frontiers | Research Topics

Measuring, modeling and predicting the seismic site effect

Edited by
Yefei Ren, Giovanni Lanzano, Yadab P. Dhakal,
Behzad Hassani and Kun Ji

Published in
Frontiers in Earth Science

ISSN 1664-8714
ISBN 978-2-8325-4009-1
DOI 10.3389/978-2-8325-4009-1

About Frontiers

Frontiers is more than just an open access publisher of scholarly articles: it is a pioneering approach to the world of academia, radically improving the way scholarly research is managed. The grand vision of Frontiers is a world where all people have an equal opportunity to seek, share and generate knowledge. Frontiers provides immediate and permanent online open access to all its publications, but this alone is not enough to realize our grand goals.

Frontiers journal series

The Frontiers journal series is a multi-tier and interdisciplinary set of open-access, online journals, promising a paradigm shift from the current review, selection and dissemination processes in academic publishing. All Frontiers journals are driven by researchers for researchers; therefore, they constitute a service to the scholarly community. At the same time, the *Frontiers journal series* operates on a revolutionary invention, the tiered publishing system, initially addressing specific communities of scholars, and gradually climbing up to broader public understanding, thus serving the interests of the lay society, too.

Dedication to quality

Each Frontiers article is a landmark of the highest quality, thanks to genuinely collaborative interactions between authors and review editors, who include some of the world's best academicians. Research must be certified by peers before entering a stream of knowledge that may eventually reach the public - and shape society; therefore, Frontiers only applies the most rigorous and unbiased reviews. Frontiers revolutionizes research publishing by freely delivering the most outstanding research, evaluated with no bias from both the academic and social point of view. By applying the most advanced information technologies, Frontiers is catapulting scholarly publishing into a new generation.

What are Frontiers Research Topics?

Frontiers Research Topics are very popular trademarks of the *Frontiers journals series*: they are collections of at least ten articles, all centered on a particular subject. With their unique mix of varied contributions from Original Research to Review Articles, Frontiers Research Topics unify the most influential researchers, the latest key findings and historical advances in a hot research area.

Find out more on how to host your own Frontiers Research Topic or contribute to one as an author by contacting the Frontiers editorial office: frontiersin.org/about/contact

Measuring, modeling and predicting the seismic site effect

Topic editors
Yefei Ren — Institute of Engineering Mechanics, China Earthquake Administration, China
Giovanni Lanzano — National Institute of Geophysics and Volcanology (INGV), Italy
Yadab P. Dhakal — National Research Institute for Earth Science and Disaster Resilience (NIED), Japan
Behzad Hassani — BC Hydro, Canada
Kun Ji — Hohai University, China

Citation
Ren, Y., Lanzano, G., Dhakal, Y. P., Hassani, B., Ji, K., eds. (2024). *Measuring, modeling and predicting the seismic site effect*. Lausanne: Frontiers Media SA.
doi: 10.3389/978-2-8325-4009-1

Table of contents

frontiers | Frontiers in Earth Science

ORIGINAL RESEARCH
published: 22 June 2022
doi: 10.3389/feart.2022.938514

Novel Evaluation Method for Site Effect on Earthquake Ground Motion Based on Modified Horizontal to Vertical Spectral Ratio

Xiaojun Li*, Na Li, Mianshui Rong and Qing Dong

Key Laboratory of Urban Security and Disaster Engineering of China Ministry of Education, Beijing University of Technology, Beijing, China

The effect of local site conditions on the earthquake ground motion is a very important factor to be considered in engineering seismic fortification. Many methods, such as numerical simulation methods based on site analysis models and statistical empirical relation methods based on the earthquake ground motion observations and numerical simulation data, have been used to consider the site effects in actual engineering seismic fortification and earthquake disaster assessment. The statistical analysis to obtain characteristic parameters of site condition effect based on strong motion and microtremor records become an economical and practical method of determining the designed ground motion of engineering sites, especially for large survey areas and engineering sites where it is difficult to carry out a site survey. In this paper, a novel evaluation method for site effect on earthquake ground motion is proposed. The new method is based on the horizontal to vertical spectral ratio (HVSR) method, but the original HVSR is replaced by a modified HVSR considering the effect of the soil layer on the vertical ground motion. In order to build the model and determine the corresponding parameters of the modified HVSR, first, the ground motions in the bedrock below the soil layer are calculated using the one-dimensional equivalent linear method. These calculated records are independent of the influence of the downgoing wavefield, and the differences between the ground surface to bedrock spectral ratio (SBSR). The HVSR for the local sites of ground motion observation stations are analyzed using the strong ground motion records from the Kiban-Kyoshin network (KiK-net) in Japan. The statistical characteristics of the relationship between SBSR and HVSR are revealed, and then, a quantitative relationship between SBSR/HVSR and HVSR is established. The proposed evaluation method for the site effect has the advantage that the original HVSR method only requires ground motion records on the ground surface of the site, and it further considers the influence of the vertical seismic effect on the accuracy of the HVSR method. The proposed method can characterize the influence of the site conditions on ground motion more reasonably than the conventional method.

Keywords: site condition, site effect, strong motion record, KiK-net, horizontal to vertical spectral ratio

Edited by:
Kun Ji,
Hohai University, China

Reviewed by:
Jinjun Hu,
China Earthquake Administration, China
John Zhao,
Shandong Jianzhu University, China

****Correspondence:***
Xiaojun Li
beerli@vip.sina.com

Specialty section:
This article was submitted to Structural Geology and Tectonics, a section of the journal Frontiers in Earth Science

Received: *07 May 2022*
Accepted: *23 May 2022*
Published: *22 June 2022*

Citation:
Li X, Li N, Rong M and Dong Q (2022) Novel Evaluation Method for Site Effect on Earthquake Ground Motion Based on Modified Horizontal to Vertical Spectral Ratio.
Front. Earth Sci. 10:938514.
doi: 10.3389/feart.2022.938514

INTRODUCTION

Surveys and investigations of earthquake disasters have shown that the spatial variations in the local site conditions are the main factor leading to the differences in earthquake disasters in local areas during large earthquakes (Wood, 1908; Liu, 2002). The conclusion that the important effect of local site conditions on the propagation of seismic waves has been repeatedly confirmed in large earthquakes and has been broadly studied and applied in practical engineering (Borcherdt et al., 1976; Seed et al., 1976a, 1976b, 1988; Li, 1992; Guo et al., 2013; Zhang et al., 2020). The "local site" conditions generally refer to the variations in the shallow engineering geological structures and surface topography within a region of tens to hundreds of meters. In studies of the effect of site conditions on ground motions, certain classification indicators are usually used to classify sites into different categories and to characterize the differences in the site conditions (Lee et al., 2001; Building Seismic Safety Council, 2004; Huang et al., 2009; Ministry of Housing and Urban-Rural, 2016; Li, 2013; Li et al., 2019). Based on the site classification in the statistical analysis of strong-motion records or numerical simulation methods of site models, the characteristic parameters and empirical relationships are obtained to characterize the effect of the site conditions on ground motions (Hwang et al., 1997; Li et al., 2001; Lu et al., 2008; Pitilakis et al., 2013). To provide a reference for engineering design under complex site conditions, a ground motion parameter adjustment model is used to account for the effects of the different site conditions on ground motions. A simple classification of sites is often insufficient when representing the effects of specific sites on ground motions. For this reason, it is necessary to carry out a drilling survey of the site conditions for important engineering projects and to perform site seismic response simulations for the specific site conditions to account for their impact on the ground motion. For sites that involve a large scope (such as new district construction planning and old city reconstruction) and for sites that pose difficulties to the execution of drilling survey (such as construction sites in alpine canyon areas or on islands and reefs), economical and practical methods need to be utilized for acquiring the characteristics of the site effects and to determine the seismic design of the engineering site, such as methods based on the analysis and statistics of strong-motion records and microtremors.

As early as 1970, Borcherdt (1970) proposed a transfer function spectral ratio method for calculating sedimentary site effects using records of strong motions observed by site stations and referencing bedrock stations. This type of method is the most direct method of site effect analysis and is referred to as the classical standard spectral ratio method. The surface to bedrock spectral ratio (SBSR) method is based on the records of borehole arrays (Wen et al., 1995; Régnier et al., 2013), and the ground motion records at the borehole bedrock are used as the reference ground motion. Compared with the standard spectral ratio method, the SBSR method can effectively solve the difficult problem of selecting a reference free-surface bedrock. In addition, since it is believed that the ground motion records of a vertical array on the ground surface and those of borehole bedrock contain the same source effect and propagation path effect, the SBSR can better characterize the effect of the site conditions on ground motions. Nevertheless, it is imperative to note that the records for the bedrock below the soil layers are disturbed by the downgoing wavefield (Bonilla et al., 2002; Régnier et al., 2013).

In the late 1980s, the Japanese scholar Nakamura proposed a method for estimating the influence of the characteristics of a site on ground motions based on the Fourier amplitude spectral ratio of the horizontal and vertical components of a microtremor (Nakamura, 1989), which later became known as the horizontal to vertical spectral ratio method (referred to as the HVSR method or the Nakamura method). The HVSR method includes the following basic assumptions: 1) for site microtremor observations in different periods, the spectral characteristics of the microtremors are basically the same, and the amplification effect is mainly related to the dynamic characteristics of the soil media; 2) the value of HVSR at the bedrock is 1; 3) the horizontal component of the microtremors is amplified by the soil layers, but the vertical component is basically not amplified.

The HVSR method derives from microtremor observations and analysis, and it was first used in the study of microearthquakes (Konno et al., 1998; Chen et al., 2009). It was later applied to the analysis of strong-motion observations and then, it was expanded into the research of site effects on ground motions (Lermo et al., 1993; Yamazaki et al., 1997; Zhao et al., 2006; Fukushima et al., 2007; Wen et al., 2010; Kawase, 2011; Nagashima et al., 2014; Rong et al., 2016). The validity and scope of the application of the HVSR method in the analysis of the site effect on ground motions have always been subject to some debate and controversy. This is mainly because the HVSR method assumes that the HVSR at the bedrock is one and the vertical component is basically not amplified. At present, there still is no consistent conclusion regarding these issues, but a common notion is that the HVSR method can effectively extract the predominant period of the site effects on ground motions. However, there can be large errors in the estimation of the site effect amplification (Rong et al., 2016).

In this study, we present our results of the study on the strong motion records of the Kiban-Kyoshin network (KiK-net) in Japan, and we examined the different characteristics of the SBSR and HVSR at the sites of strong-motion recording stations and the variations in the SBSR/HVSR with the spectral period. Then, a novel site effect evaluation method that uses seismic records was developed based on a modified HVSR and the statistical relationship between the SBSR and HVSR.

THE IDEA OF THE NEW METHOD

Theoretically, compared with the HVSR method, the SBSR method can more reasonably evaluate the effects of the site conditions under a seismic, but it needs to use the observed ground motion records on the ground surface of the site and the corresponding bedrock below soil layers, separately. Therefore, it is necessary to conduct site drilling and borehole observations,

TABLE 1 | Selected stations and related information in this study.

No.	Site code	Latitude N/(°)	Longitude E/(°)	Depth/m	$V_{S,30}$/(m·s^{-1})	NEHRP classification
1	AKTH02	39.6634	140.5721	100	620.404	C
2	AKTH13	39.9819	140.4072	100	535.723	C
3	AOMH05	40.8564	141.1033	312	238.302	D
4	AOMH13	40.5794	141.4451	150	154.274	E
5	AOMH16	40.4624	141.0923	150	225.750	D
6	AOMH17	40.4624	141.3374	114	378.362	C
7	FKSH11	37.2006	140.3386	115	239.826	D
8	FKSH14	37.0264	140.9702	147	236.561	D
9	FKSH20	37.4911	140.9871	109	350.000	D
10	HDKH01	42.7031	142.2296	100	368.252	C
11	HDKH04	42.5126	142.0381	220	235.026	D
12	IBRH10	36.1112	139.9889	900	144.138	E
13	IBRH13	36.7955	140.575	100	335.369	D
14	IBRH17	36.0864	140.314	510	300.774	D
15	IBUH01	42.8739	141.8191	101	306.785	D
16	IWTH02	39.825	141.3826	102	389.567	C
17	IWTH06	40.2611	141.1709	100	431.655	C
18	IWTH08	40.2686	141.7831	100	304.521	D
19	IWTH24	39.1979	141.0118	150	486.412	C
20	IWTH27	39.0307	141.532	100	670.313	C
21	KMMH01	33.109	130.695	100	574.631	C
22	KSRH06	43.22	144.4285	237	326.193	D
23	KSRH07	43.1359	144.3274	222	204.104	D
24	KSRH10	43.2084	145.1168	255	212.875	D
25	MYGH13	38.699	141.418	100	570.591	C
26	NIGH11	37.1728	138.744	205	375.000	C
27	NMRH04	43.3978	145.1224	216	168.103	E
28	SMNH12	35.1634	132.8558	101	590.200	C
29	TCGH12	36.6959	139.9842	120	343.678	D
30	TKCH08	42.4865	143.152	100	353.208	D

which is expensive and time-consuming. The HVSR method only requires ground motion records, but there are some unreasonable problems in the basic assumptions listed above. Therefore, the constructuion of an indirect evaluation method for the SBSR was developed in this study.

Based on the SBSR method the following relationship can be assumed,

$$\boldsymbol{SBSR_H} = \frac{\boldsymbol{S_{S,H}}}{\boldsymbol{S_{B,H}}}, \tag{1}$$

where $SBSR_H$ is the SBSR value of the horizontal motion on the ground surface and in the corresponding bedrock, $S_{S,H}$ is the Fourier amplitude spectrum of the horizontal-component on the ground surface, $S_{B,H}$ is the Fourier amplitude spectrum of the horizontal-component in the bedrock. **Eq. 1** can be rewritten as

$$\begin{aligned}\boldsymbol{SBSR_H} &= \frac{\boldsymbol{S_{S,H}}}{\boldsymbol{S_{S,V}}} \times \frac{\boldsymbol{S_{S,V}}}{\boldsymbol{S_{B,V}}} \times \frac{\boldsymbol{S_{B,V}}}{\boldsymbol{S_{B,H}}} = \frac{\boldsymbol{S_{S,H}}}{\boldsymbol{S_{S,V}}} \times \frac{\boldsymbol{S_{S,V}}}{\boldsymbol{S_{B,V}}} \times \frac{1}{\boldsymbol{S_{B,H}}/\boldsymbol{S_{B,V}}} \\ &= \boldsymbol{HVSR_S} \times \frac{\boldsymbol{SBSR_V}}{\boldsymbol{HVSR_B}}.\end{aligned} \tag{2}$$

where $S_{S,V}$ is the Fourier amplitude spectrum of the vertical motion on the ground surface, $S_{B,V}$ is the Fourier amplitude spectrum of the vertical motion in the bedrock, $HVSR_S$ is the HVSR value in the ground surface, $HVSR_B$ is the HVSR value in the bedrock, $SBSR_V$ is the SBSR value of the vertical on the ground surface and in the corresponding bedrock.

If the Fourier amplitude spectrum transfer function of the horizontal motion from the bedrock to the ground surface (TF_H) i.e., the $SBSR_H$, is used to express the effect of the site conditions on the horizontal motion, then based on **Eq. 2**,

$$\boldsymbol{TF_H} = \boldsymbol{HVSR_S} \times \boldsymbol{SBSR_V}/\boldsymbol{HVSR_B}, \tag{3}$$

According to the basic assumption of the HVSR method,

$$\begin{cases} \boldsymbol{HVSR_B} = 1 \\ \boldsymbol{SBSR_V} = 1 \end{cases}, \tag{4}$$

Then, based on **Eq. 3**,

$$\boldsymbol{TF_H} = \boldsymbol{HVSR_S}, \tag{5}$$

Therefore, TF_H can be approximately calculated using the HVSR method. However, there are some errors that needed to be considered in order to obtain a more reasonable evaluation value of TF_H. A novel evaluation method for site effect was developed to evaluate the site effect on earthquake ground motions.

$$\boldsymbol{TF_H} = \boldsymbol{\alpha} \bullet \boldsymbol{HVSR_S}, \tag{6}$$

where α is a modified parameter that describes the impacts of $SBSR_V$ and $HVSR_B$, which needs to be obtained via statistical analysis of ground motion records. This is a special issue investigated in this study.

SELECTION AND PROCESSING OF STRONG MOTION RECORDS

Japan's National Institute of Earth Science and Disaster Prevention (NIED) has established two strong motion observation networks, K-NET and KiK-net, with a total of more than 1,700 stations nationwide. The average distance between stations is less than 20 km. The stations in the KiK-net strong motion observation network are all multi-point borehole arrays (i.e., a vertical array). Each station is equipped with tri-axial strong motion observation instruments on the ground surface and at the bottom bedrock in the borehole. They can simultaneously observe ground motions on the ground surface and in the bedrock below the soil layers. The borehole depths of the KiK-net stations are all 100 m or greater. Except for a few individual station sites, the boreholes all reach the engineering bedrock surface ($V_S > 760$ m/s). The KiK-net was put into service in 1997, and a large number of observation records have been obtained.

Selection of Strong Motion Records

The focus of this study was analysis of the influence of the soil layers on the ground motion. Therefore, when selecting the KiK-net observation records for this study, it was necessary to examine whether the observation station site could be regarded as a layered site, i.e., whether it could be simplified to a one-dimensional site model. First, the stations used in this study were selected from the 662 stations in the KiK-net network that had obtained a certain number of strong-motion records. The selection criteria were as follows. 1) The number of records with a peak ground acceleration (PGA) of $PGA > 100$ gal was two or more. 2) The number of records with $PGA > 10$ gal was at least 100. Then, for the stations with ground motion records met the above criteria, their transfer functions of the horizontal ground motions were calculated according to the one-dimensional site models (referred to as the calculated transfer function TF_{HC}), and the $SBSR_H$ of the horizontal ground motions were calculated using the ground motion records (referred to as the statistical transfer function TF_{HS}). To obtain the calculated transfer function TF_{HC}, the one-dimensional site models were established using the borehole and test data of the station sites. We statistically analyzed the logarithmic mean standard deviation σ of TF_{HS} and the correlation coefficient r between TF_{HS} and TF_{HC} for each station site. We selected the station sites that satisfied both $\sigma < 0.35$ and $r > 0.6$ as the sites that met the criteria of this study. In total, 30 stations were finally selected, as shown in **Table 1**.

Based on a comparison of the site responses to the main shocks and aftershocks of large earthquakes, earlier researchers have speculated that the threshold for nonlinear site responses is 100–200 gal (Wen et al., 1994; 1995). However, recent studies have shown that a slight nonlinearity of site responses appears in records with medium-level intensities (PGA = 20–80 gal) (Baise, 2000; Régnier et al., 2013). Thus, we divided the 19,002 sets of three-component strong motion records obtained from the 30 stations into six groups, with peak ground accelerations of 10–20, 20–100, 100–200, 200–300, and >300 gal (**Table 2**). Since the records with PGAs of < 10 gal are of little engineering significance, they were not considered in this study.

TABLE 2 | The number of strong-motion records in the different PGA groups.

Site class	Site code	PGA/gal				
		10~20	20~100	100~200	200~300	>300
C	AKTH02	74	54	2	0	0
	AKTH13	122	79	9	0	0
	AOMH17	299	106	9	4	0
	HDKH01	127	60	3	0	4
	IWTH02	876	667	42	11	14
	IWTH06	181	85	6	0	0
	IWTH24	185	112	10	3	2
	IWTH27	1,079	504	31	8	8
	KMMH01	99	39	6	2	0
	MYGH13	675	311	13	1	2
	NIGH11	146	110	9	3	3
	SMNH12	52	52	6	4	0
D	AOMH05	417	207	15	3	0
	AOMH16	428	171	9	2	0
	FKSH11	622	285	12	2	3
	FKSH14	635	283	18	2	2
	FKSH20	393	238	21	0	2
	HDKH04	119	56	4	1	2
	IBRH13	1,175	732	79	23	33
	IBRH17	796	424	21	2	3
	IBUH01	317	136	10	3	4
	IWTH08	423	182	13	0	2
	KSRH06	349	155	3	1	8
	KSRH07	286	149	8	1	4
	KSRH10	273	174	11	3	5
	TCGH12	680	338	6	0	2
	TKCH08	197	117	10	0	1
E	AOMH13	213	86	7	0	0
	IBRH10	522	248	16	2	0
	NMRH04	328	150	8	0	2

Processing of Strong Motion Records

In studies of site condition effects using strong motion records, as much attention as possible should be given to the recorded S-wave time section. Therefore, before calculating the Fourier amplitude of the ground motion, a time window with a reasonable length should be chosen. The time window should not only contain the main energy of the shear waves, but it should also avoid the influence of the surface waves on the amplitude spectrum. For this reason, the time window for the ground motion record was chosen to be from the first arrival of the P wave to the time when the seismic wave energy reached 80% of the total energy (the cut-off time). In the specific analysis, the cut-off time was calculated using the ground motion energy by the Arias intensity formula (**Eq. 7**), and the signal-to-noise ratio (SNR) was calculated using **Eq. 8**. The first 15 s of the record were treated as noise to eliminate the records with an SNR of less than 5 dB in the 0.05–20 Hz frequency, to reduce the dispersion of the results caused by unreasonable statistical data,

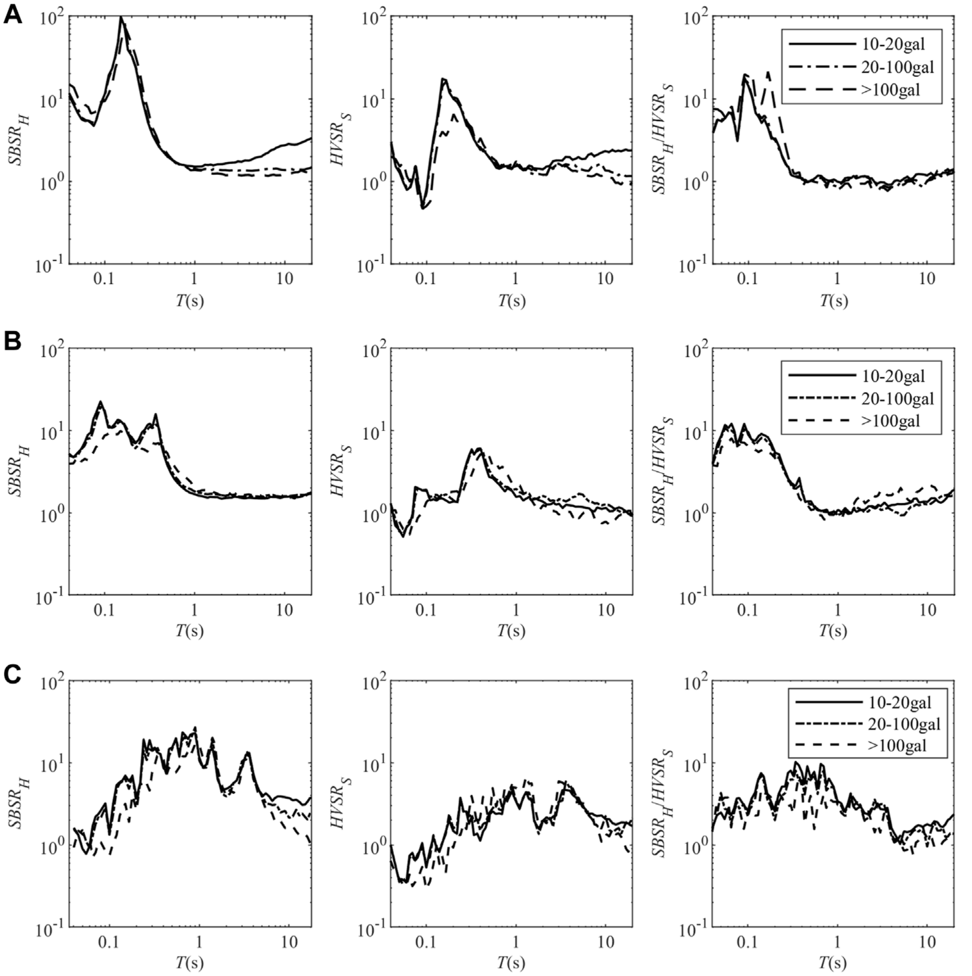

FIGURE 1 | The average values of $SBSR_H$, $HVSR_S$, and $SBSR_H/HVSR_S$ for the strong-motion records with different PGA ranges at one station. **(A)** recordings for IWTH02 (class C). **(B)** recordings for IBRH13 (class D). **(C)** recordings for IBRH10 (class E).

and to improve the accuracy of the analysis results. The ground motion energy I_a is defined as

$$\boldsymbol{I_a} = \frac{\pi}{2\boldsymbol{g}} \int_0^{T_e} \boldsymbol{a}^2(\boldsymbol{t})\boldsymbol{dt}, \tag{7}$$

where T_e is the ground motion duration. The SNR is defined as

$$\boldsymbol{SNR}(\boldsymbol{f}) = 10 \log \frac{\boldsymbol{A_{signal}}(\boldsymbol{f})}{\boldsymbol{A_{noise}}(\boldsymbol{f})}. \tag{8}$$

where A_{signal} (f) is the Fourier amplitude spectrum of the ground motion record, and A_{noise} (f) is the Fourier amplitude spectrum of the noise signal.

ANALYSIS OF THE DIFFERENCE BETWEEN SBSR AND HVSR

To calculate $SBSR_H$ and $HVSR_S$ of the ground motion records, the average values were obtained in three PGA ranges: 10–20, 20–100, and >100 gal. Because there were few $PGA > 200$ gal records, $PGA > 100$ gal was used as the statistical range. **Figures 1A–C** show the average values of $SBSR_H$ and $HVSR_S$ in the different PGA ranges.

The data presented in **Figures 1A–C** show that the mean values of $SBSR_H$ and $HVSR_S$ of the ground motions recorded by each station did not exhibit any significant differences when $PGA < 100$ gal, but there were significant differences when $PGA > 100$ gal, which indicates the nonlinear effect of the soil layers on ground motions. For this reason, no distinction was made between the 10–20 and 20–100 gal categories in the subsequent statistical analysis.

Figure 2 shows the average $SBSR_H/HVSR_S$ values of the ground motions recorded by each station and the average value plus or minus one standard deviation. Over the entire period, the average $SBSR_H/HVSR_S$ values were greater than 1, that is, the average $SBSR_H$ values were greater than of the average $HVSR_S$ values. This confirmed the existence of the site effect on the vertical ground motion. The average value and variance of $SBSR_H/HVSR_S$ were approximately constant

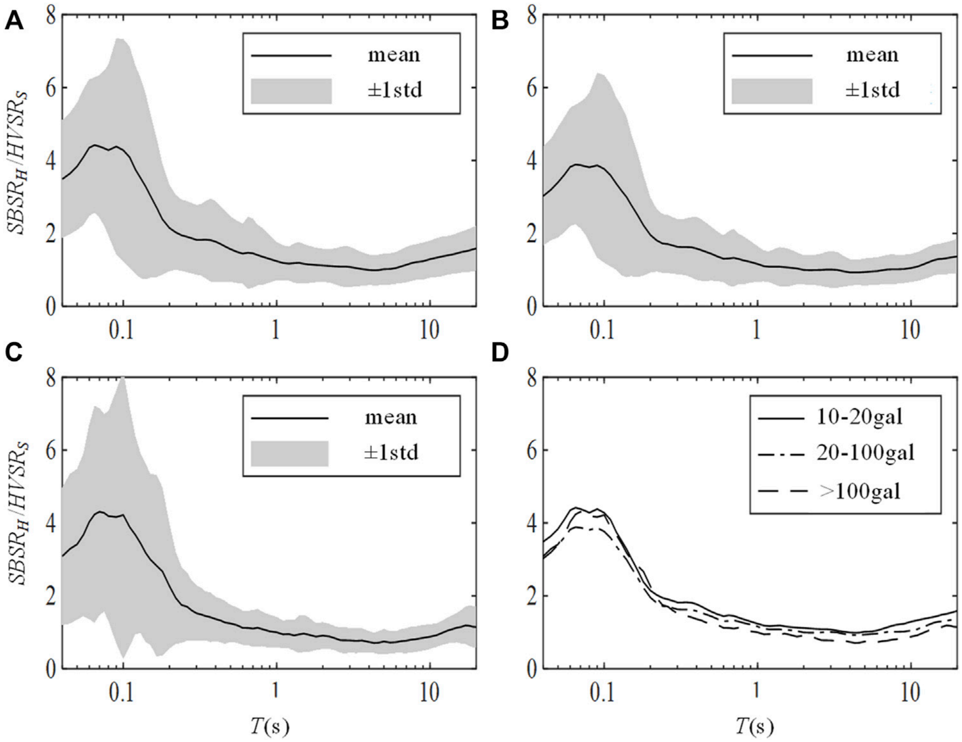

FIGURE 2 | Variations in $SBSR_H/HVSR_S$ with period. **(A)** *PGA* = 10~20 gal. **(B)** *PGA* = 20~100 gal. **(C)** *PGA* > 100 gal. **(D)** comparison of the different PGA ranges.

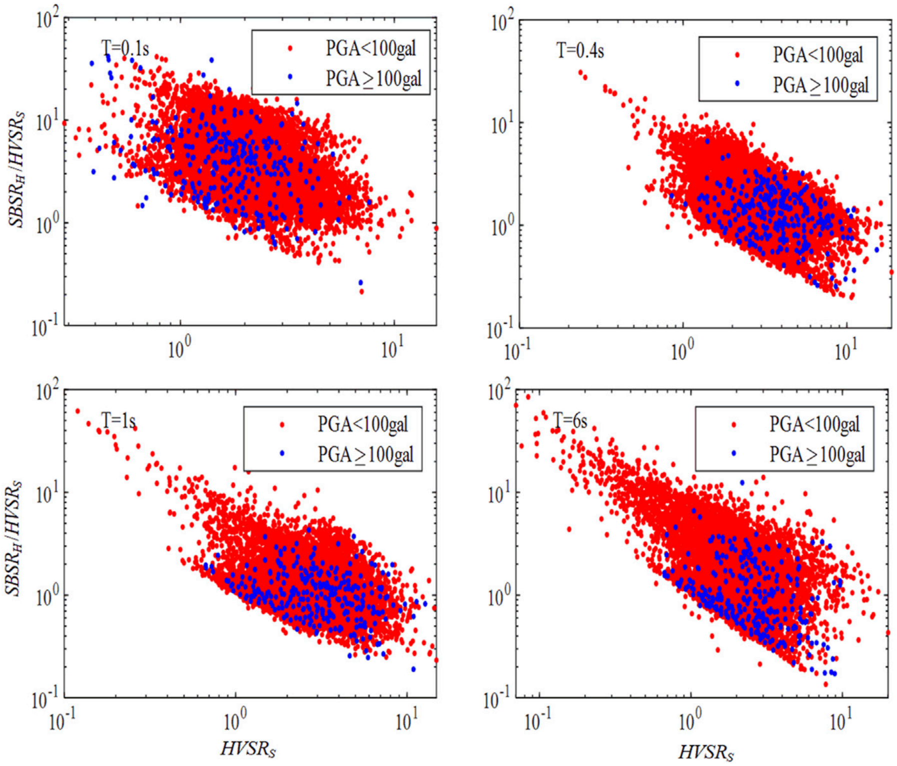

FIGURE 3 | Variations in $SBSR_H/HVSR_S$ with $HVSR_S$.

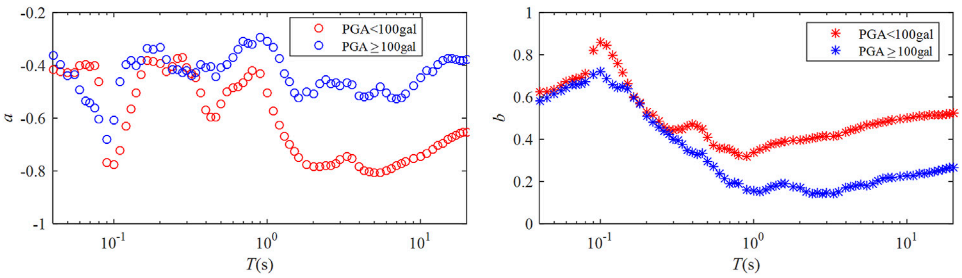

FIGURE 4 | Variations in the statistical values of parameters *a* and *b* with period *T*.

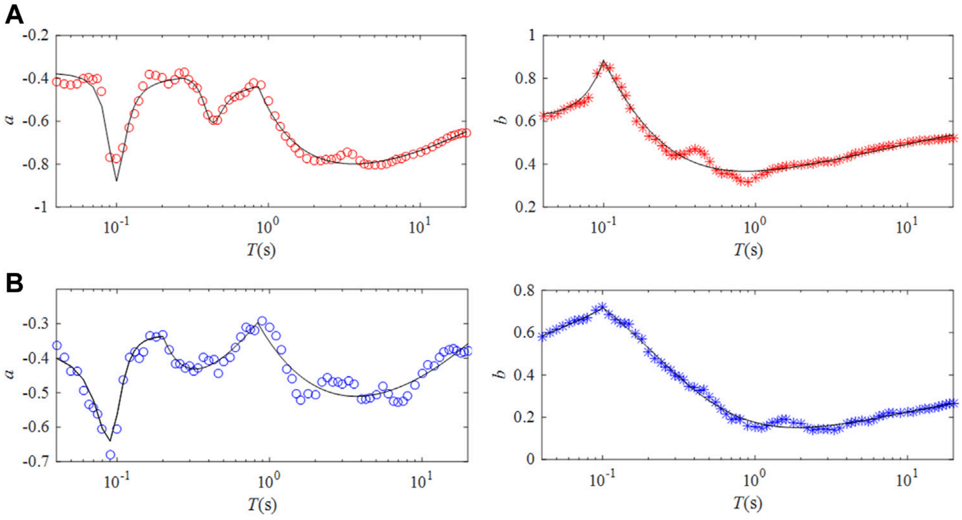

FIGURE 5 | Regression curves of the parameters *a* and *b* under different ground motion intensities. **(A)** under weak motions (*PGA* < 100 gal). **(B)** under strong motions (*PGA* > 100 gal).

TABLE 3 | Coefficients for the relationships between parameters *a* and *b* and the period *T*.

Parameter	*PGA*/gal	Period *T*/s	Coefficients						
			p_1	p_2	p_3	q_1	q_2	q_3	*R*
a	<100	(0.04, 0.27)	–0.376	–0.762	–0.391	1	2.014	1.019	0.902
		(0.27, 0.86)	–0.404	–0.318	–0.067	1	0.768	0.154	0.957
		(0.86,20.00)	0.538	–1.404	–0.354	0	1.000	0.656	0.952
	≥100	(0.04,0.20)	–0.348	–0.707	-0.365	1	2.066	1.077	0.958
		(0.20, 0.84)	0.813	0.361	–0.277	0	1.000	1.090	0.874
		(0.84, 20.00)	0.879	–1.510	–0.634	0	1.000	1.799	0.789
b	<100	(0.04, 0.10)	–0.250	–0.118	–0.072	0	1.000	0.763	0.962
		(0.10, 20.00)	1.124	1.103	1.114	1	2.745	3.032	0.966
	≥100	(0.04, 0.10)	0.309	1.307	0.964	0	1.000	0.951	0.985
		(0.10, 20.00)	0.670	-0.117	0.282	1	1.120	1.607	0.992

in the period of 0.4–20 s, and they changed very little with the period. However, they changed significantly in the period of less than 0.4 s.

Figure 3 shows the variations in $SBSR_H/HVSR_S$ with $HVSR_S$ for the different periods. The variations in the period range of 0.04–20 s exhibited a high regularity, and there was a logarithmic correlation between $SBSR_H/HVSR_S$ and $HVSR_S$. This provided a basis for establishing a novel evaluation method for site amplification by modifying the HVSR method to take into account the site effect on the vertical ground motion.

Based on the above calculation and analysis results and using the logarithmic coordinate linear fitting method, we obtained the following quantitative relationship between the HVSR and SBSR under different ground motion levels in the period range of 0.04–20 s:

$$\boldsymbol{\alpha}(\boldsymbol{T}) = \frac{\boldsymbol{SBSR_H}(\boldsymbol{T})}{\boldsymbol{HVSR_S}(\boldsymbol{T})} = \boldsymbol{a}(\boldsymbol{T})\boldsymbol{HVSR_S}(\boldsymbol{T}) + \boldsymbol{b}(\boldsymbol{T}), \tag{9}$$

where T is the period, and a and b are statistical constants.

Based on previous studies, the statistical values of a and b were obtained, and the results of their changes with the period T are shown in **Figure 4**. These values vary significantly with T and fluctuate up and down, especially the values of a. For this reason, we used the following parametric model to fit the curves of a and b in the period ranges.

$$\boldsymbol{Y} = \frac{\boldsymbol{p}_1\boldsymbol{x}^2 + \boldsymbol{p}_2\boldsymbol{x} + \boldsymbol{p}_3}{\boldsymbol{q}_1\boldsymbol{x}^2 + \boldsymbol{q}_2\boldsymbol{x} + \boldsymbol{q}_3}. \tag{10}$$

where Y represents a or b, x represents the base-10 logarithmic period, and p_1, p_2, p_3, q_1, q_2, and q_3 are the model parameters. The variations in a and b with T were obtained through fitting, as shown in **Figures 5A,B**, and the model coefficients are shown in **Table 3**.

NOVEL EVALUATION METHOD FOR SITE EFFECT

Through comprehensive consideration of **Eqs 6**, **9**, **10**, we obtained the following equations for a novel method of evaluating the site effect:

$$\boldsymbol{TF_H}(\boldsymbol{T}) = (\boldsymbol{a}(\boldsymbol{T})\boldsymbol{HVSR_S}(\boldsymbol{T}) + \boldsymbol{b}(\boldsymbol{T}))\,\boldsymbol{HVSR_S}(\boldsymbol{T}), \tag{11}$$

$$\boldsymbol{a}(\boldsymbol{T}) = \frac{\boldsymbol{p}_{1a}(\mathbf{log}\boldsymbol{T})^2 + \boldsymbol{p}_{2a}\mathbf{log}\boldsymbol{T} + \boldsymbol{p}_{3a}}{\boldsymbol{q}_{1a}(\mathbf{log}\boldsymbol{T})^2 + \boldsymbol{q}_{2a}\mathbf{log}\boldsymbol{T} + \boldsymbol{q}_{3a}}, \tag{12}$$

$$\boldsymbol{b}(\boldsymbol{T}) = \frac{\boldsymbol{p}_{1b}(\mathbf{log}\boldsymbol{T})^2 + \boldsymbol{p}_{2b}\mathbf{log}\boldsymbol{T} + \boldsymbol{p}_{3b}}{\boldsymbol{q}_{1b}(\mathbf{log}\boldsymbol{T})^2 + \boldsymbol{q}_{2b}\mathbf{log}\boldsymbol{T} + \boldsymbol{q}_{3b}}. \tag{13}$$

where TF_H is the Fourier amplitude spectrum transfer function of the horizontal ground motions from the bedrock to the ground surface, $HVSR_S$ is the HVSR value of the ground motion on the surface, T is the period, and p_{1a}, p_{2a}, p_{3a}, q_{1a}, q_{2a}, q_{3a}, p_{1b}, p_{2b}, p_{3b}, q_{1b}, q_{2b}, and q_{3b} are empirical constants which are listed in **Table 3**.

CONCLUSION

Using 19,002 sets of acceleration record data from 30 strong motion observation stations in Japan's KiK-net, we performed statistical analysis of the relationship between the SBSR and HVSR of the station sites and obtained a log-linear correlation between the SBSR/HVSR and HVSR. We also obtained a quantitative statistical relationship. Based on the statistical analysis results, we developed a novel evaluation method for site effect using a modified HVSR formula to characterize the influence of the soil layers on the ground motion. The modified HVSR formula accounts for the influence of the vertical ground motion effect of the site and the nonlinear characteristics of the soil layers. The proposed method can more accurately evaluate the effects of the soil layers on the ground motions.

The SBSR is similar as the transfer function of the ground motions from the bedrock to the surface, but it cannot be regarded as the complete amplification function of the site effect on the ground motion. The incident wave at the bedrock below the soil layers was obtained using a one-dimensional equivalent linearization method, which yields the recording for the reference bedrock site. Although this operation can eliminate the influence of the downgoing wavefield on the ground motion record of the bedrock below the soil layers, it also introduces errors into the calculation of the ground motion record at the reference bedrock. Improving the accuracy of the reference bedrock record will to be studied in the future.

DATA AVAILABILITY STATEMENT

Publicly available datasets were analyzed in this study. This data can be found here: https://www.kyoshin.bosai.go.jp/kyoshin/data/index_en.html.

AUTHOR CONTRIBUTIONS

XL and NL contributed to conception and design of the study. NL performed the statistical analysis and wrote the first draft of the manuscript. XL, NL, and MR wrote sections of the manuscript. All authors contributed to manuscript revision, read, and approved the submitted version.

FUNDING

This study is supported by the Natural Science Foundation of China (U1839202, 51421005, 51878625).

ACKNOWLEDGMENTS

We thank the editors and reviewers for their helpful comments and suggestions for improving the manuscript.

SUPPLEMENTARY MATERIAL

The Supplementary Material for this article can be found online at: https://www.frontiersin.org/articles/10.3389/feart.2022.938514/full#supplementary-material

REFERENCES

Afshari, K., and Stewart, J. P. (2021). *Effectiveness of 1D Ground Response Analyses at Predicting Site Response at California Vertical Array Sites*. Los Angeles.University of California.

Baise, L. G. (2000). *Investigations in Site Response from Ground Motion Observations in Vertical Arrays*. Berkeley: University of California.

Bonilla, L. F., Steidl, J. H., Gariel, J., and Archuleta, R. J. (2002). Borehole Response Studies at the Garner Valley Downhole Array, Southern California. *Bull. Seismol. Soc. Am.* 92 (8), 3165–3179. doi:10.1785/0120010235

Boore, D. M. (2007). *Some Thoughts on Relating Density to Velocity*. Notes on Personal Web.

Borcherdt, R. D. (1970). Effects of Local Geology on Ground Motion Near San Francisco Bay. *Bull. Seismol. Soc. Am.* 60 (1), 29–61. doi:10.1785/BSSA0600010029

Borcherdt, R. D., and Gibbs, J. F. (1976). Effects of Local Geological Conditions in the San Francisco Bay Region on Ground Motions and the Intensities of the 1906 Earthquake. *Bull. Seismol. Soc. Am.* 66 (2), 467–500. doi:10.1785/bssa0660020467

Building Seismic Safety Council (2003). *NEHPR Recommended Provisions for Seismic Regulations for New Buildings and Other Structures (FEMA 450), Part 1 (Provisions)*. Washington D C: Building Seismic Safety Council, National Institute of Building Sciences, 19.

Chen, Q. F., Liu, L. B., Wang, W. J., and Rohrbach, E. (2009). Site Effects on Earthquake Ground Motion Based on Microtremor Measurements for Metropolitan Beijing. *Chin. Sci. Bull.* 54 (2), 280–287. doi:10.1007/s11434-008-0422-2

Fukushima, Y., Bonilla, L. F., Scotti, O., and Douglas, J. (2007). Site Classification Using Horizontal-To-Vertical Response Spectral Ratios and its Impact when Deriving Empirical Ground-Motion Prediction Equations. *J. Earthq. Eng.* 11 (5), 712–724. doi:10.1080/13632460701457116

Guo, M. Z., Zhao, F., and Zhao, F. X. (2013). A Review of the Effect of Small-Scale Surface Topography on Ground Motions. *Technol. Earthq. Disaster Prev.* 8 (3), 311.

Huang, Y. H., Lu, Y. J., and Peng, Y. J. (2009). Study on the Relations of Site Classification Methods in Seismic Design Standards between china and Abroad. *Technol. Earthq. Disaster Prev.* 4 (1), 80.

Hwang, H. H. M., Lin, H. J., and Huo, J. R. (1997). Site Coefficients for Design of Buildings in Eastern United States. *Soil Dyn. Earthq. Eng.* 16 (1), 29–40. doi:10.1016/s0267-7261(96)00031-0

Kawase, H., Sánchez-Sesma, F. J., and Matsushima, S. (2011). The Optimal Use of Horizontal-To-Vertical Spectral Ratios of Earthquake Motions for Velocity Inversions Based on Diffuse-Field Theory for Plane Waves. *Bull. Seismol. Soc. Am.* 101 (5), 2001–2004. doi:10.1785/0120100263

Konno, K., and Ohmachi, T. (1998). Ground-motion Characteristics Estimated from Spectral Ratio between Horizontal and Vertical Components of Microtremor. *Bull. Seismol. Soc. Am.* 88 (1), 228–241. doi:10.1785/bssa0880010228

Lee, C. T., Cheng, C. T., Liao, C. W., and Tsai, Y. B. (2001). Site Classification of Taiwan Free-Field Strong-Motion Stations. *Bull. Seismol. Soc. Am.* 91 (5), 1283–1297. doi:10.1785/0120000736

Lermo, J., and Chávez-García, F. J. (1993). Site Effect Evaluation Using Spectral Ratios with Only One Station. *Bull. Seismol. Soc. Am.* 83 (5), 1574–1594. doi:10.1785/bssa0830051574

Li, X. J. (2013). Adjustment of Seismic Ground Motion Parameters Considering Site Effects in Seismic Zonation Map. *Chin. J. Geotechnical Eng.* 35 (S2), 21.

Li, X. J. (1992). An Analysis Method of the Influence of Site Soil Layer on Earthquake Ground Motion. *World Earthq. Eng.* 8 (2), 49.

Li, X. J., Jing, B. B., Liu, C., and Yin, J. (2019). Site Classification Method Based on Geomorphological and Geological Characteristics and its Application in China. *Bull. Seismol. Soc. Am.* 109 (5), 1843–1854. doi:10.1785/0120190058

Li, X. J., and Pen, Q. (2001). Calculation and Analysis of Earthquake Ground Motion Parameters for Different Site Categories. *Earthq. Eng. Eng. Motion* 21 (1), 29.

Liu, H. X. (2002). *The Great Tangshan Earthquake of 1976*. California: Earthquake Engineering Research Laboratory, California Institute of Technology, 171.

Lu, Y. J., Peng, Y. J., and Lan, J. Y. (2008). Some Key Problems about Site Effects on Seismic Ground Motion Parameters. *Technol. Earthq. Disaster Prev.* 3 (2), 126.

Ministry of Housing and Urban-Rural (2016). *Development of the People's Republic of China, General Administration of Quality Supervision, Inspection and Quarantine of the People's Republic of China. GB 50011-2010 Code for Seismic Design of Buildings*. Edition. Beijing: China Architecture and Building Press.

Nagashima, F., Matsushima, S., Kawase, H., and Sanchez-Sesma, F. J. (2014). Application of Horizontal-To-Vertical Spectral Ratios of Earthquake Ground Motions to Identify Subsurface Structures at and Around the K-NET Site in Tohoku, Japan. *Bull. Seismol. Soc. Am.* 104 (5), 2288–2302. doi:10.1785/0120130219

Nakamura, Y. (1989). A Method for Dynamic Characteristics Estimation of Subsurface Using Microtremor on the Ground Surface. *Q. Rep. Railw. Tech. Res. Inst.* 30 (1), 25.

Pitilakis, K., Riga, E., and Anastasiadis, A. (2013). New Code Site Classification, Amplification Factors and Normalized Response Spectra Based on a Worldwide Ground-Motion Database. *Bull. Earthq. Eng.* 11 (4), 925–966. doi:10.1007/s10518-013-9429-4

Régnier, J., Cadet, H., Bonilla, L. F., Bertrand, E., and Semblat, J. F. (2013). Assessing Nonlinear Behavior of Soils in Seismic Site Response: Statistical Analysis on KiK-Net Strong-Motion Data. *Bull. Seismol. Soc. Am.* 103 (3), 1750–1770. doi:10.1785/0120120240

Rong, M. S., Li, X. J., Wang, Z. M., and Lv, Y. J. (2016). Applicability of HVSR in Analysis of Site-Effects Caused by Earthquakes. *Chin. J. Geophys.* 59 (8), 2878–2891. doi:10.1002/cjg2.30008

Seed, H. B., Murarka, R., Lysmer, J., and Idriss, I. M. (1976). Relationships of Maximum Acceleration, Maximum Velocity, Distance from Source, and Local Site Conditions for Moderately Strong Earthquakes. *Bull. Seismol. Soc. Am.* 66 (4), 1323–1342. doi:10.1785/BSSA0660041323

Seed, H. B., Romo, M. P., Sun, J. I., Jaime, A., and Lysmer, J. (1988). The Mexico Earthquake of September 19, 1985—relationships between Soil Conditions and Earthquake Ground Motions. *Earthq. Spectra* 4 (4), 687–729. doi:10.1193/1.1585498

Seed, H. B., Ugas, C., and Lysmer, J. (1976). Site-dependent Spectra for Earthquake-Resistant Design. *Bull. Seismol. Soc. Am.* 66 (1), 221–243. doi:10.1785/bssa0660010221

Shearer, P. M., and Orcutt, J. A. (1987). Surface and Near-Surface Effects on Seismic Waves-Theory and Borehole Seismometer Results. *Bull. Seismol. Soc. Am.* 77 (4), 1168–1196. doi:10.1785/bssa0770041168

Thompson, E. M., Baise, L. G., and Tanaka, Y. (2012). A Taxonomy of Site Response Complexity. *Soil Dyn. Earthq. Eng.* 41, 32.

Thompson, E. M., Baise, L. G., Kayen, R. E., and Guzina, B. B. (2009). Impediments to Predicting Site Response: Seismic Property Estimation and Modeling Simplifications. *Bull. Seismol. Soc. Am.* 99 (5), 2927–2949. doi:10.1785/0120080224

Wen, K. L., Beresnev, I. A., and Yeh, Y. T. (1995). Investigation of Non-linear Site Amplification at Two Bore Strong Ground Motion Arrays in Taiwan. *Earthq. Eng. Struct. Dyn.* 24 (3), 313–324. doi:10.1002/eqe.4290240302

Wen, K. L., Beresnev, I. A., and Yeh, Y. T. (1994). Nonlinear Soil Amplification Inferred from Downhole Strong Seismic Motion Data. *Geophys. Res. Lett.* 21 (24), 2625–2628. doi:10.1029/94gl02407

Wen, R. Z., Ren, Y. F., Zhou, Z. H., and Shi, D. (2010). Preliminary Site Classification of Free-Field Strong Motion Stations Based on Wenchuan Earthquake Records. *Earthq. Sci.* 23 (1), 101–110. doi:10.1007/s11589-009-0048-8

Wood, H. O. (1908). "Distribution of Apparent Intensity in San Francisco," in *The California Earthquake of April 18, 1906, Report of the State Earthquake Investigation Commission* (Washington DC: Carnegie Institution of Washington).

Yamazaki, F., and Ansary, M. A. (1997). Horizontal-to-vertical Spectrum Ratio of Earthquake Ground Motion for Site Characterization. *Earthq. Eng. Struct. Dyn.* 26 (7), 671–689. doi:10.1002/(sici)1096-9845(199707)26:7<671:aid-eqe669>3.0.co;2-s

Zhang, X. L., Peng, X. B., Li, X. J., Zhou, Z., Mebarki, A., Dou, Z., et al. (2020). Seismic Effects of a Small Sedimentary Basin in the Eastern Tibetan Plateau Based on Numerical Simulation and Ground Motion Records from Aftershocks of the 2008 Mw7.9 Wenchuan, China Earthquake. *J. Asian Earth Sci.* 192, 104257. doi:10.1016/j.jseaes.2020.104257

Zhao, J. X., Irikura, K., Zhang, J., Fukushima, Y., Somerville, P. G., Asano, A., et al. (2006). An Empirical Site-Classification Method for Strong-Motion Stations in Japan Using H/V Response Spectral Ratio. *Bull. Seismol. Soc. Am.* 96 (3), 914–925. doi:10.1785/0120050124

Conflict of Interest: The authors declare that the research was conducted in the absence of any commercial or financial relationships that could be construed as a potential conflict of interest.

Frontiers in Earth Science

TYPE Original Research
PUBLISHED 08 August 2022
DOI 10.3389/feart.2022.948697

OPEN ACCESS

EDITED BY
Yefei Ren,
Institute of Engineering Mechanics,
China Earthquake Administration, China

REVIEWED BY
Dun Wang,
China University of Geosciences
Wuhan, China
Lihua Fang,
Institute of Geophysics, China
Earthquake Administration, China

*CORRESPONDENCE
Fu Li-Yun,
lfu@upc.edu.cn

SPECIALTY SECTION
This article was submitted to Structural Geology and Tectonics,
a section of the journal
Frontiers in Earth Science

RECEIVED 20 May 2022
ACCEPTED 13 July 2022
PUBLISHED 08 August 2022

CITATION
Mianshui R, Li-Yun F, Francisco José S-S and Weijia S (2022), Joint inversion of earthquake-based horizontal-to-vertical spectral ratio and phase velocity dispersion: Applications to Garner Valley.
Front. Earth Sci. 10:948697.
doi: 10.3389/feart.2022.948697

Joint inversion of earthquake-based horizontal-to-vertical spectral ratio and phase velocity dispersion: Applications to Garner Valley

Rong Mianshui[1], Fu Li-Yun[2]*, Sánchez-Sesma Francisco José[3] and Sun Weijia[4]

[1]Key Laboratory of Urban Security and Disaster Engineering of China Ministry of Education, Beijing University of Technology, Beijing, China, [2]School of Geosciences, China University of Petroleum (East China), Qingdao, China, [3]Instituto de Ingeniería, Universidad Nacional Autónoma de México, Mexico City, Mexico, [4]Key Laboratory of Earth and Planetary Physics, Institute of Geology and Geophysics, Chinese Academy of Sciences, Beijing, China

Joint inversion of horizontal-to-vertical spectral ratios (HVSRs) and dispersion curves (DCs) from seismic noise recordings has been extensively used to overcome the lack of inversion uniqueness in the noise-based HVSR (NHV) or DC inversions alone. Earthquake recordings contain information about the structural properties of sedimentary layers and provide body-wave data complementary to seismic noise recordings to estimate site velocity structures, particularly in the high-frequency band. We propose a joint inversion of the Rayleigh wave DC obtained from array measurements and earthquake-based HVSR (EHV). The EHV is derived from earthquake motions rather than from microtremors based on the diffuse-field theory of plane waves. We investigated the complementarity of EHV and surface-wave DC in the joint inversion through sensitivity analyses. The DC is sensitive to bedrock shear-wave velocities in the low-frequency range and is supplemented to some degree by the EHV in the high-frequency range. The EHV is more sensitive to sediment thicknesses almost over the entire frequency range. The joint inversion is implemented by a hybrid global optimization scheme that combines genetic algorithm (GA) and simulated annealing (SA) to avoid premature convergence in the GA. The sensitivity of inversion parameters was tested to demonstrate that the P- and S-wave velocities and thicknesses of soil layers are the dominant parameters influencing EHV and DC responses. The proposed method was validated by using synthetic models to compare the joint inversion with EHV or DC inversions alone. The joint inversion was applied to the Garner Valley Downhole Array (GVDA) data for identifying the velocity structures of the site based on earthquake and noise observations. The inversion results for the P- and S-wave velocities and thicknesses of soil layers strongly suggest that the joint inversion is an efficient method to estimate site velocity structures.

KEYWORDS

earthquake-based HVSR (EHV), joint inversion, site velocity structures, Garner valley site, dispersion curve (DC)

Introduction

It is well known that the site effect can affect the characteristics of strong ground motions and consequently influence the distribution of damage during earthquakes. The shear-wave velocity (V_S) and thickness of soil layers are essential parameters for the quantitative evaluation of site effects. Empirical methods based on surface seismic recordings have been widely used to study site effects for estimating the Vs. profile. Among these methods, the horizontal-to-vertical spectral ratio (HVSR) proposed by Nakamura (1989) typically has a conspicuous peak that is a good estimator of dominant frequency and soon became popular because of its economy and effectiveness. Moreover, the HVSR has been widely used to estimate velocity structures from observed earthquake ground motions and microtremor measurements (Kawase, et al., 2018). In this study, to make full use of the available earthquake and noise measurement data, we propose a joint inversion of earthquake-based HVSR (hereafter, EHV) and phase velocity dispersion curve (hereafter, DC), where the HVSR is derived from earthquake motions rather than from microtremors based on the diffuse-field theory of plane waves (Kawase, et al., 2011).

Velocity profiles (particularly, the shear-wave velocity one) are often retrieved from surface recording data of passive sources, such as seismic ambient noise. The pioneering SPAC method (Aki, 1957) has been widely used. This approach has been rapidly developed through the continuous accumulation of observation data and has gained wide interest owing to its cost effectiveness. The shear-wave velocity profile can be obtained by the inversion of Rayleigh wave DCs (Aki, 1957; Louie, 2001; Wathelet, 2005; Gouedard et al., 2008; Tada et al., 2009) or by the combined inversion of the DC and ellipticity of Rayleigh waves (e.g., Scherbaum et al., 2003). Generally, the Rayleigh waves DC are derived from microtremors recorded by several instruments; therefore, the detecting instruments should form an array with a certain scale. In contrast, the HVSR inversion based on single-station recordings is much more convenient. The HVSR inversion methods can be classified into four typical categories: (1) HVSR based on the Rayleigh wave ellipticity (Fäh et al., 2001; Sherbaum et al., 2003), (2) HVSR based on the contributions of Rayleigh and Love waves (Arai and Tokimatsu, 2004), (3) HVSR based on the contribution of body waves (Herak, 2008; Bignardi et al., 2016), and (4) HVSR based on the contribution of the body and surface waves according to the diffuse wave field theory (Kawase et al., 2011; Sánchez Sesma et al., 2011; Nagashima et al., 2014). Although the HVSR inversion method is advanced, its use is hampered by the phenomenon of the non-uniqueness of the solution as demonstrated by Picozzi et al. (2005) and Picozzi and Albarello (2007).

To overcome this problem, Scherbaum et al. (2003) proposed a joint inversion of HVSR and phase velocity dispersion to determine the soil profile. Parolai et al. (2005) and Picozzi et al. (2005) performed joint inversions of the phase velocity dispersion and HVSR curves. In these joint inversions, the HVSR and DCs were obtained from ambient noise observations. Although the forward modeling calculation of noise-based HVSR (NHV) improved by García-Jerez et al. (2016) and Pina-Flores et al. (2017) is more efficient than the conventional wavenumber-integration schemes, the inversion still needs thousands of iterations and each is time-consuming for general applications. In contrast, the EHV can be easily calculated by considering only the single-wavenumber contribution of body waves (Kawase et al., 2018).

In recent years, several studies proved that the one-dimensional (1D) velocity structure could be obtained through the inversion of HVSR from earthquake motions (Kawase et al., 2011; Nagashima et al., 2014). Commonly the S-wave window of earthquake motion is adopted to calculate the EHV, under this situation, the EHV inversion is dominated by body-wave contributions. Therefore, it is natural to combine the EHV with phase velocity DCs for integrating surface- and body-wave components and they both are modeled from the layered system properties under scrutiny. The joint inversion can add extra constraints to reduce the non-uniqueness of the solutions associated with the single EHV inversion. Therefore, this strategy improves the efficiency and accuracy of the inversion for soil profiles. For an area where EHV can be easily obtained, the joint inversion of EHV and DC is especially appropriate and does not impose any additional computational cost on collecting earthquake motion data. For example, many strong ground motion stations in western China offer abundant earthquake recordings, but soil profiles are not available. With the joint inversion method, these ground motions can be used to estimate site velocity structures if some small-scale noise arrays are set up to extract DCs from microtremor measurements. To the best of our knowledge, such a joint inversion implementation has not been reported yet.

From the viewpoint of the inversion algorithm, the genetic algorithm (GA) has been widely used to deal with sundry HVSR measurements (Scherbaum et al., 2003; Parolai et al., 2005; Picozzi et al., 2005). However, during the inversion process, the algorithm tends to stall away from the global optimal solution. This phenomenon is called premature convergence (Mosegaard and Sambridge, 2002). To overcome this problem, often different optimization methods are combined (Santos et al., 2005); for example, hybrid GA and linearized (LIN) algorithms (Picozzi and Albarello, 2007) and hybrid simulated annealing (SA) and GA (Cui, 2004). The simulation shows that the premature convergence of GA and the search inefficiency of SA can be improved simultaneously in the hybrid scheme. The combinational strategy of SA and GA was applied to the inversion of EHV (Rong et al., 2018). In this study, the global optimization scheme of hybrid SA and GA was applied to the proposed joint inversion.

In this study, we conducted the joint inversion of EHV and phase velocity dispersion for site velocity structures. The EHV is obtained based on the diffuse-field theory for plane waves. In order to construct neatly the synthetic 1D diffuse illumination. Thus, only the S-wave part (which certainly includes other waves) is used to calculate EHV. The DC derived from array measurements is an essential constraint to the EHV. To delve into the effectiveness of the combined application of these two different methods, we investigated their complementarity in the inversion. The NHV is a byproduct of these noise measurements. The benefit of the joint inversion using earthquake data to determine the HVSR comes from the fast forward computations. . . .To examine our joint inversion in detail, we investigated the complementarity of EHV and surface-wave DC through sensitivity analyses. The inversion was implemented using a global optimization algorithm of hybrid GA and SA algorithms. We discussed the sensitivity of various parameters (S- and P-wave velocities, thickness, and density) to the inversion. We validated the proposed method by using a synthetic example to compare the performances of the joint inversion of NHV and DC with those of EHV or DC inversions alone. Finally, the joint inversion was applied to the Garner Valley Downhole Array (GVDA) data for identifying site velocity structures.

Methodology

Both single-station HVSR and phase velocity DCs can capture the mechanical and structural properties of sedimentary layers. The combined application of the two datasets can constrain the *V*s. structure better. The proposed joint inversion includes two steps, namely, (1) the forward calculation of EHV and DCs, and (2) the global optimization for searching the best structural model by the hybrid GA and SA algorithms.

Forward calculation of EHV and DCs

Arai and Tokimatsu (2004) improved the forward calculation of HVSR from microtremor measurements by considering the higher modes. Based on the diffuse-field theory, Sánchez-Sesma et al. (2011) linked the average measurements of HVSR to the intrinsic property of the media by regarding the power spectrum of measurements as proportional to the directional energy densities. This simplifies the forward calculation considering the full-wave HVSR as proportional to the imaginary part of the Green's function (Wu et al., 2017). . . .To extend the diffuse-field theory to earthquake records, Kawase et al. (2011) showed that for body waves incident to a 1D layered structure, the EHV can be calculated as

$$\mathbf{EHV}(f) = \sqrt{\frac{2\alpha}{\beta}}\frac{|\mathbf{TF}_S(f)|}{|\mathbf{TF}_P(f)|}, \tag{1}$$

where $\mathbf{TF}_S(f)$ and $\mathbf{TF}_P(f)$ are the transfer functions of the S- and P-waves, respectively, and *f* represents frequency, and α and β are the P- and S-wave velocities at the bedrock, respectively. The application of Eq. 1 to the EHV inversion of layered structures has been established (Kawase et al., 2011; Nagashima et al., 2014).

We used Eq. 1 to calculate the EHV curves in the proposed joint inversion. Figure 1A presents the theoretical EHV of the GVDA site. The measured profile data (Bonilla et al., 2002) are listed in Table 1. The model parameters in the table include the P-wave velocity (V_P), S-wave velocity (V_s), density (ρ), and thickness (h) for individual layers. Based on these parameters that define a 1D model whose properties vary with the depth, we calculated the theoretical DC using "gpdc" program, a routine in the GEOPSY software package (Wathelet et al., 2020). Figure 1B shows the resulting theoretical DC for the GVDA array site. The calculation of experimental DC was made from microtremor measurements in and array using the frequency-wavenumber method (Wathelet, 2005).

Objective functions for joint inversion

Since the aim of the inversion is to retrieve a 1D subsurface structure, we need a criterion to decide which set of simulated curves best reproduces the experimental data. Hence, we introduce an objective function that is a positive, real valued function of the subsurface parameters. The objective function becomes important in the proposed joint inversion because EHV and DC are physically different, have nonidentical dominant frequencies, and are related to subsurface velocity profiles in distinct ways and to different degrees. A reasonable objective function is a good representation of the impacts of different types of data on the inversion.

The problem of determining underground velocity structures by the joint inversion of EHV and DC can be simplified as the problem of finding the global minimum value of the objective function that relates soil parameters to EHV and DC curves. Following Parolai et al. (2005), we defined the objective function as

$$\boldsymbol{\Phi}(\boldsymbol{P}) = \boldsymbol{\Phi}_{\mathrm{DC}}(\boldsymbol{P}) \cdot \boldsymbol{\Phi}_{\mathrm{HV}}(\boldsymbol{P}), \tag{2}$$

where $\boldsymbol{\Phi}_{\mathrm{DC}}$ and $\boldsymbol{\Phi}_{\mathrm{HV}}$ are the objective functions for dispersion and EHV curves, respectively, and $\boldsymbol{P}= (x_1,x_2,x_3, \ldots ,x_N)^{\mathrm{T}}$ is the parameter vector of the model with *N* soil layers.

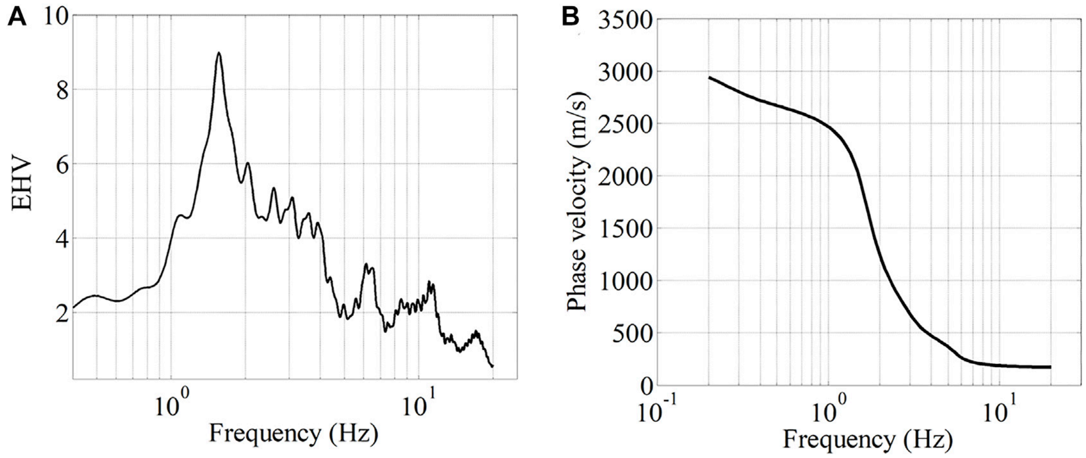

FIGURE 1
Forward calculation of the theoretical EHV **(A)** and DC **(B)** for the GVDA site (Bonilla et al., 2002).

TABLE 1 Measured model of GVDA site (Bonilla et al., 2002).

Layer	*h*(m)	ρ(kg/m³)	V_P(m/s)	V_S(m/s)	Q_P	Q_S
1	6	2000	1225	175	15	10
2	9	2000	1525	200	15	10
3	7	2200	1600	320	15	10
4	36	2400	2000	550	20	15
5	29	2800	2150	650	20	15
6	132	2800	2820	1632	50	30
7	381	2800	5190	3000	100	50
8	4400	2800	5250	3050	1000	500
9	4400	2800	6220	3490	1000	500

Similar to Lawrence and Wiens (2004), the objective functions Φ_{DC} and Φ_{HV} in Eq. 2 can be expressed as

$$\begin{cases} \boldsymbol{\Phi}_{\mathbf{DC}}(\boldsymbol{P}) = \left(\dfrac{\mathbf{DC_t}(f) - \mathbf{DC_o}(f)}{\max(\mathbf{DC_o}(f))}\right)^2 \\ \boldsymbol{\Phi}_{\mathbf{HV}}(\boldsymbol{P}) = \left(\dfrac{\mathbf{EHV_t}(f) - \mathbf{EHV_o}(f)}{\max(\mathbf{EHV_o}(f))}\right)^2, \end{cases} \quad (3)$$

where $\mathrm{DC_t}(f)$ and $\mathrm{DC_o}(f)$ represent the theoretical and observed DCs, respectively, and $\mathrm{EHV_t}(f)$ and $\mathrm{EHV_o}(f)$ indicate the theoretical and observed EHV curves, respectively. We see that Eq. 3 represents the difference in the amplitudes and spectral shapes of the simulated and observed curves. For multilayer soil structures, $\Phi(\boldsymbol{P})$ is usually a nonlinear function of multiple parameters (V_P, V_S, h, ρ); that is, the joint inversion is a problem of multiple extreme values.

In this study, we incorporated the SA into the GA in an attempt to seek the global minimum of the multiple extreme value problems. The hybrid global optimization method considers the effects of S- and P-wave velocities, thicknesses, and densities on the EHV and DC curves.

Inversion procedure

The global optimization method of hybrid GA and SA (Rong et al., 2018), which was originally developed for EHV inversions, was modified to consider the EHV and DCs simultaneously for the joint inversion. In this hybrid implementation, the premature convergence of GA is avoided by the SA annealing operation and the search inefficiency of SA is improved by the GA global optimizing operation.

We denote the set of parameters of the ith layer by $p_i = (V_{Si}, V_{Pi}, h_i, \rho_i)$, with $i = 1,2,3,\ldots,N$. Some background parameters should be set in advance. These parameters include the genetic population size (M), variable dimension (maximum number of variables considered in the inversion), binary digits, initial temperature T_0 for SA, and the iteration number of generations (L) at a certain temperature.

The hybrid GA and SA method relies mainly on the GA and is supplemented by the SA. We first initialize the genetic population model by calculating its objective function and every individual relative fitness. Each individual in the population model is denoted by a string of binary codes with 0 and 1. Then the objective functions for individuals are calculated and ranked. According to the ranking of objective functions, the fitness value are normalized and assigned as values between −2 and 2.

The fitness value describes the superiority or inferiority of individuals. It is used to determine the next genetic operation: selection, crossover, or mutation. The initial population can be

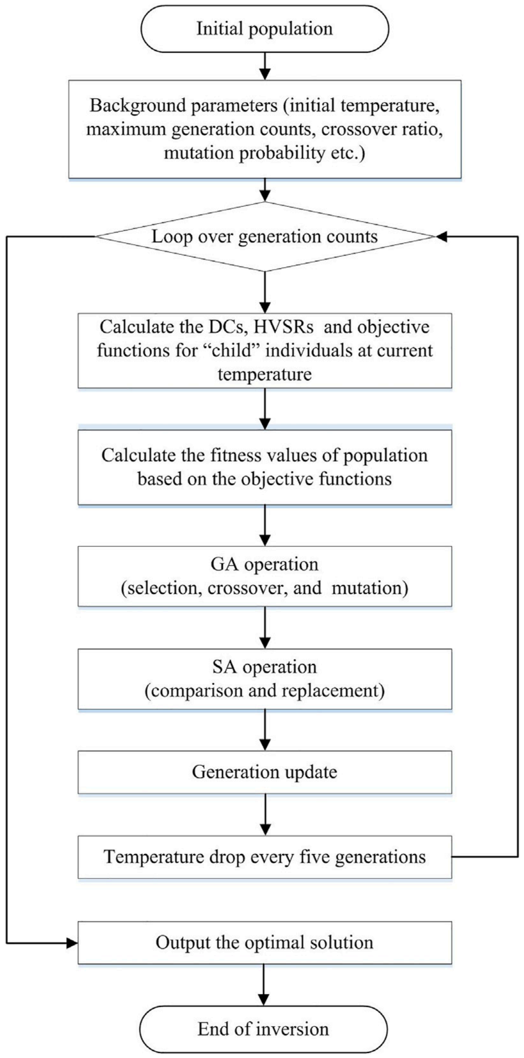

FIGURE 2
Flow chart of the proposed joint inversion.

evolved into the next generation. The larger the fitness of an individual, the higher is the probability that the individual will be reproduced and passed down into the next generation.

The SA operation is introduced to reduce the premature convergence of the GA. In this operation, we compare the objective functions of "child" individuals (Φ_{child}) with "parent" individuals (Φ_{parent}), and then we calculate their differences ($\Delta\Phi = \Phi_{child} - \Phi_{parent}$). The child individual with $\Delta\Phi$ <0 passes down into the next generation; for the other child individuals, we must perform an annealing operation of random disturbance by a probability of $\exp(-\Delta\Phi/T_k)$, where T_k is the temperature of the kth iteration of SA. T_k decreases with increasing number of generations (l) according to

$$T_k = T_0 \cdot c^{k-l}, \tag{4}$$

where c is the temperature attenuation coefficient, which is typically a constant less than one.

The computational flow for the hybrid implementation of the GA and SA is principally based on the GA. Figure 2 depicts the flow chart of the inversion with the following main steps.

Step 1. Create the initial population.

Step 2. Set up the background parameters—the initial temperature, maximum generation counts, crossover ratio, mutation probability, etc.

Step 3. Loop over the generation counts to calculate the DCs, EHVs, and objective functions of child individuals at the current temperature; then, compute the fitness value of the population based on the objective functions.

Step 4. Perform the GA operations of each generation loop to conduct selection, crossover, and mutation.

Step 5. Perform the SA operations of each generation loop to compare the objective functions of Φ_{child} and Φ_{parent} to see if the child individuals can be replaced according to random disturbances by an acceptable probability at the current temperature.

Step 6. Output the optimal solution to end the inversion process.

Sensitivity analyses

The joint inversion by combining Rayleigh wave DC and EHV is based on their complementarity in the inversion. We investigated the complementarity and provided some supplementation through sensitivity analyses by using a simple model. The use of multiple parameters (V_P, V_S, h, and ρ) makes the model space of inversion very large, significantly reducing the efficiency of calculations. The sensitivity analysis of inversion parameters can reduce the spatial dimension of inversion problems to some extent.

Following Arai and Tokimatsu (2004), we defined the following absolute value of the nondimensional partial derivative of inversion parameters as the sensitivity of inversion

$$D^{P}_{ji}(f) = \left|\frac{P}{\mathrm{NHV}(f)}\frac{\partial \mathrm{NHV}(f)}{\partial P}\right|_{P=P_{ji}}, \tag{5}$$

where $P_{ji} = (V_{Pj}, V_{Sj}, h_j, \rho_j)$ represents the ith set of parameters in the jth layer. We see that the objective function varies with individual parameters in every soil layer. A larger $D^{P}_{ji}(f)$ indicates the greater sensitivity of $\mathrm{NHV}(f)$ to P_{ji}. Kawase et al. (2011) demonstrated a sensitivity analysis by using a

TABLE 2 A simplified soil structure (Kawase et al., 2011).

Layer	h(m)	ρ(kg/m3)	V_P(m/s)	V_S(m/s)	Poisson's ratio v
1	50	1800	867	500	0.25
2	∞	2700	5888	3400	0.25

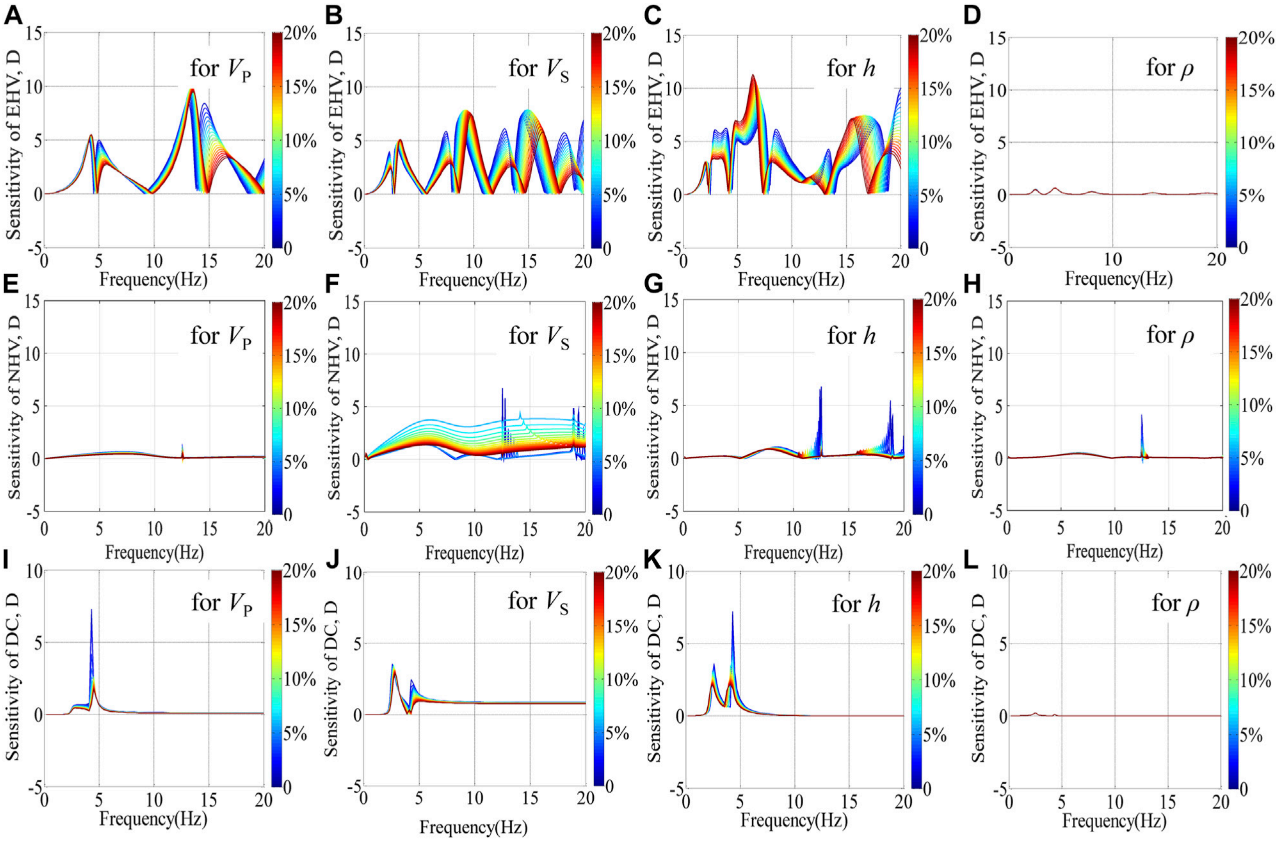

FIGURE 3
The sensitivity of different parameters to the EHV, NHV or DC, **(A)** V_P to the EHV, **(B)** V_S to the EHV, **(C)** h to the EHV, **(D)** ρ to the EHV, **(E)** V_P to the NHV, **(F)** V_S to the NHV, **(G)** h to the NHV, **(H)** ρ to the NHV, **(I)** V_P to the DC, **(J)** V_S. to the DC, **(K)** h to the DC, **(L)** ρ to the DC. The color bar is calibrated in terms of the variability of parameters. We consider 0–20% for the variation range of parameters.

simplified soil model. The model contains a single soft layer in the half-space bedrock, with the relative parameters listed in Table 2. We used the same model for the sensitivity analyses of the proposed joint inversion.

In the joint inversion, parameters such as thicknesses, S- and P-wave velocities, and densities affect the EHV, NHV, and DC curves in distinct ways and to different degrees. The computation of NHV was proposed by Sánchez-Sesma et al. (2011) and corresponds to the square root of the spectral ratio of the horizontal components of Green's function to that of the vertical counterpart. Based on the soil model in Table 2, we calculated $D_{ji}^{P}(f)$ as a function of frequency with respect to the S- and P-wave velocities, thicknesses, and densities. The results are shown in Figure 3. The color bar is calibrated in terms of the variability of parameters. We considered a 0–20% variation range of the parameters, and we increased the values of V_P, V_S, h, and ρ in the sediment layer. The $D_{ji}^{P}(f)$ values indicate that the S- and P-wave velocities and thicknesses are more sensitive than densities in the range of 0–20 Hz. This conclusion shows that it is reasonable to consider V_S, V_P, and h as the independent variables in the joint inversion.

The HVSR can be approximately interpreted as a receiver function in the frequency domain (Yu et al., 2017) having in mind that neither the azimuth nor the incidence angle are

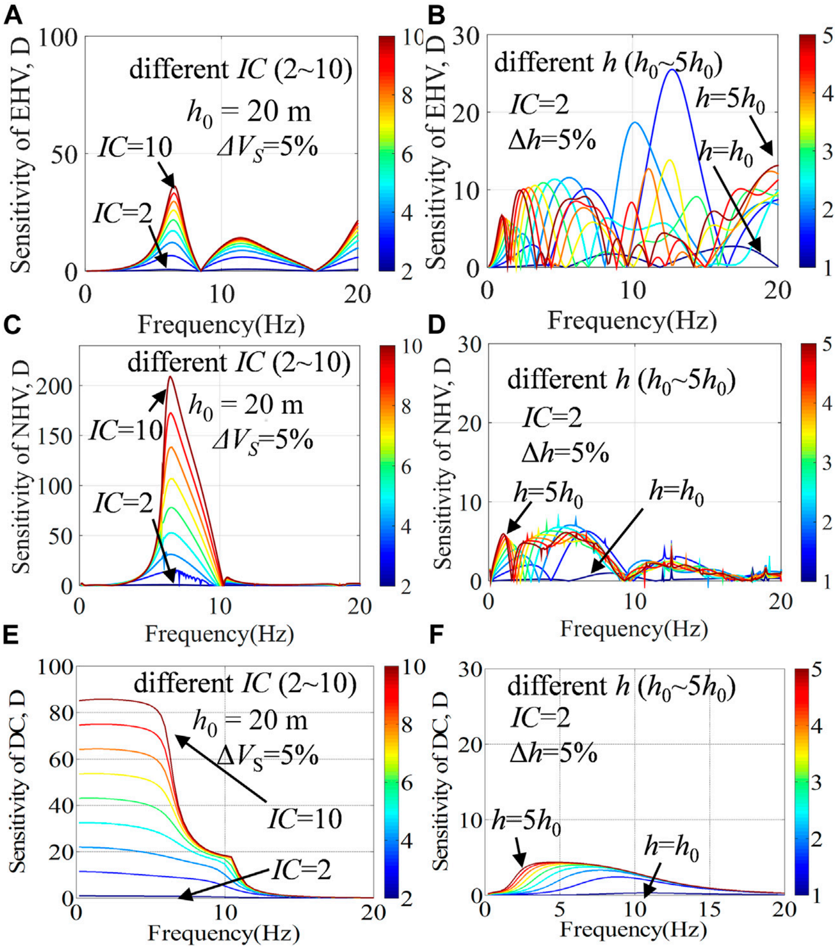

FIGURE 4
The sensitivity of bedrock S-wave velocities **(A)**, and sediment thicknesses **(B)** to the EHV; The sensitivity of bedrock S-wave velocities **(C)**, and sediment thicknesses **(D)** to the NHV; The sensitivity of bedrock S-wave velocities **(E)**, and sediment thicknesses **(F)** to the DC. For the **(A) (C)**, and **(E)**, we fix the sediment thickness h = 20 m with the other relevant properties listed in Table 2, and then change the bedrock S-wave velocity to make the sediment-bedrock impedance contrast IC = 2–10, with the color bar calibrated in terms of the sediment-bedrock impedance contrast. For the **(B)**, **(D)** and **(F)**, we fix the bedrock S-wave velocity by setting IC = 2, and then change the sediment thickness from h_0 to $5h_0$ (h_0 = 20 m), with the color bar calibrated in terms of sediment thicknesses for a variation range of 5%.

known. We only consider it is sensitive to impedance contrasts (i.e., strata interfaces), whereas the DC is sensitive to shear-wave velocities. Parolai et al. (2005) found that the joint inversion of HVSRs and DCs from seismic noise recordings can reduce the problem of trade-off between the velocity and thickness of layers. Picozzi et al. (2005) further showed that the bedrock S-wave velocity can be well constrained through this joint inversion. However, the HVSR in the previous joint inversions were based on seismic noise recordings and therefore based on the assumption of surface waves. However, as we know, NHV and EHV are quite distinct in terms of their frequency contents and propagation paths and modes because of the differences between surface and body waves. In addition, to the best of our knowledge, the complementarity of EHV and surface-wave DC in inverse problems has not be specifically clarified until now.

As a preliminary attempt in this regard, we extended sensitivity analyses using equation (5) to identify the complementarity of EHV and DC using the model detailed in Table 2. We tested the sensitivity of EHV, NHV, and surface-wave DC separately to the bedrock S-wave velocities and sediment thicknesses. We conducted two groups of tests. For the first group, we fixed the sediment thickness at 20 m with the other relevant properties as listed in Table 2, and then, we changed the bedrock S-wave velocity from 667 to 3333 m/s as the corresponding P-wave velocity was varied from 1155 to 5773 m/s to maintain the Poisson's ratio of the bedrock at 0.25. The sediment–bedrock impedance contrast (*IC*) varied

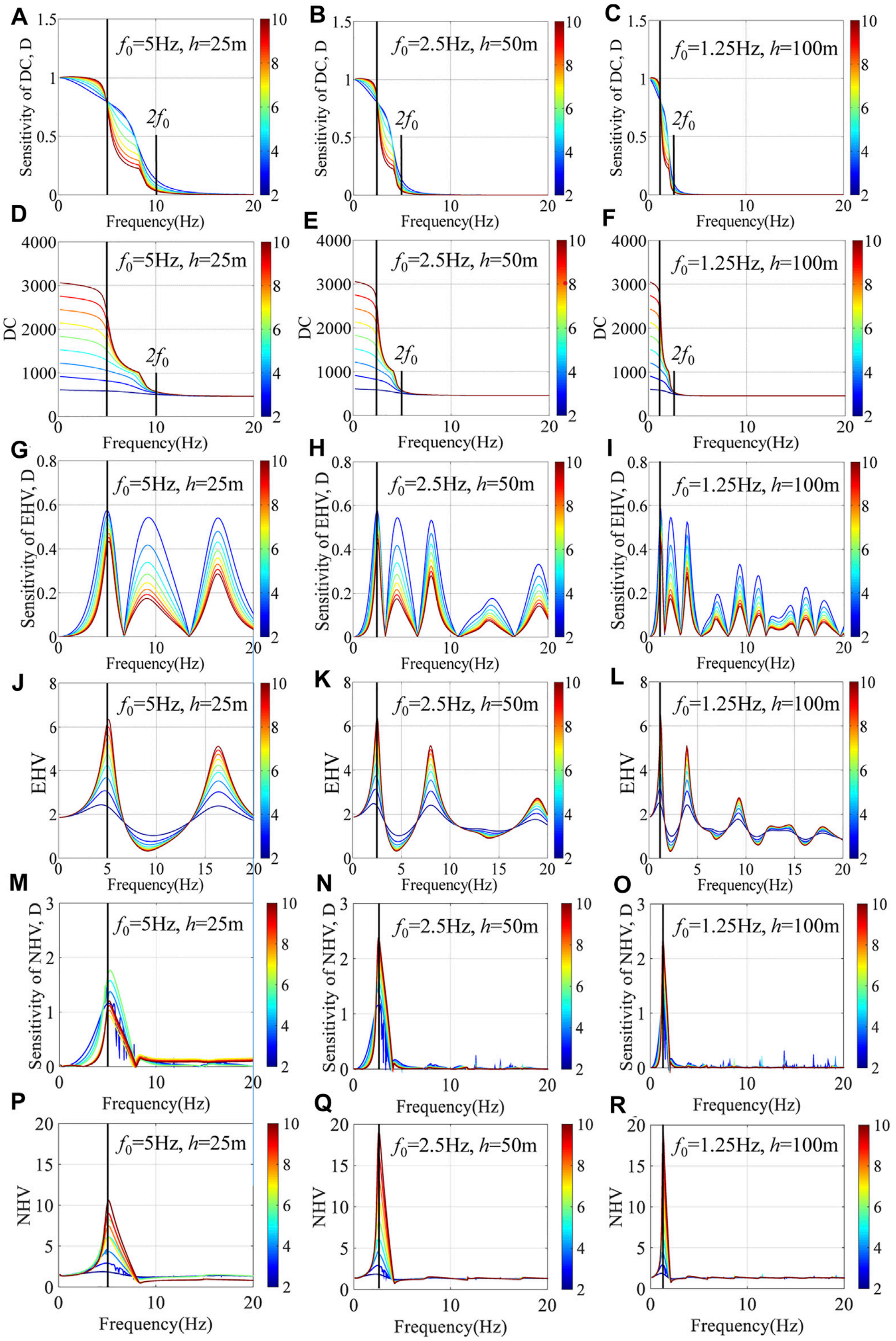

FIGURE 5
The sensitivity of the DC, EHV and NHV to bedrock S-wave velocities, along with the corresponding DC, EHV and NHV curves. The left **(A,D,G,J,M,P)**, middle **(B,E,H,K,N,Q)**, and right **(C,F,I,L,O,R)** panels result from the numerical experiments with three fixed parameter pairs of predominant frequency and sediment thickness: (5 Hz, 25 m) (2.5 Hz, 50 m), and (1.25 Hz, 100 m). The color bar is calibrated in terms of the sediment-bedrock impedance contrast IC = 2–10.

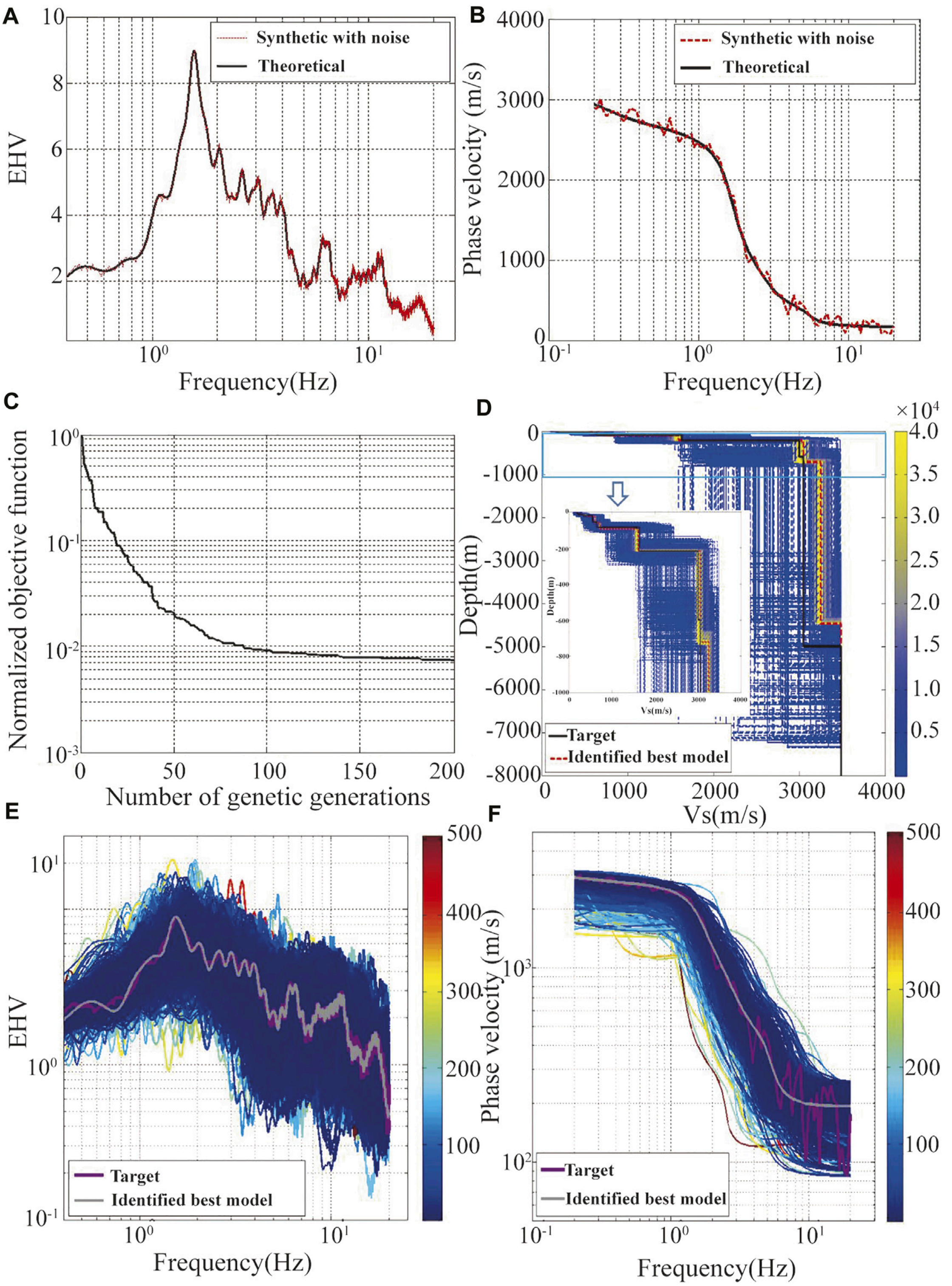

FIGURE 6
Verification of joint inversion of EHV and DC by the noise-contaminated synthetic case with the GVDA model. **(A)** The theoretical (solid line) and noise-contaminated synthetic (red dashed line) HVSRs of the GVDA mode. **(B)** The theoretical (solid line) and noise-contaminated synthetic (red dashed line) DCs of the GVDA mode. **(C)** Iterative convergence curve by objective functions versus generation numbers. **(D)** Inverted velocity profiles. the color bar is calibrated in terms of the order of appearance of the individuals. **(E)** and **(F)** The corresponding HVSR and DC curves of all the iterative models colored in terms of the value of objective functions which converge to the target curves (purple lines) with decreasing objective functions.

TABLE 3 Verification of joint inversion by the noise-contaminated synthetic case with the GVDA model (see Table 1): initial and identified models.

Model	Layer	h(m)	ρ(kg/m3)	V_P(m/s)	V_S(m/s)
Initial model	1	3.0–9.0	2000*	612.5–1837.5	87.5–262.5
	2	4.5–13.5	2000*	762.5–2287.5	100.0–300.0
	3	3.5–10.5	2200*	800.0–2400.0	160.0–480.0
	4	18.0–54.0	2400*	1000.0–3000.0	275.0–825.0
	5	14.5–43.5	2800*	1075.0–3225.0	325.0–975.0
	6	63.0–198.0	2800*	1410.0–4230.0	816.0–2448.0
	7	190.5–571.5	2800*	2595.0–6220.0	1500.0–3490.0
	8	2200.0–6600.0	2800*	2625.0–6220.0	1525.0–3490.0
	9	4400*	2800*	6220*	3490*
Identified model	1	4.3(3.5–5.5)	2000*	1444.4(940.3–1938.3)	202.8(172.7–237.8)
	2	12.4(9.9–14.6)	2000*	1481.7(1210.8–1744.2)	202.5(182.1–223.5)
	3	7.8(6.5–9.1)	2200*	2119.8(1655.8–2379.8)	381.8(309.0–438.5)
	4	37.6(33.1–43.1)	2400*	2352.0(1930.0–2669.4)	590.2(523.5–710.8)
	5	32.7(26.2–39.4)	2800*	2182.3(1740.8–2455.5)	719.6(625.6–822.9)
	6	124.7(97.4–141.7)	2800*	2685.8(2260.2–3030.3)	1602.6(1239.4–1835.5)
	7	502.8(349.7–596.6)	2800*	4922.0(4486.5–5246.8)	3049.5(2529.7–3458.6)
	8	3754.9(2965.6–4542.2)	2800*	4639.0(4281.1–5021.3)	3249.6(3092.0–3441.0)
	9	4400*	2800*	6220*	3490*

Asterisk (*) denotes fixed parameters. Values in parentheses are 95% confidence limits for parameters.

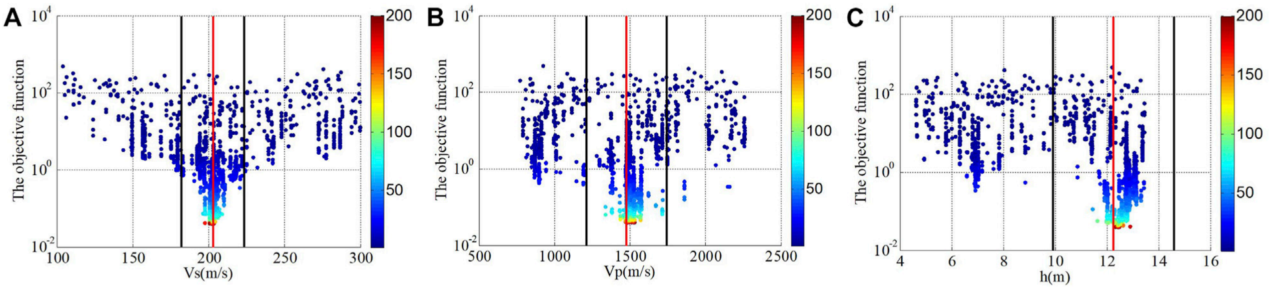

FIGURE 7
Variability of inverted parameters (Vs, Vp, and **(H)** for the second layer versus objective functions during the converging process, with color bars calibrated in terms of generations. Red and black lines represent the averages and the 95% confidence limits of all the tested parameters. **(A)** Vs., **(B)** Vp, **(C)** *h*.

correspondingly from 2 to 10. We emphasize that because the sediment velocities (see Table 2) and sediment and bedrock densities were fixed, the sediment–bedrock *IC* values mainly reflect the change in the bedrock S-wave velocities. The fundamental resonance frequency (f_0) used in these tests was 6.25 Hz because only impedance contrasts were considered. For the second group, we fixed the bedrock S-wave velocity by setting $IC = 2$ and then changed the sediment thickness from h_0 to $5h_0$ with $h_0 = 20$ m.

Figure 4 shows the resultant sensitivity of the EHV, NHV, and DC to S-wave velocities (by fixing $h = 20$ m) and sediment thicknesses (by fixing $IC = 2$). We considered a 5% variation range for velocities and thicknesses. The EHV, NHV, and DC exhibited different sensitivities for different frequency ranges. The EHV is more sensitive to the variation in sediment thicknesses almost throughout the frequency range, especially in the high-frequency range (>10 Hz). As expected, it is less sensitive to bedrock S-wave velocities. On the other hand, the DC is more sensitive to changes in the bedrock shear-wave velocities in the low-frequency range (<10 Hz), and less sensitive to sediment thicknesses. The NHV exhibits has similar sensitivity characteristics as the DC; for example, the NHV is also more sensitive to changes in the bedrock shear-wave velocities in the frequency range less than 10 Hz and less sensitive to sediment

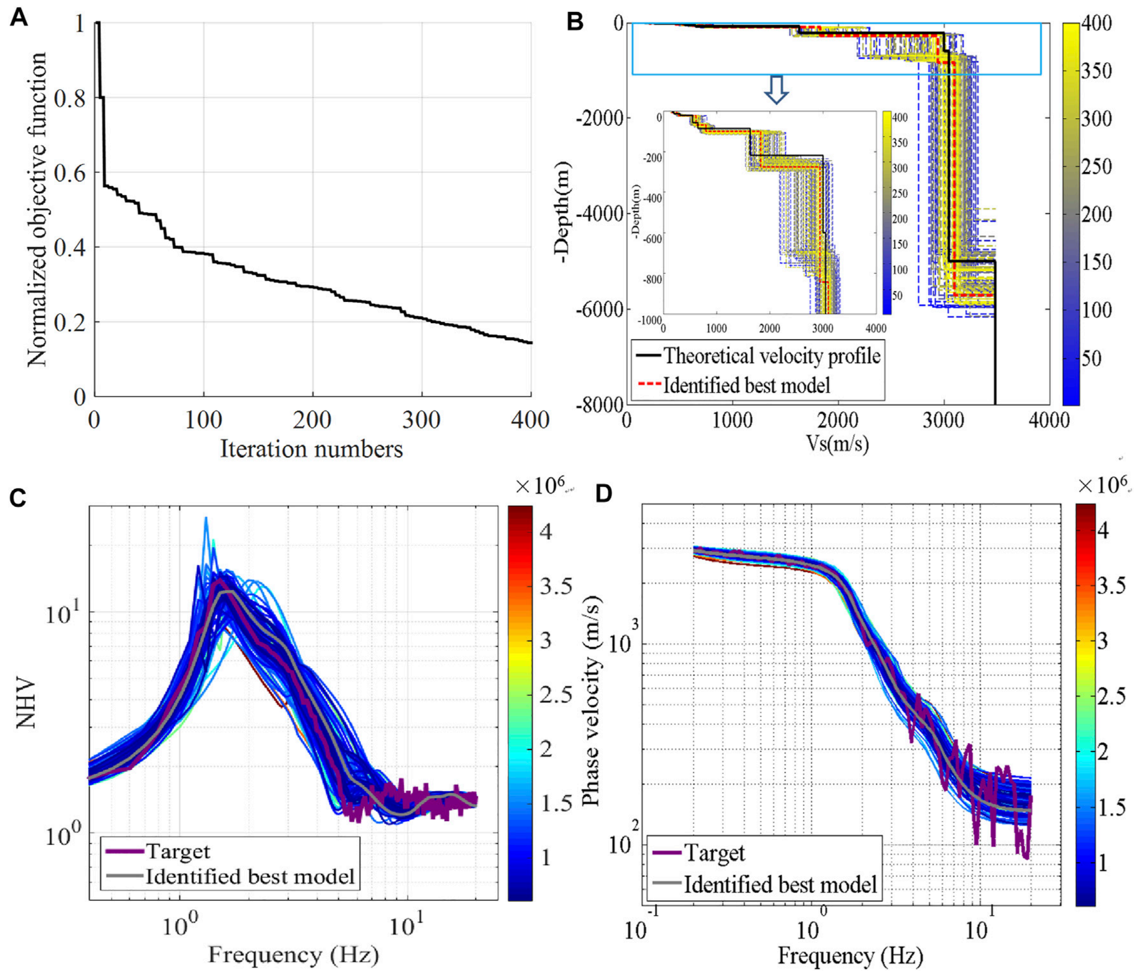

FIGURE 8
The joint inversion of NHV and DC by the noise-contaminated synthetic case with the GVDA model **(A)** Iterative convergence curve by objective functions versus iteration numbers **(B)** All the inverted Vs. models, the color bar is calibrated in terms of the order of appearance of the individuals. **(C)** and **(D)** The corresponding NHV and DC curves of all the iterative models colored in terms of the value of objective functions which converge to the target curves (purple lines) with decreasing objective functions.

thicknesses. This is because NHV and DC are derived from microtremor measurements, which mainly consist of surface waves, so that the peaks associated with higher modes are not be as prominent as those in the case of EHV. The EHV is derived from earthquake ground motions, which mainly consist of upwardly propagating plain body waves, and hence, the higher mode resonances can be seen at high frequencies. This result indicates that from the viewpoint of sensitive frequency range, the joint inversion of the EHV and DC is more complementary than that of the NHV and DC. The former method can exploit the complementarity of the EHV and DC to achieve a reliable inversion for bedrock shear-wave velocities and sediment thicknesses.

Figure 4 clearly shows that the contribution of the EHV covers the whole frequency range and the contribution of the DC mainly lies in low and middle frequencies. It implies that the joint inversion of EHV and DC has complementarity from the aspect of frequency. However, the joint inversion for bedrock S-wave velocities does not appear as reliable in the middle-to-high-frequency band because there is almost no contribution of the DC. We need to identify the contribution of the EHV in this frequency band. For this purpose, the first group of tests, described previously, to test the sensitivity of the EHV and DC to different sediment–bedrock *ICs* for a sediment thickness $h = 20$ m and a fundamental resonance frequency $f_0 = 6.25$ Hz, is extended to different sediment thicknesses ($h = 25$, 50, and 100 m) and corresponding predominant frequencies ($f_0 = 5$, 2.5, and 1.25 Hz, respectively).

Figure 5 shows the resultant sensitivity of the EHV and DC to bedrock S-wave velocities for three fixed predominant

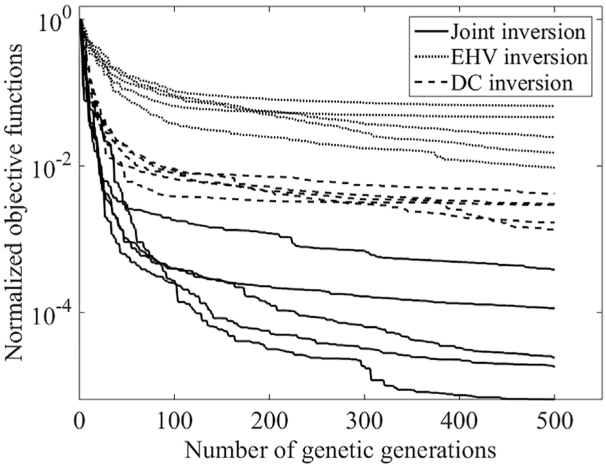

FIGURE 9
Convergence curves with normalized objective functions versus generation numbers by three inversion methods with each for five random numerical experiments.

frequency–sediment thickness pairs: 5 Hz and 25 m; 2.5 Hz and 50 m; and 1.25 Hz and 100 m. We see that the EHV and DC curves exhibit great changes for different parameter pairs. The responses of the DC to bedrock S-wave velocities mainly lie in the frequency range less than $2f_0$, whereas the EHV is sensitive to bedrock S-wave velocities over a wide range of frequencies around f_0 and beyond. That is, the frequency complementarity of the EHV and DC can assure the joint inversion for bedrock shear-wave velocities.

Verification of joint inversion by a synthetic example

We considered the example of the GVDA site to validate the proposed joint inversion. The detailed velocity model for this site has been studied widely (e.g. Gibbs, 1989; Pecker and Mohammadioun, 1993; Theodulidis et al., 1996). As per the details in Table 1, the model was improved by the best fitting of the time-domain simulations and observed data (Bonilla et al., 2002). It has been widely used as a standard model to test various inversion algorithms.

The theoretical EHV and DC curves of the GVDA model are shown in Figure 1. Gaussian noise with a signal-to-noise ratio of 30 dB were added to these theoretical curves to test the robustness of the joint inversion algorithm. The resulting target curves are shown as red curves in Figures 6A,B. Although no initial model is required for our hybrid global optimization inversion, it is preferable to have one to constrain the search range of parameters. In this synthetic case, the P- and S-wave velocities and layer thicknesses were used as the unknown parameters based on the parameter sensitivity analysis described in the previous section. The bottommost layer was used as the bedrock with its parameters fixed in the inversion. The P- and S-wave velocities (V_{P0} and V_{S0}) and thickness (h_0) of the measured GVDA model (listed in Table 1) were used to determine the search ranges of all the model parameters. For example, the search ranges of each layer were set as (0.5–1.5) V_{P0} (0.5–1.5) V_{S0}, and (0.5–1.5) h_0 for P- and S-wave velocities and thickness, respectively. Details of the resultant initial model for inversion are listed in Table 3.

For the joint inversion of the EHV and DC, the background parameters of inversion were set as follows: the number of generations was 200; the popular size of each generation was 200; the generation gap of the GA was 0.9, the crossover rate was 0.7; the mutation rate was 0.01; and the initial temperature and scale factor (c_0) of the SA were 10 ˚C and 0.99, respectively. The joint inversion process for the minimum objective function ended at the 200th generation, with an inverted structure model as detailed in Table 3. From Figure 6C, we see that the objective function decreases quickly until the number of genetic generations reaches 100, implying that the 200 generations set in the joint inversion are reasonable for this case study. Figure 6D shows that all the iterative models for the *V*s. profile, which are colored in terms of generations. We see that these models converge from the searching range to a narrow white area with an increasing number of generations. The corresponding EHV and DC curves of all the possible models colored in terms of values of objective functions are shown in Figures 6E,F; these curves converge to the target curves (the best model) with decreasing objective functions. Figure 7 shows the variability of the inverted parameters (V_S, V_P, and h) for the second layer along with the objective functions during the convergence. As the objective functions decrease with increasing generation numbers, and the fluctuation range of parameters gradually narrows, and the parameters approach their best values. To estimate the uncertainty associated with the inverted parameters, we calculated the average of the inverted parameters (Avg.), as shown in Table 3. We see that most inverted parameters lie in the range of 95% confidence limits, implying that the best model can be identified for the noise-contaminated EHVs and DCs.

To compare with the joint inversion of EHV and DC, the “HV-Inv” program proposed by García-Jerez et al. (2016) and Piña-Flores et al. (2017) was used to conduct a joint inversion of the NHV and DC. The modified SA is adopted as the global optimization method. The inversion parameters were set as follows: the iteration number was 300; the initial population had 200 models; the perturbation range was 10%, and the initial temperature was controlled by the relative misfit increment and probability of acceptance, i.e., 0.1 and 0.5, respectively; the cooling schedule was controlled by the temperature ratio (0.9). From Figure 8A, we see that the objective function reduces quickly with an increase in the number of iterations. Figure 8B shows all the inverted *V*s. models. These models converge from the search range to a narrow yellow area with

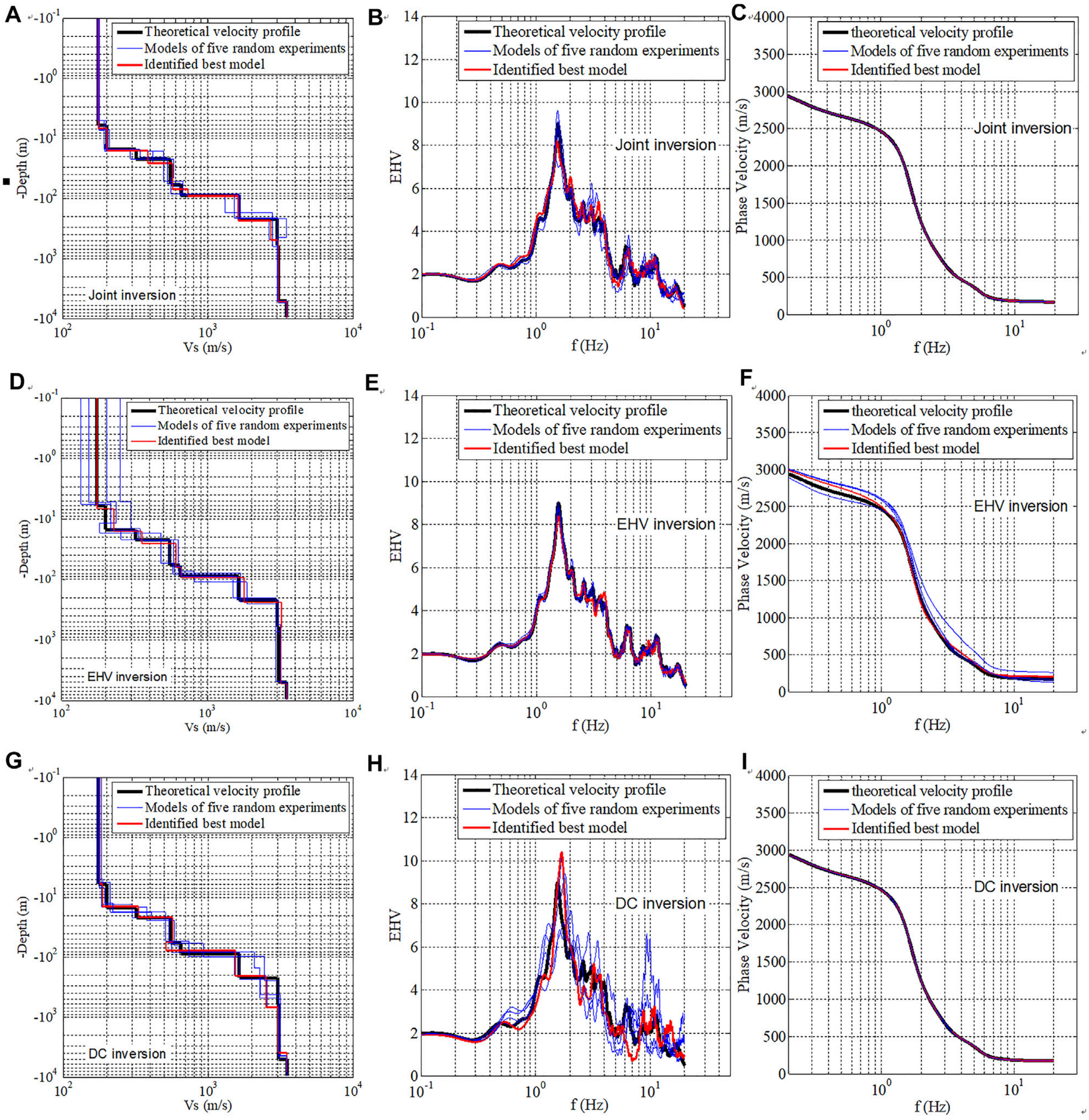

FIGURE 10
Comparison of the theoretical and inverted profiles, EHVs, and DCs by different inversion methods. **(A–C)** The theoretical and inverted profiles, EHVs, and DCs by proposed joint inversion method. **(D–F)** The theoretical and inverted profiles, EHVs, and DCs by the EHV inversion alone. **(G–I)** The theoretical and inverted profiles, EHVs, and DCs by the DC inversion alone. For every inversion methods, five random numerical experiments are conducted.

increasing order of appearance of the individuals. Meanwhile, the NHV (Figure 8C) and DC (Figure 8D) also converge to the corresponding target curves. These results show that the HV-Inv is a powerful tool for obtaining subsurface velocity profiles. Because of the vast differences between the two joint inversion methods in terms of their mechanism and inversion algorithms, it is difficult to directly compare them and judge which one is better. However, from the perspective of the inversion result, the best model identified from the joint inversion of the EHV and DC agrees considerably better with

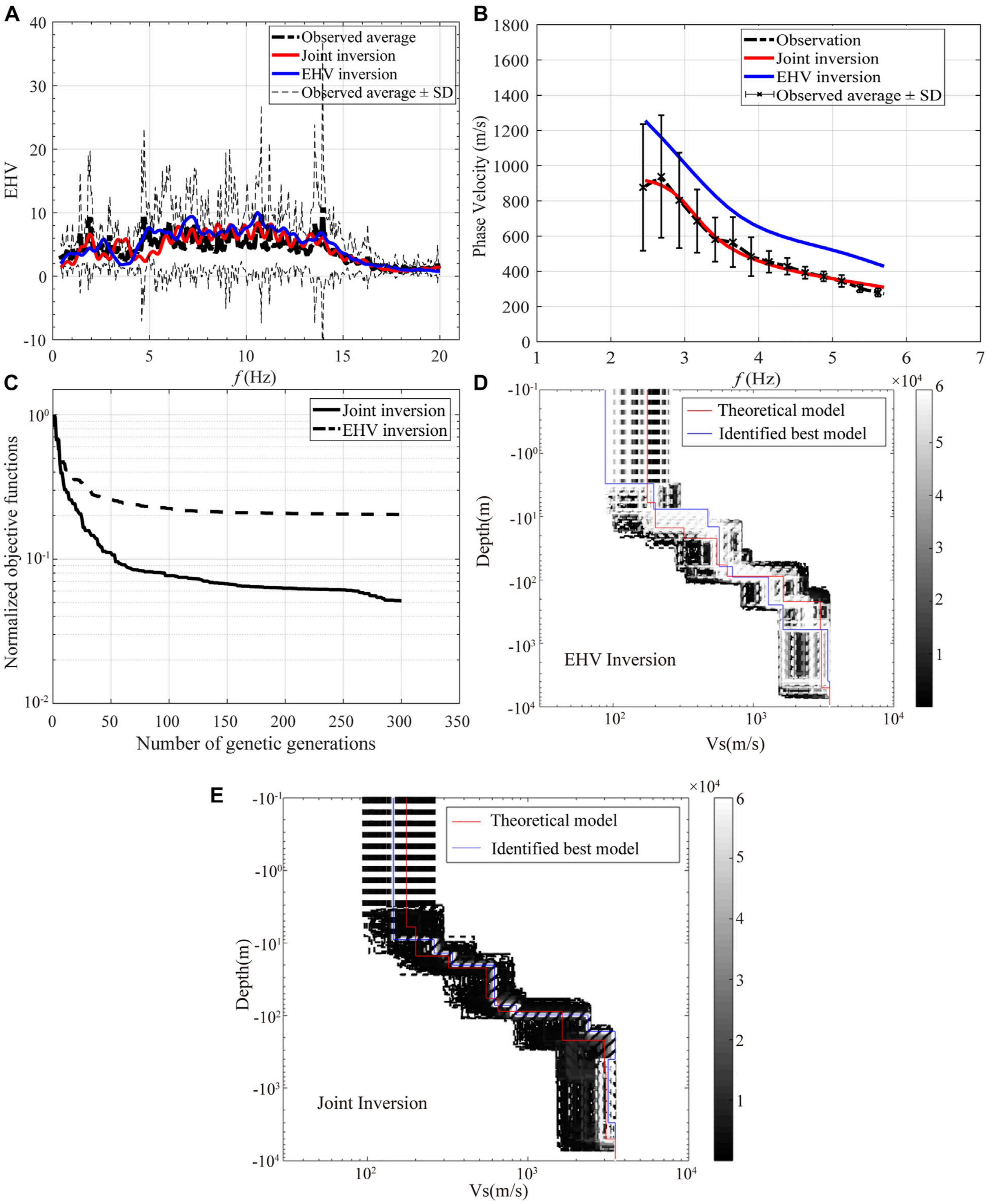

FIGURE 11
(A) Comparison of observed and inverted EHVs by the joint inversion and the EHV inversion alone. The bold black dotted line denotes the observed average EHVs. The thin black dotted lines represent the average ±1 standard deviation (SD) of observations. The red and blue lines denote the best inverted EHVs by the joint inversion and the EHV inversion, respectively. **(B)** Comparison of observed and inverted DCs. The marked points are measurement points derived from ambient noise array observations. The light error bar represents ±1 SD of observations. The black dotted line is the fitting line of measurement points. The red and blue lines represent the best inverted DCs by the joint inversion and the EHV inversion, respectively. **(C)** Comparison of convergence curves. **(D)** Inverted velocity profiles by the EHV inversion alone. **(E)** Inverted velocity profiles by the

(*Continued*)

FIGURE 11
joint inversion. In **(D)** and **(E)**, all the tested models by both the methods are colored in terms of the order of appearance of the individuals. The red and blue lines denote the observed and inverted model profiles, respectively.

TABLE 4 Earthquake parameters of used accelerograms and corresponding PGAs of vertical array sites.

No.	Time(UTC)	M	Depth(km)	Epi. Dis.(km)	Long. (°)	Lat. (°)	PGA(cm/s^2)
1	2008-06-03 23:06:33	2.4	16.9	4.8	−116.72	33.68	67.27
2	2017-06-09 09:24:02	2.7	13.7	6.2	−116.73	33.63	127.34
3	2013-10-16 13:43:42	2.9	17.1	4.1	−116.72	33.68	82.39
4	2018-04-20 12:33:03	2.9	18.4	5.6	−116.72	33.70	65.01
5	2008-06-03 23:06:33	3.0	16.2	5.5	−116.73	33.67	57.17
6	2006-07-30 13:32:53	3.2	15.3	11.6	−116.80	33.69	146.25
7	2016-01-09 11:43:11	3.3	13.6	9.3	−116.77	33.66	75.11
8	2005-11-08 22:03:46	3.4	12.9	15.7	−116.69	33.53	61.91
9	2013-06-28 17:45:48	3.4	15.6	5.4	−116.70	33.62	58.33
10	2009-07-26 04:54:04	3.5	14	5.8	-116.72	33.63	57.17
11	2008-11-17 12:35:42	4.1	12.2	25.6	-116.86	33.50	61.06
12	2010-01-16 12:03:26	4.3	13.9	43.7	−117.02	33.93	77.47
13	2016-01-06 14:42:35	4.4	16.7	37.9	−116.89	33.96	105.01
14	2013-03-11 16:56:06	4.7	13.1	27.3	−116.46	33.50	141.96
15	2005-06-16 20:53:26	4.9	11.6	53.4	−117.01	34.06	80.35
16	2016-06-10 08:04:39	5.2	12.3	34.1	−116.44	33.43	80.62
17	2005-06-12 15:41:46	5.2	14.2	18.1	−116.57	33.53	71.89
18	2010-07-07 23:53:34	5.4	14.0	32.5	−116.49	33.42	76.37

the theoretical velocity profile than the best model identified from the joint inversion of the NHV and DC, especially for depths less than 1000 m. Correspondingly, the genetic generations of the joint inversion of the EHV and DC is 200, which is less than the number of iterations for the joint inversion of the NHV and DC, which is 400 in our case.

To highlight the advantage of joint inversion, we compared its performance with the one of EHV or DC inversion alone. The EHV and DC inversions follow the same procedure as the joint inversion, except that their objective functions are $\Phi_{\mathrm{HV}}(\mathbf{X})$ and $\Phi_{\mathrm{DC}}(\mathbf{X})$, respectively. The corresponding theoretical EHV and DC of the GVDA model were used as the target curves (see Figure 1). To highlight the discrepancy between these inversions, we conducted five random numerical experiments for each method. In these experiments, the fixed parameters, background parameters of inversion, parameters for GA and SA operations, and search ranges of P- and S-wave velocities and layer thicknesses are identical to those set up previously. To assure the convergence of the EHV and DC inversions, we set the maximum iteration number of generations at 500 and the popular size of each generation at 600. The resulting convergence curves for these three inversion methods are shown in Figure 9 in terms of the normalized objective functions versus generation numbers. The normalized objective function, which is defined as the objective function normalized by its maximum value, can describe the fitting accuracy of target curves. We see that the normalized objective function curves decrease sharply in the first 100 generations and become flat after 500 generations. The minimum normalized objective functions of the joint inversion are clearly smaller than those of the other two methods, which implies that the joint inversion is better than the inversion only by either of the two methods.

Figure 10 shows a comparison of these inverted profiles and the corresponding EHV and DC curves obtained by different methods. We see that the joint inversion reproduces the theoretical velocity profile very well (Figure 10A), and the EHV (Figure 10B) and DC (Figure 10C) of the identified best model agree well with the corresponding curves of the theoretical velocity profile. The EHV inversion alone (Figures 10D–F) achieves a good fit to the theoretical EHVs, but the fit for the theoretical DCs is not as good as that for the joint inversion. On the other hand, the DC inversion alone (Figures 10G–I) shows a good fit for the theoretical DCs, but shows a bad fit for the theoretical EHVs.

Applications to observed data

The proposed joint inversion was applied to observed data from the GVDA site for the P- and S-wave velocities and layer thicknesses. The observed EHV and DC curves were set as target curves, as shown in Figure 11. The observed EHV curve is the average of the EHV curves from several earthquakes. We selected the effective earthquakes that could generate peak ground accelerations greater than 20 cm/s^2 and less than 150 cm/s^2 in the range of 100 km. As listed in Table 4, 18 events recorded between 1 January 2004, and 31 January 2019, satisfy this requirement. These earthquakes have magnitudes of M2.4–M5.4 with epicentral distances in the range of 4.8–53.4 km. The resulting peak accelerations on the surface of the site range from 57.17 to 146.25 cm/s^2. We calculated the EHV curve of each earthquake following the data-processing steps of Rong et al. (2018). There are three processing steps: first, the baseline correction and Chebyshev bandpass filter with a band of 0.1–50 Hz were applied to all the records. Second, a window of more than 5 s, beginning 0.5–1 s before the onset of the S-wave, was taken from each record, and the S-wave onset was visually picked by comparing the horizontal and vertical components for each earthquake. The minimum and maximum S-wave window durations were 5 and 10 s, respectively. Then, the S-wave Fourier spectra were calculated and smoothed by using the Hanning window. Finally, the EHV curve was obtained from the ratio of the geometric mean spectra between the horizontal and vertical components.

The observed DC curve is the fitting curve of the phase velocities measured by Liu et al. (2000), as shown in Figure 11B. The measured phase velocities were derived from microtremor recordings by a 10-element nested-triangular array of 100 m aperture on the GVDA site. Although the observed DC curve was only available for about 2–6 Hz, the curve is believed to play an important role in reducing the nonuniqueness in the joint inversion. For comparison, the EHV inversion alone was also conducted following the same procedure and using the relevant parameters. The number of genetic generations for both the inversions was set as 300. The upper and lower limits of velocity and thickness for each layer were in the following ranges $(0.5–1.5)V_{P0}$ $(0.5–1.5)V_{S0}$, and $(0.5–1.5)h_0$, with V_{P0}, V_{S0}, and h_0 being the P- and S-wave velocities and layer thickness of the measured model, respectively. The other parameters of inversion were set as follows: the popular size of each generation was 200; the generation gap was 0.9; the crossover rate was 0.7; the mutation rate was 0.01; and the initial temperature and scale factor (c_0) of the SA were 10°C and 0.99, respectively.

Figure 11 compares the observed and inverted EHVs and DCs for these two inversion methods. We see that the EHV inversion produces a good fit to EHVs but shows obvious discrepancies in the DC curves. The joint inversion produces a good fit for both the EHVs and DCs. Figure 11 compares the convergence curves and inverted velocity profiles obtained by these two inversion methods. We see that the convergence performance (see Figure 11C) of the joint inversion is much better than that of the EHV inversion. The best model identified from the joint inversion in Figure 11E agrees well with the observed model profile with all the tested models colored in terms of generations converging quickly to a narrow white area, and the agreement is much better than in the case of the results (see Figure 11D) obtained by only the EHV inversion. In conclusion, the joint inversion can effectively constrain the model by reducing the non-uniqueness of inversion.

Conclusion

Conventional joint inversions combine the EHV and DC curves with those obtained from array measurements. Such inversions are regarded as the best solution to the non-uniqueness problem arising in the case of the use of EHV or DC inversions alone. To make full use of the additional information of the velocity profile, we proposed an improved joint inversion that combines the Rayleigh wave DCs obtained from array measurements and the EHV obtained from earthquake recordings. We investigated the complementarity of the EHV and surface-wave DCs in the joint inversion through sensitivity analyses. A hybrid global optimization procedure was adopted by combining the GA and SA algorithms. The sensitivity of the inversion parameters was examined to reduce the spatial dimension of inverse problems. We validated the proposed joint inversion by considering a synthetic case of the GVDA model and comparing the results with those obtained by the EHV or DC inversions alone. The proposed method was applied to observation data from the GVDA site for the velocities and thicknesses of soil layers. The main conclusions are summarized as follows:

1. The EHV is more sensitive to sediment thicknesses, especially in the high-frequency range (>10 Hz), and less sensitive to bedrock S-wave velocities. Conversely, the DC is more sensitive to bedrock shear-wave velocities in the low-frequency range (<10 Hz) and less sensitivity to

sediment thicknesses. The joint inversion can exploit the complementarity of the EHV and DC to achieve reliable inversion for bedrock shear-wave velocities and sediment thicknesses.
2. The responses of the DC to bedrock S-wave velocities mainly lie in the frequency range less than 2f0, whereas the EHV is sensitive to bedrock S-wave velocities over a wide range of frequencies around f0 and beyond. The frequency complementarity of the EHV and DC can assure the joint inversion for bedrock shear-wave velocities.
3. The sensitivity of inversion parameters demonstrates that the P- and S-wave velocities and thicknesses of soil layers are dominant parameters that affect the EHV or DC responses. It is reasonable to consider V_S, V_P, and h as the independent variables in the joint inversion.
4. The joint inversion was validated by considering a synthetic case of GVDA site. With increasing generations, the iterative models converged to the measured model rapidly, with most of the inverted model parameters lying in the range of 95% confidence limit. The measured model was identified for the noise-contaminated EHVs and DCs.
5. The joint inversion effectively constrained the model by reducing the non-uniqueness of the inversion. Applications to observed data from the GVDA site achieved perfect convergence of the velocity profiles, with good fits for both the EHVs and DCs. The EHV inversion alone causes obvious discrepancies in the DCs.

Data and resources

All the information of the GVDA, Southern California, used in this study were gathered and authorized by the Earth Research Institute at UCSB. The corresponding observation data can be obtained from http://www.nees.org/(last accessed April 2022). The "gpdc" program used to calculate the theoretical DC can be obtained from http://www.geopsy.org/download.php (last accessed April 2022).

Data availability statement

The original contributions presented in the study are included in the article/supplementary material, further inquiries can be directed to the corresponding author.

Author contributions

Conceptualization, MR; methodology, MR; validation, MR and LF; formal analysis, MR and LF; investigation, MR; resources, MR and FS; data curation, MR; writing-original draft preparation, MR, LF and FS; writing-review and editing, LF, FS and WS; visualization, MR and WS; supervision, LF, WS and FS; project administration, MR; funding acquisition, MR and FS. All authors have read and agreed to the published version of the manuscript.

Funding

This study is supported by the Natural Science Foundation of China (Grants No. 41720104006 and 51878625) and by DGAPA-UNAM under (Project IN107720).

Acknowledgments

The authors wish to thank S. Parolai who offered references and helped in the joint inversion method. The authors also appreciate J.E. Plata and G. Sánchez and their team of the Unidad de Servicios de Información (USI) of the Institute of Engineering-UNAM for locating useful references.

Conflict of interest

The authors declare that the research was conducted in the absence of any commercial or financial relationships that could be construed as a potential conflict of interest.

Publisher's note

References

Aki, K. (1957). Space and time spectra of stationary stochastic waves with special reference to microtremors. *Bull. Earthq. Res. Inst.* 35, 415

Arai, H., and Tokimatsu, K. (2004). S-wave velocity profiling by inversion of microtremor H/V spectrum. *Bull. Seismol. Soc. Am.* 94 (1), 53–63. doi:10.1785/0120030028

Bignardi, S., Mantovani, A., and Abu Zeid, N. (2016). OpenHVSR: Imaging the subsurface 2D/3D elastic properties through multiple HVSR modeling and inversion. *Comput. Geosci.* 93, 103–113. doi:10.1016/j.cageo.2016.05.009

Bonilla, L. F., Steidl, J. H., Gariel, J. C., and Archuleta, R. J. (2002). Borehole response studies at the garner valley downhole array, southern California. *Bull. Seismol. Soc. Am.* 92 (8), 3165–3179. doi:10.1785/0120010235

Cui, J. W. (2004). An improved global optimization method and its application to the inversion of surface wave dispersion curves. *Chin. J. Geophys.* 47 (3), 521.

Fäh, D., Kind, F., and Giardini, D. (2001). A theoretical investigation of average H/V ratios. *Geophys. J. Int.* 145 (2), 535–549. doi:10.1046/j.0956-540x.2001.01406.x

García-Jerez, A., Piña-Flores, J., Sánchez-Sesma, F. J., Luzón, F., and Perton, M. (2016). A computer code for forward calculation and inversion of the H/V spectral ratio under the diffuse field assumption. *Comput. Geosciences* 97, 67–78. doi:10.1016/j.cageo.2016.06.016

Gibbs, J. F. (1989). Near-surface P- and S- wave velocities from borehole measurements near Lake Hemet, California. *U.S. Geol. Surv. Open File rept.* 89, 630.

Gouedard, P., Cornou, C., and Roux, P. (2008). Phase-velocity dispersion curves and small scale geophysics using noise correlation slantstack technique. *Geophys. J. Int.* 172 (3), 971–981. doi:10.1111/j.1365-246x.2007.03654.x

Herak, M. (2008). Model HVSR-A Matlab tool to model horizontal-to-vertical spectral ratio of ambient noise. *Comput. Geosci.* 34, 1514–1526. doi:10.1016/j.cageo.2007.07.009

Kawase, H., Mori, Y., and Nagashima, F. (2018). Difference of horizontal-to-vertical spectral ratios of observed earthquakes and microtremors and its application to S-wave velocity inversion based on the diffuse field concept. *Earth Planets Space* 70 (1), 1. doi:10.1186/s40623-017-0766-4

Kawase, H., Sánchez-Sesma, F. J., and Matsushima, S. (2011). The optimal use of Horizontal-to-Vertical spectral ratios of earthquake motions for velocity inversions based on diffuse field theory for plane waves. *Bull. Seismol. Soc. Am.* 101 (5), 2001–2014. doi:10.1785/0120100263

Lawrence, J. F., and Wiens, D. A. (2004). Combined receiver-function and surface wave phase-velocity inversion using a niching genetic algorithm: application to patagonia. *Bull. Seismol. Soc. Am.* 94 (3), 977–987. doi:10.1785/0120030172

Liu, H. P., Boore, D. M., Joyner, W. B., Oppenheimer, D. H., Warrick, R. E., Zhang, W. B., et al. (2000). Comparison of phase velocities from array measurements of Rayleigh waves associated with microtremor and results calculated from borehole shear-wave velocity profiles. *Bull. Seismol. Soc. Am.* 90 (3), 666–678. doi:10.1785/0119980186

Louie, J. N. (2001). Faster, better: Shear-wave velocity to 100 meters depth from refraction microtremor arrays. *Bull. Seismol. Soc. Am.* 91 (2), 347–364. doi:10.1785/0120000098

Mosegaard, K., and Sambridge, M. (2002). Monte Carlo analysis of inverse problems. *Inverse Probl.* 18, 29–54. doi:10.1088/0266-5611/18/3/201

Nagashima, F., Matsushima, S., Kawase, H., Sanchez-Sesma, F. J., Hyakawa, T., Satoh, T., et al. (2014). Application of horizontal-to-vertical spectral ratios of earthquake ground motions to identify subsurface structures at and around the K-net site in tohoku, Japan. *Bull. Seismol. Soc. Am.* 104 (5), 2288–2302. doi:10.1785/0120130219

Nakamura, Y. (1989). A method for dynamic characteristics estimation of subsurface using microtremor on ground surface. *QR Railw. Tech. Res. Inst.* 30 (1), 25

Parolai, S., Picozzi, M., Richwalski, S. M., and Milkereit, C. (2005). Joint inversion of phase velocity dispersion and H/V ratio curves from seismic noise recordings using a genetic algorithm, considering higher modes. *Geophys. Res. Lett.* 32, L01303. doi:10.1029/2004gl021115

Pecker, A., and Mohammadioum, B. (1993). "Garner Valley: analyse statistique de 218 enregistrements seismiques," in *Proceeings of the 3eme colloque national AFPS. France: Saint-Remy-les-Chevreuse*, Paris.

Picozzi, M., and Albarello, D. (2007). Combining genetic and linearized algorithms for a two-step joint inversion of Rayleigh wave dispersion and*H/V*spectral ratio curves. *Geophys. J. Int.* 169, 189–200. doi:10.1111/j.1365-246x.2006.03282.x

Picozzi, M., Parolai, S., and Richwalski, S. M. (2005). Joint inversion of H/V ratios and dispersion curves from seismic noise: estimating the S-wave velocity of bedrock. *Geophys. Res. Lett.* 32 (11), L11308. doi:10.1029/2005gl022878

Pina-Flores, J., Perton, M., Garcia-Jerez, A., Carmona, E., Luzon, F., Molina-Villegas, J. C., et al. (2017). The inversion of spectral ratio H/V in a layered system using the diffuse field assumption (DFA). *Geophys. J. Int.* 208 (1), 577–588.

Rong, M. S., Fu, L. Y., and Li, X. J. (2018). Inversion of site velocity structure using a hybrid optimization algorithm based on HVSRs of accelerograms recorded by a single station. *Chin. J. Geophys.* 61 (3), 938. doi:10.6038/cjg2018L0171

Sánchez-Sesma, F. J., Rodriguez, M., Iturraran-Viveros, U., Luzon, F., Campillo, M., Margerin, L., et al. (2011). A theory for microtremor H/V spectral ratio: application for a layered medium. *Geophys. J. Int.* 186 (1), 221–225. doi:10.1111/j.1365-246x.2011.05064.x

Santos, A. B., Sampaio, E. E. S., and Porsani, M. J. (2005). A robust two-step inversion of complex magnetotelluric apparent resistivity data. *Stud. Geophys. Geod.* 49 (1), 109–125. doi:10.1007/s11200-005-1628-2

Scherbaum, F., Hinzen, K. G., Ohrnberger, M., Ohrnberger, M., and Herrmann, R. B. (2003). Determination of shallow shear wave velocity profiles in the Cologne, Germany area using ambient vibrations. *Geophys. J. Int.* 152 (3), 597–612. doi:10.1046/j.1365-246x.2003.01856.x

Tada, T., Cho, I., and Shinozaki, Y. (2009). New circular-array microtremor techniques to infer love-wave phase velocities. *Bull. Seismol. Soc. Am.* 99 (5), 2912–2926. doi:10.1785/0120090014

Theodulidis, N., Bard, P. Y., Archuleta, R., and Bouchon, M. (1996). Horizontal-to-vertical spectral ratio and geological conditions: the case of Garner valley downhole array in southern california. *Bull. Seismol. Soc. Am.* 86 (2), 306–319. doi:10.1785/bssa0860020306

Wathelet, M. (2005). *Array recordings of ambient vibrations: surface-wave inversion*. Liège: University of Liège. [dissertation/doctor's thesis]. [Belgium].

Wathelet, M., Chatelain, J., Cornou, C., Giulio, G. D., Guillier, B., Ohrnberger, M., et al. (2020). Geopsy: a user-friendly open-source tool set for ambient vibration processing. *Seismol. Res. Lett.* 91 (3), 1878–1889. doi:10.1785/0220190360

Wu, H., Masaki, K., Irikura, K., and Sánchez-Sesma, F. J. (2017). Application of a simplified calculation for full-wave microtremor H/V spectral ratio based on the diffuse field approximation to identify underground velocity structures. *Earth Planets Space* 69, 162. doi:10.1186/s40623-017-0746-8

Yu, J., Han, C., Wang, X., Yuan, J., Fu, X., Zhang, W., et al. (2017). Seismic amplification effect and geological structure: observation and analysis of seismic waves for the yuhuangguan area in front of the longmenshan. *Chin. J. Geophys.* 60 (6), 2239. doi:10.6038/cjg20170617

frontiers | Frontiers in Earth Science

TYPE Original Research
PUBLISHED 29 August 2022
DOI 10.3389/feart.2022.934206

The study of ground motion amplification based on an SMASS array site

Ping Li[1,2,3]* and Kai Zhou[1,2]*

[1]Hebei Key Laboratory of Earthquake Disaster Prevention and Risk Assessment, Sanhe, China, [2]Institute of Disaster Prevention, Sanhe, China, [3]Key Laboratory of Earthquake Engineering and Engineering Vibration, Institute of Engineering Mechanics, China Earthquake Administration, Harbin, China

OPEN ACCESS

EDITED BY
Yefei Ren,
Institute of Engineering Mechanics,
China Earthquake Administration, China

REVIEWED BY
Jingyan Lan,
Guilin University of Technology, China
Bhavesh Pandey,
Sarathy Geotech and Engineering
Services Pvt ltd., India

*CORRESPONDENCE
Ping Li,
chinaliping1981@126.com,
Kai Zhou,
729814560@qq.com

SPECIALTY SECTION
This article was submitted to Structural Geology and Tectonics,
a section of the journal
Frontiers in Earth Science

RECEIVED 02 May 2022
ACCEPTED 01 August 2022
PUBLISHED 29 August 2022

CITATION
Li P and Zhou K (2022), The study of ground motion amplification based on an SMASS array site.
Front. Earth Sci. 10:934206.
doi: 10.3389/feart.2022.934206

There is a consensus in earthquake engineering that different soil structures have significant effects on ground motion. Three main methods can be used to study this issue: theoretical analysis, numerical simulation, and earthquake records analysis. Notably, the combined analysis of strong-motion records and station site information appears to be the most effective and reliable approach. In this study, we used site information from the Seismic Monitoring Array of Site and Structure (SMASS) of the Institute of Disaster Prevention and a record of the earthquake that occurred in Guye, China: a point on the bedrock was considered as reference for studying the amplification effect of the soil structure on ground motion through traditional spectral ratio analysis. Our main conclusions are the following. (1) The SMASS array data indicated that the shallow soil had an amplifying effect on ground motion: the frequency bands amplifying the horizontal ground motion were mainly those between 3.4 and 6.8, 11.3–13, and 15–20.8 Hz, while the frequency bands amplifying the vertical ground vibration were mainly those between 5 and 9.9, 13.5–15.9, and 18.5–21.9 Hz (2) The SMASS array data indicated that the influence of the deep soil on the horizontal ground motion frequency component was more significant than that of vertical ground motion. (3) Overall, the SMASS array site amplified the effects of both the high (3.4–20.8 Hz) and low (0.4–2.2 Hz) frequency components of ground motion with the depth decreases of buried depth; notably, the amplification effect of the high-frequency components grew much faster than that of the low-frequency components. (4) The groundwater table had an amplification effect on the vertical ground motion; therefore, its influence is also important to consider.

KEYWORDS

the seismic site effect, the traditional spectral ratio method, ground motion, amplification, SMASS array site

1 Introduction

Field surveys have shown that the damages caused by a single earthquake can often differ from site to site. For instance (Wood 1908), studied the damage data relative to the 1906 San Francisco (United States) earthquake (Ms 7.8), finding that buildings located on soft soil sites presented much greater damages than those on near hard soil. In the case of the 1923 Kanto (Japan) (Ms 7.9) and 1976 Tangshan (Ms 7.8) earthquake in China, a strong correlation was noted between the damage of buildings (structures) and the thickness of the soil layer (Ohsaki, 1969; Liu and Cha, 1982; Gao and Hu, 1987). Interestingly, the damage rate of high-rise buildings was found to increase with the thickness of the soil layer in the case of the 1967 Venezuela earthquake (Ms 6.5) (Seed et al., 1986; Drake and San, 1993). During the 1985 Mexico earthquake (Ms 8.1), mid-rise buildings in Mexico City (at 400 km from the epicenter) were severely damaged, while low- and high-rise buildings (with more that 23 stories) were not damaged (Seed et al., 1988). Furthermore, the 2008 Wenchuan earthquake (Ms 8.0) produced high intensity anomalies in the Hanyuan County (at 200 km from the epicenter), which were mainly due to the amplification of ground motion by the local soil structure (Bo et al., 2009; Qi et al., 2010; Li et al., 2012). Overall, numerous earthquake damage field surveys and studies have shown that site characteristics can affect ground motion. The main reasons are the following: (1) the occurrence of resonance phenomena caused by the natural frequency of buildings that are similar to the predominant period of the site; (2) the local soil structure acting as a filter, which selectively amplifies or reduces the frequency components of ground motion (when ground motion is transmitted from the bedrock to the surface, its frequency components and amplitude values change significantly). The site amplification effect on ground motion is therefore a fundamental issue in seismology and earthquake engineering, since it has an important theoretical value and practical significance for earthquake fortification.

Ground response analysis methods based on strong motion observation data can be classified as reference or non-reference site methods, according to the availability of rock sites. The earliest reference site method (i.e., the traditional spectral ratio method) was proposed by Borcherdt (1970): the site amplification effect is defined based on the ratio of the Fourier spectrum of strong earthquake records at the soil site to that of the nearby rock site. This method considers the direction of the earthquake source and the path effect when the soil and rock sites are far away from each other. For example, Bonilla et al. (1997) studied the site amplification effect in the intensity anomaly zone of the San Fernando Valley (California) based on the aftershock records of the 1994 Northridge earthquake using this method. Moreover, Wang and Xie (2010) analyzed the Wenchuan main shock records recorded by the Zigong landform array based on the traditional spectral ratio method, finding that the landform and the soil site had a large influence on ground motion. Furthermore, Wang (2011) analyzed the strong earthquake records recorded by the digital strong-motion networks deployed in the Weihe Basin by the traditional spectral ratio method. He found that the Ⅶ-degree-intensity abnormal region distributed along the basin edge (from Baoji to Meixian) and associated with the Wenchuan earthquake resulted from a combination of basin edge effect and ground motion's amplification by the soil site. Based on the main shock records of the Wenchuan earthquake (which were recorded at six stations around the Anning River) and the traditional spectral ratio method, Li et al. (2016) studied the amplification of ground motion at the station sites. A good correlation was identified between the amplification effect of the regional site on ground motion and the engineering geological zoning, and the different engineering geological zones were analyzed in detail. Lan et al. (2020) designed and constructed a centrifugal model test for medium–hard free fields, analyzed the correspondent results based on the traditional spectral ratio method, systematically investigated the nonlinear ground motion effect of the soil layer, and obtained the variation law of the ground motion amplification effect with depth.

So far, due to the limitation of data, most studies have been conducted to analyze the amplification effect of station soil sites by calculating the spectral ratios between the strong motions recorded at those stations and those recorded at nearby rock sites (through the traditional spectral ratio method). However, the soil structure below the surface of each station located in a certain region always includes more than one soil layer; therefore, the site amplification effect observed during the transmission of the ground motion from the bedrock to the surface would derive from the frequency filtering of all these soil layers. Because of the small number of domestic and foreign site soil arrays and strong motion records, studies on the amplification effect of ground motion at different depths below the surface have mostly focused on theoretical analysis and numerical simulation, while only a few studies have been based on actual strong motion records. This study was based on strong motion records collected in Guye (China) by the Seismic Monitoring Array of Site and Structure (SMASS) of the Institute of Disaster Prevention. These records were processed and analyzed by the traditional spectral ratio method, obtaining the spectral ratios for different depths. In this way, it was possible to conduct a systematic and comprehensive study of the amplification effect of ground motion by the soil structure at different bury depths. The obtained results are expected to be useful for future research on site ground motion effects.

2 Materials and methods

2.1 THE SMASS

The SMASS array, which belongs to the Key Laboratory of Seismic Defense and Risk Assessment of the Hebei Province, consists of both local effect and structure response arrays and is

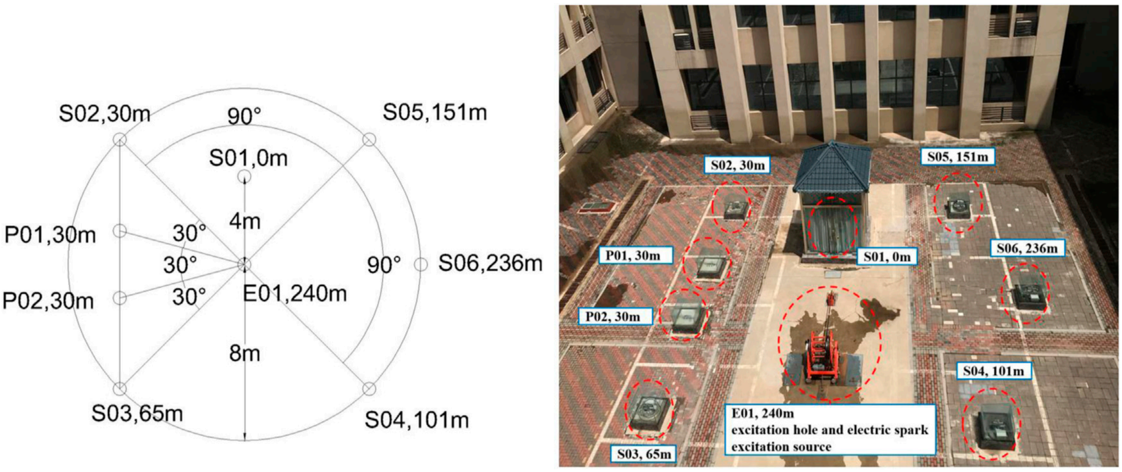

FIGURE 1
Local effect array measurement point plan.

located at a site characterized by a soil layer thickness of ~ 230 m, a flat bedrock surface, and a groundwater table of ~ 20 m. Such configuration is ideal for studying the seismic response of soil sites. Notably, the SMASS array is located within the potential seismic source zone of magnitude 8.0, at ~ 12 km from the macroscopic epicenter of the magnitude 8.0 Sanhe-Pinggu earthquake that occurred on 2 September 1,679. Hence, this site is suitable for strong motion observations in the near field of major earthquakes.

During the construction of the SMASS array, continuous core sampling and logging were carried out. Notably, the deepest drilled hole reached the inside of the bedrock (depth = 240.2 m). Based on the core samples, and according to geological drilling description requirements, we identified a total of 69 soil layers. These were then integrated into 38 layers according to the requirements of site effect observation under strong motion. The P- and S-wave velocities at different depths of the SMASS array were obtained by cross-hole seismic CT, the VSP logging technique, and the single-hole method. The soil samples were subjected to screening, liquid–plastic limit, dynamic triaxial, and resonant column tests to determine the static and dynamic parameters of each soil layer in the array. These data will be useful for future research focusing on the soil layer seismic response.

2.2 Composition and spatial arrangement of SMASS

A total of six measurement points (No. S01-S06) were deployed to monitor strong vibrations in the local effect array. Five of the measurement points (No. S02-S06) was positioned on a concentric circle with a radius of 8 m This measurement points were located in correspondence of observation peep holes: the accelerometers were placed at the bottom of the peep holes (i.e., at 30 m, 65 m, 101 m, 151 m underground and 236 m at the top of the rock layer). Besides, two groundwater pressure measurement points (No. P01 and P02) were located between S02 and S03. The water column was instead 30 m below the observation peep holes: it was possible to monitor the changes of pore water pressure in the saturated stratum. At the same time, an excitation hole 240 m deep was set at the center of a concentric circle. The electric spark excitation source was placed within this circle. The local effect array measurement point plan and the instrument layout table are shown in Figure 1 and Table 1, respectively.

2.3 Strong earthquake records

The SMASS array monitored two strong earthquake records after its installation: the Fengnan earthquake (Ms 4.5), which occurred on 5 December 2019, and the Guye earthquake (Ms 5.1), which occurred on 12 July 2020. The epicenter of the Fengnan earthquake was located at 39.31°N, 118.04°E, (focal depth = 10 km): its epicenter was at ~ 130 km from the SMASS array. Meanwhile, the epicenter of the Guye earthquake was located at 39.78°N, 118.44°E (focal depth = 10 km): its epicenter was at ~ 143 km from the SMASS array. Since the magnitude of the Fengnan earthquake was small and the quality of the strong earthquake records was poor, we chose the records of the Guye earthquake for this study. (Figure 2)

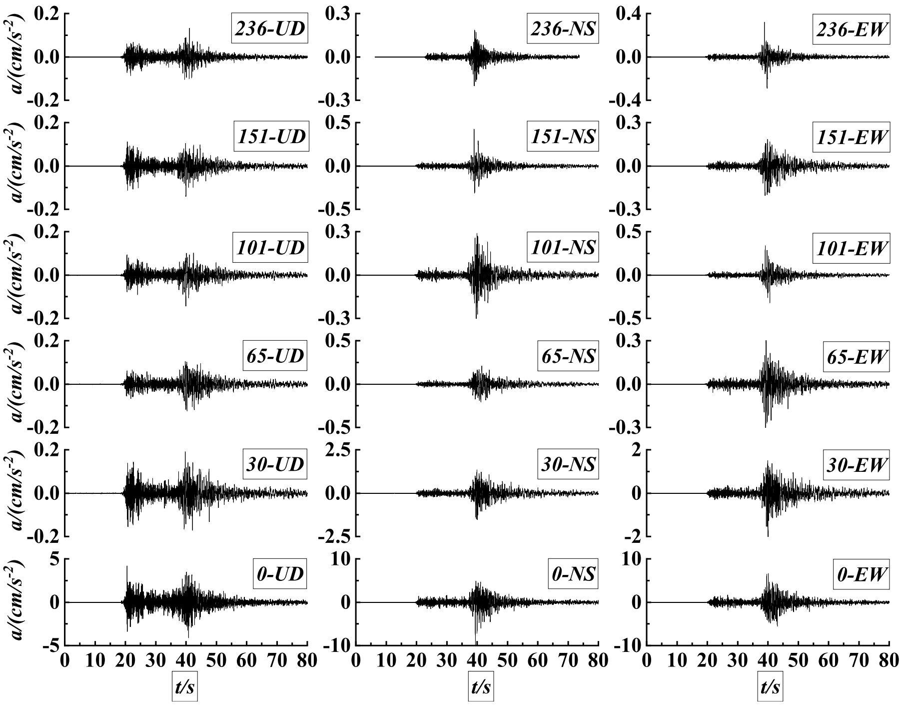

FIGURE 2
Guye strong earthquake acceleration time course.

TABLE 1 Information on the instrument layout.

Measurement point number	Location of the measurement points	Instrument	Soil layer	Shear wave speed (m/s)
S01	Surface (0 m depth)	ES-T three-directional force balance accelerometer	—	—
S02	29.8 m underground	SBEPI shallow-well three-directional accelerometer	Silty clay	409
S03	65.2 m underground	SBEPI shallow-well three-directional accelerometer	Powdered earth	486
S04	101.6 m underground	ES-DH deep-well three- directional accelerometer	Clay	486
S05	151 m underground	ES-DH deep-well three-divisional accelerometer	Powdered sand	563
S06	236.3 m underground	ES-DH deep-well three-divisional accelerometer	Sandstone	800

2.4 Data processing

Only part of the raw strong-motion data collected during the Guye earthquake could be used in the study. In fact, various factors may cause interference in the data from the moment of the motion triggering until the end of the recording of the strong motion seismograph: the direct use of raw strong earthquake records for data analysis, containing false component signals, would greatly affect the results. Processing the original strong-motion recordings was therefore an essential part of the data analysis. Here, we processed the strong-motion record of the Guye earthquake in four main steps: recording discrimination, filtering, smoothing, and horizontal component synthesis.

2.4.1 Strong earthquake record discrimination

According to Zhou (2012), defective records can be mainly classified into "asymmetric waveforms" (Department of Earthquake Damage Prevention, China Earthquake Administration, 2008; Shin et al., 2008; Tobita et al., 2010), "small burr waveforms" (Rajesh Rupakhety, 2010), and "palpus phenomena" (Department of Earthquake Damage Prevention, China Earthquake Administration, 2008).

TABLE 2 Ratios of the strong Guye earthquake records.

Serial number	Depth of tunnel	Direction	PGA (cm/s^{-2})	Left ratio	Right ratio
1	236	UD	0.133	1.032	1.008
2	236	NS	−0.200	1.020	1.040
3	236	EW	0.323	1.018	1.023
4	151	UD	−0.140	1.038	1.007
5	151	NS	0.428	1.027	1.013
6	151	EW	−0.204	1.013	1.007
7	101	UD	−0.142	1.017	1.001
8	101	NS	−0.322	1.011	1.009
9	101	EW	0.341	1.027	1.010
10	65	UD	−0.124	1.005	1.040
11	65	NS	0.210	1.012	1.015
12	65	EW	−0.487	1.028	1.009
13	30	UD	0.191	1.006	1.016
14	30	NS	−1.517	1.006	1.037
15	30	EW	−2.060	1.019	1.016
16	0	UD	4.183	1.071	1.001
17	0	NS	−9.934	1.028	1.004
18	0	EW	6.652	1.001	1.022

In this study, the ratio of the peak acceleration points to the adjacent sampling points (i.e., the case in which this value exceeded 1.1) and the occurrence of dissimilarities were considered discriminant conditions. In the case of complex palpus phenomena, the ratio of the peak acceleration points to the adjacent sampling points is expected to be too large and anisotropy might occur. The ratios of the peak acceleration points to the adjacent sampling points in the Guye strong-motion records are indicated in Table 2: the ratios never exceeded 1.1 and dissimilarity occurred.

2.4.2 Filtering

The main purpose of the filtering step is typically to minimize the interference of noise in strong motion records and, hence, to provide realistic information for any subsequent data analysis. A reasonable cut-off frequency can in fact reduce the interference of noise signals, while an unreasonable one may lead to the loss of original components in the strong motion recordings. A large number of scholars have therefore researched filtering cut-off frequencies. So far, cut-off frequencies have been determined by four types of methods: empirical formulas (Trifunac, 1971; Trifunac and Lee, 1973; Shakal et al., 1988), pseudo-velocity spectra (Syun'itiro et al., 1988), noise spectra (Lee et al., 1982), and the earthquake focus theory (Trifunac and Todorovska, 2001; Shakal et al., 2003). So the filtering cut-off frequencies is selected according to noise spectra (Lee et al., 1982).

We extracted the 17s signal before the arrival of the P-wave of the ground motion recorded by the Guye strong earthquake as a noise spectrum; moreover, the high and low cut-off frequencies were determined by the trend of the original signal Fourier spectrum amplitude and by the intersection position of the original signal Fourier spectrum with the noise signal Fourier spectrum. In the low-frequency part of the record, since the noise signal lasted 17 s, the low cut-off frequency needed to be greater than 0.06 Hz: We found that the low-frequency part of the noise spectrum amplitude was always lower than the signal spectrum amplitude. Furthermore, the signal spectrum amplitude increased with frequency over 0.2 Hz: 0.2 Hz was identified as the low cut-off frequency. We found that the signal and noise Fourier spectra began to intersect at ~ 20–30 Hz in the high-frequency part, after this point, the frequency component of the original signal may have been contaminated by the noise signal, and the original signal spectrum amplitude increased with frequency. Therefore, 25 Hz was taken as the high cut-off frequency. The original signal was filtered by using the Butteworth filter (of the fourth order) and the Fourier spectrum of the original signal was compared with that of the filtered signal. The peak acceleration values of the ground motion time history at different depths were given after filtering (Table 3).

2.4.3 Smoothing treatment

After the baseline correction and filtering of the strong motion records, we observed a high number of burrs in the Fourier transformed spectra (Figures 3–5). In this case and should the records be used directly for the calculation of the

TABLE 3 Peak acceleration in n relation to depth of tunnel.

Depth of tunnel (m)	Vertical peak acceleration (cm/s^{-2})	North–south peak acceleration (cm/s^{-2})	East–west peak acceleration (cm/s^{-2})
236	0.14	0.20	0.32
151	0.13	0.40	0.20
101	0.15	0.30	0.34
65	0.12	0.22	0.48
30	0.18	1.57	2.06
0	4.17	9.29	6.56

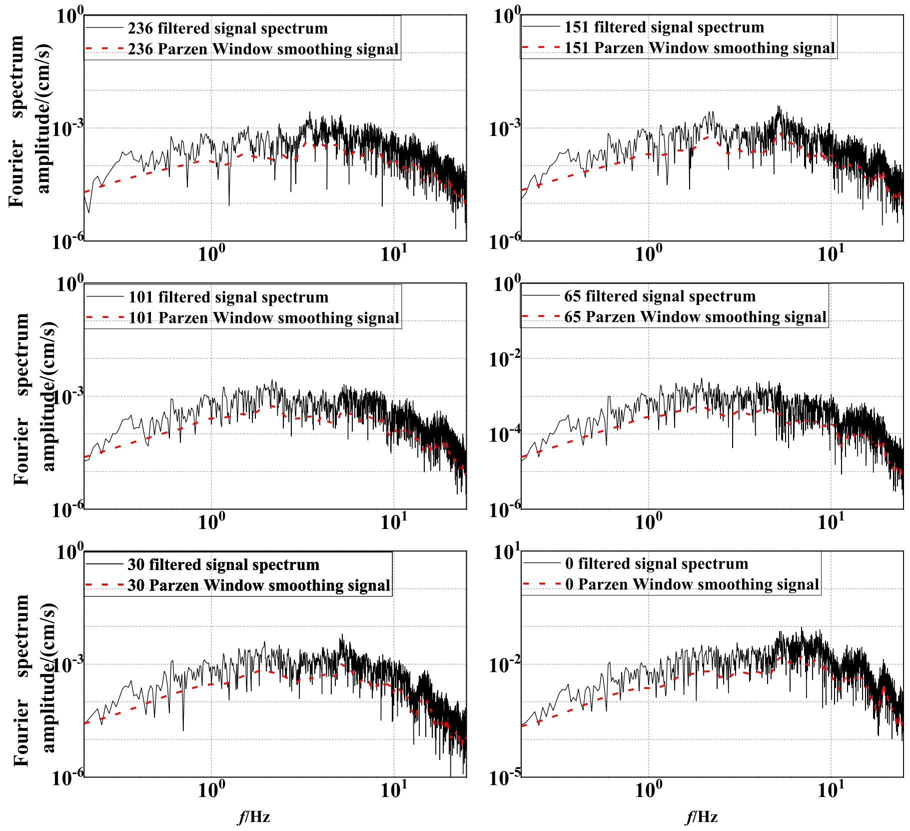

FIGURE 3
Guye strong motion record smoothing effects (vertical direction).

spectral ratio without previous smoothing, it would be difficult to determine the frequency band and energy distributions. This, in turn, would increase the difficulty of identifying the predominant frequency at the study site. Two types of burr processing methods are generally applied to strong motion recording data: (1) the addition of a smoothing window in the time domain and (2) the addition of a smoothing window in the frequency domain (Osaki, 2008). In study, the Parzen window and K-window length of 0.8 Hz (Konno and Ohmachi, 1995) were used to smooth the Fourier spectrum of the Guye strong motion records. Through several tests and comparisons, we found that the best smoothing effect was obtained for a Pazen window length of 0.8 Hz: in this case, the burrs were effectively removed and the error was within a reasonable range. Based on these results, we decided to apply a Parzen window with a window length of 0.8 Hz to smooth the Fourier spectra of the filtered strong motion records: the correspondent smoothing effects are shown in Figures 3–5.

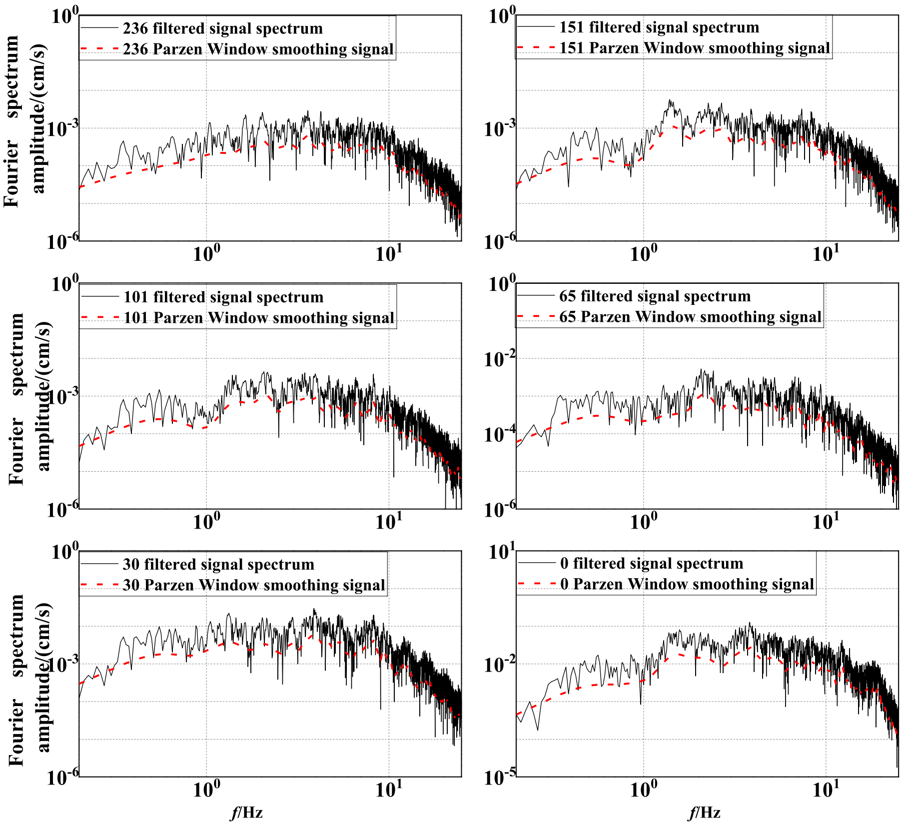

FIGURE 4
Guye strong motion record smoothing effects (north–south direction).

2.4.4 Synthesis of the horizontal components

If the direction of the strong motion seismograph is not the same as the actual direction during the placement, a new horizontal component increment may be generated. Here, we focused on the amplification effect of soil structure on ground motion. To improve the accuracy of our predictions, the strong motion records in the east–west direction were synthesized with those in the north–south direction before obtaining the spectral ratio; notably, only the amplification effects of the soil structure on the horizontal and vertical ground motions were considered. Eq. (1) (Yu, 2003) represents the synthesis formula, where $H(Ps, f)$ is the horizontal Fourier spectrum, $N(Ps, f)$ is the north–south direction Fourier spectrum, and $E(Ps, f)$ is the east–west direction Fourier spectrum:

$$H(Ps, f) = \sqrt{N^2(Ps, f) + E^2(Ps, f)} \tag{1}$$

2.4.5 Analysis methods

Ground motion is mainly affected by three factors during its propagation: the source effect $E(f)$, the path effect $P(f)$, and the site effect $S(f)$. The relationship between these factors is explained by Eq. 2. The traditional spectral ratio method considers a rock site station near the site station: the ground motions recorded by the two stations are expected to have the same source effect and almost the same path effect during the earthquake occurrence; moreover, these ground motions can be spectrally compared to obtain the site effect (if the distance between the two stations is far, the path effect needs to be considered). In this study, the SMASS array was 143 km away from the epicenter and the six observation points were arranged in concentric circles with radiuses of 8 m. The distance between each two observation points was expected to have the same epicenter and path effects compared with the hypocenter distance.

Wang Haiyun (2011) found that the interference of the upward and downward wave fields caused by different velocity interfaces at the surface and within the soil body can lead to the so-called “spectral hole” phenomenon. Therefore, based on the concept of stemming function proposed by (Steidl 1996). In their study, further analysis is carried out to obtain the site response at the surface or at a certain depth in the ground by multiplying the stemming function with the Fourier spectral ratio. The coherence function can be expressed by the equation

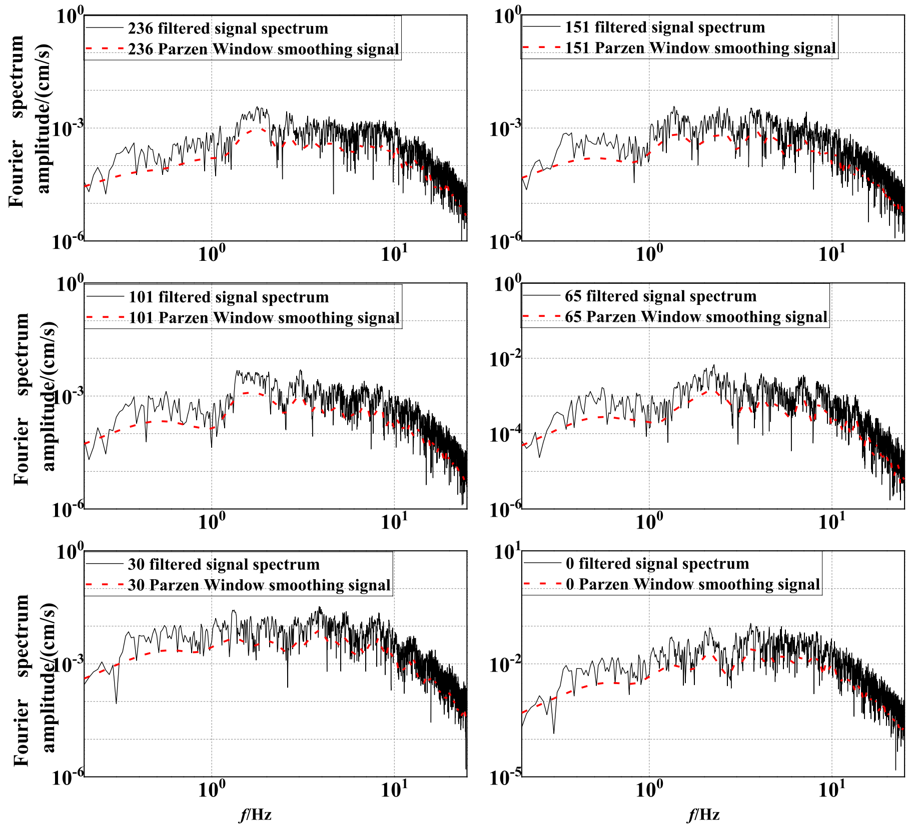

FIGURE 5
Guye strong motion record smoothing effects (east–west direction).

$$r_{12}(f) = \frac{|S_{12}(f)|}{\sqrt{s_{11}(f)s_{22}f}} \tag{2}$$

$S_{12}(f)$ is the ground vibration inter-spectrum at the depth of d1 and bedrock respectively, $s_{11}(f)$ is the ground vibration autospectrum at the surface or a depth below ground, $s_{22}(f)$ is the ground vibration autospectrum at bedrock.

Therefore, we used the traditional spectral ratio method to determine the site effect: the strong motion records observed at the five measurement points were compared with those observed at the bedrock measurement point.

$$O(f) = E(f)*P(f)*S(f) \tag{3}$$

As a matter of fact, a Fourier transformation consists in the conversion of a signal from the time domain to the frequency domain. A Fourier spectrum, which can be described as a simple harmonic wave frequency in horizontal coordinates and as a simple harmonic wave amplitude in vertical coordinates, can reflect the frequency spectral characteristics of a ground motion time history. The horizontal coordinates of the response spectrum represent the period, while the vertical coordinates represent the maximum response amplitude generated by different single-degree-of-freedom systems under the excitation of a ground motion time history, which can also reflect the frequency spectral characteristics of the ground motion time history. Luo et al. (2019) deduced that the Fourier and zero-damped velocity response spectra can both represent the energy in a vibrator system. The response and Fourier spectra are similar in which they can both record strong motions under the neglect of damping; moreover, the Fourier spectrum curve is always included in the velocity response spectrum. Therefore, we decided to use the spectral ratio of the Fourier spectrum to the velocity response spectrum with zero damping for our contrast, and observe whether the two spectral ratios agree.

3 Results

In this study, the traditional spectral ratio method was used to analyze the site amplification effect of the SMASS site array. The bedrock (depth = 236 m) was taken as the reference site:

TABLE 4 Amplification factors and corresponding amplification frequencies observed at different bury depths of the SMASS table array in the Guye strong motion records (Fourier spectrum ratios).

Bury depth (m)	Horizontal		Vertical	
	Fourier spectrum ratio		Fourier spectrum ratio	
	Frequency (Hz)	Spectral ratio	Frequency (Hz)	Spectral ratio
151	1.3	2.95	2.2	4.10
101	3.1	2.96	2.2	3.87
65	2.3	4.19	1.9	3.29
30	4.0	24.11	2.2	4.18
0	18.5	84.22	14.4	113.54

TABLE 5 Amplification factors and corresponding amplification frequencies observed at different bury depths of the SMASS table array in the Guye strong motion records (response spectrum ratios).

Bury depth (m)	Horizontal response spectrum ratio		Vertical response spectrum ratio	
	Frequency (Hz)	Spectral ratio	Frequency (Hz)	Spectral ratio
151	1.4	4.34	2.2	9.81
101	3.1	3.81	2.2	9.77
65	2.2	5.26	2.2	8.81
30	3.9	35.38	2.0	11.28
0	19.2	112.03	8.6	160.04

the Fourier and response spectra of strong motion records at different depths were compared with those in correspondence of the bedrock to study the variation of ground motion in different soil structures. The correspondent results are shown in and Tables 4, 5.

Figures 6, 7 show how most of the Fourier spectral ratio curves were located between the reaction spectral ratio curves and had similar shapes (Luo et al., 2019); therefore, the reaction spectrum with zero damping was considered to be feasible for our spectral ratio analyses. The data in Tables 4, 5 show instead how, during the diffusion of the horizontal ground motion from the bedrock to 65 m below ground, the spectral ratio first increased and then fluctuated within a certain range; furthermore, as the horizontal ground motion continued to diffuse upward, the spectral ratio increased significantly. Finally, from 30 m below ground to the surface, the growth rate of the spectral ratio increased further. The changes in spectral ratio during the diffusion of the vertical ground motion from the bedrock upward were slightly different from that just described: from the bedrock to 30 m below ground, there were no obvious variations. However, from 30 m below ground to the surface, the spectrum ratio increased sharply and its growth rate was larger than that of the horizontal ground motion within the same depth interval.

Figure 6 shows how the amplification effect of the soil layer on the horizontal ground motion was different at different depths. When the horizontal ground motion diffused from the bedrock to 151 m underground, the ground motion amplification by the soil layer structure was mainly concentrated around 1.3 and 2.1 Hz, and the spectral ratio was maximum at 1.3 Hz. Meanwhile, when the horizontal ground motion diffused from 151 to 101 m underground, the magnitude of the spectral ratio did not change significantly, but the frequency corresponding to the maximum spectral ratio changed from 1.3 to 3.1 Hz. When the horizontal ground motion diffused instead from 101 to 65 m below ground, the peak at 1.04 Hz disappeared (suggesting that the soil structure between 151 and 101 m below ground should have selectively filtered the ground vibration frequency components and amplified the frequencies around 0.5 and 2.3 Hz) and the spectral ratio reached its maximum at 2.3 Hz. When the horizontal ground motion diffused from 65 to 30 m

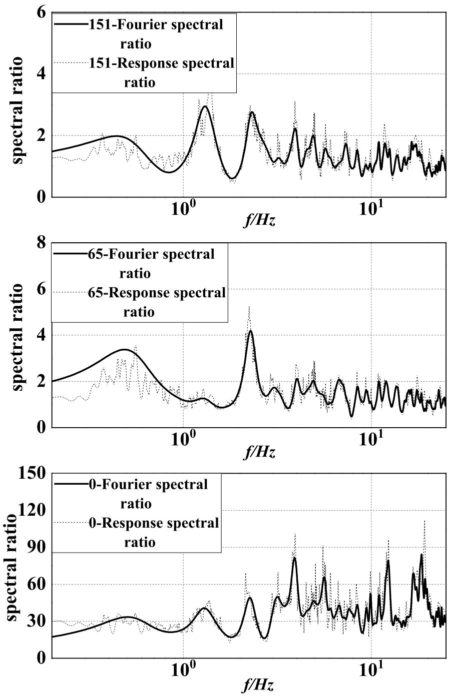

FIGURE 6
Fourier and response spectral ratios in the horizontal direction (Guye strong motion records).

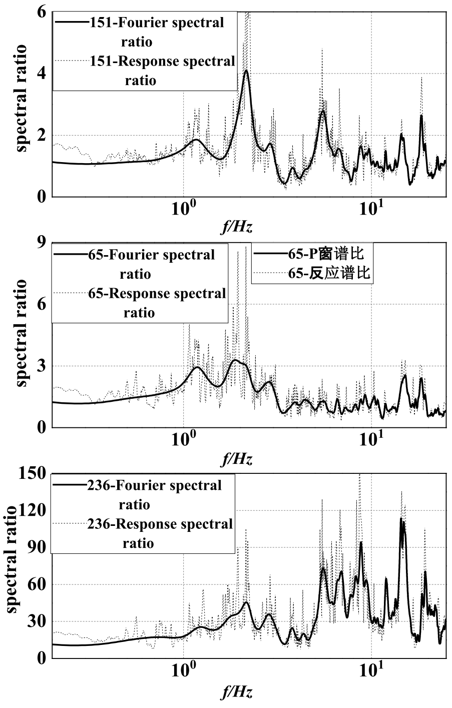

FIGURE 7
Fourier and response spectral ratios in the vertical direction (Guye strong motion records).

underground, the spectral ratio increased significantly and the frequency of the maximum spectral ratio increased, with small peaks increasing after 4 Hz. Finally, when the horizontal ground motion diffused from 30 m underground to the surface, the correspondent soil layer amplified both the low- and high-frequency components of ground motion; however, the amplification of the former was less obvious than that of the latter, and the spectral ratio was maximum at a frequency of 18.5 Hz.

As shown in Figure 7, the amplification of the vertical ground motion occurred mainly around 2.2, 5.5, and 18 Hz for the soil layer structure between the bedrock and 151 m underground and the spectral ratio was maximum at 2.2 Hz. As the ground motion continued to diffuse upward, the soil layer between 151 and 101 m underground selectively filtered the vertical ground motion frequency components, resulting in a decrease of the spectral ratio at 5.5 Hz; meanwhile, the frequency corresponding to the maximum spectral ratio did not change (was still 2.2 Hz). When the vertical ground motion reached 65 m underground, the frequency band near 1.9 Hz gradually broadened and the frequency corresponding to the maximum spectral ratio changed from 2.2 to 1.9 Hz, while the maximum spectral ratio and the peak acceleration did not change significantly. When the vertical ground motion reached 30 m underground, the small peak of the high-frequency components after 4 Hz started to increase and the frequency corresponding to the maximum spectral ratio increased from 1.9 to 2.2 Hz, while the spectral ratio did not change significantly. Finally, when the vertical ground motion diffused from 30 m underground to the surface, the spectral ratio increased rapidly and the frequency corresponding to the maximum spectral ratio increased, reaching 14.4 Hz at the surface.

4 Conclusion

The main findings are summarized below.

1) The soil layer structure amplified the ground motion in the SMASS array site mainly in correspondence of the shallow soil layer (above 30 m depth). In the deeper soil layer, the amplification effect occurred but it was not obvious: the amplification effect increased with the decrease of the bury depth.
2) The amplification effect of the soil layers on the horizontal ground motion changed with depth. In fact, the amplification effect of the soil layer between the bedrock and 151 m underground was mainly concentrated at 1.3 and 2.1 Hz (maximum spectral ratio at 1.3 Hz); meanwhile, at 151 m underground the maximum spectral ratio corresponded to a remarkable frequency change (from 1.3 to 3.1 Hz). At 65 m underground, the spectral ratio reached its maximum at 2.3 Hz, while the small spikes started to increase at frequencies >4 Hz at 30 m underground. Finally, the soil layer between 30 m underground and the surface amplified both the low- and high-frequency components of ground motion, but the amplification effect on the former components was less obvious than that on the latter components, and the maximum spectral ratio corresponded to a frequency of 18.5 Hz.
3) An amplification effect of the SMASS array site on both the high- and low-frequency components of ground motion was noted; however, when the bury depth was deeper, the amplification effect on the high-frequency components of ground motion was not obvious and the amplification frequency band was mainly concentrated between ~ 1–3 Hz. With the decrease of the bury depth, the amplification of the low-frequency component of the band gradually grew; notably, the amplification of the high-frequency component grew much faster than that of the low-frequency components from 4 to 18.5 Hz.
4) From the SMASS array spectral ratio results, we infer that the groundwater level can have an amplifying effect on the peak vertical ground vibration acceleration; however, further studies are needed to determine the quantitative effects.

5 Discussion

We investigated the amplification of ground motion by the traditional spectral ratio method and based on the SMASS array, finding that the source effect and path effect were negligible: the only factor causing changes in ground motion is the effect of different soil structures during its diffusion.

5.1 Influence of soil structure

As the ground motion diffused from the bedrock upward, different soil layer structures filtered its frequency components in different ways and selectively amplified the components having frequencies similar to their own.

1) Our results clearly indicated that the soil layer structure between the bedrock surface and 151 m underground amplified both the horizontal and vertical components of ground motion; meanwhile, the soil structure between 151 and 65 m underground affected the transmission of ground motion, but the spectral ratios varied within a restricted range and this variation was not obvious.
2) The spectral ratio results indicate that the amplification effect of the deep soil layer was not obvious during the upward diffusion of the horizontal ground motion from the bedrock side: the spectral ratio and the peak ground acceleration of ground motion started to increase

significantly only when the horizontal ground motion diffused upward from 65 m underground. The shear wave velocity was 486 m/s at 65 m underground, suggesting that at this depth the soil changed from hard to soft and explaining its increasing amplifying effect on the horizontal ground motion in the upward direction.

3) By comparing the spectral ratios of the horizontal and vertical ground motions at 151, 101, and 65 m underground, we noticed the following: the frequencies corresponding to the maximum spectral ratios in the case of the horizontal ground motions were 1.3, 3.1, and 2.3 Hz, respectively, while those in the case of the vertical ground motions were 2.2, 2.2, and 1.9 Hz, respectively. Moreover, the shape changes of the horizontal ground motion spectral ratios were larger than those of the vertical ground motion spectral ratios. Overall, these results indicate that changes in the soil layer structure had a greater influence on the horizontal, rather than on the vertical ground motion frequency components.
4) When the horizontal and vertical ground motions diffused upward from 65 m underground, the maximum spectral ratio corresponded to the superior frequency and the small spikes in the high-frequency part started to increase. This indicates that the shallow soil layer of the SMASS array site had a greater influence on the amplification of ground shaking, and that the amplification of the high-frequency component of ground motion was stronger than that of the low-frequency component.

5.2 Influence of the groundwater level on the vertical ground vibration

The above results clearly indicate that the soil layer structure influenced both the horizontal and vertical components of ground motion, although it had a greater influence on the former. When the horizontal ground motion diffused upward from 65 to 30 m underground, the spectral ratio and the PGA started to increase significantly, and the frequency corresponding to the maximum spectral ratio increased. Meanwhile, the frequency corresponding to the maximum spectral ratio of vertical ground motion also increased, but this change was not obvious and the spectral ratio and the PGA hardly varied. Chen et al. conducted a 3D seismic response analysis of a soft soil site in Shanghai (Chen et al., 2011). By considering various groundwater level depths, they found that the amplification effect of the horizontal peak acceleration increased with the rise of the groundwater level, although this variation was not significant; at the same time, any changes in the depth of the groundwater level had a significant effect on the amplification coefficient of the vertical peak acceleration. In this study, we considered an SMASS array with a perennial groundwater level at ~ 20 m depth. When the vertical ground motion diffused upward from the bedrock surface to 30 m underground, the maximum spectral ratio did not change significantly; however, when it diffused upward from 30 m underground, the maximum spectral ratio and the PGA increased significantly (the growth rate in this case being greater than that of the horizontal ground shaking). On this basis, we infer that the groundwater level should have had a great influence on the maximum spectral ratio and on the PGA of the vertical ground motion.

5.3 Considerations on the application of seismic response analysis methods to the investigation of soil layers

Recent research on the amplification effect of ground motion at different depths below the surface has been mostly based on theoretical analysis and numerical simulation. Unfortunately, the low number of arrays and strong motion records has led to a scarcity of works analysis methods aimed at testing the soil seismic response under actual strong earthquake records. The shear wave velocity is an indication of the softness and stiffness of the soil layer to a certain extent. The results of our analyses suggest that the soil layer with shear wave velocity <486 m/s significantly amplified the horizontal ground motion. In this case, it is reasonable to choose the soil layer with shear wave velocity = 500 m/s as input interface for obtaining the soil layer seismic response. The results obtained from these calculations can then be applied to the construction of anti-seismic building structures. However, for important or can lead to secondary disaster of the building (structure), for safety reasons should be specifically studied to determine the input interface.

5.3.1 Selection of the vertical ground motion parameters

The ground motions generated during earthquakes are complex and multi-dimensional. In particular, vertical ground motions are sometimes very strong and can cause serious damages to buildings. In the "Code for Seismic Design of Buildings" (GB50011-2010), the vertical earthquake influence coefficient is usually taken as 65% of the maximum horizontal earthquake influence coefficient for determining the vertical seismic action. From the analyses, we found that the peak acceleration of the vertical ground motion in correspondence of the bedrock was much smaller than the correspondent peak acceleration of the horizontal ground motion; moreover, when the ground motion diffused to the shallow soil layer, the growth rate of the peak acceleration of the vertical ground motion was much larger than that of the horizontal ground motion due to the influence of the groundwater level. Finally, when the ground motion reached the surface, the peak acceleration of the vertical ground motion was close to that of the horizontal ground motion: the value of vertical ground motion was low, suggesting that it should be increased for different structural.

Data availability statement

The original contributions presented in the study are included in the article/supplementary material, further inquiries can be directed to the corresponding authors.

Author contributions

PL was involved in writing the manuscript. KZ contributed to data analysis and paper writing. PL and KZ read and approved the final manuscript.

Funding

This study is funded by the China Earthquake Administration Spark Project of Earthquake Science and Technology (XH204401).

Acknowledgments

The authors thank the SMASS, Hebei Key Laboratory of Earthquake Disaster Prevention and Risk Assessment for providing data.

Conflict of interest

The authors declare that the research was conducted in the absence of any commercial or financial relationships that could be construed as a potential conflict of interest.

Publisher's note

References

Aoi, S., Kunugi, T., and Fujiwara, H. (2008). Trampoline effect in extreme ground motion. *Science* 322 (5902), 727–730. doi:10.1126/science.1163113

Bo, J. S., Qi, W. H., Liu, H. S., Liu, B., Liu, D. D., and Sun, Y. W. (2009). Abnormality of seismic intensity in Hanyuan during Wenchuan earthquake. *Earthq. Eng. Eng. Dyn.* 29 (06), 53–64.

Bonilla, L. F., Steidl, J. H., Lindley, G. T., Tumarkin, A. G., and Ar-chuleta, R. J. (1997). Site amplification in the San Fernando Valley, California: Variability of site-effect estimation using the *S*-wave, coda, and *H/V* methods. *Bull. Seismol. Soc. Am.* 87 (3), 710–730. doi:10.1785/bssa0870030710

Borcherdt, R. D. (1970). Effects of local geology on ground motion near San Francisco Bay. *Bull. Seism. Soc. Am.* 60 (1), 29–61.

Chen, Q. S., Gao, G. Y., and He, J. F. (2011). Three-dimensional nonlinear analysis of seismic ground response of soft soil sites in Shanghai. *Rock. Soil. Mech.* 32 (11), 3461–3467. doi:10.3969/j.issn.1000-7598.2011.11.043

Department of Earthquake Damage Prevention, China Earthquake Administration (2008). *Report on strong earthquake records in China episode 12 volume 1 uncorrected acceleration records of the wenchuan 8.0 magnitude earthquake.* Germany: Earthquake Press.

Drake, L. A., and San, C. O. (1993). Germany: St. Augustine. Ground motion and building damage: Caracas 29 july 1967 and Mexico city, 19 september 1985 Proceedings of the Caribbean Conference on Natural Hazard: Volcanoes, Earthquakes, Windstorms, Floods.

Gao, Z. H., and Hu, B. R. (1987). The influence of local site conditions on earthquake damage——analysis of earthquake damage in fengrun county during the tangshan earthquake. *North. China. Earthq. Sci.* 5 (S1), 208–213.

Ji, K., Ren, Y. F., and Wen, R. Z. (2017). Review on site classification with spectra ratio method. *World. Earthq. Eng.* 33 (01), 91–99.

Ji, K., Wen, R. Z., Ren, Y. F., and Wang, H. W. (2014). Analysis of site characteristics based on strong-motion records of Lushan aftershocks, Earthquake. *Eng. Eng. Dyn.* 34 (5), 35–42. doi:10.13197/j.eeev.2014.05.35.jik.005

Konno, K., and Ohmachi, T. (1995). A smoothing function suitable for estimation of amplification factor of the surface ground from microtremor and its application. *Dob. Gakkai Ronbunshu*, 247–259. doi:10.2208/jscej.1995.525_247

Lan, J. Y., Song, X. J., Liu, J., and Wang, Y. W. (2020). Study on the variation ground motion amplification effect of medium-hard free fields with depth under earthquake action. *Chin. J. Rock Mech. Eng.* 39 (S2), 3696–3705. doi:10.13722/j.cnki.jrme.2019.1249

Lee, V. W., Trifunac, M. D., and Amini, A. (1982). Noise in earthquake accelerograms. *J. Engrg. Mech. Div.* 108 (6), 1121–1129. doi:10.1061/jmcea3.0002894

Li, P., Bo, J. S., Li, X. B., and Xiao, R. J. (2016). Amplification effect of soil sites on ground motion in Anning River valley and Qionghai Lake area. *Chin. J. Geotech. Eng.* 38 (02), 362–369. doi:10.11779/CJGE201602022

Li, P., Bo, J. S., Qi, W. H., Liu, D. D., and Xiao, R. J. (2012). Effects of soil structure on abnormal intensity in Hanyuan old town. *Acta Seismol. Sin.* 34 (06), 851–857.

Liu, S. K., and Cha, X. G. (1982). The influence of site conditions on earthquake damage in the high intensity area of the Tangshan earthquake. *China Earthq. Eng. J.* 4 (02), 67–74.

Luo, G. C., Li, X. J., Fu, L., and Wang, Y. S. (2019). Study on nonlinearity of site effect with the HVSR spectral ratio. *J. Seismol. Res.* 42 (04), 546–554+650.

Ministry of Housing and Urban-Rural Development of the People's Republic of China (2010). *GB50011-2010 code for seismic Design of buildings*. Beijing: Building Industry Press.

Ohsaki, Y. (1969). *Proceedings of the seventh IC SMFE specialty session on soil dynamics*. Mexico: Building Industry Press.The effects of local soil conditions upon earthquake damage.

Osaki, Y. (2008). *Introduction to spectral analysis of ground motion*. Beijing: Seismological Press.

Qi, W. H., Bo, J. S., Liu, X. Guo D. D., and Liu, Q. B. (2010). Preliminary study on a special site in the Wenchuan earthquake. *Earthq. Eng. Eng. Dyn.* 30 (3), 53–58. doi:10.1785/0120090132

Rupakhety, R. (2010). *Contemporary issues in earthquake engineering research: Processing of accelerometric data,modelling of inelastic structural response, and quantification of near_fault effects*. Reykjavik: Faculty of Civil and Environmental Engineering School of Engineering and Natural Sciences University of Iceland.

Seed, H. B., Romo, M. P., Sun, J. I., Jaime, A., and Lysmer, J. (1988). The Mexico earthquake of September 19, 1985- Relationships between soil conditions and earthquake ground motions. *Earthq. Spectra* 4 (4), 687–729. doi:10.1193/1.1585498

Seed, H. B., Wong, R. T., Idriss, I. M., and Tokimatsu, K. (1986). Moduli and damping factors for dynamic analyses of Cohesionless soils. *J. Geotech. Engrg.* 112 (11), 1016–1032. doi:10.1061/(asce)0733-9410(1986)112

Shakal, A. F., Huang, M. J., and Cao, T. Q. (1988). *Proceedings of the second workshop on processing of seismic strong motion records*. Tokyo: Springer. Processing of 9wcee strong motion workshop test records by CSMIP.

Shakal, A. F., Huang, M. J., and Graizer, V. M. (2003). 58 Strong-motion data processing. *Int. Geophys.* 81 (3), 967–981. doi:10.1016/S0074-6142(03)80172-9

Steidl, J. H., Tumarkin, A. G., and Archuleta, A. J. (1996). What is a reference site? *Bull. Seismol. Soc. Am.* 86 (6), 1733–1748. doi:10.1785/bssa0860061733

Syun'itiro, O., Tokiharu, O., and Shigeto, H. (1988). *Data processing method for acceleration records and its application results, Processings of the second workshop on processing of seismic strong motion records*. Tokyo: Springer, 119–135.

Tobita, T., Iai, S., and Iwata, T. (2010). Numerical analysis of near-field asymmetric vertical motion. *Bull. Seismol. Soc. Am.* 100 (4), 1456–1469. doi:10.1785/0120090301

Trifunac, M. D. (1971). Zero baseline correction of strong-motion accelerograms. *Bull. Seismol. Soc. Am.* 61 (5), 1201–1211. doi:10.1785/bssa0610051201

Trifunac, M. D., and Lee, V. W. (1973). *Routine computer processing of strong-motion accelerograms*. Pasadena: Earthquake Engineering Research Laboratory. Report EERL 73-03.

Trifunac, M. D., and Todorovska, M. I. (2001). A note on the useable dynamic range of accelerographs recording translation. *Soil Dyn. Earthq. Eng.* 21, 275–286. doi:10.1016/s0267-7261(01)00014-8

Wang, H. Y. (2011). Amplication effects of soil sites on ground motion in the Weihe basin. *Chin. J. Geophys.* 54 (01), 137–150. doi:10.3969/j.issn.0001-5733.2011.01.015

Wang, H. Y., and Xie, L. L. (2010). Effects of topography on ground motion in the Xishan park, Zigong city. *Chin. J. Geophys.* 53 (7), 1631–1638. doi:10.3969/j.issn.0001-5733.2010.07.014

Wood, H. O. (1908). *Distribution of apparent intensity in san Francisco, report of the state earthquake commission*. Geophysical: Carnegie Institute of Washington.

Yu, J. (2003). The choice of reference sites for seismic ground amplification analyses: Case study at parkway, New Zealand. *Bull. Seismol. Soc. Am.* 93 (2), 713–723. doi:10.1785/0120010289

Zhou, B. F. (2012). *Some key issues on the strong motion observation*. China Earthquake Administration: Institute of Engineering Mechanics.

frontiers | Frontiers in Earth Science

TYPE Methods
PUBLISHED 22 December 2022
DOI 10.3389/feart.2022.1056583

OPEN ACCESS

EDITED BY
Kun Ji,
Hohai University, China

REVIEWED BY
Qingzhi Hou,
Tianjin University, China
Maryam Khosravi,
Isfahan University of Technology, Iran

*CORRESPONDENCE
Xiaojun Li,
64482261@qq.com,
beerli@vip.sina.com

SPECIALTY SECTION
This article was submitted to Structural Geology and Tectonics, a section of the journal Frontiers in Earth Science

RECEIVED 29 September 2022
ACCEPTED 08 December 2022
PUBLISHED 22 December 2022

CITATION
Yang Y, Li X, Rong M and Yang Z (2022), Strategy for eliminating high-frequency instability caused by multi-transmitting boundary in numerical simulation of seismic site effect.
Front. Earth Sci. 10:1056583.
doi: 10.3389/feart.2022.1056583

Strategy for eliminating high-frequency instability caused by multi-transmitting boundary in numerical simulation of seismic site effect

Yu Yang[1], Xiaojun Li[2,3]*, Mianshui Rong[2] and Zhibo Yang[1]

[1]Nuclear and Radiation Safety Center MEE, Beijing, China, [2]Key Laboratory of Urban Security and Disaster Engineering of Ministry of Education, Beijing University of Technology, Beijing, China, [3]Institute of Geophysics, China Earthquake Administration, Beijing, China

A multi-transmitting boundary is a local artificial boundary widely used for numerically simulating seismic site effects. However, similar to other artificial boundaries, the multi-transmitting boundary has instability issue in numerical simulation. Based on the concept of multi-directional transmitting formula, a strategy for eliminating the high-frequency instability of the transmitting boundary is studied and a measure is proposed using a neighbour node of a boundary node to realize smoothing filtering. The proposed measure is verified through numerical analysis. The smoothing coefficient chosen for this measure provides a reference for deriving the coefficient of multidirectional transmitting formula in the time domain.

KEYWORDS

seismic site effect, wave propagating simulation, multi-transmitting boundary, high-frequency instability, multi-direction transmitting formula

1 Introduction

The influence of local topography on ground motion is fundamentally a wave scattering problem. Hence, simulating near-field waves is crucial to the numerical simulation of seismic site effects. The accuracy of near-field wave numerical simulations directly depends on whether artificial boundary conditions can accurately simulate an infinite domain. Since the 1960s, several achievements have been attained in the study of artificial boundaries (Liao, 1984, 2002; Wolf, 1988; Givoli, 1992; Cheng et al., 1995; Wolf, 1996; Xu et al., 2018; Xing et al., 2021). Among the established artificial boundary conditions, the multi-transmitting boundary (Liao et al., 1984a; Liao et al., 1984b; Xing et al., 2017a; Xing et al., 2017b) has a wide application range and high precision. Moreover, combined with the finite element method, the multi-transmitting boundary can facilitate decoupling.

Similar to other local artificial boundaries, the transmitting boundary's computational stability is a key issue that requires further study. High-frequency oscillation and low-frequency drift are two types of numerical instability phenomena that may occur when the multi-transmission boundary is combined with the finite element method (Li et al., 2012; Yang et al., 2014). In this paper, a strategy for eliminating the instability of high-frequency oscillations of the multi-transmission boundary is suggested.

Smoothing factor filtering is an effective measure for restraining high-frequency instability of transmission boundary (Liao et al., 1989; Liao et al., 1992; Liao et al., 2002). Another measure to restrain high-frequency instability is utilizing the energy consumption characteristics of explicit integration scheme. This measure inhibits high-frequency instability by increasing damping in proportion to strain velocity (Li et al., 1992; Li et al., 2007; Tang et al., 2010). Modifying the internal node motion equation and stiffness of the finite element is also an effective measure for stabilizing the high-frequency of multi-transmission boundary (Xie et al., 2012; Zhang et al., 2021).

This paper proposes an improved measure for existing strategies to restrain high-frequency instability using a smoothing factor. When considering only the high-frequency error oscillation perpendicular to the artificial boundary and ignoring the high-frequency oscillation parallel to the artificial boundary, the current method only smooths the points perpendicular to the boundary. Based on the concept of a multidirectional transmitting formula, this paper proposes smoothing the points on the artificial boundary to restrain high-frequency instability.

2 Multi-transmitting formula and its instability of high-frequency oscillation for restraining instability

2.1 Multi-transmitting formula (MTF)

The multi-transmitting boundary is also called Multi-transmitting formula (MTF), which is a boundary condition using the general expression of a one-sided traveling wave solution to simulate an external wave crossing the boundary at a point on the artificial boundary. It uses internal point displacement to represent the boundary point displacement. MTF was proposed by Liao et al. (Liao, 1984, 2002). In the finite element discrete model (Figure 1), the MTF of the arbitrary artificial boundary point J can be expressed as

$$u_J^{P+1} = \sum_{n=1}^{N} (-1)^{n+1} C_n^N \overline{T_n}\,\overline{u_n} \tag{1}$$

where J of u_J^{P+1} represents the position in the discrete grid (e.g., point J in Figure 1), ***P + 1*** of u_J^{P+1} represents moment P+1, ***N*** is the order of MTF, and C_n^N is a binomial coefficient ($C_n^N = N!/((N-n)!n!)$). The following yields $\overline{T_n}$ and $\overline{u_n}$:

$$\begin{cases} \overline{u_n} = \left[u_J^{P-n+1}, u_{J-1}^{P-n+1}, \cdots, u_{J-2n}^{P-n+1}\right]^T \\ \overline{T_n} = [T_1, T_2, \cdots, T_{2n+1}] \\ T_K = \sum t_{K_1} t_{K_2} \cdots t_{K_n} (K = 1, 2, \cdots, 2n+1) \end{cases} \tag{2}$$

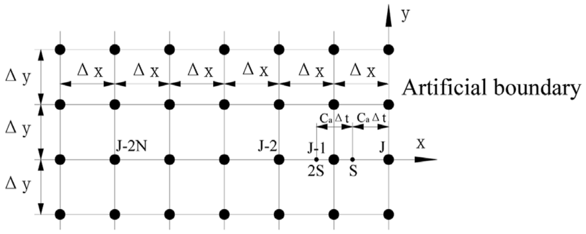

FIGURE 1
Discrete model of multi-transmitting boundary.

where T_K and t_{K_n} are dimensionless parameters. Here, T_K is obtained by summing t_{K_n} to satisfy the following:

$$K_1 + K_2 + \cdots + K_n = K + n - 1, K_1, K_2, \cdots, K_n = 1, 2, 3 \tag{3}$$

$$\begin{cases} t_1 = \dfrac{(2-s)(1-s)}{2} \\ t_2 = s(2-s) \\ t_3 = \dfrac{s(s-1)}{2} \\ s = \dfrac{c_a \Delta t}{\Delta x} \end{cases} \tag{4}$$

In Eq. 4, c_a is the artificial wave velocity. The wave unilaterally travels at velocity c and transmits in the direction of angle θ with a boundary surface ($c_a = c/\cos\theta$). As shown in Figure 1, Δx is the spatial step of the discrete grid in the direction perpendicular to the artificial boundary; Δt is the time step of the finite element calculation; and s is a dimensionless parameter.

For first-order transmission (N=1), under the condition that Eq. 3 is satisfied, Eq. 1 can be written as follows:

$$u_J^{P+1} = [t_1, t_2, t_3]\left[u_J^P, u_{J-1}^P, u_{J-2}^P\right]^T \tag{5}$$

By substituting Eq. 4 into Eq. 5, the first-order MTF can be derived as

$$u_J^{P+1} = \frac{1}{2}(1-s)(2-s)u_J^P + s(2-s)u_{J-1}^P + \frac{1}{2}s(s-1)u_{J-2}^P \tag{6}$$

2.2 Analysis of the instability of high-frequency oscillations

The most intuitive explanation for high-frequency oscillation instability of MTF is the reflection amplification of high-frequency wave component in the artificial boundary. An amplification error wave is reflected to the artificial boundary in the finite calculation area and then amplified again, resulting in the instability of the artificial boundary. Such error wave amplification only occurs in high-frequency waves approaching the cut-off frequency. These high-frequency fluctuations causing oscillation instability are outside the scope of the frequency components considered in numerical simulation; and they do not benefit the computational stability of numerical simulation. In the numerical simulation, the high-frequency waves approaching the cut-off frequency have an insignificant effect on the accuracy of frequency bands. These high-frequency fluctuations exist perpendicular and parallel to the artificial boundary. Therefore, the elimination of useless high-frequency fluctuations in all directions can stabilize high-frequency oscillation without affecting the calculation accuracy.

2.3 Fundamental ideas of stabilization measures

In the meaningful frequency band of the finite element (or finite difference) simulation of the wave, the transmission boundary does not produce oscillation instability. Oscillation instability only occurs in the high-frequency band approaching the cut-off frequency. Therefore, the guiding principle of stabilization is to eliminate meaningless high-frequency components without affecting the low-frequency components meaningful for wave simulation.

In this paper, the proposed measure for suppressing oscillation instability is inspired by the concept of a multi-directional transmitting formula (Liao et al., 1993). The fundamental concept of the multi-direction transmitting formula is that the scattering wave from various directions radiates to the artificial boundary. This abandons the assumption that the scattering wave is based on a single direction and only uses the motion information of the node in the normal direction of the boundary. Instead, the transmission boundary formula is established using the motion information of all nodes adjacent to the artificial boundary node (including those on the artificial boundary and normal line).

The node position is shown in Figure 2 (I is the target node, and smooth filtering is performed using the nodes adjacent to point I on the boundary). When smoothing using three points, I, I − 1, and I + 1 are involved. When five points are used, I − 2, I − 1, I, I + 1, and I+2 are involved. In this regard, the following three considerations are emphasized.

1) Smoothing is performed after calculating the artificial boundary point at time P + 1.
2) Three or five points are selected to be used in smoothing; all points use their P + 1 values of time. For example, if the smoothing target point is I on the boundary, the participating points include point I on the boundary and the points adjacent to the boundary.
3) Smoothing is performed not only for displacement but also for the velocity values of the boundary point. This is implemented after calculating the displacement and velocity of the artificial boundary point at time P + 1.

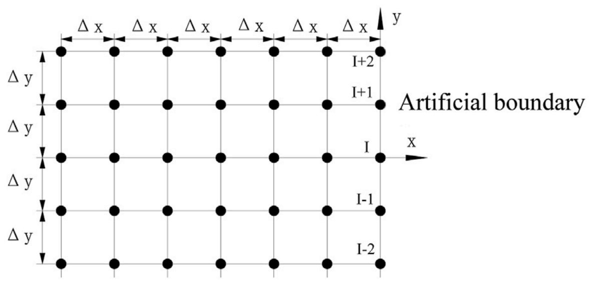

FIGURE 2
Position of the boundary point involvedin filtering.

After calculating the movement of the artificial boundary point at P + 1 using MTF (Eq. 1), the displacement and velocity values of the artificial boundary point I at P + 1 are smoothed. For point I on the boundary shown in Figure 2, three-point smoothing involves I − 1, I, and I + 1, and five-point smoothing involves I − 2, I − 1, I, I + 1, and I + 2. If three-point smoothing is used, the displacement and velocity can be calculated using Eqs 7, 9, respectively. If five-point smoothing is used, the displacement and velocity can be calculated using Eqs 8, 10, respectively. The displacement and velocity of point I after smoothing at P+1 are $\tilde{u}_i^{P+1}$ and $\tilde{\dot{u}}_i^{P+1}$, respectively. Coefficients β_1, β_2, and β_3 in Eqs 7, 9 are three-point smoothing coefficients, and coefficients β_1, β_2, β_3, β_4, and β_5 in Eqs 8, 10 are five-point smoothing coefficients. The values of the smoothing coefficients in Eqs 7–10 are presented in Section 2.4 of this paper.

$$\tilde{u}_i^{P+1} = \beta_1 u_i^{P+1} + \beta_2 u_{i-1}^{P+1} + \beta_3 u_{i+1}^{P+1} \tag{7}$$

$$\tilde{u}_i^{P+1} = \beta_1 u_i^{P+1} + \beta_2 u_{i-1}^{P+1} + \beta_3 u_{i+1}^{P+1} + \beta_4 u_{i-2}^{P+1} + \beta_5 u_{i+2}^{P+1} \tag{8}$$

$$\tilde{\dot{u}}_i^{P+1} = \beta_1 \dot{u}_i^{P+1} + \beta_2 \dot{u}_{i-1}^{P+1} + \beta_3 \dot{u}_{i+1}^{P+1} \tag{9}$$

$$\tilde{\dot{u}}_i^{P+1} = \beta_1 \dot{u}_i^{P+1} + \beta_2 \dot{u}_{i-1}^{P+1} + \beta_3 \dot{u}_{i+1}^{P+1} + \beta_4 \dot{u}_{i-2}^{P+1} + \beta_5 \dot{u}_{i+2}^{P+1} \tag{10}$$

2.4 Derivation of smoothing formula coefficient

For the foregoing smoothing formula, the key problem is the means for determining the value of the smoothing coefficient. The values of the smoothing coefficients are discussed as follows.

The relationship between the wavelength that may cause high-frequency instability at the boundary point and the mesh size of the finite element calculation is simplified into four cases, as shown in Figure 3.

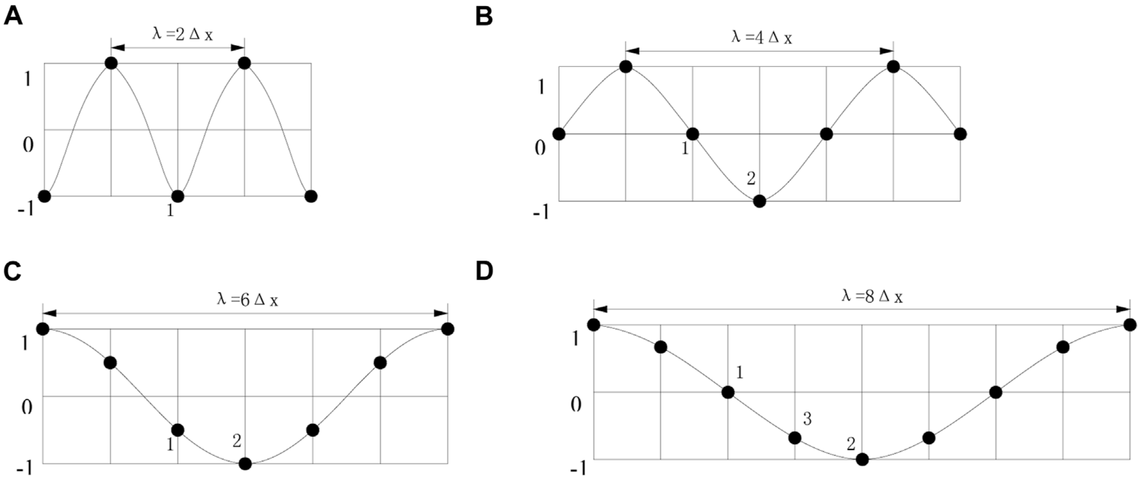

FIGURE 3
Wavelength and mesh size. **(A)** Wavelength and mesh size of case **(a)**. **(B)** Wavelength and mesh size of case **(b)**. **(C)** Wavelength and mesh size of case **(c)**. **(D)** Wavelength and mesh size of case **(d)**.

The smoothing effect of the coefficients considering four wavelengths shown in the figure is evaluated. Consider three-point smoothing as an example. The following four situations are discussed:

1) For case (a), the amplitude at point 1 in Figure 3A represents all points under the case. At point 1, the amplitudes before and after smoothing are −1 and ½ × (−1) + ¼ ×1 + ¼ × 1 = 0, respectively. The smoothed amplitude is found to be 0% of the original amplitude.
2) For case (b), the amplitudes at points 1 and 2 in Figure 3B represent those at all points. The amplitudes before and after smoothing at point 1 are 0 and ½ × 0 + ¼ × (−1) + ¼ × 1 = 0, respectively. The smoothed amplitude is found to be 0% of the original amplitude. At point 2, the amplitudes before and after smoothing are −1 and ½ × (−1) + ¼ × 0 + ¼ × 0 = −½, respectively. The smoothed amplitude is observed to be 50% of the original amplitude.
3) In case (c), the amplitudes at points 1 and 2 in Figure 3C represent those at all points in the case. At point 1, the amplitudes before and after smoothing are -1/2 and ½ × (−½) + ¼ × ½ + ¼ × (−1) = −3/8, respectively. The smoothed amplitude is observed to be 75% of the original amplitude. At point 2, the amplitudes before and after smoothing are −1 and ½ × (−1) + ¼× (−½) + ¼ × (−½) = −3/4, respectively. The smoothed amplitude is 75% of the original amplitude.
4) For case (d), the amplitudes at points 1, 2, and 3 in Figure 3D represent those at all points. At point 1, the amplitudes before and after smoothing are 0 and ½ × 0 + ¼ × ½ + ¼ × (−½) = 0, respectively. The smoothed amplitude is 0% of the original amplitude. At point 2, the amplitudes before and after smoothing are −1 and ½ × (−1) + ¼ × (−½) + ¼ × (−½) = −3/4, respectively. The smoothed amplitude is observed to be 75% of the original amplitude. At point 3, the amplitudes before and after smoothing are −½ and ½ × (−½) + ¼× 0 + ¼× (−1) = −½, respectively. The smoothed amplitude is 100% of the original amplitude.

Table 1 summarizes the smoothing values of using three coefficients in the four wavelength cases. The values in the table are amplitude percentages after smoothing relative to the original amplitude.

With this filtering method, the amplitudes of the high-frequency and low-frequency waves are expected to decrease after smoothing. The foregoing eliminates meaningless high-frequency components without affecting the low-frequency part of the wave simulation. The percentage values corresponding to the calculation in this study after smoothing situations (a) and (b) are anticipated to be lower than those before smoothing. The percentage values after smoothing situations (c) and (d) must be higher than those before smoothing.

Table 1 indicates that the effect of values resulting from three-point smoothing is closest to that expected, followed by the effect of the five-point smoothing coefficient values (1/3, 1/4, 1/4, 1/12, and 1/12). The five-point smoothing coefficient values (1/2, 1/6, 1/6, 1/12, and 1/12) have the worst effect. Later, numerical tests are conducted to verify the effects.

3 Modified formula of the MTF with stabilization measure proposed

First-order and three-point smoothing are considered as an example to discuss the MTF after smoothing. With point I on the

TABLE 1 Smoothed amplitude percentage.

		Three-point smoothing	Five-point smoothing (1)	Five-point smoothing (2)
		(1/2, 1/4,1/4)	(1/3, 1/4, 1/4,1/12, 1/12)	(1/2, 1/6, 1/6, 1/12, 1/12)
		(%)	(%)	(%)
case (a)	Point 1	0	0	30
case (b)	Point 1	0	0	0
	Point 2	50	17	30
case (c)	Point 1	75	50	50
	Point 2	75	50	50
case (d)	Point 1	0	0	0
	Point 2	100	83	83
	Point 3	100	60	70

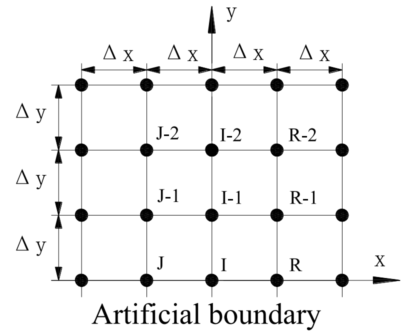

FIGURE 4
Discrete model of multi-transmitting boundary area.

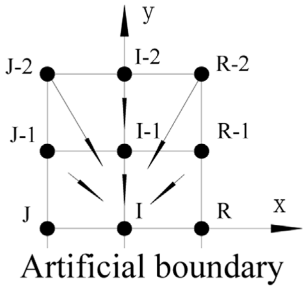

FIGURE 5
Multi-directional transmitting boundary.

boundary shown in Figure 4 as the target point, three points, I, J, and R, on the boundary are involved in smoothing point I. According to Eq. 7, the motion expression of point I after smoothing at time P + 1 is.

$$\tilde{u}_I^{P+1} = \beta_1 u_I^{P+1} + \beta_2 u_J^{P+1} + \beta_3 u_R^{P+1} \tag{11}$$

According to Eq. 6, the motion expressions of I, J, and R at time P + 1 are Eqs 12–14, respectively:

$$u_I^{P+1} = \frac{1}{2}(1-S)(2-S)u_I^P + S(2-S)u_{I-1}^P + \frac{1}{2}S(S-1)u_{I-2}^P \tag{12}$$

$$u_J^{P+1} = \frac{1}{2}(1-S)(2-S)u_J^P + S(2-S)u_{J-1}^P + \frac{1}{2}S(S-1)u_{J-2}^P \tag{13}$$

$$u_R^{P+1} = \frac{1}{2}(1-S)(2-S)u_R^P + S(2-S)u_{R-1}^P + \frac{1}{2}S(S-1)u_{R-2}^P \tag{14}$$

By substituting Eqs 12–14 into Eq. 11, the motion expression of point I after smoothing at time P + 1 is derived as follows:

$$\begin{aligned}\tilde{u}_I^{P+1} = &\frac{1}{2}(1-S)(2-S)\left(\beta_1 u_I^P + \beta_2 u_J^P + \beta_3 u_R^P\right)\\ &+ S(2-S)\left(\beta_1 u_{I-1}^P + \beta_2 u_{J-1}^P + \beta_3 u_{R-1}^P\right)\\ &+ \frac{1}{2}S(S-1)\left(\beta_1 u_{I-2}^P + \beta_2 u_{J-2}^P + \beta_3 u_{R-2}^P\right)\end{aligned} \tag{15}$$

Eq. 15 can also be regarded as a multi-directional transmitting formula constructed using the information of all nodes (including I − 1, I − 2, J, J − 1, J − 2, R, R − 1, and R −2) around boundary node I, as shown in Figure 5. Coefficients β_1, β_2, and β_3 in Eq.15 can be considered as the share coefficients of node participation in transmission.

Next, to verify the effectiveness of the proposed measure in suppressing high-frequency instability, numerical tests are conducted.

4 Numerical test

As an example, the wave propagation is simulated for a semi-infinite space model, as shown in Figure 6. The coordinates of the observation points are as follows: point 1 (0 m, 0 m); point 2

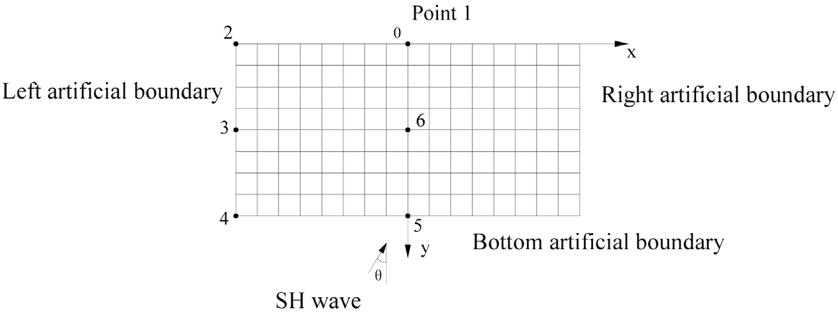

FIGURE 6
Calculation model.

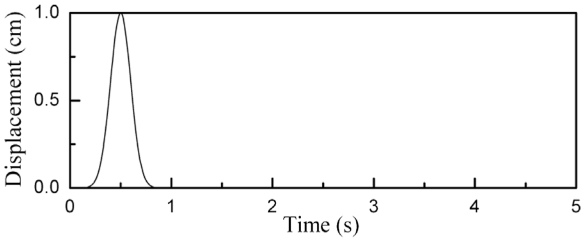

FIGURE 7
Displacement pulse.

(−500 m, 0 m); point 3 (−500 m, −500 m); point 4 (−500 m, −1,000 m); point 5 (0 m, −1,000 m); and point 6 (0 m, −500 m). The input SH wave pulse–time history is shown in Figure 7. The incident angle is 0°, and the wave velocity is 2000 m/s. The mesh size is $\Delta x = 10$ m and $\Delta y = 5$ m. The calculated time step is $\Delta t = 0.0025$ s.

Figure 8 shows the comparison results between implementing and not implementing the proposed measures for eliminating high-frequency instability. As shown in Figure 8, the coefficients are as follows: in three-point smoothing, $\beta_1 = 1/2$ and $\beta_2 = \beta_3 = ¼$; in five-point smoothing (1), $\beta_1 = 1/3$, $\beta_2 = \beta_3 = ¼$, and $\beta_4 = \beta_5 = 1/12$; and in five-point smoothing (2), $\beta_1 = 1/2$, $\beta_2 = \beta_3 = 1/6$, and $\beta_4 = \beta_5 = 1/12$.

By analysing the results of the displacement–time history comparison of observation points in Figure 8, the following are deduced.

1) The processing method of adjacent nodes participating in filtering smoothing on the artificial boundary is effective for suppressing the instability of high-frequency oscillations.
2) The corresponding curve of the three-point smoothing measure does not exhibit high-frequency oscillations, indicating that the measure has a satisfactory effect on suppressing high-frequency instability.
3) The time history curve of the observation point obtained using the five-point smoothing measure exhibits slight oscillations. Between the two values yielded by five-point smoothing, the following coefficients is the worst: 1/2, 1/6, 1/6, 1/12, and 1/12. In Figure 8B, C, E, the time history curves corresponding to the foregoing set of values have small high-frequency oscillations, indicating that this group of values cannot completely eliminate high-frequency instability.
4) In Figure 8E, F, the curves corresponding to the two five-point smoothing measures have distinct abnormal fluctuations between 2 and 3 s. No abnormal fluctuations are observed in the curves corresponding to those in which no measure for eliminating high-frequency oscillation is applied and the curves corresponding to the three-point smoothing measure. This shows that the abnormal fluctuation is caused by the disturbance from numerous low-frequency components introduced by the five-point smoothing method while filtering high-frequency components. The disturbance due to numerous low-frequency components causes abnormal fluctuations. This also demonstrates that the effect of the three-point smoothing measure is superior to that of the five-point smoothing one.

Table 2 lists the peak displacement–time histories of each observation point shown in Figure 8. The data in Table 2 indicate

TABLE 2 Displacement peak of observation point.

	Point 1	Point 2	Point 3	Point 4	Point 5	Point 6
No measures	1.9999	1.9999	0.9999	0.9999	0.9999	1.0000
Three-point smoothing	2.0000	1.9974	0.9991	1.0083	1.0000	1.0001
Five-point smoothing (1)	2.0002	1.9944	0.9979	1.0452	1.0000	1.0001
Five-point smoothing (2)	2.0002	1.9937	0.9974	1.0565	1.0000	1.0001

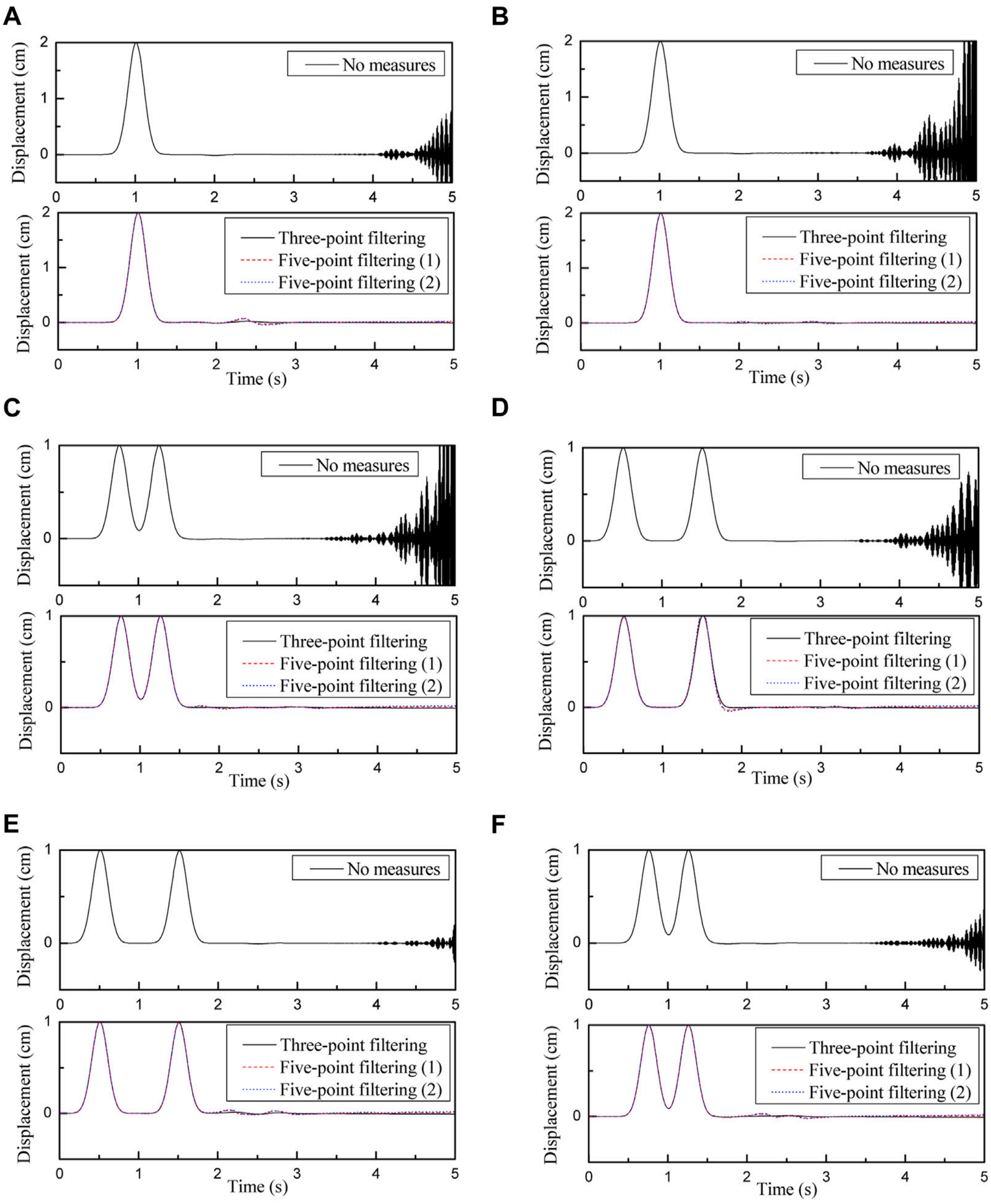

FIGURE 8
Displacement time history, **(A)** Observation point 1 **(B)** Observation point 2, **(C)** Observation point 3 **(D)** Observation point 4, **(E)** Observation point 5 **(F)** Observation point 6

that the peak value of point 4 significantly differs. The peak value error obtained by the three-point smoothing measure is only 0.83%, whereas the errors obtained by the five-point smoothing one are 4.5% and 5.6%. This further demonstrates that three-point smoothing measure is better than five-point smoothing one. By considering the results in Figure 8; Table 2, the three-point smoothing measure is found to resolve the high-frequency instability, and the peak value of the observation point is least disturbed. This verifies the observation presented in Section 1.4. In terms of practical implementation, three-point smoothing is simpler than five-point smoothing. Accordingly, the use of the three-point smoothing measure is recommended.

5 Conclusion

Inspired by the multi-directional transmitting formula, and considering the high-frequency wave oscillation in the vertical and parallel directions with the artificial boundary, a strategy for filtering and smoothing adjacent nodes on the artificial boundary is proposed in this paper to suppress the instability of high-frequency oscillations of the multi-transmitting boundary. A reasonable smoothing coefficient value was obtained, and the effectiveness of the measure was verified through numerical tests. The main findings of the study are summarized as follows.

1) The smoothing filtering strategy using the adjacent nodes of the artificial boundary is effective in suppressing the instability of high-frequency oscillations of the multi-transmitting boundary.
2) This paper presents three types of smoothing coefficient value combinations. Both three-point and five-point smoothing measures are effective in suppressing high-frequency instability of the multi-transmitting boundary; however, the three-point smoothing measure exhibits better performance. This is because low-frequency components are inevitably introduced when high-frequency components are filtered. Five-point smoothing measure introduces more low-frequency interference factors than three-point smoothing one. Consequently, excessive low-frequency disturbances cause the time history curve to fluctuate and affect calculation accuracy.
3) This study analyses the conceptual similarity between the smoothing of the motion calculated by the boundary point and multi-directional transmitting formulas. Hence, it provides a reference for establishing the coefficient value of the multi-directional transmitting formula in the time domain.

Data availability statement

The original contributions presented in the study are included in the article/Supplementary Material, further inquiries can be directed to the corresponding author.

Author contributions

YY is the main author of this paper. XL made an important contribution to the innovation of this paper. MR and ZY gave good suggestions in the completion of the paper.

Funding

This study is supported by the National Natural Science Foundation of China (U1839202) and National Key Research and Development Program (2019YFB1900900).

Conflict of interest

The authors declare that the research was conducted in the absence of any commercial or financial relationships that could be construed as a potential conflict of interest.

Publisher's note

References

Cheng, N., and Cheng, C. H. (1995). Relationship between Liao and Clayton-Engquist absorbing boundary conditions: Acoustic case. *Bull. Seismol. Soc. Am.* 85 (3), 954–956. doi:10.1785/bssa0850030954

Givoli, D. (1992). *Numerical methods for problems in infinite domain.* Amsterdam: Elsevier.

Li, X. J., Liao, Z. P., and Du, X. L. (1992). An explicit finite difference method for viscoelastic dynamic problem. *Earthq. Eng. Eng. Vib.* 12 (4), 74–80. *in Chinese.*

Li, X. J., and Tang, H. (2007). Numerical dissipation property of an explicit integration scheme for dynamic equation of structural system. *Eng. Mech.* 24 (2), 28–33. *in Chinese.*doi:10.1080/13632469.2017.1326423

Li, X. J., and Yang, Y. (2012). Measure for stability of transmitting boundary. *Chin. J. Geotechnical Eng.* 34 (4), 641–645. *in Chinese.*doi:10.1371/journal.pone.0243979

Liao, Z. P., and Liu, J. B. (1989). Finite element simulation of wave motion–basic problem and conceptual aspects. *Earthq. Eng. Eng. Vib.* 9 (4), 1–14. *in Chinese.*

Liao, Z. P., and Liu, J. B. (1992). Fundamental problems in finite element simulation of wave motion. *Sci. China (Series B)* 34 (8), 874–882. *in Chinese*.

Liao, Z. P., Zhou, Z. H., and ZhangY, H. (2002). Stable implementation of transmitting boundary in numerical simulation of wave motion. *Chin. J. Geophys.* 45 (4), 554–568. *in Chinese*. doi:10.1002/cjg2.269

Liao, Z. P. (1984). A finite element method for near-field wave motion in heterogeneous materials. *Earthq. Eng. Eng. Vib.* 4 (2), 1–14. *in Chinese*.doi:10.1098/rspa.2016.0738

Liao, Z. P. (2002). *Introduction to wave motion theories in engineering*. second edition. Beijing: Science Press. *in Chinese*.

Liao, Z. P., and Wong, H. L. (1984). A transmitting boundary for the numerical simulation of elastic wave propagation. *Soil Dyn. Earthq. Eng.* 3, 174–183. doi:10.1016/0261-7277(84)90033-0

Liao, Z. P., Wong, H. L., Yang, B., and Yuan, Y. (1984). A transmitting boundary for transient wave analyses. *Sci. Sin. Ser. A.* 27 (10), 1063–1076.doi:10.1360/YA1984-27-10-1063

Liao, Z. P., and Yang, G. (1993). Multi-directional transmitting boundaries for steady-state SH waves. *Earthq. Eng. Structrual Dyn.* 24, 361–371. doi:10.1002/eqe.4290240305

Tang, H., Li, X. J., and Li, Z. (2010). The effect of the explicit in tegration for defressing and eliminating the high- frequency instability induced by local transmitting boundary. *World Earthq. Eng.* 26 (4), 50–54. *in Chinese*.doi:10.1007/BF02650573

Wolf, P., and Song, C. (1996). *Finite-element modelling of unbounded media*. Chichester: John Wiley & Sons.

Wolf, P. (1988). *Soil-structure dynamic interaction analysis in time domain*. Englewood Cliffs, NJ: Prentice-Hall.

Xie, Z. N., and Liao, Z. P. (2012). Mechanism of high frequency instability caused by transmitting boundary and method of its elimination—SH wave. *Chin. J. Theor. Appl. Mech.* 44 (4), 745–752. *in Chinese*.doi:10.6052/0459-1879-11-312

Xing, H. J., and Li, H. J. (2017a). Implementation of multi- transmitting boundary condition for wave motion simulation by spectral element method: One dimension case. *Chin. J. Theor. Appl. Mech.* 49 (2), 367–379. *in Chinese*.doi:10.6052/0459-1879-16-393

Xing, H. J., and Li, H. J. (2017b). Implementation of multi- transmitting boundary condition for wave motion simulation by spectral element method: Two dimension case. *Chin. J. Theor. Appl. Mech.* 49 (4), 894–906. *in Chinese*.doi:10.6052/0459-1879-16-393

Xing, H. J., Li, X. J., Liu, A. W., Li, H. J., Zhou, Z. H., and Chen, S. (2021). Extrapolation-type artificial boundary conditions in the numerical simulation of wave motion. *Chin. J. Theor. Appl. Mech.* 53 (5), 1480–1495. *in Chinese*.

Xu, S. G., and Liu, Y. (2018). 3D acoustic and elastic VTI modeling with optimal finite-difference schemes and hybrid absorbing boundary conditions. *Chin. J. Geophys.* 61 (7), 2950–2968. *in Chinese*.doi:10.6038/cjg2018L0250

Yang, Y., Li, X. J., He, Q. M., and Wang, L. (2014). Comparison of measures for eliminating high-frequency instability of a multi-transmitting boundary in scattering problems. *China Earthq. Eng. J.* 36 (3), 476–481. *in Chinese*.doi:10.1002/cnm.1394

Zhang, X. B., Liao, Z. P., and Xie, Z. N. (2021). Mechanism of high frequency instability and stable implementation for transmitting boundary—P-SV wave motion. *Chin. J. Geophys.* 64 (10), 3646–3656. *in Chinese*.doi:10.6052/0459-1879-11-312

frontiers | Frontiers in Earth Science

TYPE Original Research
PUBLISHED 04 January 2023
DOI 10.3389/feart.2022.1057316

OPEN ACCESS

EDITED BY
Yefei Ren,
Institute of Engineering Mechanics,
China Earthquake Administration, China

REVIEWED BY
Zhang Yushan,
China Earthquake Disaster Prevention
Centre, China
Wujian Yan,
Lanzhou Earthquake Research Institute,
China Earthquake Administration, China

*CORRESPONDENCE
Junju Xie,
✉ xiejunjv05@mails.ucas.ac.cn

SPECIALTY SECTION
This article was submitted to Structural Geology and Tectonics,
a section of the journal
Frontiers in Earth Science

RECEIVED 29 September 2022
ACCEPTED 05 December 2022
PUBLISHED 04 January 2023

CITATION
Jiao H, Xie J, Zhao M, Huang J, Du X and Wang J (2023), Seismic response analysis of slope sites exposed to obliquely incident P waves.
Front. Earth Sci. 10:1057316.
doi: 10.3389/feart.2022.1057316

Seismic response analysis of slope sites exposed to obliquely incident P waves

Hongyun Jiao[1], Junju Xie[1]*, Mi Zhao[2], Jingqi Huang[3], Xiuli Du[2] and Juke Wang[1]

[1]Institute of Geophysics, China Earthquake Administration, Beijing, China, [2]Key Laboratory of Urban Security and Disaster Engineering, Ministry of Education, Beijing University of Technology, Beijing, China, [3]Beijing Key Laboratory of Urban Underground Space Engineering, School of Civil and Resource Engineering, University of Science and Technology Beijing, Beijing, China

This study proposes a seismic input method for layered slope sites exposed to obliquely-incident seismic waves which transforms the waves into equivalent nodal forces that act on the truncated boundary of a finite element model. The equivalent nodal forces at the left and right boundaries are obtained by combining the free field response of a one-dimensional layered model with a viscoelastic boundary. The equivalent nodal forces at the bottom boundary are obtained by combining the incident wave field with the viscoelastic boundary. This proposed seismic input method for slope sites exposed to obliquely incident seismic waves is implemented with the aid of MATLAB software; it is applied to the seismic response analysis of slope sites in the commercial finite element ABAQUS software. The calculation results are compared with the reference solutions obtained by using the extended model to verify the correctness of the established seismic input method. The proposed seismic input method is then employed to investigate the influencing factors of the seismic response of layered slope sites exposed to oblique incidence P waves. The results show that the angle of incidence, location of the interface between soft and hard rocks, and impedance ratio have significant effects on the seismic landslide.

KEYWORDS

seismic input method, obliquely incident P waves, layered slope site, influencing factors, seismic landslide

1 Introduction

Landslides are frequent during earthquakes in mountainous and hilly areas (Prestininzi and Romeo, 2000; Chigira et al., 2005; Sato et al., 2007; Semblat et al., 2011). Hillside topography can magnify seismic intensity and change seismic frequency content—termed "topographic effects". Landslide disasters caused by earthquakes have been a frequent subject of geological hazard research because of their wide distribution, considerable quantity, and great harm (Bird et al., 2004; Owen et al., 2008). Since the 1960s, scholars have begun identifying and analyzing the seismic response of slope sites exposed to seismic waves (Cavallin and Slejko, 1986; Jibson et al., 2000; Pareek and Arora, 2010; Li et al., 2022). Analysis methods have included landslide observation, model testing, and numerical simulations (Keeper, 1984). The finite element method (FEM) is the most common numerical method; it can effectively simulate the geometric and material non-linear characteristics of slope sites.

When analyzing the seismic response of slope sites based on FEM, it is necessary to introduce artificial boundary conditions at the truncated boundaries of the finite domain to simulate the radiation damping effect of the infinite domain on the finite domain. The artificial boundary appropriate to the characteristics and specific conditions of the research object must be deduced. Due to the irregular terrain of slope sites, poor geological conditions, and the existence of free surfaces, the topographic effect of slope site has attracted research attention (Gischig et al., 2015; Poursartip et al., 2017). It is necessary to deduce the appropriate artificial boundary according to the characteristics of the research object and the specific situation. In previous finite element analysis of the seismic response of slope sites, most scholars have assumed that the bottom boundary of the model is rigid, while the lateral side boundaries adopt roller boundaries (Rizzitano et al., 2014), viscous boundaries (Lysmer and Kuhlemeyer, 1969; Athanasopoulo et al., 1999; Pelekis, 2017), viscoelastic boundaries (Deeks and Randolph, 1994; Liu et al., 2006; Maleki and Khodakarami, 2017), transmissive boundaries (Liao and Wong, 1984), paraxial approximate boundaries (Clayton and Engquist, 1977), and infinite element boundaries (Bettess, 1977; Astley, 2000). Seismic input is completed by converting the seismic wave action into the equivalent forces applied to boundaries; however, this treatment method is not applicable in cases where the lower part of the site model is not bedrock.

Much recent research has been conducted on the seismic response analysis of slope sites with non-rigid bedrock at the bottom of the site model. Based on the viscous boundary, Bouckovalas and Papadimitriou (2005) presented numerical analyses for the seismic response of step-like ground slopes in uniform viscoelastic soil under vertically propagating SV seismic waves. Assimaki et al. (2005) employed the viscous boundary to address vertically incident seismic wave action and obtained a seismic input method suitable for layered slopes. Based on the viscous boundary, Lenti and Martino (2012) studied a landslide disaster on a stepped slope under the action of a vertically incident seismic wave. Nakamura (2012) adopted the energy-transmitting boundary to study the seismic input and established the seismic response analysis method for the layered slope. However, when the source is shallow or the site is far from the epicenter, the seismic input cannot be assumed to be vertically incident seismic waves but can be considered obliquely incident.

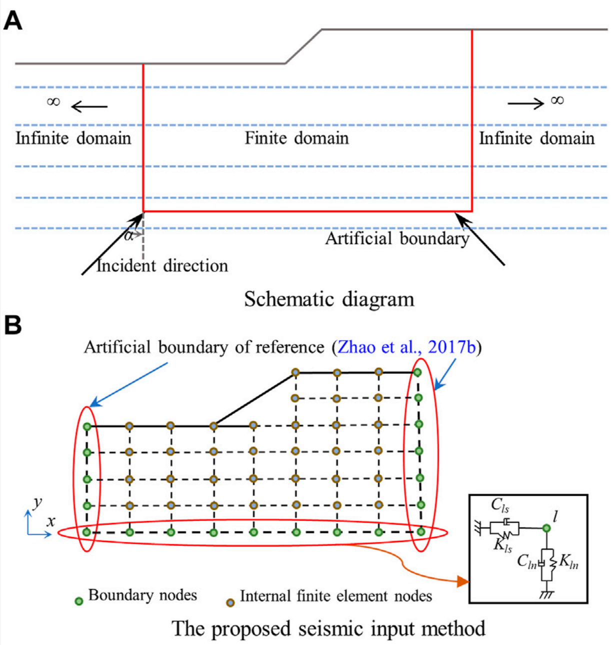

FIGURE 1
Model of a layered slope site under obliquely incident P waves. **(A)** Schematic diagram. **(B)** Proposed seismic input method.

Scholars have thus conducted research on the seismic response of regular sites under the action of obliquely incident seismic waves. Liu and Lu (1998) proposed a seismic input method based on spring-buffer boundary conditions that convert seismic waves with arbitrary incident angles into equivalent nodal forces acting on boundary nodes. Based on the viscoelasticity boundary, Huang et al. (2017a) and Huang et al. (2017b) used the FEM to analyze the non-linear seismic response of tunnels with a normal fault ground subjected to obliquely incident seismic waves. Bazyar and Song (2017) expressed such a wave as the boundary condition applied to the near field by the proportional boundary FEM. Based on the one-dimensional time-domain FEM proposed by Liu and Wang (2007), Zhao et al. (2013) and Zhao et al. (2017) proposed an improvement by establishing a site response analysis method and applying it to study the influence of the oblique incidence of ground motion on the seismic response of subway stations. However, previous seismic input methods have been established for seismic response analysis of regular sites under the action of obliquely incident seismic waves; this is not applicable to the seismic response of slope sites under the action of obliquely incident seismic waves. There are few studies on the seismic input method of slope sites exposed to obliquely incident seismic waves.

In this paper, obliquely incident seismic waves are transformed into equivalent nodal forces that act on the truncated boundary of the finite element model as the seismic input. Based on the viscoelastic artificial boundary, the free field responses of one-dimensional layered sites with different heights are taken as the seismic input for the left and right boundaries, and the incident wave field is used as the

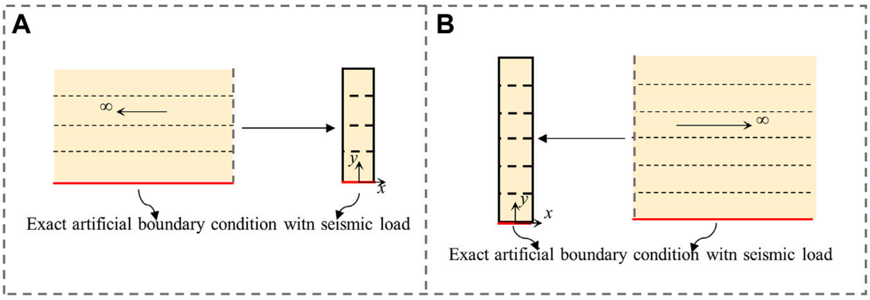

FIGURE 2
One-dimensional finite element model. **(A)** Left boundary. **(B)** Right boundary.

seismic input for the bottom. Then, the proposed seismic input method for slope sites under the action of obliquely incident seismic waves is implemented with the aid of MATLAB software and is applied to the seismic response analysis of slope sites in the commercial finite element ABAQUS software. Accordingly, the numerical simulation results of a two-dimensional layered slope site obtained using the established seismic input method are compared with the numerical results of an extended computational model to verify the accuracy of this method. Finally, with the aid of the proposed seismic input method, the influencing factors of the seismic response of layered slope sites under oblique incidence P waves are determined.

2 Seismic input mechanism for the slope site

2.1 Governing equations

Figure 1A illustrates the schematic diagram of the seismic response analysis of a layered slope site subjected to P waves obliquely incident at an angle of α. When analyzing the seismic response of a two-dimensional layered slope site with the aid of the FEM, the finite computational domain needs to be cut off from the infinite ground. Artificial boundaries are usually used to simulate waves scattered by target structures and the non-reflecting wave effect of truncated infinite domains (Du et al., 2006; Huang et al., 2016; Zhao et al., 2019; Li et al., 2020). The stable and accurate viscoelasticity artificial boundary developed by Du et al. (2006) is adopted in this study. For a given boundary node l (x_l, y_l, z_l), one pair of dashpots and springs in the normal and tangential directions of the boundary plane are established respectively (Figure 1B).

At a given boundary node l (x_l, y_l) of the 2-D finite element model, the parameters for the springs and dashpots are

$$\begin{cases} K_{ln} = A_l \dfrac{1}{(1+a_r)} \dfrac{\lambda + 2G}{R}, & C_{\mathrm{ln}} = A_l b_r \rho c_p \\ K_{ls} = A_l \dfrac{1}{(1+a_r)} \dfrac{G}{R}, & C_{ls} = A_l b_r \rho c_s, \end{cases} \tag{1}$$

where K_{ln} and K_{ls} denote the normal and tangential spring stiffnesses at the boundary node l (x_l, y_l); C_{ln} and C_{ls} denote the normal and tangential damping coefficients at the boundary node l (x_l, y_l); A_l is half of the total length of all boundary elements containing the boundary node l (x_l, y_l); R is the distance between the scattering source and the artificial boundary node; λ, G, and ρ are the Lamé constant, shear modulus, and mass density of the ground, respectively; c_s and c_p represent the shear and compression wave velocities of the ground, respectively; a_r and b_r are the modified coefficients with good values of 0.8 and 1.1, respectively (Du et al., 2006).

The dynamic finite element equation for the finite domain has the form

$$\begin{bmatrix} \boldsymbol{M}_{\mathrm{II}} & \boldsymbol{M}_{\mathrm{IB}} \\ \boldsymbol{M}_{\mathrm{BI}} & \boldsymbol{M}_{\mathrm{BB}} \end{bmatrix} \left\{ \ddot{\boldsymbol{u}}_{\mathrm{I}}\ \ddot{\boldsymbol{u}}_{\mathrm{B}} \right\} + \begin{bmatrix} \boldsymbol{C}_{\mathrm{II}} & \boldsymbol{C}_{\mathrm{IB}} \\ \boldsymbol{C}_{\mathrm{BI}} & \boldsymbol{C}_{\mathrm{BB}} \end{bmatrix} \begin{Bmatrix} \dot{\boldsymbol{u}}_{\mathrm{I}} \\ \dot{\boldsymbol{u}}_{\mathrm{B}} \end{Bmatrix} + \begin{bmatrix} \boldsymbol{K}_{\mathrm{II}} & \boldsymbol{K}_{\mathrm{IB}} \\ \boldsymbol{K}_{\mathrm{BI}} & \boldsymbol{K}_{\mathrm{BB}} \end{bmatrix} \begin{Bmatrix} \boldsymbol{u}_{\mathrm{I}} \\ \boldsymbol{u}_{\mathrm{B}} \end{Bmatrix} = \begin{Bmatrix} \boldsymbol{F}_{\mathrm{I}} \\ \boldsymbol{F}_{\mathrm{B}} \end{Bmatrix} \tag{2}$$

where subscript $_{\mathrm{B}}$ represents the boundary node and subscript $_{\mathrm{I}}$ represents the internal node, $\boldsymbol{u}$, $\dot{\boldsymbol{u}}$, $\ddot{\boldsymbol{u}}$ and $\boldsymbol{F}$ represent displacement, velocity, displacement and force vectors, and $\boldsymbol{M}$, **C** and **K** represent the mass matrix, damping matrix, and stiffness matrix.

The seismic waves can be separated into the free field motion of the infinite domain and scattering wave motion generated by all scattering sources. The free field motion in the infinite domain or engineering site is expressed by the superscript ^{f}, and the scattering wave motion is expressed by the superscript ^{s}. The displacement $\boldsymbol{u}_l$, velocity $\dot{\boldsymbol{u}}_l$, and force F_l at a given boundary node l (x_l, y_l) of the 2-D finite element model can be written as

$$\boldsymbol{u}_l = \boldsymbol{u}_l^f + \boldsymbol{u}_l^s, \tag{3}$$

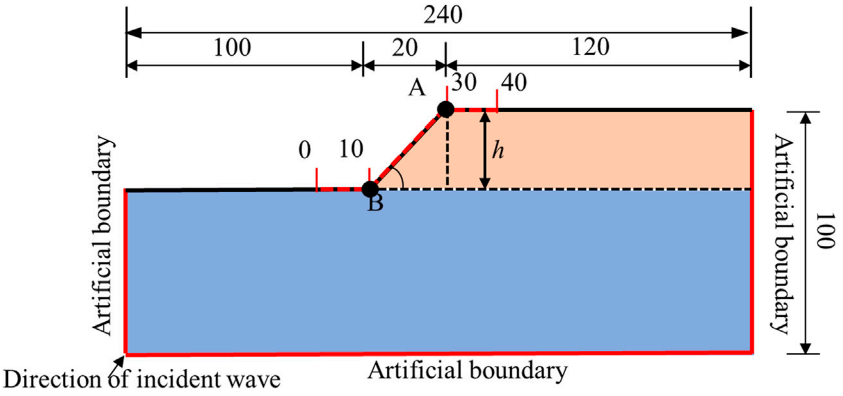

FIGURE 3
Calculation model for the layered slope site exposed to obliquely incident P waves.

TABLE 1 Material constants of the soil.

Layer	Density ρ (kg/m^3)	Elastic modulus E (Pa)	Poisson's ratio υ	Internal friction angle φ (°)	Cohesion c (Pa)	C_P (m/s)	C_{SV} (m/s)
Upper	1700	1e9	0.45	20	0.05e6	1494	450
Lower	2400	17.7e9	0.26	45	1.4e6	3004	1711

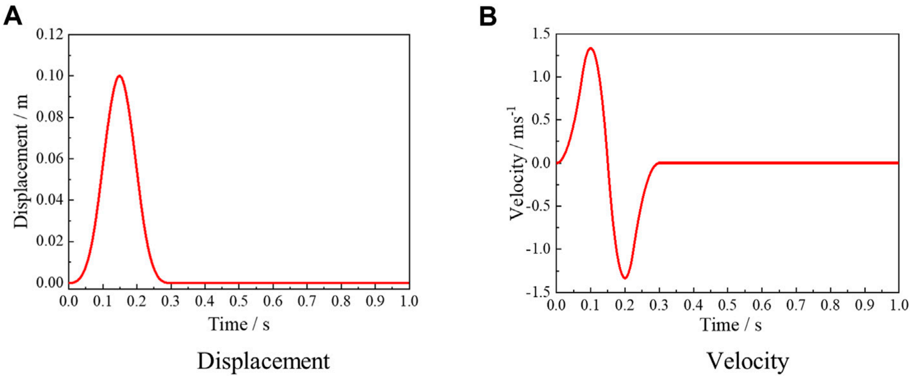

FIGURE 4
Time history curve of the input seismic wave. **(A)** Displacement. **(B)** Velocity.

$$\dot{\boldsymbol{u}}_l = \dot{\boldsymbol{u}}_l^f + \dot{\boldsymbol{u}}_l^s, \tag{4}$$

$$\boldsymbol{F}_l = \boldsymbol{F}_l^f + \boldsymbol{F}_l^s. \tag{5}$$

where $\mathbf{u}_l^T = [u_x u_y]$, $\dot{\mathbf{u}}_l^T = [\dot{u}_x \dot{u}_y]$, and $\mathbf{F}_l^T = [F_x F_y]$. The load $\mathbf{F}_l^s$ due to the scattering wave motion can be expressed as

$$\boldsymbol{F}_l^s = -\boldsymbol{K}_l \boldsymbol{u}_l^s - \boldsymbol{C}_l \dot{\boldsymbol{u}}_l^s, \tag{6}$$

where K_{li} and C_{li} represent the spring component and damping component of the stiffness matrix $\mathbf{K}_l$ and damping matrix $\mathbf{C}_l$ at an artificial boundary node l in the i direction, respectively.

Substituting Eqs 3–5 into Eq. 6 after rearrangement, the following equation can be obtained:

$$\boldsymbol{F}_l = \boldsymbol{K}_l \boldsymbol{u}_l^f + \boldsymbol{C}_l \dot{\boldsymbol{u}}_l^f + \boldsymbol{A}_l \boldsymbol{f}_l^f - \boldsymbol{K}_l \boldsymbol{u}_l - \boldsymbol{C}_l \dot{\boldsymbol{u}}_l, \tag{7}$$

where $f_l^f = [f_x^f \ f_y^f]^T$ is the stress vector induced by free field motion.

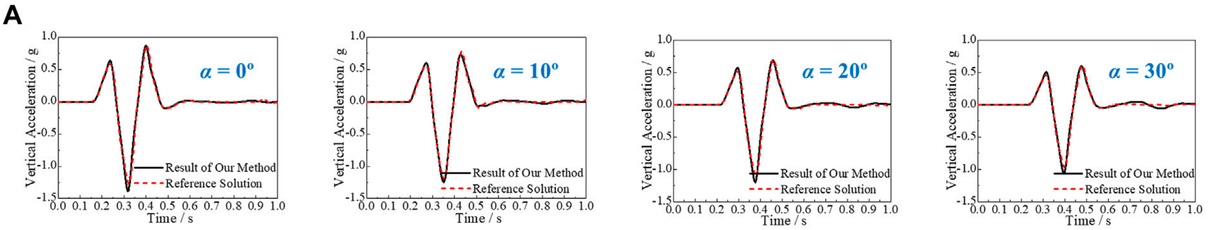

Comparison results of vertical acceleration of node A under different input angles.

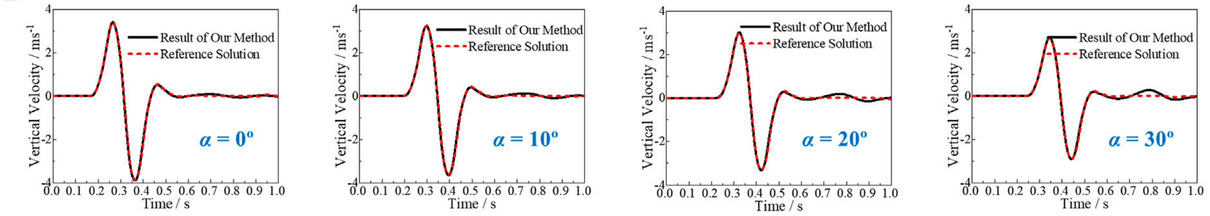

Comparison results of vertical velocity of node A under different input angles.

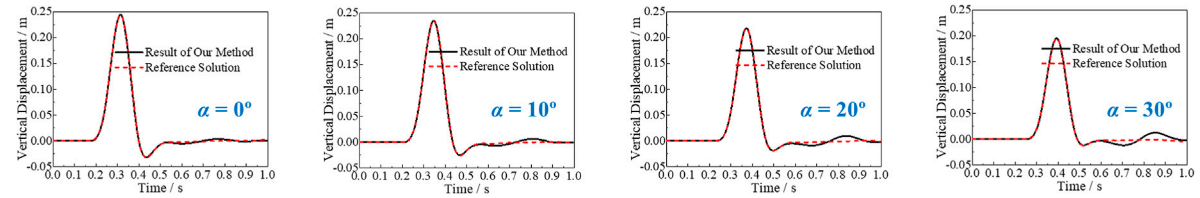

Comparison results of vertical displacement of node A under different input angles.

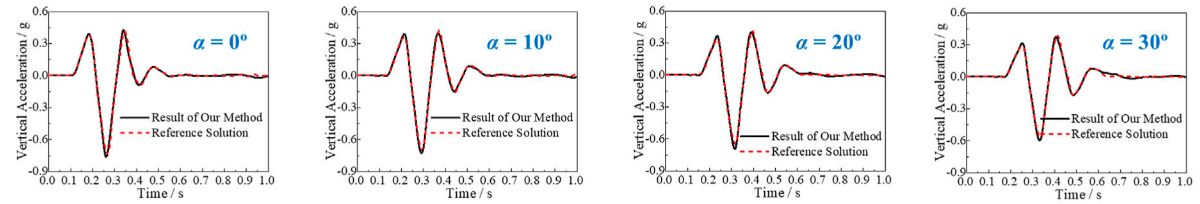

Comparison results of vertical acceleration of node B under different input angles.

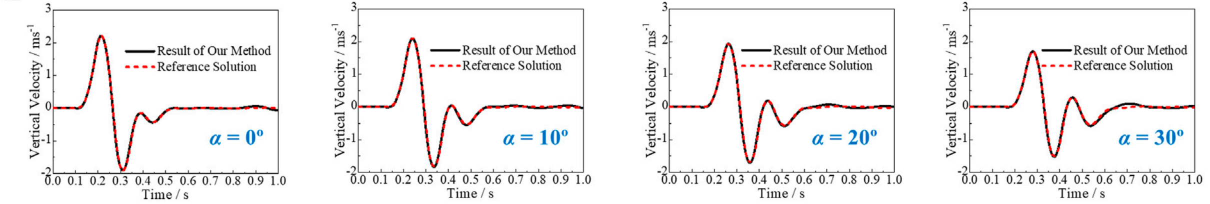

Comparison results of vertical velocity of node B under different input angles.

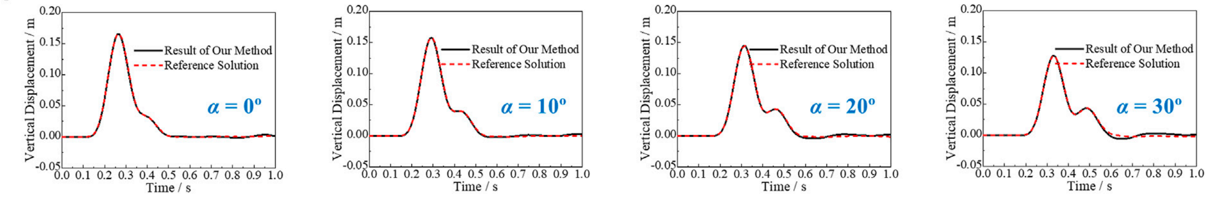

Comparison results of vertical displacement of node B under different input angles.

FIGURE 5
Comparison results at different input angles. **(A)** Comparison of the vertical acceleration results of node A at different input angles. **(B)** Comparison of the vertical velocity results of node A at different input angles. **(C)** Comparison of the vertical displacement results of node A at different input angles. **(D)** Comparison of the vertical acceleration results of node B at different input angles. **(E)** Comparison of the vertical velocity results of node B at different input angles. **(F)** Comparison of the vertical displacement results of node B at different input angles.

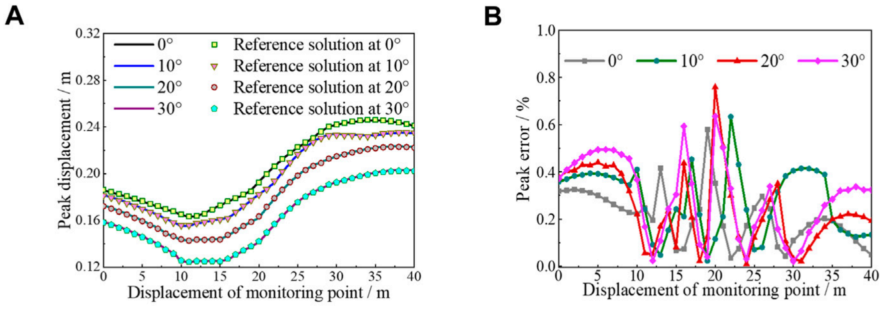

Comparison results of the vertical displacement peaks　Relative errors

FIGURE 6
Comparison of the results and relative errors of the vertical displacement peaks of each observation node on the free surface. **(A)** Comparison of the results of the vertical displacement peaks. **(B)** Relative errors.

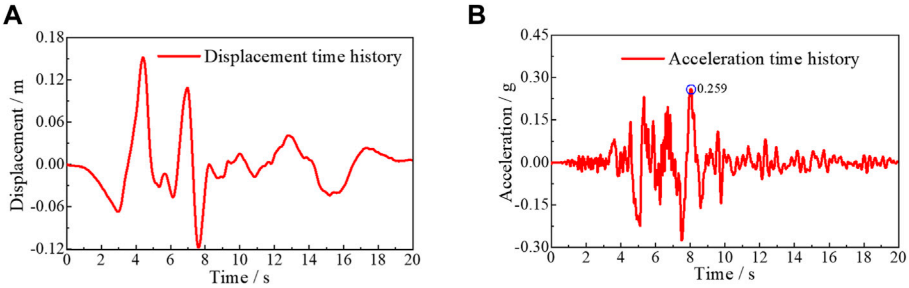

Time history of displacement　Time history of acceleration

FIGURE 7
Time histories of the Kobe wave for Kobe University. **(A)** Time history of displacement. **(B)** Time history of acceleration.

Then, substituting Eq. 7 into Eq. 2, the dynamic finite element equation is:

$$\begin{bmatrix} \boldsymbol{M}_{\mathrm{II}} & \boldsymbol{M}_{\mathrm{IB}} \\ \boldsymbol{M}_{\mathrm{BI}} & \boldsymbol{M}_{\mathrm{BB}} \end{bmatrix} \{\ddot{\boldsymbol{u}}_{\mathrm{I}}\ \ddot{\boldsymbol{u}}_{\mathrm{B}}\} + \begin{bmatrix} \boldsymbol{C}_{\mathrm{II}} & \boldsymbol{C}_{\mathrm{RI}} \\ \boldsymbol{C}_{\mathrm{BI}} & \boldsymbol{C}_{\mathrm{BB}} + \boldsymbol{C}_{\mathrm{B}} \end{bmatrix} \begin{Bmatrix} \dot{\boldsymbol{u}}_{\mathrm{I}} \\ \dot{\boldsymbol{u}}_{\mathrm{B}} \end{Bmatrix}$$
$$+ \begin{bmatrix} \boldsymbol{K}_{\mathrm{II}} & \boldsymbol{K}_{\mathrm{IB}} \\ \boldsymbol{K}_{\mathrm{BI}} & \boldsymbol{K}_{\mathrm{BB}} + \boldsymbol{K}_{\mathrm{B}} \end{bmatrix} \begin{Bmatrix} \boldsymbol{u}_{\mathrm{I}} \\ \boldsymbol{u}_{\mathrm{B}} \end{Bmatrix}$$
$$= \begin{Bmatrix} 0 \\ \boldsymbol{F}^f \end{Bmatrix}, \tag{8}$$

where submatrices $[\boldsymbol{C}_{\mathrm{B}}]$ and $[\boldsymbol{K}_{\mathrm{B}}]$ are both diagonal. For the boundary node l (x_l, y_l), $[\mathrm{C}_{\mathrm{B}}]_l = \boldsymbol{C}_l$, $[\boldsymbol{K}_{\mathrm{B}}]_l = \boldsymbol{K}_l$. $[\boldsymbol{F}^f]$ represents the equivalent seismic forces acting on the artificial boundary. F_l^f is the equivalent nodal force and has the form

$$\boldsymbol{F}_l^f = \boldsymbol{K}_l \boldsymbol{u}_l^f + \boldsymbol{C}_l \dot{\boldsymbol{u}}_l^f + \boldsymbol{A}_l \boldsymbol{f}_l^f. \tag{9}$$

Equation 9 provides the method of converting seismic waves into equivalent nodal forces that act on artificial boundary nodes to realize the seismic wave input in the seismic response analysis of the finite element model. To calculate the equivalent node force at each boundary node, it is necessary to provide the free field velocity, displacement, and stress at the node.

2.2 Equivalent nodal forces for the slope site

For the incidence of the seismic waves, the wave motions can be transferred into equivalent node forces applied at the boundary nodes. However, due to the topographic effect of the slope site, the seismic input wave fields at the left, right, and bottom boundaries of the two-dimensional finite element model are different. Realization of the seismic wave input at the left and right artificial boundaries requires the free field response calculation for a one-dimensional layered site. Because of the different heights of the left and right sides of the slope terrain, one-dimensional FEM calculations are necessary (Figure 2) (Zhao et al., 2017). The equivalent nodal forces at the left and right boundaries are then obtained by combining the calculation

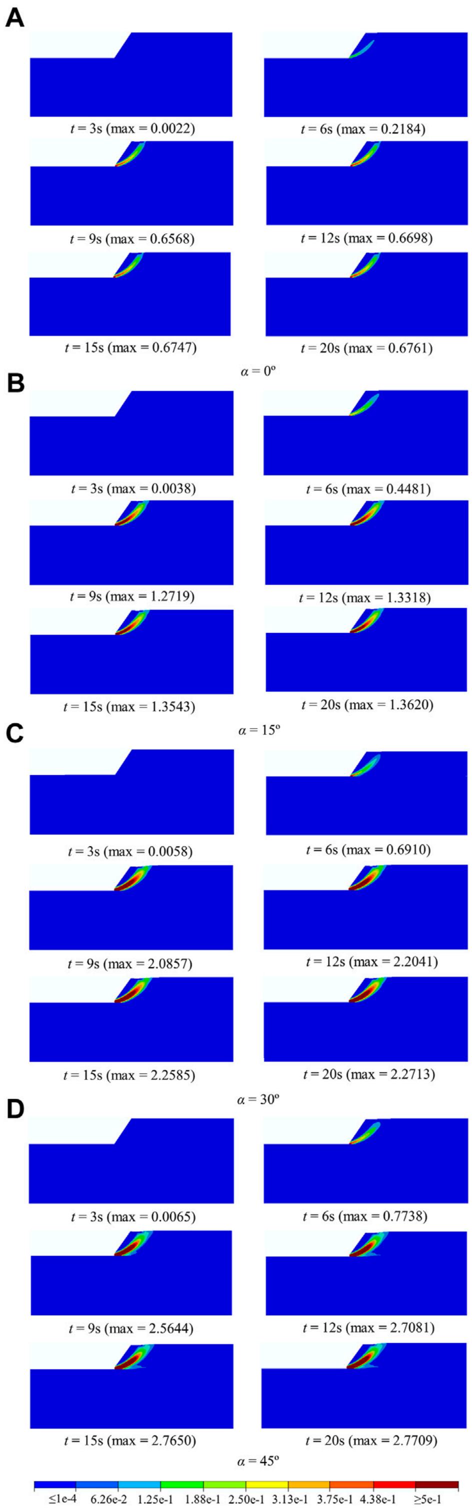

FIGURE 8
Plastic strain nephograms of the slope at different timing with different incident angles. **(A)** $\alpha = 0^\circ$. **(B)** $\alpha = 15^\circ$. **(C)** $\alpha = 30^\circ$. **(D)** $\alpha = 45^\circ$.

results of the one-dimensional FEM with the viscoelastic artificial boundary to complete the seismic input at the left and right boundaries.

For node $l\,(x_l, y_l)$ on the left or right boundary, the equivalent nodal forces of obliquely incident P waves can be given as

$$\begin{cases} F_x = K_{ln}u_x + C_{ln}\dot{u}_x + \delta A_l f_x \\ F_y = K_{ls}u_y + C_{ls}\dot{u}_y + \delta A_l f_y \end{cases}, \tag{10}$$

where u_x, $\dot{u}_x$, and f_x are the displacement, velocity, and internal stress of the one-dimensional finite element model at node l in the x direction respectively; u_y, $\dot{u}_y$, and f_y are the displacement, velocity, and internal stress of the one-dimensional finite element model at node l in the y direction, respectively; the boundary-dependent parameter δ values are -1 for the left boundary and 1 for the right boundary.

For node $l\ (x_l,\ 0)$ on the bottom boundary, the equivalent nodal forces of obliquely incident P waves can be given as

$$\begin{cases} F_x = K_{ls}u_{bx} + C_{ls}\dot{u}_{bx} - A_l f_{bx} \\ F_y = K_{ln}u_{by} + C_{ln}\dot{u}_{by} - A_l f_{by} \end{cases}, \tag{11}$$

where u_{bx} and $\dot{u}_{bx}$ are the displacement and velocity of the bottom boundary node in x the direction, respectively; u_{by} and $\dot{u}_{by}$ are the displacement and velocity of the bottom boundary node in the y direction, respectively; f_{bx} and f_{by} are the stresses of the bottom boundary node in the x and y directions, respectively.

Since the P waves are obliquely incident at an angle of α, there is a time delay in the response of any node on the bottom boundary relative to that of the initial incident node in the finite element model. $u_0(t)$ and $\dot{u}_0(t)$ are the displacement and velocity at the initial incident node with an angle of α, respectively. Therefore, the displacement and velocity of each node at the bottom boundary are expressed as

$$\begin{cases} u_{bx} = u_0(t-\Delta t)\cdot\sin\alpha \\ u_{by} = u_0(t-\Delta t)\cdot\cos\alpha \end{cases}, \tag{12}$$

$$\begin{cases} \dot{u}_{bx} = \dot{u}_0(t-\Delta t)\cdot\sin\alpha \\ \dot{u}_{by} = \dot{u}_0(t-\Delta t)\cdot\cos\alpha \end{cases}, \tag{13}$$

where $\Delta t = (x_l \sin\alpha / c_P)$ is the time delay in the response of any node on the bottom boundary relative to that of the initial incident node.

The stresses along and perpendicular to the incident direction of the P wave are expressed as

$$\begin{cases} \sigma_1 = \dfrac{(\lambda + 2G)}{c_p}\dot{u}_0(t-\Delta t) \\ \\ \sigma_2 = \dfrac{\lambda}{c_p}\dot{u}_0(t-\Delta t). \end{cases}, \tag{14}$$

The stresses f_{bx} and f_{by} of the bottom boundary node in the x and y directions are

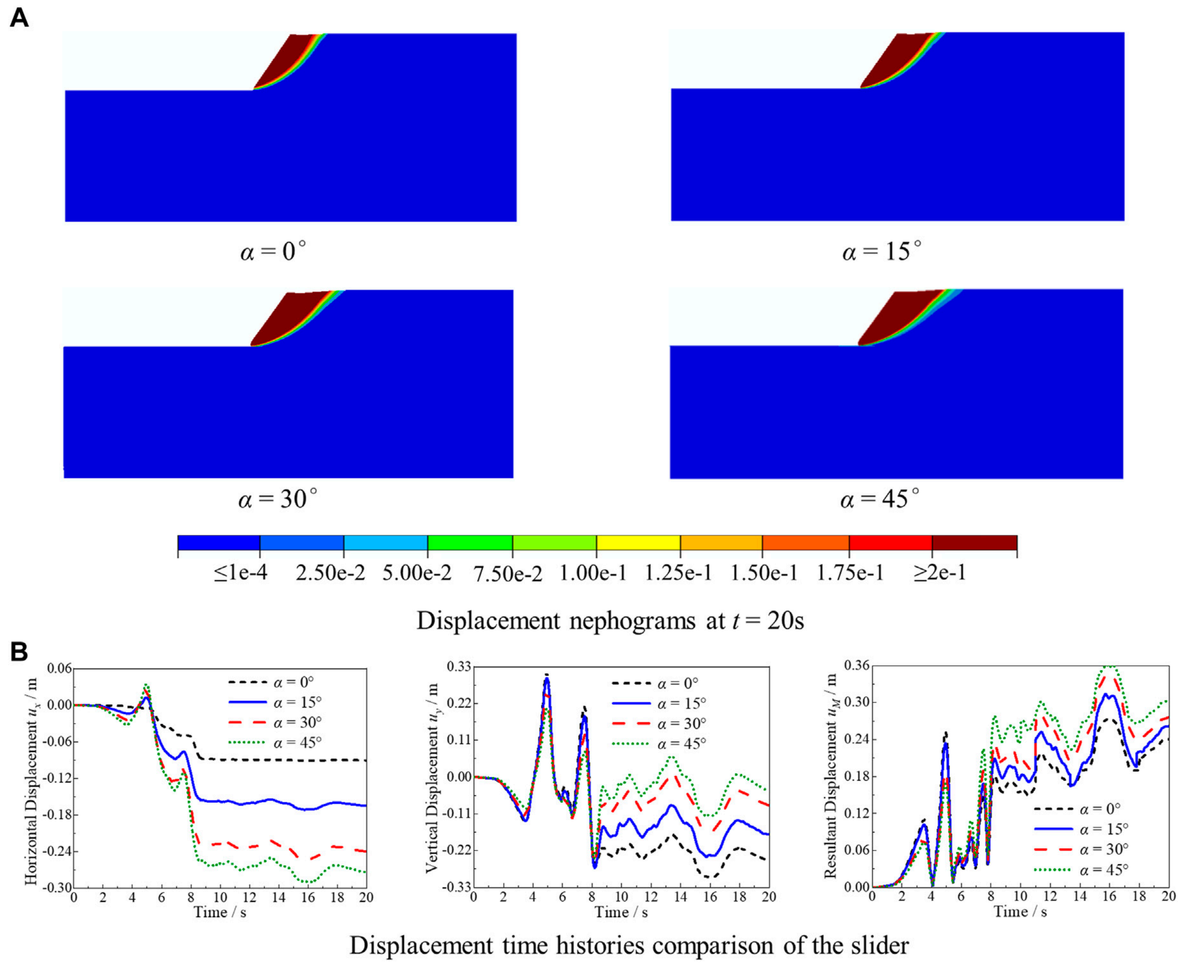

FIGURE 9
Displacement of the slope at different incident angles. **(A)** Displacement nephograms at *t* = 20 s. **(B)** Displacement time history comparison of the slider.

$$\begin{cases} f_{bx} = (\sigma_1 - \sigma_2)\cdot \sin\alpha \cdot \cos\alpha = \dfrac{2G\cdot \sin\alpha\cdot \cos\alpha}{c_p}\dot{u}_0(t-\Delta t) \\ f_{by} = \sigma_1 \cdot \cos^2\alpha + \sigma_2 \cdot \sin^2\alpha = \dfrac{\lambda + 2G\cos^2\alpha}{c_p}\dot{u}_0(t-\Delta t) \end{cases}. \tag{15}$$

3 Method validation

The seismic input method established in Section 2 is realized through programming with MATLAB software and is applied to the seismic response analysis of slope sites in the commercial finite element ABAQUS software. To verify the accuracy of the proposed seismic input method, this section simulates the free field response of a layered slope site under the action of obliquely incident P waves. The size of the finite element model of the two-dimensional slope site is 240 m long, 70 m high on the left side, and 100 m high on the right side (Figure 3). *h* represents the thickness of soft layer; in this section, *h* = 30 m. The reference solution is the calculation result of an extended computational model with a length of 4100 m, a right-side height of 2100 m, and a left-side height of 2070 m. The slope site is meshed by solid elements, with a mesh size of 1 m. The material parameters of each layer of the slope site are shown in Table 1 (JTG/T D70-2010, 2010). The form of the obliquely incident pulse wave with an incident angle of *α* acting on the slope site calculation model is shown in Figure 4.

In verifying the seismic input method for the layered slope site, the P wave is incident from the left corner of the model with angles of 0°, 10°, 20°, and 30°. The observation nodes are arranged at each node of the free surface within the range of 10 m from the left side of the slope toe to 10 m from the right side of the slope top (Figure 3). Top node A and toe node B are the main observation nodes. The results of the acceleration, velocity, and displacement time history of the layered slope site model, calculated on the established seismic input method, are compared with the results of the extended model. The comparison results are shown in Figure 5. The results obtained with the aid of the established seismic input method agree well with the reference solutions. The accuracy and applicability of the established seismic wave input method for slope sites are thus verified.

The relative error of the peak displacement value is used to measure the accuracy of the calculation results; the calculation formula is

$$R = \frac{\left||r(t)|_{\max} - |r_0(t)|_{\max}\right|}{|r_0(t)|_{\max}}, \tag{16}$$

where $r_0(t)$ is the displacement reference solution, $r(t)$ is the displacement calculation result obtained using the seismic input method proposed in this paper, | | represents the absolute value, and the subscript $_{\max}$ is used to evaluate the maximum value.

The comparison of the results and relative errors of the vertical displacement peaks of each observation node on the free surface are shown in Figure 6. The change in the dynamic amplification effect of the displacement peak with topographic relief is negligible, and the maximum error of the displacement peak at four incident angles is less than 1%. Therefore, by comparing the calculated results of the small model of the slope site with the numerical results of the extended model, the high accuracy of the developed seismic input method is further demonstrated.

4 Parameter study

This section discusses the effects of incident angles, soft-hard rock interface positions, and impedance ratios on the seismic responses of slope sites exposed to obliquely incident P waves. The seismic input method of the slope site established in Section 2 is employed.

The upper soft rock and lower hard rock of the slope site is modeled in ABAQUS software, and the Mohr-Coulomb elastic-plastic model is selected for the constitutive relationship. The model dimensions are shown in Figure 3. The Kobe wave (Figure 7) is input by the seismic input method proposed in this paper to study the factors that influence seismic landslides.

4.1 Input angle of the seismic wave

This subsection investigates the influence of the different incident angles (α = 0°, 15°, 30°, and 45°) of P waves on the dynamic responses of the slope site. The site parameters are

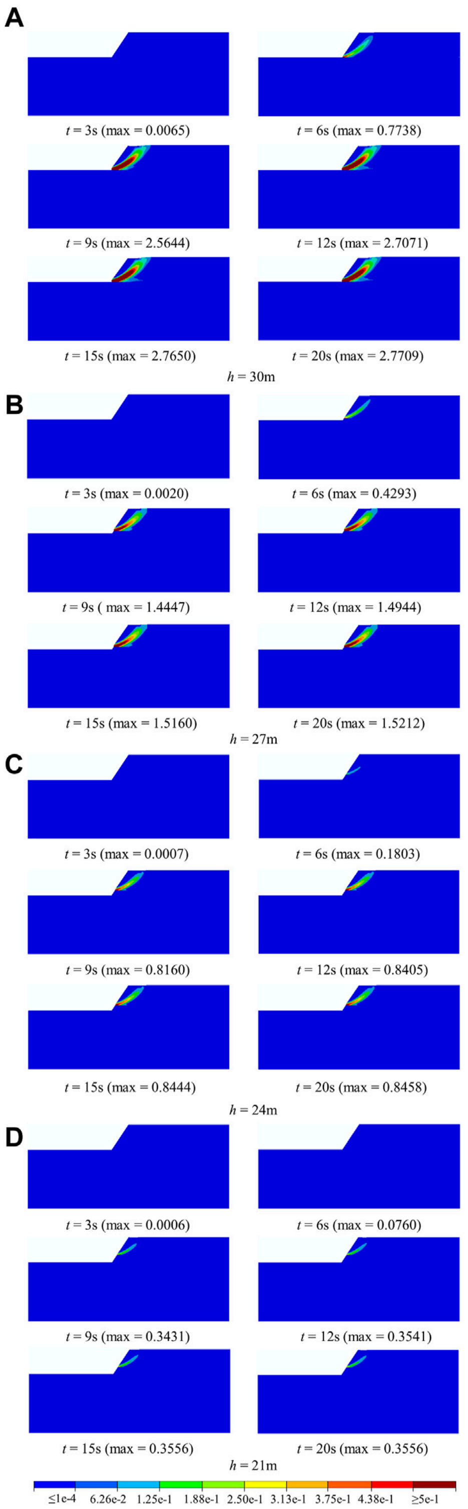

FIGURE 10
Plastic strain nephograms of the slope at different timings with different soft–hard rock interface positions. **(A)** h = 30 m. **(B)** h = 27 m. **(C)** h = 24 m. **(D)** h = 21 m.

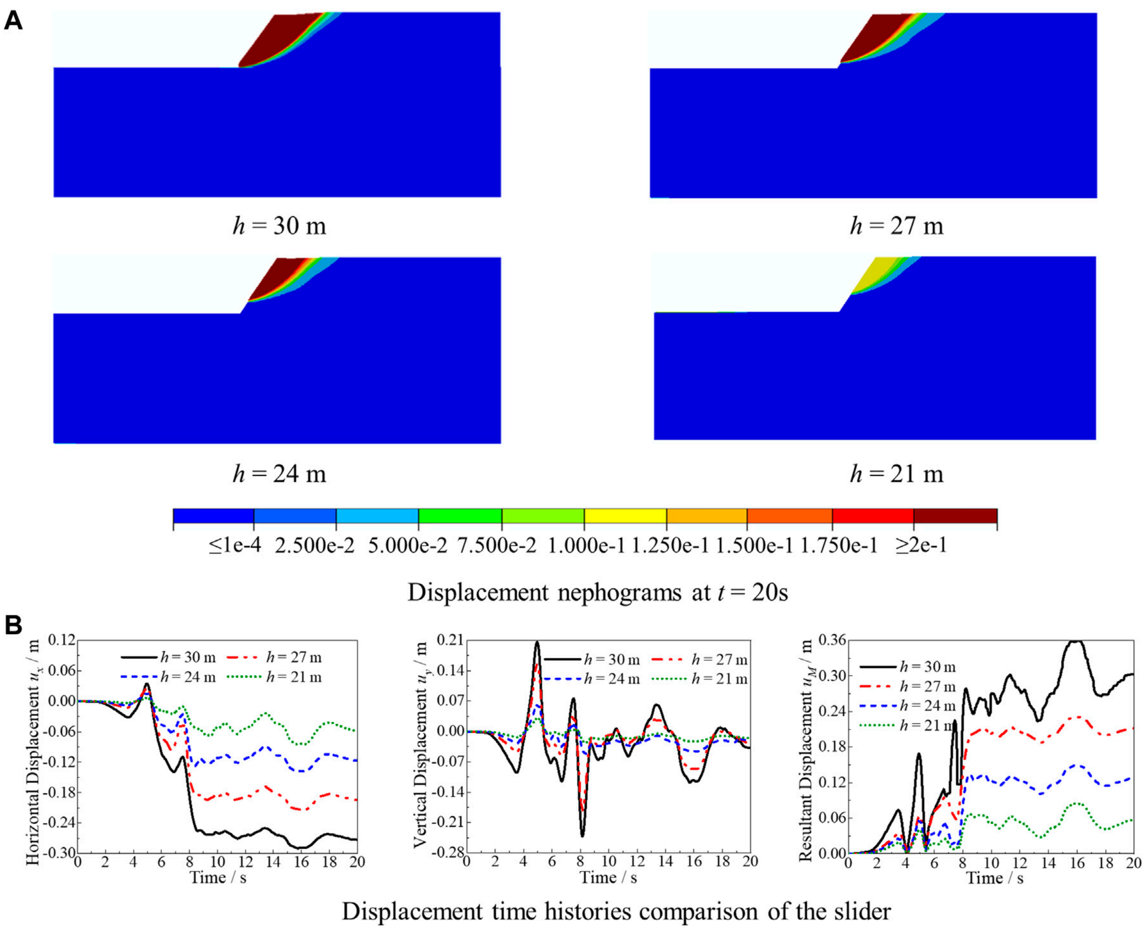

FIGURE 11
Displacement of the slope at different interface positions of soft and hard rock. **(A)** Displacement nephograms at t = 20 s. **(B)** Displacement time history comparison of the slider.

TABLE 2 Material constants of the slope site.

Case	Impedance ratio a	Layer	Density ρ (kg/m^3)	Elastic modulus E (Pa)	Poisson's ratio υ	Internal friction angle φ (°)	Cohesion c (Pa)	C_P (m/s)	C_{SV} (m/s)
Case 1	0.2	Upper	1700	1.2e9	0.42	21	0.08e6	1342	499
		Lower	2500	20.2e9	0.25	50	1.5e6	3114	1798
Case 2	0.4	Upper	1700	1.2e9	0.42	21	0.08e6	1342	499
		Lower	2200	5.8e9	0.31	37	0.6e6	1912	1003
Case 3	0.6	Upper	1700	1.2e9	0.42	21	0.08e6	1342	499
		Lower	2100	2.7e9	0.32	31	0.35e6	1356	698
Case 4	0.8	Upper	1700	1.2e9	0.42	21	0.08e6	1342	499
		Lower	1900	1.68e9	0.37	25	0.16e6	1251	568
Case 5	1.0	Upper	1700	1.2e9	0.42	21	0.08e6	1342	499
		Lower	1700	1.2e9	0.42	21	0.08e6	1342	499

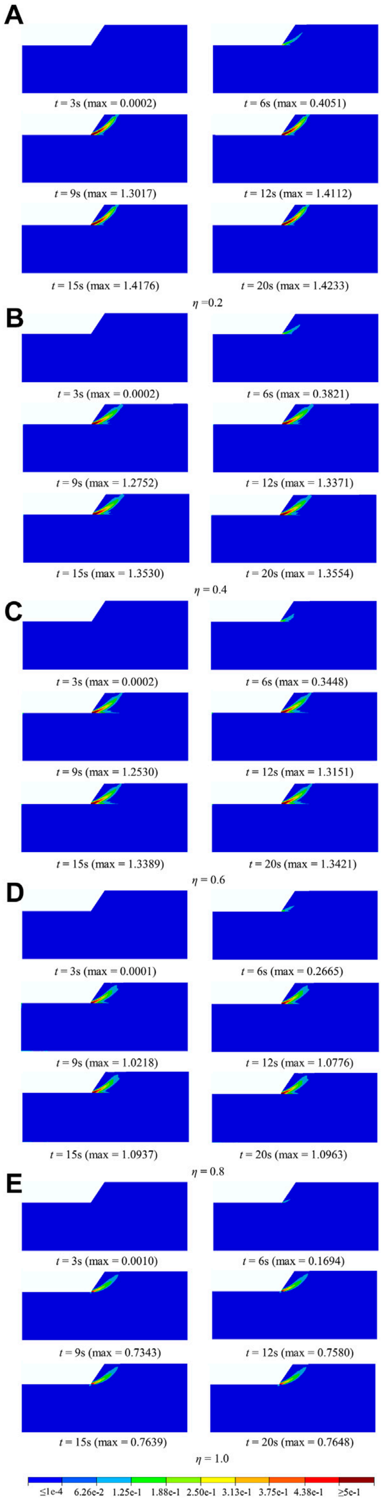

FIGURE 12
Plastic strain nephograms of the slope at different timing with different impedance ratios. **(A)** $\eta = 0.2$. **(B)** $\eta = 0.4$. **(C)** $\eta = 0.6$. **(D)** $\eta = 0.8$. **(E)** $\eta = 1.0$.

shown in Table 1, with the soft and hard rock interface 30 m from the slope top. Figure 8 shows the plastic strain nephograms of the slope site at different timing exposed to obliquely incident P waves with different angles. The displacement nephograms of the slope site at $t = 20$ s are illustrated in Figure 9A.

As shown in Figure 8, landslides occur in the slope sites of upper soft rock and lower hard rock exposed to obliquely incident P waves with different incident angles. Landslide surfaces appear on the slope bodies, and the blocks slide down along the landslide surfaces. With increasing incident angle, the maximum plastic strain value increases, and the plastic zone of the slope site enlarges. Meanwhile, the landslide surface starts earlier at larger incident angles. Figure 9A shows that the volume and sliding displacement of the landslide mass increase with an increasing incident angle, and the sliding slope surface changes from steep to gentle. This means that the landslide hazard becomes higher with an increase in the oblique incidence angle of the P wave.

To better reflect the displacement of each slider at different incident angles, Figure 9B shows the displacement time history comparison of a slider at such angles. As shown in Figure 9B, the absolute value of the horizontal average displacement of the slider increases with an increase of the incident angle, while the absolute value of the vertical average displacement decreases. The resultant displacement of the sliding block first decreases and then increases with an increase of the incidence angle, and the corresponding deformation of the slope site gradually changes from elastic to plastic deformation.

4.2 Positions of the soft-hard rock interface

This subsection analyzes the effect of the soft and hard rock interface positions on the dynamic response of the slope site by adopting the slope site model of the upper soft rock and lower hard rock shown in Figure 3. The distances between the soft–hard rock interface and the slope top are $h = 30$, 27, 24, and 21 m, respectively. The smaller the distance between the soft-hard rock interface and the slope top, the thinner the soft rock overburden is above the hard rock. The site parameters are shown in Table 1.

P waves are obliquely incident at an angle of $\alpha = 45^\circ$ from the lower left corner of the model. Figure 10 shows the plastic strain nephograms of the slope site under the action of obliquely incident P waves with different soft–hard rock interface positions at different timings. Figure 11A depicts the displacement nephograms of the slope site at $t = 20$ s. Figures 10, 11A show that, for the slope site with upper soft rock and lower hard rock, the plastic zones first appear at the interfaces between soft rock and hard rock and then continuously develop

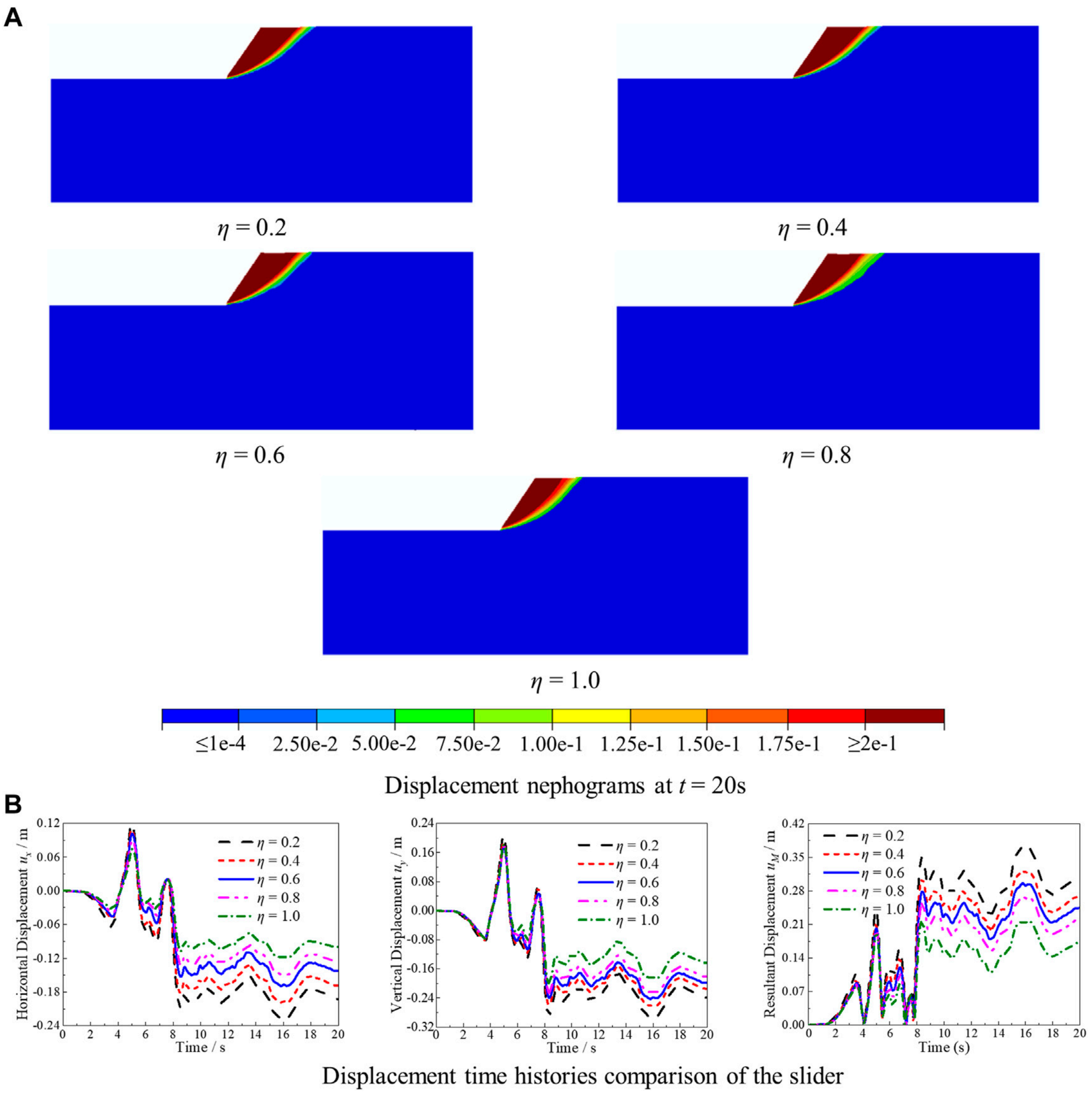

FIGURE 13
Displacement of the slope at different impedance ratios. **(A)** Displacement nephograms at t = 20 s. **(B)** Displacement time history comparison of the slider.

upward to form landslide surfaces. A thicker soft-rock overburden tends to cause an earlier appearance of the plastic strain zone, faster sliding surface formation, a greater plastic zone and plastic deformation, and stronger sliding.

In order to better reflect the influence of the soft–hard rock interface position on the sliding displacement of the slider, Figure 11B describes the displacement time history comparison results of the slider at different positions of the soft–hard rock interface. Thus, the absolute value of the horizontal and vertical average displacement and the resultant displacement of the slider all increase as the distance between the soft–hard rock interface to the top of the slope changes from near to far.

According to the comprehensive analysis in Figures 10, 11, on slope sites of upper soft rock and lower hard rock, the smaller the thickness of the soft rock layer, the safer the site will be. When the interface between soft and hard rock is 21 m from the slope top, the plastic strain zone appears late, and the plastic strain and sliding displacement of the slider are small. The thickness of soft rock is small enough to prevent landslides.

4.3 Impedance ratio

This subsection analyzes the dynamic responses of the layered slope site at different impedance ratios (η = 0.2, 0.4, 0.6, 0.8, and 1.0) of the upper and lower layers. The size of the slope site finite element model is the same as in Section 4.1; the site parameters are shown in Table 2. P waves are obliquely incident at an angle of $\alpha = 15^\circ$ from the lower left corner of the model.

Plastic strain nephograms of the slope with different impedance ratios are given in Figure 12. The greater the impedance ratio between the upper and lower media, the later the plastic strain zone appears, the slower the development speed, and the later the landslide surface will occur. The maximum plastic strain of the slope site decreases with increasing impedance ratio between the upper and lower media.

Figure 13A illustrates the displacement nephograms of the slope site with different impedance ratios at $t = 20$ s. The impedance ratio has no effect on the position of the landslide surface and the volume of the sliding block but has a significant effect on the sliding displacement of the sliding block.

To better reflect the influence of the impedance ratio between the upper and lower media on the sliding displacement of the slider, Figure 13B describes the displacement time history comparison results of the slider at different impedance ratios. It can be concluded that the absolute value of the horizontal and vertical average displacement and the resultant displacement of the slider have the same change trend under different impedance ratios, and that they all decrease with the increase in impedance ratio. With this increase, the landslide hazard of the slope site decreases significantly.

5 Summary and conclusion

Landslide seismic disasters have become a focus of geological hazard research because of their wide distribution, frequency, and great harm. Due to the topographic effect of slope sites, the seismic input method of regular sites is no longer applicable. This paper combines viscoelastic boundary with a seismic input method for slope sites under the action of obliquely incident P waves. Application is made with MATLAB programming software. The finite element model of the slope site is established in the application software ABAQUS, and the seismic mechanical behavior of the slope site is simulated by the Mohr-Coulomb model. Compared with the calculation results of the extended model, the established seismic input method is verified as correct. The established seismic input method is applied to analyze the parameters of landslide disasters in slope sites with upper soft rock and lower hard rock.

Under all calculation working conditions, the landslide hazard occurrence process of the slope site is basically the same, but the severity of the landslide hazard is different. Under the action of obliquely incident P waves, a small range of plastic deformation in upper soft rock slopes and lower hard rock slopes first occurs at the soft–hard rock interface. Next, the plastic zone expands upward to form a small-scale plastic zone, and the maximum plastic strain value increases continuously; the input velocity time history is then close to the peak. Thereafter, the plastic zone expands upward. When the input seismic wave reaches peak value, an obvious slip surface is formed. The slope body slides downward along this, and the deformation of the slope top is obvious. After the peak value is reached, there is no obvious change in the size of the plastic zone, but the maximum plastic strain value still increases in a small range over time. The details are as follows.

(1) For the slope site with upper soft rock and lower hard rock, the plastic zone and plastic strain value increase as the incident angle of the P wave changes from 0° to 45°. The larger the incident angle of the P wave, the earlier the landslide surface will form, the larger the landslide volume and sliding displacement, and the more serious the landslide disaster will be.
(2) For slope sites with upper soft rock and lower hard rock, the plastic zones first appear at the soft–hard rock interface and then continuously develop upward to form the landslide surfaces. The farther the soft–hard interface is from the slope top, the earlier the plastic strain zone will appear, and the faster the slip surface forms. With the thickening of the soft rock overburden, the plastic zone area and plastic deformation increase, and the sliding displacement of the slider is more obvious.
(3) The greater the impedance ratio between the upper and lower media of the layered slope site, the later the plastic strain zone will appear, and the slower the plastic zone develops. At different impedance ratios, the location of the landslide surface and the volume of the sliding block are basically the same. The maximum plastic strain and sliding displacement of the sliding block decrease with the increase of impedance ratio.

Some limitations should be noted with this paper. As the type of seismic failure of hard rock slopes is different from that studied in this paper, the proposed method is not suitable for such slopes. These conclusions and findings are based on the simulation results of the calculation model of the soft rock slope site and slope site with upper soft rock and lower hard rock. Due to the complexity of the problems, the validity of these conclusions and findings for calculating a model of hard rock slope sites or soil slope sites need much more study. Moreover, the simulation of the material of the slope site is based on the Mohr-Coulomb model without considering the existence of cracks and structural planes in rock mass materials. In general, the limits mentioned above should be addressed in future work.

Finally, the proposed method only discusses seismic landslides under the action of P waves, and further research is needed on seismic landslides under the action of shear waves and Rayleigh waves. Follow-up study regarding these issues is needed.

Data availability statement

The original contributions presented in the study are included in the article/supplementary material; further inquiries can be directed to the corresponding author.

Author contributions

HJ: data curation, writing—original draft preparation, and program. JX: conceptualization, writing-reviewing, and fund support. MZ: guide the establishment of method and writing-reviewing. JH: software and assist in the establishment of the method. XD: resources, supervision, writing—review and editing. JW: visualization and data curation.

Funding

This work was supported by Postdoctoral Science Foundation of China (2022M722929), the Special Fund of the Institute of Geophysics, China Earthquake Administration (DQJB20B23), and Beijing Natural Science Foundation Program (JQ19029). The support is gratefully acknowledged.

Conflict of interest

The authors declare that the research was conducted in the absence of any commercial or financial relationships that could be construed as a potential conflict of interest.

Publisher's note

References

Assimaki, D., Gazetas, G., and Kausel, E. (2005). Effects of local soil conditions on the topographic aggravation of seismic motion: Parametric investigation and recorded field evidence from the 1999 athens earthquake. *Bull. Seismol. Soc. Am.* 95 (3), 1059–1089. doi:10.1785/0120040055

Astley, R. J. (2000). Infinite elements for wave problems: A review of current formulations and an assessment of accuracy. *Int. J. Numer. Methods Eng.* 49 (7), 951–976. doi:10.1002/1097-0207(20001110)49:7<951::aid-nme989>3.0.co;2-t

Athanasopoulos, G. A., Pelekis, P. C., and Leonidou, E. A. (1999). Effects of surface topography on seismic ground response in the Egion (Greece) 15 June 1995 earthquake. *Soil Dyn. Earthq. Eng.* 18 (2), 135–149. doi:10.1016/s0267-7261(98)00041-4

Bazyar, M. H., and Song, C. (2017). Analysis of transient wave scattering and its applications to site response analysis using the scaled boundary finite-element method. *Soil Dyn. Earthq. Eng.* 98, 191–205. doi:10.1016/j.soildyn.2017.04.010

Bettess, P. (1977). Infinite elements. *Int. J. Numer. Methods Eng.* 11 (1), 53–64. doi:10.1002/nme.1620110107

Bird, J. F., and Bommer, J. J. (2004). Earthquake losses due to ground failure. *Eng. Geol.* 75 (2), 147–179. doi:10.1016/j.enggeo.2004.05.006

Bouckovalas, G. D., and Papadimitriou, A. G. (2005). Numerical evaluation of slope topography effects on seismic ground motion. *Soil Dyn. Earthq. Eng.* 25 (7-10), 547–558. doi:10.1016/j.soildyn.2004.11.008

Cavallin, A., and Slejko, D. (1986). Statistical approach to landslide and soil liquefaction hazards in seismic areas. *Geol. Appl. E Idrogeol.* 21 (2), 231–236.

Chigira, M., and Yagi, H. (2005). Geological and geomorphological characteristics of landslides triggered by the 2004 Mid Niigta prefecture earthquake in Japan. *Eng. Geol.* 82 (4), 202–221. doi:10.1016/j.enggeo.2005.10.006

Clayton, R., and Engquist, B. (1977). Absorbing boundary conditions for acoustic and elastic wave equations. *Bull. Seismol. Soc. Am.* 67 (6), 1529–1540. doi:10.1785/bssa0670061529

Deeks, A. J., and Randolph, M. F. (1994). Axisymmetric time-domain transmitting boundaries. *J. Eng. Mech.* 120 (1), 25–42. doi:10.1061/(asce)0733-9399(1994)120:1(25)

Du, X. L., Zhao, M., and Wang, J. T. (2006). A stress artificial boundary in FEA for near-field wave problem. *Chin. J. Theor. Appl. Mech.* 38, 49–56.

Gischig, V. S., Eberhardt, E., Moore, J. R., and Hungr, O. (2015). On the seismic response of deep-seated rock slope instabilities—insights from numerical modeling. *Eng. Geol.* 193, 1–18. doi:10.1016/j.enggeo.2015.04.003

Huang, J. Q., Du, X. L., Jin, L., and Zhao, M. (2016). Impact of incident angles of P waves on the dynamic responses of long lined tunnels. *Earthq. Eng. Struct. Dyn.* 45 (15), 2435–2454. doi:10.1002/eqe.2772

Huang, J. Q., Du, X. L., Zhao, M., and Zhao, X. (2017b). Impact of incident angles of earthquake shear (S) waves on 3-D non-linear seismic responses of long lined tunnels. *Eng. Geol.* 222, 168–185. doi:10.1016/j.enggeo.2017.03.017

Huang, J. Q., Zhao, M., and Du, X. L. (2017a). Non-linear seismic responses of tunnels within normal fault ground under obliquely incident P waves. *Tunn. Undergr. Space Technol.* 61, 26–39. doi:10.1016/j.tust.2016.09.006

Jibson, R. W., Harp, E. L., and Michael, J. A. (2000). A method for producing digital probabilistic seismic landslide hazard maps. *Eng. Geol.* 58 (3), 271–289. doi:10.1016/s0013-7952(00)00039-9

JTG/T D70-2010 (2010). Guidelines for Design of Highway Tunnel. *The People's Republic of China: Industry Recommended Standards of the People's Republic of China*, 35–48 (In Chinese).

Keeper, D. K. (1984). Landslides caused by earthquakes. *Geol. Soc. Am. Bull.* 95 (4), 406. doi:10.1130/0016-7606(1984)95<406:lcbe>2.0.co;2

Lenti, L., and Martino, S. (2012). The interaction of seismic waves with step-like slopes and its influence on landslide movements. *Eng. Geol.* 126, 19–36. doi:10.1016/j.enggeo.2011.12.002

Li, C., He, J., Wang, Y., and Wang, G. (2022). A novel approach to probabilistic seismic landslide hazard mapping using Monte Carlo simulations. *Eng. Geol.* 301, 106616. doi:10.1016/j.enggeo.2022.106616

Li, H. F., Zhao, M., and Du, X. L. (2020). Accurate H-shaped absorbing boundary condition in frequency domain for scalar wave propagation in layered half-space. *Int. J. Numer. Methods Eng.* 121, 4268–4291. doi:10.1002/nme.6424

Liao, Z. P., and Wong, H. L. (1984). A transmitting boundary for the numerical simulation of elastic wave propagation. *Int. J. Soil Dyn. Earthq. Eng.* 3 (4), 174–183. doi:10.1016/0261-7277(84)90033-0

Liu, J. B., Du, Y. X., Du, X. L., Wang, Z. Y., and Wu, J. (2006). 3D viscous-spring artificial boundary in time domain. *Earthq. Engin. Engin. Vib.* 5 (1), 93–102. doi:10.1007/s11803-006-0585-2

Liu, J. B., and Lu, Y. D. (1998). A direct method for analysis of dynamic soil-structure interaction based on interface idea. *Dev. Geotechnical Eng.* 83 (3), 261–276. doi:10.1016/s0165-1250(98)80018-7

Liu, J. B., and Wang, Y. (2007). A 1D Time-domain method for inplane wave motion of free field in layered media. *Chin. J. Eng. Mech.* 24 (7), 16–22.

Lysmer, J., and Kuhlemeyer, R. L. (1969). Finite dynamic model for infinite media. *J. Engrg. Mech. Div.* 95 (4), 859–877. doi:10.1061/jmcea3.0001144

Maleki, M., and Khodakarami, M. I. (2017). Feasibility analysis of using MetaSoil scatterers on the attenuation of seismic amplification in a site with triangular hill due to SV-waves. *Soil Dyn. Earthq. Eng.* 100, 169–182. doi:10.1016/j.soildyn.2017.05.036

Nakamura, N. (2012). Two-dimensional energy transmitting boundary in the time domain. *Earthquakes Struct.* 3 (2), 97–115. doi:10.12989/eas.2012.3.2.097

Owen, L. A., Kamp, U., Khattak, G. A., Harp, E. L., Keefer, D. K., and Bauer, M. A. (2008). Landslides triggered by the 8 october 2005 kashmir earthquake. *Geomorphology* 94 (1-2), 1–9. doi:10.1016/j.geomorph.2007.04.007

Pareek, N., Arora, S., and Arora, M. K. (2010). Impact of seismic factors on landslide susceptibility zonation: A case study in part of Indian himalayas. *Landslides* 7, 191–201. doi:10.1007/s10346-009-0192-1

Pelekis, P., Batilas, A., Pefani, E., Vlachakis, V., and Athanasopoulos, G. (2017). Surface topography and site stratigraphy effects on the seismic response of a slope in the Achaia-Ilia (Greece) 2008 Mw6. 4 earthquake. *Soil Dyn. Earthq. Eng.* 100, 538–554. doi:10.1016/j.soildyn.2017.05.038

Poursartip, B., Fathi, A., and Kallivokas, L. F. (2017). Seismic wave amplification by topographic features: A parametric study. *Soil Dyn. Earthq. Eng.* 92, 503–527. doi:10.1016/j.soildyn.2016.10.031

Prestininzi, A., and Romeo, R. W. (2000). Earthquake-induced ground failures in Italy. *Eng. Geol.* 58 (3-4), 387–397. doi:10.1016/s0013-7952(00)00044-2

Rizzitano, S., Cascone, E., and Biondi, G. (2014). Coupling of topographic and stratigraphic effects on seismic response of slopes through 2D linear and equivalent linear analyses. *Soil Dyn. Earthq. Eng.* 67, 66–84. doi:10.1016/j.soildyn.2014.09.003

Sato, P. H., Hasegawa, H., Fujiwara, S., Tobita, M., Koarai, M., Une, H., et al. (2007). Interpretation of landslide distribution triggered by the 2005 Northern Pakistan earthquake using SPOT 5 imagery. *Landslides* 4 (2), 113–122. doi:10.1007/s10346-006-0069-5

Semblat, J. F. (2011). Modeling seismic wave propagation and amplification in 1D/2D/3D linear and nonlinear unbounded media. *Int. J. Geomech.* 11 (6), 440–448. doi:10.1061/(asce)gm.1943-5622.0000023

Zhao, M., Gao, Z. D., Du, X. L., Wang, J. T., and Zhong, Z. L. (2019). Response spectrum method for seismic soil-structure interaction analysis of underground structure. *Bull. Earthq. Eng.* 17, 5339–5363. doi:10.1007/s10518-019-00673-6

Zhao, M., Gao, Z. D., Wang, L. T., Du, X. L., Huang, J. Q., and Li, Y. (2017). Obliquely incident earthquake input for soil-structure interaction in layered half space. *Earthquakes Struct.* 13 (06), 573–588.

Zhao, M., Yin, H. Q., Du, X. L., Liu, J. B., and Liang, L. (2013). 1D finite element artificial boundary method for layered half space site response from obliquely incident earthquake. *Earthquakes Struct.* 1 (9), 173–194. doi:10.12989/eas.2015.9.1.173

frontiers | Frontiers in Earth Science

TYPE Original Research
PUBLISHED 05 January 2023
DOI 10.3389/feart.2022.1118079

OPEN ACCESS

EDITED BY
Yefei Ren,
Institute of Engineering Mechanics, China Earthquake Administration, China

REVIEWED BY
Weibing Gong,
University of California, Berkeley, United States
Ning Zhang,
Anhui Jianzhu University, China

*CORRESPONDENCE
Zhenghua Zhou,
✉ bjsmoc@163.com

SPECIALTY SECTION
This article was submitted to Structural Geology and Tectonics, a section of the journal Frontiers in Earth Science

RECEIVED 07 December 2022
ACCEPTED 20 December 2022
PUBLISHED 05 January 2023

CITATION
Du L, Jin L and Zhou Z (2023), Analysis of the seismic effects of the local slope site of Longtoushan market town in Ludian Ms6.5 earthquake.
Front. Earth Sci. 10:1118079.
doi: 10.3389/feart.2022.1118079

Analysis of the seismic effects of the local slope site of Longtoushan market town in Ludian Ms6.5 earthquake

Liting Du[1], Liguo Jin[2] and Zhenghua Zhou[1]*

[1]College of Transportation Engineering, Nanjing Tech University, Nanjing, China, [2]Institute of Geophysics, China Earthquake Administration, Beijing, China

In the Ludian Ms6.5 earthquake (Yunnan, China), Longtoushan market town and its vicinity showed significant differences in earthquake damage. To explain this phenomenon, this paper discusses the local engineering geological conditions, local topographic effects, and seismic response of the soil layer in Longtoushan market town. The results show that complex topography and varied engineering geological conditions will lead to significant differences in ground motion, and then lead to significant differences in building earthquake damage. Slope topography has an obvious influence on ground motion. From the foot of the slope to the top of the slope, the degree of influence gradually increases, and the influence in different directions is different, as shown: the closer to the top of the slope, the more significant the difference. This indicates that the serious damage to buildings built on the slope is caused by the amplification effect of local terrain and the differential effect of ground motion. Although the site belongs to Class II site, the near-surface geotechnical properties and their combination characteristics, the physical state and thickness of the overlying soil layer, the variation characteristics of shear wave velocity, the non-linear dynamic characteristics of the soil, and other factors play a decisive role in the amplification degree of ground motion. The significant difference in ground motion on the surface of the slope site leads to a significant difference in seismic damage to buildings on the site. The covering soil layer has a significant effect on the acceleration response spectrum. The conclusions obtained in this paper can provide a scientific basis for the site selection of engineering construction and seismic design of building structures.

KEYWORDS

ground motion, site effect, local topography, response spectrum, ground pulsation

1 Introduction

China has been hit by several destructive earthquakes since 2000, causing heavy casualties and economic losses. For example, the Wenchuan Ms8.0 earthquake in 2008 caused more than 100,000 casualties and hundreds of billions of direct economic losses (Peng et al., 2011). In 2010, the Yushu Ms7.1 earthquake in Qinghai Province killed more than 2000 people (Ni et al., 2010). The Lushan Ms7.0 earthquake in Sichuan Province in 2013 caused hundreds of casualties (Li et al., 2013). The Jinggu Ms6.6 earthquake in Yunnan Province in 2014 also caused hundreds of casualties and economic losses of 5 billion yuan (Jia et al., 2016). Ludian Ms6.5 earthquake in Yunnan Province on 3 August 2014, caused 617 deaths, 112 missing, and 3,143 injured, and the direct economic losses is 23.578 billion yuan (Hao et al., 2016). In the Ludian earthquake, the seismic intensity of Longtoushan market town was IX, which caused serious building damages, as shown in Figure 1.

In the Ludian earthquake, the strong-motion seismograph located in the Bureau of Finance of Longtoushan Market Town recorded a maximum acceleration value of 949 cm/s^2 in the EW direction, which is the largest peak ground acceleration (PGA) recorded in the meizoseismal area in the mainland of China so far (Cui et al., 2014). The investigation of the earthquake damage in the meizoseismal area shows that there is a large difference in the earthquake damage to buildings in Longtoushan Market Town, which is shown as "moderate earthquake but great disaster". The study of the abnormal earthquake damage phenomenon is helpful to reveal the mechanism of the abnormal earthquake damage, which has important reference value for the revision of the seismic design code of buildings and the site selection of construction projects.

Earthquake magnitude, propagation path, and local site conditions are the main factors affecting earthquake damage (Mayoral et al., 2019; Jin et al., 2020; Pamuk and Ozer., 2020). In the case of the Ludian earthquake, a mere Ms6.5 earthquake would not have been enough to cause such severe damage to Longtoushan Market Town. The only possible reason for the significant difference in earthquake damage, under the condition of a similar transmission path, is that the local site conditions have a significant impact on earthquake damage.

Local site conditions have a significant influence on earthquake damage to buildings (Panzera et al., 2018; Brando et al., 2020; Cetin et al., 2022; Huang et al., 2022). Borcherd et al. (1976) analyzed the San Francisco earthquake in 1906 and found that the earthquake damage to buildings located on bedrock or the hard site was light, while the earthquake damage to buildings located on soft ground was heavy. They pointed out that the site conditions have an important influence on earthquake damage. Subsequent earthquakes also show that site conditions have a significant impact on building earthquake damage (Estrella et al., 2003). For example, the Mexico earthquake in 1985, the Jiji earthquake in Taiwan in 1999 (Wang et al., 2002), and the Wenchuan earthquake in Sichuan in 2008 (Bo et al., 2009) all confirmed this conclusion. In addition, the influence of local terrain on building earthquake damage is mainly reflected in the amplification of local terrain on ground motion and the non-uniformity of spatial distribution (Geli et al., 1988; Çelebi et al., 1991; Shiann-Jong et al., 2009; Sun et al., 2011; Yang et al., 2018). This shows that for buildings located on complex terrain, it is necessary to consider local topographic effects in site selection and seismic design of engineering structures to ensure their safety under earthquakes.

The detailed seismic damage investigation data, strong motion records, and engineering geological data of the Ludian earthquake provide abundant materials for the analysis of local ground motion effects in Longtoushan Market Town. This paper will study the ground motion effect of the local slope site in Longtoushan Market Town through the analysis of local geological conditions, local topographic effect and seismic response of the soil layer, and then reveal the mechanism of serious earthquake damage in Longtoushan Market Town, so as to provide the basis for land planning, the site selection for engineering construction and building seismic design in Longtoushan Market Town.

2 Engineering geological condition

The Ludian earthquake area is located in the south-central section of the south-north-trending seismic belt on the eastern margin of the Qinghai-Tibet Plateau. The geological structure here is very complex, mainly the NE- and NW- trending fault structures. The NE-trending fault is mainly the Zhaotong-Ludian fault, which consists of three secondary faults. The NW-trending fault is mainly the Baogunao-Xiaohe fault, which consists of several short faults. Longtoushan Market Town is just in the intersection area of the Zhaotong-Ludian fault and the Baogunao-Xiaohe fault (Pang et al., 2016).

According to the investigation of Ludian earthquake damage, the geomorphic features of Longtoushan market town are mainly structural erosion canyons and denudating landforms of low mountain mounds, among which Longquan River and Shaba River pass through the town. Longtoushan market town is located between the foot of the mountain and the Longquan River, and the construction site is mostly the gentle slope landform formed by the accumulation of rivers. The overlying soil layer of bedrock mainly includes medium compressible clay containing gravel, pebbled silty clay, gravel soil, pebble, silty clay, and so on. Such complex topography and changeable geological conditions will have a significant impact on

FIGURE 1
Earthquake damage in Longtoushan market town.

the ground motion, and then cause significant differences and zoning of earthquake damage.

3 Analysis of local topographic effect based on ground pulsation

The houses in Longtoushan market town are mainly built along the slope, and some of them are seriously damaged by the earthquake, as shown in Figure 2A. The methods of studying local topographic effects mainly include the analytical method, numerical simulation, and experimental study (physical model test and site observation). With the improvement of instrument observation accuracy and resolution, site observation, especially ground pulsation observation, has been widely used in the study of local topographic seismic effects. The research on the dynamic characteristics of a site based on ground pulsation (Nurwidyanto et al., 2021; Molnar et al., 2022) began in the 1960s, and the HVSR spectral ratio method proposed by Nakamura et al. (Pandey et al., 2018), has been the most widely used.

To analyze the amplification effect of the slope topography on ground motion in Longtoushan market town, the author takes the west slope of the family planning service station of Longtoushan Market Town as the observation object and carries out ground pulsation observation. The slope has an angle of about 18°. A total of six observation points were laid for the slope topography, as shown in Figures 2B, C. The instrument used in the field test is the ETNA2 accelerometer. The instrument has a built-in EpiSensor force-balance accelerometer, which can simultaneously record two horizontal and vertical acceleration time-histories at the observation point. ETNA2 accelerometer has a GPS time calibration function and has two modes of continuous recording and trigger recording. The sampling rate was 200 sps.

Through the observation of ground pulsation at six points, a total of about 3,000 s of ground pulsation has been recorded. After baseline correction, digital filtering, and segmental superposition and averaging of ground pulsation records, the time-history records that can be used for final analysis are obtained. Then Fourier transform is applied to the ground pulsation records after processing. Based on the transfer function method (reference point spectral ratio method) (Haghshenas et al., 2008), the two horizontal spectral ratio peaks of the 5 observation points (P_2-P_6) on the slope relative to the point P_1 at the slope foot and their corresponding frequencies can be obtained through calculation, as shown in Figure 3. The calculation results are shown in Table 1.

It can be seen from Table 1 that, the ratios between the peaks of the spectral ratio of the observation point (P_2-P_6) on the slope and that of the observation point P_1 are all greater than 1. From the foot of the slope to the top, the peaks of the spectral ratio become larger. The peak of the spectral ratio at the slope top (point P_6) is the largest, with the EW direction being 2.835 and the NS direction being 8.422. The frequencies corresponding to the peaks of the spectral ratio are also different. The frequency corresponding to the peak of the EW direction is always larger than that of the NS direction. The frequency range corresponding to the peak of the EW direction is 5.4 ~ 6.0 Hz, and the NS direction is 4.6 ~ 5.4 Hz. The peaks of the spectral ratio of the NS direction are always larger than that of the EW direction. The closer to the top of the slope, the more significant the difference in the spectral ratio peak.

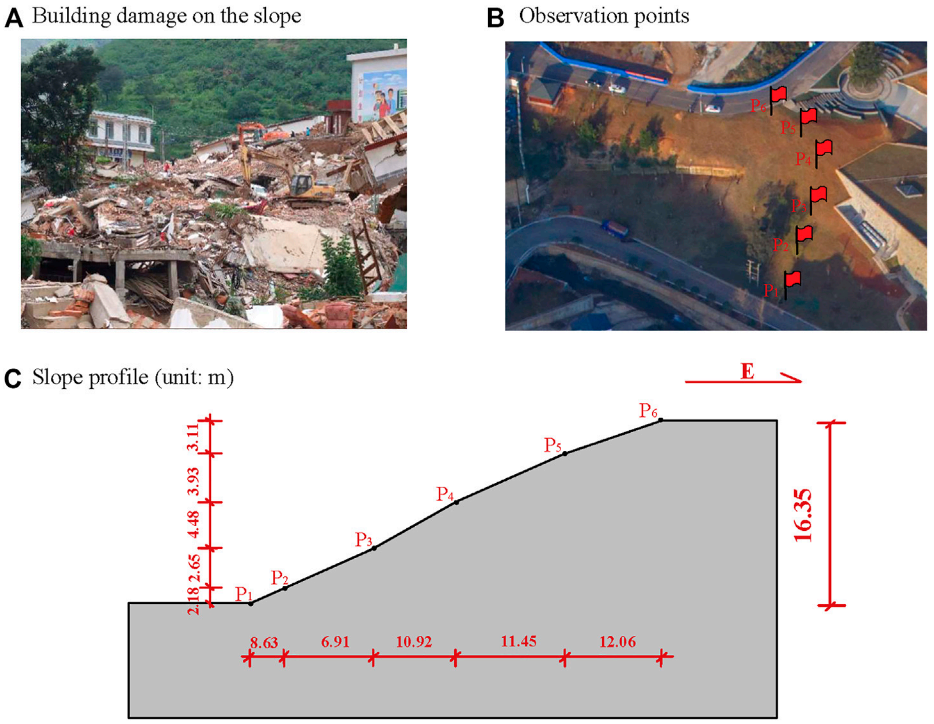

FIGURE 2
Building damage and observation point for ground pulsation on the slope site in Longtoushan Market Town.

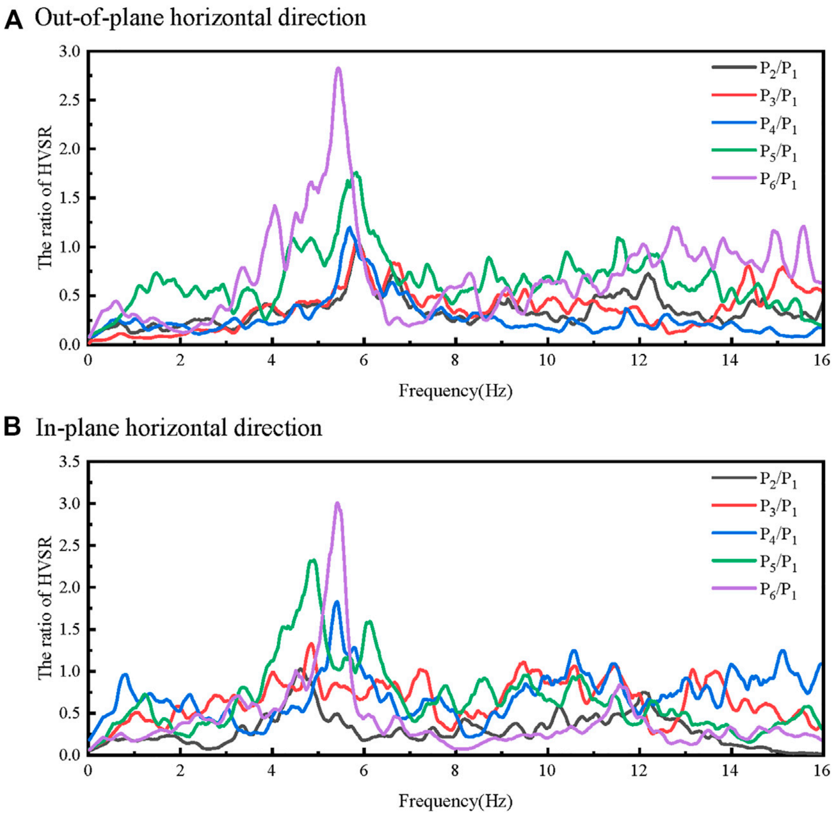

FIGURE 3
The ratio of HVSR between the observation points P_2–P_6 and P_1.

TABLE 1 Spectrum ratio of observation points on the slope.

Measuring point	Direction	Frequency of spectrum ratio (Hz)	Spectral peak value
P_2	EW	6.0	1.005
	NS	4.6	1.026
P_3	EW	5.8	1.044
	NS	4.9	1.330
P_4	EW	5.7	1.203
	NS	5.4	1.825
P_5	EW	5.8	1.760
	NS	4.9	2.332
P_6	EW	5.4	2.835
	NS	5.4	8.422

It can be seen that the slope site has a significant amplification effect on ground motion. The amplification effect is different from the foot of the slope to the top of the slope, and the top of the slope has the largest amplification effect. Meanwhile, the amplification effect in the slope site also has a significant difference in different directions. It can be inferred that the serious damage to buildings built on slopes is caused by the amplification effect of local terrain and the difference in ground motion.

To confirm the conclusion obtained by the ground pulsation test, the finite element method is used to analyze the dynamic characteristics of the slope topography. Based on ABAQUS® software, the numerical calculation model was established, as shown in Figure 4A. According to Liao et al. (1984), the model mesh size is determined by 1/10 ~ 1/8 of the wavelength that corresponds to the cutoff frequency. To ensure the accuracy and efficiency of calculation, the size of the grid is taken as 1 m × 1 m. In this paper, two conditions are considered: 1) the soil is the completely weathered rock, with a shear wave velocity of 300 m/s and Poisson's ratio of 0.35; ② the soil is the bedrock, with shear wave velocity of 500 m/s and Poisson's ratio is 0.25. In both cases, the soil is assumed to be elastic homogeneous isotropic, with mass density of 2,350 kg/m³. For eliminating the influence of artificial boundaries, the viscoelastic artificial boundaries were applied to the bottom and the two side boundaries of the model (Liu et al., 2020). The input is an approximate δ-pulse incident vertically at the bottom boundary (Liao et al., 1981; Hao et al., 2014). The approximate δ-pulse and its Fourier amplitude spectrum are shown in Figure 4B, and the cutoff frequency of the pulse is 12 Hz.

The horizontal and vertical displacement time histories of each observation point on the slope terrain are shown in Figures 5A, B. The authors determined the dynamic amplification coefficient of the observation point relative to the input pulse (the ratio of the peak displacement of the observation points to that of the input pulse), and obtained the variation trend of the dynamic amplification coefficient of the site along the slope terrain, as shown in Figure 5C. As can be seen from the figure, as the observation point gradually rises along the slope, the dynamic amplification coefficient gradually increases, and the observation point at the top of the slope has the largest dynamic amplification coefficient. The dynamic amplification coefficients of the observation points A_1–A_6 and A_{12}–A_{16} are close to the free-field results, which indicates that the influence of the slope can be ignored when the distance from the slope terrain is more than 2 times the slope height. It can be seen from Table 1 and Figure 5 that, the numerical simulation is basically consistent with the pulsation test at the top and foot of the slope, thus confirming each other.

4 Analysis of earthquake response of slope site

Based on the boreholes (DZK1-DZK6) data and experimental data corresponding to the six observation points, the one-dimensional equivalent linearization method (Astroza et al., 2017; Rui et al., 2021) is adopted to calculate the site seismic response at the six observation points. Through this calculation, the influence of the near-surface covering soil layer on ground motion is analyzed, and then the earthquake damage to buildings is discussed. Tables 2, 3 respectively give the soil layer information and the dynamic characteristic parameters of the soil at the observation points.

According to the data shown in Table 2, the equivalent shear wave velocity of each borehole (DZK1-DZK6) at 20 m depth is 273.5, 270.3, 373.4, 347.4, 401.9, and 254.6 m/s respectively; the thickness of the covered soil layers is 26.0, 59.1, 24.3, 59.0, and 28.3/18.7 m, respectively. According to Code for Seismic Design of Buildings (GB 50011–2010) in China, the slope site belongs to Class II building site.

A Schematic diagram of 2D finite element analysis model of slope(Unit: m)

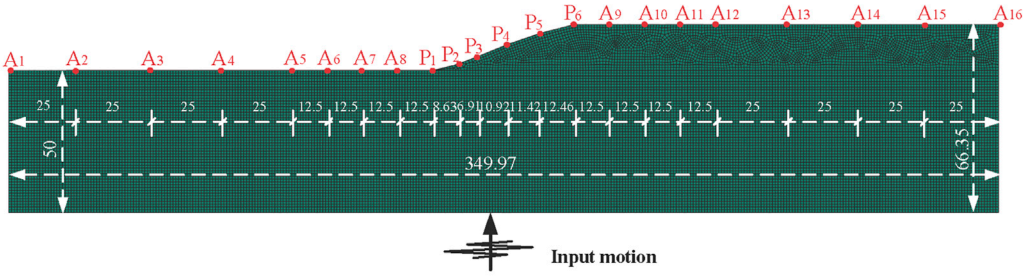

B Input pulse ground motion and its Fourier amplitude spectrum

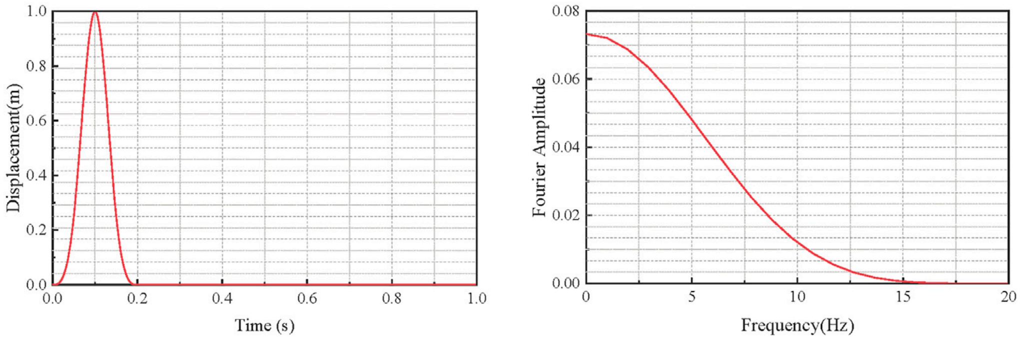

FIGURE 4
Finite element model of the slope site and the input pulse.

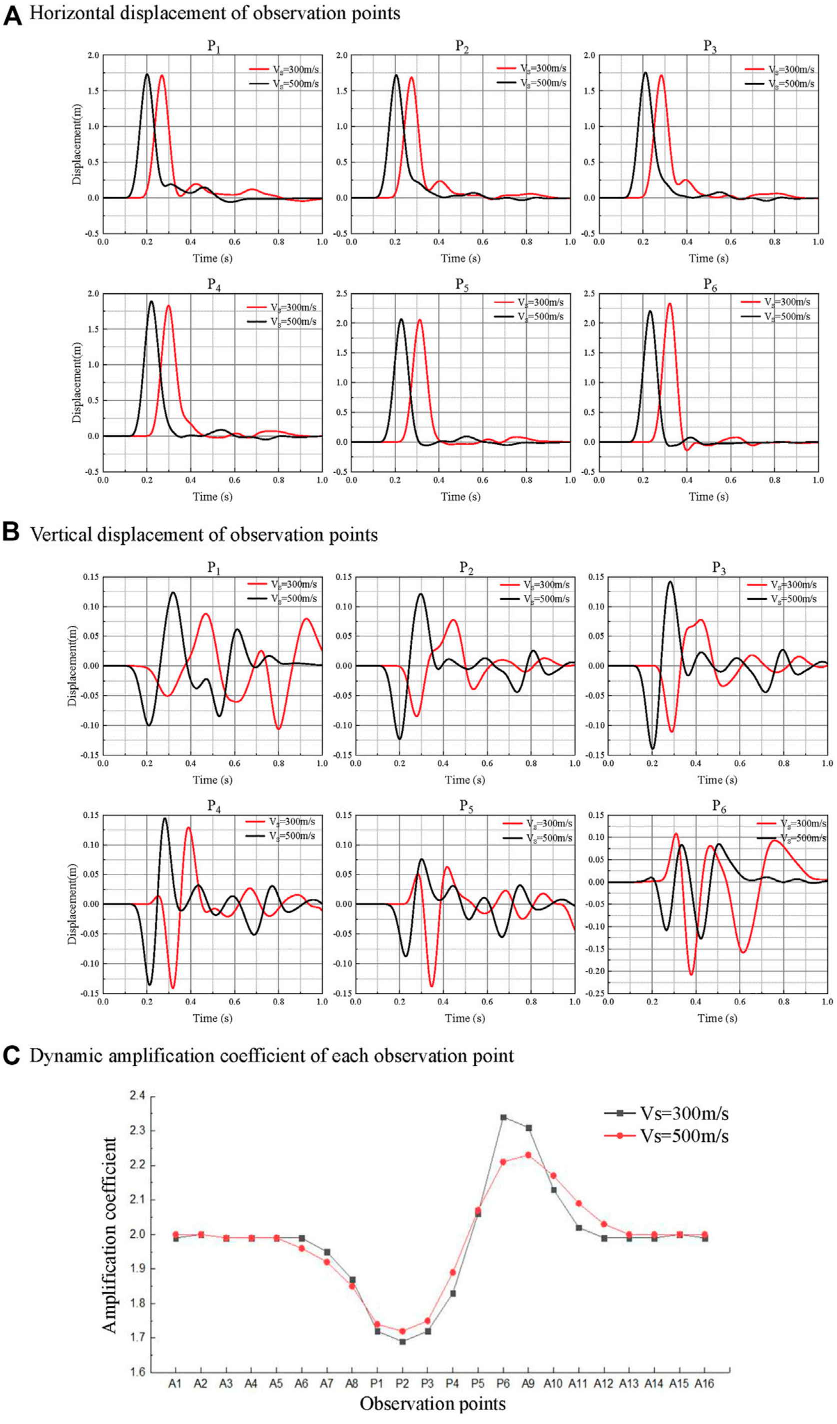

FIGURE 5
Calculation result of the finite element model of the 2D slope site.

In the Ludian Ms6.5 earthquake, there was a strong motion observation station (53LLT) near the DZK1 borehole, which is less than 10 km away from the epicenter (Cui et al., 2014; Ji et al., 2014). The station recorded the strong motion time-history in the EW direction, NS direction, and vertical direction, with the peak acceleration of 949, 706, and 504 cm/s^2, respectively. These are the maximum acceleration records during the Ludian earthquake. Therefore, in the one-dimensional seismic response analysis of the site, we multiply the EW-direction acceleration record by the reduction coefficient of 0.5 to obtain the input ground motion from the base. The input ground motion and its response spectrum are shown in Figure 6. It can be seen that the input ground motion has a wide frequency band, and the characteristic period is about 0.7 s, rich in long-period components.

By calculating the horizontal seismic response of each borehole, the horizontal ground acceleration time-history and response

TABLE 2 Information of the soil layers corresponding to the boreholes.

DZK	Layer	Soil	Depth (m)	Height (m)	Shear wave velocity (m/s)	Density (t/m^3)	Soil type number
DZK1	1	Miscellaneous fill	3.2	3.2	185.0	1.87	24
	2	Round gravel	11.8	8.6	281.0	2.25	1
	3	Round gravel	19.1	7.3	327.0	2.25	2
	4	Gravelly sand	23.0	3.9	310.0	2.15	3
	5	Gravelly sand	26.0	3.0	310.0	2.15	4
	6	Computational base	—	—	758.0	2.50	26
DZK2	1	Plain fill	1.2	1.2	201.0	1.72	24
	2	Round gravel	4.5	3.3	277.0	2.25	12
	3	Silt	5.1	0.6	270.0	1.96	5
	4	Round gravel	7.0	1.9	328.0	2.25	1
	5	Boulder	7.8	0.8	542.0	2.45	26
	6	Weathered quartz sand	15.6	7.8	453.0	2.23	6
	7	Fault breccia	18.0	2.4	521.0	2.45	26
	8	Weathered quartz sand	59.1	41.1	496.0	2.23	6
	9	Computational base	—	—	586.0	2.50	26
DZK3	1	Miscellaneous fill	1.2	1.2	190.0	1.87	24
	2	Round gravel	9.9	8.7	379.0	2.25	1
	3	Gravel silty clay	12.1	2.2	332.0	1.94	7
	4	Dust	13.5	1.4	445.0	2.10	25
	5	Broken stone	16.0	2.5	472.0	2.10	25
	6	Gravelly sand	21.2	5.2	434.0	2.15	3
	7	Gravel silty clay	24.3	3.1	431.0	1.99	9
	8	Computational base	—	—	539.0	2.50	26
DZK4	1	Miscellaneous fill	3.2	3.2	211.0	1.87	24
	2	Pebble	4.7	1.5	432.0	2.10	25
	3	Round gravel	9.8	5.1	417.0	2.25	1
	4	Gravel silty clay	12.5	2.7	375.0	1.94	7
	5	silt	13.2	0.7	379.0	1.96	5
	6	Gravel silty clay	18.0	4.8	385.0	1.97	8
	7	Gravel silty clay	24.0	6.0	385.0	1.99	9
	8	Gravel silty clay	30.1	6.1	385.0	2.00	10
	9	Weathered limestone	59.0	28.9	462.0	2.20	11
	10	Computational base	—	—	510.0	2.50	26
DZK5	1	Plain fill	1.0	1.0	281.0	1.72	24
	2	Round gravel	6.7	5.7	391.0	2.25	12
	3	Pebble	7.7	1.0	440.0	2.10	25
	4	Round gravel	9.5	1.8	419.0	2.25	13
	5	Round gravel	11.5	2.0	419.0	2.25	14
	6	Round gravel	15.0	3.5	419.0	2.25	15

(Continued on following page)

TABLE 2 (*Continued*) **Information of the soil layers corresponding to the boreholes.**

DZK	Layer	Soil	Depth (m)	Height (m)	Shear wave velocity (m/s)	Density (t/m^3)	Soil type number
	7	Round gravel	21.8	6.8	419.0	2.25	16
	8	Weathered limestone	22.5	0.7	545.0	2.20	11
	9	Fault gouge	23.1	0.6	392.0	1.86	17
	10	Moderately limestone	27.5	4.4	759.0	2.50	26
	11	Fault gouge	28.3	0.8	392.0	1.86	17
	12	Computational base	—	—	759.0	2.50	26
DZK6	1	Plain fill	1.0	1.0	165.0	1.72	24
	2	Silty clay	4.4	3.4	217.0	1.92	18
	3	Clay	6.5	2.1	213.0	1.86	19
	4	Gravel silty clay	9.2	2.7	234.0	1.86	20
	5	Gravelly sand	10.8	1.6	274.0	2.15	3
	6	Clay	11.6	0.8	321.0	1.86	19
	7	Gravelly sand	13.7	2.1	259.0	2.15	3
	8	Silty clay	15.5	1.8	360.0	2.03	21
	9	Silty clay	18.7	3.2	360.0	1.85	22
	10	Weathered limestone	26.5	7.8	703.0	2.20	23
	11	Computational base	—	—	804.0	2.50	26

spectrum at each borehole can be obtained. The peak of horizontal acceleration of the ground surface at the location of each borehole and the ratios with the peak of input motion (Peak acceleration ratio) are shown in Figure 7A. The response spectrum (damping ratio 5%) for the boreholes is shown in Figure 7B.

It can be seen from Figure 7A that, there are significant differences in peak values of ground surface acceleration at different observation points. DZK6 borehole has the maximum peak value of ground acceleration, and the ratio between it and the peak recorded (input motion shown in Figure 6) by the 53LLT observation station is 1.81. The peaks of ground surface acceleration corresponding to DZK1, DZK3 and DZK5 boreholes are similar, and all of them are slightly higher than those recorded by the 53LLT observation station, with the ratios of peak acceleration are 1.11, 1.16, and 1.12, respectively. Similarly, the ratios of peak ground surface acceleration corresponding to DZK2 and DZK4 boreholes are 0.78 and 0.47 respectively, which is close to the peak acceleration recorded by the 53LLT observation station. It should be noted that the DZK4 borehole has the lowest peak ground acceleration which is smaller than the peak of the input ground motion. The results show that the ground motion amplification effect at DZK1, DZK3, DZK5 and DZK6 boreholes is higher than that of 53LLT observation station, especially at the location of the DZK6 borehole. However, the ground motions at DZK2 and DZK4 boreholes have different degrees of attenuation, and the attenuation at the position of the DZK4 borehole is the most obvious. It can be seen that the amplification effect of the site on ground motion is jointly determined by the properties of the rock and soil near the ground surface and their composition, the physical state and thickness of the overlying soil, the velocity variation characteristics, and the non-linear dynamic characteristics of the soil.

The response spectrum shown in Figure 7B demonstrates that the response spectra of the ground surface acceleration time-histories that correspond to different boreholes are also significantly different. The acceleration response spectra that correspond to DZK1, DZK3, and DZK5 boreholes are close to each other and close to that of the 53LLT observation station in the period range of 0.2–0.45 s and 1.4–20 s. The difference in the response spectrum of ground surface acceleration corresponding to DZK4 and DZK6 is obvious. When the period is less than 1.2 s, the response spectrum value of the DZK4 borehole is smaller than that of the 53LLT observation station, but it is similar for the rest of the period. For the DZK6 borehole, when the period is less than 0.9 s, the value of the response spectrum is larger than that of the 53LLT observation station but similar for the rest period. In addition, in the period range of 0.65–1.6 s, the response spectra corresponding to DZK1 and DZK5 boreholes are slightly higher than that of the 53LLT observation station. It can be seen that the soil layer close to the ground surface has a significant influence on the acceleration response spectrum, and it is period-dependent.

From the above analysis, it can be seen that although the engineering site corresponding to the six boreholes is Class II site, due to the differences in geotechnical properties and their combination characteristics, the physical state and layer thickness of the overlying soil layer, the change of shear wave velocity, and

TABLE 3 Dynamic non-linear parameters of different soil layers.

Soil type number	Soil	Modulus ratio	Shearing strain γ (10^{-4})							
		Damping ratio	0.05	0.1	0.5	1	5	10	50	100
1	Round gravel	G/G_{max}	0.9976	0.9952	0.9765	0.9541	0.8061	0.6752	0.2937	0.1721
		λ	0.0060	0.0093	0.0252	0.0382	0.0942	0.1301	0.2116	0.2337
2	Round gravel	G/G_{max}	0.9954	0.9909	0.9560	0.9157	0.6847	0.5206	0.1784	0.0980
		λ	0.0037	0.0063	0.0212	0.0351	0.0976	0.1350	0.2049	0.2203
3	Gravelly sand	G/G_{max}	0.9975	0.9950	0.9757	0.9526	0.8007	0.6676	0.2866	0.1673
		λ	0.0052	0.0082	0.0232	0.0361	0.0927	0.1298	0.2145	0.2374
4	Gravelly sand	G/G_{max}	0.9933	0.9868	0.9371	0.8817	0.5984	0.4270	0.1297	0.0693
		λ	0.0076	0.0123	0.0365	0.0569	0.1339	0.1717	0.2301	0.2412
5	Silt	G/G_{max}	0.9970	0.9940	0.9706	0.9429	0.7675	0.6227	0.2482	0.1417
		λ	0.0026	0.0043	0.0143	0.0237	0.0684	0.0985	0.1659	0.1834
6	Weathered sandstone	G/G_{max}	0.9938	0.9878	0.9416	0.8897	0.6173	0.4465	0.1389	0.0746
		λ	0.0010	0.0021	0.0112	0.0222	0.0833	0.1235	0.1977	0.2135
7	Gravel silty clay	G/G_{max}	0.9980	0.9960	0.9804	0.9616	0.8337	0.7148	0.3339	0.2004
		λ	0.0006	0.0012	0.0055	0.0105	0.0430	0.0722	0.1627	0.1939
8	Gravel silty clay	G/G_{max}	0.9937	0.9876	0.9408	0.8882	0.6137	0.4427	0.1371	0.0736
		λ	0.0005	0.0012	0.0077	0.0164	0.0711	0.1098	0.1844	0.2005
9	Gravel silty clay	G/G_{max}	0.9942	0.9885	0.9453	0.8962	0.6333	0.4633	0.1472	0.0795
		λ	0.0133	0.0196	0.0470	0.0673	0.1365	0.1690	0.2190	0.2286
10	Gravel silty clay	G/G_{max}	0.9968	0.9937	0.9692	0.9402	0.7586	0.6111	0.2392	0.1358
		λ	0.0066	0.0102	0.0275	0.0416	0.0998	0.1345	0.2049	0.2219
11	Weathered limestone	G/G_{max}	0.9862	0.9728	0.8772	0.7812	0.4166	0.2631	0.0666	0.0345
		λ	0.0083	0.0138	0.0431	0.0666	0.1397	0.1667	0.1993	0.2045
12	Round gravel	G/G_{max}	0.9872	0.9746	0.8849	0.7935	0.4345	0.2776	0.0714	0.0370
		λ	0.0082	0.0136	0.0427	0.0663	0.1415	0.1702	0.2057	0.2114
13	Round gravel	G/G_{max}	0.9975	0.9950	0.9754	0.9520	0.7987	0.6648	0.2840	0.1655
		λ	0.0007	0.0014	0.0065	0.0124	0.0494	0.0807	0.1678	0.1944
14	Round gravel	G/G_{max}	0.9941	0.9833	0.9443	0.8945	0.6291	0.4589	0.1450	0.0782
		λ	0.0030	0.0053	0.0192	0.0323	0.0902	0.1229	0.1786	0.1900
15	Round gravel	G/G_{max}	0.9979	0.9959	0.9796	0.9601	0.8280	0.7065	0.3249	0.1940
		λ	0.0005	0.0011	0.0055	0.0110	0.0493	0.0854	0.2007	0.2407
16	Round gravel	G/G_{max}	0.9912	0.9826	0.9189	0.8499	0.5311	0.3615	0.1017	0.0536
		λ	0.0112	0.0174	0.0464	0.0686	0.1417	0.1725	0.2145	0.2217
17	Fault gouge	G/G_{max}	0.9956	0.9912	0.9575	0.9184	0.6924	0.5295	0.1837	0.1012
		λ	0.0033	0.0058	0.0207	0.0351	0.1030	0.1454	0.2273	0.2458
18	Silty clay	G/G_{max}	0.9988	0.9975	0.9878	0.9758	0.8897	0.8013	0.4465	0.2874
		λ	0.0025	0.0041	0.0124	0.0199	0.0570	0.0856	0.1742	0.2075
19	Clay	G/G_{max}	0.9982	0.9964	0.9821	0.9648	0.8458	0.7328	0.3542	0.2152
		λ	0.0005	0.0009	0.0047	0.0092	0.0412	0.0720	0.1760	0.2144

(Continued on following page)

TABLE 3 (*Continued*) Dynamic non-linear parameters of different soil layers.

Soil type number	Soil	Modulus ratio	Shearing strain γ (10^{-4})							
		Damping ratio	0.05	0.1	0.5	1	5	10	50	100
20	Gravel silty clay	G/G_{max}	0.9989	0.9978	0.9892	0.9787	0.9018	0.8211	0.4786	0.3146
		λ	0.0069	0.0101	0.0245	0.0358	0.0835	0.1164	0.2107	0.2453
21	Silty clay	G/G_{max}	0.9961	0.9922	0.9620	0.9268	0.7170	0.5589	0.2022	0.1125
		λ	0.0015	0.0027	0.0111	0.0200	0.0673	0.1002	0.1704	0.1875
22	Silty clay	G/G_{max}	0.9991	0.9982	0.9913	0.9828	0.9193	0.8507	0.5326	0.3630
		λ	0.0034	0.0052	0.0134	0.0201	0.0504	0.0726	0.1430	0.1719
23	Weathered limestone	G/G_{max}	0.9941	0.9883	0.9441	0.8940	0.6279	0.4576	0.1444	0.0778
		λ	0.0008	0.0018	0.0103	0.0211	0.0858	0.1307	0.2176	0.2366
24	Filling	G/G_{max}	0.960	0.950	0.800	0.700	0.300	0.200	0.150	0.100
		λ	0.025	0.028	0.030	0.035	0.080	0.100	0.110	0.120
25	Gravel/crushed stone	G/G_{max}	0.990	0.970	0.900	0.850	0.700	0.550	0.320	0.200
		λ	0.004	0.006	0.019	0.030	0.075	0.090	0.110	0.120
26	Bedrock	G/G_{max}	1.000	1.000	1.000	1.000	1.000	1.000	1.000	1.000
		λ	0.050	0.050	0.050	0.050	0.050	0.050	0.050	0.050

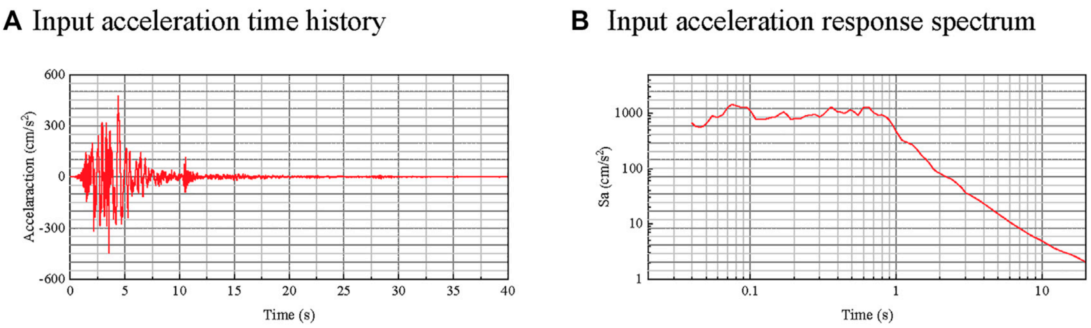

FIGURE 6
Input ground motion for site seismic response analysis and its response spectrum.

the dynamic non-linear characteristics of the soil, the amplification effect on the ground motion at different borehole position is significantly different, which will cause a significant difference in the seismic damage of the house at the location of different borehole.

Figure 8 shows the damage to the buildings located at different borehole positions. The locations of boreholes DZK1, DZK3, DZK5, and DZK6 respectively correspond to the 53LLTobservation station, the west side of the administration office area, the old block, and the living area. In these areas, the houses are more severely damaged. The DZK2 borehole is located on a middle school campus where the damage to the buildings is relatively light. The DZK4 borehole is located in a kindergarten where the main structure of the buildings has not been seriously damaged. The seismic response analysis of the site showed that the amplification effect on the ground motion at the positions of DZK1, DZK3, DZK5, and DZK6 boreholes is most significant compared with that at the location of the DZK4 borehole, while the amplification effect on the ground motion at the location of DZK2 borehole is relatively small. This feature is consistent with the actual earthquake damage, that is, where the amplification of ground motion is stronger, the damage to the building is heavier. This can show that the amplification effect of the site on the ground motion has a significant impact on building damage, and the more significant the amplification on ground motion, the more serious the building damage.

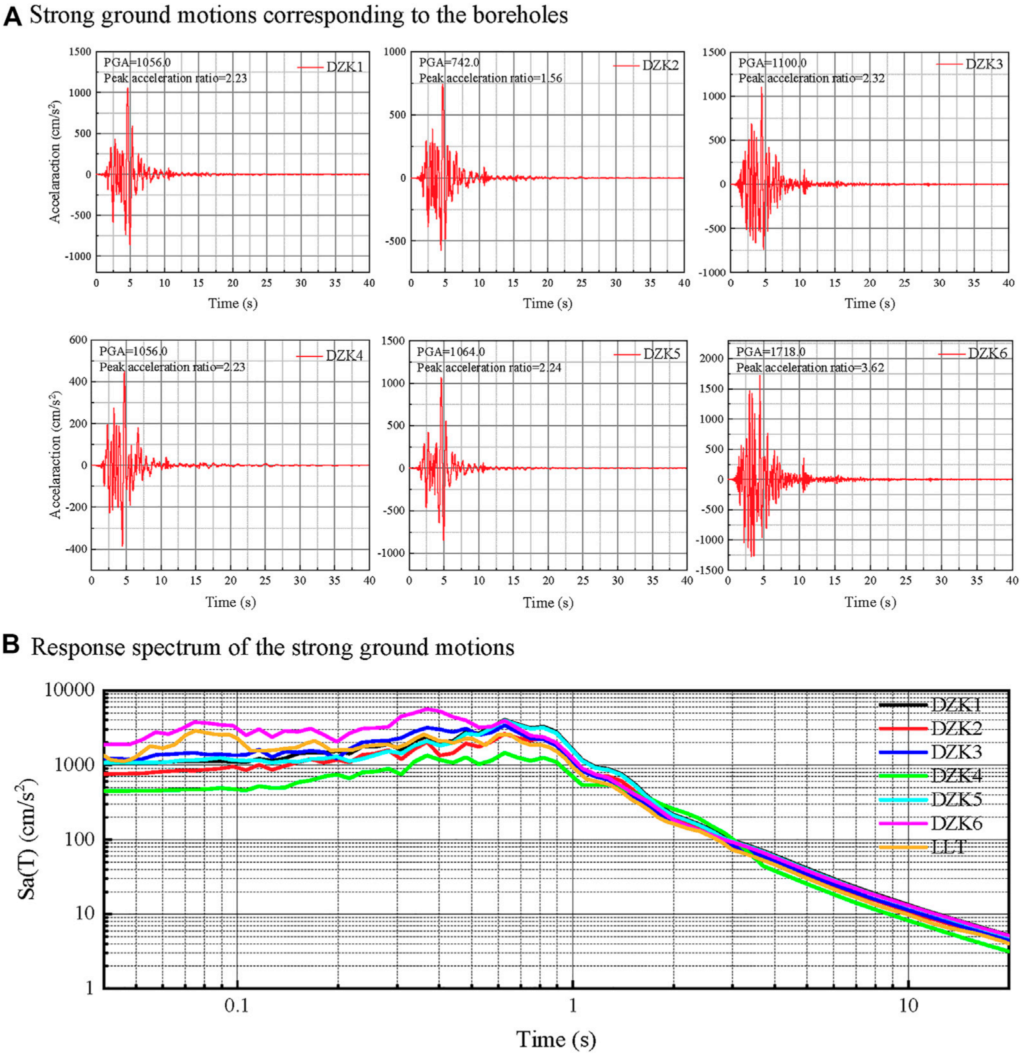

FIGURE 7
Site seismic response calculation based on one-dimensional equivalent linearization method.

FIGURE 8
Earthquake damage in Longtoushan Market Town.

5 Conclusion

In this paper, the amplification effect of the slope site on ground motion in Longtoushan Market Town is discussed through the analysis of local site engineering geological conditions, local topographic effects and seismic response analysis of the slope site, and its influence on building earthquake damage is further investigated. The main findings and conclusions are as follows:

1) Complex topography and variable engineering geological conditions will lead to significant differences in ground motion, which in turn will lead to significant differences in seismic damage to buildings. For slope sites, from the foot of the slope to the top of the slope, the amplification effect of the site on ground motion gradually becomes stronger. In different directions of the same location of the site, the site amplifies ground motion differently.
2) The strength of the amplification effect of the site on ground motion is determined by the properties of the rock and soil near the ground surface and their composition, the physical state and thickness of the overlying soil layer, the changes of shear wave speed, and the dynamic non-linear characteristics of the soil. This will lead to significant differences in ground motion amplification effects at different locations of the site, which in turn will lead to significant differences in the seismic damage of houses located at different locations on the site.
3) The soil layer close to the ground surface has a significant influence on the ground motion acceleration response spectrum, and it is period-dependent. The analysis of the site seismic response is consistent with the actual seismic damage investigation. The amplification effect of the site on the ground motion has a significant impact on building damage, and the more significant the amplification on ground motion, the more serious the building damage.

Data availability statement

The original contributions presented in the study are included in the article/supplementary material, further inquiries can be directed to the corresponding author.

Author contributions

LD: Validation, Formal analysis, Visualization. LJ: Conceptualization, Validation, Formal analysis, Data curation, Visualization, Writing—original draft—review and editing. ZZ: Software, Data curation, Supervision, Writing—review and editing.

Funding

This study is supported by the National Natural Science Foundation of China (Grant No. U2039208, U1839202).

Conflict of interest

The authors declare that the research was conducted in the absence of any commercial or financial relationships that could be construed as a potential conflict of interest.

Publisher's note

References

Astroza, R., César., P., and Ochoa-Cornejo, F. (2017). Site response analysis using one-dimensional equivalent-linear method and bayesian filtering. *Comput. Geotechnics* 89, 43–54. doi:10.1016/j.compgeo.2017.04.004

Bo, J., Qi, W., and Liu, H. (2009). Abnormality of seismic intensity in hanyuan during wenchuan earthquake. *Earthq. Eng. Eng. Vib.* 29 (6), 53–64.

Borcherdt, R., and Gibbs, J. (1976). Effects of local geological conditions in the San Francisco Bay region on ground motions and the intensities of the 1906 earthquake. *Bull. Seismol. Soc. Am. (United States)* 66 (2), 467–500. doi:10.1785/bssa0660020467

Brando, G., Pagliaroli, A., Cocco, G., and Di, B. (2020). Site effects and damage scenarios: The case study of two historic centers following the 2016 central Italy earthquake. *Eng. Geol.* 272, 105647. doi:10.1016/j.enggeo.2020.105647

Çelebi, M. (1991). Topographical and geological amplification: Case studies and engineering implications. *Struct. Saf.* 10, 199–217. doi:10.1016/0167-4730(91)90015-2

Cetin, L., Kemal, O., Altun, S., Askan, A., Sezer, A., Kincal, C., et al. (2022). The site effects in izmir bay of october 30 2020, M7.0 samos earthquake. *Soil Dyn. Earthq. Eng.* 152, 107051. doi:10.1016/j.soildyn.2021.107051

Cui, J., Liu, Q., and Duan, J. (2014). Strong-motion recordings of MS6.5 ludian earthquake in yunnan in 2014 and their preliminary analysis. *J. Seismol. Res.* 37 (4), 542–548.

Estrella, H., and González, J. (2003). Spac: An alternative method to estimate earthquake site effects in Mexico city. *Geofísica Int.* 42 (2), 227–236. doi:10.22201/igeof.00167169p.2003.42.2.267

Geli, L., Bard, P. Y., and Jullien, B. (1988). The effect of topography on earthquake ground motion: A review and new results. *BSSA* 78 (1), 42–63. doi:10.1785/bssa0780010042

Haghshenas, E., Bard, P. Y., and Theodulidis, N., (2008). Empirical Evaluation of microtremor H/V spectral ratio. *Bull. Earthq. Eng.* 6 (01), 75–108. doi:10.1007/s10518-007-9058-x

Hao, C., Xie, Q., Dai, B., Zhang, H., and Chen, H. (2016). Seismic damage to structures in the Ms6.5 ludian earthquake. *Earthq. Eng. Eng. Vib.* 5 (01), 173–186. doi:10.1007/s11803-016-0314-4

Hao, M., Zhang, Y., and Zhao, F. (2021). Analysis of slope terrain effect on the properties of ground motion. *Technol. Earthq. Disaster Prev.* 16 (2), 229–236. (in Chinese).

Huang, Z. K., Zhang, D. M., Pitilakis, K., Tsinidis, G., Huang, H. W., Zhang, D., et al. (2022). Resilience assessment of tunnels: Framework and application for tunnels in alluvial deposits exposed to seismic hazard. *Soil Dyn. Earthq. Eng.* 162, 107456. doi:10.1016/j.soildyn.2022.107456

Ji, K., Wen, R., and Cui, J. (2014). Observation of strong motion and damage investigation for M_S6.5 ludian earthquake. *Technol. Earthq. Disaster Prev.* 9 (3), 325–339.

Jia, H., Chen, F., Fan, Y., and Pan, D. (2016). Comparison of two large earthquakes in China: The ms 6.6 yunnan jinggu earthquake and the ms 6.5 yunnan ludian earthquake in 2014. *Int. J. Disaster Risk Reduct.* 16, 99–107. doi:10.1016/j.ijdrr.2016.01.006

Jin, K., Lee, J., Lee, K., Kyung, J., and Kim, Y. (2020). Earthquake damage and related factors associated with the 2016 ML = 5.8 Gyeongju earthquake, southeast Korea. *Geosciences J.* 24 (2), 141–157. doi:10.1007/s12303-019-0024-9

Li, Z., Hou, J., and Li, Yang. (2013). Analysis on the characteristics of the MS7. 0 Lushan, Sichuan province, earthquake hazard on April 20, 2013. *Seismol. Geol.* 35 (2), 398–410.

Liao, Z. (1984). A finite element method for near-field wave motion in heterogeneous materials. *Earthq. Eng. Eng. Vib.* 4 (2), 1–14.

Liao, Z., Yang, B., and Yuan, Y. (1981). Effects of three-dimensional topography on earthquake ground motion. *Earthq. Eng. Eng. Vib.* 1 (1), 56–77.

Liu, J., Bao, X., and Tan, H. (2020). Seismic wave input method for soil-structure dynamic interaction analysis based on internal substructure. *China Civ. Eng. J.* 53 (8), 87–96. (in Chinese).

Mayoral, J., Asimaki, D., Tepalcapa, S., Wood, C., Roman-de, l., Hutchinson, T., et al. (2019). Site effects in Mexico City basin: Past and present. *Soil Dyn. Earthq. Eng.* 121, 369–382. doi:10.1016/j.soildyn.2019.02.028

Molnar, S., Sirohey, A., Assaf, J., Bard, P. Y., Castellaro, S., Cornou, C., et al. (2022). A review of the microtremor horizontal-to-vertical spectral ratio (MHVSR) method. *J. Seismol.* 26, 653–685. doi:10.1007/s10950-021-10062-9

Ni, S., Wang, W., and Li, L. (2010). The april 14th, 2010 Yushu earthquake, a devastating earthquake with foreshocks. *Sci. China (Earth Sci.* 53 (06), 791–793. doi:10.1007/s11430-010-0083-2

Nurwidyanto, M., Irhama, C., Zainuri, M., Yuliyanto, G., and Wirasatriya, A. (2021). Measurement of ground response of semarang coastal region risk of earthquakes by horizontal to vertical spectral ratio (HVSR) microtremor method. *J. Phys. Conf. Ser.* 1943 (1), 012033. doi:10.1088/1742-6596/1943/1/012033

Pamuk, E., and Ozer, C. (2020). The site effect investigation with using horizontal-to-vertical spectral ratio method on earthquake data, south of Turkey. *Geotectonics* 54 (4), 563–576. doi:10.1134/s001685212004010x

Pandey, A. K., Roy, P. N. S., Baidya, P. R., and Gupta, A. K. (2018). Estimation of current seismic hazard using Nakamura technique for the Northeast India. *Nat. Hazards* 93 (02), 1013–1027. doi:10.1007/s11069-018-3338-4

Pang, W., Yang, R., and Chen, J. (2016). High density resistivity exploration method for ludian MS6. 5 earthquake in area of longtoushan town in 2014. *J. Seismol. Res.* 39 (4), 622–629.

Panzera, F., Lombardo, G., Imposa, S., Grassi, S., Gresta, S., Catalano, S., et al. (2018). Correlation between earthquake damage and seismic site effects: The study case of lentini and carlentini, Italy. *Eng. Geol.* 240, 149–162. doi:10.1016/j.enggeo.2018.04.014

Peng, X., Liu, L., Li, X., and Sun, P. (2011). Study on correlation between building damage and strong motion parameters in wenchuan earthquake. *J. Basic Sci. Eng.* 19 (4), 574–582.

Rui, S., and Xiao, M. (2021). A holistic equivalent linear method for site response analysis. *Soil Dyn. Earthq. Eng.* 140 (1), 106476. doi:10.1016/j.soildyn.2020.106476

Shiann-Jong, L., Dimitri, K., Bor-Shouh, H., and Jeroen, T. (2009). Effects of topography on seismic-wave propagation: An example from northern taiwan. *BSSA* 99 (1), 314–325. doi:10.1785/0120080020

Sun, C., Ming, X., and Zhou, M. (2011). Influence of local topography on ground motion in mountain region of southern gansu province. *Northwest. Seismol. J.* 33 (4), 331–335.

Wang, G., Zhou, X., Zhang, P., and Igel, H. (2002). Characteristics of amplitude and duration for near fault strong ground motion from the 1999 chi-chi, taiwan earthquake. *Soil Dyn. Earthq. Eng.* 22 (1), 73–96. doi:10.1016/s0267-7261(01)00047-1

Yang, Y., Zhu, X., and Yang, Z. (2018). Analytic solution for diffraction of plane P waves by a circular alluvial valley in wedge-shaped space. *Technol. Earthq. Disaster Prev.* 13 (4), 810–821.

frontiers | Frontiers in Earth Science

TYPE Original Research
PUBLISHED 05 January 2023
DOI 10.3389/feart.2022.1016096

OPEN ACCESS

EDITED BY
Yefei Ren,
Institute of Engineering Mechanics,
China Earthquake Administration, China

REVIEWED BY
Ying Zhou,
Jilin Jianzhu University, China
Yosuke Aoki,
The University of Tokyo, Japan

*CORRESPONDENCE
Martin Chapman,
mcc@vt.edu

SPECIALTY SECTION
This article was submitted to Structural Geology and Tectonics,
a section of the journal
Frontiers in Earth Science

RECEIVED 10 August 2022
ACCEPTED 21 September 2022
PUBLISHED 05 January 2023

CITATION
Guo Z and Chapman M (2023), A study of site response in the Longmen Shan and adjacent regions and site response models for the Sichuan Basin.
Front. Earth Sci. 10:1016096.
doi: 10.3389/feart.2022.1016096

A study of site response in the Longmen Shan and adjacent regions and site response models for the Sichuan Basin

Zhen Guo[1] and Martin Chapman[2]*

[1]School of Science, Jiangnan University, Wuxi, Jiangsu, China, [2]Department of Geosciences, Virginia Tech, Blacksburg, VA, United States

We investigated the regional attenuation and site responses in the Sichuan Basin and adjacent Songpan-Ganze terrane of the Tibetan Plateau using seismic data recorded at 41 stations from regional earthquakes occurring between January 2009 and October 2020. Fourier amplitude spectra of Lg waves were computed and binned into 18 frequency bins with center frequencies ranging from 0.1 Hz to 20.4 Hz. The quality factor is estimated as $Q(f) = 313f^{0.74}$ for the Sichuan Basin and $Q(f) = 568f^{0.34}$ for the Songpan-Ganze terrane, reflecting significant differences in the crustal structure beneath these two regions. Relative to the Songpan-Ganze terrane, site responses in the Sichuan Basin are characterized by strong amplification effects at frequencies lower than 6 Hz and obvious attenuation at higher frequencies (>10 Hz). κ_0 of stations in the Sichuan Basin show clearly geographical dependence with an average value of 0.045 s, whereas stations in the Songpan-Ganze terrane generally have smaller κ_0 values with an average value of 0.028 s. In particular, site response and κ_0 of stations in the Sichuan Basin are found to be dependent on the geographically variable thickness of the sedimentary deposits (sediment thickness). These units are comprised of sedimentary rock and semi-consolidated sediments, with a maximum thickness reaching approximately 10 km. Site response terms in the Sichuan Basin derived from the Lg Fourier spectra exhibit consistent patterns versus sediment thickness as frequency increases. We developed site response models as functions of sediment thickness for stations in the Sichuan Basin. The site response model derived from Lg site terms is consistent with that based on site response terms from coda amplitude spectra and horizontal to vertical (H/V) spectral ratios. The models were then incorporated in the stochastic method of ground motion predictions in the Sichuan Basin for six earthquakes occurring between October 2020 and June 2022. Residual analysis suggests that incorporating the site response models as functions of sediment thickness can improve the ground motion prediction model for the Sichuan Basin from moderate earthquakes.

KEYWORDS

ground motion prediction, site response, sediment thickness, Sichuan Basin, attenuation

Introduction

The Longmen Shan region is the most active seismic region in southwestern China, which has been struck by several big earthquakes since 2008, including the 12 May 2008 Ms 8.0 Wenchuan earthquake and the 20 April 2013 Ms 7.0 Lushan earthquake. The design seismic accelerations for most of the Longmen Shan and adjacent regions have been increased to 0.15–0.25 g in the latest version of seismic ground motion parameters zonation map of China issued in 2015 (AQSIQ 2001) whereas the values were 0.10–0.20 g in the previous version issued in 2001 (AQSIQ 2001). This requires that the seismic-proof demand should be raised one level or even two levels for these regions (Wang et al., 2018). Therefore, the Longmen Shan and adjacent regions, including the Sichuan Basin and Songpan-Garze Terrane (Figure 1), are currently exposed to high seismic hazard.

Ground motion prediction equations or simulations of ground motion time series play essential roles in seismic hazard analysis and other seismic engineering problems. The seismic source spectrum, path effect and site response are the three key factors in determining earthquake ground motions, where site response describes the effects of local geological conditions. It has long been recognized that near-surface geological conditions can have significant effects on earthquake ground motions. Even for rock sites, the weathering and cracking of the bedrock will amplify ground motions in certain frequency range (Steidl et al., 1996; Castro et al., 2017). For sites on unconsolidated sediments, ground motions can be strongly amplified relative to nearby rock sites whereas the high-frequency ground motions will be attenuated significantly when the sedimentary layer is thick enough (Field et al., 1997; Borcherdt 2002; Frankel et al., 2002; Wang et al., 2013; Guo and Chapman 2019; Pratt and Schleicher 2021; Wang and Wen 2021; Wang et al., 2022). Developing regional models to account for the site response effects can be challenging due to the varying geological structures beneath the seismic stations. Correction factors based on Vs. 30, which is the averaged shear-wave velocity in the top 30 m under the site, are usually adopted in ground motion prediction equations to account for the site effects (Wen et al., 2010; Bora et al., 2016; Li et al., 2018a; Stewart et al., 2020; Xu et al., 2020).

Across the Longmen Shan, the crustal thickness increases sharply from ~40 km in the western Sichuan Basin to ~60 km in the Songpan-Ganze terrane with an elevation change of ~5 km (Chen et al., 1986; Wang et al., 2007; Zheng et al., 2019; Wei et al., 2020). The Songpan-Ganze terrane is a triangular tectonic block located at the eastern margin of the Tibetan Plateau, west to the Longmen Shan thrust belt (Figure 1). This region is underlain by thick Paleozoic platform and surrounded by pre-Sinian

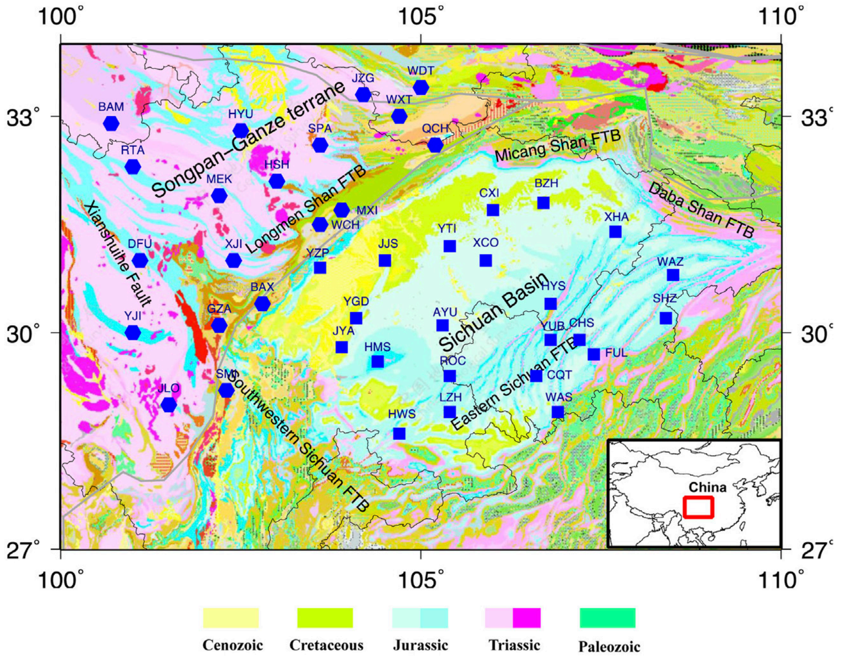

FIGURE 1
Geologic map of the Sichuan Basin and the Songpan-Ganze terrane, including the surrounding structural belts, Longmen Shan fold and thrust belt (FTB), Micang Shan FTB, Daba Shan FTB, Eastern Sichuan FTB and Southwestern Sichuan FTB. Locations of broadband stations used in this study are plotted as squares (in the Sichuan Basin) and hexagons (in the Songpan-Ganze terrane). The thick rectangle in the inset map shows the location of the study region. Geologic map is adapted from the 1:500,000 digital geological map of China, China Geological Survey (CGS, 2003).

continental basement (Zheng et al., 2016). The terrane is widely covered by Triassic marine deposits which were metamorphosed and strongly folded during late Triassic. Late Jurassic-Cenozoic sedimentary strata are lacking in this area but it does include several intrusive Miocene plutons along the deeply seated Xianshuihe fault (Chang 2000; Tian et al., 2016; Zheng et al., 2016). The Sichuan Basin is located to the east of Longmen Shan, which is a diamond-shaped compressional basin in central China and western Yangze Craton. The basin is underlain by Proterozoic rocks of the Yangtze Platform with a quite thick (up to 10 km) sedimentary cover of Mesozoic and Cenozoic marine and terrestrial sediments (Burchfiel et al., 1995; Guo et al., 1996; Meng et al., 2005; Wang et al., 2016; Xia et al., 2021). The Jurassic to Cretaceous sedimentary strata known as the “red beds,” reach a thickness of ~4–6 km in the western and central basin (Guo et al., 1996; Sha et al., 2010; Li et al., 2016; Li et al., 2018b). Cenozoic sediments in the Sichuan Basin are less than 0.7 km thick and restricted to the southwestern foreland basins (Burchfiel et al., 1995; Kirby et al., 2002). The sedimentary deposits in the Sichuan Basin are characterized by wedge-shaped post-Late-Triassic strata thinning from the north and northwest towards the southeast underlain by layer-cake Early to Middle Triassic sedimentary sequences, with a total thickness varying from 2 to 10 km (Meng et al., 2005; Wang et al., 2016; Liu et al., 2021).

Previous studies have shown that the crustal quality factor, which is usually described as $Q(f) = Q_0 f^{\alpha}$, shows a smaller Q_0 but higher α in the Sichuan Basin compared to the Songpan-Ganze region suggesting different crustal structures beneath these two regions (Hua et al., 2009; Fu et al., 2018; Fu et al., 2019). Site responses in the Sichuan Basin and Songpan-Ganze region were also found to be quite different. Fu et al. (2019) studied site responses in western Sichuan Basin and the Songpan-Ganze Orogen using broadband seismograms from 88 regional earthquakes occurring between 2009 and 2013. Their results show clear differences in site responses of stations in the Sichuan Basin relative to those in the Songpan-Ganze Orogen. They also reported larger average κ_0 for stations in the western Sichuan Basin relative to the Songpan-Ganze region, coinciding with results from Fu and Li, 2016 and Li et al. (2020) using strong motion data. κ_0 here is the zero-distance kappa in Anderson and Hough (1984), which represents the attenuation effects of the near-surface geological conditions in the top hundreds of meters or even a few kilometers beneath the station. These differences in site responses are due to the various near-surface sedimentary structures in the Sichuan Basin and Songpan-Ganze terrane. Properly estimating and modeling site responses in the Longmen Shan and adjacent regions is a key step in seismic hazard analysis for southwestern China.

For regions covered by thick sediments as the Sichuan Basin, various studies have shown that the site responses are most likely controlled by the structure of the whole sedimentary column. Fu et al. (2019) found that κ_0 in the Longmen Shan region correlates apparently with the low shear-wave velocity anomaly averaged over the depth range of 0–10 km. Wang et al. (2013) studied the site responses of three stations in the Qionghai Basin to the southwest corner of the Sichuan Basin and found that site amplifications in the frequency range 0.1–10 Hz at the three stations are significantly dependent on sediment thickness in the basin. In addition, correlations between κ_0 and sediment thickness have been reported in Taiwan, the New Madrid seismic zone and the Gulf Coastal Plain (Liu et al., 1994; Campbell 2009; Chapman and Conn 2016; Chang et al., 2019). Attempts have been made to investigate and describe the correlation between the site effects and thickness of the sedimentary strata in central and eastern United States. Chapman and Conn (2016) derived a linear kappa model versus sediment thickness in the Gulf Coastal Plain and applied it into the stochastic ground motion prediction models. They showed that the kappa model significantly improved the high-frequency ground motion predictions from regional earthquakes. Following their work, Guo and Chapman (2019) investigated the site responses in the Atlantic and Gulf Coastal Plain using the spectral ratio method. They found that the site terms show obvious dependence on sediment thickness and can be modeled using piecewise linear functions versus sediment thickness at low frequencies. For the Atlantic Coastal Plain, different functions have been proposed to model the site responses with respect to sediment thickness by Harmon et al. (2019) and Pratt and Schleicher (2021) using various data sets and methods. Similar correlations between site responses and deeper sedimentary structures as well as site response models based on features of the whole sedimentary strata are expected for the Sichuan Basin.

The first objective of this paper is to compare site responses in the Songpan-Ganze terrane and Sichuan Basin due to the significantly different geological conditions. We downloaded broadband recordings from 189 regional earthquakes and computed the Fourier spectra of Lg waves which usually have the largest amplitudes in regional seismograms. Site responses and crustal attenuation were inverted simultaneously for the Sichuan Basin and Songpan-Ganze terrane respectively. The second objective of this paper is to introduce and evaluate site response models as functions of sediment thickness for the Sichuan Basin, which account for the effects of the thick sediments. In this paper, we focused on estimating the site responses and κ_0 for stations in the Sichuan Basin and Songpan-Ganze terrane using the Lg spectral amplitudes. We also obtained site response terms using coda spectral ratios and the H/V spectral ratios for stations in the Sichuan Basin, with the detailed description and comparison of the three sets of site terms of stations in the Sichuan Basin documented in a separate paper (Guo et al., 2022). The site response models for the Sichuan Basin were incorporated into the stochastic ground motion predictions for six recent earthquakes that were not included in our dataset for the inversions. The results in this paper are hoped to shed

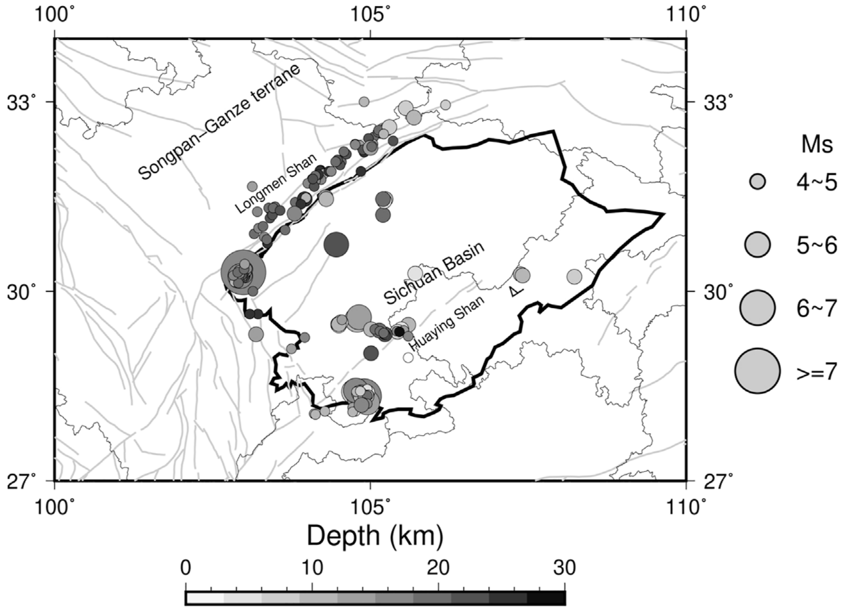

FIGURE 2
Map showing locations of the 189 earthquakes used in this study along with the earthquake source depths. Major faults in the study region are indicated by the gray lines. Magnitudes (Ms) of the earthquakes are used to scale the sizes of the circles.

light on developing regional site response models for the Longmen Shan and adjacent regions.

Data and method

Dataset

The China Digital Seismological Observation Network includes 145 broadband stations from the national seismic network and 806 broadband stations from regional seismic networks which were deployed before the end of 2007. The average spatial distance for these permanent stations is ~30–60 km except in Xinjiang and Tibet. 22 stations located in the Sichuan Basin and 19 stations in the Songpan-Ganze terrane were used in this study as shown in Figure 1. These stations have a common sample rate of 100 Hz and provide good coverage over the study region.

We collected broadband seismograms recorded at the stations from earthquakes with magnitudes $4.0 \leq Ms \leq 7.0$ happening between January 2009 and October 2020. The epicentral distances are less than 1,000 km and the focal depths are less than 30 km (Figure 2). Most of the earthquakes occurred along the Longmen Shan fault zone to the west of the Sichuan Basin and clustered in southern Sichuan Basin near the Huaying Shan fault zone as shown in Figure 2. Three-component seismograms were downloaded from the China Earthquake Network Center (CENC), beginning 2 min prior to the direct p wave with a duration of 60 min. We first obtained ground accelerations from the raw seismograms using the instrument transfer functions and rotated the two horizontal components to radial and transverse directions. The acceleration seismograms were then filtered using a high-pass filter with the corner frequency of 0.01 Hz.

To calculate the Fourier amplitude spectra of Lg waves, we adopted the following model for predicting Lg arrival time in the study region:

$$T = T_0 + \frac{r}{3.57} \tag{1}$$

where r is the epicentral distance in km and T_0 denotes the earthquake origin time. The Lg arrival time model (Eq. 1) is determined using handpicked Lg arrival times recorded at stations in the Sichuan Basin and Songpan-Ganze terrane from three earthquakes in southeastern Sichuan on 17 June, 22 June and 4 July 2019 with magnitudes Ms 5.1–5.7. The crustal velocity of Lg waves in the study region is estimated as 3.57 km/s. The length of the time window for spectral calculation is determined as 70% energy duration of the Lg waves (Chapman and Conn 2016; Guo and Chapman 2019). We tapered the time windows at both edges with 15% duration using a cosine taper and computed the Fourier amplitude spectra. Then the geometric mean of the radial and transverse Lg spectra were calculated. The noise spectra were computed simultaneously with time windows beginning at the start of the seismograms and of the same lengths as the corresponding Lg

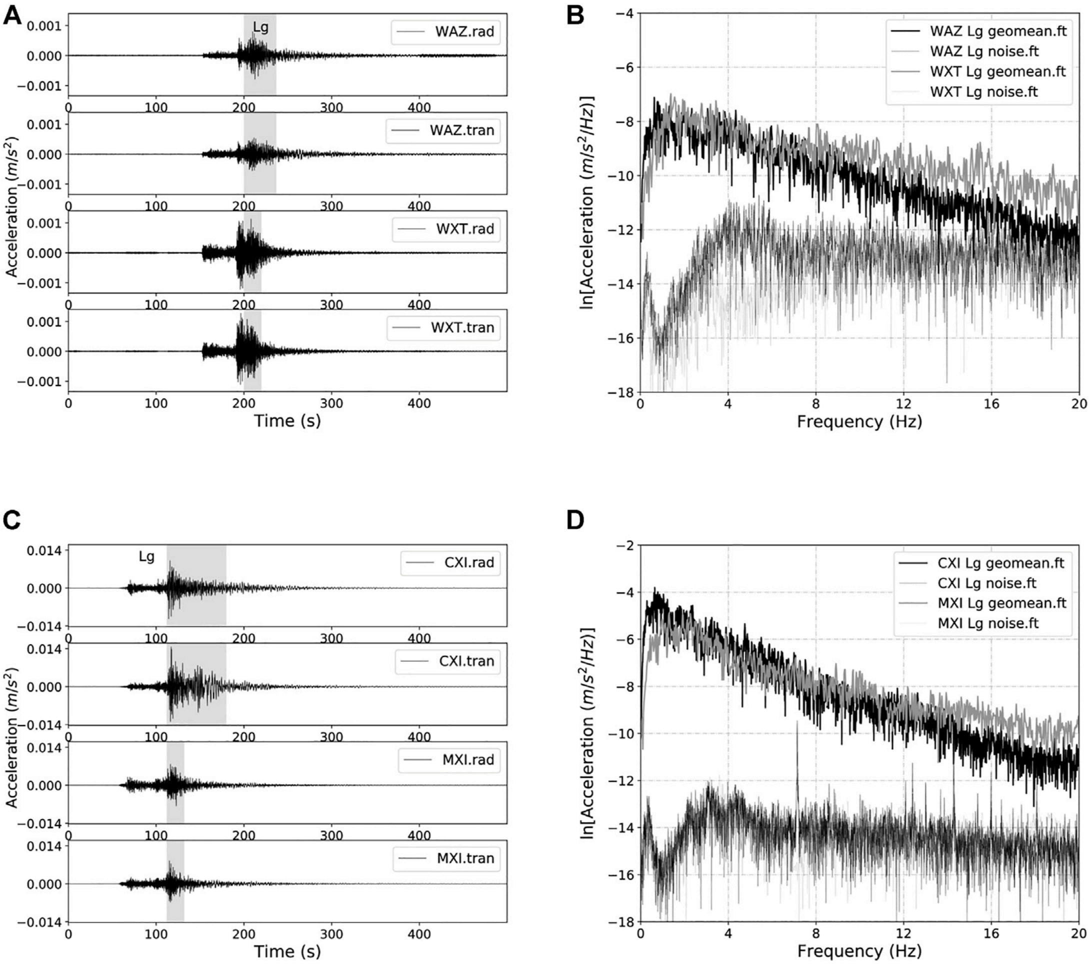

FIGURE 3
(A) Horizontal-component acceleration seismograms from the 18 December 2019 Ms 5.2 Zizhong earthquake recorded at stations WAZ (in northeastern Sichuan Basin) and WXT (in northeastern Songpan-Ganze terrane). The epicentral distances for both stations are ~374 km. The shaded areas indicate time windows used for Lg spectral calculations. **(B)** Corresponding geometric mean of Lg and noise spectra at stations WAZ and WXT. **(C)** and **(D)** are the same as **(A)** and **(B)** but from the 17 June 2019 Ms 6.0 Changning earthquake recorded at station CXI (in northwestern Sichuan Basin) and station MXI (in eastern Songpan-Ganze terrane) with epicentral distances of ~385 km.

windows. We rejected Lg spectra with signal-to-noise ratios less than three and visually inspected the spectra to exclude those with strong modulations. The final dataset consists of seismograms from 189 earthquakes with more than 5,800 event-station pairs. Supplementary Tables S1, S2 list information of the 22 stations in the Sichuan Basin and 19 stations in the Songpan Ganze terrane respectively, in which thickness of sediments beneath each individual basin station was estimated as the thickness of Cenozoic and Mesozoic sedimentary sequence from Wang et al. (2016) and Xia et al. (2021).

Figure 3 compares some examples of seismograms and Lg spectra recorded at stations in the Sichuan Basin and Songpan-Ganze terrane. In the top panel, we showed the horizontal-component seismograms and the corresponding Lg spectra recorded at station WAZ at the northeastern corner of the Sichuan Basin and station WXT in northeastern Songpan-Ganze terrane from the 18 December 2019 Ms 5.2 Zizhong, Sichuan earthquake. The acceleration amplitudes of Lg waves recorded at station WAZ are obviously smaller than station WXT though the epicentral distances are both ~374 km, corresponding to strong attenuation of Lg Fourier amplitudes relative to WXT at frequencies higher than 6–8 Hz. At lower frequencies (<1–2 Hz), we observed amplifications in Lg spectral amplitudes at station WAZ compared to WXT. Similar low-frequency amplification and high-frequency attenuation in spectral amplitudes were observed in Lg waves recorded at station CXI in northwestern Sichuan Basin and station MXI at the eastern margin of the Songpan-Ganze terrane from the 17 June 2019 Ms 6.0 Changning earthquake in southern Sichuan with epicentral distance of

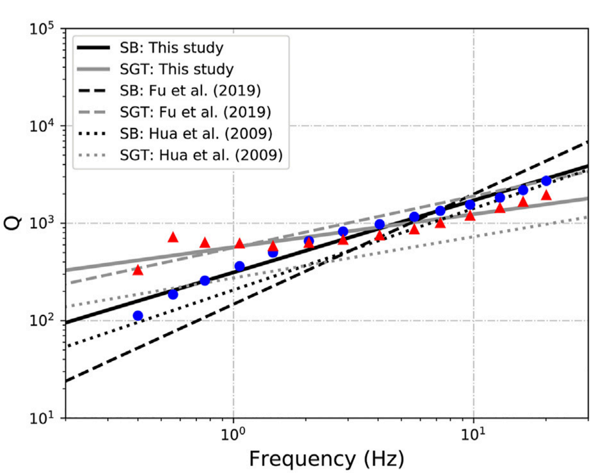

FIGURE 4
Q estimates of the Sichuan Basin (circles) and Songpan-Ganze terrane (triangles) in the frequency range of 0.4–20.04 Hz in this study. Results of least-square fits to the data are plotted as black solid line for the Sichuan Basin with $Q(f) = 335f^{0.72}$ and gray solid line for the Songpan-Ganze terrane with $Q(f) = 568f^{0.338}$ respectively. The black and gray dotted lines indicate models from Hua et al. (2009) with $Q(f) = 206.7f^{0.836}$ and $Q(f) = 274.6f^{0.423}$ for the Sichuan Basin and Songpan-Ganze terrane respectively. The black and gray dashed lines show models from Fu et al. (2019) with $Q(f) = 147.5f^{1.13}$ and $Q(f) = 274.6f^{0.53}$ for the basin and terrane respectively.

~385 km. For further analysis, we computed the mean spectral amplitudes within 18 frequency intervals with center frequencies 0.1, 0.2, 0.3, 0.4, 0.56, 0.76, 1.06, 1.46, 2.06, 2.86, 4.06, 5.66, 7.26, 9.66, 12.86, 16.06, and 20.06 Hz respectively.

Lg spectral analysis

The spectral amplitude of Lg waves at frequency f recorded at the ith station from the kth earthquake can be modeled as the following:

$$A_{ik}(f, r_{ik}) = E_k(f) G(r_{ik}) e^{-\frac{\pi r_{ik} f}{Q(f) v}} S_i(f) \tag{2}$$

where r_{ik} is the hypocentral distance, $E_k(f)$ represents the source spectrum of the kth earthquake and $G(r_{ik})$ is the geometrical spreading term. V is the shear-wave velocity and $Q(f)$ is the quality factor in the crust. The site response term at ith station is denoted as $S_i(f)$.

Our goal is to invert for the crustal quality factor $Q(f)$ and site response term $S_i(f)$ for sites in the Sichuan Basin and Songpan-Ganze terrane, which requires appropriate modeling of the source term and geometrical spreading effect according to Eq. 2. Here we modeled the source spectrum of kth earthquake using an omega-square source model, the Brune source spectral model (Brune, 1970, 1971), as the following equation:

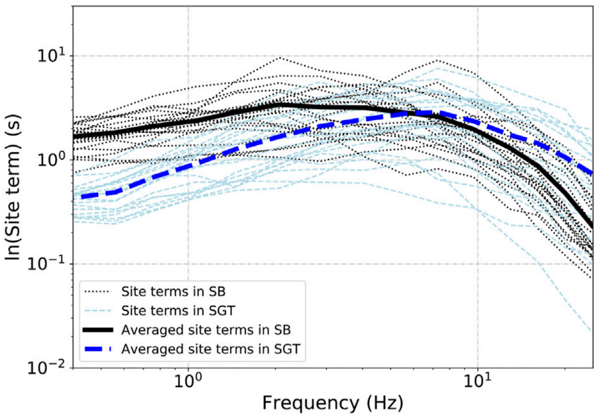

FIGURE 5
Site responses of individual stations in the Sichuan Basin (thinner dotted lines) and Songpan-Ganze terrane (thinner dashed lines) as functions of frequency. The average site response curves of stations in the Sichuan Basin and those in the Songpan-Ganze terrane are plotted as thick solid line and thick dashed line respectively.

$$E_k(f) = R_{\theta\phi} F_S V \frac{M_0 (2\pi f)^2}{1 + \left(\frac{f}{f_c}\right)^2} \frac{1}{4\pi\rho\beta^3} \tag{3}$$

in which $R_{\theta\phi} = 0.55$ is the radiation pattern averaged over a proper range of take-off angles and azimuths, $F_S = 2$ represents the free-surface effect and V accounts for the partition of S-wave energy into the horizontal components set to 0.71. ρ and β are density and shear-wave velocity near the source, assumed to be 2.7 g/cm^3 and 3.57×10^5 cm/s respectively. M_0 is the earthquake seismic moment. The corner frequency $f_c = 0.491\beta \left(\frac{\Delta\sigma}{M_0}\right)^{\frac{1}{3}}$, in which M_0 is in units of dyn·cm, $\beta$is in units of cm/s and $\Delta\sigma$ denotes the earthquake stress drop in units of dyn/cm^2. Here we adopted a stress drop value of 1 MPa according to the results from Fu et al. (2018), Wang et al. (2018) and Li et al. (2020) for earthquakes occurring along the Longmen Shan fault zone and clustered in the southern Sichuan Basin.

Geometrical spreading of S and Lg waves at near-source distances is known to be complex due to the effects of radiation pattern, focal depth, source directivity and postcritical reflections from the Moho and intra-crustal velocity contrasts (Burger et al., 1987; Ou and Herrmann 1990; Atkinson and Mereu 1992; Atkinson and Boore, 2014). At larger distances, the Lg geometrical spreading can be simply modeled as $G(r_{ik}) = r_{ik}^{-0.5}$ (Kennett 1986). We used trilinear models similar to those of Atkinson and Mereu (1992) to account for the geometrical spreading effects in the Sichuan Basin and Songpan-Ganze terrane:

TABLE 1 Kappa (κ_0) estimates from Lg Fourier spectral amplitudes of stations in the Sichuan Basin and Songpan-Ganze terrane.

Station (sichuan Basin)	κ_0 (s)	Station (songpan-ganze terrane)	κ_0 (s)
YZP	0.047	SPA	0.03
CHS	0.059	HYU	0.057
CQT	0.046	HSH	0.035
FUL	0.041	MEK	0.023
ROC	0.058	XJI	0.022
SHZ	0.034	BAM	0.022
WAZ	0.046	RTA	0.033
YUB	0.022	DFU	0.064
AYU	0.06	YJI	0.023
BZH	0.052	JLO	0.038
CXI	0.071	BAX	0.025
HMS	0.027	GZA	0.024
HWS	0.04	SMI	0.029
HYS	0.025	JZG	0.013
JJS	0.081	WDT	0.024
JYA	0.05	WXT	0.011
LZH	0.038	QCH	0.022
XCO	0.056	MXI	0.017
XHA	0.03	WCH	0.028
YGD	0.051		
YTI	0.044		
WAS	0.022		

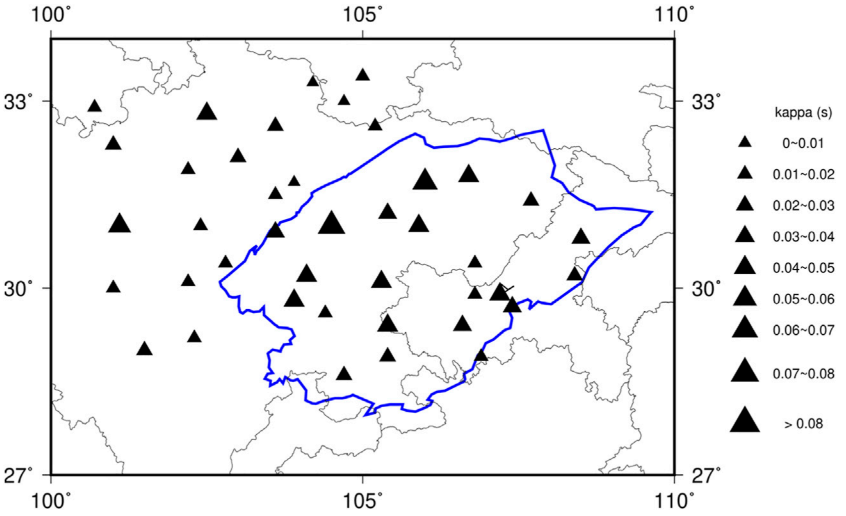

FIGURE 6
κ_0 of stations in the Sichuan Basin and Songpan-Ganze terrane plotted at the geographical locations of the corresponding stations. Sizes of the triangles are scaled to the values of κ_0 in seconds. The margin of the Sichuan Basin is shown by the thick line.

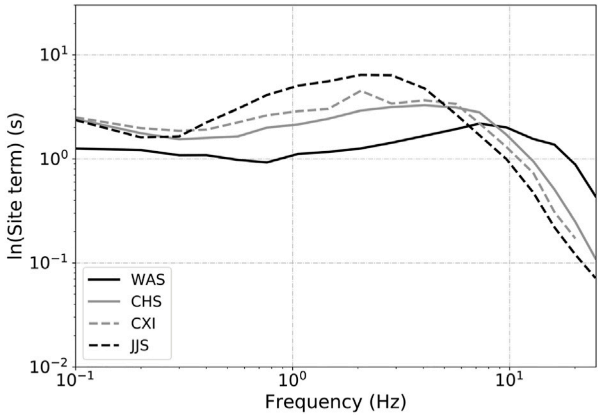

FIGURE 7
Comparison of site responses versus frequency of four stations WAS, CHS, CXI, and JJS in the Sichuan Basin. The thicknesses of sediments underlying stations WAS, CHS, CXI, and JJS are 2.0, 5.2, 7.7 and 10.0 km respectively. The value of sediment thickness is estimated as the thickness of the Cenozoic and Mesozoic sedimentary sequence based on results from Wu et al. (2016).

TABLE 2 Linear regression coefficients of natural logarithms of Lg site terms and all three sets of site terms as a function of sediment thickness in km at each center frequency (*f*).

f (Hz)	Lg site term		All site term	
	a	b	*a*	b
0.1	0.0648	0.3456	0.0623	0.1742
0.56	0.0866	0.0816	0.0621	0.0550
0.76	0.1136	0.0698	0.0892	0.0373
1.06	0.1150	0.1874	0.0893	0.1564
2.06	0.1359	0.3654	0.1111	0.2121
4.06	0.1304	0.3594	0.1104	0.0599
5.66	0.0825	0.4946	0.0780	0.0795
7.26	0.0055	0.7808	-0.0013	0.3793

$$G(r_{ik}) = \begin{cases} r_{ik}^{-1.0}, & r_{ik} \leq 1.5\,H \\ (1.5H)^{-1.0}, & 1.5H < r_{ik} < 2.5\,H \\ (1.5H)^{-1.0}\left(\frac{r_{ik}}{2.5H}\right)^{-0.5}, & r_{ik} \geq 2.5\,H \end{cases} \tag{4}$$

where H is the Moho depth. Here we took $H = 42$ km for the Sichuan Basin and $H = 60$km for the Songpan-Ganze terrane according to results in Wang et al. (2007), Li et al. (2011) and Wei et al. (2020).

For inversion, we wrote Eq. 2 as the following:

$$\ln\left[\frac{A_{ik}(f, r_{ik})}{E_k(f)G(r_{ik})}\right] = -\frac{\pi f r_{ik}}{Q(f)v} + \ln[S_i(f)] \tag{5}$$

The quality factor $Q(f)$ and site term $S_i(f)$ at each centered frequency f can be estimated from the linear regression of Eq. 5 with respect to hypocentral distance r_{ik}. All the 189 earthquakes were used in the inversion for the Sichuan Basin while we only used seismic data from 149 earthquakes along the Longmen Shan fault zone in the inversion for the Songpan-Ganze terrane to ensure that most of the propagation paths are within the terrane. The site terms for *ith* station at high frequencies can be modeled as the following:

$$\ln[S_i(f)] = \ln[C_i] - \pi\kappa_i f \tag{6}$$

where C_i is a constant and κ_i is the zero-distance kappa (κ_0) at the *ith* station. We then estimated κ_i from a linear regression of Eq. 6 with respect to frequency. The frequency range of the linear regression is constrained by the signal-to-noise ratios and the linear trend of the natural logarithms of the site terms.

Results

Q in the Sichuan Basin and Songpan-Ganze terrane

The Lg wave is typically the most prominent phase in seismograms at regional distances over continental paths. The Lg attenuation in the crustal wave guide was found to be sensitive to the lateral changes in crustal structure, intrinsic properties and deformation of the crust (Frankel 1991; Baqer and Mitchell 1998; Xie et al., 2006; Pasyanos et al., 2009; Zhao et al., 2010). Figure 4 shows the quality factor Q inverted from Eq. 5 for the Sichuan Basin and Songpan-Ganze terrane. The Q values in both regions generally increase with frequency. At frequencies higher than 2 Hz, both sets of Q exhibit good linear trends versus frequency in log-log scale and the quality factor in the basin is larger than that in the Songpan-Ganze terrane, suggesting less attenuation of high frequency motion through the basin crust. The least square fits to the Q values are plotted as solid lines in Figure 4, corresponding to the following models:

$$Q(f) = 313 f^{0.74} \tag{7}$$

for the Sichuan Basin, and

$$Q(f) = 568 f^{0.34} \tag{8}$$

for the Songpan-Ganze terrane. Q models for these two regions from Fu et al. (2019) and Hua et al. (2009) were also plotted in Figure 4. In general, Q models in the three studies all show larger low-frequency Q and smaller high-frequency Q in the Songpan-Ganze region relative to the Sichuan Basin. The Q models in this study have larger Q_0 (Q at 1Hz) values and smaller slopes compared to previous studies, for both regions. $Q(f)$ for the Songpan-Ganze terrane from Hua et al. (2009) predicted obviously smaller values than the other two models. Discrepancies in Q models among the three studies are

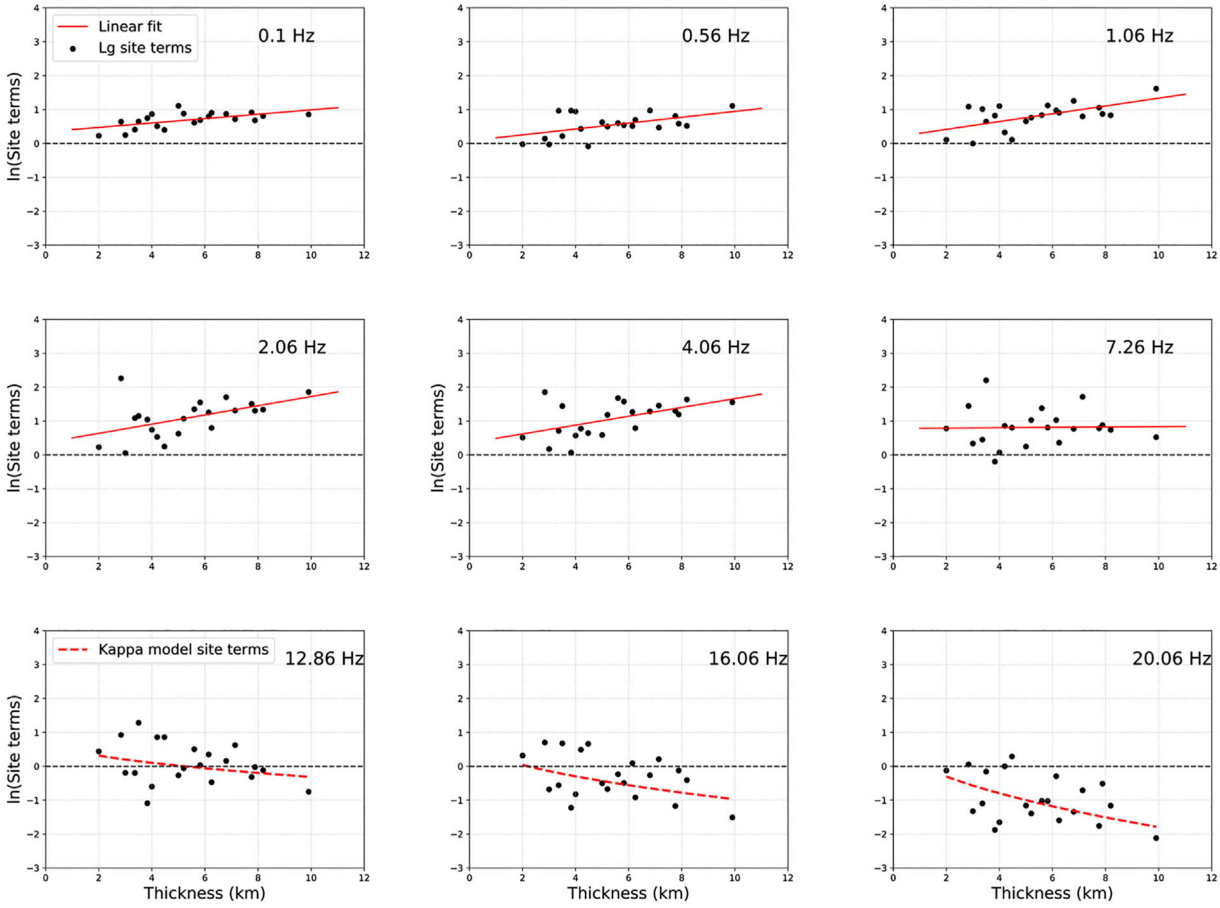

FIGURE 8
Natural logarithms of site terms (dots) estimated from linear regression of Eq. 8 using Lg waves for stations in the Sichuan Basin versus sediment thickness over frequency range 0.1–7.26 Hz. The solid lines indicate linear regression results of the Lg site terms with respect to sediment thickness. The dashed lines show estimates calculated using Eq. 6 and the κ_0 model represented by Eq. 10.

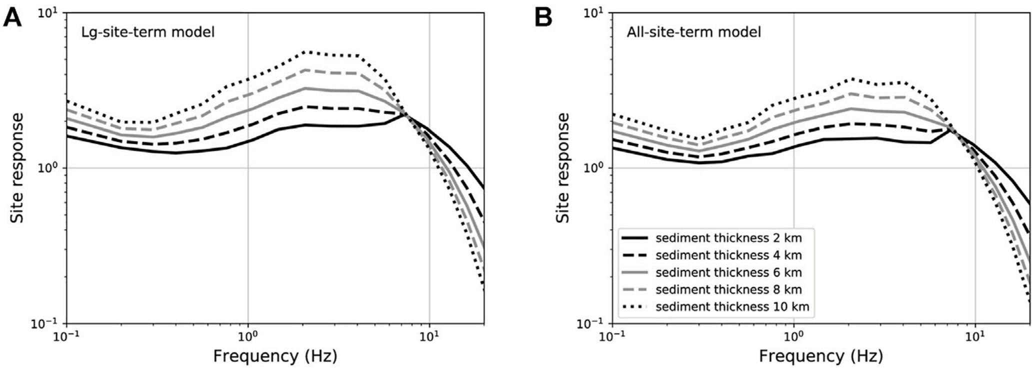

FIGURE 9
Site responses calculated using Eqs 9, 11 for sites in the Sichuan Basin with different sediment thicknesses.

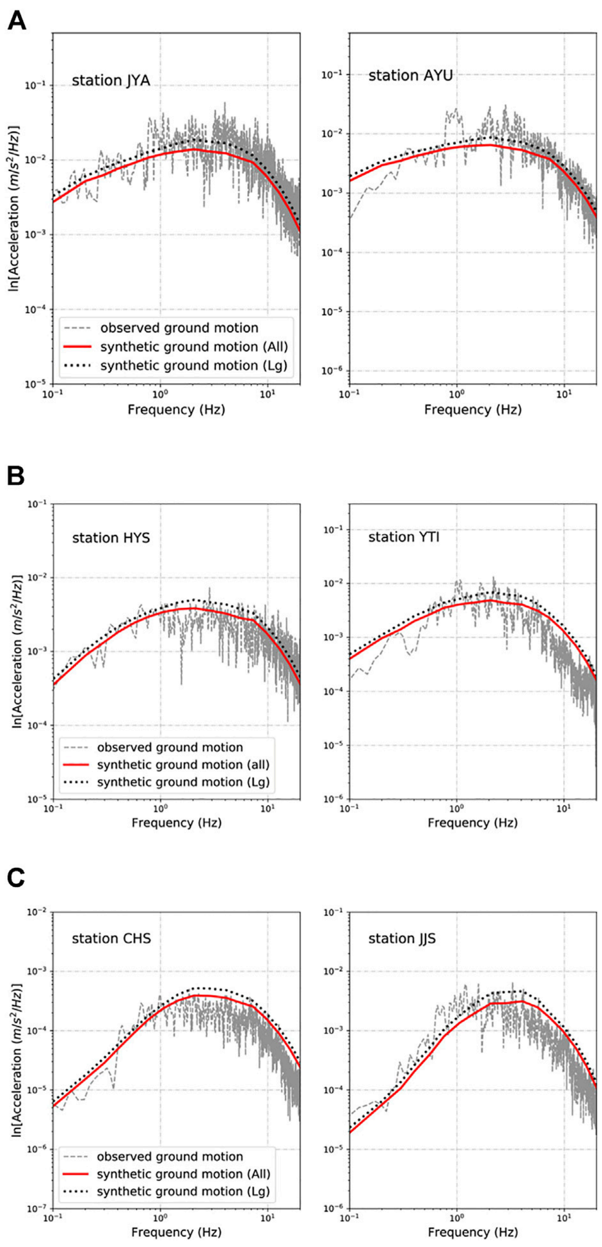

FIGURE 10
(A) The gray dashed lines show the Lg spectra recorded at stations JYA and AYU in the Sichuan Basin from the 1 June 2022 Ms 6.1 Lushan earthquake respectively. The dotted and solid lines indicate the corresponding target spectra calculated using Eq. 2 based on site response terms with Lg site term coefficients and all site term coefficients listed in Table 2 respectively. **(B)** The same as **(A)** but for Lg waves recorded at stations HYS and YTI in the Sichuan Basin from the 15 September 2021 Ms 6.0 earthquake. **(C)** The same as **(A)** and **(B)** but for Lg waves recorded at stations CHS and JJS in the Sichuan Basin from the 21 October 2020 Ms 4.6 earthquake in central Sichuan.

attributed to the different dataset, methods and study area covered by the ray paths. At high frequencies (f > 4 Hz), larger Q values in the Sichuan Basin may indicate less heterogeneities in the deep crust beneath the basin sedimentary sequence. It is important to note that, from Eq. 2, the Q estimates above reflect the distance dependent part of the total attenuation through the path, and presumably quantify Q in the deeper crust. Distance independent attenuation occurring essentially beneath the receivers (zero distance) and presumably at shallower depths is captured by the $S_i(f)$ site terms in Eq. 2. The total path attenuation (the product of both the exponential and site terms on the right-hand side of Eq. 2) at most sites in the Sichuan Basin at high frequencies (f > 4 Hz) is actually greater than at most sites in the Songpan-Ganze terrane. Attenuation occurring along the part of the path essentially beneath the receivers is quantified by larger average values of κ_0 in the Sichuan Basin compared to the Songman-Ganze terrane. We discuss this complex behavior of site response in the following sections.

Site responses in the Sichuan Basin and Songpan-Ganze terrane

In Figure 5, we showed the site response terms of stations in the Sichuan Basin and Songpan-Ganze terrane. Site responses for most of the stations exhibit a wide frequency range of amplification instead of a distinguishable resonant peak and site responses in the Sichuan Basin are significantly different from those in the Songpan-Ganze terrane. The peak amplifications for sites in the Sichuan Basin mainly occur between 1 and 4 Hz, whereas they exist between 2 and 11 Hz for stations in the Songpan-Ganze terrane. This can be clearly observed in the average site response curves for the two regions shown in Figure 5. The average site response in the Sichuan Basin indicates strong amplifications over the frequency range up to ~15 Hz while stations in the Songpan-Ganze terrane tend to amplify ground motions in the frequency range of 1.7–18 Hz. At frequencies lower than 1.7 Hz, average de-amplifications are observed for the Songpan-Ganze stations. The average site response in the Sichuan Basin shows much stronger amplification at low frequencies (<6 Hz) and more obvious attenuation at frequencies higher than 10 Hz relative to the Songpan-Ganze terrane. The average peak frequency for sites in the Sichuan Basin is ~2 Hz with an amplification factor of ~3.3 while it migrates to ~7 Hz with a peak factor of ~2.4 in the Songpan-Ganze terrane. For individual sites, the peak amplification factor could reach up to ~10 in the Sichuan Basin. Fu et al. (2019) calculated site responses for 16 stations

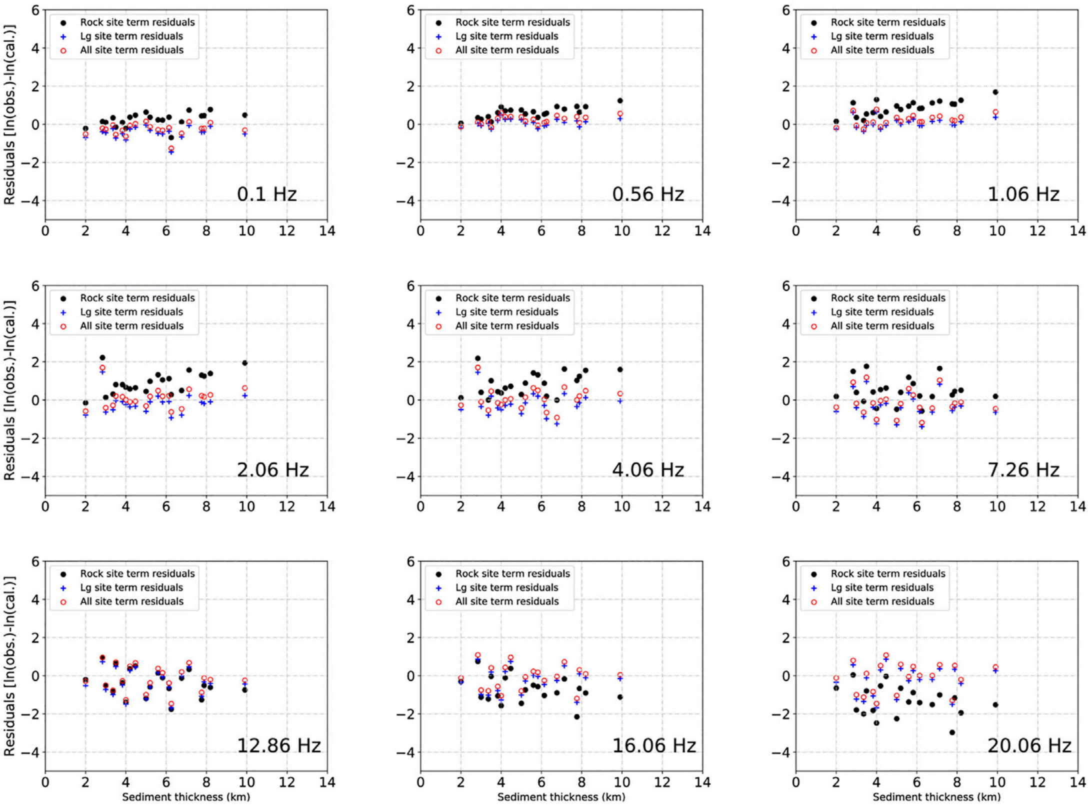

FIGURE 11
Rock site term residuals (filled circles), Lg site term residuals (pluses) and all site term residuals (open circles) of stations in the Sichuan Basin at different frequencies plotted with respect to sediment thickness in the basin for the 1 June 2022 Ms 6.1 Lushan earthquake.

in western Sichuan Basin and 12 stations in eastern Songpan-Ganze terrane using the generalized inversion technique (GIT). Their results are similar to the site responses in our Figure 5.

Table 1 lists the estimates of κ_0 from Lg Fourier spectra for the stations in the Sichuan Basin and Songpan-Ganze terrane which were plotted at the geographical locations of the corresponding stations in Figure 6. The largest κ_0 values occur in western and central Sichuan Basin while κ_0 of stations in eastern Sichuan Basin and the Songpan-Ganze terrane are generally smaller. κ_0 values in the Songpan-Ganze terrane are within 0.011–0.038 s except for stations DFU and HYU with κ_0 values of 0.064 s and 0.057 s respectively, whereas κ_0 varies significantly from 0.02 s to 0.08 s across the Sichuan Basin. The average κ_0 in the Sichuan Basin is 0.045 s, larger than the average κ_0 in the Songpan-Ganze terrane with a value of 0.028 s. Fu et al. (2019) obtained similar results with average κ_0 values of 0.0423 s and 0.0227 s for western Sichuan Basin and the Songpan-Ganze Orogen respectively using the GIT. The stronger high-frequency attenuation effects implied by the larger κ_0 values in the Sichuan Basin relative to the Songpan-Ganze terrane are likely due to the thick unconsolidated and semi-consolidated Post-Triassic sediments accumulated in the basin. Geographical variation of κ_0 in the Sichuan Basin is significant and it is notable that the κ_0 generally decreases from northwest towards southeast within the basin coinciding with the changes of sediment thickness (Meng et al., 2005; Wang et al., 2016; Li et al., 2020).

Site response models for the Sichuan Basin

The Sichuan Basin is the most populated and industrialized area in southwestern China, and therefore exposed to higher seismic hazard than adjacent regions near the Longmen Shan fold and thrust belt. Developing appropriate ground motion prediction models for the Sichuan Basin is in urgent demand for seismic hazard analysis, which will require an appropriate site response model to account for the amplification and attenuation effects of the thick sediments in the basin.

Figure 7 shows site response terms versus frequency for four stations in the Sichuan Basin underlain by sedimentary columns of different thicknesses. As the sediment thickness increases, the peak frequency of amplifications generally migrates to lower

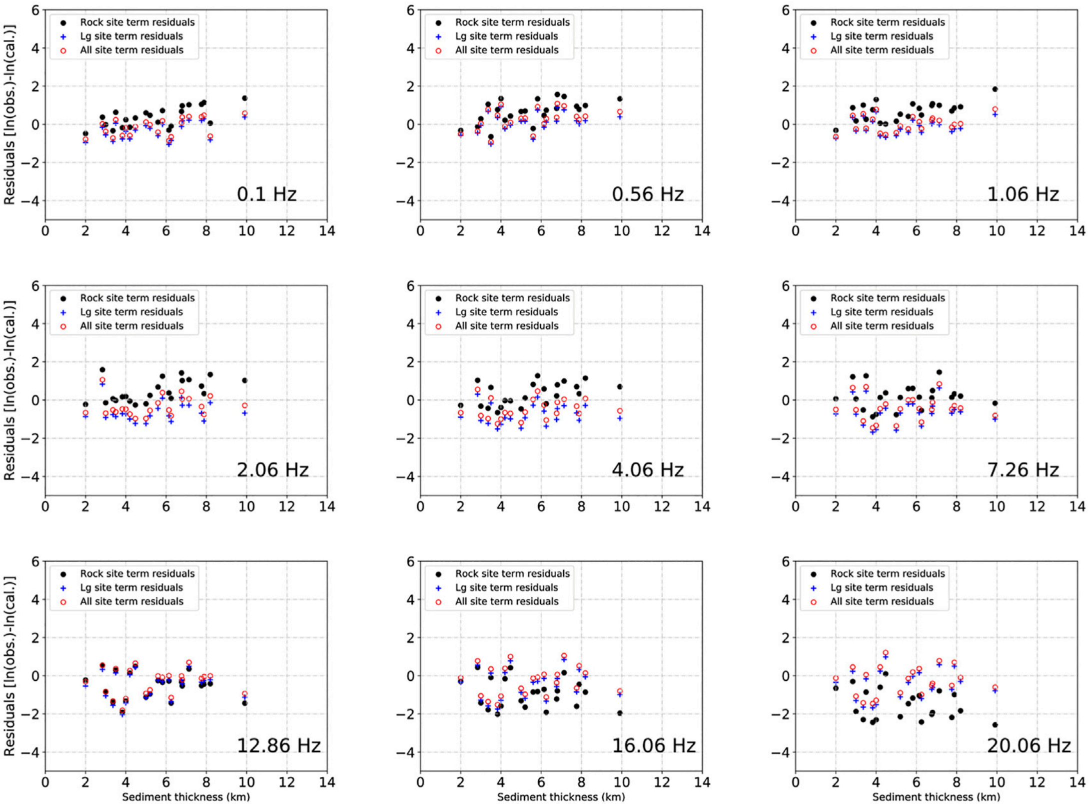

FIGURE 12
Same as Figure 11 but for the 21 October 2020 Ms 4.6 earthquake in central Sichuan.

frequencies and the amplitudes of amplifications become larger. At high frequencies (>10 Hz), we observed stronger attenuation effects at stations overlying thicker sediments. These observations imply that site responses in the Sichuan Basin are strongly correlated with sediment thickness.

In Figure 8, we plotted the natural logarithms of the site terms derived from Lg Fourier spectra with respect to sediment thickness at nine center frequencies ranging from 0.1 to 20.06 Hz. Some patterns can be observed, even though the scatter is large. At lower frequencies ($\le$ 4.06 Hz), the site responses were dominated by amplifications and exhibit positive correlations with sediment thickness. As frequency increases, the positive trend becomes flat and gradually turns into a negative trend within the frequency range of 7–12 Hz. The site responses show dominant attenuations at frequencies higher than 12.86 Hz and the attenuation effects become more significant as sediment thickness increases. To verify the sediment-thickness dependence of the site response terms, we also calculated site responses in the Sichuan Basin using the H/V spectral ratios and coda spectral ratios. The results show that site response terms derived from the three different methods behave consistently versus sediment thickness as frequency increases. Detailed description of the three sets of site response terms has been documented in a separate paper (Guo et al., 2022).

We model the site responses at frequency f in the Sichuan Basin using the following linear relationship between the natural logarithm of the site terms and sediment thickness:

$$\ln[S(f, Z)] = aZ + b \tag{9}$$

where Z is sediment thickness in km. Eq. 9 is only used to model the site responses within the frequency range of 0.1–7.26 Hz and the linear regression results are plotted as solid lines in Figure 8. At higher frequencies, the site responses are controlled by κ_0 according to Eq. 6. κ_0 values of stations in the Sichuan Basin derived from Lg spectral amplitudes agreed well with those from the coda spectral ratios as shown in Supplementary Figure S1 (Supplementary Materials), and both sets of κ_0 exhibit a clear positive correlation with sediment thickness. κ_0 estimates from Fu et al. (2019) are also within the scatter range of our κ_0 values. We modeled κ_0 in the Sichuan Basin as a function of sediment thickness following Guo and Chapman (2019):

$$\kappa_0 = 0.019Z^{0.545} \tag{10}$$

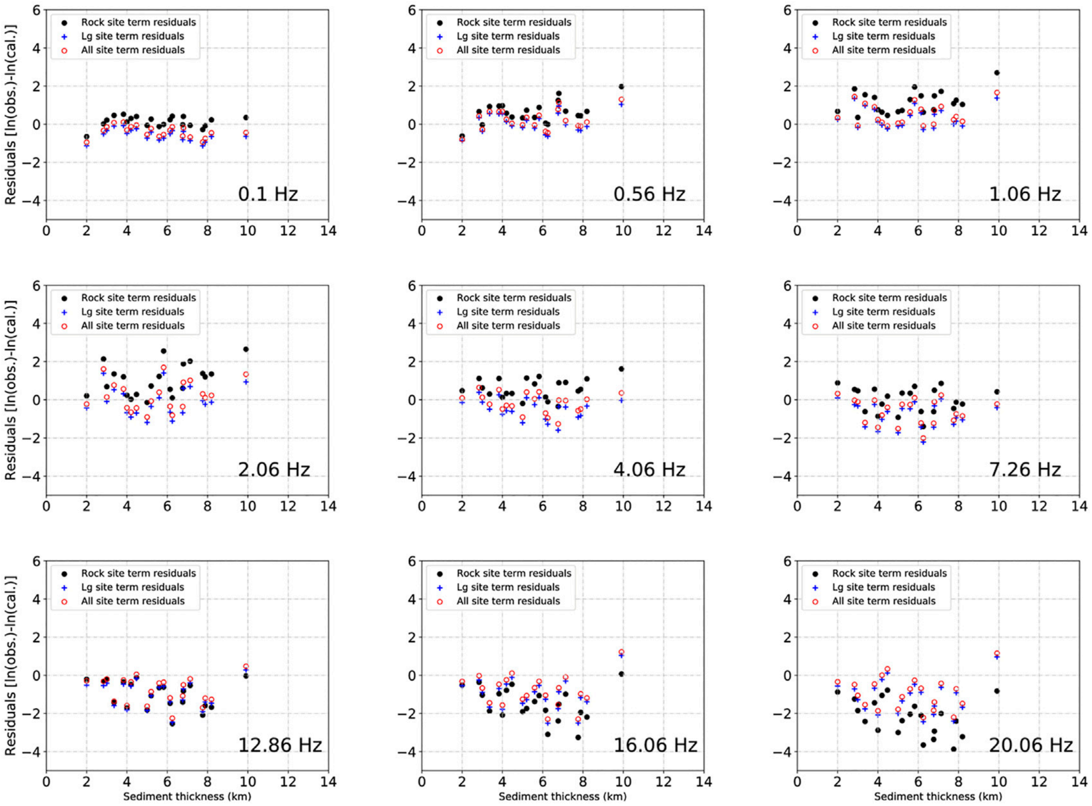

FIGURE 13
Same as Figure 11 but for the 15 September 2021 Ms 6.0 earthquake.

Here the units for κ_0 and sediment thickness are seconds and kilometers respectively. For frequencies higher than 7.26 Hz, the site responses are modeled as the following:

$$\ln[S(f,Z)] = \ln[S(7.26\,Hz,Z)]e^{-\pi\kappa_0(f-7.26)} \tag{11}$$

where κ_0 is defined by Eq. 10 as a function of sediment thickness. As shown by the dashed lines in Figure 8, the model represented by Eq. 11 fits the observed Lg site terms well.

Table 2 lists the coefficients for linear regressions of the Lg site terms in the frequency range of 0.1–7.26 Hz. For comparison, we also listed the linear regression coefficients of all site response terms estimated from the three different methods in Table 2. Figure 9 shows some examples of site response models $S(f,Z)$ versus frequency for the Sichuan Basin. Site response curves for sediment thickness ranging from 2 to 10 km in Figure 9A were calculated using the Lg site term coefficients while those in Figure 9B were calculated using the all site term coefficients. The Lg site term model is similar to the corresponding all site term model but has slightly larger amplitudes.

Evaluation of the site response models

To evaluate the site response models defined by Eqs 9, 11 as functions of frequency and sediment thickness, we applied the models using the stochastic method of ground motion simulation for the Sichuan Basin following Guo and Chapman (2019). We selected six earthquakes occurring between October 2020 and June 2022 with magnitude (Ms) of 4.6–6.1 for analysis. Seismograms from these earthquakes were not included in the dataset for estimating the quality factor and site response: therefore, they can be used for an unbiased test of our attenuation and site response model. Detailed information for the six earthquakes was listed in Supplementary Table S3. Three of the earthquakes were located along the western boundary of the Sichuan Basin and the rest of them occurred in the southern part of the basin.

We first calculated the synthetic Fourier amplitude spectrum (i.e., target spectrum) for each station-event pair using Eq. 2 based on the stochastic method. The source and geometrical spreading terms are given by Eqs 3, 4, and the quality factor $Q(f)$ in the Sichuan Basin is modeled as Eq. 7. The site response term is defined by Eqs 9, 11. Figure 10 shows examples of observed and target spectra from three of the earthquakes in Supplementary Table S3. In Figure 10A, we showed the target spectra for stations JYA and AYU from the 1 June 2022 Ms 6.1 Lushan earthquake calculated using the site response models based on the Lg site term and all site term coefficients listed in Table 2 respectively. The target spectrum based on Lg site term coefficients has slightly higher amplitudes than that based on all of the site term coefficients. In general, the shape and amplitudes of the observed Lg spectra have been well-captured by both target spectra.

For further investigation, we computed three sets of residuals which are differences between the observed and target spectra for each station-event pair. Two sets of the residuals were calculated using target spectra based on site response models defined in Eqs 9, 11 with Lg site term and all site term coefficients respectively. We denoted these two sets of residuals as “Lg site term residuals” and “all site term residuals” hereafter. The third set of residuals were calculated using the site response term for generic rock sites defined as the following equation:

$$S_r(f) = C_r e^{-\pi \kappa_r f} \tag{12}$$

in which C_r is the crustal amplification factor from Boore and Thompson (2015) for rock sites with a V_{S30}=2.0 km/s, and κ_r = 0.006 *s* which is representative of hard rock sites. We denoted the third set of residuals as “rock site term residuals”.

Figure 11 shows the three sets of residuals versus sediment thickness at nine frequencies for the 1 June 2022 Ms 6.1 Lushan earthquake, which occurred near the southwestern corner of the Sichuan Basin. The rock site term residuals show a strong frequency dependence with positive amplitudes at frequencies lower than 4.06 Hz while the amplitudes decrease to negative values at higher frequencies (≥ 12.84 Hz). Sediment thickness dependence was clearly observed in the rock site term residuals. The amplitudes of the residuals become more positive for sites on larger thicknesses of sediment at frequencies lower than 4.06 Hz whereas they decrease to more negative values as thickness increases at higher frequencies (≥ 12.84 Hz). The Lg site term and all site term residuals behaved consistently with each other and showed minor differences over the frequency range. Relative to the rock site term residuals, the Lg and all site term residuals exhibit a lack of thickness dependence and the amplitudes are brought down to near zero at frequencies ranging from 0.56 to 4.06 Hz and increase to near zero at frequencies higher than 12.86 Hz. Similar reductions in residual bias when using the site response models derived in this study were observed in residuals for the 21 October 2020 Ms 4.6 earthquake in central Sichuan and the 15 September 2021 Ms 6.0 earthquake in southern Sichuan Basin as shown in Figures 12, 13. For the Ms 6.0 earthquake in the southern Sichuan Basin, the ground motion prediction models with Lg and all site term coefficients tend to overestimate the ground motions at high frequencies (≥ 12.86 Hz). However, the thickness dependence in the rock site term residuals is absent in the Lg and all site term residuals and the site response models with Lg and all site term coefficients greatly improved the prediction of high-frequency ground motions relative to that with the rock site term. Supplementary Figure S2 shows residuals for the remaining three earthquakes in Supplementary Table S3 which share similar behaviors with the residuals in Figures 11–13. At certain frequency range (especially 4.06–7.26 Hz), the average values of the Lg and all site term residuals for the six earthquakes deviated from zero suggesting the site response models defined by Eqs 9, 11 are not working well for these frequencies. However, the ground motion prediction models with Lg and all site term coefficients generally worked better in predicting ground motions in the Sichuan Basin for the six earthquakes relative to the prediction model using the rock site term. Overall, the all site term residuals seem to behave better than the Lg site term residuals, especially at higher frequencies. The site response models for the Sichuan Basin were derived using Fourier spectra, which can be used to develop site terms applicable for prediction models of the PSA response spectra following the procedure in Chapman and Guo, 2021.

Conclusion

The crustal quality factor and site response in the Sichuan Basin and the Songpan-Ganze terrane were estimated using more than 5,800 three-component broadband seismograms from 189 earthquakes occurring between January 2009 and October 2020. We obtained $Q(f) = 313 f^{0.74}$ and $Q(f) = 568 f^{0.338}$ for the Sichuan Basin and Songpan-Ganze terrane respectively, which is in good agreement with the $Q(f)$ models found in previous studies. Site responses of stations in the Sichuan Basin differed strongly from those in the Songpan-Ganze terrane, which is attributed to the different geological conditions between the two regions. The average site response in the basin shows stronger amplification effects at frequencies lower than 6 Hz and strong attenuation effects at higher frequencies (>10 Hz) relative to the Songpan-Ganze terrane. κ_0 estimates of stations in the basin are generally larger than those in the Songpan-Ganze terrane and the average κ_0 is ~1.6 times larger in the basin than the Songpan-Ganze terrane. Site response terms and κ_0 of stations in the Sichuan Basin were found to be correlated with sediment thickness. We developed site response models for the Sichuan Basin from site response terms obtained using Lg Fourier amplitudes, coda spectral ratios and H/V spectral ratios. The site response models depend on the sediment thickness and were incorporated in the stochastic method of ground motion predictions for six recent earthquakes, to establish an independent means to test the derived models. The rock site term residuals for the earthquakes exhibit strong bias, and dependence on sediment thickness, exhibiting an underestimation of low-frequency ground motions and overestimation of high-frequency ground motions in the Sichuan Basin. This bias of ground motion prediction residuals is greatly reduced using the site response models derived here. Generally, the Lg results and the results using all site term coefficients presented in this study worked well in predicting ground motions for the six earthquakes used to independently test the models. The site response models defined by Eqs 9, 11 are the first models developed for the whole Sichuan Basin which can be directly used in predicting the Fourier spectra recorded at stations with given sediment thickness. Site corrections based on our site response models can be used to reduce the bias in determining magnitudes and other source parameters of the earthquakes in the Longmen Shan and adjacent regions. In addition, site terms for predicting PSA response spectra can be developed from our site response models following the method in Chapman and Guo 2021, which can be incorporated into calculations of probabilistic seismic hazard assessment. Soc,

Data and resources

The seismic data used in this study are provided by Data Management Centre of China National Seismic Network at Institute of Geophysics (SEISDMC, doi:10.11998/SeisDmc/SN), China Earthquake Networks Center and AH, BJ, BU, CQ, FJ, GD, GS, GX, GZ, HA, HB, HE, HI, HL, HN, JL, JS, JX, LN, NM, NX, QH, SC, SD, SH, SN, SX, TJ, XJ, XZ, YN, ZJ Seismic Networks, China Earthquake Administration (http://www.esdc.ac.cn/; last accessed June 2022). We made some of the figures using the Generic Mapping Tools version 5.2.1 (GMT, Wessel et al., 2013) and Matplotlib version 1.5.1 (Hunter, 2007).

Data availability statement

The original contributions presented in the study are included in the article/Supplementary Material, further inquiries can be directed to the corresponding author.

Author contributions

ZG: The first author collected and processed all the seismic data used in the study. She wrote the manuscript and plotted all the figures in the paper. MC: The corresponding author wrote and tested the fortran programs for the inversion and provided fortran programs for calculating the residuals. He described and explained some of the results during oral communications. He also revised the manuscript.

Funding

This study was supported by the National Natural Science Foundation of China (Grant No. 42004035), the Natural Science Foundation of Jiangsu Province (Grant No. BK20200609), and the Fundamental Research Funds for the Central Universities (Grant No. JUSRP121050).

Acknowledgments

We thank the Earthquake Science Data Center for providing the seismic data. We thank the associate editor YR and two reviewers for comments that improved the study.

Conflict of interest

The authors declare that the research was conducted in the absence of any commercial or financial relationships that could be construed as a potential conflict of interest.

Publisher's note

Supplementary material

The Supplementary Material for this article can be found online at: https://www.frontiersin.org/articles/10.3389/feart.2022.1016096/full#supplementary-material

References

Anderson, J. G., and Hough, S. E. (1984). A model for the shape of the Fourier amplitude spectrum of acceleration at high frequencies. *Bull. Seismol. Soc. Am.* 74, 1969–1993.

AQSIQ (2001). *GB18306—2011 seismic ground motion parameters zonation map of China*. first edition. Beijing: Standard Press of China, 165–189. AvaliableAt: https://www.nssi.org.cn/nssi/front/5138636.html.

Atkinson, G. M., and Mereu, R. F. (1992). The shape of ground motion attenuation curves in southeastern Canada. *Bull. Seismol. Soc. Am.* 82 (5), 2014–2031. doi:10.1785/bssa0820052014

Atkinson, G. M., and Boore, D. M. (2014). The attenuation of Fourier amplitudes for rock sites in eastern North America. *Bull. Seismol. Soc. Am.* 104, 513–528. doi:10.1785/0120130136

Baqer, S., and Mitchell, B. (1998). Regional variation of. *Pure Appl. Geophys.* 153 (4), 613–638. doi:10.1007/s000240050210

Bora, S. S., Scherbaum, F., Kuehn, N., and Stafford, P. (2016). On the relationship between Fourier and response spectra: Implications for the adjustment of empirical ground-motion prediction equations (GMPEs). *Bull. Seismol. Soc. Am.* 106 (3), 1235–1253. doi:10.1785/0120150129

Borcherdt, R. D. (2002). Empirical evidence for acceleration-depen- dent amplification factors. *Bull. Seismol. Soc. Am.* 92, 761–782. doi:10.1785/0120010170

Boore, D. M., and Thompson, E. M. (2015). Revisions to some parameters used in stochastic-method simulations of ground motion. *Bull. Seismol. Soc. Am.* 105, 1029–1041. doi:10.1785/0120140281

Brune, J. N. (1971). Correction. *J. Geophys. Res.* 76, 5002.

Brune, J. N. (1970). Tectonic stress and the spectra of seismic shear waves from earthquakes. *J. Geophys. Res.* 75, 4997–5009. doi:10.1029/jb075i026p04997

Burchfiel, B. C., Chen, Z. L., Liu, Y. P., and Royden, L. H. (1995). Tectonics of the longmen Shan and adjacent regions, central China. *Int. Geol. Rev.* 37 (8), 661–735. doi:10.1080/00206819509465424

Burger, R. W., Somerville, P. G., Barker, J. S., Herrmann, R. B., and Helmberger, D. V. (1987). The effect of crustal structure on strong ground motion attenuation relations in eastern North America. *Bull. Seismol. Soc. Am.* 77, 420–439.

Campbell, K. W. (2009). Estimates of shear-wave Q and 0 for unconsolidated and semiconsolidated sediments in eastern north Americafor unconsolidated and semiconsolidated sediments in eastern north America. *Bull. Seismol. Soc. Am.* 99 (4), 2365–2392. doi:10.1785/0120080116

Castro, R. R., Stock, J. M., Hauksson, E., and Clayton, R. W. (2017). Source functions and path. Report.

Chang, E. Z. (2000). Geology and tectonics of the songpan-ganzi fold belt, southwestern China. *Int. Geol. Rev.* 42 (9), 813–831. doi:10.1080/00206810009465113

Chang, S. C., Wen, K. L., Huang, M. W., Kuo, C. H., Lin, C. M., Chen, C. T., and Huang, J. Y. (2019). The high-frequency decay parameter (Kappa) in Taiwan. *Pure Appl. Geophys.* 176, 4861–4879. doi:10.1007/s00024-019-02219-y

Chapman, M., and Conn, A. (2016). A model for Lg propagation in the Gulf Coastal Plain of the southern United States. *Bull. Seismol. Soc. Am.* 106 (2), 349–363. doi:10.1785/0120150197

Chapman, M., and Guo, Z. (2021). A response spectral ratio model to account for amplification and attenuation effects in the atlantic and Gulf Coastal Plain. *Bull. Seismol. Soc. Am.* 111 (4), 1849–1867. doi:10.1785/0120200322

Chen, X. B., Wu, Y. Q., Du, P. S., Li, J. S., Wu, Y. R., and Jiang, G. F. (1986). "Crustal velocity structure at two sides of Longmenshan tectonic belt (in Chinese)," in *Developments in the research of deep structure of China's continent* (Beijing: Seismol. Press), 112–127.

Field, E. H., Johnson, P. A., Beresnew, l. A., and Zeng, Y. (1997). Nonlinear ground-motion amplification by sediments during the 1994 Northridge earthquake. *Nature* 390 (11), 599–602. doi:10.1038/37586

Frankel, A. D., Carver, D. L., and Williams, R. A. (2002). Nonlinear and linear site response and basin effects in Seattle for the M 6.8 Nisqually, Washington, earthquake. *Bull. Seismol. Soc. Am.* 92 (6), 2090–2109. doi:10.1785/0120010254

Frankel, A. (1991). Mechanisms of seismic attenuation in the crust: Scattering and anelasticity in New York state, south Africa, and southern California. *J. Geophys. Res.* 96, 6269–6289. doi:10.1029/91jb00192

Fu, L., and Li, X. (2016). The characteristics of high-frequency attenuation of shear waves in the Longmen Shan and adjacent regions. *Bull. Seismol. Soc. Am.* 106 (5), 1979–1990. doi:10.1785/0120160002

Fu, L., Li, X., Wang, F., and Chen, S. (2019). A study of site response and regional attenuation in the Longmen Shan region, eastern Tibetan Plateau, SW China, from seismic recordings using the generalized inversion method. *J. Asian Earth Sci.* 181, 103887. doi:10.1016/j.jseaes.2019.103887

Fu, L., Li, X. J., Rong, M. S., Chen, S., and Zhou, Y. (2018). Parameter estimation of ground-motion prediction model in Longmen Shan region based on strong motion data. *Acta Seismol. Sin.* 40, 374–386. doi:10.11939/jass.20170215

Guo, Z., and Chapman, M. C. (2019). An examination of amplification and attenuation effects in the Atlantic and Gulf Coastal Plain using spectral ratios. *Bull. Seismol. Soc. Am.* 109 (5), 1855–1877. doi:10.1785/0120190071

Guo, Z., Guan, M., and Chapman, M. C. (2022). Amplification and attenuation due to geologic conditions in the Sichuan Basin, central China. *Seismol. Res. Lett.* XX, 1–15. doi:10.1785/0220220030

Guo, Z. W., Deng, K., and Han, Y. (1996). *Formation and evolution of the Sichuan Basin*. Beijing: Geologic Publishing House, 200.

Harmon, J., Hashash, Y. M. A., Stewart, J. P., Rathje, E. M., Campbell, K. W., and Silva, W. J. (2019). Site amplification functions for central and eastern North America—Part II: Modular simulation-based models. *Earthq. Spectra* 35 (2), 815–847. doi:10.1193/091117EQS179M

Hua, W., Chen, Z. L., and Zheng, S. H. (2009). A study on segmentation characteristics of aftershock source parameters of Wenchuan M8.0 earthquake in 2008. *Chin. J. Geophys.* 52, 365–371. doi:10.1002/cjg2.1334

Hunter, J. D. (2007). Matplotlib: A 2D graphics environment. *Comput. Sci. Eng.* 9 (3), 90–95. doi:10.1109/mcse.2007.55

Kennett, B. L. N. (1986). Lg waves and structural boundaries. *Bull. Seismol. Soc. Am.* 76, 1133–1141.

Kirby, E., Reiners, P. W., Krol, M. A., Whipple, K. X., Hodges, K. V., and Farley, K. A. (2002). Late Cenozoic evolution of the eastern margin of the Tibetan Plateau: Inferences from ^{40}Ar/^{39}Ar and (U-Th)/He thermochronology. *Tectonics* 21, 1–20. doi:10.1029/2000TC001246

Li, J., Zhou, B., Rong, M., Chen, S., and Zhou, Y. (2020). Estimation of source spectra, attenuation, and site responses from strong-motion data recorded in the 2019 changning earthquake sequence. *Bull. Seismol. Soc. Am.* 110 (2), 410–426. doi:10.1785/0120190207

Li, X., Zhai, C., Wen, W., and Xie, L. (2018a). Ground motion prediction model for horizontal PGA, 5% damped response spectrum in sichuan-yunnan region of China. *J. Earthq. Eng.* 24, 1829–1866. doi:10.1080/13632469.2018.1485600

Li, Y., He, D., Li, D., Lu, R., Fan, C., and Sun, Y. (2018b). Sedimentary provenance constraints on the jurassic to cretaceous paleogeography of Sichuan Basin, SW China. *Gondwana Res.* 60, 15–33. doi:10.1016/j.gr.2018.03.015

Li, Y. Q., He, D. F., Chen, L. B., Mei, Q. H., Li, C. X., and Zhang, L. (2016). Cretaceous sedimentary ba- sins in sichuan, SW China: Restoration of tectonic and depositional environments. *Cretac. Res.* 57, 50–65. doi:10.1016/j.cretres.2015.07.013

Li, Z. W., Xu, Y., Huang, R. Q., Hao, T. Y., Xu, Y., Liu, J. S., et al. (2011). Crustal P-wave velocity structure of the Longmen Shan region and its tectonic implications for the 2008 Wenchuan earthquake. *Sci. China Earth Sci.* 54, 1386–1393. doi:10.1007/s11430-011-4177-2

Liu, S., Yang, Y., Deng, B., Zhong, Y., Wen, L., Sun, W., et al. (2021). Tectonic evolution of the Sichuan Basin, southwest China. *Earth. Sci. Rev.* 213, 103470. doi:10.1016/j.earscirev.2020.103470

Liu, Z., Wuenscher, M. E., and Herrmann, R. B. (1994). Attenuation of body waves in the central New Madrid seismic zone. *Bull. Seismol. Soc. Am.* 84, 1112–1122.

Meng, Q. R., Wang, E. C., and Hu, J. M. (2005). Mesozoic sedimentary evolution of the northwest Sichuan basin: Implication for continued clockwise rotation of the South China block. *Geol. Soc. Am. Bull.* 117, 396–410. doi:10.1130/b25407.1

Ou, G. B., and Herrmann, R. B. (1990). A statistical model for ground motion produced by earthquakes at local and regional distances. *Bull. Seismol. Soc. Am.* 80 (6A), 1397–1417. doi:10.1785/bssa08006a1397

Pasyanos, M. E., Matzel, E. M., Walter, W. R., and Rodgers, A. J. (2009). Broad-band*Lg*attenuation modelling in the Middle East. *Geophys. J. Int.* 177, 1166–1176. doi:10.1111/j.1365-246x.2009.04128.x

Pratt, T. L., and Schleicher, L. S. (2021). Characterizing ground- motion amplification by extensive flat-lying sediments: The seismic response of the eastern U.S. Atlantic Coastal Plain strata. *Bull. Seismol. Soc. Am.* 111, 1795–1823. doi:10.1785/0120200328

Sha, J. G., Shi, X. Y., Zhou, Z. H., and Wang, Y. D. (2010). *The terrestrial triassic and jurassic sys- tems in the Sichuan Basin*. ChinaHefei: University of Science & Technology of China Press, 1–214.

Steidl, J. H., Tumarkin, A. G., and Archuleta, R. J. (1996). What is a reference site? *Bull. Seismol.* 86, 1733–1748.

Stewart, J. P., Parker, G. A., Atkinson, G. M., Boore, D. A., Hashash, Y. M. A., and Silva, W. J. (2020). Ergodic site amplification model for central and eastern North America. *Earthq. Spectra* 36 (1), 42–68. doi:10.1177/8755293019878185

Tian, Y., Kohn, B. P., Phillips, D., Hu, S., Gleadow, A. J. W., and Carter, A. (2016). Late Cretaceous–earliest Paleogene deformation in the Longmen Shan fold- and-thrust belt, eastern Tibetan Plateau margin: Pre-Cenozoic thickened crust? *Tectonics* 35, 2293–2312. doi:10.1002/2016TC004182

Wang, C.-Y., Han, W.-B., Wu, J.-P., Lou, H., and Chan, W. W. (2007). Crustal structure beneath the eastern margin of the Tibetan Plateau and its tectonic implications. *J. Geophys. Res.* 112, B07307. doi:10.1029/2005JB003873

Wang, H., Xie, L., Wang, S., and Ye, P. (2013). Site response in the Qionghai Basin in the wenchuan earthquake. *Earthq. Eng. Eng. Vib.* 12, 195–199. doi:10.1007/s11803-013-0162-4

Wang, H., Li, C., Wen, R., and Ren, Y. (2022). Integrating effects of source-dependent factors on sediment-depth scaling of additional site amplification to ground-motion prediction equation. *Bull. Seismol. Soc. Am.* 112 (1), 400–418. doi:10.1785/0120210134

Wang, H., Ren, Y., and Wen, R. (2018). Source parameters, path attenuation and site effects from strong-motion recordings of the Wenchuan aftershocks (2008-2013) using a non-parametric generalized inversion technique. *Geophys. J. Int.* 212, 872–890. doi:10.1093/gji/ggx447

Wang, H., and Wen, R. (2021). Attenuation and basin amplification revealed by the dense ground motions of the 12 July 2020 MS 5.1 Tangshan, China, earthquake. *Seismol. Res. Lett.* 94 (2), 2109–2121. doi:10.1785/0220200400

Wang, M. M., Hubbard, J., Plesch, A., Shaw, J. H., and Wang, L. N. (2016). Three-dimensional seismic velocity structure in the Sichuan basin, China. *J. Geophys. Res. Solid Earth* 121 (2), 1007–1022. doi:10.1002/2015jb012644

Wei, Z., Chu, R., Chen, L., Wu, S., Jiang, H., and He, B. (2020). The structure of the sedimentary cover and crystalline crust in the Sichuan Basin and its tectonic implications. *Geophys. J. Int.* 223 (3), 1879–1887. doi:10.1093/gji/ggaa420

Wen, R., Ren, Y., Zhou, Z., and Shi, D. (2010). Preliminary site classification of free-field strong motion stations based on Wenchuan earthquake records. *Earthq. Sci.* 23, 101–110. doi:10.1007/s11589-009-0048-8

Wessel, P., Smith, W. H. F., Scharroo, R., Luis, J. F., and Wobbe, F. (2013). Generic mapping Tools: Improved version released. *Eos Trans. AGU.* 94, 409–410. doi:10.1002/2013eo450001

Wu, W. W., Su, J. R., Wei, Y. L., Wu, P., Li, J., and Sun, W. (2016). Discussion on attenuation characteristics, site response and magnitude determination in Sichuan. *Seimol. Geol.* 38, 1005–1018. doi:10.3969/j.issn.0253-4967.2016.04016

Xia, X., Li, Z., Bao, F., Xie, J., Shi, Y., You, Q., et al. (2021). Sedimentary structure of the Sichuan Basin derived from seismic ambient noise tomography. *Geophys. J. Int.* 225, 54–67. doi:10.1093/gji/ggaa578

Xie, J., Wu, Z., Liu, R., Schaff, D., Liu, Y., and Liang, J. (2006). Tomographic regionalization of crustal Lg Q in eastern Eurasia. *Geophys. Res. Lett.* 33, L03315. doi:10.1029/2005GL024410

Xu, P., Ren, Y., Wen, N., and Wang, H. (2020). Observations on regional variability in ground-motion amplitude from six mw ~ 6.0 earthquakes of the north–south seismic zone in China. *Pure Appl. Geophys.* 177, 247–264. doi:10.1007/s00024-019-02176-6

Zhao, L.-F., Xie, X.-B., Wang, W.-M., Zhang, J.-H., and Yao, Z.-X. (2010). Seismic Lg-wave Q tomography in and around Northeast China. *J. Geophys. Res.* 115, B08307. doi:10.1029/2009JB007157

Zheng, C., Zhang, R., Wu, Q., Li, Y., Zhang, F., Shi, K., et al. (2019). Variations in crustal and uppermost mantle structures across eastern Tibet and adjacent regions: Implications of crustal flow and asthenospheric upwelling combined for expansions of the Tibetan plateau. *Tectonics* 38, 3167–3181. doi:10.1029/2018TC005276

Zheng, Y., Li, H., Sun, Z., Wang, H., Zhang, J., Li, C., et al. (2016). New geochronology constraints on timing and depth of the ancient earthquakes along the Longmen Shan fault belt, eastern Tibet. *Tectonics* 35, 2781–2806. doi:10.1002/2016TC004210

frontiers | Frontiers in Earth Science

TYPE Original Research
PUBLISHED 05 January 2023
DOI 10.3389/feart.2022.996389

OPEN ACCESS

EDITED BY
Kun Ji,
Hohai University, China

REVIEWED BY
Haiping Ding,
Suzhou University of Science and Technology, China
Zailin Yang,
Harbin Engineering University, China

*CORRESPONDENCE
Qiang Ma,
maqiang@iem.ac.cn

SPECIALTY SECTION
This article was submitted to Structural Geology and Tectonics,
a section of the journal
Frontiers in Earth Science

RECEIVED 17 July 2022
ACCEPTED 20 September 2022
PUBLISHED 05 January 2023

CITATION
Wang F, Ma Q, Tao D and Xie Q (2023), A numerical study of 3D topographic site effects considering wavefield incident direction and geomorphometric parameters.
Front. Earth Sci. 10:996389.
doi: 10.3389/feart.2022.996389

A numerical study of 3D topographic site effects considering wavefield incident direction and geomorphometric parameters

Fuchen Wang[1,2], Qiang Ma[1,2]*, Dongwang Tao[1,2] and Quancai Xie[1,2]

[1]Key Laboratory of Earthquake Engineering and Engineering Vibration, Institute of Engineering Mechanics, China Earthquake Administration, Harbin, China, [2]Key Laboratory of Earthquake Disaster Mitigation, Ministry of Emergency Management, Harbin, China

The topographic site effect plays a vital role in controlling the characteristics of earthquake ground motions. Due to its complexity, the factors affecting topographic amplification have not been fully identified. In this study, 100 ground motion simulations generated by double-couple point sources in the homogeneous linear elastic half-space are performed based on the 3D (three-dimensional) Spectral Element Method, taking the Menyuan area of Qinghai Province, China as a local testbed site. A relationship between incident direction and the strength of topographic amplification has been observed. The horizontal ground motion is affected by the back-azimuth, which is typically chosen to be the direction from seismic station to seismic source measured clockwise from north. Specifically, the east-west PGA (Peak Ground-motion Acceleration) is significantly amplified when back-azimuth is about 90° or 270°, and the north-south PGA is significantly amplified when back-azimuth is around 0° or 180°. The vertical ground motion is affected by the dipping angle, which is the angle from vertical at which an incoming seismic wave arrives. The vertical PGA is strongly amplified when the seismic wave is almost horizontally incident (e.g., dipping angle = 78°). A correlation study between geomorphometric parameters and frequency-dependent topographic amplification indicates that relative elevation and smoothed curvature contain similar information, both of which are closely related to the topographic amplification of horizontal components, but not the vertical component. Our study reveals the influence of source and propagation path on topographic amplification and provides a reference for considering the topographic site effect in real engineering sites.

KEYWORDS

topographic site effect, spectral element method, back-azimuth, dipping angle, relative elevation, smoothed curvature

Introduction

The topographic site effect refers to the scattering of seismic waves by topographic irregularities, which generally manifests as the ground motion amplified at the convex features such as hilltops and deamplified at the concave features such as valleys. The interaction between seismic waves and irregular topographic features can be dramatic: a high peak ground acceleration (PGA) of 1.78 g was recorded at the Tarzana hilltop stations during the 1994 Northridge earthquake (Bouchon and Barker, 1996; Ashford and Sitar, 1997); A PGA of 1.25 g recorded by the Pacoima Dam site during the 1971 San Fernando earthquake (Trifunac and Hudson, 1971); For moderate earthquakes, severe damage can also be partially attributed to the scattering effect of topography (e.g., Kang et al. 2019).

Although empirical evidence pointing out the contributions of topography do exist in various seismic scenarios (Hartzell et al., 1994; Harris, 1998; Buech et al., 2010; Hough et al., 2010; Pischiutta et al., 2010; Luo et al., 2014), topographic site effects have received less attention compared with stratigraphic site effects. Topographic site effects are often invoked to explain abnormal ground motion amplitudes in local areas, and its complexity makes the relevant research encounter challenges in reproducing the amplification value accurately. More specifically, the relevant information of the source, propagation path, and engineering site are all covered in the ground motion records. Among these, the site condition includes stratified soil, topography, sedimentary basin structure, etc. To perform quantitative analysis, the contribution of the topography itself needs to be extracted separately from the ground motion records, and the influence of source, stratified soil, and other factors on the topographic amplification value cannot be ignored. Asimaki and Mohammadi (2018) emphasized a non-linear coupling between the amplification effects from surface topography and subsurface stratified soil. The thickness, shear wave velocity, damping ratio, and lateral heterogeneity of the underlying geologic materials all affect the topographic amplification (Assimaki and Gazetas, 2004; Assimaki et al., 2005a; Assimaki et al., 2005b; Bouckovalas and Papadimitriou, 2005; Wang et al., 2019; Luo et al., 2020; Song et al., 2020). The source and propagation path indirectly affect the topographic site effect by determining the azimuth and frequency content of the incoming wavefield, and there are few related studies. Using three-dimensional finite difference methods, Mayoral et al. (2019) indicates that for hill slopes, subduction earthquakes led to deep failure surfaces, whereas normal events to shallow failure surfaces.

At present, there are three kinds of methods to study the topographic site effects: experimental method (e.g., Tucker et al., 1984; Wood and Cox, 2016; Stolte et al., 2017), analytical and semi-analytical method (e.g., Yuan and Liao, 1996; Paolucci, 2002) and numerical simulation methods (e.g., Boore, 1972; Geli et al., 1988; Hartzell et al., 2017). The standard spectral ratio (SSR) method (Borcherdt, 1970) is the spectral ratio of ground motions between the target station and the adjacent reference station. It is widely used in the study of topographic site effects due to its ease of operation and clear physical context, but the reference station needs to be located on the bedrock site and cannot be affected by the adjacent topographic features, which limits the amount of available ground motion data. The Nakamura (HVSR, horizontal-to-vertical spectral ratio) method, which avoids the selection of the reference station by using the horizontal to the vertical spectral ratio of the same station to characterize site effects (Nakamura, 1989). However, the topographic amplification of vertical ground motion reduces the accuracy of the estimation of amplification. Some scholars used microtremors to make up for the lack of ground motion records (e.g., Stolte et al., 2017; La Rocca et al., 2020). Numerical simulations also have helped augment the observational record, but the numerical results are usually smaller than those of experiments (Geli et al., 1988; Lovati et al., 2011). The reason is that the underground shear wave velocity structure and soil layer information are usually unclear, and the accuracy of the elevation data used in the numerical simulation is also limited, which greatly affects the accuracy of the numerical modeling (Moore et al., 2011; Burjánek et al., 2012; Burjánek et al., 2014). However, with the growth in computational capabilities, the development of codes capable of handling complex topographies, and more high-quality near-surface geologic data available, it is becoming easier to directly model ground-motion amplification due to topography. Some studies that consider surface topography has obtained simulation results that are in good agreement with observed ground motions (Magnoni et al., 2013; Galvez et al., 2021; Wang et al., 2021).

In this paper, we first adopt the spectral element method to establish a ground motion synthetic database, and then explore the influence of the incident direction of the incoming seismic wavefield on the topographic amplification; in addition, the correlation between geomorphometric parameters, which commonly used to build the ground-motion models (GMMs), and topographic amplification values have also been analyzed. Finally, we discuss the physical mechanism behind the source-site interaction and make recommendations for considering the topographical site effect in real engineering sites.

Ground-motion synthetic database

A powerful and freely available spectral element software, called SPECFEM3D, is adopted to generate the synthetic ground motion data. The Spectral Element Method (SEM) enjoys the geometrical flexibility of the Finite Element Method and the accuracy of the Pseudo-Spectral Method. High-degree Lagrange interpolants are used to express functions in SEM. Therefore, the accuracy of the simulation can be ensured by adjusting the polynomial degree and the representative element size. The

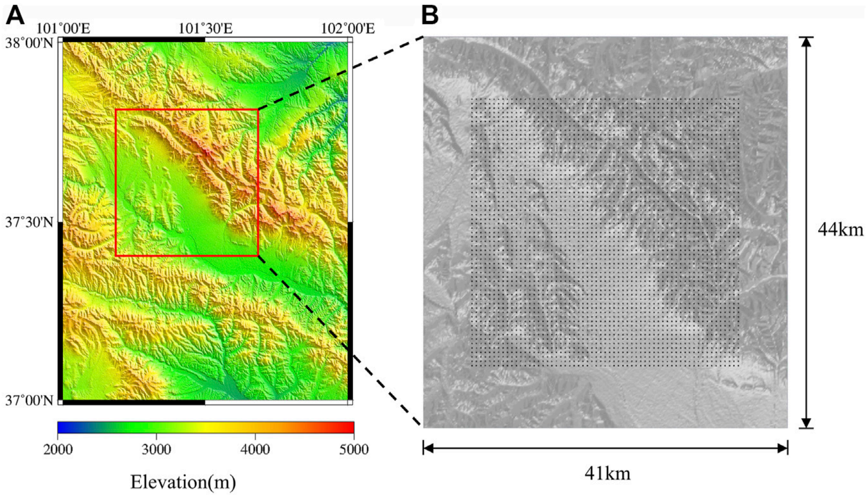

FIGURE 1
(A) Menyuan area elevation map and study region (red box); **(B)** Locations of the square array of 3,721 virtual receivers (black dots, one station every 500 m).

polynomial degree is set to 4 in our study [following Komatitsch et al., 2005; Igel, 2017; Yuan et al., 2021], which means one SEM element per wavelength has been found to be accurate. As a comparison, the spatial element size in some finite difference methods must be smaller than approximately one-tenth to one-eighth of the wavelength, which leads to a great number of elements (e.g., Ma et al., 2021). The SEM allows for systematic diagonalization of the mass matrix, which then allows for easy parallelization.

Menyuan area, Qinghai Province, China is located northeast of the Qinghai Tibet Plateau, with a great difference in elevation and the average elevation is 2,866 m. The overall terrain is high in the northwest, low in the southeast, high in the north and south, and low in the middle. The north is adjacent to the Qilian Mountains, and the Datong River Valley in the middle is relatively flat. As shown in Figure 1A, the topography is complex, including ridges, isolated hills, valleys, canyons, and flat surfaces, which cover a large variety of topographic features often present in real cases in which 3D site effects may occur. Therefore, A 3D model with dimensions of 41 × 44 × 15 km^3 surrounding the Menyuan area is established to understand the mechanism of topographic site effect. The digital elevation data comes from the ASTER Global Digital Elevation Model (GDEM) Version 3, with a spatial resolution of 1 arc-s (approximately 30-m horizontal posting at the equator). 3,721 virtual receivers (black dots in Figure 1B) are regularly distributed in a 30 × 30 km^2 area that covers the main topographic features of the computational domain. The ground motion of three components [corresponding to east-west (X), north-south (Y), and vertical (Z)] can be recorded by each receiver.

To isolate topographic site effects from heterogeneities in the subsurface materials, we assume isotropic homogeneous linear elastic half-space with properties given by $V_p = 5600$ m/s, $V_s = 3354$ m/s, and $\rho = 2636$ kg/m^3 (Brocher, 2005; Zuo and Chen, 2018). Therefore, the grid size needs to be less than 670 m to simulate ground motion below 5 Hz. The size of the lower grid cell is set to about 620 m, and the size of the upper grid cell is about 210 m, as illustrated in Figure 2A. Two buffer layers (a smoothed version of the surface topography) are introduced to damped mesh distortions of the surface topography (Lee et al., 2008) (Figure 2B). In addition, the mesh between the two buffer layers is refined after balancing the computation cost and accuracy of surface topography modeling.

100 Mw 4.5 double couple point sources with Gaussian source time function are used as the input of simulations. The focal mechanisms and locations of each source are randomly generated by uniform distribution, and the rise time is obtained by the empirical scaling relations (Somerville et al., 1999). It should be noted that the rupture area of Mw 4.5 is generally about 2–3 km^2 (Somerville et al., 1999; Leonard, 2010). The hypocenter depth is limited to above 5 km to ensure the validity of the point source hypothesis. Finding a suitable reference site is not an easy task in the empirical method. But this problem can be easily solved by numerical simulation. An SEM model with a flat ground surface is adopted (the size, medium parameters, and receiver locations of the model are consistent with the previous model) to simulate the reference ground motion. All raw ground motion records in our database need to be filtered by a 4th order Butterworth low-pass filter with a cut-off frequency of 5 Hz before subsequent analysis. Then the three-component ground

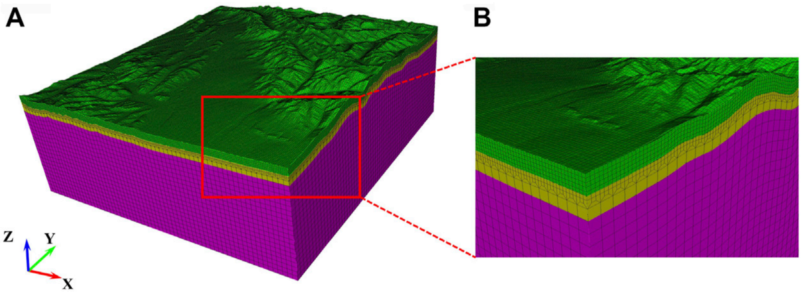

FIGURE 2
(A) Global view of the 3D SEM model; **(B)** Buffer layer indicate by the red box in (A).

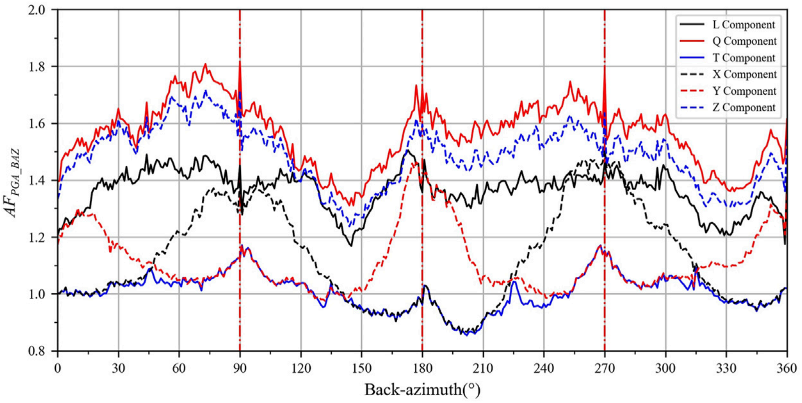

FIGURE 3
The relationship of AF_{PGA_BAZ} with back-azimuth, taking 1° as the interval. The solid black, red, and blue lines correspond to the L, Q, and T components, respectively; the dashed black, red, and blue lines correspond to the X, Y, and Z components, respectively. The red vertical dashdot lines are at 0° (360°), 90°, 180°, and 270°for reference.

motion amplification factors of 3,721 receivers can be obtained with the input of each double couple source.

Influence of incident direction on topographic site effects

The amplification factor of PGA, AF_{PGA}, is defined as the PGA on the topography surface divided by the PGA on the flat ground surface. The data set is divided into 360 subsets based on different back-azimuths (taking 1° as the interval), and then the relationship between the mean AF_{PGA} of each subset (Abbreviated as AF_{PGA_BAZ}) and the back-azimuth is obtained, as shown in Figure 3. The LQT coordinate system is obtained by rotating the XYZ coordinate system based on the specified dipping angle and azimuth, and L, Q, and T represent the polarization directions of P, SV, and SH waves respectively. It can be observed that the AF_{PGA_BAZ} of the T component is consistent with the Y component when the back-azimuth equals to 90° or 270°, and consistent with the X component when the back-azimuth equals to 0° (360°) or 180°, which demonstrates that the coordinate rotation is correct.

For the LQT coordinate system (solid line in Figure 3), the PGA of L and Q components is significantly amplified by the topography, while the AF_{PGA_BAZ} of T component varies around 1.0. The topographic amplification value of SV wave exceeds those of P wave. The curve shapes of L and Q components in Figure 3 are similar, and they both have no obvious correlation with the back-azimuth. For the XYZ coordinate system (dashed line in Figure 3), the AF_{PGA_BAZ} of X component is relatively larger when the back-azimuth is around 90° or 270°; the AF_{PGA_BAZ} of Y component is relatively larger when the back-azimuth is around 0° (360°) or 180°. Considering that 80% of the dipping angles in our database are greater than

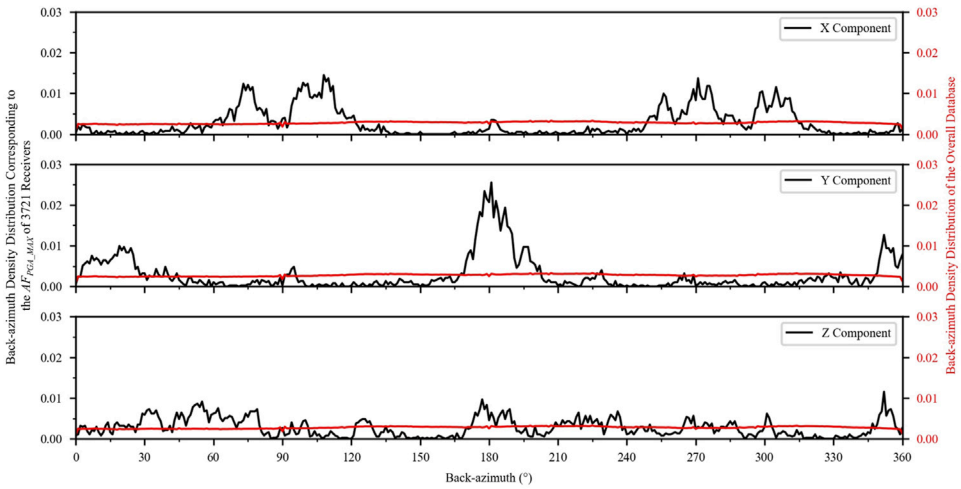

FIGURE 4
The density distribution of back-azimuth. The black solid line represents the density distribution of the back-azimuth corresponding to the AF_{PGA_MAX} of 3,721 receivers (From top to bottom: the X, Y, and Z components, respectively); the solid red line represents the back-azimuth density distribution of the overall database.

45°, the particle motion of P wave is mainly projected on the horizontal plane, resulting in the ground motion amplification of X component (or Y component) being more consistent with that of L component (P wave) in the corresponding back-azimuth. For example, since the topographic amplification of P wave is stronger than that of SH wave, the AF_{PGA} of X component will be relatively higher when the particle motion direction of P wave coincides with the *X* direction (back-azimuth=90° or 270°), and relatively small when the particle motion direction of SH wave coincides with the *X* direction (back-azimuth=0° or 180°).

The maximum AF_{PGA} of one receiver with 100 source inputs is defined as AF_{PGA_MAX}. The back-azimuths corresponding to the AF_{PGA_MAX} in X, Y, and Z components of all 3,721 receivers is counted, and the density distribution with an interval of 1° is shown in Figure 4. The distribution of back-azimuths of the overall database (red solid line) is uniform in the range of 0° to 360°. 41.6% of the AF_{PGA_MAX} in X component occurred in the back-azimuth range of 90° ± 15° and 270° ± 15°, 55.1% of the AF_{PGA_MAX} in Y component occurred in the back-azimuth range of 0° ± 15° and 180° ± 15°. Compared with Figures 3, 4 further illustrates that the AF_{PGA_MAX} of horizontal components are correlated with the back-azimuth.

The data set is also divided into 90 subsets based on different dipping angles (taking 1° as the interval), the mean AF_{PGA} of each subset is defined as AF_{PGA_DIP}. The influence of dipping angles on AF_{PGA} is also shown in Figure 5. As expected, the AF_{PGA_DIP} of Z component in Figure 5A (blue dashed line) is close to that of the L component (black solid line) when dipping angle is equal to 0° and close to that of the Q component (red solid line) when the dipping angle is about 80°. Ding et al. (2017) and Gu et al. (2017) analyzed the seismic ground motion of the scarp topography, and reported that when the slope angle is unchanged, for the inclined P waves, the amplification factor of X component increases, while the amplification factor of Z component decrease with the increase of dipping angle; for the inclined SV waves, the amplification factor of X component decrease, while the amplification factor of Z component increase with the increase of dipping angle. The reason for this phenomenon is also that the increase of the dipping angle will make the P wave project more on the horizontal plane and make the SV wave project more in the vertical direction. It worth noting that topography itself has no influence on dipping angle, but the combination of topographic relief and different dipping angles leads to different forms of ground motion amplification. Due to the amplification of P and SV waves by topography, the AF_{PGA_DIP} of Z component presents a shape of high on both sides and low in the middle. It is worth noting that the double-couple point source and real topographic surface are adopted in this study, so the situation is more complicated than Ding et al. (2017) and Gu et al. (2017).

The dipping angle density distribution of the overall database is mainly concentrated above 45° (red solid line in Figure 5B), which leads to the particle motion of SV wave is mainly projected in the vertical direction, so the AF_{PGA_BAZ} of Z component is more consistent with that of Q component (SV wave). The AF_{PGA_BAZ} of Z component is greater than that of horizontal components due to that the topographic amplification of SV wave is greater than that of the P and SH waves.

Figure 5B further indicates that the PGA of Z component is strongly amplified when the incident seismic

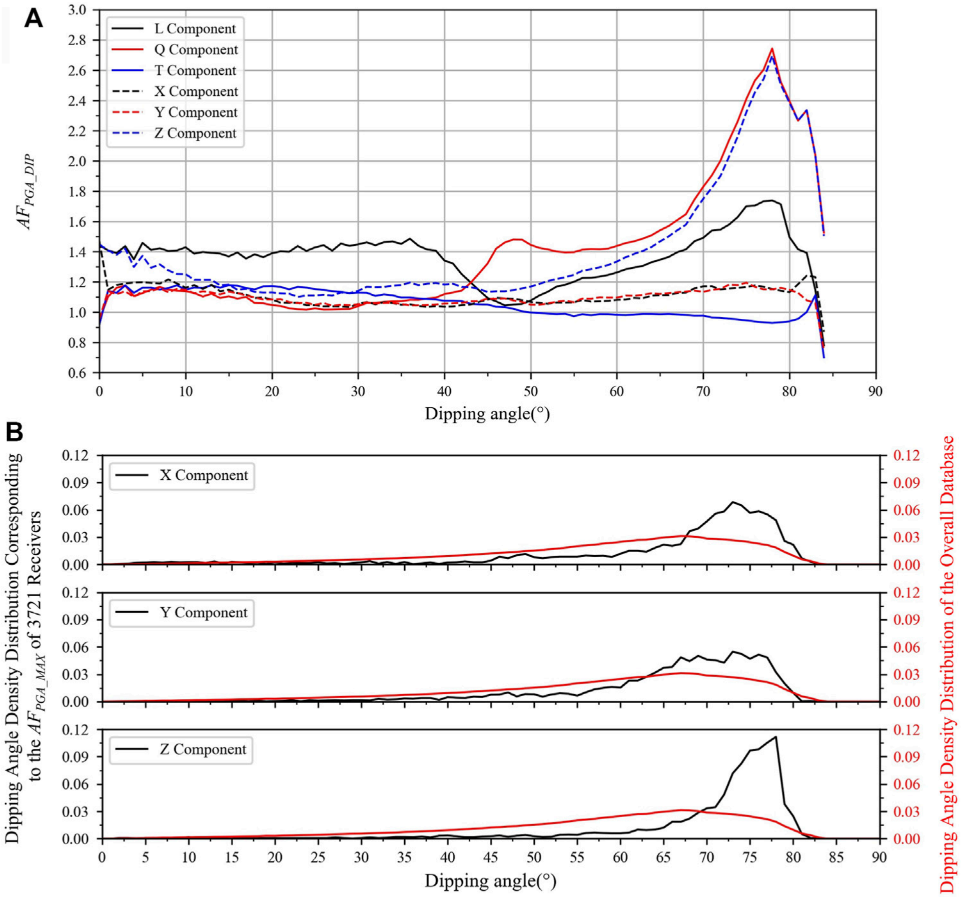

FIGURE 5
The influence of dipping angle on AF_{PGA}. **(A)** The relationship of AF_{PGA_DIP} with dipping angle, taking 1° as the interval; **(B)** The density distribution of dipping angle.

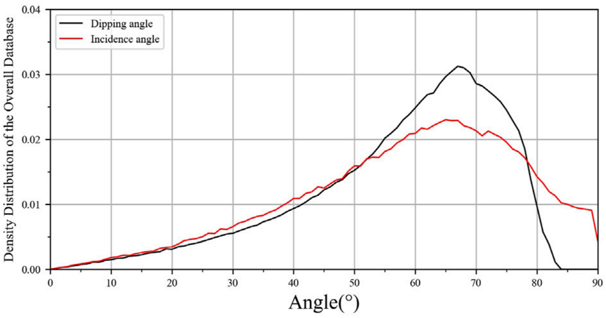

FIGURE 6
Density distribution of dipping angle (black solid line) and incidence angle (red solid line) in the overall database.

wave is approximately horizontal. For example, 74.5% of the AF_{PGA_MAX} in Z component occurred in the dipping angle range of 75° ± 5°, while only 24.8% of the dipping angle in the overall database is in the range of 75° ± 5°.

Our simulation data show that the amplification of P and SV waves is independent of back-azimuth, but correlates with dipping angle. Taking the SV wave as an example, when the dipping angle is smaller than 45°, the AF_{PGA_DIP} of Q component is small; when the dipping angle is larger than 55°, the AF_{PGA_DIP} of Q component increases with the dipping angle, and reaches the peak when the dipping angle is about 78°, then decreases rapidly. This phenomenon may be related to the scattering effect of topography, which will be discussed in Discussion section.

Figure 6 represents the density distribution of the dipping angle and the incidence angle, where the incidence angle refers to the angle between the incident direction of seismic wave and the normal to the topography surface at the location of the receiver. The incidence angle in this study is also mainly above 45°, and the relationship between PGA amplification factor and dipping angle is similar to that of the incidence angle, so we will not repeat them here.

Correlation between geomorphometric parameters and topographic site effects

Topographic site effect prediction models based on geomorphometric parameters have been established by previous studies (Maufroy et al., 2015; Zhou et al., 2020). However, due to topographic site effects varying strongly with the stratigraphy and material properties of the underlying geologic material, some researchers believe that topographic site effects cannot be well characterized by studying the effects of ground surface geometry alone (Asimaki and Mohammadi, 2018; Pitarka et al., 2021). Based on the synthetic database, this section studies the correlation between commonly used geomorphometric parameters and topographic amplification to explore whether this correlation can remain stable with different incident directions. The relative elevation and smoothed curvature are initially selected.

Relative elevation (H_r) is defined as the difference between the elevation at a point on the surface and the mean elevation within a specified neighborhood of the point. A circular neighborhood with a radius r is used to compute the mean elevation. A positive H_r of a point indicates that the point has a higher elevation relative to the surrounding area, such as the crest; a negative H_r of a point indicates that the point has a lower elevation relative to the surrounding area, such as a valley or the base of a ridge. Note that the value of H_r also depends on the selection of r. The H_r is smooth and continuous with the different r, and the H_r at a position may both have positive and negative values. The r in this study is set to half of the seismic wavelength, as shown in Eq. 1, where λ is the seismic wavelength and the seismic frequency f ranges from 0.4 to 5 Hz with intervals of 0.1 Hz. The minimum value of the frequency range is limited by the size of the model. Our leftmost station is 5500 m from the left boundary of the model. Therefore, the radius we use to calculate the relative elevation cannot exceed 5500 m. Bring it into Eq. 1, and we can get the highest frequency of 0.304 Hz. So we set the lower limit of the frequency range to 0. 4 Hz.The maximum value of the frequency range is limited by the grid division. So we set the upper limit of the frequency range to 5 Hz.The variation range of r in this study is 335.4–4,192.5 m.

$$r = \frac{\lambda}{2} = \frac{V_s}{2f} \tag{1}$$

Referring to AF_{PGA_MAX}, the mean AF_{PGA} of one receiver with 100 source inputs is defined as AF_{PGA_MEAN}. The Pearson correlation coefficients (Abbreviated as PCC) between AF_{PGA_MEAN} of different components and H_r by varying the radius of surrounding circular area are shown in Figure 7A, in which the PGA of Horizontal component (PGA_{hor}) and 3D component (PGA_{3D}) are obtained following Eq. 2, in which $Acc(t)$ is the acceleration time history of ground motion and the subscripts X, Y and Z indicate the corresponding components respectively.

$$\begin{gathered} PGA_{hor} = Maximum\left(\sqrt{Acc_X(t)^2 + Acc_Y(t)^2}\right) \\ PGA_{3D} = Maximum\left(\sqrt{Acc_X(t)^2 + Acc_Y(t)^2 + Acc_Z(t)^2}\right) \end{gathered} \tag{2}$$

It can be observed from Figure 7A that the PCCs of all components increase first and then decrease with r, and AF_{PGA_MEAN} no longer correlate with H_r when r is large to a certain extent, which demonstrates that for a specific site, its topographic site effect (AF_{PGA}) is affected by the surrounding topographic features within a certain range, but not by the topography at a long distance. The AF_{PGA_MEAN} of X and Y components are found to have a strong correlation with the relative elevation, but not that of Z component. Therefore, the PCC of the horizontal component is greater than that of the 3D component and reaches the peak of 0.64 when r is equal to 400 (red dot in Figure 7A). The increase of AF_{PGA_MEAN} with H_r can be observed in the Figure 7B, which is consistent with our expectation. That is, the amplification of ground motion is easy to occurs near the crest with large H_r, while the de-amplification generally occurs near the foot of the hill or valley with small H_r.

Wang et al. (2018) also studied the correlation between geomorphometric parameters and PGA amplification. They used the vertically incident plane wave as the input ground motion, without considering the variation of incidence angle. After considering the incidence angle, Figure 7 shows that the correlation is found to be weaker than that of Wang et al. (2018). In addition, Figure 7 also indicates that it is hard to determine the r when AF_{PGA_MEAN} and H_r is best correlated, and the distribution of the scatter points in Figure 7B is quite dispersed, which suggesting that topography-induced PGA amplification cannot be accurately estimated by relying on relative elevation alone.

Topographic amplification is frequency-dependent. The ground motion spectral amplification in this study is defined as $AF(f)$, which varying with frequency f. The Fourier amplitude spectrum $O(f)$ is obtained by transforming the acceleration time history $Acc(t)$ from time domain to frequency domain. The amplitude spectra of the horizontal and 3D components are both obtained from the vector amplitudes; that is, $O_{hor}(f) = \sqrt{O_X(f)^2 + O_Y(f)^2}$ and $O_{3D}(f) = \sqrt{O_X(f)^2 + O_Y(f)^2 + O_Z(f)^2}$, respectively. Then the spectrum is smoothed by a 0.2 Hz Parzen window. After that$AF(f)$ can be obtained by dividing the Fourier amplitude spectra of the receiver on the topography surface by the receiver on the flat ground surface.

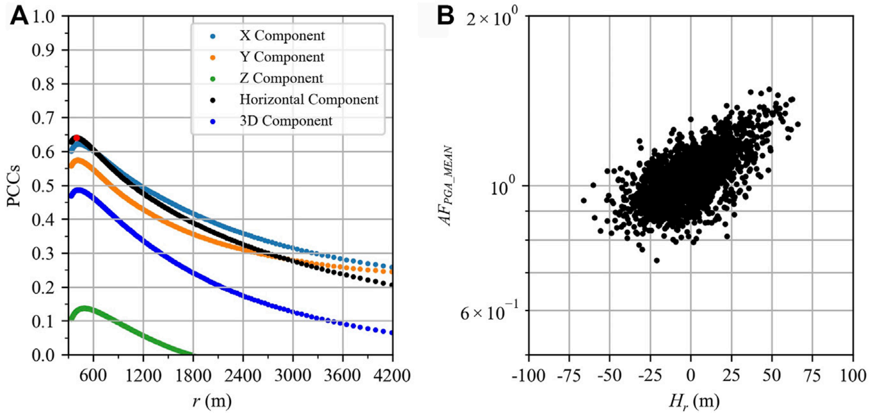

FIGURE 7
Correlation between AF_{PGA_mean} and H_r. **(A)** PCCs of serval components obtained between H_r and AF_{PGA_MEAN}; **(B)** The horizontal AF_{PGA_MEAN} and H_r of the 3,721 receivers indicated by the red dot in **(A)**.

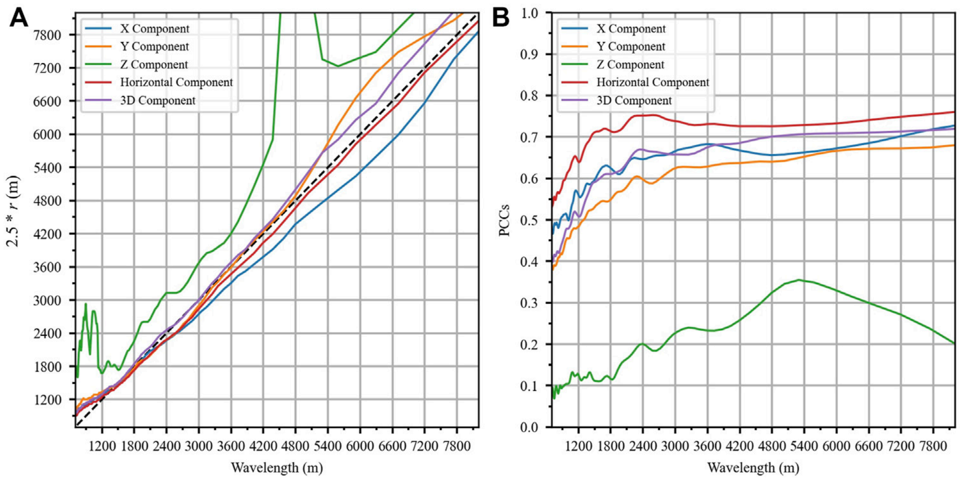

FIGURE 8
The relationship between $AF(f)$ and H_r; **(A)** The relationship between wavelength and r when $AF(f)$and $H_r$is best correlated; **(B)** The maximum PCCs over different seismic wavelengths. Solid lines of different colors in **(A)** and **(B)** correspond to different components (see legend in the upper left for details), and the black dashed line in **(A)** indicates that the value of the abscissa is equal to the ordinate.

We calculate the PCCs between $AF(f_i)$ of 3,721 receivers at the sampling frequency f_i and relative elevation H_r with varying r.When f_i is unchanged, each r corresponds to a PCC. All PCCs of f_i can be obtained after traversing all r values, and the relationship between the r value corresponding to the largest PCC and the seismic wavelength λ at the f_i is shown in Figure 8A. It is found that when the seismic wavelength is about 2.5 times the r, the $AF(f)$ except for the Z component is best correlated with the H_r, and the maximum PCC over different seismic wavelengths is given in Figure 8B. Among all the components, relative elevation H_r has the strongest correlation with $AF(f)$ of horizontal component and the weakest correlation with $AF(f)$ of Z component. The PCC between $AF(f)$ and H_r is larger at low frequency (large wavelength) than at high frequency (small wavelength), and the reason can be attributed to two aspects: the first is the selection of r value. As mentioned earlier, $AF(f)$ and H_r are most correlated when the wavelength is equal to 2.5 times r, but the r is set to half the wavelength [see Eq. 1]. This means that in the high-frequency band, the r corresponding to the maximum PCC will be outside the range of r. For example, the wavelength of a 5 Hz seismic wave in this study is 670.8 m, and the r corresponding to the

TABLE 1 PCCs between smoothed curvature and AF_{PGA}.

Components	X	Y	Z	Horizontal	3D
PCCs	0.31	0.26	0.07	0.31	0.23

maximum PCC should equal to 670.8/2.5 = 268.32 m, but the minimum value of r is only 335.4 m. Second, the 4th order Butterworth low-pass filter cannot completely filter out the ground motion information above 5 Hz, and the accuracy of numerical simulation may also decline in the high-frequency band.

By comparing Figure 7A with Figure 8B, we can easily find that H_r has stronger correlation with $AF(f)$ than that of AF_{PGA}. We infer that the frequency-dependent topographic amplification is closely related to the scale of topography: large-scale features are correlated to amplification of low-frequency waves, and small-scale features are correlated to amplification of high-frequency waves. H_r with varying r covers topographic feature information in different scales and can better describe $AF(f)$.

The surface curvature is defined as the second spatial derivative of the elevation map. Following the work of Zevenbergen and Thorne (1987), the Digital Elevation Model (DEM) of the region E should be a rectangular matrix of evenly spaced elevation values with space increment h, note that h should be in the same units as the elevations in E (e.g., meters in our study). The curvature at any point (x_i, y_i) is given by

$$\boldsymbol{C}(x_i, y_i) = \boldsymbol{E}''(x_i, y_i) \approx -2(\delta + \varepsilon) \times 100 \tag{3}$$

In which δ and ε are second-order derivatives of elevation in x and y components, which are approximated by finite differences as

$$\delta = \frac{1}{h^2}\left[\frac{\boldsymbol{E}(x_{i-1}, y_i) + \boldsymbol{E}(x_{i+1}, y_i)}{2} - \boldsymbol{E}(x_i, y_i)\right] \tag{4}$$

and

$$\varepsilon = \frac{1}{h^2}\left[\frac{\boldsymbol{E}(x_i, y_{i-1}) + \boldsymbol{E}(x_i, y_{i+1})}{2} - \boldsymbol{E}(x_i, y_i)\right] \tag{5}$$

As shown in Table 1, the PCCs between smoothed curvature and AF_{PGA} is low. However, we can find that horizontal PCCs are greater than that of vertical, which means that smoothed curvature also mainly contains information of the horizontal topographic amplification.

To characterize the spatial correlation between smoothed curvature and ground-motion amplification as a function of frequency, Maufroy et al. (2015) introduced a smoothing operator, which is to convolve matrix $\boldsymbol{C}$ twice (one per derivative) with a $n \times n$ unit matrix normalized by a factor n^4. The smoothed curvature $\boldsymbol{C}_s$ is given by

$$\boldsymbol{C}_s = \frac{1}{n^4}\left[\boldsymbol{C}^* \begin{pmatrix} 1_{11} & \cdots & 1_{1n} \\ \vdots & \ddots & \vdots \\ 1_{n1} & \cdots & 1_{nn} \end{pmatrix}^* \begin{pmatrix} 1_{11} & \cdots & 1_{1n} \\ \vdots & \ddots & \vdots \\ 1_{n1} & \cdots & 1_{nn} \end{pmatrix}\right] \tag{6}$$

The characteristic length is defined as $L_s = 2 \times n \times h$. According to Maufroy et al. (2015), the highest correlation between frequency-dependent topographic amplification and the smoothed curvature is reached when the curvature is smoothed over a characteristic length equal to half of the S wavelength, which is also confirmed in Figure 9A. In addition, Figures 7–9 show that the geomorphometric parameters have the best correlation with the horizontal topographic amplification and the worst in the vertical component.

Based on the above analysis, it is easy to notice the strong similarity between relative elevation H_r and smoothed curvature $\boldsymbol{C}_s$. Rai et al. (2016) demonstrated that H_r and $\boldsymbol{C}_s$ are highly correlated. Wang et al. (2018) took Hong Kong Island as a local testbed site and used a square neighborhood with the length defined as L_h to calculate H_r. They found that the best correlation between H_r and $\boldsymbol{C}_s$ is obtained when $L_h = 1.5 \times L_s$ and the corresponding coefficient of determination R^2 is as high as 0.94. Based on the DEM of this study, the relationship between relative elevation and smooth curvature is analyzed. As shown in Figure 10, the R^2 between H_r and $\boldsymbol{C}_s$ in this study is as high as 0.975 when $L_s = 1.25r$. Considering that a circular area of radius r is used in this study, Figure 10 is consistent with Wang et al. (2018). In addition, Figure 10 further indicates that the strong correlation between H_r and $\boldsymbol{C}_s$ is not limited by the study area, which means that relative elevation and smooth curvature with given length scales represent the same information of the topography. The initially acquired surface topography data is usually unprocessed digital elevation data, and considering the algorithmic complexity, relative elevation H_r is recommended as a proxy for topographic site effects.

Discussion

The influence of the incident direction of seismic waves on the topographic site effect is revealed in this work based on a large number of 3D numerical simulations, which is useful for us to explain the spatial distribution characteristics of ground motion. However, the applicability of these findings in real earthquake scenarios needs to be discussed.

The homogeneous velocity model introduced in this study leads to some discrepancies between the numerical simulation results and the real earthquake cases, one of which is the difference in dipping angle. In real earthquake scenarios, the shear velocity increase with depth whether it is homogeneous rock or unconsolidated sediments (Kanamori and Schubert, 2015). Based on Snell's law, when the seismic wave is transmitted from the larger shear velocity medium to the smaller shear velocity medium, the direction of the refracted

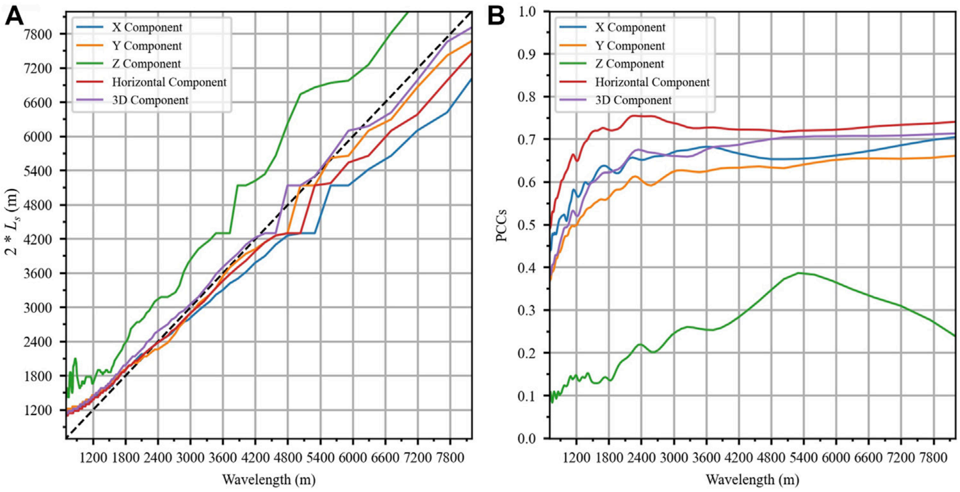

FIGURE 9
The relationship between *AF* (*f*) and C_s; **(A)** The relationship between wavelength and L_s when *AF* (*f*)and $\mathbf{C}_s$is best correlated; **(B)** The maximum PCCs over different seismic wavelengths. Solid lines of different colors in **(A,B)** correspond to different components (see legend in the upper left for details), and black dashed line in **(A)** indicates that the value of the abscissa is equal to the ordinate.

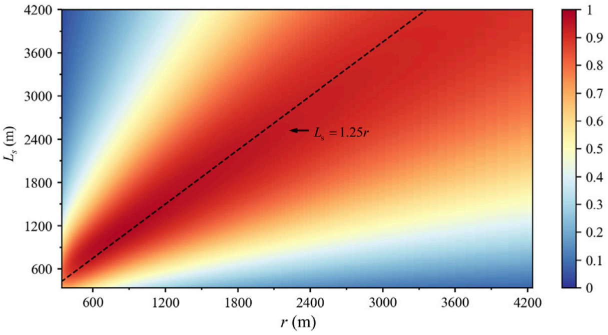

FIGURE 10
Coefficients of determination between relative elevation and smoothed curvature with various *r* and L_s.

wave will approach the normal direction. Even if the initial dipping angle is very large, the propagating path of the seismic wave will become approximately vertical in the near-surface after several refractions. Since seismic waves do not refract in the medium with uniform shear velocity (e.g., numerical models used in this work), the dipping angle of seismic waves at the ground surface will be much larger than that in the real world. Based on the discussion of Figure 5 above, the larger dipping angle is part of the reason why the AF_{PGA} of vertical component is greater than that of the horizontal components, while investigation of historical earthquakes generally shows that topography has a much larger ground motion amplification effect on the horizontal components than on the vertical component. The relationship between back-azimuth and the strength of topographic amplification should be available at bedrock sites [such as Classes A in NEHRP (National Earthquake Hazards Reduction Program) Site Classification] under shallow earthquakes with large hypocenter distances (The point source assumptions). While the point source assumption is not met, there is not a clear relationship between the back-azimuth and the degree of amplification (e.g., Stone et al., 2022).

Numerical simulations and model experiment show that the scattering of body waves to surface waves can be induced by topographic features in homogeneous linear elastic half-space (Gangi and Wesson, 1978; Boore et al., 1981; Ohtsuki and Harumi, 1983; Li and Liao, 2002). We also confirm the existence of converted surface wave based on the spectral element method, see Supplementary Material document for details. The dipping angle may be related to the strength of the generated surface wave. Li and Liao (2002) indicates that the top corner of cliff scatter stronger Rayleigh wave under inclined body waves than vertical body waves and the maximum amplitude of converted Rayleigh wave is about 1.1 times of the free field surface displacement. Assimaki et al. (2005a) demonstrated that all the incident energy with the critical incidence angle (i.e., $\arcsin\left(V_S/V_P\right)$ for Poisson’s ratio of the elastic medium is 0.35) practically transforms into surface waves. Tsai et al. (2017) and Kang et al. (2019) also indicated that large incidence angles increase the possibility of surface wave generation. We speculate that the increase of dipping angle will strengthen the converted surface wave, and then the constructive interference between the generated surface wave and the direct SV wave results in the strong amplification of L and Q components. Since the total energy remains unchanged, the amplification factors of T component become decrease.

Although numerical simulations alone are not as powerful as simulations used in conjunction with real data, it is currently one of the best ways to understand the mechanisms of topographic site effects. The role of different factors in controlling the highly variable amplification effects is unclear, and the numerical simulation methods are very flexible and can solve these problems to a certain extent. Previous studies have built appropriate models according to the research targets to study the influence of a specific factor on the ground motion (e.g., Lee et al., 2009a; Lee et al., 2009b). It is difficult to explore the influence of back-azimuth on topographic site effect based on real data. The challenges are mainly manifested in two aspects: the first is there are many limitations when selecting a reference station, which is related to the reliability of the topographic amplification factors. The second is that there should be enough historical ground motion records. To ensure the robustness of the conclusion, at least one or two historical earthquakes are required in every 1° back-azimuth. However, with the construction of stations and the increase of observation records, our conclusions are expected to be verified in the future.

We found that the relative elevation is indeed closely related to the horizontal ground motion amplification, but even for the idealized numerical model used in this paper, this correlation still shows a certain discreteness, which imposes a challenge to the accuracy of the GMM; on the other hand, post-earthquake disaster assessment generally focuses on specific sites that including both muti-layer subsurface structures and topographic features, which imposes a challenge to the applicability of the GMM. Therefore, we plan to classify the topographic features based on the geomorphometric parameters, and then combine it with the site classification (e.g., NEHRP site classification) to evaluate the ground motion amplification level in the real engineering site.

Conclusion

In this paper, we study the influence of back-azimuth and dipping angle on the topographic amplification based on the ground motion synthetic database constructed by the spectral element method. In addition, the correlation between geomorphometric parameters (relative elevation and smooth curvature) and frequency-dependent topographic amplification value is also analyzed. For the isotropic homogeneous numerical model with double couple point sources as the input, the following conclusions can be obtained:

(1) When the dipping angle is smaller than 45°, topography has a strong amplification effect on P waves; When the dipping angle is greater than 45°, topography has a strong amplification effect on SV wave, followed by P wave, and it has the least amplification effect on SH wave.

(2) When the dipping angle is large, the topographic amplification of P wave is more projected on the horizontal components. More specifically, When the back-azimuth angle is around 90° or 270°, the PGA amplification of the X component increases obviously; when the back-azimuth is around 0° or 180°, the PGA amplification of the Y component increases obviously. The PGA amplification of Z component is independent of the back-azimuth and similar to that of SV wave.

(3) The relative elevation and smoothed curvature cover the same information of topography, Considering the algorithmic complexity, relative elevation is recommended as a proxy for topographic site effects.

(4) The correlation of geomorphometric parameters (relative elevation and smoothed curvature) with spectral amplification is stronger than that of geomorphometric parameters with PGA amplification.

(5) The relative elevation and smoothed curvature are both closely related to the horizontal topographic amplification, but independent of that in the vertical component.

Data availability statement

The original contributions presented in the study are included in the article/Supplementary Material, further inquiries can be directed to the corresponding author.

Author contributions

FW implemented the numerical simulations and specifically writing the initial draft. QM determined the research goals and contributed to designing the methodology. DT and QX provided important suggestions for the interpretation of the results and revised the manuscript. All authors contributed to the redaction and final revision of the manuscript.

Funding

This research was partially supported by Scientific Research Fund of Institute of Engineering Mechanics, China Earthquake

Administration (Grant No. 2016A03), and National Natural Science Foundation of China (Grant No. U2039209 and 5150082083).

Acknowledgments

We thank NASA's (National Aeronautics and Space Administration) EOSDIS (Earth Observing System Data and Information System) (https://search.earthdata.nasa.gov) for providing DEM (Digital Elevation Model) data. Some plots were made using Generic Mapping Tools v.5.2.1 and the matplotlib module in Python.

Conflict of interest

The authors declare that the research was conducted in the absence of any commercial or financial relationships that could be construed as a potential conflict of interest.

Publisher's note

Supplementary material

The Supplementary Material for this article can be found online at: https://www.frontiersin.org/articles/10.3389/feart.2022.996389/full#supplementary-material

SUPPLEMENTARY TABLES S1–S2
Show the coordinate positions of seismic events and stations in the numerical model, respectively.

References

Ashford, S. A., and Sitar, N. (1997). Analysis of topographic amplification of inclined shear waves in a steep coastal bluff. *Bull. Seismol. Soc. Am.* 87, 692–700. doi:10.1785/BSSA0870030692

Asimaki, D., and Mohammadi, K. (2018). On the complexity of seismic waves trapped in irregular topographies. *Soil Dyn. Earthq. Eng.* 114, 424–437. doi:10.1016/j.soildyn.2018.07.020

Assimaki, D., Gazetas, G., and Kausel, E. (2005a). Effects of local soil conditions on the topographic aggravation of seismic motion: Parametric investigation and recorded field evidence from the 1999 athens earthquake. *Bull. Seismol. Soc. Am.* 95, 1059–1089. doi:10.1785/0120040055

Assimaki, D., and Gazetas, G. (2004). Soil and topographic amplification on canyon banks and the 1999 Athens earthquake. *J. Earth. Eng.* 8, 1–43. doi:10.1142/S1363246904001250

Assimaki, D., Kausel, E., and Gazetas, G. (2005b). Soil-dependent topographic effects: A case study from the 1999 athens earthquake. *Earthq. Spectra* 21, 929–966. doi:10.1193/1.2068135

Boore, D. M. (1972). A note on the effect of simple topography on seismic SH waves. *Bull. Seismol. Soc. Am.* 62, 275–284. doi:10.1785/BSSA0620010275

Boore, D. M., Harmsen, S. C., and Harding, S. T. (1981). Wave scattering from a step change in surface topography. *Bull. Seismol. Soc. Am.* 71, 117–125. doi:10.1785/BSSA0710010117

Borcherdt, R. D. (1970). Effects of local geology on ground motion near San Francisco Bay. *Bull. Seismol. Soc. Am.* 60, 29–61. doi:10.1785/BSSA0600010029

Bouchon, M., and Barker, J. S. (1996). Seismic response of a hill: The example of Tarzana, California. *Bull. Seismol. Soc. Am.* 86, 66–72. doi:10.1785/BSSA08601A0066

Bouckovalas, G. D., and Papadimitriou, A. G. (2005). Numerical evaluation of slope topography effects on seismic ground motion. *Soil Dyn. Earthq. Eng.* 25, 547–558. doi:10.1016/j.soildyn.2004.11.008

Brocher, T. M. (2005). Empirical relations between elastic wavespeeds and density in the earth's crust. *Bull. Seismol. Soc. Am.* 95, 2081–2092. doi:10.1785/0120050077

Buech, F., Davies, T., and Pettinga, J. (2010). The little red hill seismic experimental study: Topographic effects on ground motion at a bedrock-dominated mountain edifice. *Bull. Seismol. Soc. Am.* 100, 2219–2229. doi:10.1785/0120090345

Burjánek, J., Edwards, B., and Fäh, D. (2014). Empirical evidence of local seismic effects at sites with pronounced topography: A systematic approach. *Geophys. J. Int.* 197, 608–619. doi:10.1093/gji/ggu014

Burjánek, J., Moore, J. R., Yugsi Molina, F. X., and Fäh, D. (2012). Instrumental evidence of normal mode rock slope vibration. *Geophys. J. Int.* 188, 559–569. doi:10.1111/j.1365-246X.2011.05272.x

Ding, H., Yu, Y., and Zheng, Z. (2017). Effects of scarp topography on seismic ground motion under inclined P waves. *Rock Soil Mech.* 38, 1716–1724+1732. doi:10.16285/j.rsm.2017.06.021

Galvez, P., Petukhin, A., Somerville, P., Ampuero, J. P., Miyakoshi, K., Peter, D., et al. (2021). Multicycle simulation of strike-slip earthquake rupture for use in near-source ground-motion simulations. *Bull. Seismol. Soc. Am.* 111, 2463–2485. doi:10.1785/0120210104

Gangi, A. F., and Wesson, R. L. (1978). P-wave to Rayleigh-wave conversion coefficients for wedge corners; model experiments. *J. Comput. Phys.* 29, 370–388. doi:10.1016/0021-9991(78)90140-7

Geli, L., Bard, P.-Y., and Jullien, B. (1988). The effect of topography on earthquake ground motion: A review and new results. *Bull. Seismol. Soc. Am.* 78, 42–63. doi:10.1785/BSSA0780010042

Gu, L., Ding, H., and Yu, Y. (2017). Effects of scarp topography on seismic ground motion under inclined SV waves. *J. Nat. Disast.* 26, 39–47. doi:10.13577/j.jnd.2017.0405

Harris, R. A. (1998). Forecasts of the 1989 loma prieta, California, earthquake. *Bull. Seismol. Soc. Am.* 88, 898–916. doi:10.1785/BSSA0880040898

Hartzell, S. H., Carver, D. L., and King, K. W. (1994). Initial investigation of site and topographic effects at Robinwood Ridge, California. *Bull. Seismol. Soc. Am.* 84, 1336–1349. doi:10.1785/BSSA0840051336

Hartzell, S., Ramírez-Guzmán, L., Meremonte, M., and Leeds, A. (2017). Ground motion in the presence of complex topography II: Earthquake sources and 3D simulations. *Bull. Seismol. Soc. Am.* 107, 344–358. doi:10.1785/0120160159

Hough, S. E., Altidor, J. R., Anglade, D., Given, D., Janvier, M. G., Maharrey, J. Z., et al. (2010). Localized damage caused by topographic amplification during the 2010 M 7.0 Haiti earthquake. *Nat. Geosci.* 3, 778–782. doi:10.1038/ngeo988

Igel, H. (2017). *Computational seismology: A practical introduction*. Oxford, United Kingdom: Oxford University Press.

Kanamori, H., and Schubert, G. (2015). *Treatise on geophysics: Earthquake seismology*. Amsterdam, Netherlands: Elsevier Press.

Kang, S., Kim, B., Cho, H., Lee, J., Kim, K., Bae, S., et al. (2019). Ground-motion amplifications in small-size hills: Case study of gokgang-ri, South Korea, during the 2017 M_L 5.4 pohang earthquake sequence. *Bull. Seismol. Soc. Am.* 109, 2626–2643. doi:10.1785/0120190064

Komatitsch, D., Tsuboi, S., Tromp, J., Levander, A., and Nolet, G. (2005). The spectral-element method in seismology. *Geoph. Mono. Am. Geoph.Un.* 157, 205.

La Rocca, M., Chiappetta, G. D., Gervasi, A., and Festa, R. L. (2020). Non-stability of the noise HVSR at sites near or on topographic heights. *Geophys. J. Int.* 222, 2162–2171. doi:10.1093/gji/ggaa297

Lee, S.-J., Chan, Y.-C., Komatitsch, D., Huang, B.-S., and Tromp, J. (2009a). Effects of realistic surface topography on seismic ground motion in the Yangminshan region of Taiwan based upon the Spectral-Element Method and LiDAR DTM. *Bull. Seismol. Soc. Am.* 99, 681–693. doi:10.1785/0120080264

Lee, S.-J., Chen, H.-W., Liu, Q., Komatitsch, D., Huang, B.-S., and Tromp, J. (2008). Three-dimensional simulations of seismic-wave propagation in the Taipei Basin with realistic topography based upon the spectral-element method. *Bull. Seismol. Soc. Am.* 98, 253–264. doi:10.1785/0120070033

Lee, S.-J., Komatitsch, D., Huang, B.-S., and Tromp, J. (2009b). Effects of topography on seismic-wave propagation: An example from northern Taiwan. *Bull. Seismol. Soc. Am.* 99, 314–325. doi:10.1785/0120080020

Leonard, M. (2010). Earthquake fault scaling: Self-consistent relating of rupture length, width, average displacement, and moment release. *Bull. Seismol. Soc. Am.* 100, 1971–1988. doi:10.1785/0120090189

Li, S. Y., and Liao, Z. P. (2002). Wave-type conversion caused by a step topography subjected to inclined seismic body wave. *Earthq. Eng. Eng. Vib.* 22, 9–15. doi:10.13197/j.eeev.2002.04.002

Lovati, S., Bakavoli, M. K. H., Massa, M., Ferretti, G., Pacor, F., Paolucci, R., et al. (2011). Estimation of topographical effects at Narni ridge (Central Italy): Comparisons between experimental results and numerical modelling. *Bull. Earthq. Eng.* 9, 1987–2005. doi:10.1007/s10518-011-9315-x

Luo, Y., Del Gaudio, V., Huang, R., Wang, Y., and Wasowski, J. (2014). Evidence of hillslope directional amplification from accelerometer recordings at qiaozhuang (sichuan — China). *Eng. Geol.* 183, 193–207. doi:10.1016/j.enggeo.2014.10.015

Luo, Y., Fan, X., Huang, R., Wang, Y., Yunus, A. P., and Havenith, H.-B. (2020). Topographic and near-surface stratigraphic amplification of the seismic response of a mountain slope revealed by field monitoring and numerical simulations. *Eng. Geol.* 271, 105607. doi:10.1016/j.enggeo.2020.105607

Ma, Q., Wang, F., Tao, D., Xie, Q., Liu, H., and Jiang, P. (2021). Topographic site effects of Xishan Park ridge in Zigong city, Sichuan considering epicentral distance. *J. Seismol.* 25, 1537–1555. doi:10.1007/s10950-021-10048-7

Magnoni, F., Casarotti, E., Michelini, A., Piersanti, A., Komatitsch, D., Peter, D., et al. (2013). Spectral-Element simulations of seismic waves generated by the 2009 L'Aquila earthquake. *Bull. Seismol. Soc. Am.* 104, 73–94. doi:10.1785/0120130106

Maufroy, E., Cruz-Atienza, V. M., Cotton, F., and Gaffet, S. (2015). Frequency-Scaled curvature as a proxy for topographic site-effect amplification and ground-motion variability. *Bull. Seismol. Soc. Am.* 105, 354–367. doi:10.1785/0120140089

Mayoral, J. M., De la Rosa, D., and Tepalcapa, S. (2019). Topographic effects during the September 19, 2017 Mexico city earthquake. *Soil Dyn. Earthq. Eng.* 125, 105732. doi:10.1016/j.soildyn.2019.105732

Moore, J. R., Gischig, V., Burjanek, J., Loew, S., and Fäh, D. (2011). Site effects in unstable rock slopes: Dynamic behavior of the Randa instability (Switzerland). *Bull. Seismol. Soc. Am.* 101, 3110–3116. doi:10.1785/0120110127

Nakamura, Y. (1989). A method for dynamic characteristics estimation of subsurface using microtremor on the ground surface. *Q. Rep. Railw. Tech. Res. Inst.* 30, 25–33.

Ohtsuki, A., and Harumi, K. (1983). Effect of topography and subsurface inhomogeneities on seismic SV waves. *Earthq. Eng. Struct. Dyn.* 11, 441–462. doi:10.1002/eqe.4290110402

Paolucci, R. (2002). Amplification of earthquake ground motion by steep topographic irregularities. *Earthq. Eng. Struct. Dyn.* 31, 1831–1853. doi:10.1002/eqe.192

Pischiutta, M., Cultrera, G., Caserta, A., Luzi, L., and Rovelli, A. (2010). Topographic effects on the hill of Nocera Umbra, central Italy. *Geophys. J. Int.* 182, 977–987. doi:10.1111/j.1365-246X.2010.04654.x

Pitarka, A., Akinci, A., De Gori, P., and Buttinelli, M. (2021). Deterministic 3D ground-motion simulations (0–5 Hz) and surface topography effects of the 30 October 2016 Mw 6.5 Norcia, Italy, earthquake. *Bull. Seismol. Soc. Am.* 112, 262–286. doi:10.1785/0120210133

Rai, M., Rodriguez-Marek, A., and Yong, A. (2016). An empirical model to predict topographic effects in strong ground motion using California small- to medium-magnitude earthquake database. *Earthq. Spectra* 32, 1033–1054. doi:10.1193/113014eqs202m

Somerville, P., Irikura, K., Graves, R., Sawada, S., Wald, D., Abrahamson, N., et al. (1999). Characterizing crustal earthquake slip models for the prediction of strong ground motion. *Seismol. Res. Lett.* 70, 59–80. doi:10.1785/gssrl.70.1.59

Song, J., Gao, Y., and Feng, T. (2020). Influence of interactions between topographic and soil layer amplification on seismic response of sliding mass and slope displacement. *Soil Dyn. Earthq. Eng.* 129, 105901. doi:10.1016/j.soildyn.2019.105901

Stolte, A. C., Cox, B. R., and Lee, R. C. (2017). An experimental topographic amplification study at Los Alamos National Laboratory using ambient vibrations. *Bull. Seismol. Soc. Am.* 107, 1386–1401. doi:10.1785/0120160269

Stone, I., Wirth, E. A., and Frankel, A. D. (2022). Topographic response to simulated Mw 6.5–7.0 earthquakes on the seattle fault. *Bull. Seismol. Soc. Am.* 112, 1436–1462. doi:10.1785/0120210269

Trifunac, M. D., and Hudson, D. E. (1971). Analysis of the Pacoima Dam accelerogram-san Fernando, California, earthquake of 1971. *Bull. Seismol. Soc. Am.* 61, 1393–1141. doi:10.1785/BSSA0610051393

Tsai, V. C., Bowden, D. C., and Kanamori, H. (2017). Explaining extreme ground motion in Osaka basin during the 2011 Tohoku earthquake. *Geophys. Res. Lett.* 44, 7239–7244. doi:10.1002/2017GL074120

Tucker, B. E., King, J. L., Hatzfeld, D., and Nersesov, I. L. (1984). Observations of hard-rock site effects. *Bull. Seismol. Soc. Am.* 74, 121–136. doi:10.1785/BSSA0740010121

Wang, G., Du, C., Huang, D., Jin, F., Roo, R. C. H., and Kwan, J. S. H. (2018). Parametric models for 3D topographic amplification of ground motions considering subsurface soils. *Soil Dyn. Earthq. Eng.* 115, 41–54. doi:10.1016/j.soildyn.2018.07.018

Wang, L., Wu, Z., Xia, K., Liu, K., Wang, P., Pu, X., et al. (2019). Amplification of thickness and topography of loess deposit on seismic ground motion and its seismic design methods. *Soil Dyn. Earthq. Eng.* 126, 105090. doi:10.1016/j.soildyn.2018.02.021

Wang, X., Wang, J., Zhang, L., and He, C. (2021). Broadband ground-motion simulations by coupling regional velocity structures with the geophysical information of specific sites. *Soil Dyn. Earthq. Eng.* 145, 106695. doi:10.1016/j.soildyn.2021.106695

Wood, C. M., and Cox, B. R. (2016). Comparison of field data processing methods for the evaluation of topographic effects. *Earthq. Spectra* 32, 2127–2147. doi:10.1193/111515eqs170m

Yuan, X., and Liao, Z. (1996). Scattering of plane SH waves by arbitrary circular convex topography. *Earthq. Eng. Eng. Vib.* 16, 1–13. doi:10.13197/j.eeev.1996.02.001

Yuan, Y. O., Lacasse, M. D., and Liu, F. (2021). Full-wavefield, full-domain deterministic modeling of shallow low-magnitude events for improving regional ground-motion predictions. *Bull. Seismol. Soc. Am.* 111, 2617–2634. doi:10.1785/0120210031

Zevenbergen, L. W., and Thorne, C. R. (1987). Quantitative analysis of land surface topography. *Earth Surf. Process. Landf.* 12, 47–56. doi:10.1002/esp.3290120107

Zhou, H., Li, J., and Chen, X. (2020). Establishment of a seismic topographic effect prediction model in the Lushan Ms 7.0 earthquake area. *Geophys. J. Int.* 221, 273–288. doi:10.1093/gji/ggaa003

Zuo, K., and Chen, J. (2018). 3D body-wave velocity structure of crust and relocation of earthquakes in the Menyuan area. *Chin. J. Geophys.* 61, 2788–2801. doi:10.6038/cjg2018L0537

frontiers | Frontiers in Earth Science

TYPE Original Research
PUBLISHED 09 January 2023
DOI 10.3389/feart.2022.1107921

EDITED BY
Kun Ji,
Hohai University, China

REVIEWED BY
Mianshui Rong,
Beijing University of Technology, China
Zhao Xiaofen,
China Earthquake Administration, China

*CORRESPONDENCE
Hongwei Wang,
✉ whw1990413@163.com

SPECIALTY SECTION
This article was submitted to Structural Geology and Tectonics, a section of the journal Frontiers in Earth Science

RECEIVED 25 November 2022
ACCEPTED 08 December 2022
PUBLISHED 09 January 2023

CITATION
Yao X, Zhang P, Zhao Y, Wang H and Wang D (2023), Region-dependent site conditions in China: Evidence from borehole data statistics.
Front. Earth Sci. 10:1107921.
doi: 10.3389/feart.2022.1107921

Region-dependent site conditions in China: Evidence from borehole data statistics

Xinxin Yao[1,2], Peng Zhang[1,2], Yu Zhao[1,2], Hongwei Wang[1,2]* and Daren Wang[1,2]

[1]Key Laboratory of Earthquake Engineering and Engineering Vibration, Institute of Engineering Mechanics, China Earthquake Administration, Harbin, China, [2]Key Laboratory of Earthquake Disaster Mitigation, Ministry of Emergency Management, Harbin, China

Consideration of site effects is vital in modeling and predicting earthquake ground motions. However, site conditions can vary markedly between different localities. The regional dependency of site conditions in China has not yet been investigated systematically. In this study, profiles of 6,179 boreholes were collected from four regions in China, i.e., the Capital Metropolitan (CM), Xinjiang (XJ), Guangdong—Guangxi (GG), and Sichuan–Yunnan (SY) areas. Quantitative characteristic parameters including site category, equivalent shear wave velocity (V_{se}), and the thickness of the overlying soil layer (H) defined by the Chinese seismic code, and V_{S30} and the median shear wave profile were all analyzed to confirm the dependency on site conditions among the four regions. Investigation revealed that the majority of sites in most regions are classified as Class-II sites with no Class-IV sites, except in CM. In comparison with the other three regions, a larger number of GG sites are classified as Class-I. Sites in XJ are generally characterized by small H values (<20 m) and large V_{se} values (250 –450 m/s), while those in CM are characterized by large H values (average: ~50 m) and small V_{se} values (150 –300 m/s). Generally, the V_{se} and H values are similar in GG and SY, i.e., the sites are covered by an overlying soil layer that is ~20 m thick with an average V_{se} value of ~250 m/s. A very thin (<5 m) overlying soil layer is observed at many more sites in GG than at sites in the other three regions. The V_{S30} values in CM, SY, and GG all approximately follow a lognormal distribution with various logarithmic means, i.e., 257.2, 299.6, and 360.9 m/s, respectively. However, the V_{S30} values of most sites in XJ broadly follow a uniform distribution with a range of 200 –550 m/s. We summarized the characteristics of the median V_S profiles of each V_{S30}-based category (C1, C2, and C3) for each region. The median V_S profiles between any two regions are mainly manifested as parallel trends for sites in category C1, whereas they present trends of intersection for sites in categories C2 and C3. The findings of this study could serve as a basis for the establishment of a regional empirical model for site-dependent seismic response in China.

KEYWORDS

site condition, site borehole profiles, regional dependency, site category, V_{S30}

1 Introduction

The spatial distribution of ground motion is highly influenced by local site conditions, which can be determined on the basis of borehole profile characteristics that include the thickness of the overlying soil, shear wave velocity (V_S), and the geotechnical category and properties of each soil layer. Site effects are vital factors that must be considered in seismic design (e.g., GB 50011, 2010), seismic zonation (e.g., Mucciarelli, 2011), and ground motion predictions (e.g., Wen et al., 2018). Previous studies found that seismic response can vary markedly among sites with similar values of the time-weighted average shear wave velocity of the upper 30 m (V_{S30}) owing to substantial differences between borehole profiles (e.g., Ren et al., 2013; Rong et al., 2017). Qi et al. (2013) investigated the seismic response at sites with similar equivalent shear wave velocity and thickness of the overlying soil layer, and found notable dependency on the vertical arrangement of various soil layers. Kamai et al. (2016) observed obvious regional dependency of median V_S profiles in the same V_{S30} bin in three disparate regions (i.e., California, Taiwan, and Japan), and suggested the development of individual site-response prediction models for California and Japan.

Most previous related studies focused on verification of the regional dependency of soil dynamic parameters through dynamic testing of soil, which can provide important information for calculating site seismic response using the one-dimensional equivalent linear method (e.g., Yuan et al., 2000; Lv et al., 2003; Chen et al., 2005). On this basis, soil dynamic parameters have been recommended for use in various regions. However, few studies have addressed the regional dependency of site conditions. In regions with the same sedimentary environment and geological background, borehole profiles of the near-surface material should be broadly similar (Zhang et al., 2022). Theoretically, the borehole profiles vary from one region to another. Boore et al. (2011) found that the V_{S30} empirical estimation model developed for California (USA) is inapplicable to Japan because of substantial differences in borehole profiles. Wang et al. (2022) confirmed that commonly used V_{S30} extrapolation models are inapplicable to Xinjiang (China) owing to the special borehole profiles. Overall, no systematic studies have been performed previously to investigate the regional dependency of site conditions in China.

This study collected site borehole profiles in four regions of China, i.e., the Capital Metropolitan (CM), Xinjiang (XJ), Guangdong–Guangxi (GG), and Sichuan–Yunnan (SY) areas. We compared the site classes in each of the four regions, as defined on the basis of the Code for Seismic Design of Buildings of China (GB50011-2010) and three characteristic site parameters, i.e., the equivalent shear wave velocity (V_{se}), thickness of the overlying soil layer (H), and V_{S30}. We also compared the median V_S profiles for Class-II sites and sites categorized with the same V_{S30}–based category to investigate the potential dependency on site conditions among the four regions. The findings of this study could serve as the basis for establishment of a regional empirical model for site seismic response in China.

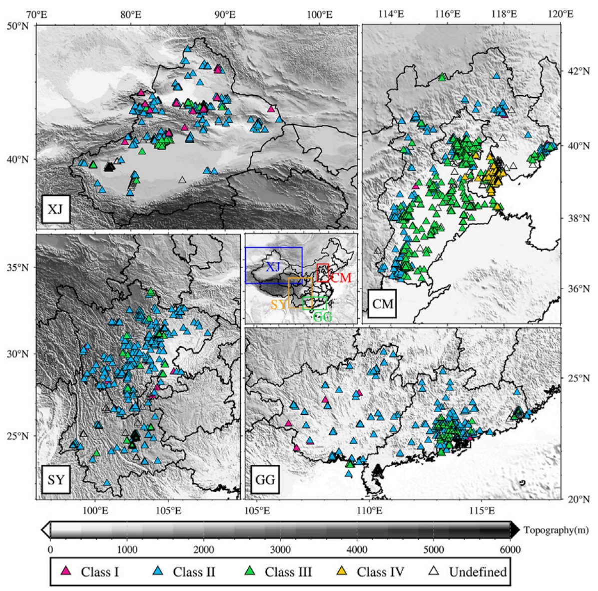

FIGURE 1
Locations of borehole sites in the four regions considered in this study, i.e., the Capital Metropolitan (CM), Xinjiang (XJ), Guangdong−Guangxi (GG), and Sichuan−Yunnan (SY) areas. Different colors are used to represent the various site classes defined by China's seismic code.

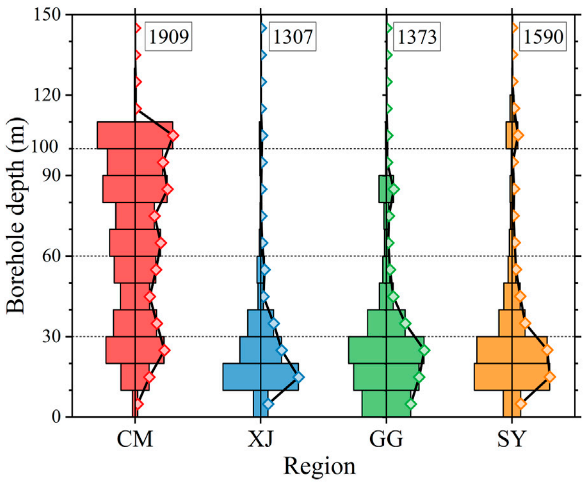

FIGURE 2
Histograms of the distribution of borehole depth at sites in CM, XJ, GG, and SY. The numbers within the box represent the total number of the sites in different regions, the rectangles with different colors stand for the number of sites in each bin, and the polylines with squares represent the proportion of the number of sites in each bin to the total.

TABLE 1 **Site categories defined by the Code for Seismic Design of Buildings of China (GB 50011, 2010).**

Equivalent shear-wave velocity V_{se} (m·s^{-1})	Thickness of overlying soil layer, H (m)				
	I_0	I_1	II	III	IV
>800	0				
$500 < V_{se} \le 800$		0			
$250 < V_{se} \le 500$		<5	≥5		
$150 < V_{se} \le 250$		<3	$3 \le H \le 50$	>50	
≤150		<3	$3 \le H \le 15$	$15 < H \le 80$	>80

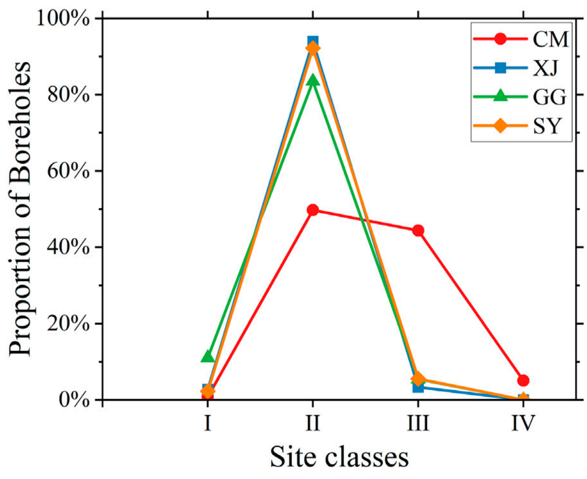

FIGURE 3
Proportions of borehole sites associated with different site classes in SY, XJ, GG, and CM.

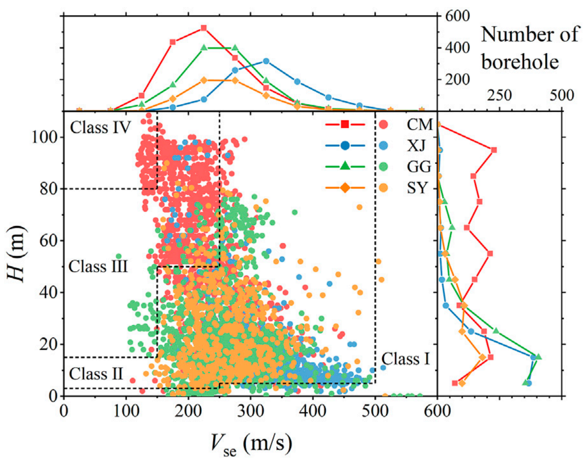

FIGURE 4
Scatter plots of V_{se} *versus* H for sites in CM, XJ, GG, and SY, together with histograms of V_{se} and H values. The polygonal lines distinguish the ranges of V_{se} and H for different site classes as defined by the Chinese seismic code.

2 Datasets

In total, 6,179 borehole profiles from sites in CM, XJ, GG, and SY were collected. The borehole profiles were mainly derived from the engineering site exploration, seismic safety evaluation, *etc*. The boreholes in CM, SY show a uniform spatial distribution. However, most boreholes in GG cluster in the Pearl River Delta Region, and boreholes in XJ are mainly spread along the north and south foot of Tianshan Mountain.

These profiles were then reorganized uniformly in terms of their geographic coordinates, V_S values, thickness, and the geotechnical category and properties of each soil layer. Figure 1 shows the geographical distribution of the borehole sites in China.

Figure 2 shows distribution histograms of the borehole depths at the sites in the four regions. The borehole depths at most sites are <30 m in XJ, GG, and SY, but a very small number of sites have borehole depths of >100 m. The sites in CM located on the North China Plain with a thick sedimentary layer have much deeper borehole depths, i.e., more than half the sites have borehole depths of >60 m, while a certain quantity have depths of >100 m.

In the Code for Seismic Design of Buildings of China (GB 50011, 2010), engineering sites are classified into four categories (Class-I, II, III, and IV) according to V_{se} and H, as listed in Table 1. Class-I sites include two subcategories (I_0 and I_1). In the code, V_{se} is defined as the time-weighted average V_S over the upper soil layer with minimum depth of 20 m and H. The code also definitely stipulates how to determine values of H according to various cases. Generally, H is defined as the depth to the upper surface of a soil layer for which V_S is not <500 m/s, and where the V_S value of the underlying soil layer is always not <500 m/s.

The V_{se} and H values were calculated according to the site borehole profiles and used to categorize the site classes. Note that some boreholes were not included in the following analysis because the H values were unascertainable owing to the limited number of borehole depths. Figure 3 shows the proportion of sites divided into

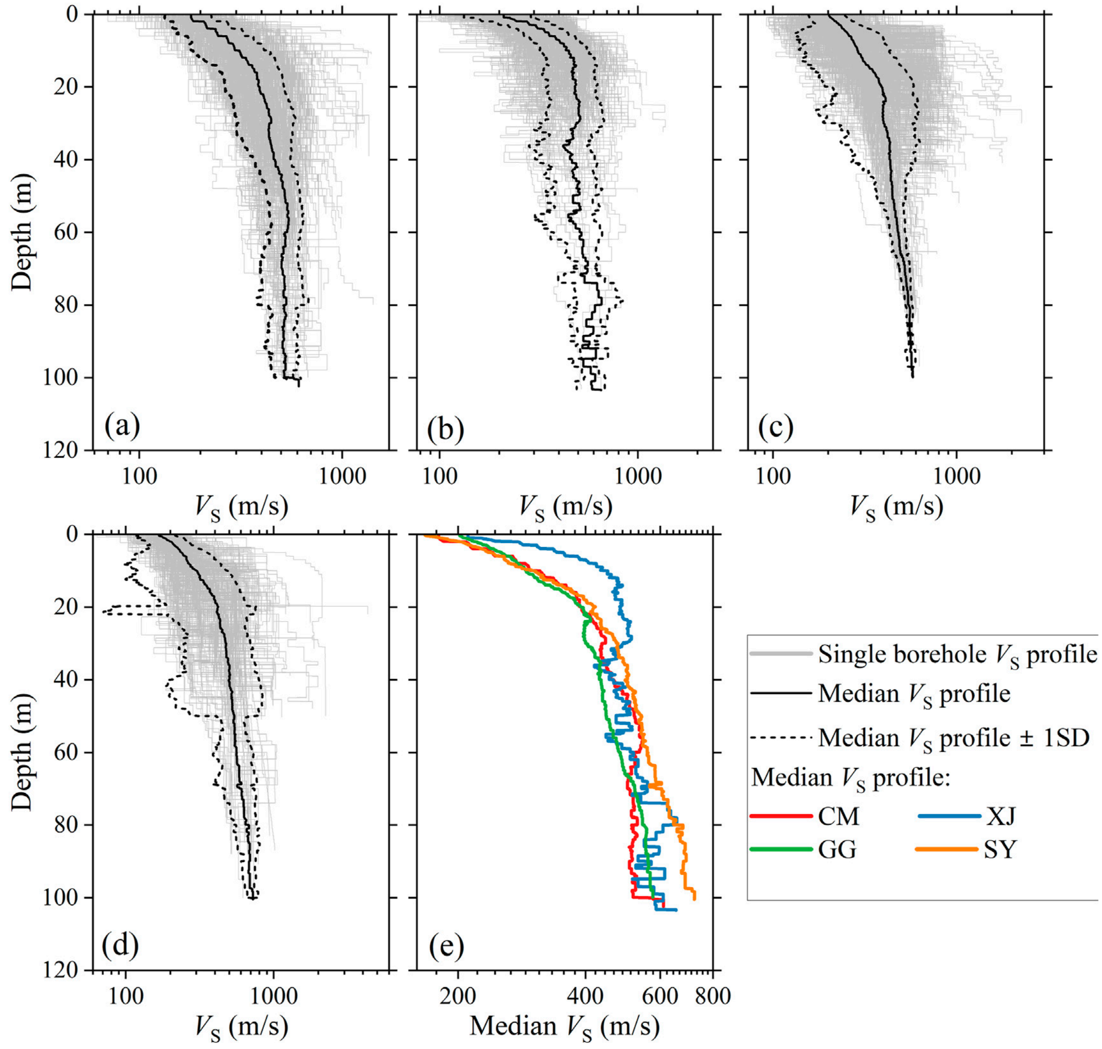

FIGURE 5
The V_S profiles of Class-II sites in **(A)** SY, **(B)** GG, **(C)** CM, and **(D)** XJ areas. Solid and dotted lines indicate the median V_S profile and the one standard deviation range, respectively, for each region. **(E)** The median V_S profiles of the Class-II sites in the four regions are compared in panel.

the various site classes for the four regions. The overwhelming majority of sites in XJ, GG, and SY are classified as Class-II sites, while only a few are classified as Class-I and Class-III sites. No site in XJ, GG, or SY is assigned to the Class-IV group. We also note that the proportion of Class-I sites in GG is substantially higher than that in either XJ or SY. In contrast, in CM, the number of Class-III sites is slightly lower than that of Class-II sites, and Class-II and Class-III sites account for the majority. In CM, some sites are classified as Class-IV sites, and their proportion is far greater than that of the Class-I sites. As shown in Figure 1, the Class-III and Class-IV sites in CM are generally distributed around the coastal area with very soft and deep soils. The common characteristic that Class-II sites account for the majority is also the result determined using the Chinese seismic code with a wide interval of Class-II sites.

3 Regional dependency of site conditions

3.1 Regional dependency of H and V_{se}

Figure 4 presents V_{se}–H scatter plots for the four studied regions, together with histograms of the H and V_{se} values. The H values of XJ sites are generally <20 m, while the V_{se} values are at a comparatively high level (250 –450 m/s), indicating that most sites in XJ are covered by thin and hard soil (e.g., sand and silty clay). In contrast, CM sites generally show an approximately uniform distribution of H values in the range of 0 –100 m (average: ~50 m) and lower V_{se} values in the range of 150 –300 m/s, indicating deep and soft surficial soil. The

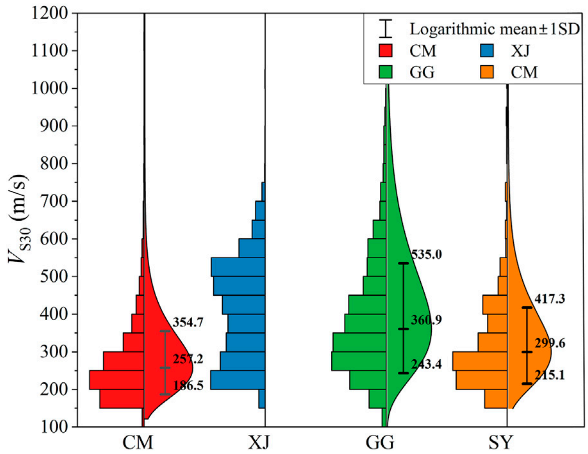

FIGURE 6
Frequency distributions of V_{S30} values in the four studied regions.

V_{se}–H scatter plots present similar distributions for GG and SY. Generally, the ground surface in both regions is covered by an overlying soil layer that is ~20 m thick with an average V_{se} value of ~250 m/s. However, in comparison with the other three regions, the overlying soil layer is very thin (<5 m) at many more sites in GG. In comparison with those sites with a very deep overlying soil layer (i.e., >80 m) in XJ, CM, and SY, some of the sites in CM are characterized by very low V_{se} (i.e., <150 m/s), and sites with higher V_{se} values account for a larger proportion of such sites in SY. The above results fully reflect the major differences in H and V_{se} at the various sites in the four studied regions.

3.2 Regional dependency of V_S profiles

The potential regional dependency in the V_S profiles was investigated based on the boreholes of the Class-II sites in the four regions. Figure 5 shows the variation of V_S with depth for each Class-II site, as well as the V_S median and the one standard deviation range for each region. Very obvious differences are evident in the V_S profiles of the Class-II sites in the four regions. The median V_S profiles for the four regions are also plotted in Figure 5 for comparison purposes. The sites in the four regions show some similarities in terms of the characteristics of the variation in median V_S with depth, i.e., a sharp increase in V_S in shallow soil layers from the ground surface to a critical depth, and notably slower increase in deeper soil layers beneath the critical depth. The differences in the median V_S profiles for the four regions were investigated. The median V_S profile in XJ shows a much shallower critical depth (~13 km) than that in the other three regions (~20 km). The median V_S values (increasing from ~220; to ~480 m/s) in the shallow soil layers in XJ are much larger than those (increasing from ~200; to ~400 m/s) in the other regions. The median V_S value in XJ appears to exhibit faster increase in shallow soil depths than that in the other regions. The median V_S values of the deeper soil layers in XJ generally show no

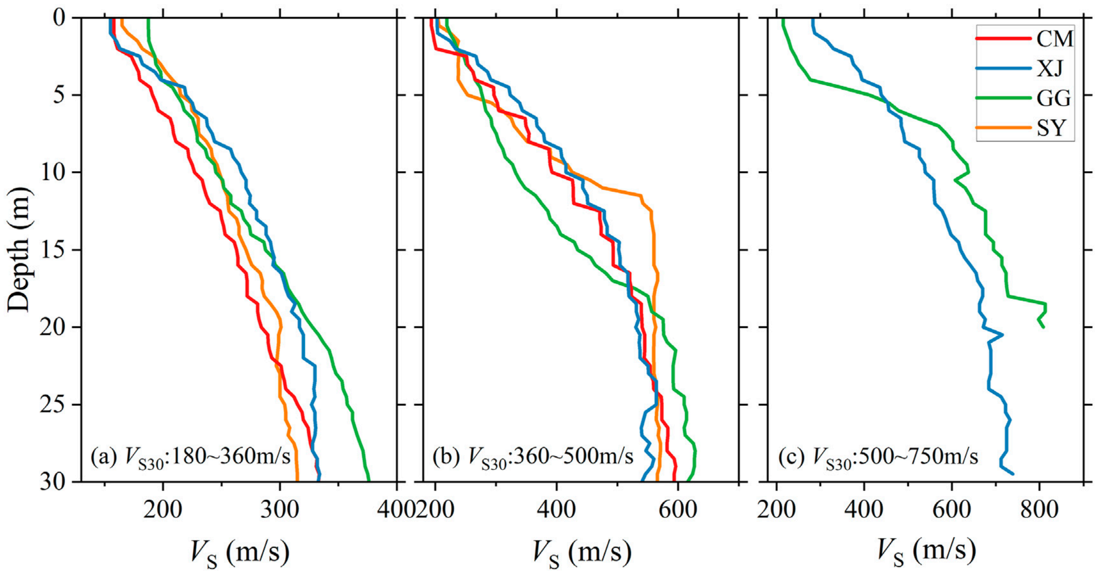

FIGURE 7
Median V_S profiles for sites belonging to each V_{S30}-based category in the four regions considered in this study: **(A)** category C1 for V_{S30} = 180–360 m/s, **(B)** category C2 for V_{S30} = 360–500 m/s, and **(C)** category C3 for V_{S30} = 500–750 m/s.

TABLE 2 Trends describing the regional dependency between any two regions for each V_{S30}-based site category.

	Sites within C1 category			Sites within C2 category			Sites within C3 category		
	XJ	GG	SY	XJ	GG	SY	XJ	GG	SY
CM	○	○	×	●	×	×			
XJ		×	○		×	×		×	
GG			○			×			

Noting ○ indicates the parallel median V_S profiles, ● indicates the overlapped median V_S profiles, and × indicates the intersecting median V_S profiles.

obvious increase with depth. Such a phenomenon is also observed in many of the deeper soil layers (>60 m) in CM. In GG and SY, the median V_S values of the deeper soil layers maintain continuous increase with depth, i.e., from 400; to 580 m/s and to 700 m/s, respectively. Our results indicate that it is necessary to consider regionally dependent site amplification effects in seismic design.

3.3 Regional dependency of V_{S30}

Although the Chinese seismic code uses site categories to characterize the effects of local site conditions on ground motions, V_{S30} is also an important parameter commonly used to characterize local site amplification. The potential regional dependency of V_{S30} was further investigated on the basis of the borehole data from the four studied regions. The V_{S30} values were estimated for sites with borehole depths of <30 m using the constant extrapolation model (Wang et al., 2022) if a rock layer was situated at the bottom of the borehole, and using the linear extrapolation model if a soil layer was situated at the bottom of the borehole.

Frequency distributions of the V_{S30} values in the four studied regions are plotted in Figure 6. The V_{S30} distributions in CM, SY, and GG all approximately follow a lognormal distribution with logarithmic means of 257.2, 299.6, and 360.9 m/s, respectively. The range of one standard deviation in CM, SY, and GG is 186.5–354.7, 215.1–417.3, and 243.4–535.0 m/s, respectively, indicating that the near-surface soil layer in the upper 30 m is on average hardest in GG and softest in CM. The V_{S30} values at a certain proportion of sites in GG are measured or estimated to be >800 m/s, corresponding to hard soil or rock sites, while barely any such sites are found in CM. However, the near-surface site conditions in CM could be confirmed to be most similar owing to the narrowest dispersion of V_{S30} values, while the widest dispersion in GG indicates greatest discrepancy. Different from the other three regions, the V_{S30} values of XJ sites do not follow a lognormal distribution. Instead, the V_{S30} values for most sites fall within a wide range of 200 –550 m/s, approximately following a uniform distribution with an average of ~400 m/s.

The V_{S30}-related empirical relations are often used to characterize site amplification effects, e.g., in predicting ground motions. Moreover, the empirical relations associated with site categories are also used (e.g., Bindi et al., 2011). However, in such cases, the same amplification effects appear associated with sites belonging to the same site category but with different measured V_{S30} values. Therefore, we explored the potential regional dependency of V_{S30} values measured or estimated at sites belonging to the same site category. Referring to the seismic code of China and other countries and regions, most sites considered in this study were divided into three categories on the basis of the V_{S30} values, i.e., C1 for V_{S30} = 180 –360 m/s, C2 for V_{S30} = 360 –500 m/s, and C3 for V_{S30} = 500 –750 m/s.

The median V_S profiles for sites belonging to each category were computed for each of the four regions and illustrated in Figure 7. Note that the median V_S profiles for sites within category C3 in SY and CM are not presented owing to the limited number of samples which is less than 10% of the total number of sites. Substantial regional dependency is also observed in the median V_S profiles of sites within the same category. To clearly express the regional dependency of median V_S profiles of each category, we defined three trends to describe the regional dependency between any two regions considered in this study, i.e., 1) parallel median V_S profiles between two regions that indicate similar V_S variation with depth and greater V_S values in one region in comparison with those in another; 2) intersecting median V_S profiles of two regions that indicate dissimilar V_S variation with depth and greater (lower) V_S in the upper (lower) soil layers in one region in comparison with those in another; and 3) overlapping median V_S profiles at certain depths for both regions indicating consistent V_S values. The three trends between any two regions for each V_{S30}-based site category are listed in Table 2. For sites belonging to category C1, the median V_S profiles between two regions are mainly manifested as a parallel trend, while a trend of intersection appears for XJ–GG and XJ–SY pairings. However, for sites belonging to categories C2 and C3, the median V_S profiles between two regions are predominantly shown as intersection trends, while only the XJ–CM pairing in category C2 shows as an overlapping trend. It is worth noting that the median V_S profiles for categories C2 show an intersection trend with the other three regions and categories C3 intersect with XJ in GG. The median V_S values of the upper soil layers in GG are relatively small but relatively large in the lower soil layers, reflecting the higher impedance ratio and the corresponding stronger site seismic responses in GG. The trends of the median V_S profiles for the same V_{S30}-based category between any two regions fully demonstrate the regional dependency of the V_{S30} values measured or estimated at sites belonging to the same site category. Even if the V_{S30} values among the four regions are similar, the V_S profiles can differ substantially, which could cause huge differences in site seismic responses.

4 Conclusion

This study collected over 6,000 borehole profiles from sites in four regions (i.e., XJ, CM, GG, and SY) in China to investigate the potential regional dependency of site conditions. These sites were first classified into corresponding site categories as defined by the Chinese seismic code. The regional dependencies in V_{se}, H, and V_{S30}, and also in the V_S profiles, were clearly observed at the various sites among the four regions. The following conclusions were drawn.

1) The proportion of Class-II sites is the highest among all four regions. Sites in XJ are generally characterized by small H values (<20 m) and large V_{se} values (250 –500 m/s); conversely, the H values are large and the V_{se} values are small in CM. Except for XJ sites, the V_{se} values all follow a Gaussian distribution with an average of ~250 m/s. The H values in CM exhibit an approximately uniform distribution in the range of 0 –100 m, while those in other regions are concentrated mainly in a range of 0 –30 m.
2) The V_{S30} values for the majority of sites in CM and SY are not >500 m/s, while some sites in XJ and GG show high V_{S30} values in the range of 500 –750 m/s. Except for XJ sites, the V_{S30} values in CM, SY, and GG all approximately follow a lognormal distribution with a logarithmic means of 257.2, 299.6, and 360.9 m/s, respectively. However, the V_{S30} values of XJ sites fall mainly within a wide range of 200 –550 m/s.
3) We defined three trends to describe the regional dependency of the median V_S profiles of each V_{S30}-based category (i.e., C1, C2, and C3) between any two regions. For sites belonging to category C1, C2 and C3, the median V_S profiles between two regions are manifested as a trend of parallel and intersection, respectively. The median V_S values of the upper soil layers in GG are relatively small but relatively large in lower soil layers, reflecting the higher impedance ratio and the corresponding stronger site seismic responses in GG.

The above conclusions were obtained statistically using available borehole data that represent the average characteristics of site conditions in the studied regions. These results might be subject to change when additional borehole data are incorporated in the future. However, the regional dependency of site conditions is evident, and it is recommended that it should be considered in seismic zonation mapping and seismic design codes.

Data availability statement

The original contributions presented in the study are included in the article/supplementary material, further inquiries can be directed to the corresponding author.

Author contributions

XY analyzed the data, interpreted the results, and drafted the manuscript. PZ encoded the borehole data, interpreted the results, and corrected the manuscript. YZ processed the borehole data and corrected the manuscript. HW collected the borehole data and reviewed the manuscript. DW processed the borehole data. All authors read and approved the final manuscript.

Funding

This work is supported by National Key R&D Program of China under grant number 2019YFE0115700; Chinese National Natural Science Fund under grant number 51878632; Natural Science Foundation of Heilongjiang Province under grant number YQ2019E036; Heilongjiang Touyan Innovation Team Program.

Conflict of interest

The authors declare that the research was conducted in the absence of any commercial or financial relationships that could be construed as a potential conflict of interest.

Publisher's note

References

Bindi, D., Pacor, F., Luzi, L., Puglia, R., Massa, M., Ameri, G., et al. (2011). Ground motion prediction equations derived from the Italian strong motion database. *Bull. Earthq. Eng.* 9, 1899–1920. doi:10.1007/s10518-011-9313-z

Boore, D. M., Thompson, E. M., and Cadet, H. (2011). Regional correlations of V_{S30} and velocities averaged over depths less than and greater than 30 meters. *Bull. Seismol. Soc. Am.* 101 (6), 3046–3059. doi:10.1785/0120110071

Chen, G. X., Liu, X. Z., Zhu, D. H., and Hu, Q. X. (2005). Study on dynamic characteristics of recently deposited soils in southern area of jiangsu Province. *Chin. J. Undergr. Space. Eng.* 1 (7), 1139–1142. (in Chinese with English abstract). doi:10.3969/j.issn.1673-0836.2005.z1.042

GB 50011 (2010). *Code for seismic design of buildings*. Beijing: China Architecture Industry Press. (in Chinese).

Kamai, R., Abrahamson, N. A., and Silva, W. J. (2016). V_{S30} in the NGA GMPEs: Regional differences and suggested practice. *Earthq. Spectra.* 32 (4), 2083–2108. doi:10.1193/072615EQS121M

Lv, Y. J., Tang, R. Y., and Sha, H. J. (2003). Experimental study on dynamic shear modulus ratio and damping ratio of the soils of bohai seafloor. *J. Disaster. Prev. Mitig. Eng.* 23 (2), 368–374. (in Chinese with English abstract). doi:10.13409/j/cnki.jdpme.2003.02.006

Mucciarelli, M. (2011). Ambient noise measurements following the 2011 christchurch earthquake: Relationships with previous microzonation studies, liquefaction, and nonlinearity. *Seismol. Res. Lett.* 82 (6), 919–926. doi:10.1785/gssrl.82.6.919

Qi, W. H., Liu, H. S., and Bo, J. S. (2013). A new site classification index: Equivalent period of soil layer. *Earthq. Eng. Eng. Dyn.* 33 (6), 228–235. (in Chinese with English abstract). doi:10.13197/j.eeev.2013.06.228.qiwh.032

Ren, Y. F., Wen, R. Z., Yamanaka, H., and Kashima, T. (2013). Site effects by generalized inversion technique using strong motion recordings of the 2008 Wenchuan earthquake. *Earthq. Eng. Eng. Vib.* 12 (02), 165–184. doi:10.1007/s11803-013-0160-6

Rong, M. S., Fu, L. Y., Wang, Z., Li, X. J., Carpenter, N. S., Woolery, E. W., et al. (2017). On the amplitude discrepancy of HVSR and site amplification from strong-motion observations. *Bull. Seismol. Soc. Am.* 107 (6), 2873–2884. doi:10.1785/0120170118

Wang, D. R., Ren, Y. F., Zhang, Y. T., Ji, K., Wang, H. W., and Wen, R. Z. (2022). Method for correcting extrapolation model of engineering site parameter V_{S30}. *J. Harbin. Inst. Technol. Online Publ*. (in Chinese with English abstract). doi:10.11918/202110086

Wen, R. Z., Xu, P. B., Wang, H. W., and Ren, Y. F. (2018). Single-station standard deviation using strong-motion data from sichuan region, China. *Bull. Seismol. Soc. Am.* 108 (4), 2237–2247. doi:10.1785/0120170276

Yuan, X. M., Sun, R., Sun, J., Meng, S. J., and Shi, Z. J. (2000). Laboratory experimental study on dynamic shear modulus ratio and damping ratio of soils. *Earthq. Eng. Eng. Dyn.* 20 (4), 133–139. (in Chinese with English abstract). doi:10.13197/j.eeev.2000.04.020

Zhang, Y. T., Ren, Y. F., Wen, Z., and Wang, D. R. (2022). A method of site parameter estimation based on decision tree theory considering terrain features. *Chinses J. Geophys.* 65 (2), 698–710. (in Chinses with English abstract). doi:10.6038/cjg2022P0021

frontiers | Frontiers in Earth Science

TYPE Original Research
PUBLISHED 10 January 2023
DOI 10.3389/feart.2022.1112202

EDITED BY
Yefei Ren,
Institute of Engineering Mechanics, China Earthquake Administration, China

REVIEWED BY
Haiping Ding,
Suzhou University of Science and Technology, China
Zhinan Xie,
Institute of Engineering Mechanics, China Earthquake Administration, China

*CORRESPONDENCE
Yushi Wang,
✉ wangyushi@bjut.edu.cn

SPECIALTY SECTION
This article was submitted to Structural Geology and Tectonics, a section of the journal Frontiers in Earth Science

RECEIVED 30 November 2022
ACCEPTED 20 December 2022
PUBLISHED 10 January 2023

CITATION
Wang Y, Ding Y and Li X (2023), Scaling ratios for spectral accelerations caused by seismic site effect under site condition classifications in China.
Front. Earth Sci. 10:1112202.
doi: 10.3389/feart.2022.1112202

Scaling ratios for spectral accelerations caused by seismic site effect under site condition classifications in China

Yushi Wang*, Yi Ding and Xiaojun Li

Key Laboratory of Urban Security and Disaster Engineering of China Ministry of Education, Beijing University of Technology, Beijing, China

The spectral accelerations (Sa), which are widely used as ground motion inputs in structural seismic designing, are significantly affected by local site conditions classified by near-surface geology. A novel approach of quantifying the scaling ratios for Sa on site class I, II, III, and IV under the site condition classifications in Chinese seismic codes, was proposed. In this integrated approach, the scaling ratios for Sa on each site class were subordinated to three constituents, i.e., scaling ratios for peak ground acceleration (PGA), scaling ratios for PGA-normalized Sa, and non-linear decay exponents. The scaling ratios for peak ground acceleration were derived from recent studies and numerical simulations of 1,138 borehole models in China, the scaling ratios for PGA-normalized Sa were derived from 3,584 strong motion records in NGA West two database, and the non-linear decay exponents were derived from about 140 thousand borehole observation data recorded by KiK-net. Consequently, this approach was solidly based on statistics of observation data in company with numerical simulations, which resulted in more reasonable and more reliable scaling ratios for Sa caused by the seismic site effect under site condition classifications in China.

KEYWORDS

seismic site effect, local site condition, site scaling ratio, near-surface geology, spectral acceleration, strong motion record, NGA West 2 database, KiK-net

1 Introduction

Seismic damage data and strong motion records showed that local site conditions have a significant impact on the characteristics of ground motions, especially the medium-to-long period components are significantly amplified by soft overburdens, which should be sufficiently considered during the determination of ground motion inputs for structural seismic designing (Seed et al., 1969; Hu et al., 1980; Aki, 1993; Hu, 2006). For an important engineering structure, it is generally necessary to carry out engineering geological survey, establish a local site model, and conduct numerical simulation of site seismic response considering the influence of seismic environment, strong motion attenuation, and other factors to determine the ground motion inputs related to the local site condition. Meanwhile, for general projects with large quantities and a wide range of areas, it is necessary to establish the scaling ratios for ground motion induced by the seismic site effect on homologous site conditions for the convenience of engineering applications (Li et al., 2001a; Stewart and Seyhan, 2013; Bo et al., 2021).

Based on the site condition classifications in China, different scaling ratios for ground motion parameters caused by the seismic site effect were given (Lu et al., 2008; Li, 2013), in which the ground motion parameter most commonly concerned was peak ground acceleration (PGA), while effective peak acceleration (EPA) and spectral acceleration (Sa) were also frequently used. The research methods included the conversion of foreign achievements (Lü et al., 2007), the numerical simulation of borehole models (Li et al., 2001b; Lan et al.,

TABLE 1 Site condition classification criteria in China.

V_S or V_{SE} (m·s^{-1})	I_0	I_1	II	III	IV
	Overburden thickness (m)				
$V_S > 800$	0	—	—	—	—
$800 \geq V_S > 500$	—	0	—	—	—
$500 \geq V_{SE} > 250$	—	<5	≥5	—	—
$250 \geq V_{SE} > 150$	—	<3	3–50	>50	—
$V_{SE} \leq 150$	—	<3	3–15	15–80	>80

2012), and statistics based on strong motion records in western United States (Bo, 1998; Geng, 2005; Liu et al., 2009; Zhao et al., 2009) or Japan (Guo et al., 2011; Cui et al., 2016; Bian et al., 2017), but there were obvious inconsistencies among these results.

Based on the strong motion records now available, a novel approach of quantifying the scaling ratios for Sa under the site condition classifications in China were proposed in this study.

2 Site condition classifications

2.1 Site condition classifications in China

According to "GB 50011: Code for Seismic Design of Buildings" in China (General Administration of Quality Supervision, Inspection and Quarantine of the People's republic of China, 2016), site conditions were classified into I_0, I_1, II, III, and IV in accordance with shear-wave velocity and overburden thickness, as shown in Table 1, where V_S was the shear-wave velocity of the surface rock on the rock site, V_{SE} was the equivalent shear-wave velocity on the soil site. V_{SE} was defined as following:

$$V_{SE} = \sum_{i=1}^{n}(d_i) \Big/ \sum_{i=1}^{n}(d_i/V_{Si}) \tag{1}$$

where d_i was the thickness of the i^{th} layer of soil within the shallower of overburden thickness and 20 m, and V_{Si} was shear-wave velocity of the i^{th} layer of soil.

2.2 Site condition classifications in this study

The shear-wave velocity structures of the 1,138 borehole models and 140 thousand KiK-net observation data were available, and therefore the corresponding site class could be determined according to Table 1. But in the NGA West two database, the shear-wave velocity structures were not listed, hence the empirical relationship between V_{S30} (the time-averaged shear-wave velocity to 30 m depth in m·s^{-1}) and V_{S20} (the time-averaged shear-wave velocity to 20 m depth in m·s^{-1}) (Boore, 2004)

$$\log_{10}(V_{S30}) = 0.025439 + 1.0095 \log_{10}(V_{S20}) \pm 0.03018 \tag{2}$$

was used to classify the site conditions. If V_{S20} was treated to be identical to V_{SE}, it could be calculated that $V_{S30} > 562$ m s^{-1} on site class I, 562 m s$^{-1} \geq V_{S30} > 280$ m s^{-1} on site class II, 279 m s$^{-1} \geq V_{S30} > 167$ m s^{-1} on site class III, and $V_{S30} < 167$ m s^{-1} on site class IV under the site condition classification criteria in China. As a result of data insufficiency, the site class I_0 was not subdivided from site class I in the following statistics.

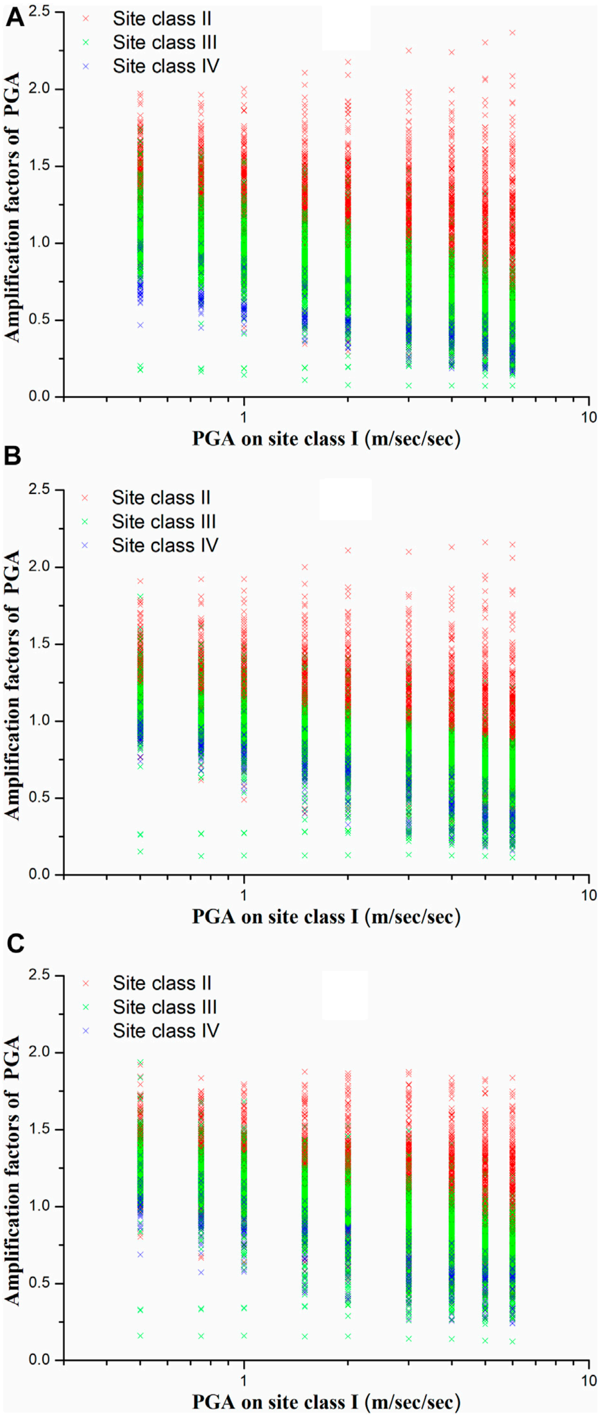

FIGURE 1
PGA amplification factors on site class II, III, and IV versus on site class I_0 given by borehole numerical simulations when the motion inputs of subterrane bottom interface were artificial acceleration time series synthesized according to the average PGA-normalized Sa for **(A)** M_W = 5.0–6.0, **(B)** M_W = 6.0–7.0, and **(C)** M_W = 7.0–8.0.

TABLE 2 Fitting coefficients for PGA amplification factors given by numerical simulations.

Sit class	PGA-normalized Sa input	*a*	*b*	σ
Sit class II	M_W = 5.0–6.0	1.3648	−.4086	.2869
	M_W = 6.0–7.0	1.2523	−.3029	.2269
	M_W = 7.0–8.0	1.3757	−.3275	.2284
	Total	1.3322	−.3464	.2534
Sit class III	M_W = 5.0–6.0	1.0821	−.5388	.1721
	M_W = 6.0–7.0	1.0578	−.4141	.1536
	M_W = 7.0–8.0	1.2292	−.5202	.1704
	Total	1.1231	−.4911	.1793
Sit class IV	M_W = 5.0–6.0	.7474	−.4130	.1040
	M_W = 6.0–7.0	.9412	−.5388	.1043
	M_W = 7.0–8.0	1.0301	−.5312	.1291
	Total	.9062	−.4946	.1443

3 Scaling ratios for PGA

3.1 Numerical simulations of borehole models

One-dimensional equivalent linearization models for 492 boreholes on site class II, 596 boreholes on site class III, and 50 boreholes on site class IV drilled in Sichuan, Yunnan, Xinjiang and Eastern China, were established. The strong motion inputs of subterrane bottom interface were artificial acceleration time series synthesized according to the average PGA-normalized Sa on site class I for moment magnitude 5.0–6.0, 6.0–7.0, and 7.0–8.0 as shown in Figure 3 scaled by PGA = .5, .75, 1.0, 1.5, 2.0, 3.0, 4.0, 5.0, and 6.0 m/s^{-2}. The amplification factors of PGA induced from the numerical simulation results were shown in Figure 1. The linear fittings for amplification factors of PGA under semi-logarithmic coordinates were calculated. The linear fittings formula was

$$A_i = a + b\log_{10}\frac{PGA_{\mathrm{I}}}{0.5} \pm \sigma \tag{3}$$

where the site class i = II, III, or IV, A_i was the amplification factor on site class i versus on site class I_0, PGA_{I} was the peak ground acceleration on site class I_0 in meter/s/second (m s^{-2}), and the coefficients a, b and standard deviation σ were listed in Table 2.

3.2 Statistical results in recent studies

PGA amplification factors proposed in recent studies when PGA ≤ .5 m s^{-2} on site class I_1 were listed in Table 3, and the PGA amplification factors on site class II, III, and IV versus site class I_1 were shown in Figure 2. Considering the differences between the site class I_0 and the site class I_1, the PGA amplification factors given by numerical simulations in Table 2 were divided by 0.80 according to Table 5. It could be concluded that PGA amplification of soft overburden layers had reached consensus, but the specific values of amplification factors were not identical in different studies, even when the ground motion strength was weak enough to ignore the soil non-linearity (Wang et al., 2022).

3.3 Proposed scaling ratios for PGA

The median values of PGA amplification factors when PGA ≤.5 m s^{-2} on site class I_1 in recent studies shown in Table 3, i.e., 1.00 on site class I_1, 1.39 on site class II, 1.30 on site class III, and 1.16 on site class IV, were proposed to be the PGA scaling ratios as a temporary compromise. The PGA scaling ratio on site class I_0 was proposed to be .80 according to the practices of NEHRP (Stewart and Seyhan, 2013).

TABLE 3 PGA amplification factors when PGA ≤.5 m s^{-2} on site class I_1 in recent studies.

Recent study	Site class I_1	Site class II	Site class III	Site class IV	Statistical data
Bo (1998)	.98	1.00	.99	—	235 strong motion records in Western United States
Li et al. (2001b)	1.00	1.50	1.10	.80	188 borehole models in China
Geng, (2005)	.53	1.00	2.00#	.74	470 strong motion records in Western United States
Lü et al. (2007)	.80	1.00	1.20	1.60#	Dozens of borehole models in United States
Zhao et al. (2009)	1.00	1.00	3.00#	—	812 strong motion records in United States
Liu et al. (2009)	1.00	—	—	1.16	728 strong motion records in Western United States
Guo et al. (2011)	1.00	1.80	1.29	1.10	484 strong motion records in Japan
Lan et al. (2012)	.96	1.30	1.25	1.29	235 borehole models in China
Cui et al. (2016)	.70	1.00	.90	—	1,609 strong motion records in Japan
Bian et al. (2017)	.80	1.00	1.20	1.15	1,233 strong motion records in Japan
This study	1.00	1.66	1.40	1.13	1,138 borehole models in China
Mean values	1.00	1.41	1.30	1.20	
Median values	1.00	1.39	1.30	1.16	

Note: Data marked with # were excluded in statistics.

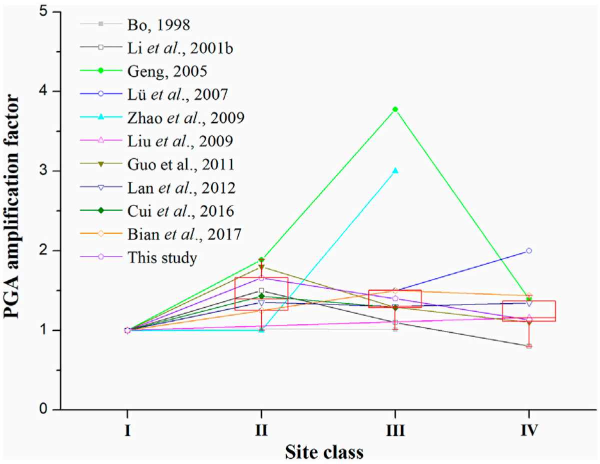

FIGURE 2
PGA amplification factors and their box-plots on site class II, III, and IV versus site class I_1 when PGA ≤ .5 m s^{-2} on site class I_1 in recent studies.

4 Scaling ratios for PGA-normalized sa

4.1 Data resource

The statistical data used in this section were from NGA-West two database of the next generation ground motion attenuation program of the Pacific Earthquake Engineering Research Center. NGA-West two database had collected and processed more than 20,000 strong motion records of shallow crustal earthquakes in active tectonic regions around the world, including detailed earthquake parameters and site information. However, strong motion records in earthquakes above moment magnitude 8.0 were not included in this database. Although abundant strong motion records were obtained in the 2011 earthquake off the Pacific coast of Tōhoku, Japan, they were excluded in this study considering that this earthquake occurred in a marine subduction zone. Almost all the destructive earthquakes in China are of another type of earthquake mechanism, i.e., inland earthquakes. Researches had shown that there were significant differences between the ground motions of the two types of earthquake mechanism, and the long-period ground motions of earthquakes in marine subduction zone were significantly lower than the inland earthquakes.

Three thousand five hundred eighty four strong motion records with moment magnitude $M_W \geq 5.0$, Joyner-Boore distance (the closest distance to the surface projection of an extended seismogenic fault) ≤200 km, and PGA ≥.3 m s^{-2} were used. The sample capacities of records on each site class grouped by moment magnitude, Joyner-Boore distance or PGA were listed in Table 4. There were most strong motion records on site class II, and their distribution was relatively uniform grouped by moment magnitude, Joyner-Boore distance or PGA. There were fewer records on site class I and site class III, and only 30 records on site class IV.

According to the lowest usable frequency of each strong motion record given by NGA-West2 database, the Sa values exceeding the corresponding period were eliminated. Consequently, 100% of the 3,584 records were used in the statistics of Sa when period $T \leq 1.0$ s, while 97.0% when 1.0 s < $T \leq 2.0$ s, 80.9% when 2.0 s < $T \leq 4.0$ s, and 70.1% when 4.0 s < $T \leq 6.0$ s.

TABLE 4 Sample capacities of records from NGA-West2 database on each site class.

Consideration	Interval	Site class I	Site class II	Site class III	Site class IV
Moment magnitude	5.0–5.5	81	303	22	0
	5.5–6.0	114	294	35	0
	6.0–6.5	227	463	206	1
	6.5–7.0	276	575	136	27
	7.0–7.5	76	272	29	0
	7.5–8.0	119	227	99	2
Joyner-Boore distance (km)	0–10	127	474	34	2
	10–30	271	460	75	6
	30–60	281	682	147	5
	60–100	158	364	172	4
	100–200	56	334	99	13
PGA (m·s^{-2})	.3–0.5	209	576	157	10
	.5–1.0	286	610	193	9
	1.0–2.0	217	581	117	6
	2.0–4.0	133	252	44	4
	>4.0	48	115	16	1
Total		893	2,134	527	30

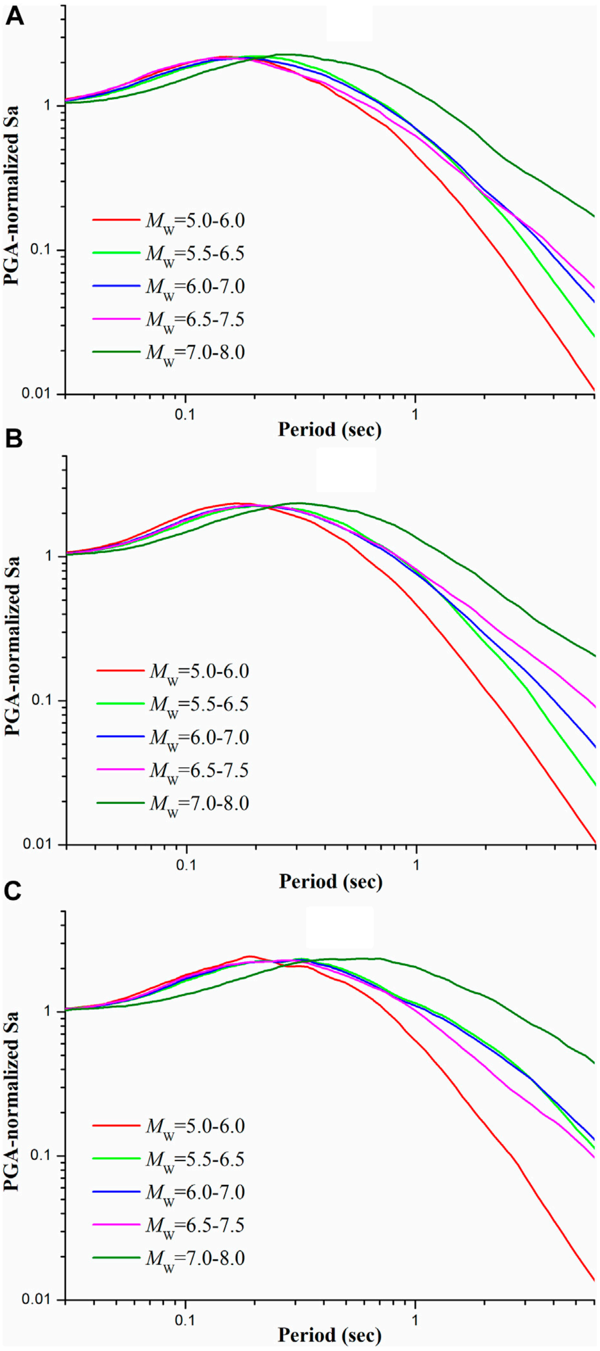

FIGURE 3
Mean values for PGA-normalized Sa with different moment magnitude intervals on **(A)** site class I, **(B)** site class II, and **(C)** site class III.

4.2 PGA-normalized Sa

The PGA-normalized Sa was defined as the quotient of Sa with 5% damping ratio divided by PGA of each strong motion record. The site condition represented by the site class, earthquake magnitude represented by the moment magnitude M_W, source distance represented by the Joyner-Boore distance, and ground motion strength represented by PGA, were selected as the key influences on PGA-normalized Sa in this study, for they significantly affected Sa. Only PGA-normalized Sa on site class I, II, and III was analysed due to the small sample capacity of records on the site class IV.

The mean values of PGA-normalized Sa with different moment magnitude intervals were shown in Figure 3, which indicated that:

1) PGA-normalized Sa was significantly affected by the moment magnitude.
2) Generally, the medium-to-long period ($T > .20$ s on site class I, $T > .24$ s on site class II, and $T > .30$ s on site class III) segments of PGA-normalized Sa remarkably increased with the increase of the moment magnitude.
3) The short period ($T < .20$ s on site class I, $T < .24$ s on site class II, and $T < .30$ s on site class III) segments of PGA-normalized Sa with moment magnitude M_W = 5.0–7.5 were almost identical to each other, while their values were slightly larger than the values with moment magnitude M_W = 7.0–8.0.
4) The differences among the PGA-normalized Sa with moment magnitude M_W = 5.5–6.5, 6.0–7.0, and 6.5–7.5, were much slighter comparing the differences among other moment magnitude intervals. It might be caused by the geometry of seismogenic faults, which could be simplified to be a point source in a small earthquake, an area source of several square kilometers in a medium earthquake, and a rectangle source tens to more than 100 km long in a great earthquake.
5) The medium period (.30 s < T < 3.00 s) segments on site class I, and long period (T > 1.00 s) segments on site class III with moment magnitude M_W = 6.5–7.5, were abnormally small.

The mean values of PGA-normalized Sa with different Joyner-Boore distance intervals and with different PGA intervals were shown in Figure 4. It could be concluded that:

1) PGA-normalized Sa was slightly affected by the Joyner-Boore distance or PGA comparing with the influence caused by the moment magnitude.
2) From a global perspective, the medium-to-long period segments of PGA-normalized Sa increased with the increase of Joyner-Boore distance, and decreased with the increase of PGA in an imperceptible degree.

4.3 Residual analyses after removing the influence of moment magnitude

In order to further analyse the dependence of the PGA-normalized Sa on the source distance and the ground motion strength, residual analyses were used to remove the influence of the most significant influence factor, namely moment magnitude. According to the moment magnitude and site class corresponding to each strong motion record, fitting values of PGA-normalized Sa of the record were obtained from the data shown in Figure 3 using linear interpolation under logarithmic coordinates. By subtracting the fitting values from the calculated PGA-normalized Sa of each strong motion record, the residuals of logarithmic PGA-normalized Sa were obtained.

The residuals of logarithmic PGA-normalized Sa with different Joyner-Boore distance intervals were shown in Figures 5A–C, which indicated that:

1) The regularity of residual curves with the Joyner-Boore distance on site class I, II and III was weak, which meant that PGA-normalized Sa and the Joyner-Boore distance had weak correlation.

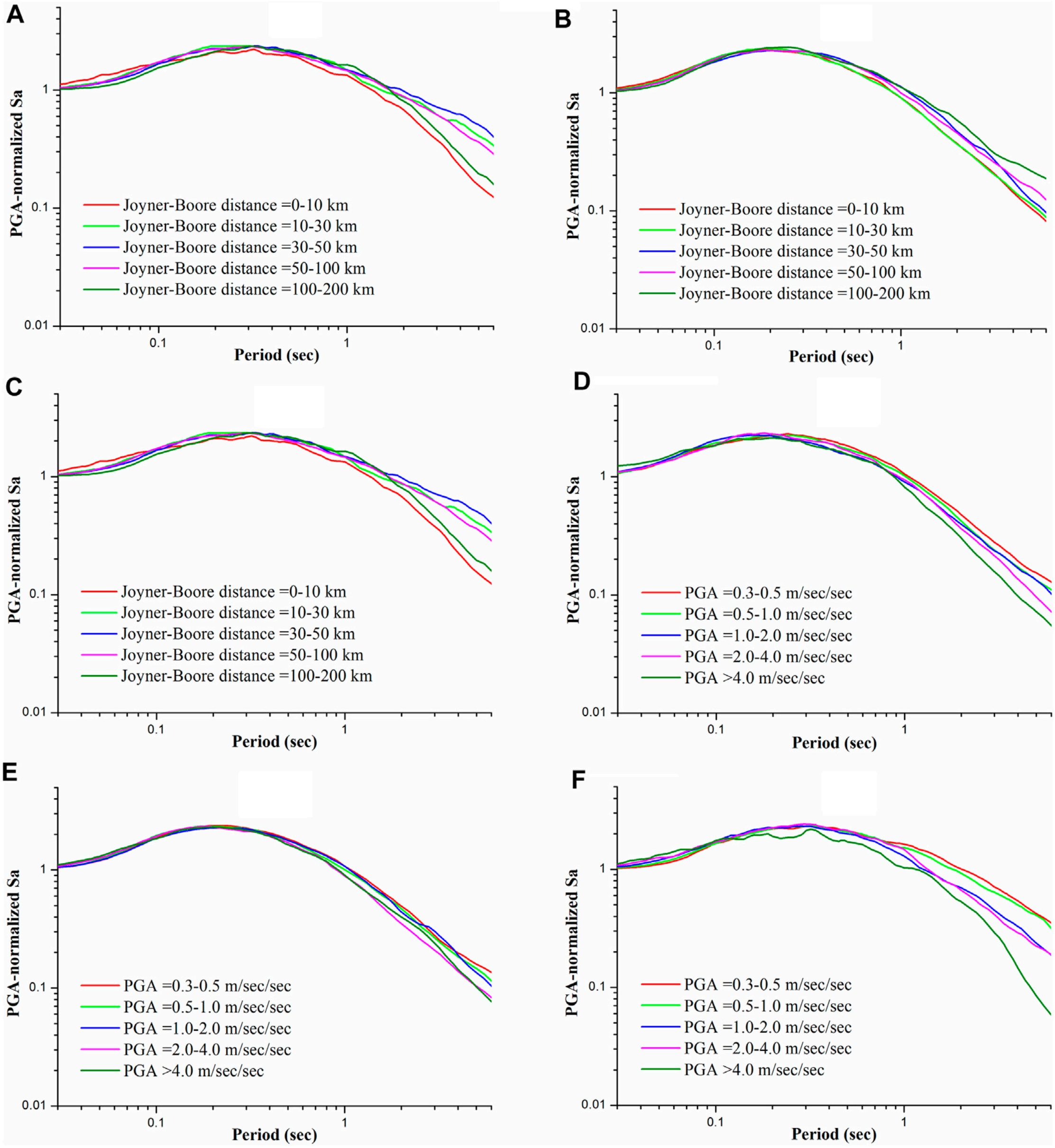

FIGURE 4
Mean values for PGA-normalized Sa with different Joyner-Boore distance intervals on **(A)** site class I, **(B)** site class II, **(C)** site class III, and mean values for PGA-normalized Sa with different PGA intervals on **(D)** site class I, **(E)** site class II, and **(F)** site class III.

2) The discreteness of residuals caused by the Joyner-Boore distance was sufficiently small, within $10^{\pm .1}$ on site class I and II, as well as on site class III when $T \leq .20$ s.

The residuals of logarithmic PGA-normalized Sa with different PGA intervals were shown in Figures 5D–F, which indicated that:

1) When $T < .20$ s, the discreteness of residuals caused by PGA was within $10^{\pm .05}$ on site class I, II, and III.
2) When $T > .30$ s, the residuals regularly decreased with the increase of PGA; meanwhile, the differences among the residuals with different PGA intervals gradually increased with the increase of periods.

Comparisons of the residuals in Figure 5 showed that the PGA-normalized Sa was much more significantly correlated with PGA than with the Joyner-Boore distance. In other words, PGA was a more sensitive variable than the Joyner-Boore distance in the determination of PGA-normalized Sa.

Incidentally, PGA and the Joyner-Boore distance were not completely independent variables in an earthquake, for PGA was negatively correlated with the source distance statistically as a result of the strong motion attenuation. Meanwhile, on rock sites with small source distances, the long-period Sa normalized by PGA was known to be smaller than that on the rock sites with large source distances; but at the same time, stronger non-linearity of overburden layers would amplify the long-period Sa on soil sites with smaller source distances. The influences on PGA-

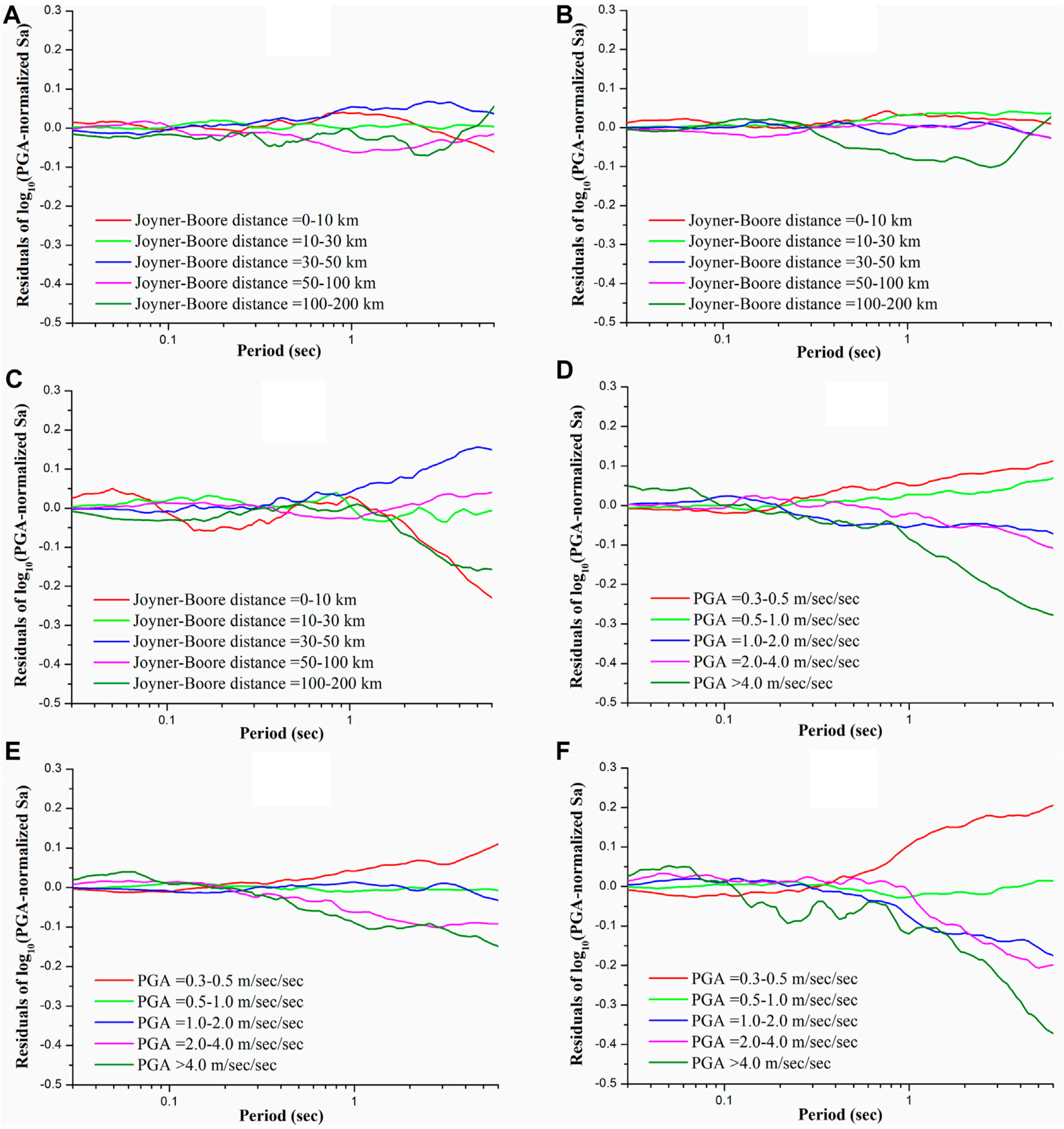

FIGURE 5
Residuals of logarithmic PGA-normalized Sa with different Joyner-Boore distance intervals on **(A)** site class I, **(B)** site class II, **(C)** site class III, and residuals of logarithmic PGA-normalized Sa with different PGA intervals on **(D)** site class I, **(E)** site class II, and **(F)** site class III.

normalized Sa caused by PGA and source distance, which offset each other, were a subject worthy of further study.

4.4 Scaling ratios for PGA-normalized Sa on site class II and III

The quotients of PGA-normalized Sa on site class II and III divided by PGA-normalized Sa on site class I with each moment magnitude interval were shown in Figures 6A, B, which indicated that:

1) When $T < 1.00$ s, the quotients with different moment magnitude intervals on the same site class were identical to each other within acceptable deviations.
2) When $T > 1.00$ s, the deviations of the quotients with different moment magnitude intervals increased with the increase of periods, and this trend was more significant on site class III than on site class II.

The above phenomenon could be explained by Figure 5, which showed that the Joyner-Boore distance and PGA significantly affected the PGA-normalized Sa when $T > 1.00$ s. Further considerations of the Joyner-Boore distance and PGA during the calculation would probably lower the deviations.

In order to eliminate the impact of source spectra differences in different earthquakes, earthquakes with no less than five strong motion records on site class I as well as on site class II or III were selected. The quotients of PGA-normalized Sa on site class II or III divided by PGA-normalized Sa on site class I in the same selected earthquake, and their mean values weighted by square roots of the sample capacities on site class I and on site class II or III, were shown in Figures 6C, D, which indicated that:

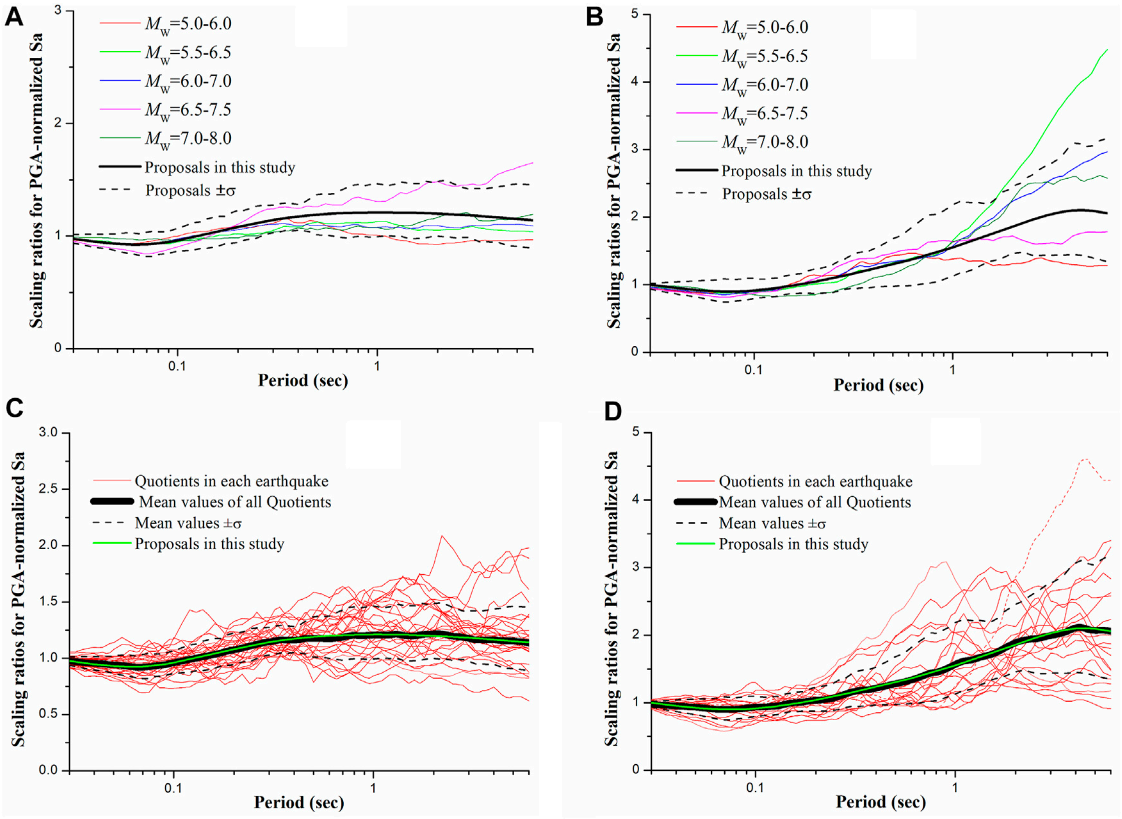

FIGURE 6
Quotients of PGA-normalized Sa on **(A)** site class II, **(B)** site class III divided by PGA-normalized Sa on site class I with different moment magnitude intervals, and quotients of PGA-normalized Sa on **(C)** site class II, **(D)** site class III divided by PGA-normalized Sa on site class I in the same selected earthquake. The scaling ratios proposed in this study were shown in green curves.

1) The deviations of the quotients calculated in the same selected earthquake were obviously larger than the deviations of quotients calculated in the same moment magnitude intervals shown in Figures 6A, B.
2) The mean values of quotients calculated in the same selected earthquake were almost identical to the average quotients calculated in the same moment magnitude intervals shown in Figures 6A,B.

The smoothen fittings for the mean values of quotients in Figures 6C,D were proposed as the scaling ratios of PGA-normalized Sa on site class II and III versus on site class I_1 in this study, which were shown as green curves. The proposed scaling ratios of PGA-normalized Sa could reflect the average impact of site conditions on spectral compositions on site class II and III as shown in Figures 6A,B, but in a particular earthquake, it would yield great error as shown in Figures 6C,D. As a consequence, the proposed scaling ratios could be used to estimate the seismic site effect for general projects with large quantities and wide areas with an acceptable accuracy in a statistical sense, but they would be non-negligible inaccurate on a particular engineering site in a particular earthquake.

4.5 Scaling ratios for PGA-normalized Sa on site class IV

The PGA-normalized Sa with different moment magnitude intervals on site class IV could not be reliably obtained because of the small sample capacity of only 30 strong motion records as listed in Table 4. So 26 strong motion records with moment magnitude M_W = 6.61–6.93 were used to calculate the PGA-normalized Sa on site class IV for second best as shown in Figure 7A. Meanwhile, the average PGA-normalized Sa on site class I with moment magnitude $M_W \approx 6.75$, which was the average moment magnitude of the 26 records on site class IV, were also calculated as shown in Figure 7A. The quotients of PGA-normalized Sa on site class IV with moment magnitude M_W = 6.61–6.93 divided by PGA-normalized Sa on site class I with moment magnitude $M_W \approx 6.75$ were shown as a black curve in Figure 7C as a black curve.

Four earthquakes with no less than five strong motion records on site class I as well as on site class IV were selected to eliminate the impact of source spectra differences, one of which was excluded in the calculation of mean values because of the excessive deviation. The quotients of PGA-normalized Sa on site class IV divided by PGA-normalized Sa on site class I in the same selected earthquake, and their mean values weighted by square roots of the sample

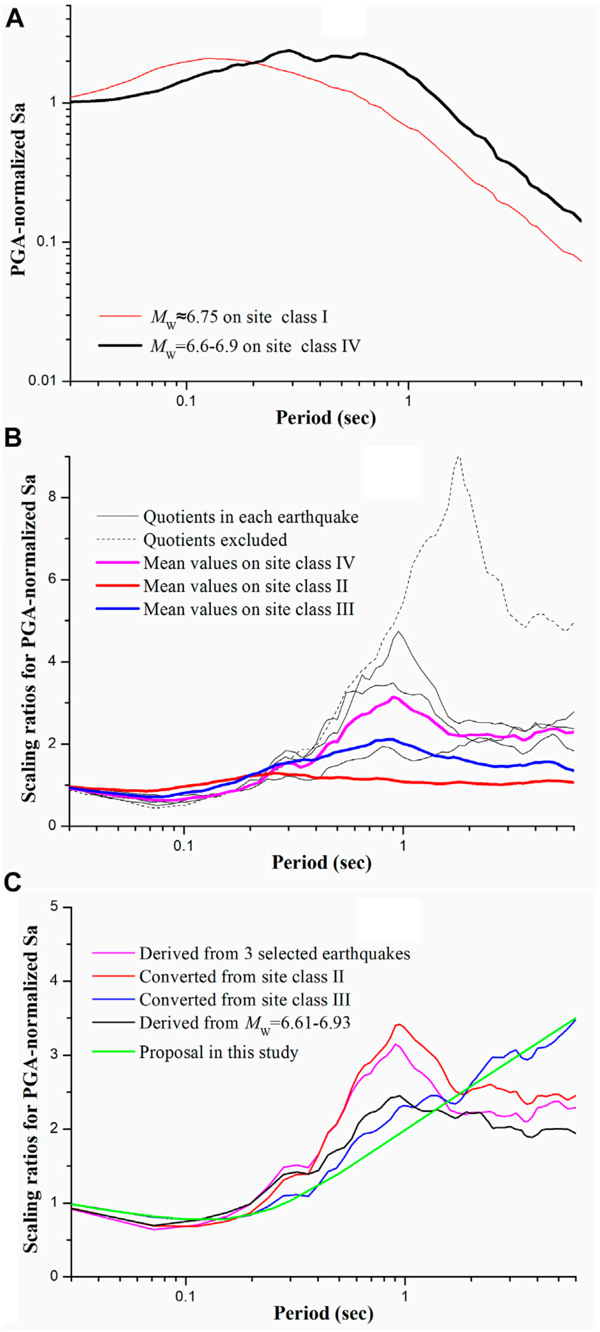

FIGURE 7
Mean values of PGA-normalized Sa on site class IV with moment magnitude M_W = 6.61–6.93 and on site class I with moment magnitude $M_W \approx 6.75$ **(A)**, the quotients for PGA-normalized Sa on site class IV given by records in the three selected earthquakes **(B)** and the indirect conversion **(C)**.

capacities on site class I and on site class IV were shown in Figure 7B, which indicated that:

1) The deviations of the quotients calculated in the same selected earthquake on site class IV were even much larger than these on site class III as shown in Figure 6D.
2) There was an obvious peak at T = .90 s on the curve of average quotients on site class IV. The period of this peak was inconsistent with the result on site class III as shown in Figure 6D.

In order to distinguish whether the obvious difference between the scaling ratios on site class IV and on site class III were caused by the source spectra of selected earthquakes, the mean values of quotients given by records in the three selected earthquakes on site class II and on site class III were also given in Figure 7B. It indicated that the trend of quotients on site class III given by records in the three earthquakes was comparable with quotients on site class IV, but significantly different from the scaling ratios on site class III given in Figure 6D. So it could be concluded that the uniqueness of source spectra in the three earthquakes might be the reason for this different trend.

Consequently, the quotients of PGA-normalized Sa on site class IV versus on site class I by an indirect conversion to eliminate the uniqueness of source spectra were shown in Figure 7C. To be more specific, the mean values of quotients of PGA-normalized Sa on site class IV in Figure 7B were divided by the quotients of PGA-normalized Sa on site class II or III in Figure 7B, and then multiplied the scaling ratios on site class II or III given in Figure 6C or Figure 6D. It could be concluded that:

1) The quotients calculated by 26 strong motion records with moment magnitude M_W = 6.61–6.93 were smaller than the mean values of quotients calculated by records in three selected earthquakes and the quotients converted from site class II. But the three of them shared the same trend, i.e., a peak at period T = .90 s, and relatively small values when period T > 2.00 s.
2) The quotients converted from site class III showed in a blue curve showed a very different trend, but they were comparable with the scaling ratios on site class III in Figure 6D.

Since the classification criteria for the site class IV were close to the site class III only with a smaller equivalent shear-wave velocity and a larger overburden thickness as listed in Table 1, and the peak at period T = .90 s was probably caused by unique source spectra, we proposed the smoothed quotients converted from site class III to be the scaling ratios for PGA-normalized Sa on the site class IV, which were shown in a green curve in Figure 7C.

5 Non-linear decay exponents

5.1 Data resource

More than 140,000 strong motion records at 137 stations in KiK-net (Kiban Kyoshin Network) were used in this section. The maximum peak acceleration of downhole records at each station ≥.75 m s^{-2}. According to the site condition classification criteria in China listed in Table 1, 15 stations were on site class I$_1$, 107 stations were on site class II, 12 stations were on site class III, and only three stations were on site class IV.

5.2 Non-linear decay of surface/borehole Sa

The quotients of Sa on the ground surface divided by Sa in the borehole, i.e., surface/borehole (S/B) Sa, obtained in the same earthquake of each station were calculated, and then the average platform value of surface/borehole Sa were determined using the similar concept as the

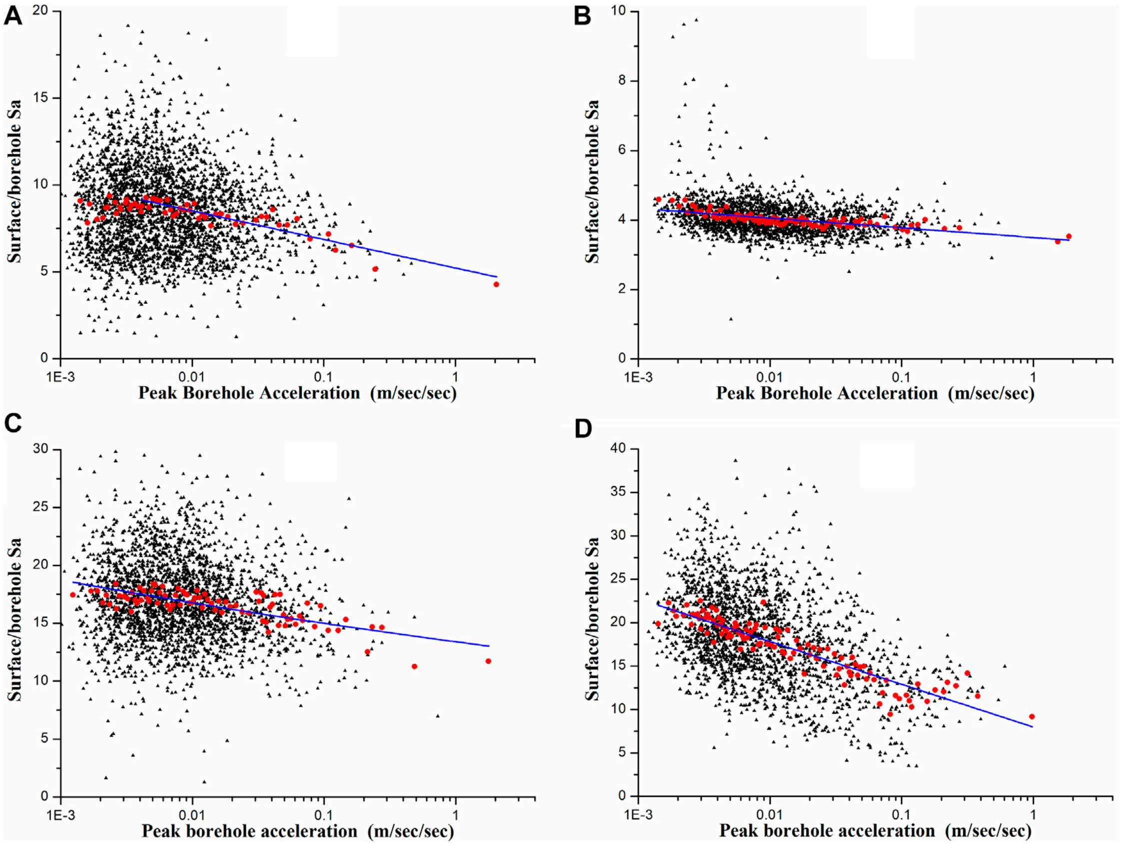

FIGURE 8
The scatter diagrams, their smoothed mean values, and linear fittings for the platform values of surface/borehole Sa at **(A)** Station TCGH10 on site class I_1, **(B)** Station FKSH11 on site class II, **(C)** Station TCGH16 on site class III, and **(D)** Station IBRH10 on site class IV.

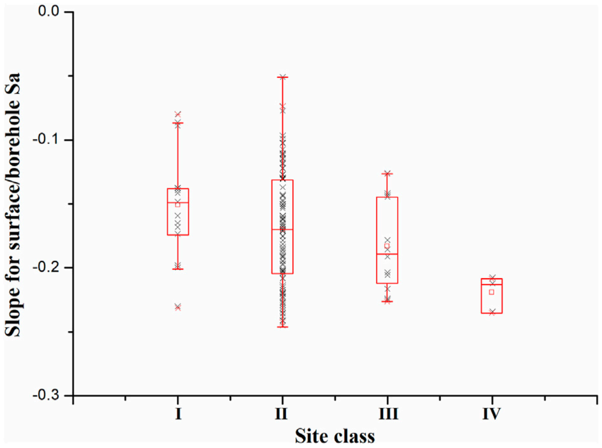

FIGURE 9
The scatter diagrams and box-plots for the slopes of the linear fittings for platform values of surface/borehole Sa for all the 137 stations on each site class.

calculation of EPA but at a variable period range (Ding et al., 2021). The scatter diagrams of the average platform values at four stations were shown in Figure 8, which indicated that large discreteness still could not hide the decay trend with strong motion strength. The mean values of the platform values in a variable sample capacity window narrowing with the increase of the strong motion strength were also shown in Figure 8 as red bold dots, which showed a clearer linear decay trend under semi-logarithmic coordinates than the platform values shown in black dots.

The slopes of the linear fittings for platform values at all the 137 station were shown in Figure 9, which indicated that the slopes were smaller on sites with softer and thicker overburdens, even though there was considerable overlap between two adjacent site classes.

5.3 Proposed non-linear decay exponents

The median slopes of the linear fittings for platform values of surface/borehole Sa under semi-logarithmic coordinates, i.e., −.150 on site class I_1, −.169 on site class II, −.182 on site class III, and −.218 on site class IV, were proposed as the non-linear decay exponents of Sa as a temporary compromise. The non-linear decay exponents on site class I_0 was proposed to be 0.

The non-linear decay exponents should be derived from the quotients of Sa on soil sites divided by Sa on rock sites, namely, soil/rock Sa, under the same strong motion inputs, or at least when the distance between the soil site and the rock site was negligible compared with their source distance. There would be an error induced by the assumption that the non-linear decay exponents of surface/borehole

TABLE 5 Scaling ratios for Sa due to site conditions varying with PGA on site class I_1.

Sa	Site class	*PGA* on site class I_1 (m s^{-2})					
		≤0.5	1.0	1.5	2.0	3.0	≥4.0
PGA (T = 0 s)	I_0	.80	.84	.86	.87	.89	.91
	I_1	1.00	1.00	1.00	1.00	1.00	1.00
	II	1.39	1.38	1.38	1.37	1.37	1.37
	III	1.30	1.29	1.28	1.27	1.27	1.26
	IV	1.16	1.14	1.12	1.11	1.10	1.09
T = .3 s	I_0	.80	.84	.86	.87	.89	.91
	I_1	1.00	1.00	1.00	1.00	1.00	1.00
	II	1.59	1.58	1.57	1.57	1.56	1.56
	III	1.49	1.48	1.47	1.47	1.46	1.45
	IV	1.19	1.17	1.16	1.15	1.13	1.12
T = 1.0 s	I_0	.80	.84	.86	.87	.89	.91
	I_1	1.00	1.00	1.00	1.00	1.00	1.00
	II	1.68	1.67	1.67	1.66	1.66	1.65
	III	2.01	2.00	1.98	1.98	1.96	1.96
	IV	2.31	2.26	2.23	2.21	2.19	2.17
T = 3.0 s	I_0	.80	.84	.86	.87	.89	.91
	I_1	1.00	1.00	1.00	1.00	1.00	1.00
	II	1.64	1.63	1.63	1.62	1.62	1.61
	III	2.64	2.61	2.60	2.59	2.57	2.56
	IV	3.39	3.32	3.28	3.25	3.21	3.18

Sa were identical to soil/rock Sa. But as there were not sufficient number of samples to obtain soil/rock Sa, the slopes of the linear fittings for platform values of surface/borehole Sa might be approximately regarded to be the non-linear decay exponents of soil/rock Sa (Li et al., 2021).

6 Proposed scaling ratios for sa

According to the scaling ratios for PGA, scaling ratios for PGA-normalized Sa, and non-linear decay exponents given by above statistics, the scaling ratios for Sa on site class I_0, I_1, II, III, and IV were proposed as following:

$$F_i\left(T, PGA_{I_1}\right) = \alpha_i \beta_i(T)\left[1 + \left(\gamma_i - \gamma_{I_1}\right)\log_{10}\frac{PGA_{I_1}}{0.5}\right] \tag{4}$$

where the site class $i = I_0, I_1$, II, III, or IV; T was the period in second; PGA_{I_1} was the peak ground acceleration on site class I_1 in m s^{-2}; $F_i(T, PGA_{I_1})$ were the scaling ratios for Sa at period T on site class i when the peak ground acceleration on site class I_1 was PGA_{I_1}; scaling ratio for PGA $\alpha_i = .80, 1.00, 1.39, 1.30$, or 1.16 for $i = I_0, I_1$, II, III, or IV when $PGA_{I_1} = .5$ m s^{-2}; non-linear decay exponent $\gamma_i = .000, -.150, -.169, -.182$, or $-.218$ for $i = I_0, I_1$, II, III, or IV; scaling ratios for PGA-normalized Sa, $\beta_i(T)$, were shown in Figures 6C, D, 7C in green curves for i = II, III, or IV, and $\beta_i(T) \equiv 1$ for $i = I_0$ and I_1.

The scaling ratios for PGA, Sa (T = .30 s), Sa (T = 1.00 s), and Sa (T = 3.00 s) varying with PGA_{I_1} were listed in Table 5, and the curves of scaling ratios for Sa when PGA_{I_1} = .5, 1.0, 1.5, 2.0, 3.0, 4.0 m s^{-2} and their corresponding values in “GB18306: Seismic ground motion parameters zonation map of China” (Ministry of Housing and Urban-Rural Development of the People's Republic of China, General Administration of Quality Supervision, Inspection and Quarantine of the People's Republic of China, 2010) were shown in Figure 10, which indicated that:

1) The non-linearities of scaling ratios for Sa varying with strong motion strength on site class I_1 were imperceptibly indeed comparing with GB18306. One reason for this phenomenon was the consideration of non-linearity on site class I_1 in this study, and another possible reason was that the non-linear decay exponents for soil/rock Sa were not identical to the non-linear decay exponents for surface/borehole Sa.
2) The scaling ratios for Sa on site class II, the scaling ratios for Sa at $T < .4$ s on site class III when $PGA_{I_1} \leq 2.0$ m s^{-2}, and the scaling ratios for Sa at $T < .6$ s on site class IV when $PGA_{I_1} \geq 3.0$ m s^{-2}, were comparable with GB18306.
3) The scaling ratios for Sa at .4 s < T < 2.0 s on site class III, and the scaling ratios for Sa at .6 s < T < 2.0 s on site class IV were smaller than or comparable with GB18306, while the scaling ratios for Sa at T > 2.0 s on site class III and IV were obviously larger than GB18306.

To sum up, the non-linearity of scaling ratios for Sa on site class I_1 was non-ignorable, and the proposed scaling ratios on site class II were comparable with GB18306, meanwhile the proposed scaling ratios on site class III and IV were smaller at medium periods .5 s < T < 2.0 s and larger at long periods T > 2.0 s than GB18306.

7 Conclusion and discussions

Based on numerical simulations of 1,138 borehole models in China, 3,584 strong motion records in NGA West two database, and about 140 thousand borehole observation data recorded by KiK-net, a novel approach assembled by scaling ratios for PGA, scaling ratios for PGA-normalized Sa, and non-linear decay exponents, was proposed.

1) The scaling ratios for PGA derived from numerical simulations of borehole models when motions were not so strong were acceptable, but one-dimensional equivalent linearization method might overestimate the non-linearity of soil when motions were strong enough for engineering significance.
2) The scaling ratios for PGA-normalized Sa derived from the strong motion records in NGA-West two database could reflect the average impact of site conditions on spectral compositions, but they would yield great errors in a particular earthquake on an actual site.
3) The non-linear decay exponents of surface/borehole Sa were negatively correlated with site classes, and the non-linear decay exponent on site class I_1 was non-ignorable.

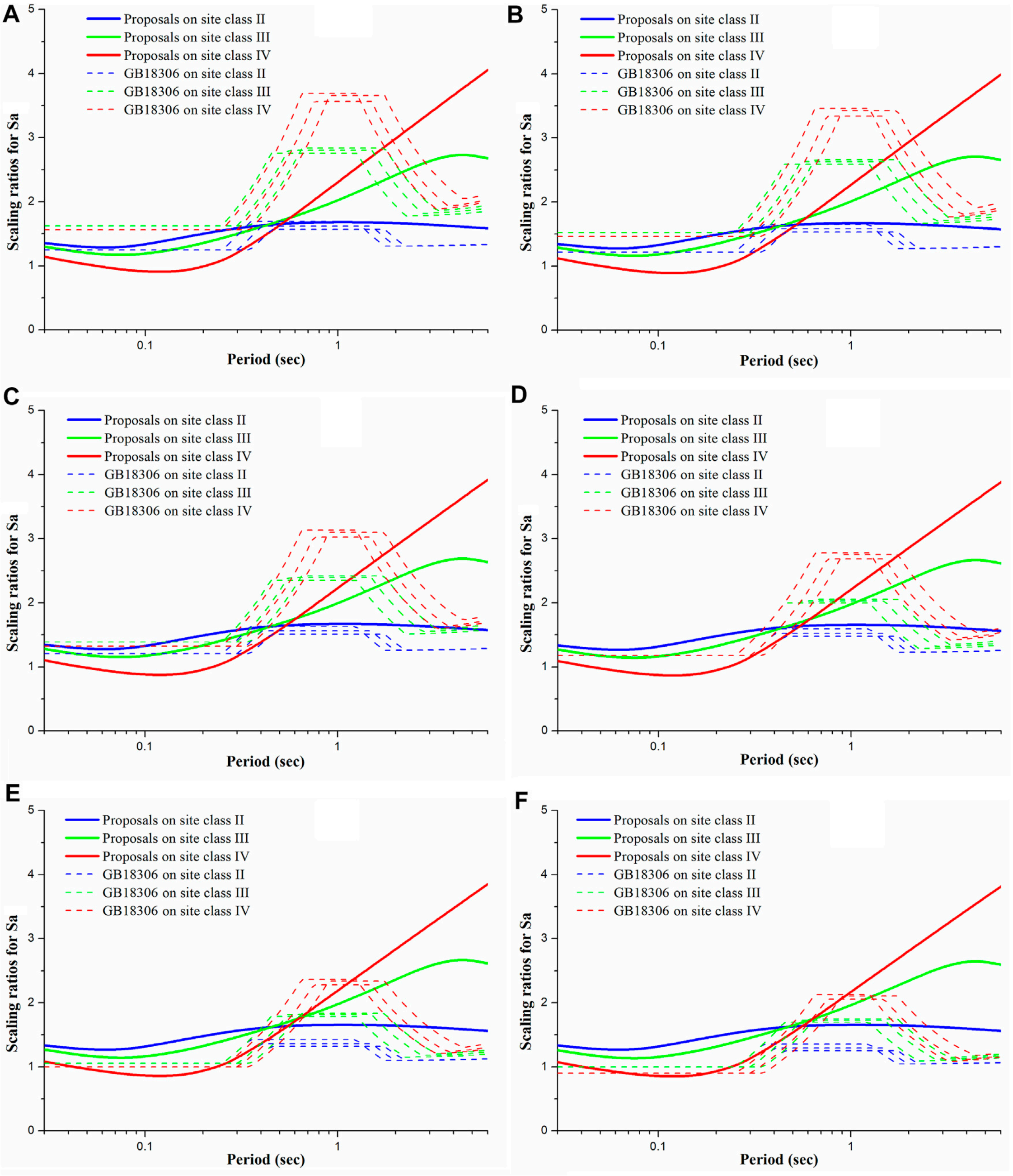

FIGURE 10
Scaling ratios for Sa on site class II, III, and IV when PGA on site class I$_1$ **(A)** ≤.5 m s^{-2}, **(B)** = 1.0 m s^{-2}, **(C)** = 1.5 m s^{-2} **(D)** = 2.0 m s^{-2}, **(E)** = 3.0 m s^{-2}, and **(F)** ≥4.0 m s^{-2}.

4) The scaling ratios for Sa proposed in this study offered an option to determine the impact on Sa caused by seismic site effect on each site class under site condition classifications in China.

Further improvements were also needed to improve the reliability and applicability of the proposed scaling ratios for Sa.

1) The influences of the source distance and the strong motion strength on PGA-normalized Sa needed more considerations.
2) The strong motions on site class I$_0$ and on site class I$_1$ should be distinguished in detail, especially in the determination of non-linear decay exponents. Ignorance of non-linearity on site class I$_1$ might significantly affect the non-linearity of scaling ratios for Sa on all the site classes, which was a common problem in recent studies and current regulations.
3) The non-linear decay exponents of soil/rock Sa needed to be built considering the inconsistency between the soil/rock Sa and surface/borehole Sa.
4) Additionally, scaling ratios on site class IV needed to be paid more attentions because of limited sample capacity.

Data availability statement

The original contributions presented in the study are included in the article/Supplementary Material, further inquiries can be directed to the corresponding author.

Author contributions

All authors listed have made a contribution to conception and design of the study, and approved it for publication. Scaling ratios for PGA: XL. Non-linear decay exponents: YD. Scaling ratios for PGA-normalized Sa and other sections: YW. Writing-original Draft: YW. Writing-reviewing and editing: YW and XL. All authors contributed to manuscript revision, read, and approved the submitted version.

Funding

This study is supported by the National Key R&D Program of China (2022YFC3003503) and National Natural Science Foundation of China (52192675).

Acknowledgments

We acknowledge with thanks the strong motion data from KiK-net of National Research Institute for Earth Science and Disaster Resilience (NIED), and from NGA-West2 database of the Pacific Earthquake Engineering Research Center (PEER). We also owed sincere thanks to two reviewers for their constructive comments optimizing our statistical results.

Conflict of interest

The authors declare that the research was conducted in the absence of any commercial or financial relationships that could be construed as a potential conflict of interest.

Publisher's note

Supplementary material

The Supplementary Material for this article can be found online at: https://www.frontiersin.org/articles/10.3389/feart.2022.1112202/full#supplementary-material

References

Aki, K. (1993). Local site effects on weak and strong ground motion. *Tectonophysics* 218 (1-3), 93–111. doi:10.1016/0040-1951(93)90262-i

Bian, F. D., and Ding, H. P. (2017). Estimation and application of depth correction factor for site coefficient based on KiK-net strong-motion seismograph network. *J. Suzhou Univ. Sci. Technol. Eng. Technol.* 30 (4), 1456–1519.

Bo, J. S., Li, Q., Qi, W. H., Yuting, W., Xinlong, Z., et al. (2021). Research progress and discussion of site condition effect on ground motion and earthquake damage. *J. Jilin Univ. (Earth Sci. Ed.* 51 (5), 1295–1305.

Bo, J. S. (1998). *Site classification and design response spectrum adjustment method*. Harbin, China, Earthquake Administration: Institute of Engineering Mechanics.

Boore, D. M. (2004). Estimating s(30) (or NEHRP site classes) from shallow velocity models (depths < 30 m). *Bull. Seismol. Soc. Am.* 94 (2), 591–597. doi:10.1785/0120030105

Cui, H., and Ding, H. P. (2016). Estimation of site coefficient based on KiK-net strong-motion seismograph network. *Earthq. Eng. Eng. Vib.* 36 (4), 147–152.

Ding, Y., Wang, Y. S., Wang, N., et al. (2021). Study on nonlinear statistical characteristics of surface/downhole response spectrum ratio and influencing factors. *Technol. Earthq. Disaster Prev.* 16 (2), 362–370.

General Administration of Quality Supervision, Inspection and Quarantine of the People's republic of China (2016). *Seismic ground motion parameters zonation map of China* (Beijing, China: China Quality and Standards Publishing & Media Co.,Ltd), GB18306.

Geng, S. W. (2005). *Strong ground motion input parameter for seismic design*. Harbin, China, Earthquake Administration: Institute of Engineering Mechanics, 44–69.

Guo, F., Wu, D. M., Xu, G. F., et al. (2011). Effect of site condition on the maximum value of seismic design response spectrum. *J. Civ. Eng. Manag.* 28 (1), 69–72.

Hu, Y. X. (2006). *Earthquake engineering*. 2nd. Beijing, China: Seismological Press.

Hu, Y. X., Sun, P. S., Zhang, Z. Y., et al. (1980). Effects of site conditions on earthquake damage and ground motion. *Earthq. Eng. Eng. Vib.* 0 (0), 34–41.

Lan, J. Y., Lv, Y. J., and Liu, H. S. (2012). Influence of intensity and frequency of ground motion on site earthquake response. *Technol. Earthq. Disaster Prev.* 7 (1), 37–45.

Li, X. J. (2013). Adjustment of seismic ground motion parameters considering site effects in seismic zonation map. *Chin. J. Geotechnical Eng.* 35 (S2), 21–29.

Li, X. J., Li, N., Wang, J. K., et al. (2021). Difference between horizontal-to-vertical spectral ratio and surface-to-bedrock spectral ratio of strong-motion and modified horizontal-to-vertical spectral ratio method. *Technol. Earthq. Disaster Prev.* 16 (1), 81–90.

Li, X. J., Pen, Q., and Liu, W. Z. (2001). Consideration of site effects for determination of design earthquake ground motion parameters. *Word Inf. Earthq. Eng.* 17 (4), 34–41.

Li, X. J., and Peng, Q. (2001). Calculation and analysis of earthquake ground motion parameters for different site categories. *Earthq. Eng. Eng. Vib.* 21 (1), 29–36.

Liu, Z., Shen, J. W., Shi, S. Z., et al. (2009). Soft soil amplification of peak ground acceleration. *J. Tongji Univ. Nat. Sci.* 37 (5), 607–611.

Lü, H. S., and Zhao, F. X. (2007). Site coefficients suitable to China site category. *Acta Seismol. Sin.* 29 (1), 71–79. doi:10.1007/s11589-007-0071-6

Lu, Y. J., Peng, Y. J., Lan, J. Y., et al. (2008). Some key problems about site effects on seismic ground motion parameters. *Technol. Earthq. Disaster Prev.* 3 (2), 126–135.

Ministry of Housing and Urban-Rural Development of the People's Republic of China, General Administration of Quality Supervision, Inspection and Quarantine of the People's Republic of China, (2010). *Code for seismic design of buildings*. Beijing, China: China Architecture & Building Press, GB50011, 18–35.

Seed, H. B., and Idriss, I. M. (1969). Influence of soil conditions on ground motions during earthquakes. *J. Soil Mech. Found. Div.* 95 (1), 99–137. doi:10.1061/jsfeaq.0001260

Stewart, J. P., and Seyhan, E. (2013). *Semi-empirical nonlinear site amplification and its application in NEHRP site factors*. Oakland, CA, USA: University of California.

Wang, Y., Li, X., Li, M., et al. (2022). Study on scaling ratios for spectral accelerations of ground motion due to site conditions. *Technol. Earthq. Disaster Prev.* 17 (3), 464–472.

Zhao, Y., Guo, M. Z., Li, H. M., et al. (2009). Contrast analysis of effect of site condition on the maximum of design response spectra. *Seismol. Geol.* 31 (1), 186–196.

frontiers | Frontiers in Earth Science

TYPE Technology and Code
PUBLISHED 10 January 2023
DOI 10.3389/feart.2022.1056485

OPEN ACCESS

EDITED BY
Yefei Ren,
Institute of Engineering Mechanics, China Earthquake Administration, China

REVIEWED BY
Andrea Montanino,
University of Naples Federico II, Italy
Ba Zhenning,
Tianjin University, China

*CORRESPONDENCE
Chen Shaolin,
✉ iemcsl@nuaa.edu.cn

SPECIALTY SECTION
This article was submitted to Structural Geology and Tectonics, a section of the journal Frontiers in Earth Science

RECEIVED 28 September 2022
ACCEPTED 19 December 2022
PUBLISHED 10 January 2023

CITATION
Jirong S, Shaolin C, Jiao Z and Puxin C (2023), Unified framework based parallel FEM code for simulating marine seismoacoustic scattering.
Front. Earth Sci. 10:1056485.
doi: 10.3389/feart.2022.1056485

Unified framework based parallel FEM code for simulating marine seismoacoustic scattering

Shen Jirong[1], Chen Shaolin[1,2]*, Zhang Jiao[1] and Cai Puxin[2]

[1]College of Aerospace Engineering, Nanjing University of Aeronautics and Astronautics, Nanjing, China,
[2]College of Civil Aviation, Nanjing University of Aeronautics and Astronautics, Nanjing, China

The simulation of seismic wave propagation in marine areas, which belongs to seismoacoustic scattering problem, is complicated due to the fluid-solid interaction between seawater and seabed, especially when the seabed is saturated with fluid. Meanwhile, huge computation resources are required for large-scale marine seismic wave simulation. In the paper, an efficient parallel simulation code is developed to solve the near-field seismoacoustic scattering problem. The method and technologies used in this code includes: 1) Unified framework for acoustic-solid-poroelastic interaction analysis, in which seawater and dry bedrock are considered as generalized saturated porous media with porosity equals to one and zero, respectively, and the coupling between seawater, saturated seabed and dry bedrock can be analyzed in the unified framework of generalized saturated porous media and avoid interaction between solvers of different differential equation; 2) Element-by-element strategy and voxel finite-element method (VFEM), with these strategies, it only needs to calculate several classes of element matrix and avoid assembling and storing the global system matrices, which significantly reduces the amount of memory required; 3) Domain-partitioning procedure and parallel computation technology, it performs 3D and 2D model partitioning for the 3D and 2D codes respectively, sets up the velocity structure model for the partitioned domain on each CPU or CPU core, and calculates the seismic wave propagation in the domain using Message Passing Interface data communication at each time step; 4) Local transmitting boundary condition, we adopt multi-transmitting formula, which is independent of specific wave equations, to minimize reflections from the boundaries of the computational model. A horizontal layered model with the plane P-wave incident vertically from bottom is used to demonstrate the computational efficiency and accuracy of our code. Then, the code is used to simulate the wave propagation in Tokyo Bay. All codes were written following to the standards of Fortran 95.

KEYWORDS

fluid-solid interaction, generalized saturated porous medium, marine seismoacoustic scattering, parallel computation, Tokyo Bay

1 Introduction

With the increasing exploitation and utilization of marine resources, a large number of marine engineering structures and infrastructures, such as oil platforms, cross-sea bridges, submarine tunnels, and artificial islands, have been constructed. In order to ensure the safety of these offshore structures under the action of earthquake, it is necessary to accurately predict the ground motion of the sea area. Currently, there are mainly three categories of ground motion predictions, which are known as prediction based on the attenuation relationship of ground motion, theoretical analysis prediction and numerical simulation prediction. For the prediction based on the attenuation relationship of ground motion, fewer offshore strong-motion records are gathered than the onshore strong-motion records, coupled with the lack of material parameters and spatial distribution of marine soil layers, which makes it difficult to determine the attenuation relationship of marine ground motions. Consequently, onshore strong-motion records are commonly selected for the seismic design of offshore structures. However, Nakamura et al. (2014) investigated the seismic wave amplification in and around the Kii peninsula using observation data analyses and numerical simulations from land (K-net) and seafloor stations (DONET), and the results indicate that the amplifications at the marine sites with low-velocity sediment layers partially contribute to an overestimation of magnitude, if the same empirical equations as those used for data observed at land stations are applied without any correction allowed for seismic amplification caused by ocean-specific structures. Similarly, Hu et al. (2020) pointed out that the seismic attenuation relationship of offshore site is significantly different from that of onshore site due to the deep soft sediment layer. For the theoretical analysis prediction, many researchers have simplified the sea area terrain into a regular model, and solved the marine ground motion response by theoretical methods (Brekhovskikh, 1980; Zhu, 1988; Okamoto and Takenaka, 1999; Li et al., 2017; Ke et al., 2019). However, this kind of method can only be applied to sites with regular terrain (such as horizontally layered sites), and cannot be directly used for ground motion simulation of offshore sites with complex terrain.

With the development of computer technology and the maturity of numerical calculation methods, some researchers have begun to use numerical simulation methods to solve the ground motion response of complex sea areas in the last few decades. Morency and Tromp (2008) based upon domain decomposition, described wave propagation in different media and discussed the interfacial continuity conditions used to deal with the discontinuities between different media. Link et al. (2009) deduced the 2D finite element format of fluid-solid-acoustic field interaction. Nakamura et al. (2012) simulated ground motions in the Suruga Bay, and the results showed that the seawater layer and the irregular topography of the sea area have a significant impact on the amplitude and duration to the coda part of S-wave. Liu et al. (2019) simulated the wave radiation effect of infinite fluid and solid domains on the reef-seawater system through the corresponding artificial boundary conditions. In the above numerical methods, fluid, solid, and poroelastic medium are analyzed by independent solvers, and then mutual interfacial coupling is performed through data exchange, which is very inconvenient. Chen et al. (2019a) and Chen et al. (2019b) proposed a decoupling simulation technique to model seismoacoustic scattering in marine areas when a seismic wave is incident. Different media (fluid, saturated porous medium, solid) are successfully unified into the generalized saturated porous media framework by extending Biot's saturated porous media theory and continuous conditions between different media. In the unified framework, different media can be simulated simultaneously in a single solver by assigning the corresponding parameters (porosity, wave velocity, density, etc.) to generalized saturated porous media.

Although researchers have proposed many methods to simulate the seismoacoustic scattering of marine sites, the ground motion simulation of 3D large-scale sea areas is still limited by computer hardware and computing time. In the exiting research, only the long period ($T > 2$ s) synthetic waveforms fit well with the observed waveforms (Nakamura et al., 2015; Okamoto et al., 2017; Takemura et al., 2019; Oba et al., 2020; Takemura et al., 2021). Therefore, it is necessary to build high-resolution models for broadband marine wave propagation simulation. In addition, previous studies have shown that 3D oceanographic models can simulate seafloor ground motion more accurately than 1D/2D models, especially in areas with drastic topographic changes (Takemura et al., 2020; Wang and Zhan, 2020; Bao et al., 2022). Compared with the 1D/2D model, if the 3D model is used to simulate the seismoacoustic scattering in marine areas with high spatial resolution, the demand of computational resources increases rapidly, and the traditional calculation can no longer meet the calculation requirements. In order to improve computing efficiency and make full use of computer performance, Okamoto et al. (2010), Liu et al. (2017), and Maeda et al. (2017) used GPU parallelism, CPU master-slave communication parallelism, and CPU cache communication parallelism to accelerate the simulation of ground motions for 3D sites, respectively.

Compared with numerical methods that use a structured grid, FEM with an unstructured grid has a greater capability of analyzing a body with complicated configuration. However, using FEM to simulating wave propagation in models constructed by irregular computational grids requires vast amounts of computational resources for computing stiffness matrix. In addition, the model discretization by 3D unstructured elements is often laborious (Ho-Le 1988). A so-called voxel finite-element method (VFEM) has been proposed to resolve these difficulties of FEM with an unstructured grid (Koketsu et al., 2004), which avoids generating distorted elements. In addition, the combination of VFEM and EBE method can significantly reduce the demand for computational memory and improves the robustness of computing.

In this study, a new VFEM simulation code based on unified framework and parallel computational strategy is developed to realize high performance computing for marine acoustics and submarine earthquake in the 2D/3D marine field. The unified framework of generalized porous media is applied to simulate the fluid-solid interaction in marine areas (Chen et al., 2019a; Chen et al., 2019b), which avoid exchanging the interfacial response between different solvers. In addition, parallel technology is also used to improve the computing efficiency. The large-scale site is divided into several small models, and the wave propagation simulation of each small model is assigned to each CPUs. The coupling between different CPUs is realized by Message Passing Interface (MPI) data communication at each time step.

In the following, we briefly review the strategy of the generalized saturated porous media framework in Section 2. In Section 3, the numerical techniques adopted in the present code are described, and a 3D horizontal layered field with the plane P-wave input vertically from bottom is used for the benchmark test of our code. Finally, in Section 4, the seismoacoustic scattering simulation in the Tokyo Bay with the vertically incident plane P/SV wave is performed by our code.

2 Methods

In this section, we briefly introduce the FEM based on unified computational framework for simulating wave motion in water-saturated seabed-bedrock system and the algorithms adopted in our code. The details of theories can be found in Chen et al. (2003, 2019a, 2019b).

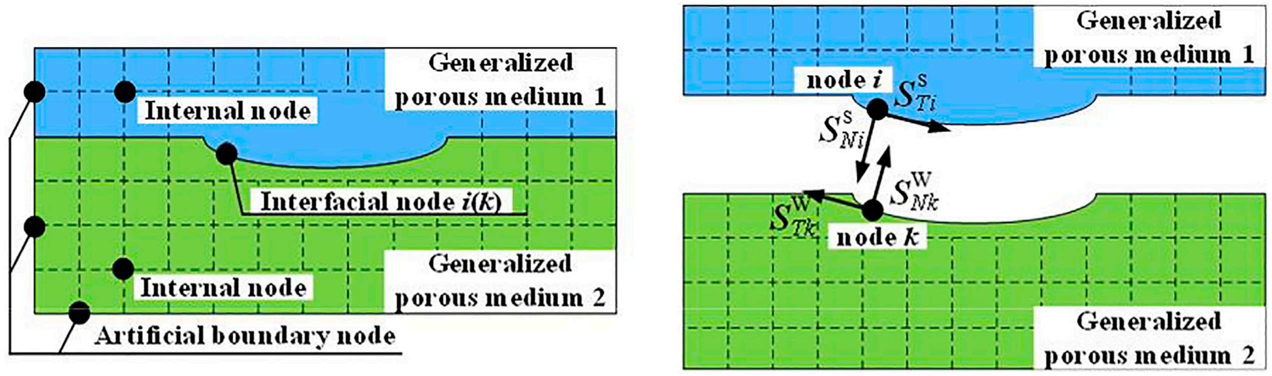

FIGURE 1
Schematic diagram of interfacial force.

2.1 Mathematical model of generalized saturated porous media dynamics

Theoretically, solid and fluid media are special cases of saturated porous media with porosity of 0 and 1, respectively, and the coupling between different media can all be described in the generalized saturated porous media system.

2.1.1 Basic differential equation

According to Biot porous medium theory, the vector representation of the basic differential equations of the model are given as follows (Biot 1956; 1962):

Solid-phase equilibrium equation for saturated porous media

$$\boldsymbol{L}_s^T\boldsymbol{\sigma} - (1-\beta)\boldsymbol{L}_w^T P + b\left(\dot{\boldsymbol{U}} - \dot{\boldsymbol{u}}\right) = (1-\beta)\rho_s\ddot{\boldsymbol{u}} \tag{1}$$

Liquid-phase equilibrium equation for saturated porous media

$$-\beta\boldsymbol{L}_w^T P + b\left(\dot{\boldsymbol{u}} - \dot{\boldsymbol{U}}\right) = \beta\rho_w\ddot{\boldsymbol{U}} \tag{2}$$

Compatibility equation (considering initial pore pressure and initial body strain as zero)

$$\tau = -\beta P = E_w\left[\beta e^w + (1-\beta)e^s\right] \tag{3}$$

Where $\boldsymbol{L}_s$ and $\boldsymbol{L}_w$ are differential operator matrices, $\boldsymbol{\sigma}$ is the solid effective stress vector, $\boldsymbol{\tau}$ is the average pore pressure, which is positive under tension. P is the pore water pressure, which is positive under compression. $\boldsymbol{U}$ and $\boldsymbol{u}$ respectively represent the displacement vectors of the liquid and solid phase, $\dot{\mathbf{U}}$, $\dot{\mathbf{u}}$ are the velocity vectors, and $\ddot{\mathbf{U}}$, $\ddot{\mathbf{u}}$ are acceleration vectors. ρ_s and ρ_w are the density of the solid and liquid phase, respectively. β is the porosity, $b = \beta^2\mu_0/k_0$, k_0 is fluid permeability coefficient, μ_0 is the kinematic viscosity coefficient, E_w is the bulk modulus of the fluid, e^s and e^w respectively represent the volume strain of the solid and liquid phase.

$$\boldsymbol{L}_s = \begin{bmatrix} \partial/\partial x_1 & 0 & 0 \\ 0 & \partial/\partial x_2 & 0 \\ 0 & 0 & \partial/\partial x_3 \\ \partial/\partial x_2 & \partial/\partial x_1 & 0 \\ 0 & \partial/\partial x_3 & \partial/\partial x_2 \\ \partial/\partial x_3 & 0 & \partial/\partial x_1 \end{bmatrix} \tag{4}$$

$$\boldsymbol{L}_w = (\partial/\partial x_1, \partial/\partial x_2, \partial/\partial x_3) \tag{5}$$

Assuming $\beta = 1$, $\rho_s = 0$, $\mu_0 = 0$ and $G = 0$, which means no solid phase in the media. At this time, $\boldsymbol{\sigma}$ and b in Eqs 1, 2 are both zero. Eq. 1 is automatically satisfied, Eqs 2, 3 respectively degenerates into equilibrium equation and constitutive equation of ideal fluid i.e., $-\mathbf{L}_w^T P = \rho_w\ddot{\mathbf{U}}$ and $\tau = E_w e^w$. Similarly, assuming $\beta = 0$, $\rho_w = 0$, $\mu_0 = 0$ and $E_w = 0$, which means no fluid phase in the media, $b = 0$, Eq. 2 comes into $\boldsymbol{L}_w^T P = 0$, and Eq. 1 degenerates into solid equilibrium equation, i.e., $\mathbf{L}_s^T\boldsymbol{\sigma} = \rho_s\ddot{\mathbf{u}}$. Therefore, the ideal fluid and elastic medium can be described by the generalized saturated porous model, which extend the porosity $0 < \beta < 1$ for the saturated porous media to $0 \le \beta \le 1$.

2.1.2 Continuity conditions of the interface

The relationship between two kinds of saturated porous media $(0 < \beta < 1)$ is determined by the following continuity conditions of interface (Deresiewicz and Rice, 1964a; Deresiewicz, 1964b).

$$\boldsymbol{\sigma}_N + \boldsymbol{\tau} = \bar{\boldsymbol{\sigma}}_N + \bar{\boldsymbol{\tau}} \tag{6}$$

$$\boldsymbol{\sigma}_T = \bar{\boldsymbol{\sigma}}_T \tag{7}$$

$$\boldsymbol{P} - \bar{\boldsymbol{P}} = \boldsymbol{0} \tag{8}$$

$$\boldsymbol{u}_N = \bar{\boldsymbol{u}}_N, \boldsymbol{u}_T = \bar{\boldsymbol{u}}_T \tag{9}$$

$$\beta(\boldsymbol{U}_N - \boldsymbol{u}_N) = \bar{\beta}(\bar{\boldsymbol{U}}_N - \bar{\boldsymbol{u}}_N) \tag{10}$$

Hereafter, the term containing subscript N represents the normal component of the vector, and the term containing subscript T represents the tangential component of the vector. The terms with and without the dash at the top represent the physical quantities corresponding to the material on one side of the interface and the material on the other side, respectively. Assuming $\beta > \bar{\beta}$ we rewrite Eq. 8 ~ Eq. 10 as:

$$\bar{\beta}(P - \bar{P}) = 0 \tag{11}$$

$$(1-\beta)\boldsymbol{u}_N = (1-\beta)\bar{\boldsymbol{u}}_N, (1-\beta)\boldsymbol{u}_T = (1-\beta)\bar{\boldsymbol{u}}_T \tag{12}$$

$$\beta\boldsymbol{U}_N = \bar{\beta}(\bar{\boldsymbol{U}}_N - \bar{\boldsymbol{u}}_N) + \beta\bar{\boldsymbol{u}}_N \tag{13}$$

and extend the continuity conditions for saturated porous media-saturated porous media interface to that for generalized saturated porous media-generalized saturated porous media interface, which can be described by Eqs 6, 7, 11 ~ Eq. 13.

By assigning the corresponding values of saturated porous media as parameters of solid or fluid, the continuity conditions of four special interfaces (i.e., fluid-saturated porous medium, saturated porous medium-solid, fluid-solid, saturated porous medium-saturated porous medium), can be unified into the continuity conditions between two generalized saturated porous media.

2.1.3 Boundary conditions

The boundary conditions consist of Dirichlet boundary condition, Neumann boundary condition and artificial boundary condition. As above, we extend the boundary conditions of saturated porous media to that of the generalized saturated porous media, Dirichlet boundary condition and Neumann boundary condition may be expressed as:

Dirichlet boundary condition

$$\Gamma_{\mathrm{D}s}\colon\ (1-\beta)\boldsymbol{u} = (1-\beta)\tilde{\boldsymbol{u}} \tag{14}$$

$$\Gamma_{\mathrm{D}w}\colon\ \beta\boldsymbol{U} = \beta\tilde{\boldsymbol{U}} \tag{15}$$

Neumann boundary condition

$$\Gamma_{\mathrm{N}s}\colon\ (1-\beta)\hat{\boldsymbol{n}}\boldsymbol{\sigma} = (1-\beta)\tilde{\boldsymbol{\sigma}} \tag{16}$$

$$\Gamma_{\mathrm{N}w}\colon\ \beta\boldsymbol{n}P = \beta\boldsymbol{n}\tilde{P} \tag{17}$$

where $\Gamma_{\mathrm{D}s}$ and $\Gamma_{\mathrm{D}w}$ respectively represent the Dirichlet boundary of solid and liquid, $\Gamma_{\mathrm{N}s}$ and $\Gamma_{\mathrm{N}w}$ respectively represent the Neumann boundary of solid and liquid, $\tilde{\boldsymbol{u}}$ and $\tilde{\boldsymbol{U}}$ respectively represent the solid and liquid phase displacement vectors given on the boundary, $\tilde{\boldsymbol{\sigma}}$ and $\tilde{P}$ respectively represent the given values of average solid phase stress and true pore pressure on the boundary, $\ddot{\boldsymbol{u}}_i\boldsymbol{M}_{si} + \boldsymbol{F}_i^s + \boldsymbol{T}_i^s - \boldsymbol{S}_i^s = 0$ is the direction vector along the outer normal on the border, $\ddot{\boldsymbol{u}}_i\boldsymbol{M}_{si} + \boldsymbol{F}_i^s + \boldsymbol{T}_i^s - \boldsymbol{S}_i^s = 0$ is a matrix composed of directional derivative.

For the fluid, $\beta = 1$, Eqs 14, 16 automatically satisficed, and the boundary conditions comes into Eqs 15, 17. For the solid, $\beta = 0$, Eqs 15, 17 automatically satisficed, and the boundary conditions degenerates into Eqs 14, 16.

2.2 Discretization and solution of motion equations

Take a random node as an example, using the Galerkin method to discretize Eqs 1, 2, and considering the boundary conditions, the decoupling motion equilibrium equation of any node i can be obtained as [Chen et al. (2019)]:

$$\ddot{\boldsymbol{u}}_i\boldsymbol{M}_{si} + \boldsymbol{F}_i^s + \boldsymbol{T}_i^s - \boldsymbol{S}_i^s = \boldsymbol{f}_i^s \tag{18}$$

$$\ddot{\boldsymbol{U}}_i\boldsymbol{M}_{wi} + \boldsymbol{F}_i^w + \boldsymbol{T}_i^w - \boldsymbol{S}_i^w = \boldsymbol{f}_i^w \tag{19}$$

where $\mathbf{M}_{si}$ and $\mathbf{M}_{wi}$ respectively represent the mass matrix of the solid phase and the mass matrix of the liquid phase concentrated at the node. A purely diagonal mass matrix can be achieved by simply summing up all the columns of the consistent mass matrix along each row into the respective diagonal [Hughes (2000); Drolia et al. (2020)]. The off-diagonal terms are then set to zero. $\boldsymbol{F}_i^s$ and $\mathbf{F}_i^w$ respectively represent the vectors of solid and liquid constitutive forces concentrated at the node, $\mathbf{T}_i^s$ and $\mathbf{T}_i^w$ respectively represent the vectors of solid and liquid viscosity resistances concentrated at the node, $\mathbf{S}_i^s$ and $\mathbf{S}_i^w$ respectively represent the vectors of solid and liquid interfacial forces acting on the node. Since the seismic response is input through the free field displacement of the boundary node, $\mathbf{f}_i^s$ and $\mathbf{f}_i^w$ here represent the vectors of solid and liquid external forces other than the seismic load.

2.2.1 Internal node

For the internal nodes, $\mathbf{S}_i^s$ and $\mathbf{S}_i^w$ are both zero (Figure 1). If the constitutive relationship is given, the Eqs 18, 19 can be solved by time-step integration, which can be written as follows:

$$\boldsymbol{u}_i^{(p+1)} = 2\boldsymbol{u}_i^p - \boldsymbol{u}_i^{(p-1)} - \frac{(\Delta t)^2}{m_i^s}\left(\boldsymbol{F}_i^s + \boldsymbol{T}_i^s - \boldsymbol{f}_i^s\right) \tag{20}$$

$$\boldsymbol{U}_i^{(p+1)} = 2\boldsymbol{U}_i^p - \boldsymbol{U}_i^{(p-1)} - \frac{(\Delta t)^2}{m_i^w}\left(\boldsymbol{F}_i^w + \boldsymbol{T}_i^w - \boldsymbol{f}_i^w\right) \tag{21}$$

where m_i^s and m_i^w represent the mass of the solid phase and the mass of the liquid phase concentrated at the node, the term containing superscript $\bar{\mathbf{F}}_k^s = \sum \int_{\Omega^e} (\mathbf{L}_s\mathbf{N}_k)^T \bar{\boldsymbol{\sigma}} dV$ represents the state of the corresponding physical quantity at $\bar{\mathbf{F}}_k^s = \sum\limits_e \int_{\Omega^e} (\mathbf{L}_s\mathbf{N}_k)^T \bar{\boldsymbol{\sigma}} dV$.

2.2.2 Interfacial node

Here we discuss the situation where node i k) is the interfacial point between two different media, which is shown in Figure 1. Using the concept of isolator, and performing time-step integration on Eqs 18, 19 at time $\boldsymbol{u}_i^{(p+1)} = \hat{\boldsymbol{u}}_i^{(p+1)} + \Delta\boldsymbol{u}_{Ni}^{(p+1)} + \Delta\boldsymbol{u}_{Ti}^{(p+1)}$, we can obtain the following equation:

$$\boldsymbol{u}_i^{(p+1)} = \hat{\boldsymbol{u}}_i^{(p+1)} + +\Delta\boldsymbol{u}_{Ni}^{(p+1)} + \Delta\boldsymbol{u}_{Ti}^{(p+1)} \tag{22}$$

$$\boldsymbol{U}_i^{(p+1)} = \hat{\boldsymbol{U}}_i^{(p+1)} + \Delta\boldsymbol{U}_{Ni}^{(p+1)} + \Delta\boldsymbol{U}_{Ti}^{(p+1)} \tag{23}$$

where $\hat{\boldsymbol{u}}_i^{(p+1)}$ and $\hat{\boldsymbol{U}}_i^{(p+1)}$ denote the displacement vectors when no interfacial force is applied in solid and fluid, respectively. $\Delta\boldsymbol{u}_{Ni}^{(p+1)}$ is the solid phase displacement vector caused by the normal interfacial force $\boldsymbol{S}_{Ni}^{sp}$, and $\Delta\boldsymbol{u}_{Ti}^{(p+1)}$ is the solid phase displacement vector caused by the tangential interfacial force $\boldsymbol{S}_{Ti}^{sp}$. $\Delta\boldsymbol{U}_{Ni}^{(p+1)}$ is the liquid phase displacement vector caused by the normal interfacial force $\boldsymbol{S}_{Ni}^{wp}$, and $\Delta\boldsymbol{U}_{Ti}^{(p+1)}$ is the liquid phase displacement vector caused by the tangential interfacial force $\boldsymbol{S}_{Ti}^{wp}$. According to Eqs 22, 23, combine with the interfacial continuity conditions, the interfacial force of node i can be solved as:

$$\boldsymbol{S}_{Ni}^{sp} = \frac{A_{22}B_1 - A_{12}B_2}{A_{22}A_{11} - A_{12}A_{21}} \tag{24}$$

$$\boldsymbol{S}_{Ni}^{wp} = \frac{A_{21}B_1 - A_{11}B_2}{A_{21}A_{12} - A_{11}A_{22}} \tag{25}$$

where

$$A_{11} = (\Delta t)^2\left(m_i^s + m_k^s\right) \tag{26}$$

$$A_{12} = \left(1 - \frac{\bar{\beta}}{\beta}\right)(\Delta t)^2 m_i^s \tag{27}$$

$$B_1 = \boldsymbol{n}_i\left(\boldsymbol{n}_i \cdot \left(\widehat{\bar{\boldsymbol{u}}}_k^{(p+1)} - \hat{\boldsymbol{u}}_i^{(p+1)}\right)\right) m_i^s m_k^s \tag{28}$$

$$A_{21} = (\Delta t)^2(\beta - \bar{\beta})m_i^w \tag{29}$$

$$A_{22} = (\Delta t)^2\left[\beta m_k^s + \frac{\bar{\beta}^2}{\beta m_k^w} m_i^w m_k^s + \frac{(\bar{\beta} - \beta)^2 m_i^w}{\beta}\right] \tag{30}$$

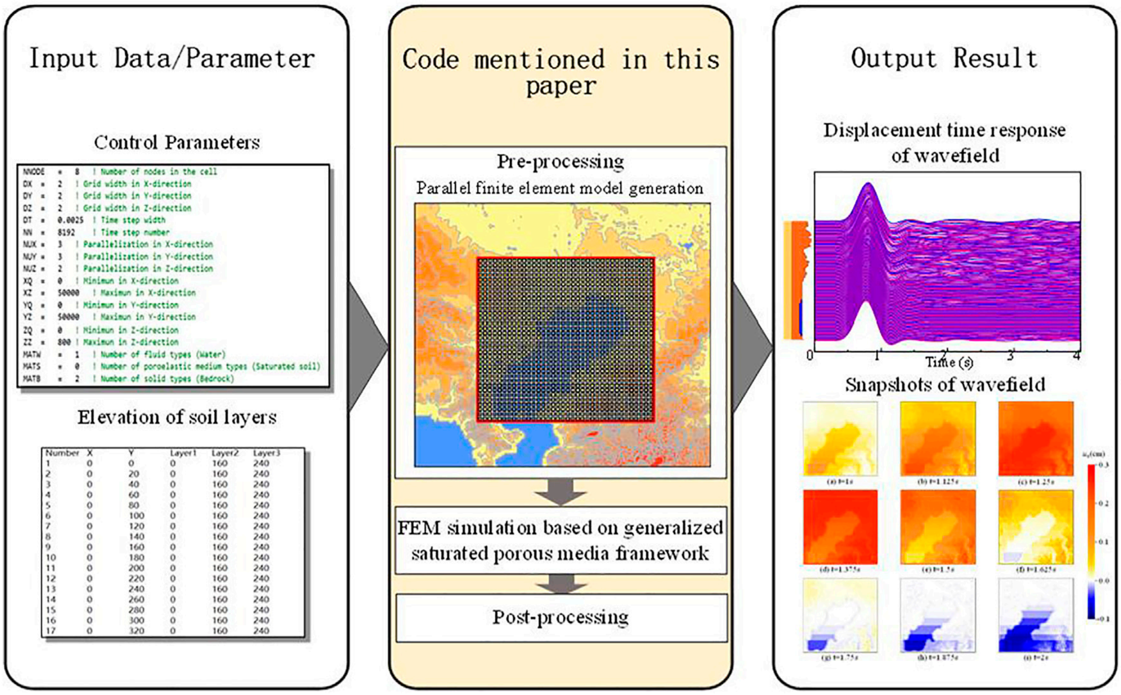

```
NNODE   =  8   ! Number of nodes in the cell
DX  =  2  ! Grid width in X-direction
DY  =  2  ! Grid width in Y-direction
DZ  =  2  ! Grid width in Z-direction
DT  =  0.0025  ! Time step width
NN  =  8192   ! Time step number
NUX =  3  ! Parallelization in X-direction
NUY =  3  ! Parallelization in Y-direction
NUZ =  2  ! Parallelization in Z-direction
XQ  =  0  ! Minimun in X-direction
XZ  =  50000  ! Maximun in X-direction
YQ  =  0  ! Minimun in Y-direction
YZ  =  50000  ! Maximun in Y-direction
ZQ  =  0  ! Minimun in Z-direction
ZZ  =  800 ! Maximun in Z-direction
MATW   =  1  ! Number of fluid types (Water)
MATS   =  0  ! Number of poroelastic medium types (Saturated soil)
MATB   =  2  ! Number of solid types (Bedrock)
```

Number	X	Y	Layer1	Layer2	Layer3
1	0	0	0	160	240
2	0	20	0	160	240
3	0	40	0	160	240
4	0	60	0	160	240
5	0	80	0	160	240
6	0	100	0	160	240
7	0	120	0	160	240
8	0	140	0	160	240
9	0	160	0	160	240
10	0	180	0	160	240
11	0	200	0	160	240
12	0	220	0	160	240
13	0	240	0	160	240
14	0	260	0	160	240
15	0	280	0	160	240
16	0	300	0	160	240
17	0	320	0	160	240

FIGURE 2
A schematic illustration of the flow of the wave propagation simulation using the code presented in this paper [Reproduced from Figure 1 of Takuto et al. (2017) with modification].

$$B_2 = \boldsymbol{n}_i\left(\boldsymbol{n}_i\cdot\left(\bar{\beta}\left(\hat{\bar{\boldsymbol{U}}}_k^{(p+1)} - \hat{\bar{\boldsymbol{u}}}_k^{(p+1)}\right) - \beta\left(\hat{\boldsymbol{U}}_i^{(p+1)} - \hat{\bar{\boldsymbol{u}}}_k^{(p+1)}\right)\right)\right) m_i^w m_k^s \tag{31}$$

After obtaining $\boldsymbol{S}_{Ni}^{sp}$ and $\boldsymbol{S}_{Ni}^{wp}$ from the Eqs 24, 25, we can solve $\bar{\boldsymbol{S}}_{Nk}^{sp}$ and $\bar{\boldsymbol{S}}_{Nk}^{wp}$ from the interfacial continuous conditions. Similarly, using the condition that the solid phase displacement at the interface is continuous, the interfacial force $\boldsymbol{S}_{Ti}^{sp}$ have the following solution:

$$\boldsymbol{S}_{Ti}^{sp} = \frac{\left(\hat{\bar{\boldsymbol{u}}}_k^{(p+1)} + \Delta\bar{\boldsymbol{u}}_{Nk}^{(p+1)} - \hat{\boldsymbol{u}}_i^{(p+1)} - \Delta\boldsymbol{u}_{Ni}^{(p+1)}\right) m_i^s m_k^s}{(\Delta t)^2\left(m_i^s + m_k^s\right)} \tag{32}$$

With the interfacial force, the displacement response of the interfacial node can be solved by Eqs 22, 23.

2.2.3 Boundary node

In order to effectively simulate the motion of the outgoing wave across the artificial boundary, we use the Multi-Transmitting Formula (MTF) proposed by Liao et al. (1984):

$$\begin{aligned}(1-\beta)u_{os}^{(p+1)} &= \sum_{j=1}^{N}(-1)^{(j+1)}C_j^N(1-\beta)u_{js}^{(p+1-j)}\\ \beta U_{os}^{(p+1)} &= \sum_{j=1}^{N}(-1)^{(j+1)}C_j^N\beta U_{js}^{(p+1-j)}\end{aligned} \tag{33}$$

where $U_{os}^{(p+1)}$ and $u_{os}^{(p+1)}$ respectively represent the liquid and solid displacement of the scattered wave at the boundary node o at $t = (P+1)\Delta t$, N is the transmitting order, C_j^N here can be expressed as:

$$C_j^N = \frac{N!}{(N-j)!\,j!} \tag{34}$$

This local artificial boundary condition is universal and has nothing to do with specific wave equations, which can be directly used for wave problems in saturated porous media (Liao et al., 1984; Chen and Liao, 2003). The total displacements W ($W = U, u$) can be separated as:

$$W = W_s + W_f \tag{35}$$

In which W_s represent scattering displacements, and W_f represent the free field displacements. At first, scattering field at time P is obtained by Eq. 35, where the total displacements at time P can be solved by the method mentioned in Section 2.2.1 and Section 2.2.2, and the free-field displacement can be obtained by the transfer matrix method (Ke et al., 2019). Then, applying Eq. 33 to scattering field of the solid-phase and liquid-phase, respectively, the scattering displacements of the boundary node at time P+1 can be obtained. Finally, adding the free field displacement at time P+1 of the boundary node to the scattering displacements, we can obtain the total displacements of the boundary node.

3 Software implementations

Based on the unified framework and the algorithms mentioned before, we developed a new code for simulating wave propagation in large-scale marine site. This code is especially designed to improve usability for non-expert users who are not familiar with numerical simulation techniques. Thus, this code also adds pre-processing and

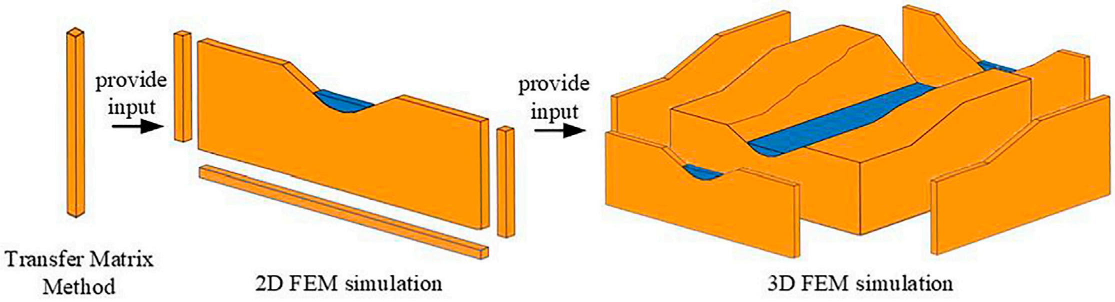

FIGURE 3
Flow chart for simulating wave propagation in 3D model with irregular boundary (Reproduced from figure 4.2 of Lokke (2019) with modification).

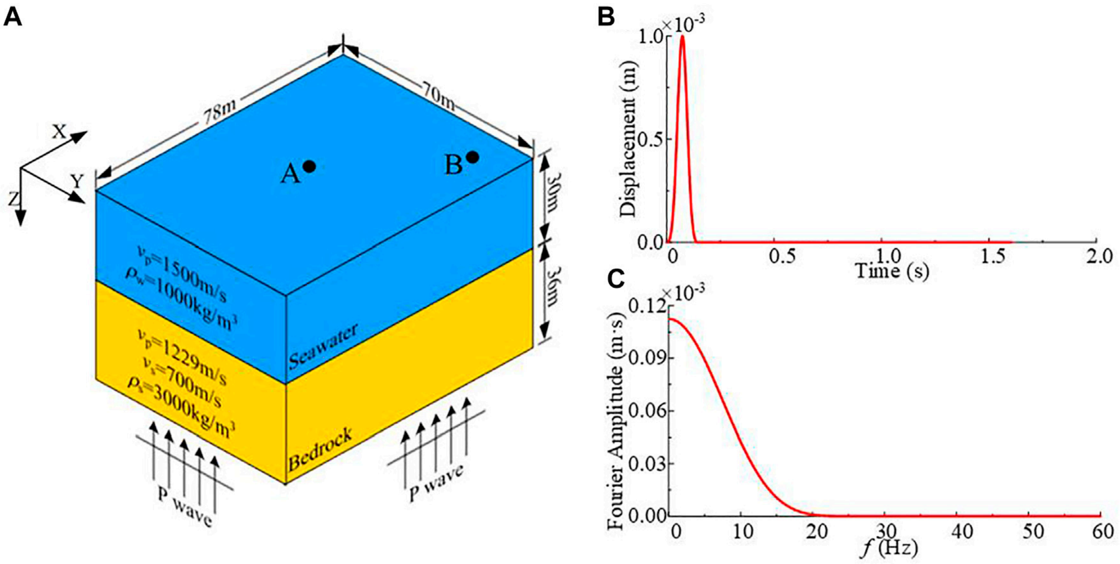

FIGURE 4
The computational model and the input pulse wave **(A)** Schematic diagram of horizontal layered computational model; **(B)** Displacement time history of the input wave; **(C)** Displacement Fourier amplitude spectrum of the input wave.

partial post-processing functions, and integrates codes between different modules through Linux script files. Users do not need to modify the code to apply it to individual simulation targets, but only needs to input the corresponding control parameters and soil layer elevation, and then the process of finite element model establishment—free field calculation—finite element simulation can be realized automatically (Figure 2).

3.1 Establishment and discretization of finite element model

Based on the comprehensive overview of geological data and borehole data, the marine site is assumed as a layered model consisting of basements and sedimentary layers. The P-wave velocities to the basements and sedimentary layers are measured by refraction and reflection surveys, the S-wave velocities are obtained by borehole logging, microtremor surveys or the empirical relationships between P- and S-wave velocities, and the density of layers is obtained by borehole logging. After that, convert time sections from seismic reflection surveys and borehole logging into depth sections using the P- and S-wave velocities. Depth sections are spatially combined with borehole data to produce the 3D model *via* interpolation, such as Bicubic spline interpolation and Kriging interpolation. Then the depth and material parameters of each soil layer can be input into our code for finite element mesh generation and subsequent marine seismoacoustic scattering simulation.

FEM can handle very complex structures with high accuracy using elements with various shapes. However, the pre-processing of FEM, i.e., grid generation, can be very time-consuming. In order to overcome the limitation of FEM, we use voxel FEM (VFEM). “Voxel” is a term in computer graphics derived from an abbreviation of “volume pixel.” It is actually a hexahedron or rectangular prism in three dimensions and its cross section forms a pixel in two dimensions (Koketsu et al., 2004). In our code, by reading the site information (such as material parameters of soil layer,

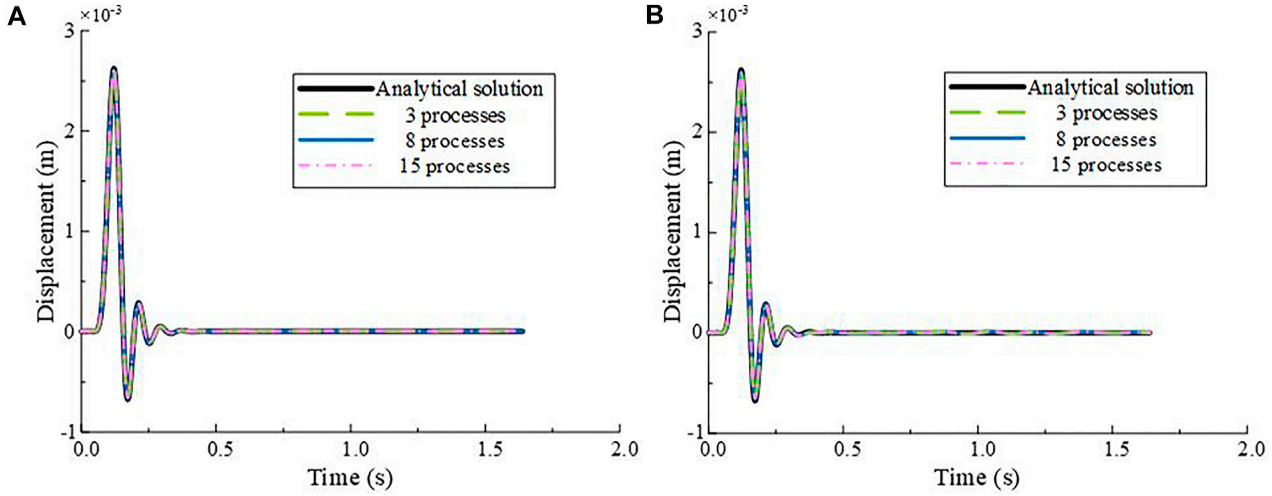

FIGURE 5
Displacement time history calculated by our code using different numbers of CPUs: **(A)** Point A; **(B)** Point B.

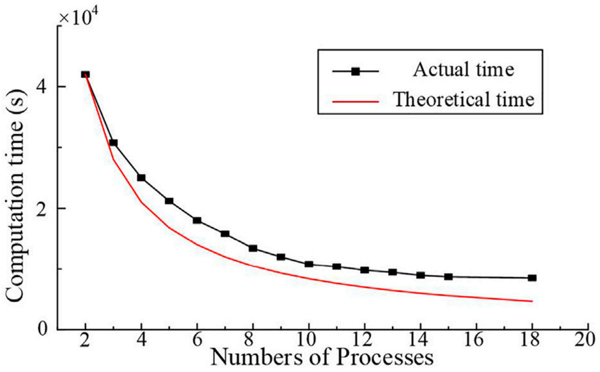

FIGURE 6
Calculation efficiency curve.

elevation, etc.) and element size input by the user, the model is discretized into regular hexahedral elements, and the corresponding material parameters are assigned. The directional derivatives at the interface of different media (fluid, saturated porous medium, solid) are also calculated and stored for subsequent finite element calculations. It is noted that the approximate treatment of a smooth boundary using voxels can lead to errors in computing displacement, and the errors become larger as the shape of the boundary becomes more irregular, but the computational accuracy requirements can generally be met by refining the mesh. VFEM mesh generation is simple and fast, and avoids generating distorted elements. Moreover, VFEM reduces the requirements of computational resources and memory.

3.2 Element-by-element and parallel computing strategy

The simulation of wave propagation in large-scale sea fields usually requires a large amount of memory and has a heavy computational load. The key to large-scale marine seismoacoustic scattering simulation is to realize the high-performance computing and save computational memory. In conventional finite element calculations, the global system matrices (including mass matrix, damping matrix, stiffness matrix etc.) usually needs to be assembled, which leads to a considerable increase in the memory usage for large-scale simulation. Therefore, the element-by-element (EBE) method is adopted in our code. It is only necessary to classify elements based on their material and size, and then calculate the mass matrix, damping matrix, and stiffness matrix for each class of elements before the solution begins, avoid assembling and storing the global system matrices. The combination of VFEM and EBE method can significantly reduce the demand for computational memory, which is suitable for large-scale marine seismoacoustic scattering simulation. When calculating the response of each node, it is only necessary to obtain the constitutive force of the node through the stiffness matrix and damping matrix of the elements around the node, and obtain the response of the node through the lumped mass and explicit integration scheme, which can avoid solving large system of equations and have high computational efficiency.

Our code also adopts a domain-partitioning procedure for the parallel computing using MPI. It performs 3D and 2D model partitioning for the 3D and 2D codes. The finite element model of each partitioned domain is set up on each CPU or CPU core, and the seismic wave propagation is calculated using MPI data communication at each time step. To ensure the continuity of the waveform across the partitioned model, the displacement and force defined at the outermost node are exchanged with those of the neighboring partitioned models at each time step using MPI.

3.3 Seismic source and input

Depending on the relative location of the model and the seismic source, the wave propagation problem can be divided into two categories: inner-source problem and scattering problem. For the inner-source problem, the seismic source is contained within the computational region. The finite fault source can be represented by

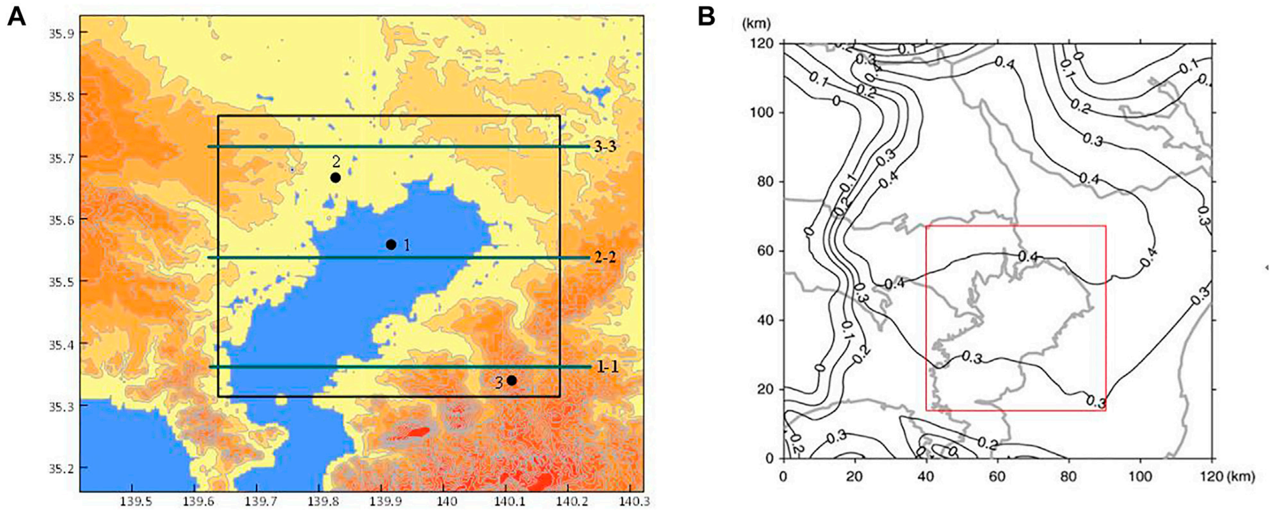

FIGURE 7
(A) Topography of the area around Tokyo Bay; **(B)** The first interface depth determined by Koketsu et al. (2009).

TABLE 1 Parameters of materials used in Tokyo Bay (Koketsu et al., 2009).

Material	Porosity/β	μ_0	ρ_s (kg·m^{-3})	ρ_w (kg·m^{-3})	ν	G (GPa)	E_w (GPa)	M (GPa)	α	k_0 (μm^2)
Seawater	1	0	0	1,000	.020	0	2.25	2.25	1	1
Bedrock1	0	0	1,850	0	.437	.666	0	1.91	0	0
Bedrock2	0	0	2,080	0	.395	2.080	0	5.80	0	0

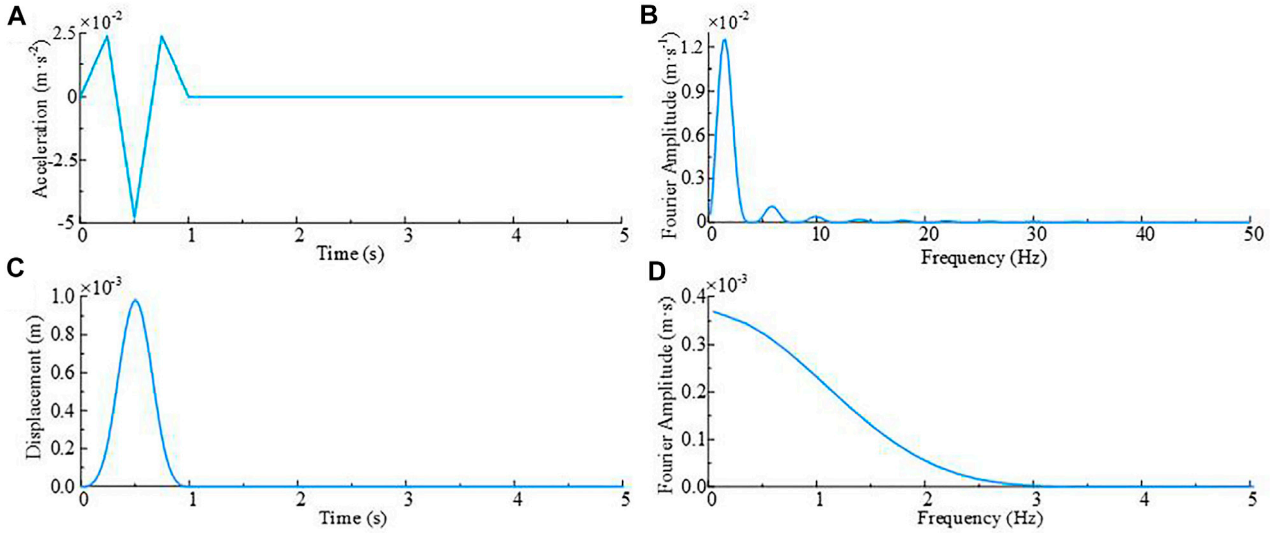

FIGURE 8
Input pulse wave: **(A)** Acceleration time history; **(B)** Acceleration Fourier amplitude spectrum; **(C)** Displacement time history; **(D)** Displacement Fourier amplitude spectrum.

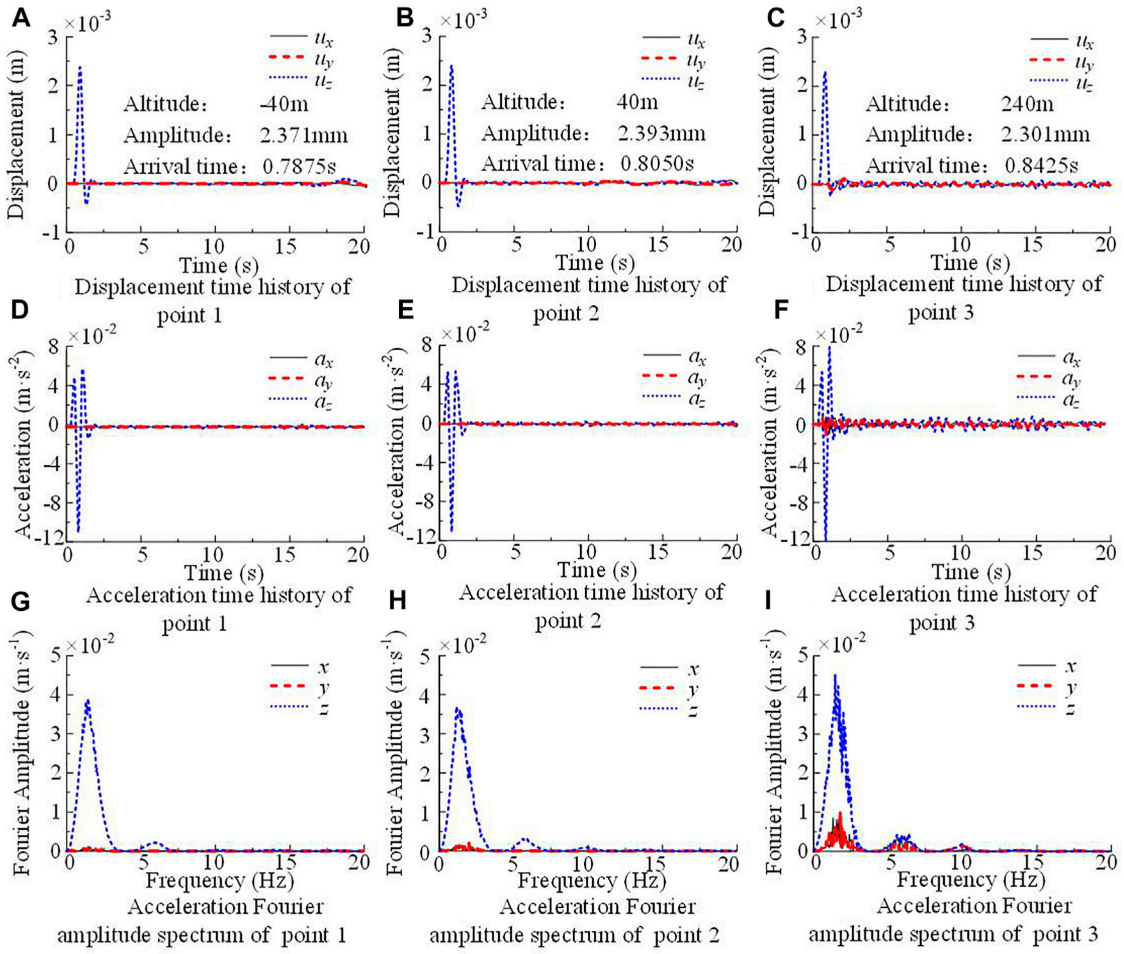

FIGURE 9
Displacement, acceleration time history curve and acceleration Fourier spectrum of observation points with P-wave input.

multiple point sources, and the seismic input can be imposed at the corresponding nodes of the model. For scattering problem, that is the case for the plane wave incidence, the seismic input is realized through free-field response (see Section 2.2.3). When the boundary of the computational model can be simplified to a horizontally layered region, the free field response can be obtained directly by the transfer matrix method (Ke et al., 2019). However, when the topography at the boundary of the model is irregular, as shown in Figure 3, we need to first develop a finite element model for the 1D column that has the same mesh density as the corner of 3D model, then obtain the response of the 1D corner column model by the transfer matrix method. After that, establish a 2D finite element model with the same mesh density as the 3D model at the cut-off boundaries, input the 1D response into the 2D model as the free field and simulate the wave propagation in 2D model, then take the 2D FEM synthetic wave field as “free fleid” and input it into the 3D model through the artificial boundary condition, as mentioned in Section 2.2.3.

In order to provide free field response for the 3D model with irregular boundaries, a code for the 2D-VFEM simulation with the incident P/SV wave is also included in our code. The 2D-VFEM simulations use the same input parameter file, except they perform the wave propagation simulations in the *x*–*z* plane, users can switch between 2D-VFEM and 3D-VFEM simulation or choose the wave motion input mode applicable to individual targets by simply setting corresponding input parameters without modifying the code, which is user friendly.

3.4 Computation performance

The computational efficiency and accuracy of the parallel simulation was examined using the following numerical test. The model used in the test is a 36-m bedrock covered with 30-m seawater (Figure 4A), and a plane P-wave with a pulse duration of .15 s (Figures 4B, C) is input from the bottom of the bedrock. The expression of the incident P-wave is:

$$s(t) = \begin{cases} 0, & \text{for } |t| > W/2 \\ 16\left(0.5-|t|/W\right)^3, & \text{for } W/4 \le |t| \le W/2 \\ 1-48\left(0.5-|t|/W\right)\left(0.5-|t|/W\right)^2, & \text{for } 0 \le |t| < W/4 \end{cases} \tag{36}$$

where W is the pulse duration. The time increment Δt = .0001 s, the number of steps n = 16,384, and the element size is 1 m × 1 m × 1 m,

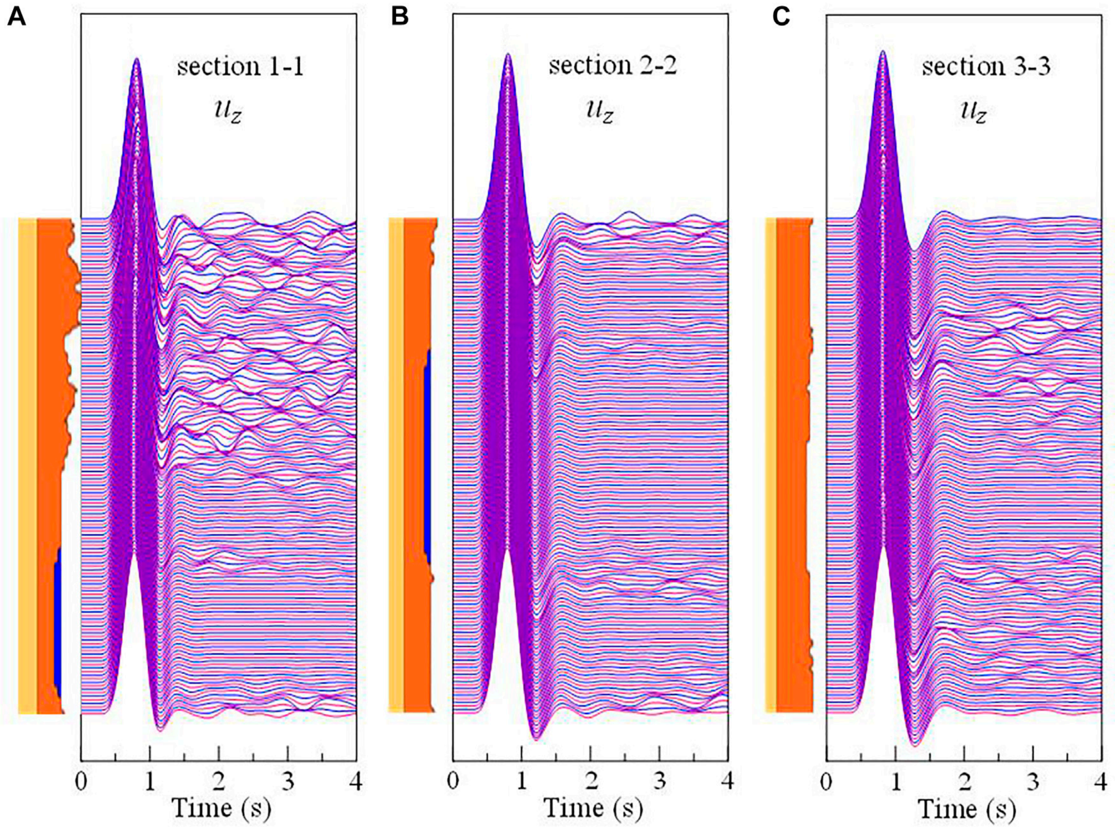

FIGURE 10
(A) Displacement waveforms in z-direction of section 1-1; **(B)** Displacement waveforms in z-direction of section 2-2; **(C)** Displacement waveforms in z-direction of section 3-3.

which is less than one-eighth of the minimum wavelength of the input wave and meet the requirement of accuracy (Moczo et al., 2000). The free field response is obtained by the transfer matrix method (Ke et al., 2019), and input from the artificial boundary through MTF. To test the computational efficiency of our code, the computation time of the numerical model is measured for parallel computing using different process numbers.

To illustrate the calculation accuracy of our code, the displacement time history of two monitoring points (point A, B, as shown in Figure 4A) in the above case simulated by our code, together with analytical solution obtained by the transfer matrix method, are plotted in Figure 5. The responses obtained by our code agree well with those obtained by the transfer matrix method.

Figure 6 shows the curve for calculating efficiency of our code. For the element-by-element parallel VFEM, at least two processes are required for parallel computation, assuming that the total computational time spent with 2 processes is t_2, and the theoretical computational time with m processes is defined as $t_m=2 \times t_2/m$. The curve demonstrates that as the number of processes increases, the computational time spent on the 3D simulation code decreases. However, when the number of processes reaches 14 or more, the computation time consumption almost does not decrease, and the gap between the theoretical computing time consumption and the actual computation time consumption increases gradually. This is due to the large number of processes used for small model simulation, the data traffic between different regions increase dramatically and resulting in over parallelization.

4 Simulation case

To demonstrate the effectiveness of our code in seismic wave propagation simulations, here we choose Tokyo Bay as the site model, and the scope of the study area is shown in Figure 7A (black frame line). The horizontal dimension of the model is 50 km × 50 km and the depth is .8 km, and artificial boundaries are applied at the boundaries of the model for absorbing the outgoing waves. It can be seen from Figure 7A that the topographic changes rapidly in the southeast of Tokyo Bay, and the rest of the area is relatively flat (the topography of the land surface and the seabed was obtained from Google Earth).

Koketsu et al. (2009) divided the soil layers in the vicinity of Tokyo Bay into four categories according to the wave speed and density, and gave the parameters of each soil layer and the depth of each interface within a range of 120 km × 120 km. According to Koketsu et al. (2009), the depth range of the first interface is 0–0.4 km (Figure 7B), and the depth of the second interface is greater than 1 km. Thus, two categories of soil layers and one interface are contained in the computational model here. Since the detailed interface depth is difficult to obtain, it can be seen from Figure 7B that the depth of the first interface is about .2–.4 km in the simulation region (red frame line), and gradually

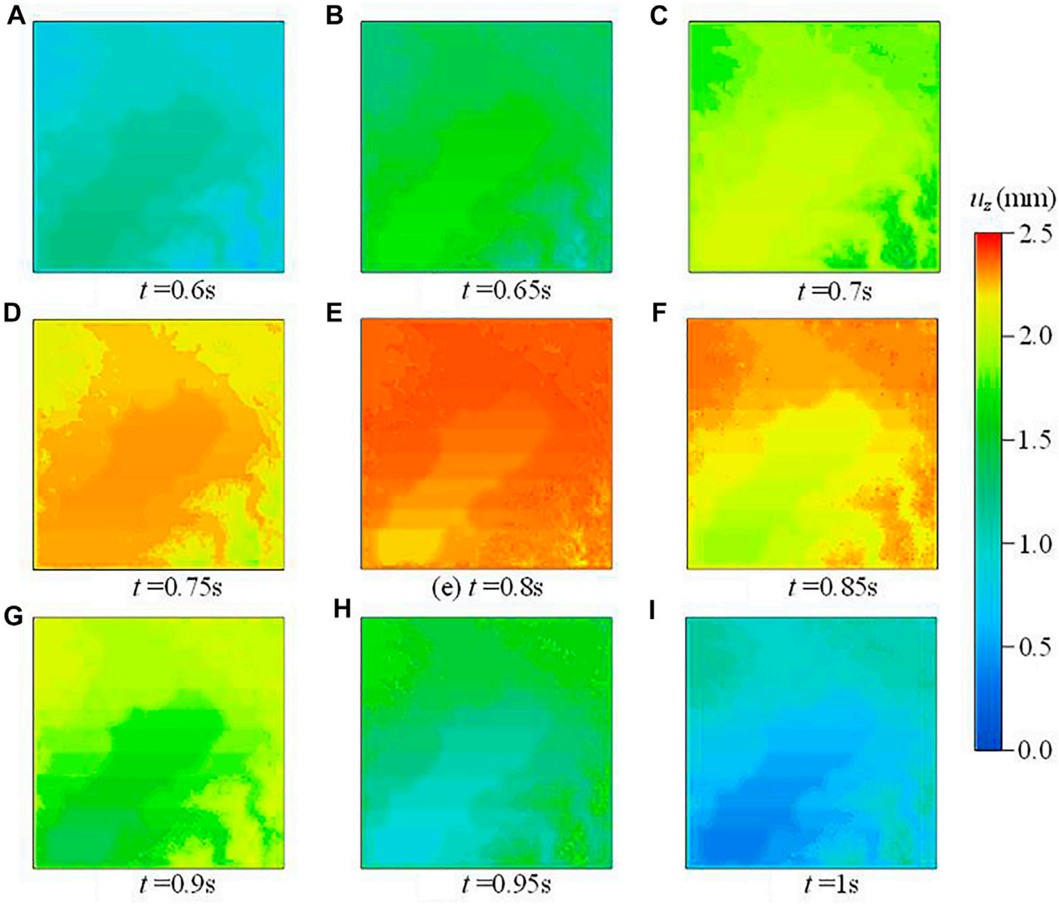

FIGURE 11
The snapshots of the displacement wavefield with P-wave input.

becomes deeper from south to north. Here we simplify the depth of the interface from south to north as a linear increase from 260 to 400 m.

Assuming that the model is only composed of seawater and elastic bedrock, and the material parameters are given in Table 1.

A plane P/SV wave with a rise time of 20 s is input from the bottom of the bedrock, and its expression is consistent with the incident wave in Section 3.4 (Eq. 36) but setting the pulse duration W = 1 s. The displacement time history, acceleration time history and corresponding Fourier spectrum of the incident wave are shown in Figure 8.

The simulation model has a grid spacing of 20 m and a time step of .0025 s with the minimum wave speed of 0.6 km/s for the shallow-most bedrock layer, which meets the requirements of numerical stability and accuracy. The model is divided into 144 domains, each domain has about 1.7 million elements, and the number of elements of the whole model is about 250 million.

Three cases are performed by our code: Case1, the seismoacoustic scattering simulation of Tokyo Bay with plane P-wave incidence; Case2, similar to case 1 but without seawater layer; Case 3, the seismoacoustic scattering simulation of Tokyo Bay with plane SV-wave incidence. In all three cases, 64 CPUs are used to simulate wave propagation in the field, and take an average of 38 h to complete the calculation. Three points shown in Figure 7A are selected as observation points, which are located on the bottom of the sea (point 1), the plain (point 2), and the top of the mountain (point 3), respectively. At the same time, three cross sections shown in Figure 7A are selected to monitor the displacement wave field at the top of the bedrock.

4.1 Plane P-wave input

The displacement time history, acceleration time history and acceleration Fourier spectrum of each observation point are shown in Figure 9. When the P-wave is vertically incident from the bottom of the model, the displacement of the three observation points in the z-direction is much larger than that in the other two directions. The reflection of the incident wave between different media can be clearly observed, and the arrival time of the first displacement peak is also delayed with increasing altitude. In addition, affected by the surrounding complex terrain, the response of point 3 in the horizontal direction is more intense than that of other two points. While points 1 and 2 are in regions with slow elevation changes, and these two points are similar in terms of displacement time history, acceleration time history, and Fourier spectrum.

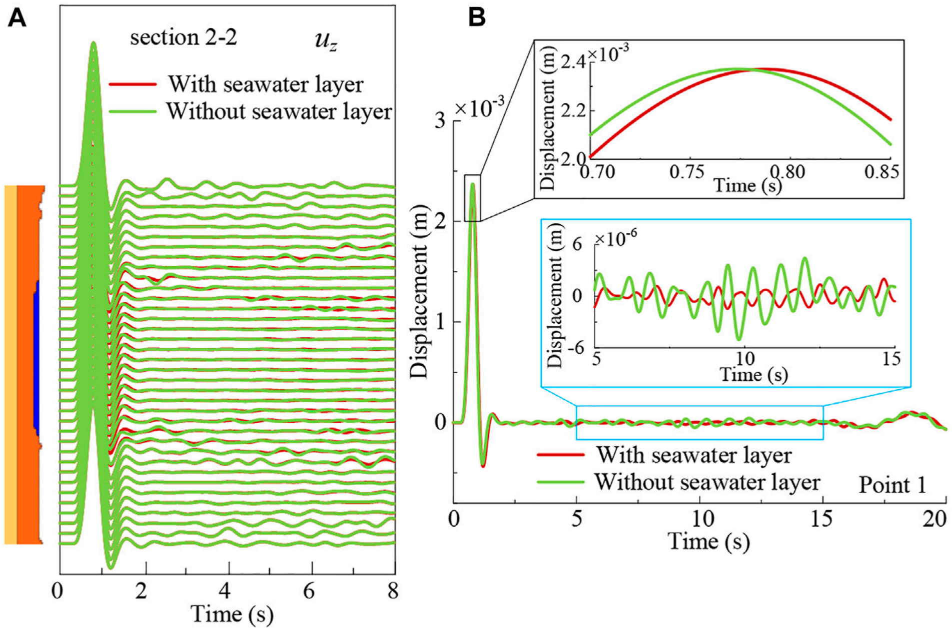

FIGURE 12
Comparison of the cases with and without sea water layer: **(A)** Displacement waveforms along the top of bedrock layer of cross section 2-2; **(B)** Displacement time history of point 1

Figure 10 illustrates the displacement time response along the top of bedrock1 of different cross sections. When the P-wave is vertically incident, the ground motions are mainly controlled by the vertical component. Section 1-1 contains both marine area and mountain area. For the marine area, the terrain is relatively flat, which makes the vertical displacements in this area stable rapidly after the end of the major response. However, in the mountainous area with drastic elevation changes, the incident wave scattered when it reaches the free surface, and the scattering waves propagate back and forth in the irregular region, triggering the complex subsequent waveforms (Figure 10A). Since the topography changes slowly in both sections 2-2 and 3-3, the peak vertical displacements as well as their arrival times are relatively coincident, and the scattering of the waves is only observed near regions with topographic change.

The snapshots of the displacement wavefield at the top of the bedrock layer are shown in Figure 11. As time going on, the incident wave first reaches the seafloor where the bedrock is the thinnest, then gradually spreads over the land, and finally reaches the mountainous area with high altitude. Furthermore, as mentioned earlier, the depth of the interface between bedrock 1 and bedrock 2 is simplified to south-to-north increasing, which means that the thickness of bedrock 2 gradually increases from north to south. Since the wave speed of bedrock 2 is greater than that of bedrock 1, the arrival time of incident wave is gradually advanced from north to south in areas with similar elevations.

The synthetic results without seawater layer are plotted in Figure 12 together with the results with seawater layer. Owing to the shallow depth of the seawater, the difference between the two cases is small, especially in the regions far from the marine area. Even so, in the offshore area, slight differences can be observed in areas where the terrain changes rapidly (Figure 12A). The displacement time history of point 1 is shown in Figure 12B for further comparison of the two cases. Since P waves can propagate in the seawater layer, the arrival time of incident wave with the seawater layer (red line in Figure 12B) is slightly later than that without the seawater layer (green line in Figure 12B). In addition, seawater acts as a “filler” on the seabed and weakens the influence of irregular terrain on the waveform, which makes the coda relatively stable.

It is worth mentioned that when our code is applied to simulating the wave propagation in the example without seawater, only need to set the material parameters of seawater such as compressive modulus and density to zero without modifying the model, which is very convenient.

4.2 Plane SV-wave input

The displacement time history, acceleration time history and acceleration Fourier spectrum of each observation point are shown in Figure 13. Similar to the case of P-wave incidence, the arrival time of the incident wave is also delayed with increasing altitude, and the ground motions are mainly controlled by the motion direction of the incident wave, here is the *x*-direction. The displacement time history of point 1 is relatively stable after 10 s, but the acceleration of point A in the *z*-direction has obvious oscillations (Figure 13D), which does not appear in the case of P-wave incidence. Since the material is assumed to be linear elastic here, the spectral characteristics of the output acceleration Fourier spectrum remain consistent with the input regardless of the terrain.

The displacement waveforms along the top of bedrock layer of different cross sections with SV-wave input are plotted in Figure 14. According to the analysis in the preceding part, in the mountainous area of section 1-1, the complexity of waveforms is triggered by the incident wave scattering in the irregular area. The effect of undulating terrain near the coast on the wave scattering is amplified due to shear waves cannot

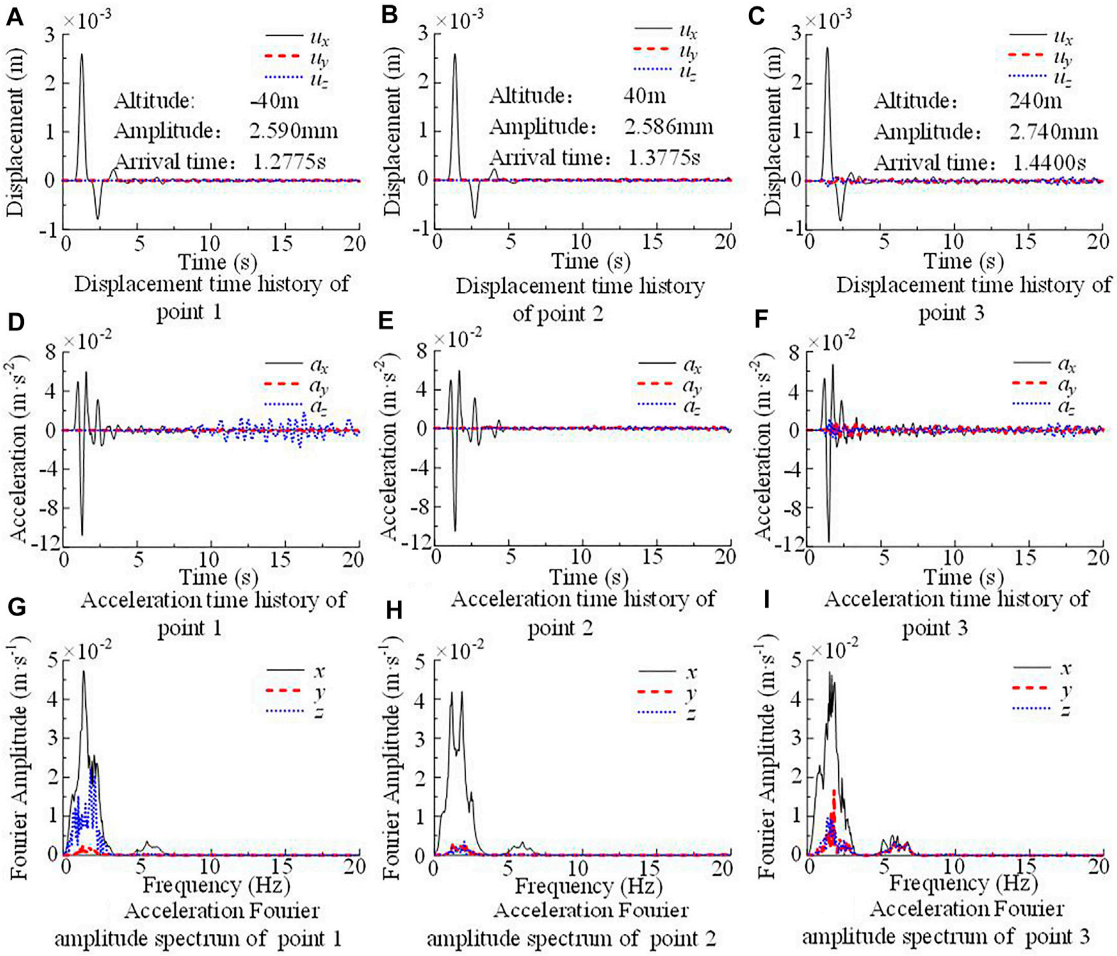

FIGURE 13
Displacement, acceleration time history curve and acceleration Fourier spectrum of observation points with SV-wave input.

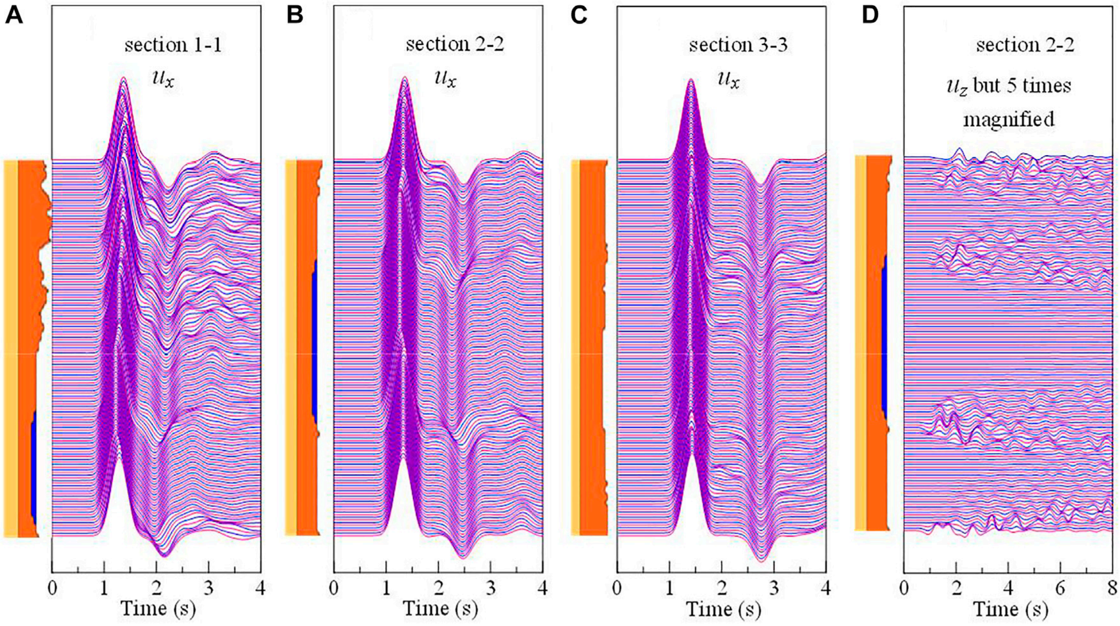

FIGURE 14
(A) Displacement waveforms in x-direction of section 1-1; **(B)** Displacement waveforms in x-direction of section 2-2; **(C)** Displacement waveforms in x-direction of section 3-3; **(D)** Displacement waveforms in z-direction of section 2-2.

propagate in seawater layer. Although the SV-wave vertically incident from the bottom of the model, they creep along the bedrock surface and bring about the vertical component displacement (Figure 14D), the vertical vibration with small amplitude gradually spread to the surrounding region over time, and causing an acceleration response in the *z*-direction (Figure 13D). The displacement waveform of section 3-3 is relatively regular, which is similar to the case of P-wave incidence.

In summary, our code can efficiently simulate marine seismoacoustic scattering in large-scale marine site.

5 Conclusion

We have developed a new FEM simulation code for efficient modeling of seismoacoustic scattering in 2D/3D large-scale marine areas. This code improves the calculation efficiency of marine seismic simulation from two aspects: calculation method and computational strategy. In terms of calculation method, different media (fluid, saturated porous medium, solid) are successfully unified into the generalized saturated porous media framework by extending Biot's saturated porous media theory and continuous conditions between different media, which means that different media can be simulated simultaneously in a single solver. The response is obtained by the lumped mass and explicit integration scheme, which can avoid solving large system of equations, and have high computational efficiency. In terms of computational strategy, regular hexahedral elements are used to discretize the computational model, and EBE parallel computing strategy is adopted, which improves the robustness of computing and reduces the demand for computational memory. The computational efficiency and accuracy of our code was examined by a 3D horizontal layered model with the plane P-wave incidence, the applicability and the effectiveness were demonstrated by simulating seismoacoustic scattering in Tokyo Bay.

In this paper, the model is discretized into cubit elements with unified size. However, when the medium wave velocity in the model varies greatly, or the surface terrain of the model changes drastically, the element size needs to be reduced to meet the numerical stability requirements, which increases the computational load. In the subsequent study, the hybrid grid would be used to discretize the model in our code, which can ensure the computational accuracy and radically reduces the computational load (Ichimura et al., 2007).

Data availability statement

The raw data supporting the conclusion of this article will be made available by the authors, without undue reservation.

Author contributions

SJ: Writing—original draft, Write the code, Numerical calculation CS: Writing—review and editing, Supervision ZJ: Write the code CP: Data curation.

Funding

This paper was supported by the National Natural Science Foundation of China (No.51978337 No.U2039209).

Acknowledgments

The author thanks the Beijing paratera tech corp., LTD., for providing computing services, and Google Earth for providing Tokyo Bay topography.

Conflict of interest

The authors declare that the research was conducted in the absence of any commercial or financial relationships that could be construed as a potential conflict of interest.

Publisher's note

References

Bao, X., Liu, J., Chen, S., and Wang, P. (2022). Seismic analysis of the reef-seawater system: Comparison between 3D and 2D models. *J. Earthq. Eng.* 26 (6), 3109–3122. doi:10.1080/13632469.2020.1785976

Biot, M. A. (1962). Mechanics of deformation and acoustic propagation in porous media. *J. Appl. Phys.* 33 (4), 1482–1498. doi:10.1063/1.1728759

Biot, M. A. (1956). Theory of propagation of elastic waves in a fluid-saturated porous solid. I. low-frequency range. *J. Acoust. Soc. Am.* 28 (2), 168–178. doi:10.1121/1.1908239

Brekhovskikh, L. M. (1980). *Waves in layered media*. 2nd edtion. NY, USA: Academic Press.

Chen, S. L., Cheng, S. L., and Ke, X. F. (2019b). A unified computational framework for fluid-solid coupling in marine earthquake engineering: Irregular interface case. *Chin. J. Theor. Appl. Mech.* 51 (5), 1517–1529. (in Chinese with English abstract).

Chen, S. L., Ke, X. F., and Zhang, H. X. (2019a). A unified computational framework for fluid-solid coupling in marine earthquake engineering. *Chin. J. Theor. Appl. Mech.* 51 (2), 594–606. (in Chinese with English abstract).

Chen, S. L., and Liao, Z. P. (2003). Multi-transmitting formula for attenuating waves. *Acta Seismol. Sin.* 16 (3), 283–291. doi:10.1007/s11589-003-0032-7

Deresiewicz, H., and Rice, J. T. (1964a). The effect of boundaries on wave propagation in a liquid-filled porous solid: V. Transmission across a plane interface. *Bull. Seismol. Soc. Am.* 54 (1), 409–416. doi:10.1785/bssa0540010409

Deresiewicz, H. (1964b). The effect of boundaries on wave propagation in a liquid-filled porous solid: VII. Surface waves in a half-space in the presence of a liquid layer. *Bull. Seismol. Soc. Am.* 54 (1), 425–430. doi:10.1785/bssa0540010425

Drolia, M., Mohamed, M. S., Laghrouche, O., Seaid, M., and Kacimi, A. E. (2020). Explicit time integration with lumped mass matrix for enriched finite elements solution of time domain wave problems. *Appl. Math. Model.* 77 (2), 1273–1293. doi:10.1016/j.apm.2019.07.054

Ho-Le, K. (1988). Finite element mesh generation methods: A review and classification. *Computer-Aided Des.* 20 (1), 27–38. doi:10.1016/0010-4485(88)90138-8

Hu, J. J., Tan, J. Y., and Zhao, J. X. (2020). New GMPEs for the Sagami bay region in Japan for moderate magnitude events with emphasis on differences on site amplifications at the seafloor and land seismic stations of K-NET. *Bull. Seismol. Soc. Am.* 110 (5), 2577–2597. doi:10.1785/0120190305

Hughes, T. (2000). *The finite element method: Linear static and dynamic finite element analysis*. Beijing China: Prentice-Hall.

Ichimura, T., Hori, M., and Kuwamoto, H. (2007). Earthquake motion simulation with multiscale finite-element analysis on hybrid grid. *Bull. Seismol. Soc. Am.* 97 (4), 1133–1143. doi:10.1785/0120060175

Ke, X. F., Chen, S. L., and Zhang, H. X. (2019). Free-field analysis of seawater-seabed system for incident plane P-SV waves. *J. Vib. Eng.* 32 (6), 966–976. (in Chinese with English abstract).

Koketsu, K., Fujiwara, H., and Ikegami, Y. (2004). Finite-element simulation of seismic ground motion with a voxel mesh. *Pure Appl. Geophys.* 161 (11-12), 2463–2478. doi:10.1007/s00024-004-2557-7

Koketsu, K., Miyake, H., Afnimar and Tanaka, Y. (2009). A proposal for a standard procedure of modeling 3-D velocity structures and its application to the Tokyo metropolitan area, Japan. *Tectonophysics* 472 (1-4), 290–300. doi:10.1016/j.tecto.2008.05.037

Li, C., Hao, H., Li, H. N., Bi, K. M., and Chen, B. K. (2017). Modeling and simulation of spatially correlated ground motions at multiple onshore and offshore sites. *J. Earthq. Eng.* 21 (3), 359–383. doi:10.1080/13632469.2016.1172375

Link, G., Kaltenbacher, M., Breuer, M., and Döllinger, M. (2009). A 2D finite-element scheme for fluid-solid-acoustic interactions and its application to human phonation. *Comput. Methods Appl. Mech. Eng.* 198 (41-44), 3321–3334. doi:10.1016/j.cma.2009.06.009

Liu, J. B., Bao, X., Wang, D. Y., and Wang, P. G. (2019). Seismic response analysis of the reef-seawater system under incident SV wave. *Ocean. Eng.* 180, 199–210. doi:10.1016/j.oceaneng.2019.03.068

Liu, S. L., Yang, D. H., Dong, X. P., Liu, Q. C., and Zheng, Y. C. (2017). Element-by-element parallel spectral-element methods for 3-D teleseismic wave modeling. *Solid earth.* 8 (5), 969–986. doi:10.5194/se-8-969-2017

Lokke, A. (2019). *Direct finite element method for nonlinear earthquake analysis of concrete dams including dam-water-foundation rock interaction*. Berkeley: Pacific Earthquake Engineering Research Center Headquarters at the University of California.

Maeda, T., Takemura, S., and Furumura, T. (2017). OpenSWPC: An open-source integrated parallel simulation code for modeling seismic wave propagation in 3D heterogeneous viscoelastic media. *Earth, Planets Space* 69 (1), 102. doi:10.1186/s40623-017-0687-2

Moczo, P., Kristek, J., and Halada, L. (2000). 3D fourth-order staggered-grid finite difference schemes: Stability and grid dispersion. *Bull. Seismol. Soc. Am.* 90 (3), 587–603. doi:10.1785/0119990119

Morency, C., and Tromp, J. (2008). Spectral-element simulations of wave propagation in porous media. *Geophys. J. Int.* 175 (1), 301–345. doi:10.1111/j.1365-246x.2008.03907.x

Nakamura, T., Nakano, M., Hayashimoto, N., Takahashi, N., Takenaka, H., Okamoto, T., et al. (2014). Anomalously large seismic amplifications in the seafloor area off the Kii peninsula. *Mar. Geophys. Res.* 35 (3), 255–270. doi:10.1007/s11001-014-9211-2

Nakamura, T., Takenaka, H., Okamoto, T., and Kaneda, Y. (2012). FDM simulation of seismic-wave propagation for an aftershock of the 2009 Suruga bay earthquake: Effects of ocean-bottom topography and seawater layer. *Bull. Seismol. Soc. Am.* 102 (6), 2420–2435. doi:10.1785/0120110356

Nakamura, T., Takenaka, H., Okamoto, T., Ohori, M., and Tsuboi, S. (2015). Long-period ocean-bottom motions in the source areas of large subduction earthquakes. *Sci. Rep.* 5 (1), 1–10. doi:10.1038/srep16648

Oba, A., Furumura, T., and Maeda, T. (2020). Data assimilation-based early forecasting of long-period ground motions for large earthquakes along the Nankai trough. *J. Geophys. Res. Solid Earth* 125 (6), 1–19. doi:10.1029/2019jb019047

Okamoto, T., and Takenaka, H. (1999). A reflection/transmission matrix formulation for seismoacoustic scattering by an irregular fluid–solid interface. *Geophys. J. Int.* 139 (2), 531–546. doi:10.1046/j.1365-246x.1999.00959.x

Okamoto, T., Takenaka, H., Nakamura, T., and Aoki, T. (2010). Accelerating large-scale simulation of seismic wave propagation by multi-GPUs and three-dimensional domain decomposition. *Earth, Planets Space* 62 (12), 939–942. doi:10.5047/eps.2010.11.009

Okamoto, T., Takenaka, H., Nakamura, T., and Hara, T. (2017). FDM simulation of earthquakes off Western Kyushu, Japan, using a land-ocean unified 3D structure model. *Earth, Planets Space* 69 (1), 88–102. doi:10.1186/s40623-017-0672-9

Takemura, S., Kubo, H., Tonegawa, T., Saito, T., and Shiomi, K. (2019). Modeling of long-period ground motions in the nankai subduction zone: Model simulation using the accretionary prism derived from oceanfloor local S-wave velocity structures. *Pure Appl. Geophys.* 176 (2), 627–647. doi:10.1007/s00024-018-2013-8

Takemura, S., Okuwaki, R., Kubota, T., Shiomi, K., Kimura, T., and Noda, A. (2020). Centroid moment tensor inversions of offshore earthquakes using a three-dimensional velocity structure model: Slip distributions on the plate boundary along the nankai trough. *Geophys. J. Int.* 222 (2), 1109–1125. doi:10.1093/gji/ggaa238

Takemura, S., Yoshimoto, K., and Shiomi, K. (2021). Long-period ground motion simulation using centroid moment tensor inversion solutions based on the regional three-dimensional model in the Kanto Region, Japan. *Earth, Planets Space* 73 (1), 15. doi:10.1186/s40623-020-01348-2

Wang, X., and Zhan, Z. W. (2020). Moving from 1-D to 3-D velocity model: Automated waveform-based earthquake moment tensor inversion in the los angeles region. *Geophys. J. Int.* 220 (1), 218–234. doi:10.1093/gji/ggz435

Zhu, J. Q. (1988). Coupled motion between sea water and sea bed-soil under earthquake action. *Earthq. Eng. Eng. Vib.* 8 (2), 37–43. (in Chinese with English abstract).

Frontiers in Earth Science

TYPE Original Research
PUBLISHED 13 January 2023
DOI 10.3389/feart.2023.1091785

OPEN ACCESS

EDITED BY
Yefei Ren,
Institute of Engineering Mechanics, China Earthquake Administration, China

REVIEWED BY
Zhen Guo,
Jiangnan University, China
Lei Fu,
Institute of Geophysics, China Earthquake Administration, China

*CORRESPONDENCE
Ying Zhou,
✉ joey052zy@163.com

SPECIALTY SECTION
This article was submitted to Structural Geology and Tectonics,
a section of the journal
Frontiers in Earth Science

RECEIVED 07 November 2022
ACCEPTED 02 January 2023
PUBLISHED 13 January 2023

CITATION
Wu H, Zhou Y, Qian Y, Yang F, Yu G, Wu G and Zhang Y (2023), Seismic-wave path attenuation and local site responses in eastern Guangdong province revealed by the ground-motion spectral analyses. *Front. Earth Sci.* 11:1091785.
doi: 10.3389/feart.2023.1091785

Seismic-wave path attenuation and local site responses in eastern Guangdong province revealed by the ground-motion spectral analyses

Huadeng Wu[1,2,3,4], Ying Zhou[5]*, Yongmei Qian[5], Fang Yang[1], Gang Yu[1,2,3,4], Guorui Wu[1] and Yi Zhang[1,2,3,4]

[1]Guangdong Province Earthquake Agency, Guangzhou, China, [2]Guangdong Science and Technology Collaborative Innovation Center for Earthquake, Prevention and Disaster Mitigation, Guangzhou, China, [3]Key Laboratory of Earthquake Monitoring and Disaster Mitigation Technology, Guangzhou, China, [4]Key Laboratory of Guang Dong Province, Earthquake Early Warning and Safety Diagnosis of Major Projects, Guangzhou, China, [5]School of Civil Engineering, Jilin Jianzhu University, Changchun, China

In an effort to investigate the attenuation characteristics and site effects in eastern Guangdong, 659 strong-motion recordings received by 27 stations were selected for spectral analysis to separate path attenuation, site effects and source spectra. The path attenuation curves are generally close to the simplest form of distance decay described by $R^{-0.5}$, and decays the slowest at a frequency of 4 Hz. We decomposed the path attenuation into a combination of geometric spreading and inelastic attenuation. The geometric spreading $R^{-0.15}$ exhibits a slower distance decay at local distances, indicating that the seismic energy close to the epicenter is not easily dissipated. The quality factors were regressed as $Q_s(f) = 114.81f^{.922}$ in the frequency range .9–20 Hz, lower than those reported for the whole Guangdong region, indicating stronger anelastic attenuation in eastern Guangdong. The site responses in eastern Guangdong show a strong correlation with geological and geotechnical characterization. The stations located in the central mountains have higher predominant frequencies (>10 Hz) accompanied by smaller site amplifications. Larger site amplification is in the southeast coastal area (i.e., Shantou area), where the surface is covered with a thicker layer of soft soil and the predominant frequency of site is relatively low (~2 Hz). The far-field earthquake will cause greater vibration and damage to this area.

KEYWORDS

earthquake ground motions, spectral analysis, path attenuation, site response, eastern Guangdong

Introduction

The coastal area of South China is located in the twisted zone between the southeast margin of the Asian continental plate and the Pacific plate, with frequent seismic activities (Zhang et al., 2013; Shu et al., 2019). Guangdong Province lies in the middle of the seismic zone along the southeast coast, with higher terrain in the north. The altitudes of the mountains to the north of Nanling are more than 1,000 m, slope toward the continental shelf of the South China Sea to 100 m below sea level. The crustal thickness is thick in the north and thin in the south. The depth of Moho discontinuity in the northern Nanling mountains is about 35 km, the depth of that in the southern coast is about 33 km. The continental shelf is a crustal thinning zone of the

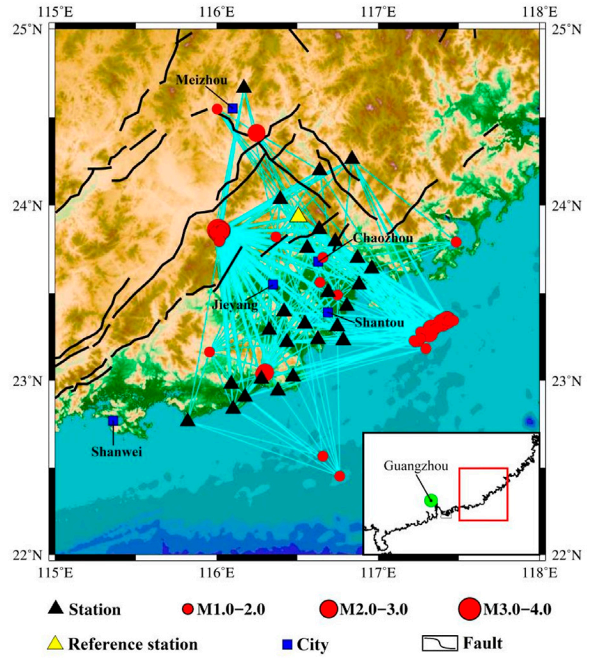

FIGURE 1
The locations of earthquakes (red circles) and stations (triangles) used in this study. The yellow triangle indicates the location of reference station FSLHX. The black discontinuous solid lines represent the faults. The cyan lines denote the propagation path from events to stations. The small scale map in the southeast shows the location and scope of the study area.

continental margin, and the depth of the Moho surface is less than 20 km (Zhang et al., 2021). Since 1900, there were 13 large-scale events with magnitude larger than 6 occurred in Guangdong province, causing heavy economic losses and social security impact (Liu et al., 2003; He, 2020).

The eastern Guangdong refers to the region from the east of the Lianhuashan fault zone to the seaside, where sedimentary rocks, intermediate-acid volcanic rocks and granites of Mesozoic Jurassic are widely distributed (Wang J. et al., 2021; Yue et al., 2022). The coastal area of eastern Guangdong is closer to the Pacific seismic zone, and the possibility of strong earthquakes is higher than that of the Pearl River Delta and western Guangdong (Zhang, 2014; Xu et al., 2019; Li et al., 2021). Moreover, the geological tectonic fault zones in Guangdong Province tend to show east-west, northeast-southwest strike (Figure 1), and the region above the fault zone has a greater probability of earthquakes (Jia et al., 2020). The eastern Guangdong is the most seismically active region in Guangdong Province, and has experienced two major earthquakes, the 1067 Chaozhou $M6^{3}/_{4}$ earthquake and the 1918 Nanao $M7.3$ earthquake (Xie 1992; Zhang et al., 2008).

As an efficient and comprehensive method of ground motion spectrum analysis, the generalized inversion technique (GIT) has been applied and improved for more than 30 years. The earliest method used a linear model (Andrews, 1986), which defined the propagation path as a linear attenuation function inversely proportional to the hypocentral distance and assumed that the attenuation term was purely parametric. Iwata and Irikura (1988) put forward the concept of quality factor, in which the attenuation was defined as two parts: the geometric spreading model related to distance and the inelastic attenuation model related to frequency, which was later called the parametric method and widely used in regional seismic characteristics research, such as the Longmenshan region (Ren et al., 2013), the Kanto Basin in Japan (Kawase and Matsuo, 2004; Tsuda, 2010; Nakano et al., 2015), the northern Italy (Pacor et al., 2016), the Uttarakhand Himalayan in India (Sharma et al., 2014), Christchurch and Wellington in New Zealand (Ren YF. et al., 2018). In fact, the material in the Earth is heterogeneous and anisotropic, and when there is a gradient in the velocity structure of the crust, the distance-dependent attenuation of seismic wave is more complex than the prespecified geometric spreading. Therefore, the solved quality factor may be abnormally large or negative in some frequency bands, which does not conform to the objective situation (Oth et al., 2008). Castro (1990) proposed a non-parametric spectral analysis method with an independent attenuation model, which uses discrete variables related to distance to represent the attenuation characteristics of seismic waves of different frequencies in the medium to obtain reliable attenuation. Bindi et al (2004) used this method to study the distance correlation and frequency correlation of the attenuation curve of Umbria-March earthquake sequence. Oth et al. (2008) improved the method to obtain multiple sets of data set results at the same time. Picozzi et al. (2017) then used genetic algorithms and neural networks on this basis to obtain more accurate source parameters. Then the method is widely used in the study of regional seismic characteristics (Ahmadzadeh et al., 2017; Jeong et al., 2020).

The strong-motion observation shows that the site conditions have great influence on the ground motion. With the deepening of research on strong-motion recordings and seismic safety assessment of engineering sites for major infrastructure, site research based on strong-motion data has become more comprehensive, such as terrain effects (Ren Y. F. et al, 2018; Fu et al., 2019), basin amplification (Wang et al., 2021b; Wang et al., 2022), site parameter estimation of (Zhang et al., 2022), site non-linear evaluation index (Ji et al., 2020), etc. In our study, the generalized inversion method is used to analyze the site effect. There are 111 seismic stations operating in the Guangdong Seismographic Network. The average distance between stations is about 54 km, which is widely distributed throughout the province for seismic data analysis and processing. In addition, Guangdong province also operates 78 earthquake early warning stations, 74 of which are established in eastern Guangdong, to monitor the characteristics of seismic waves and achieve early warning (Lin et al., 2020). Over the years, these stations have collected a lot of valuable recordings and attracted many scholars to study the characteristics of ground motion. However, previous studies were mostly focused on the whole Guangdong province (Huang et al., 2003; Xiong et al., 2020), or mainly on the Xinfengjiang reservoir area (Ye et al., 2016; Wang S. et al., 2018), and there were few studies on the ground motion characteristics in the eastern Guangdong, such as attenuation characteristics and site response. In this study, the spectral analysis was applied to the strong-motion recordings of a series of small earthquakes recorded at 27 stations in eastern Guangdong (distributed in Figure 1). The attenuation characteristics in the region, including geometric spreading and anelastic attenuation, were first systematically investigated. The site conditions and parameters of 27 stations were estimated from the borehole data and the inverted site responses, and were further used to study the site characteristics of eastern Guangdong. This study provides reference

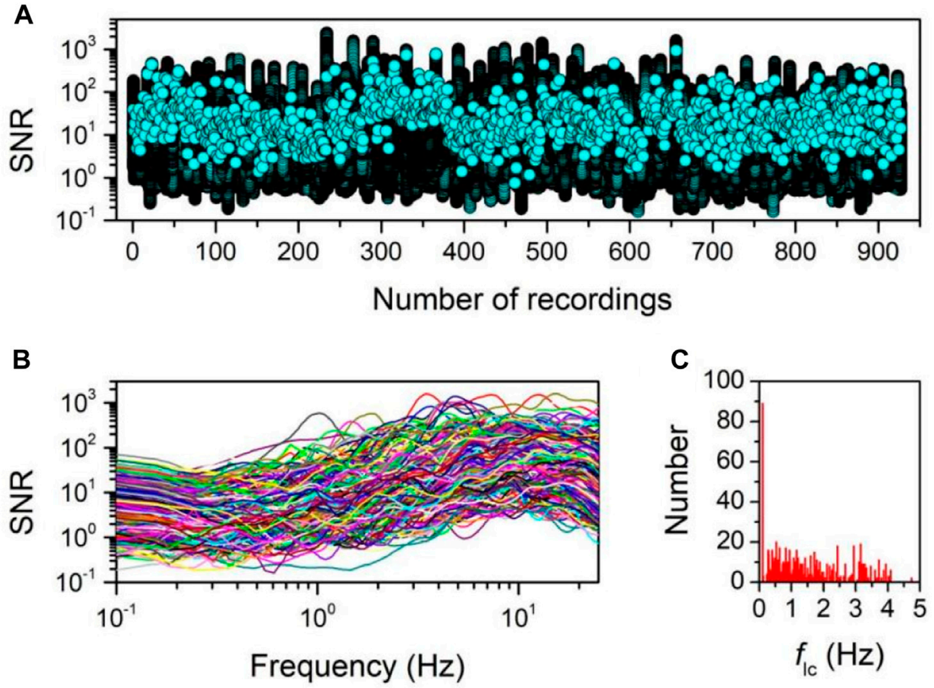

FIGURE 2
(A) The SNRs of the recordings considered in this study. **(B)** SNRs of each recording in frequency domain. **(C)** Histogram distribution of f_{lc} determined according to SNR.

for the siting of engineering and the seismic ground motion parameter zonation, and is of great significance for disaster prevention and mitigation in eastern Guangdong.

Data set and data processing

More than 900 strong-motion recordings were employed in this study, which are recorded from 27 strong-motion stations located in the eastern region of Guangdong Province (115°~118° E, 22°~25° N), China. These recordings are obtained from a series of small-scale events that occurred between January 2020 and January 2022, all but one (with a magnitude of M 3.7) of which had magnitudes below M 3.0. In spectral analysis, the S-wave of the entire waveform was applied. However, due to the small scale of the events, it is easy to make mistakes in the identification of S-wave, so we limited the maximum hypocentral distance to 120 km to minimize the interference caused by surface waves in the S wave (Ren YF. et al., 2018; Zhou et al., 2022a).

We initially manually eliminated recordings that were not available, such as incomplete recordings in three channels, apparent bad track in the channels, and the absence of P-wave or noise components in the recordings. After manual processing, baseline correction was performed on the remaining recordings. The high-cut corner frequency (f_{hc}) was uniformly set to 25 Hz, while the low-cut corner frequency (f_{lc}) was determined according to the signal-to-noise ratio (SNR) results of each recording. The calculation of SNR requires the extraction of the S-wave window and the Pre-P wave noise window of the same length as S-wave window. The arrivals of the P- and S-wave were identified as the abruptly increased point in the Husid plot (Husid, 1967), and the end of the S-wave was calculated by the energy method proposed by Pacor et al. (2016), which is related to the distance between the source and site. The end of the Pre-P wave noise window was set to 1.0 s before the P-wave onset. The SNR and f_{lc} of the recordings are shown in Figure 2. Figure 2A shows the SNR results of more than 900 recordings considered in this study, and more intuitively the SNR results of each recording in frequency domain are shown in Figure 2B. On the whole, the SNR results increased with the increase of frequency, but decreased when the frequency reached 20 Hz, indicating that the SNR results were more stable in the middle frequency band (~2–15 Hz). It should be noted that the SNR results are warped at low frequency, probably due to the large amount of noise component contained in the waveform. Figure 2C indicates a distribution of f_{lc} determined according to the SNR result, there are 88 recordings with f_{lc} of .1 Hz, and the rest are evenly distributed between .25 and 4 Hz.

The results of f_{lc} are used to perform a fourth-order Butterworth band-pass acausal filter in frequency domain (Zhou et al., 2022a). A cosine taper of 10% S-wave length was added to both ends of the extracted S-wave to eliminate truncation errors (Wang H. W. et al., 2018; Zhou et al., 2022b). The Fourier amplitude spectrum (FAS) of S-wave was calculated and smoothed by using the window function of Konno and Ohamachi with parameter $b = 20$. Using SNR as a measure of data quality (Wang et al., 2019; Wang et al., 2021b), our inversion uses a threshold of SNR = 3 (Oth et al., 2011; Jeong et al., 2020). When the frequency points with SNR <3 account for more than 15% of the total frequency points (i.e., the SNR passing rate of the recording is less than 85%), the recording was considered to be of poor quality and would be abandoned in the inversion. Figure 3A shows the available frequency band determined according to the filter and SNR. The f_{lc}

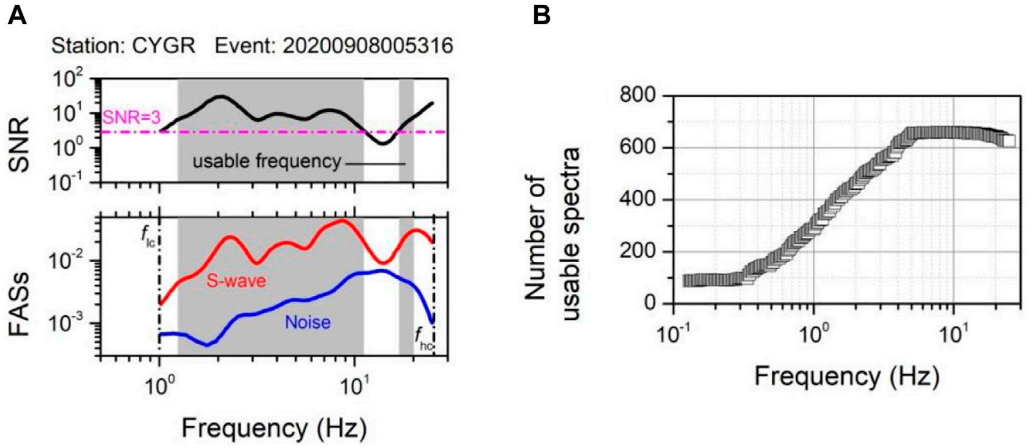

FIGURE 3
(A) The Fourier amplitude spectra for the exacted S-wave (red solid line) and the noise (blue solid line), and the corresponding SNR (dark solid line). The gray shaded areas indicated the usable frequency for inversion. **(B)** The number of usable spectra at each frequency.

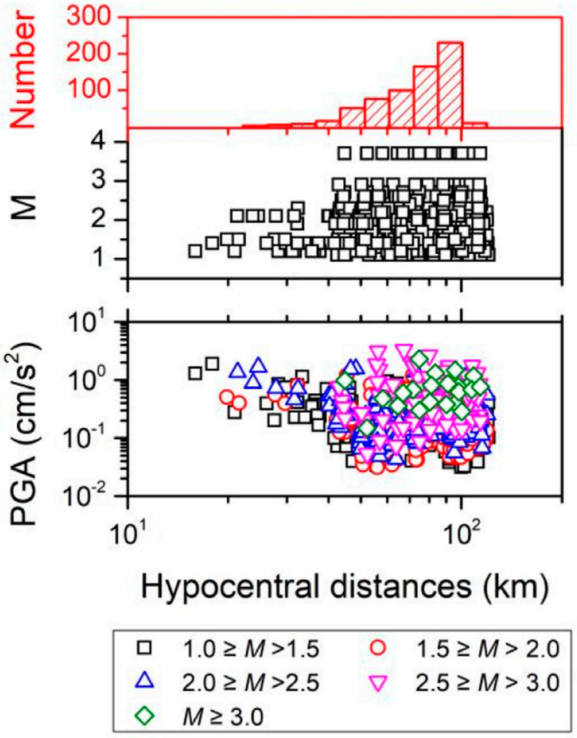

FIGURE 4
Distribution of magnitude and PGA vs. Hypocentral distances of recordings used for inversion. The red histogram is the cumulative distribution of Hypocentral distances.

and f_{hc} of the illustrated recording in Figure 3A are 1.02 and 25 Hz, and the spectra are usable (gray shaded areas) at a frequency range from $1.25f_{hc}$ to $f_{lc}/1.25$ (Abrahamson et al., 1997). The number of usable spectra at each frequency point are shown in Figure 3B. When the frequency is lower than 1 Hz, the number of usable spectra is less than half of the corresponding total number. To ensure the stability of the inversion results, each selected event should be recorded by at least four stations, and each station should collect at least four recordings.

In total, 659 strong-motion recordings from 67 events recorded at 27 strong-motion stations were assembled in the data set used for the inversion. The locations of earthquake epicenters and strong-motion stations considered in this study are shown in Figure 1. Figure 4 shows the magnitude and PGA distributed with distance of the recordings used for inversion. It was found that the PGAs were small, all of which were less than 10 gal, and tended to decrease with the increase of hypocentral distance. Twenty-four recordings were collected from event with magnitude of M 3.7, and the rest were obtained from events with $M < 3$. Although the scale of the events were small, resulting in the hypocentral distance of most recordings being within 100 km, it was sufficient to contribute a comprehensive coverage of the propagation path in the study area.

Methodology

In the frequency domain, we separated the S–wave of the observed spectral amplitude into source spectra, path attenuation, and site effect by using a one–step non–parametric generalized inversion technique (GIT) which was first proposed by Andrews (1986) and improved by Oth et al. (2011) in 2011. The propagation mechanism of seismic waves can be considered as the convolution of the above three contributions in the time domain and can be converted to the product in the frequency domain. After performing the natural logarithm operation, it can be transferred into a linear superposition in Eq. 1.

$$\ln O\left(f, M_i, R_{ij}\right) = \ln S\left(f, M_i\right) + \ln G\left(f\right) + \ln A\left(f, R_{ij}\right). \quad (1)$$

Where i represents the number of events and j represents the number of stations, in this study, $i = 1,2...67$, $j = 1,2...27$. $O(f,M_i,R_{ij})$ represents the acceleration Fourier spectrum with frequency f obtained at the j-th station resulting from the i-th earthquake with magnitude M_i. R_{ij} is the hypocentral distance, $S(f, M_i)$ accounts for the source acceleration spectrum of the i-th event, and $G(f)$ is the site

FIGURE 5
Site conditions and working environment of FSLHX station.

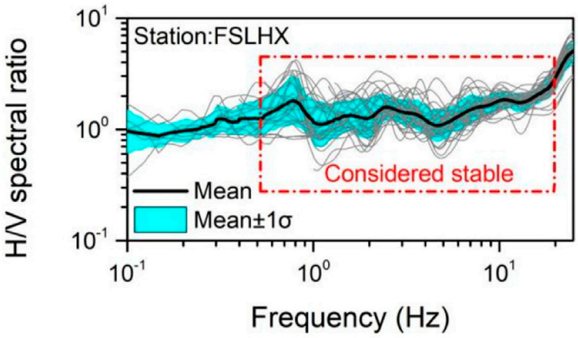

FIGURE 6
Horizontal-to-vertical (H/V) spectral ratios of the observed recordings at FSLHX station. The dark solid line and the cyan shaded area represent the mean and the range of mean plus or minus one standard deviation.

response of the j-th station. $A(f,r_{ij})$ is the attenuation term, which is a ground motion function estimated by distance, and is used to represent the attenuation characteristics of seismic waves at different frequencies in the propagation medium, including geometrical spreading, anelastic and scattering attenuation and all other factors leading to path attenuation. It is generally accepted that the amplitude of seismic waves is negatively correlated with the distance. Meanwhile, for the inelastic property of shallow crust, $A(f,r_{ij})$ should satisfies the following two assumptions: 1) $A(f,r_{ij})$ does not have any parametric functional form, and it is only constrained to be a smooth function of distance; 2) There is no path attenuation within the reference distance R_0 (the reference distance is the minimum hypocentral distance of the considered recordings, which is 15.97 km in this study), that is, $r = R_0$, the constraint of $A(f,r_{ij})$ is 1.0, independent of frequency. We adopt two weight coefficients, ω_1 and ω_2, to realize the assumptions of $A(f,r_{ij})$, which are expressed in the matrix as follow:

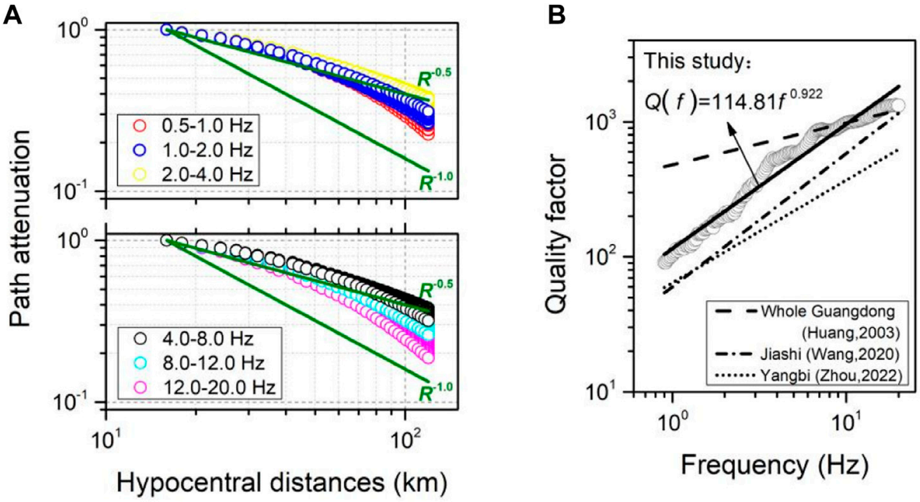

FIGURE 7
(A) .5–20 Hz path attenuation in eastern Guangdong. **(B)** .9–20.0 Hz frequency-dependent quality factor Q. Solid line represents the least squares regression curve, which is 114.81$f^{.922}$. The dashed line, dash-dotted line and dotted line indicate the quality factors of whole Guangdong province, Jiashi and Yangbi, respectively.

$$\left[\underbrace{\begin{matrix} 1 & 0 & 0 & 0 & \cdots & 0 \\ 0 & 1 & 0 & 0 & \cdots & 0 \\ \vdots & \vdots & \vdots & \vdots & \vdots & \vdots \\ 0 & 0 & 0 & 0 & \cdots & 1 \\ \omega_1 & 0 & 0 & 0 & \cdots & 0 \\ -\omega_2/2 & \omega_2 & -\omega_2/2 & 0 & \cdots & 0 \\ 0 & -\omega_2/2 & \omega_2 & -\omega_2/2 & \cdots & 0 \\ \vdots & \vdots & \vdots & \vdots & \vdots & \vdots \end{matrix}}_{N_D} \quad \underbrace{\begin{matrix} 1 & 0 & \cdots & 0 \\ 0 & 1 & \cdots & 0 \\ \vdots & \vdots & \vdots & \vdots \\ 0 & 0 & \cdots & 1 \\ 0 & 0 & \cdots & 0 \\ 0 & 0 & \cdots & 0 \\ 0 & 0 & \cdots & 0 \\ \vdots & \vdots & \vdots & \vdots \end{matrix}}_{I} \quad \underbrace{\begin{matrix} 1 & 0 & \cdots & 0 \\ 0 & 1 & \cdots & 0 \\ \vdots & \vdots & \vdots & \vdots \\ 0 & 0 & \cdots & 1 \\ 0 & 0 & \cdots & 0 \\ 0 & 0 & \cdots & 0 \\ 0 & 0 & \cdots & 0 \\ \vdots & \vdots & \vdots & \vdots \end{matrix}}_{J}\right].$$

$$\begin{bmatrix} \log A(f, R_{Bin1}) \\ \log A(f, R_{Bin2}) \\ \vdots \\ \log A(f, R_{BinN_D}) \\ \log S_1(f, M_1) \\ \vdots \\ \log S_I(f, M_I) \\ \log G_1(f) \\ \vdots \\ \log G_J(f) \end{bmatrix} = \begin{bmatrix} \log O_1(f, M_1, R_1) \\ \log O_2(f, M_2, R_2) \\ \vdots \\ \vdots \\ \log O_N(f, M_I, R_N) \\ 0 \\ 0 \\ 0 \\ \vdots \\ \vdots \end{bmatrix} \tag{2}$$

where, R_{Bin} is the minimum operation distance bin. In order to reflect the complex propagation characteristics, R_{Bin} should better as small as possible, while at the same time, it is necessary to ensure that there are enough available records in each bin. According to the distance distribution of records, R_{Bin} is taken as 3 km, and the hypocentral distances of the usable spectra at a frequency were divided into N_D bins. ω_1 specifies the attenuation of $A(f,r_{ij})$ from the reference distance and ω_2 constrain the smoothing characteristics of $A(f,r_{ij})$. After a lot of trial calculations, ω_1 and ω_2 are set as 20 and 500, respectively.

Equation 2 can be solved by using the singular value decomposition (SVD) method (Lawson and Hanson, 1974). However, there is an unconstrained degree of freedom in $I \times J$ matrix. It can be removed by specifying at least one reference site (Bindi et al., 2017; Ren YF. et al., 2018; Zhou et al., 2022b; Fu et al., 2022) or event (Fletcher & Boatwright, 1991; Moya & Irikura, 2003; Wang H. W. et al., 2018). In order to eliminate the trade-off between source and site terms, the FSLHX station was selected as the reference site, which is located on the hillside near Yongshun bridgehead, Xianfeng village. As shown in Figure 5, the FSLHX station is located on a hillside with dangerous terrain, surrounded by trees and weeds, and bare rock can be seen on the surface without covering the soil layer, which indicates that FSLHX is an accurate bedrock observation station. Next, we focus on the Horizontal-to-vertical (H/V) spectral ratios of 50 records received from the FSLHX station, see Figure 6, where the dark solid line represents the mean of the H/V spectral ratios, and the cyan shaded area is the mean plus or minus one standard deviation. The mean of H/V spectral ratio curve is flat and small in amplitude when the frequency is less than 10 Hz, demonstrating the excellent quality of bedrock stations; Until the frequency is greater than ~17 Hz, the slope of the curve becomes steep, showing obvious high-frequency amplification, which may be related to the orographic effect caused by the establishment of the FSLHX station on the hillside.

Result

Path attenuation and quality factor Q

We obtained the path attenuation in the frequency range of .5–20 Hz in eastern Guangdong. The minimum hypocentral distance is 15.97 km (reference distance R_0), and the maximum is 120 km. Taking 3 km as the minimum operation distance bin, it is divided into 36 bins from the minimum distance to the maximum distance. We calculated the path attenuation in each bin of different frequency, and the results are shown in Figure 7A. The points in these bins show a continuous decreasing trend with the increase of hypocentral distance. We divided frequencies from .5 to 20 Hz into six internals in log-average coordinates, .5–1.0 Hz, 1.0–2.0 Hz, 2.0–4.0 Hz, 4.0–8.0 Hz, 8.0–12 Hz, and 12–20 Hz. Among them, 4 Hz seems to be a turning point. When the frequency is lower than 4 Hz, the path attenuation becomes weaker with the increase of frequency, and when the frequency is higher than 4 Hz, the path attenuation becomes stronger with the increase of frequency. They are overall close to the simplest distance decay from described by $R^{-0.5}$, lower at some frequencies but higher at some frequencies.

As one of the important factors characterizing path attenuation, the quality factor $Q(f)$ value was obtained with dependent frequency. The path attenuation can be described in terms of anelastic attenuation and geometric spreading, which can be expressed as,

$$\ln A(f, R_m) = n \ln(R_0/R_m) - \pi f (R_m - R_0)/Q(f)\beta. \tag{3}$$

Where β_s is the assumed mean shear wave velocity of 3.55 km/s, n is the geometrical spreading exponent, which is obtained along with $Q(f)$ by applying the least-square method to solve Eq. 3. We obtained $n = .15$, representing the weak geometrical spreading. The frequency dependent quality factor is expressed as a power exponential form of $Q = Q_0f^{\eta}$. We obtained the regression coefficients $Q_0 = 114.81$ and $\eta = .922$ in the frequency range of .9–20 Hz, as shown in Figure 7B.

China is a country with high seismic hazard. In recent years, many moderate to large-scale earthquakes have occurred, attracting a large number of scholars to study the attenuation characteristics of seismic regions. Wang H. W. et al (2021) studied the intraregional attenuation characteristics of the Jiashi region in Xinjiang Province, and obtained the Q is $60.066f^{988}$. They found that the attenuation of near-field ground motion propagation in the Jiashi region was slower, but the attenuation in the far-field was faster due to the strong inelastic attenuation. Huang et al (2003) studied the path attenuation of the whole Guangdong province. They assumed a three-stage attenuation model of geometric spreading and obtained a quality factor of $481.5f^{31}$. Zhou et al (2022a) investigated the foreshock-mainshock-aftershock sequence of the Yangbi M 6.4 earthquake in 2021. The obtained Q was $64.27f^{76}$, which was significantly lower than that of the whole Yunnan region, indicating the stronger anelastic attenuation in the Yangbi region than the whole Yunnan region. It is found that the Q values in Jiashi and Yangbi regions were small, indicating the ground motion in the region decayed faster, especially in the far field. The relatively large Q values in eastern Guangdong indicated that the ground motion

TABLE 1 The criteria for site classification.

Equivalent shear wave velocity (V_{se}, m/s) overburden thickness (m)	Site classification				
	I_0	I_1	II	III	IV
$V_s > 800$	0				
$800 \geq V_s > 500$		0			
$500 \geq V_{se} > 250$		<5	≥5		
$250 \geq V_{se} > 150$		<3	3–50	>50	
$V_{se} \leq 150$		<3	3–15	15–80	>80

TABLE 2 Site conditions and calculated parameters at 27 stations.

Site code	Latitude (°)	Longitude (°)	Ground elevation (m)	f_p (Hz)	Max. amplification	V_{se} (m/s)	Overburden thickness (m)	Site classification
CADF	23.5052	116.6913	18.0	1.40	8.16	221	55.0	III
CAGHD	23.8638	116.6363	381.0	—	2.90	283	13.0	II
CAGHX	23.7576	116.5615	22.0	2.31	7.62	241	38.0	II
CHFX	23.4262	116.8067	22.0	2.14	25.12	136	119.0	IV
CHXN	23.5482	116.8828	24.1	1.46	12.32	128	109.0	IV
CNCD	23.2892	116.3258	12.0	3.10	13.21	204	118.0	III
CNLG	23.2201	116.4361	12.1	1.51	6.62	229	46.0	II
CYCN	23.2354	116.6279	38.1	2.49	18.26	268	65.0	II
CYGR	23.3946	116.4180	30.3	2.31	10.86	261	51.0	II
CYHX	23.3240	116.5477	21.2	8.10	16.02	182	46.2	I_1
DPFL	24.2621	116.8389	166.9	5.11	14.35	194	15.0	II
DPGB	24.1973	116.6387	61.5	2.99	18.62	298	29.0	II
FSHJ	24.0340	116.3952	49.8	15.47	9.60	172	2.5	I_1
FSLHX	23.9345	116.5072	155.7	—	5.12	$V_s > 800$	0	I_0
HJDH	23.3095	116.7480	42.0	—	3.28	394	15.0	II
HJGA	23.2296	116.7848	26.1	3.80	9.65	299	47.0	II
HLAJ	22.9809	116.0913	19.0	2.23	53.74	295	40.0	II
HLDL	23.0100	116.2777	49.0	2.99	12.57	245	1.0	I_1
HLQZ	22.9413	116.3805	24.0	3.53	36.95	370	27.0	II
HLZT	23.0220	116.4740	5.0	8.73	14.59	252	2.0	I_1
JLJC	24.6649	116.1697	132.7	4.33	7.54	231	11.0	II
LFJDD	22.9059	116.1763	9.0	3.80	9.29	358	13.0	II
LFJDX	22.8373	116.1031	12.0	3.66	13.48	324	27.0	II
LFJS	22.7650	115.8218	5.0	—	5.08	341	15.0	II
RPFB	23.7945	116.7356	330.0	—	4.14	234	11.0	II
RPJZ	23.6396	116.9614	29.0	2.44	6.63	191	7.0	II
RPQD	23.6997	116.8727	30.0	—	5.76	206	18	II

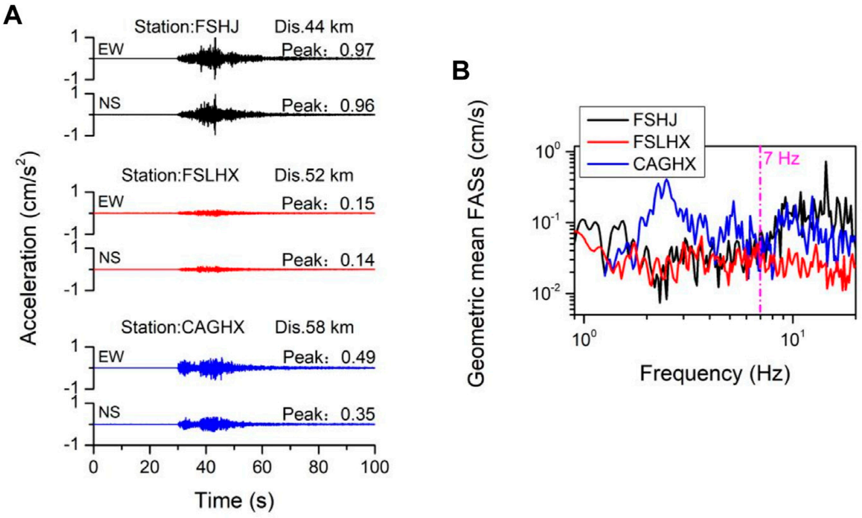

FIGURE 8
(A) Horizontal accelerations recorded by station FSHJ, FSLHX and CAGHX. **(B)** .9–20 Hz geometric mean Fourier amplitude spectrum of two horizontal components obtained by station FSHJ, FSLHX and CAGHX.

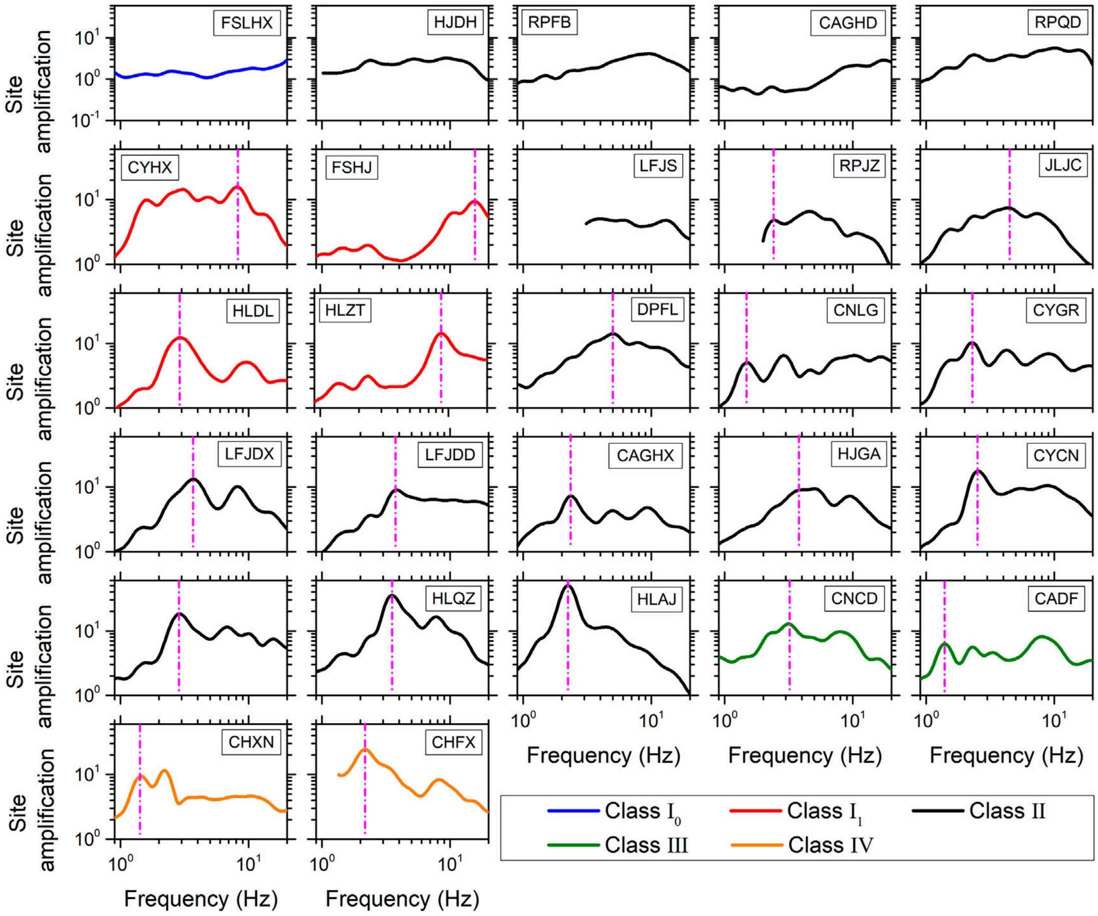

FIGURE 9
Inverted site responses of 27 stations employed in this study.

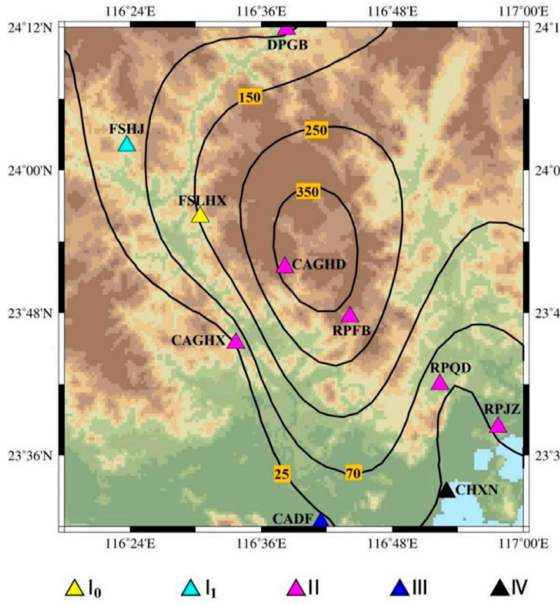

FIGURE 10
Geological conditions and elevation distribution of the stations. Yellow, cyan, pink, blue and black triangles represent sites classified as Class-I$_0$, Class-I$_1$, Class-II, Class-III, and Class-IV, respectively. The solid black lines indicate the elevation contour lines.

attenuation is slow and the capacity to dissipation seismic energy is weak, which also reflects the high regional seismic hazard.

Site classification

The site classification in our study was carried out in accordance with the relevant codes of the national standard of the People's Republic of China, "Code for Seismic Design of Buildings" (GB50011-2010, 2010). According to the equivalent shear wave velocity (V_{se}) of soil and the thickness of overburden, sites can be classified according to Table 1.

According to the definition of site classification in the national standard GB50011-2010, 27 stations employed in our study are classified into five categories, including 1 Class-I$_0$ site (uncovered rock), 4 Class-I$_1$ sites (soft rock or hard soil), 18 Class-II sites (moderately hard soil), 2 Class-III sites (deep or soft soil) and 2 Class-IV sites (very soft soil).

The equivalent shear wave velocity (V_{se}) is the average shear wave velocity in soil layer, which is defined by the principle that the propagation time of shear wave is constant from the surface to the calculated depth. It is obtained according to the condition that the time of seismic wave passing through the multi-layer soil layer within the calculated depth is equal to the time required to pass through a single soil layer. With the exception of the bedrock station FSLHX, the other 26 stations have detailed single-hole shear wave velocity reports, from which we calculated the V_{se} for the site. The specific V_{se} of each station can be found in Table 2. The small V_{se} of soil appears in the Chaoshan Basin near the coast of Nanao, which is a Quaternary neogenesis sedimentary basin. The south and southwest coasts of Chaoshan Basin are mountainous and hilly areas, with a larger V_{se}. Relatively soft sites such as Class-III (CNCD and CADF) and Class-IV (CHFX and CHXN) stations are mainly located along the coast and have a large thickness of overburden. The overlay thickness of the station CADF is 55 m, and that of the other three stations is all above 100 m.

Site response

We examined three sets of horizontal acceleration recordings recorded at stations FSHJ, FSLHX, and CAGHX, respectively (see Figure 8A), from the earthquake that occurred on 20 January 2020 (No. 20200120041711). This earthquake was the largest event in our study, with a magnitude of M 3.7 and an epicenter of 23.68°N and 116.01°E. The selection of these three recordings is mainly because the three stations have the same direction towards the event, and their hypocentral distances are relatively similar, which are 44, 52, and 58 km, respectively, to facilitate the elimination of path effect for comparative analysis. Among them, the station FSLHX is located on uncovered rock with a ground elevation of 156 m (see elevation distribution in Figure 10), and the two horizontal PGAs are .15 and .14 cm/s^2, respectively. The station FSHJ is located on the northwest slope of station FSLHX, with a ground elevation of about 50 m. The station FSHJ is closest to event 20200120041711 among the three stations, so it has a relatively large horizontal PGAs of .97 and .96 cm/s^2. The station CAGHX is located in a valley terrain with a ground elevation of 22 m The two horizontal PGAs are .49 and .35 cm/s^2, which are between station FSLHX and station FSHJ.

The .9–20 Hz geometric mean Fourier amplitude spectra of two horizontal components of three recordings are shown in Figure 8B. We found that the FAS of station FSLHX is flat and small at the whole frequency, indicating that the values obtained at each frequency of this bedrock station are relatively stable. What is interesting is that the amplitudes of stations FSHJ and CAGHX, which have the same large horizontal component, are quite different in the frequency domain. The FAS of station FSHJ is consistent with that of FSLHX when the frequency is lower than 7 Hz, and the amplitude of FAS began to increase when the frequency above 7 Hz, with a significant peak. The peak value of the FAS of station CAGHX appears between 2 and 3 Hz, and the amplitude decreases with the increase of frequency, especially in the high-frequency. This may be due to the strong attenuation of high-frequency motions caused by near-surface layer beneath station CAGHX (Guo et al., 2022). When the frequency is higher than 7 Hz, the amplitude is obviously smaller than that of FSHJ station, but still larger than that of FSLHX station.

This phenomenon is more intuitively reflected in the site response obtained by inversion of the three stations. Figure 9 shows the site responses of 27 stations employed in this study. The site response curve of station FSLHX is small and has no obvious peak value, which is consistent with the average value obtained from HVSR. The site response curve of station FSHJ has an obvious peak at 15.47 Hz, whose maximum site response is 9.60. It is generally believed that the site response of Class-I$_1$ site is small at low frequencies, and the predominant frequency (f_P) often occurs at middle to high frequencies. The larger spike values of station FSHJ at such high frequencies may be due to the topographic effects of the location. Therefore, we investigated the geographical location and elevation distribution of the stations, and the results are shown in Figure 10. The curves in

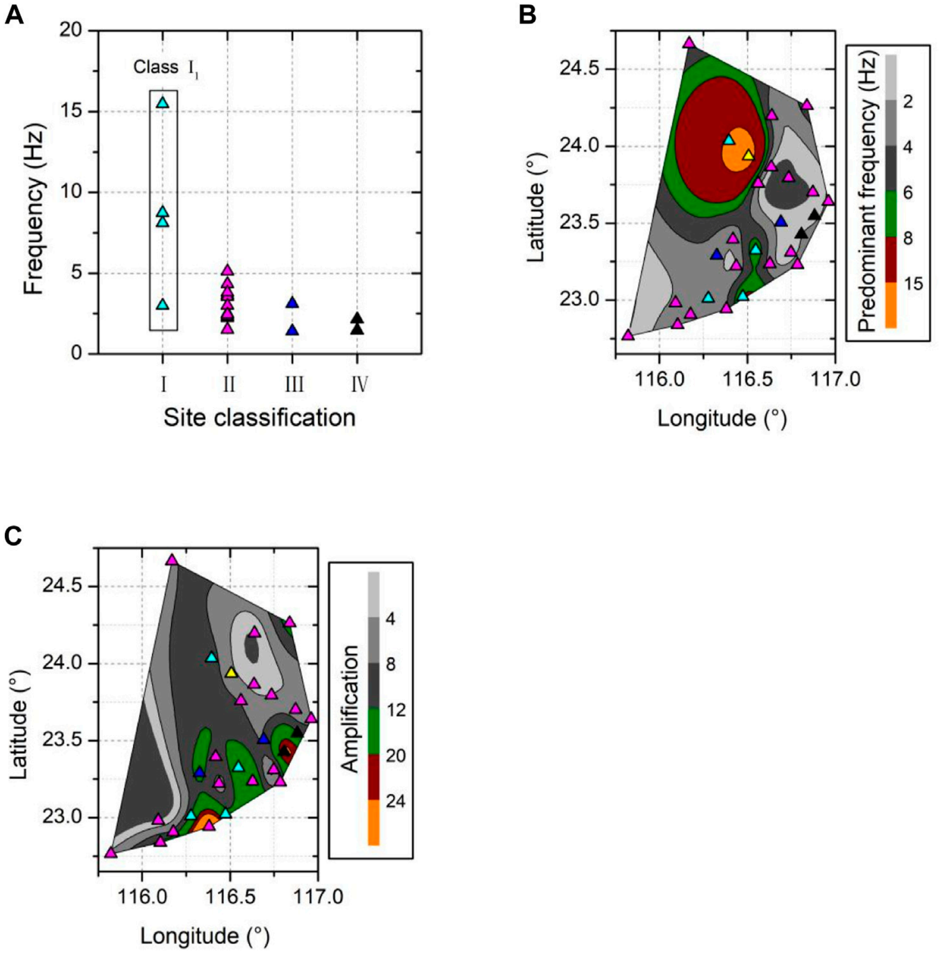

FIGURE 11
(A) Distribution of site classification vs. predominant frequency. **(B)** Predominant frequency distribution of stations. **(C)** Geographical distribution of site amplification.

the figure represent elevation contour lines, and the numbers on each line indicate the height in meter.

The geological conditions of the station FSHJ are mainly volcanic rocks and sub-volcanic rocks, whose texture is relatively soft in rocks. The rocks are covered with 2.5 m of soft soil and moderate soft soil. Moreover, the station is located in the foothills, exactly in the concave valley terrain, resulting in significant amplification at high frequencies. The station CAGHX is located on the edge of the mountain and hills, where the rock is covered from top to bottom with 13 m of moderate soft soil, 25 m of moderate hard soil and 13.5 m of hard soil. The site response of station CAGHX is more in line with the case of moderate soft soil, and there is obviously amplified at medium and low frequencies, that is, the maximum site response is 7.62 at 2.31 Hz.

Figure 11A shows the distribution of the predominant frequencies and site classification of 21 stations that can identify the predominant frequency. On the whole, the predominant frequencies tended to move to lower frequencies when the site classification ranging from Ⅰ to Ⅳ. In the case of site classification, Class-Ⅰ contains two subcategories, $Ⅰ_0$ and $Ⅰ_1$. The site response of station FSLHX of class $Ⅰ_0$ was relatively flat, and the predominant frequency could not be clearly identified. However, the site response of station FSLHX tended to increase slowly with the increase of frequency, and the corresponding frequency of the maximum site response was already greater than 20 Hz, which was the highest among all stations. There are 18 Class-II stations, among which the predominant frequencies of 5 stations (CAGHD, HJDH, LFJS, RPFB, and RPQD) can not be identified. The site responses of these 5 stations are flat, and there are no obvious frequency correlation in amplification. Their overburden thickness range from 10 to 20 m, and the surface layer is mainly covered by hard soil and moderate hard soil. The predominant frequencies of the remaining 13 stations are basically less than 5 Hz, and the overburden thickness of most of them is greater than 25 m, the surface layer is covered with moderate soft soil and moderate hard soil. The predominant frequencies of Class-III and Class-IV stations are small (almost less than 3 Hz), but the amplification of Class-IV stations is significantly larger than that of Class-III stations. The predominant frequency distribution of stations are shown in Figure 11B. The frequency band range is indicated by different chroma bands. It should be noted that the distribution of predominant frequencies does not include the results of five stations that cannot identify the predominant frequencies. The higher predominant frequency is concentrated in the location of Class-I stations. The distribution of the site amplification in geographic coordinates is shown in Figure 11C. The larger amplification was seen mainly in the two Class-IV stations located on the east coast, which, conversely, had the lower predominant frequency. In general, the soil around Shantou is relatively soft, resulting in strong site amplification during earthquakes, especially the long-period (low-frequency) ground motion, which will cause greater damage to the area.

Conclusion

The eastern Guangdong is the most seismically active region in Guangdong Province, which is distributed with geological tectonic fault zones that tend to strike east-west, northeast-southwest. A dense network of strong-motion stations has been set up in eastern Guangdong, providing sufficient information for seismic data analysis and processing. In this study, the one-step non-parametric generalized inversion technique was applied to 659 strong-motion recordings of 67 small events recorded by 27 stations in eastern Guangdong. The observation spectrum was separated simultaneously into source spectrum, path attenuation and site terms.

The inverted path attenuation curves are generally close to the simplest distance decay form described by $R^{-.5}$. In frequency, the path attenuation also show some frequency dependence, i.e. the attenuation curve decays more slowly at higher frequencies when the frequency is below 4 Hz, while the opposite is true when the frequency is above 4 Hz. We further consider the geometric spreading and inelastic attenuation to briefly describe the complex path attenuation. In the frequency range of .9–20 Hz, the non-linear least squares regression receive a geometric spreading $R^{-.15}$ and a quality factor $Q_s(f) = 114.81f^{922}$. The Q value in eastern Guangdong are larger than those in the Yangbi and Jiashi regions, showing a weaker ability to dissipate seismic energy, indicating a higher seismic hazard in eastern Guangdong.

Site conditions and parameters for 27 stations were estimated from the borehole data and inverted site response, and were further used to investigate site characteristics, i.e., predominant frequency, amplification, equivalent shear wave velocity and site classification. Site responses in eastern Guangdong exhibited strong correlation with the geological and geotechnical characterization. The stations located in mountainous area have higher fundamental frequencies and smaller amplifications during earthquakes. The stations located along the coast, especially in Shantou area, have stronger amplifications and lower fundamental frequencies, indicating that the area will suffer greater damage in far-field earthquakes.

Data availability statement

The original contributions presented in the study are included in the article/supplementary material, further inquiries can be directed to the corresponding author.

Author contributions

Conceptualization, YZ and HW; methodology, YZ, YQ, and FY; software, HW, YZ, GY, and GW; formal analysis, YZ, HW, and YZ; investigation, YZ, HW, and YQ; resources, HW, FY, and YZ; data curation, YZ, HW, and GY. All authors have read and agreed to the published version of the manuscript.

Funding

This work was supported by the Science for Earthquake Resilience of China Earthquake Administration (No. XH21023), the Science and Technology Planning Project of Guangdong Province (No. 2021B1111610008), and the Science and Technology Research Project of Jilin Provincial Department of Education (No. JJKH20230340KJ).

Acknowledgments

We would also like to thank three senior engineers, Wei Lin, Shukun Wu, and Zhujin Su, for their support in the data acquisition.

Conflict of interest

Publisher's note

References

Abrahamson, A. N., and Silva, W. J. (1997). Empirical response spectral attenuation relations for shallow crustal earthquakes. *Seismol. Res. Lett.* 68, 94–127. doi:10.1785/gssrl.68.1.941997

Ahmadzadeh, S., Parolai, S., Doloei, J., and Oth, A. (2017). Attenuation characteristics, source parameters and site effects from inversion of S waves of the March 31, 2006 Silakhor aftershocks. *Ann. Geophys.* 60 (6). doi:10.4401/ag-7520

Andrews, D. J. (1986). Objective determination of source parameters and similarity of earthquakes of different size. *Geophys. Monogr. Ser.* 37, 259–267.

Bindi, D., Castro, R., Franceschina, G., Luzi, L., and Pacor, F. (2004). The 1997–1998 umbria-marche sequence (central Italy): Source, path, and site effects estimated from strong motion data recorded in the epicentral area. *J. Geophys. Res.* 109 (B04312). doi:10.1029/2003jb002857

Bindi, D., Spallarossa, D., and Pacor, F. (2017). Between-event and between-station variability observed in the fourier and response spectra domains: Comparison with seismological models. *Geophys. J. Int.* 210 (2), 1092–1104. doi:10.1093/gji/ggx217

Castro, R. R., Anderson, J. G., and Singh, S. K. (1990). Site response, attenuation and source spectra of S waves along the Guerrero, Mexico, subduction zone. *Bull. Seismol. Soc. Am.* 80 (6), 1481–1503.

Fletcher, J. B., and Boatwright, J. (1991). Source parameters of Loma Prieta aftershocks and wave propagation characteristics along the San Francisco peninsula from a joint inversion of digital seismograms. *Bull. Seismol. Soc. Am.* 81, 1783–1812.

Fu, L., Chen, S., Li, J., Zhang, L., Xie, J., and Li, X. (2022). Regional spectral characteristics derived using the generalized inversion technique and applications to stochastic simulation of the 2021 Mw 6.1 Yangbi earthquake. *Bull. Seismol. Soc. Am.*, 1–23.XX

Fu, L., Li, X., Wang, F., and Chen, S. (2019). A study of site response and regional attenuation in the longmen Shan region, eastern Tibetan plateau, sw China, from seismic recordings using the generalized inversion method. *J. Asian Earth ences* 181 (1), 103887. doi:10.1016/j.jseaes.2019.103887SEP.

Gb50011-2010 (2010). *Code for seismic design of buildings: GB50011-2010*. Beijing, China: China Architecture & Building Press.

Guo, Z., Guan, M., and Chapman, M. C. (2022). Amplification and attenuation due to geologic conditions in the sichuan basin, central China. *Seismol. Res. Lett*, 1–15.XX.

He, P. (2020). Study of assessment method based on coupling factor of casualty in earthquake disasters in Guangdong area. *Int. J. Comput. Syst. Sci. Eng.* 2020 (3), 35.

Huang, Y. L., Zheng, S. H., Liu, J., Zhao, X. Q., and Kang, Y. (2003). Attenuation of ground motion and site response in Guangdong region. *Chin. J. Geophys.* 46 (1), 54–61.(in Chinese)

Husid, P. (1967). *Gravity effects on the earthquake response of yielding structures*. Pasadena, California: Report of Earthquake Engineering Research LaboratoryCalifornia Institute of Technology.

Iwata, T., and Irikura, K. (1988). Source parameters of the 1983 Japan sea earthquake sequence. *J. Phys. Earth* 36 (4), 155–184. doi:10.4294/jpe1952.36.155

Jeong, S. J., Stump, B. W., and Deshon, H. R. (2020). Spectral characteristics of ground motion from induced earthquakes in the fort worth basin, Texas, using the generalized inversion technique. *Bull. Seismol. Soc. Am.* 110 (5), 2058–2076. doi:10.1785/0120200097

Ji, K., Wen, R. Z., Ren, Y. F., and Dhakal, Yadab P. (2020). Nonlinear seismic site response classification using K-means clustering algorithm: Case study of the September 6, 2018 Mw6.6 Hokkaido Iburi-Tobu earthquake, Japan. *Soil Dyn. Earthq. Eng.* 128.paper ID: 105907

Jia, L. H., Mao, J. W., Liu, P., and Yu, M. (2020). Crust-mantle interaction during subduction zone processes: Insight from late Mesozoic I-type granites in eastern Guangdong, SE China. *J. Asian Earth Sci.* 192, 104284. doi:10.1016/j.jseaes.2020.104284

Kawase, H., and Matsuo, H. (2004). "Amplification characteristics of K-NET, KiK-net, and JMA Shindokei network sites based on the spectral inversion technique," in 13th World Conference on Earthquake Engineering, Vancouver, Canada, August 2004.[J]1-6 Paper Number 454

Lawson, C. L., and Hanson, R. J. (1974). *Solving least squares problems*.SIAM, Thailand.

Li, Y. H., Guo, L. T., and Yan, Y. X. (2021). Earthquake hazard evaluation of Huizhou fault and its adjacent area. *Seismol. geomagnetic observation Res.* 42 (1), 49–60.(in Chinese)

Lin, Q. X., Liang, M., Yang, X., and Jiang, X. J. (2020). The estimation of horizontal location ability for Guangdong Seismic Network. *South china J. Seismol.* 40 (4), 49–55.(in Chinese)

Liu, T. P., Yang, X. D., and Wang, Y. F. (2003). Seismicity features and seismic risk analysis in the near future in Guangdong and its neighboring region. *South China J. Seismol.* 23 (3), 35–40.(in Chinese)

Moya, A., and Irikura, K. (2003). Estimation of site effects and *Q* factor using a reference event. *Bull. Seismol. Soc. Am.* 93 (4), 1730–1745. doi:10.1785/0120020220

Nakano, K., Kawase, H., and Matsushima, S. (2015). Statistical properties of strong ground motions from the generalized spectral inversion of data observed by K-NET, KiK-net, and the JMA shindokei network in Japan. *Bull. Seismol. Soc. Am.* 105 (5), 2662–2680. doi:10.1785/0120140349

Oth, A., Bindi, D., Parolai, S., and Wenzel, F. (2008). S-Wave attenuation characteristics beneath the vrancea region in Romania: New insights from the inversion of ground-motion spectra. *Bull. Seismol. Soc. Am.* 98 (5), 2482–2497. doi:10.1785/0120080106

Oth, A., Parolai, S., and Bindi, D. (2011). Spectral analysis of k-net and kik-net data in Japan, part i: Database compilation and peculiarities. *Bull. Seismol. Soc. Am.* 101 (2), 652–666. doi:10.1785/0120100134

Pacor, F., Spallarossa, D., Oth, A., Luzi, L., Puglia, R., Cantore, L., et al. (2016). Spectral models for ground motion prediction in the L'aquila region (central Italy): Evidence for stress-drop dependence on magnitude and depth. *Geophys. J. Int.* 204, 697–718. doi:10.1093/gji/ggv448

Picozzi, M., Oth, A., Parola, S., Bindi, D., De, L., Amoroso, O., et al. (2017). Accurate estimation of seismic source parameters of induced seismicity by a combined approach of generalized inversion and genetic algorithm: Application to the geysers geothermal area, California. *J. Geophys. Res.* 2017

Ren, Y. F., Zhou, Y., Wang, H. W., Wen, R. Z., et al. (2018a). Source characteristics, site effects, and path attenuation from spectral analysis of strong-motion recordings in the 2016 kaikōura earthquake sequence. *Bull. Seismol. Soc. Am.* 108 (3B), 1757–1773. doi:10.1785/0120170290

Ren, Y. F., Wang, H. W., Xu, P. B., Dhakal, Yadab P., Wen, R. Z., Ma, Q., et al. (2018b). Strong-motion observations of the 2017 Ms7.0 jiuzhaigou earthquake: Comparison with the 2013 Ms7.0 lushan earthquake. *Seismol. Res. Lett.* 89 (4), 1354–1365. doi:10.1785/0220170238

Ren, Y. F., Wen, R. Z., Yamanaka, H., and Kashima, T. (2013). Site effects by generalized inversion technique using strong motion recordings of the 2008 Wenchuan earthquake. *Earthq. Eng. Eng. Vib.* 12, 165–184. doi:10.1007/s11803-013-0160-6

Sharma, J., Chopra, S., and Roy, K. S. (2014). Estimation of source parameters, quality factor (QS), and site characteristics using accelerograms: Uttarakhand himalaya region. *Bull. Seismol. Soc. Am.* 104 (1), 360–380. doi:10.1785/0120120304

Shu, L. S., Wang, J. Q., and Yao, J. L. (2019). Tectonic evolution of the eastern Jiangnan region, South China: New findings and implications on the assembly of the Rodinia supercontinent. *Precambrian Res.* 322, 42–65. doi:10.1016/j.precamres.2018.12.007

Tsuda, K. (2010). Inversion analysis of site responses in the kanto basin using data from a dense strong motion seismograph array. *Bull. Seismol. Soc. Am.* 100 (3), 1276–1287. doi:10.1785/0120090153

Wang, H. W., Ren, Y. F., Wen, R. Z., and Xu, P. B. (2019). Breakdown of earthquake self-similar scaling and source rupture directivity in the 2016–2017 central Italy seismic sequence. *J. Geophys. Res. Solid Earth* 124, 3898–3917. doi:10.1029/2018JB016543

Wang, H. W., Ren, Y. F., and Wen, R. Z. (2018a). Source parameters, path attenuation and site effects from strong-motion recordings of the Wenchuan aftershocks (2008–2013) using a non-parametric generalized inversion technique,path attenuation and site effects from strong-motion recordings of the Wenchuan aftershocks (2008-2013) using a non-parametric generalized inversion technique. *Geophys. J. Int.* 212, 872–890. doi:10.1093/gji/ggx447

Wang, H. W., Li, C. G., Wen, R. Z., and Ren, Y. F. (2022). Integrating effects of source-dependent factors on sediment-depth scaling of additional site amplification to ground-motion prediction equation. *Bull. Seismol. Soc. Am.* 112 (1), 400–418. doi:10.1785/0120210134

Wang, H. W., and Wen, R. Z. (2021b). Attenuation and basin amplification revealed by the dense ground motions of the 12 July 2020 MS 5.1 Tangshan, China, earthquake. *Seismol. Res. Lett.* 94 (2), 2109–2121. doi:10.1785/0220200400

Wang, H. W., Wen, R. Z., and Ren, Y. F. (2021a). Seismic ground motion simulation considering regional characteristics: A case study of the Jiashi Ms6.4 earthquake in 2020. *Seismol. Geol.* 43 (2), 430–446.(in Chinese)

Wang, J., Wang, L. M., Gong, F. Y., FanYing, G., Yan, W., ChengMing, W., et al. (2021c). Temperature and pressure conditions of dynamic metamorphism with its constraints on polymetallic mineralization of tungsten, tin and copper in Lianhuashan fault zone in eastern Guangdong Province. *Acta Petrol. Sin.* 37 (6), 1921–1932. doi:10.18654/1000-0569/2021.06.17(in Chinese)

Wang, S., Sun, X. L., Qin, J. L., et al. (2018b). Fine faults structure of Xinfengjiang water reservoir area from high-frequency ambient noise tomography. *Chin. J. Geophys.* 61 (2), 593–603.(in Chinese)

Xie, Y. S. (1992). Historical seismicity of the offshore Fujian-Guangdong region. *Acta Seismol. Sin.* 5 (3), 635–646. doi:10.1007/bf02650557

Xiong, C., Ye, X. W., and Zhang, Y. X. (2020). Site response of Guangdong seismic stations and its influence on determination of earthquake magnitude. *South China J. Seismol.* 40 (4), 18–28.(in Chinese)

Xu, Q. J., Liu, S. F., Wang, Z. F., and Zhang, B. (2019). Provenance of the east Guangdong basin and yong'an Basin in southeast China: Response to the mesozoic tectonic regime transformation. *J. Asian Earth Sci.* 185, 104024. doi:10.1016/j.jseaes.2019.104024

Ye, X. W., Huang, Y. M., and Liu, J. P. (2016). 3D P-wave velocity structure and active tectonics in the Xinfengjiang area of Guangdong. *Earthq. Res. China* 32 (3), 465–476.(in Chinese)

Yue, X. H., Liu, L., Zhang, Z. G., et al. (2022). Petrogenesis of the jurassic representative volcanic rocks in eastern Guangdong: Response to the early stage of the paleo-pacific subduction. *Geol. J. China Univ.* 28 (2), 199–210.(in Chinese)

Zhang, G. W., Guo, A. L., Wang, Y. J., Li, S., Dong, Y., Liu, S., et al. (2013). Tectonics of South China continent and its implications. *Sci. China Earth Sci.* 56, 1804–1828. doi:10.1007/s11430-013-4679-1(in Chinese)

Zhang, L. X. (2014). Seismic risk analysis in Guangzhou and its neighboring area. *Chin. J. Eng. Geophys.* 11 (4), 568–574.(in Chinese)

Zhang, Y. Q., Shi, D. N., Lü, Q. T., Xu, Y., Xu, Z., Yan, J., et al. (2021). The crustal thickness and composition in the eastern South China Block constrained by receiver functions: Implications for the geological setting and metallogenesis. *Ore Geol. Rev.* 130, 103988. doi:10.1016/j.oregeorev.2021.103988

Zhang, Y. T., Ren, Y. F., Wen, R. Z., et al. (2022). A method of site parameter estimation based on decision tree theory considering terrain features. *Chin. J. Geophys.* 65 (2), 698–710.(in Chinese)

Zhang, Z. Z., Pan, H., Wang, J., et al. (2008). Research on historical earthquakes in the eastern Guangdong. *Earthq. Res. China* 24 (3), 278–287.(in Chinese)

Zhou, Y., Miao, T. M., Yang, J., Wang, X., Wang, H., and Zheng, W. (2022b). Seismic wave attenuation characteristics from the ground motion spectral analysis around the Kanto Basin. *Buildings* 12 (318), 318. doi:10.3390/buildings12030318

Zhou, Y., Wang, H. W., Wen, R. Z., Miao, T. M., and Cui, J. W. (2022a). Source characteristics and path attenuation for the Yangbi, China seismic sequence in 2021. *Appl. Geophys.*179, (published on line)

Frontiers | Frontiers in Earth Science

TYPE Original Research
PUBLISHED 13 January 2023
DOI 10.3389/feart.2022.1081542

OPEN ACCESS

EDITED BY
Kun Ji,
Hohai University, China

REVIEWED BY
Pengfei Dang,
Guangzhou University, China
Xiaodan Sun,
Southwest Jiaotong University, China
Yuxiang Tang,
King Abdullah University of Science and Technology, Saudi Arabia

*CORRESPONDENCE
Mengtan Gao,
gaomt1957@163.com
Zongchao Li,
lizongchaoigo@163.com
Jize Sun,
sun_jize@126.com

†PRESENT ADDRESS
Zhiwei Ji and Zongchao Li,
Minzu University, Beijing, China

SPECIALTY SECTION
This article was submitted to Structural Geology and Tectonics,
a section of the journal
Frontiers in Earth Science

RECEIVED 27 October 2022
ACCEPTED 22 November 2022
PUBLISHED 13 January 2023

CITATION
Ji Z, Li Z, Sun J, Gao M, Li T, Huang T, Li N and Guo X (2023), Estimation of broadband ground motion characteristics considering source parameter uncertainty and undetermined site condition in densely populated areas of Pingwu.
Front. Earth Sci. 10:1081542.
doi: 10.3389/feart.2022.1081542

Estimation of broadband ground motion characteristics considering source parameter uncertainty and undetermined site condition in densely populated areas of Pingwu

Zhiwei Ji[1†], Zongchao Li[1*†], Jize Sun[2*], Mengtan Gao[1*], Tiefei Li[1], Ting Huang[1], Na Li[1] and Xiangyun Guo[1]

[1]Institute of Geophysics China Earthquake Administration, Beijing, China, [2]Shenzhen Academy of Disaster Prevention and Reduction, Shenzhen, China

Three destructive earthquakes occurred in Pingwu and Songpan, Sichuan Province, China, between August 16 and 23, 1976. Due to the seismic monitoring capability at that time, the ground motion characteristics of these earthquakes are very vague. Realistc and reliable strong ground motion input plays an important role in seismic building design and urban-scale earthquake damage simulation. This study reproduces the main broadband ground motion characteristics of the 1976 Ms7.2 Songpan earthquake in densely populated areas of Pingwu. The empirical Green's function method and finite difference method are used to simulate high-frequency and low-frequency ground motion, respectively, and the broadband ground motion is obtained by superposition within the frequency range. In addition, in combination with the "Recipe" source parameter scheme, various uncertainties in the source parameters are considered, including the source mechanism, source depth, asperity parameters, etc. We obtain 36 kinds of broadband ground motion at six typical locations in the Pingwu area. Moreover, we test the rationality of the obtained broadband ground motion by ground motion prediction equations(GMPEs), and the broadband ground motions are consistent with the local ground motion characteristics. The results show broadband ground motions obtained from the scenario earthquake in this paper can meet the destructive capacity of earthquakes of this magnitude. The hybrid method can effectively compensate for the lack of long-period components of the original empirical Green function method. This research also proves that the peak ground acceleration (PGA) of ground motion is mainly contributed by high-frequency ground motion components. Long-period ground motion contributes most to the peak ground velocity (PGV), and about twice the contribution of high-frequency ground motion. Concerning the Chinese seismic intensity scale (GB/T 17742-2020) and China Seismic Ground Motion Parameter Zoning Map (GB18306-2015), the basic fortification intensity in the Pingwu area is VIII. In this paper, the seismic intensity of PWN is VI-VII, indicating that the buildings at this location are less likely to be damaged after the earthquake. The seismic intensity of other regions is VII-IX and buildings are more likely to be damaged during the earthquake at these locations. There are many mountains and valleys in the Pingwu area, and the probability of landslides, debris flows, and other disasters after an earthquake is very high, and we should give special attention to the impact of secondary disasters caused by earthquakes. It is necessary to prevent dammed lakes and other disasters caused by landslides and debris flows.

KEYWORDS

broadband ground motion, uncertainty, finite difference method, green function method, recipe scheme

Introduction

On August 16, 1976, an Ms7.2 earthquake occurred at the junction of Songpan County and Pingwu County, Sichuan Province, China. Another two earthquakes occurred successively in the following week: an Ms6.7 earthquake on August 22 and an Ms7.2 earthquake on August 23 (Figure 1). The seismogenic structures of the three earthquakes are the Huya fault (Figure 1) at the east boundary of the Minshan fault block, which is located northwest of the Longmenshan fault. As the east boundary of the Minshan fault block, the Huya fault is located in the transition zone from the Bayan Hara block to the Motianling block, belonging to the geomorphic boundary between the high and middle mountains (Zhao et al., 1994; Zhou et al., 2006; Li et al., 2018). The Huya fault is also an important part of the compressional transformation tectonic system at the east end of the East Kunlun strike-slip fault (Kirby et al., 2007; Xu et al., 2008). Its seismic activity is frequent, and since historical records were initiated, many strong earthquakes with magnitudes of 6.0–7.2 have occurred along the boundary fault of the Minshan fault block. The Huya fault is located in the mountain valley area. Due to the limitation of traffic conditions, many scholars have different interpretations of its nature and segmentation. Some have reported that the Huya fault is a Quaternary thrust fault (Deng et al., 1994; Zhao et al., 1994), and some that the fault constitutes mainly strike slip with a thrust

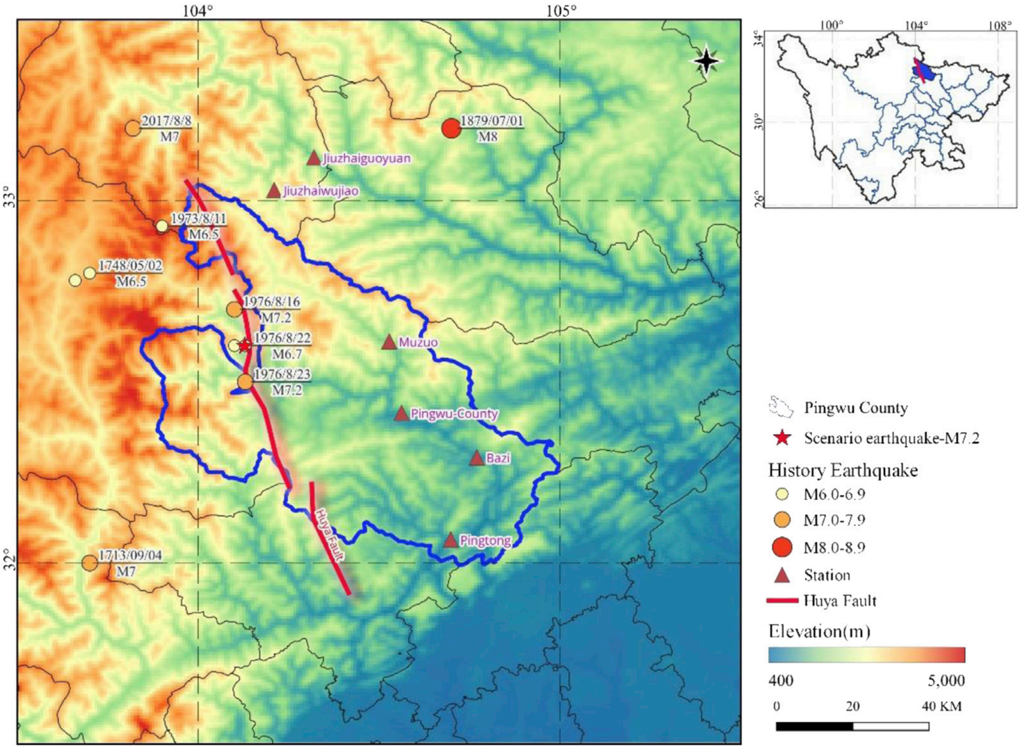

FIGURE 1
Maps showing the tectonic setting of the Pingwu Area.

nature (Jones et al., 1984; Zhou et al., 2006; Xu et al., 2008). The focal area of the Jiuzhaigou Ms7.0 earthquake in 2017 is located at the intersection of the Tazang, Minjiang and Huya faults (Xu et al., 2008), which shows that the Huya fault is still a strong active fault and that there is still the possibility of large earthquakes in the Songpan and Pingwu areas in the future.

Strong earthquakes in mountain and canyon areas are likely to cause a large number of secondary disasters in the region, such as mountain collapse, rockfall, and mud rock flow, causing severe casualties and economic losses. The Ms6.8 earthquake in Luding in 2022 was mainly associated with secondary disasters. The 1976 Songpan and Pingwu earthquake was one of the few successfully predicted earthquakes in history. Although it caused great damage to buildings, large casualties were prevented. With the development of the social economy, the economic losses caused by strong earthquakes are also increasing. Improving the seismic fortification level of buildings and improving the disaster prevention level of cities is one of the problems faced by seismic engineers and is an appropriate context for studying historical earthquakes. Because of limitations in earthquake-monitoring ability, most regions that have experienced strong earthquakes have failed to record the earthquake waveform to accurately characterize the characteristics of earthquake ground motion, which is unfortunate for most regions in the world that have experienced historical large earthquakes. To obtain a clearer understanding of the ground motion characteristics of these strong earthquakes and reduce the possible damage caused by future earthquakes, it is necessary to reproduce historical earthquakes using ground motion simulation methods.

For seismic analysis of lifeline projects and long-span structures, it is necessary to consider a wider frequency range of ground motion. Because the small-scale source information and the near-surface medium information are difficult to obtain, there is a large technical obstacle to directly simulate broadband ground motion. Therefore, the hybrid method of separately simulating low-frequency ground motion (<1 Hz) and high-frequency ground motion (>1 Hz) and superimposing them in the frequency domain is an effective means to obtain reasonable broadband ground motion. Graves and Pitarka (2010) combined a deterministic approach and a semistochastic approach to reproduce broadband ground motion of the Imperial Valley, Loma Prieta, Landers, and Northridge earthquakes. Thus far, the University of Southern California's Broadband Platform 22.4.0 platform (https://strike.scec.org/scecpedia/Broadband_Platform) has been used. A total of 9 broadband ground motion simulation schemes have been reported (Zeng et al., 1994; Motazedian and Atkinson., 2005; Graves and Pitarka., 2010; Mai et al., 2010; Schmides et al., 2010; Morikawa et al., 2011; Song, 2015; Iwaki et al., 2016a; Iwaki et al., 2016b; Pitarka et al., 2017). Three simulation schemes are based on the "Recipe" scheme proposed by Irikura and Miyake. (2011), that is, the arrangement and combination of high-frequency and low-frequency ground motion obtained by the high-frequency and low-frequency ground motion simulation method. The methods involved in the Recipe scheme include the frequency-wavenumber Green's function (FK method), Stochastic Finite-Fault method, finite difference method (FDM), and Stochastic method, etc. Hartzell et al. (1999) used the 3D finite difference method to calculate low-frequency ground motion and the Green function method to calculate high-frequency ground motion when investigating the broadband ground motion of the 1994 Northridge earthquake and evaluated the influence of different types of Green functions.

For long-period ground motion simulation, the finite element method is generally used, which can take into account the influence of complex geological structures such as terrain and basin. High-frequency ground motion simulation uses the empirical Green function method to simulate strong ground motion using small-earthquake records observed near the source area, which can effectively reproduce the ground motion characteristics of large earthquakes (Miyake et al., 2003). This method requires a sufficient number of small-earthquake records in the target area. Benefiting from China's increasingly improved earthquake-monitoring capability, we have obtained a large amount of earthquake-monitoring data and seismic waveforms in the Songping area, which gives us the opportunity to reproduce the seismic acceleration time history and corresponding seismic characteristics of the 1976 Songpan-Pingwu Ms7.2 earthquake at typical locations (densely populated areas, major project sites or lifeline project locations).

For the estimation of historical earthquakes, many parameters are uncertain, and uncertainties in the source and fault parameters affect the results of ground motion simulation (Atkinson and Beresnev, 2002; Aochi and Douglas, 2006; Sorensen et al., 2007; Causse et al., 2008; Graves et al., 2008; Ripperger et al., 2008; Wang et al., 2008; Ansal et al., 2009; Cultrera et al., 2010; Imperatori and Mai, 2012; Ji et al., 2022). Therefore, when simulating historical earthquakes, we focus on the uncertainty factors of many source parameters (such as asperity parameters, the source mechanism, and the initial rupture location), express the characteristics of ground motion with a reasonable range of values, and verify the reliability of ground motion evaluation results in combination with a variety of seismic attenuation relationships.

In this paper, the broadband ground motion simulation scheme is adopted to reproduce the ground motion characteristics of the 1976 Songpan Ms7.2 earthquake on the Huya fault at a typical location in the Pingwu area by focusing on multiple uncertainties in the source parameters. The empirical Green function is introduced based mainly on a large number of small-earthquake records recorded in the Songpan and Pingwu areas, which can take into account the rupture process of the source and the complexity of the propagation medium. The introduction of the finite difference method (FDM) is mainly due to its advantages of simple spatial discretization and high computational efficiency. In addition, considering uncertainties in the source parameters, a broadband ground motion simulation scheme is developed to simulate historical earthquakes; reproduce their broadband ground motion characteristics; provide effective data support for the seismic design of major mega projects, lifeline projects, and other research fields that need input of ground motion parameters; and provide some reference for reducing the severity of possible earthquake disasters in the Pingwu region in the future.

Recipe scheme and simulation method

Recipe broadband ground motion simulation scheme

The Recipe scheme is an optimization scheme for predicting future scenario earthquakes based on the characteristic source model. The scheme focuses on the correlation between the inhomogeneity of the fault rupture surface and uncertainties in the asperity parameters on the ground motion prediction results. Based on the empirical relationship between source parameters, the parameters of source models used to predict ground motion are divided into three categories: external parameters, internal parameters and other parameters. The external parameters are defined as the total rupture area and the total seismic moment of the fault. The internal parameters are defined as the nonuniform slip at the source, the area of the asperity, the stress drop of each asperity, etc. The fracture nucleation and termination mode is an external fault parameter related to active fault landforms (Irikura and Miyake, 2011). In the Recipe scheme, there are two important factors for predicting strong earthquake ground motion: one is the source model of each scenario earthquake, and the other is the use of an appropriate Green's function from the source to the site. Finally, the validity of the results is confirmed by comparing the historical data with the predicted ground motion. Using the Recipe scheme to estimate future scenario earthquakes can provide reasonable strong ground motion characteristics for seismic engineers, government earthquake emergency response personnel, etc., to facilitate subsequent corresponding actions (Irikura and Miyake, 2011). The present paper refers to the ground motion simulation scheme of Irikura and Miyake (2011) and develops a broadband ground motion simulation scheme (Figure 2).

Ground motion simulation method

We use the FDM to simulate the low-frequency ground motion in this paper. Aoi and Fujiwara. (1999) proposed a finite difference method based on discontinuous grids, which greatly improved the calculation efficiency on the premise of ensuring calculation accuracy. During the simulation of ground motion, the stratum medium is divided into grids of different thicknesses according to the depth, and the three-dimensional coordinates of the grids are given. The rupture area is set as the combination of finite sub faults, and the source parameters (slip, seismic moment, source time function) on the sub faults are calculated by difference to simulate the rupture process of the fault in the earthquake and then simulate the ground motion. This method can calculate the long-period ground motion of any three-dimensional heterogeneous medium structure and effectively simulate the long-period ground motion of complex geological structure areas such as fault zones and sedimentary basins (Iwaki and Iwata, 2010; Iwaki et al., 2016a; Luo et al., 2020). In this paper, the open source software Ground Motion Simulator (GMS) based on the discontinuous grid finite difference method is used to calculate the low-frequency part of broadband ground motion.

The empirical Green function method is used to simulate high-frequency ground motion in this paper. Hartzell (1978) first proposed this method, which mainly uses foreshock or aftershock records of large earthquakes as the Green function to synthesize large earthquakes. The source of a large earthquake is considered to be composed of a series of sub-earthquake sources, and an aftershock or foreshock record of appropriate size is selected as the Green function. A small earthquake is equivalent to a sub-earthquake. According to a certain rupture mode, these empirical Green functions are superposed to obtain the time history of the large earthquake ground motion. Irikura and Miyake et al. (Irikura and Kamae, 1994; Miyake et al., 2003; Irikura and Miyake, 2011) system proposed the idea of using empirical Green function method to simulate future ground motions, and verified the reliability of this method with several earthquake examples. They also summarized the general steps of the method to simulate ground motion. Through the continuous efforts of many scholars, the empirical Green function method has gradually developed into a relatively mature ground motion simulation method for strong earthquakes and has been widely recognized (Li et al., 2021, 2022).

After the low-frequency and high-frequency ground motion is simulated respectively, they are superimposed into broadband ground motion in the frequency domain. First, the two parts are filtered. The final frequency range of the high-frequency ground motion is 1–25 Hz, and the final frequency range of the low-frequency ground motion is 0.1–1.0 Hz. The high-frequency and low-frequency ground motion is superposed at a frequency of 1.0 Hz (Roten et al., 2012; Iwaki et al., 2016b), and the effective frequency band of the final broadband is 0.1–25.0 Hz (Figure 3).

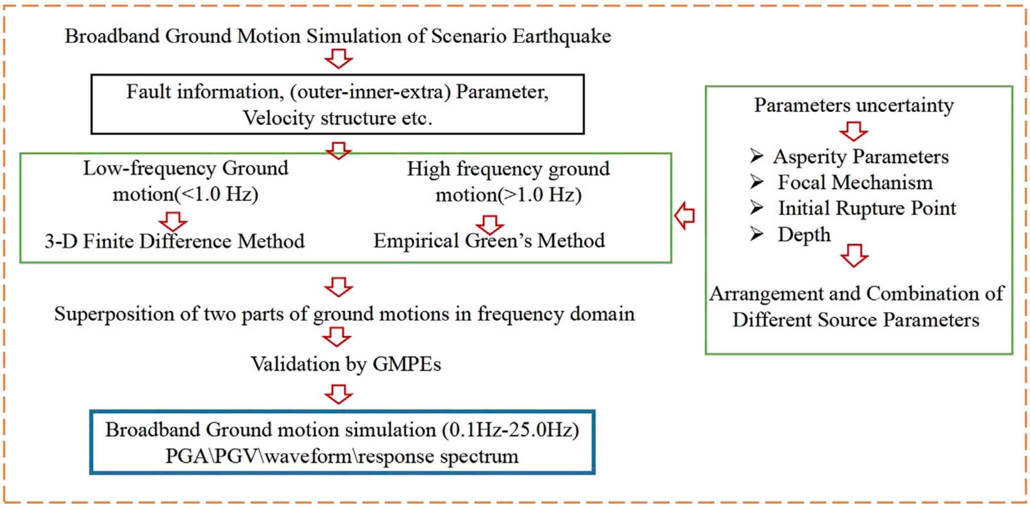

FIGURE 2
Flowchart of scenario earthquake broadband ground motion simulation in Pingwu Area.

Uncertainty in the source parameters

Uncertainties in the source parameters is the main factor to be considered in this study, arising mainly from uncertainties in the asperity parameters, the source mechanism, the source depth, the initial rupture point. The empirical Green function method and the finite difference method are used to address uncertainties in these parameters. Some parameters used in the two different methods have some difference which are caused by the difference of reference source and

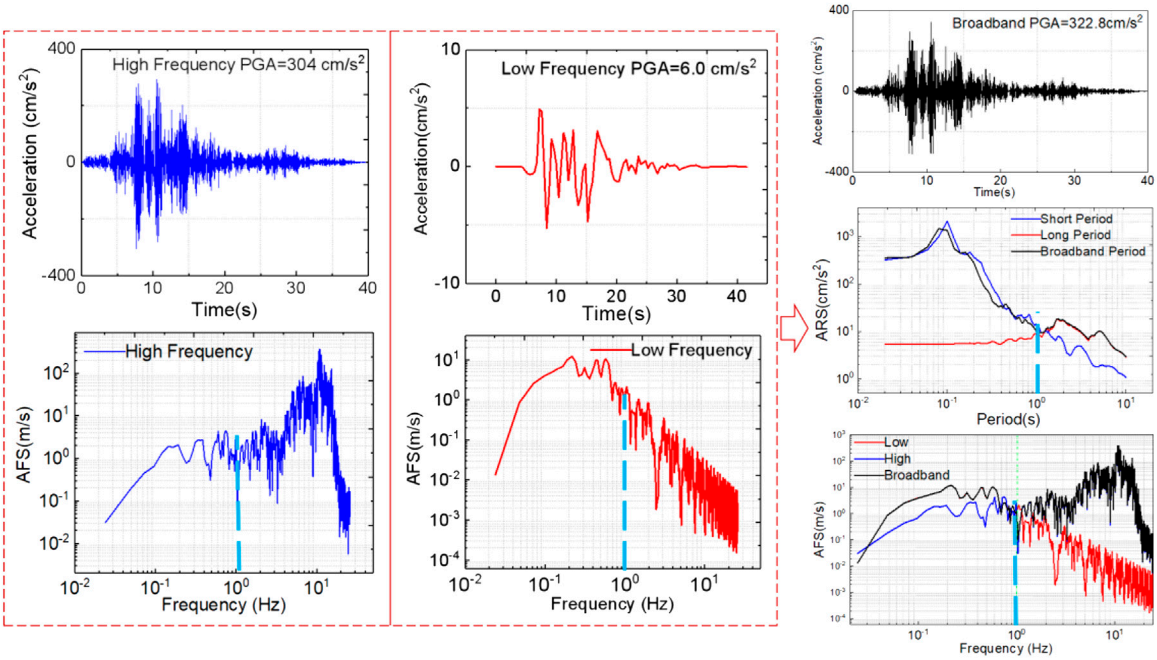

FIGURE 3
Schematic diagram of superposition of high-frequency and long-period ground motion waveforms in the frequency domain.

TABLE 1 Source parameters used by the finite difference method in the Pingwu scenario earthquake.

Source kinematics parameters	One asperity	Reference
Rupture area (km^2) = length (km)×width (km)	50 × 20	Wang, (2004)
Total seismic moment tensor M_0 (N·m)	3.98e+19	Hanks and Kanamori, (1979)
Average slip of the asperity/background area (cm)	330/115	Somerville et al., 1999; Wang, 2004
Asperity area (km^2)	220	
M_0 of the asperity/background area (N·m)	1.75e + 19/2.23e + 19	
Rise time of the asperity/background area (s)	2.987/1.493	Somerville et al. (1999)
Rupture velocity (km/s)	2.8	
Focal mechanism (strike/dip/rake)	340/Uncertainty/0	Tang and Liu, (1981)

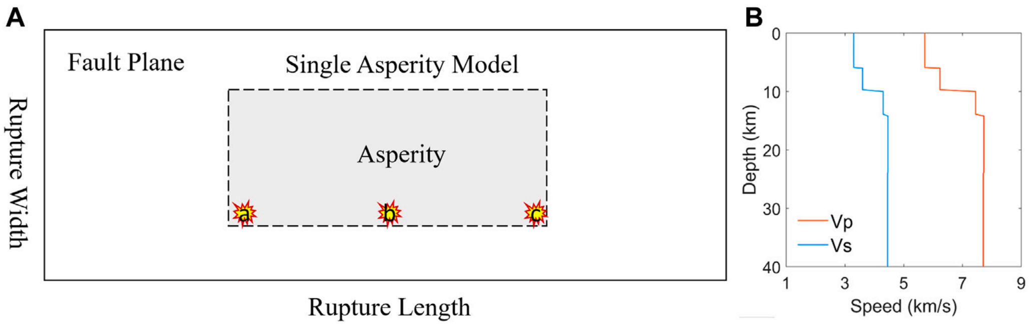

FIGURE 4
Asperity source model and crustal velocity structure used for synthesizing low-frequency ground motion **(A)** Asperity source model of the low-frequency ground motion **(B)** Velocity structure of the low-frequency ground motion.

experience relationship, such as the seismic moment-M_0 (Hanks et al., 1978; Somerville et al., 1999). The results also show that the difference of these parameters has little influence on the characteristic of ground motion when simulating the scenario earthquakes.

In this paper, the steps to obtain broadband ground motion are as follows: 1) For the source models of high-frequency and low-frequency ground motion, the uncertainties in the source parameters are considered for calculation; 2) We arrange and combine the obtained ground motion to obtain the documents required for merging broadband ground motion; and 3) the ground motion is spliced at the frequency of 1.0 Hz to output the broadband ground motion time history.

TABLE 2 Source parameters used in the empirical Green function method for Pingwu scenario earthquakes.

Source parameters		Reference
Magnitude	Ms7.2	Tang and Liu, (1981)
Seismic moment (N·m)	7.08e+19	Somerville et al. (1999)
Source depth (km)	10/15/22	Tang and Liu, (1981)
Fault area (km^2)	60× 30	Tang and Liu, (1981)
Asperity area (km^2)	28.3× 14.2	Somerville et al. (1999)
Shear wave velocity (km/s)	3.5	Yao et al. (2019)
Focal mechanism	175°–45°/60°/75°–57°	Institute of Geophysics, China Earthquake Administration

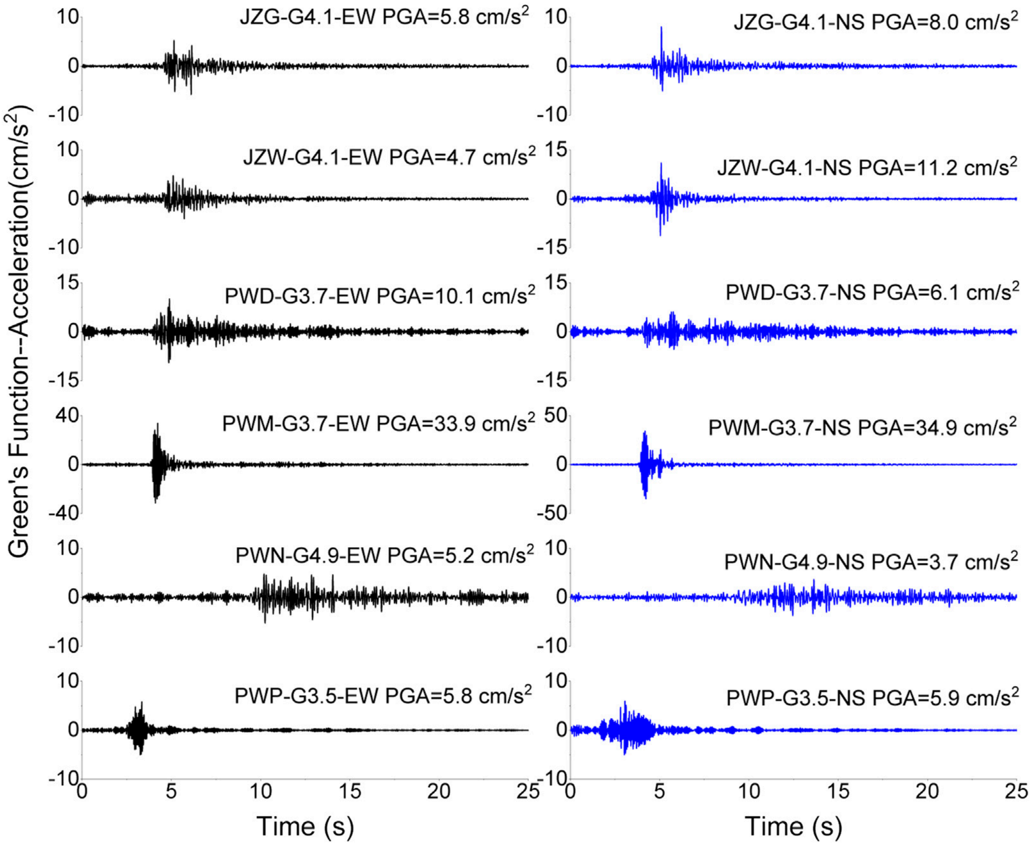

FIGURE 5
Horizontal Green function waveform and PGA at typical locations.

The source model used in the finite difference method needs to define parameters such as the rupture size, seismic moment, rise time, source mechanism, and asperity parameters (number, area). The type of fault, rupture speed and position of the initial rupture point affect the low-frequency ground motion. The uncertainty in these parameters should be taken into account when simulating low-frequency ground motion. The source parameters set for these ground motion in this paper are

TABLE 3 Key parameters of Green function taken at each typical location in the Pingwu scenario earthquake.

Minor earthquake magnitude	M3.5	M3.7	M4.9	M4.1
Stress drop ratio C of large and small earthquakes	1.96	1.96	1.96	1.96
Number of sub faults	43	34	9	22
Sub fault length × sub fault width	0.66 km×0.33 km	0.83 km×0.42 km	3.14 km×1.57 km	1.28 km×0.64 km

Note: The magnitude of small earthquakes used at each location is not fixed, and each small earthquake has corresponding key parameters for scenario earthquakes.

TABLE 4 Relative position of stations corresponding to calculation points.

Calculation position	Jiuzhai wujiao	Jiuzhai guoyuan	Pingwu	Muzuo	Bazi	Pingtong
Station NO.	JZW	JZG	PWD	PWM	PWN	PWP
Epicentral distance (km)	37.4	47.4	45.5	36.0	69.2	78.1
Azimuth (°)	8.4	16.0	116.7	87.9	119.4	137.8

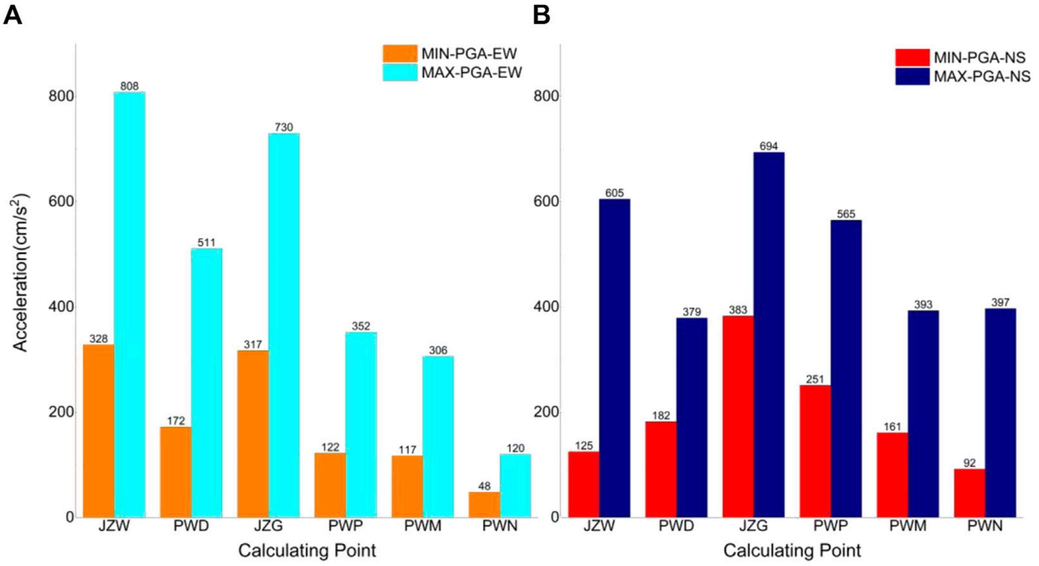

FIGURE 6
PGA value range of six typical locations. **(A)** Shows the PGA range of the EW component, **(B)** shows the PGA range of the NS component.

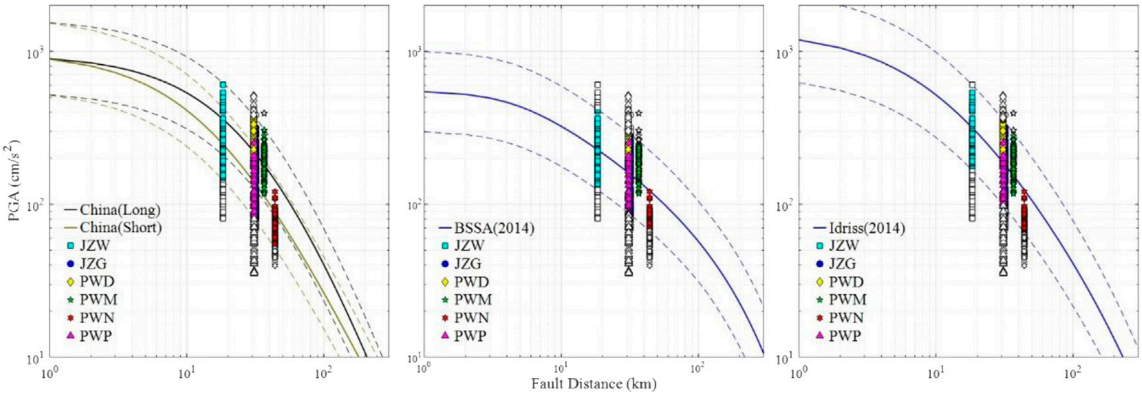

FIGURE 7
Acceleration time history of 6 calculation points selected by the three attenuation relationships.

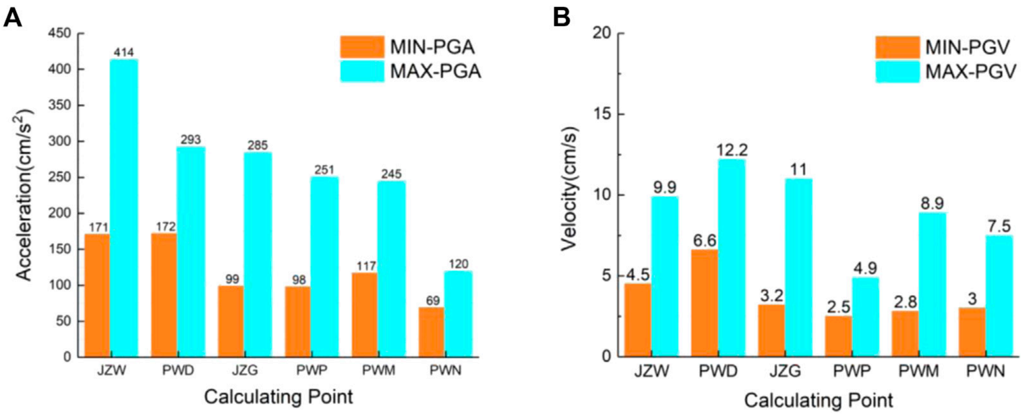

FIGURE 8
Value range of the PGA and PGV obtained from the intersection of the three types of attenuation relationships.

TABLE 5 Peak acceleration range of each typical position obtained after screening the three attenuation relationships.

GMPE	Range	PGA(cm/s^2)					
		JZW	JZG	PWD	PWM	PWN	PWP
BSSA (2014)	Max-PGA	414.37	285.35	293.07	245.00	120.39	250.79
	Min-PGA	126.01	86.33	171.72	117.00	68.62	87.76
Idris (2014)	Max-PGA	537.18	317.09	353.09	280.00	120.39	250.79
	Min-PGA	170.95	98.90	171.72	117.00	66.78	98.30
CN[China (GB18306-2015)]	Max-PGA	605.14	317.09	378.66	306.00	120.39	250.79
	Min-PGA	143.62	80.03	171.72	117.00	53.35	81.30

shown in Table 1. Among them, the parameter uncertainty includes the uncertainty in the fault dip angle and initial rupture point. The dip angles of the fault are 45°, 60°, and 75°, and the initial rupture point takes into account three uncertainties, as shown in Figure 4A. The rupture velocity is equal to 0.8Vs. (Somerville et al., 1999). The value of Vs. list in Table 2. In this paper, we calculate 36 scenario earthquakes. The finite difference method requires defining parameters related to the crustal velocity structure, fault characteristics and seismic slip distribution (Luo et al., 2020). The crustal structure parameters used to calculate low-frequency ground motion in this paper are shown in Figure 4B (Long, 2008). The quality factor of each layer of the medium is calculated according to the empirical relationship proposed by Graves et al. (2008).

High-frequency ground motion arises mainly from near-fault ruptures, specifically associated with the asperity

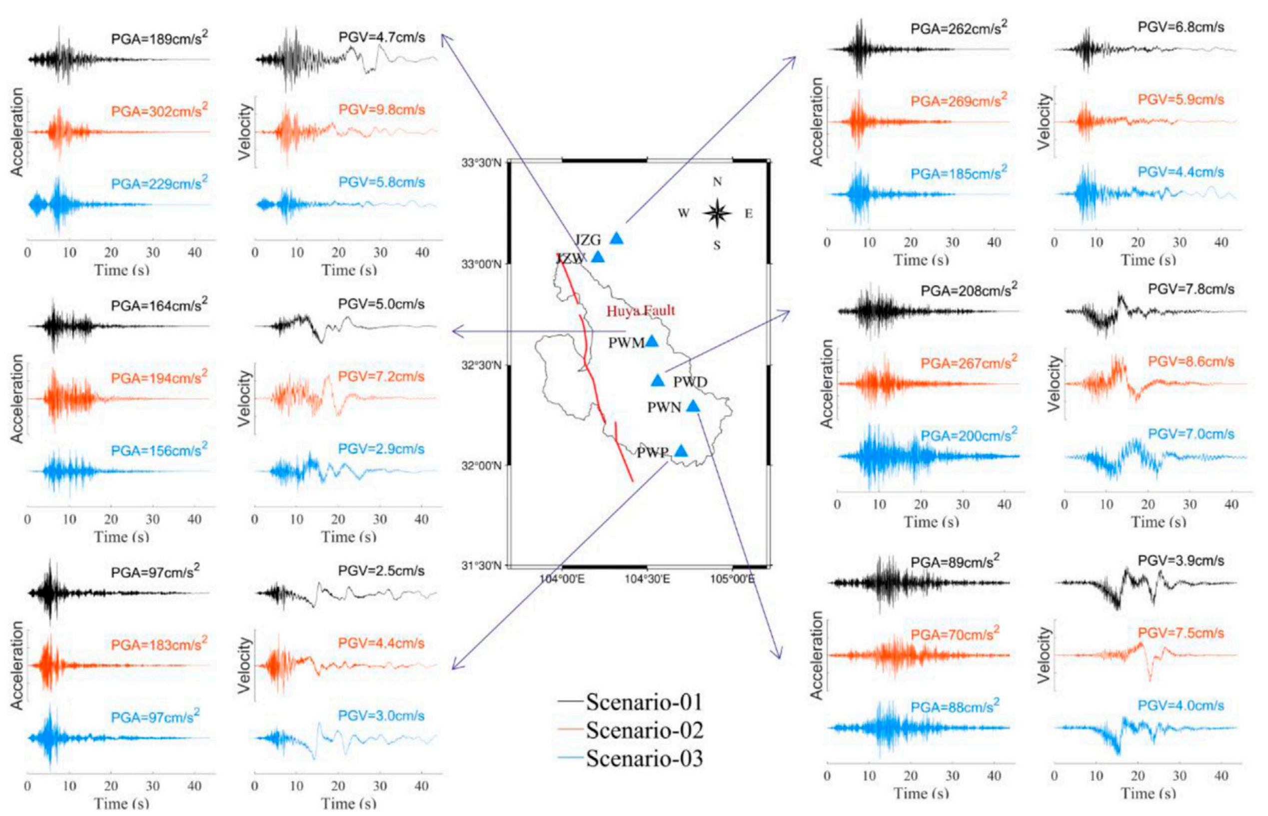

FIGURE 9
Acceleration and velocity time history of the 6 points in the partial scenarios.

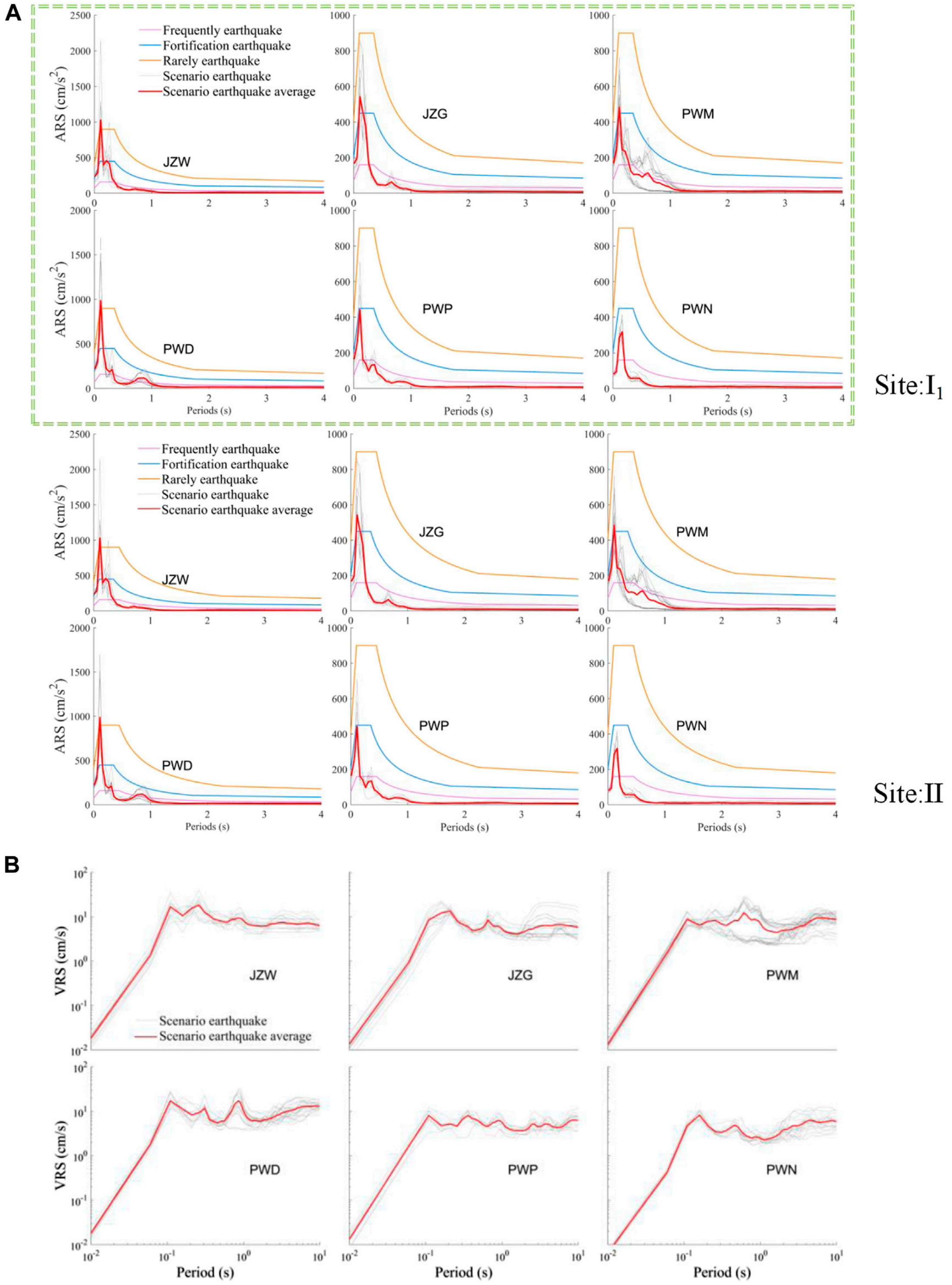

FIGURE 10
Acceleration response spectrum **(A)** and velocity response spectrum **(B)** of all scenarios in six typical locations (ARS stands for acceleration response spectrum, and VRS stands for velocity response spectrum).

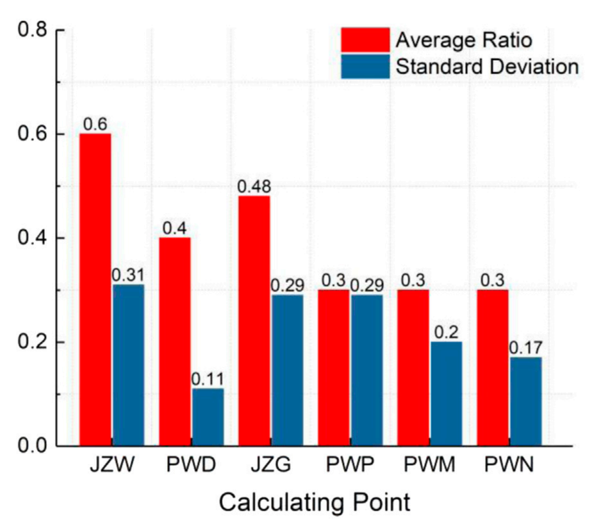

FIGURE 11
PGV contribution ratio of high-frequency ground motion to broadband ground motion.

parameters, initial rupture location, focal mechanism, and key focal parameters C (ratio of stress drop of large and small earthquakes) and N (Number of sub faults divided by the main earthquake fault plane). The parameter uncertainties mainly considered by the empirical Green function method in this paper include the parameter uncertainties in the asperity, source mechanism, initial rupture point, source depth, etc. For high-frequency earthquake ground motion simulations of scenario earthquakes, the initial exception point is generally selected from the bottom position of the asperity (Figure 4) (Miyake et al., 2003). The area of an asperity is 22% of the total fault area according to Somerville et al. (1999), and the total seismic moment of an asperity is 44% of the total seismic moment. The focal depth of the three historical large earthquakes of the 1976 Songpan Pingwu earthquake swarm (Tang and Liu, 1981) is selected as the focal depth. The focal mechanism is obtained from the focal mechanism database of the Institute of Geophysics, China Earthquake Administration, and uncertainty in the dip parameters is considered. The detailed parameters are shown in Table 3. We note here that there are differences in fault area and rupture area due to different output forms of low-frequency and high-frequency ground motion to the source model. In addition, because the seismic moment of low-frequency and high-frequency ground motion are obtained from different statistical formulas, their values are different.

Broadband ground motion simulation results

In this paper, six typical locations are selected in Figure 1, and the broadband ground motion is estimated. These six points are places where the population density in the Pingwu area is relatively high or where major projects are located. In addition, these six regions have good small-earthquake records recorded by strong seismic stations (Table 4). The waveform of small earthquakes used in each typical location area is shown in Figure 5.

After fully considering various uncertainties in the source parameters, we calculated low-frequency and high-frequency ground motion of Ms7.2 scenario earthquakes in six typical locations in the Pingwu area. We selected low-frequency and high-frequency ground motion with the same source depth, number of asperities, and initial rupture point location to conduct broadband ground motion synthesis, and 36 kinds of broadband ground motion were obtained at each point.

Figure 6 shows the range of PGA values of broadband ground motion obtained from the arrangement and combination of two parts of ground motion at each typical location. The range of values for each location shown in the figure is large; for example, the difference between the maximum and minimum PGA at JZW is nearly 0.5 g, and in fact, not every scenario earthquake is appropriate. Therefore, we adopt the scheme commonly used worldwide and use a variety of GMPEs to comprehensively determine the more reasonable broadband ground motion intensity range at each typical location. The GMPEs mainly include the Fifth Generation Seismic Ground Motion Parameter Zoning Map of China (GB18306-2015) and NGA West2 (Boore et al., 2014; Idriss, 2014) attenuation relationship. We screened the broadband ground motion under different scenarios from the perspective of ground motion attenuation characteristics (Figure 7) and ultimately obtained more reasonable peak acceleration ranges for each typical location, as shown in Table 5. To obtain a more accurate and detailed range of the peak acceleration (Figure 8A) and peak velocity (Figure 8B) of broadband ground motion at six typical locations at the calculation points, we took the

TABLE 6 Corresponding intensity range of six typical locations in the Chinese seismic intensity scale.

Station name	JZW (cm/s^2)	JZG (cm/s^2)	PWD (cm/s^2)	PWM (cm/s^2)	PWN (cm/s^2)	PWP (cm/s^2)
Max-PGA	414	285	293	245	120	251
Min-PGA	171	99	172	117	69	98
Intensity scale	VII-IX	VII-VIII	VII-VIII	VII-VIII	VI-VII	VII-VIII

intersection of the range of three types of attenuation relations (Figure 8).

Finally, after screening, we obtained 220 broadband ground motion in 6 typical locations. Figure 9 shows partial broadband acceleration time histories and velocity time histories for six typical locations. Different coloured lines represent broadband ground motion under different scenarios. Limited by the length of the article, only the time histories of three scenarios are given for each typical location, and broadband ground motion of other scenarios are given as annexes. The acceleration spectrum and velocity spectrum can provide good data support for seismic design and seismic damage analysis of buildings. Figure 10 shows the acceleration response spectrum (ARS) (Figure 10A) and velocity response spectrum (VRS) (Figure 10B) of broadband ground motion obtained at six typical locations. The grey features represent the acceleration spectrum and velocity spectrum of the scenario earthquake, and the red line represents the average value of the acceleration spectrum and velocity spectrum. The acceleration spectrum contains two site conditions (Code for seismic design of buildings, GB 500101-2010):I_1 and II. Frequently earthquake, Fortification earthquake and Rarely earthquake in Figure 10A) stand for specification spectrum of Code for seismic design of buildings (GB 500101-2010). Red line represent average response spectrum (acceleration and velocity) of scenario earthquake.The six typical locations in this paper include the city of Pingwu with a large population density, scenic spots with a large pedestrian flow, and important traffic projects (Muzuo, Bazi, Pingtong) (Table 4). In typical locations JZW and PWD, the average acceleration spectrum of scenario earthquake are exceed rarely earthquake specification spectrum.

According to the PGA value range shown in Figure 8A, corresponding to the provisions of the China Seismic Intensity Scale (GB/T 17742-2020), the corresponding seismic intensities of six typical locations are shown in Table 6. With reference to the fortification requirements of the Fifth Generation Seismic Ground Motion Parameter Zoning Map of China (GB18306-2015), the basic fortification intensity in the Pingwu area is VIII. In the results of this paper, the PGA range at the PWN location is 69 cm/s^2-120 cm/s^2, and the corresponding intensity is VI - VII, indicating that the buildings at this location were less likely to be damaged after the Ms7.2 earthquake. The PGA range at the JZW location is 171 cm/s^2-414 cm/s^2, and the seismic intensity reaches IX. The site is likely to have been damaged during the earthquake. The PGA range of other locations is 98 cm/s^2-251 cm/s^2, and the seismic intensity is VII-VIII. In mountainous and canyon areas such as Pingwu, the probability of landslides and debris flows occurring after the earthquake is very high. Special attention should be given to the impact of secondary disasters caused by the earthquake, especially the Fujiang River system flowing through Pingwu. It is necessary to prevent barrier lakes caused by landslides and debris flows. In practical application, if more detailed information about the site conditions can be obtained, it is recommended that the results in this paper should be appropriately corrected.

Upon estimating the characteristics of broadband ground motion at six typical locations, this paper also summarizes the characteristics of the synthesized broadband ground motion. The peak ground acceleration of broadband ground motion is mainly contributed by high-frequency ground motion; that is, the energy released from the asperity area accounts for most of the energy of this earthquake, while the long-period ground motion contributes less to the peak ground acceleration. However, in terms of peak ground velocity, it is mainly contributed by long-period ground motion, which account for approximately 60%–70% of the PGV (typical locations: PWD, PWP, PWM, PWN), and high-frequency ground motion accounts for approximately 30%–40% of the PGV (Figure 11). This study also shows that the expression of different physical parameters by the long-period and high-frequency spectrum components of the synthesized broadband ground motion is quite different. Therefore, when selecting the simulation method to synthesize broadband ground motion, a reasonable simulation scheme should be selected according to the actual needs.

Conclusion and discussion

By considering multiple uncertainties in the source parameters, based on the Recipe scheme, combined with the finite difference method and empirical Green function method, we obtained the acceleration time history, velocity time history, and corresponding PGA, PGV, and response spectrum of broadband ground motion of the Pingwu Ms7.2 scenario earthquake. We use GMPEs to screen the obtained broadband ground motion, providing broadband ground motion within the reasonable range of 6 typical locations. The conclusions of this paper are as follows:

(1) The broadband ground motion synthesis scheme adopted in this paper combines the advantages of low-frequency and high-frequency ground motion simulation methods, makes up for the shortcomings of the simple empirical Green function method in the context of long-period ground motion, and resolves the limitations of the finite difference method for calculating high-frequency ground motion.
(2) High-frequency ground motion is the main PGA contributor; that is, the PGA of high-frequency ground motion is almost equal to the PGA of broadband ground motion, while high-frequency and long-period ground motion strongly contribute to the PGV, of which the contribution value of high-frequency ground motion is approximately 30%–40% and the contribution of long-period ground motion to the PGV is larger as a whole.
(3) This study also shows that it is feasible to obtain the ground motion with a reasonable value range based on the research scheme of the source parameters of the Recipe scheme, and the ground motion with a reasonable value

range is also the best scheme to describe the scenario earthquake results.

(4) In the most densely populated county, Pingwu County, the ground motion PGA range is approximately 170–290 cm/s^2, and the seismic intensity is approximately VIII. It is recommended that local people note these factors and take more practical and specific long-term earthquake prevention and disaster reduction measures.

Synthesizing the characteristics of ground motion in areas lacking large earthquake records is of great significance for local seismic design and earthquake disaster prevention. In many regions where historical earthquakes have occurred or where future earthquakes may occur, due to the lack of support from seismic records, the seismic input of other regions can be used only for the seismic design of buildings and earthquake damage simulation of buildings, which makes it difficult to truly express the actual seismic characteristics of the region. The work in this paper is intended to compensate for this shortcoming. In future earthquake research, it will be necessary to select more refined standards to determine the range of ground motion values and then screen out more appropriate ground motion. In the future, we plan to synthesize more representative broadband ground motion at typical locations, which will increase the reference value of this work.

Data availability statement

The raw data supporting the conclusion of this article will be made available by the authors, without undue reservation.

Author contributions

(First Author–JZ): Methodology, data curation, formal analysis, investigation, validation, writing-original draft, writing-review,editing. (Co-First Author and Corresponding Author–LZ): Conceptualization, methodology, data curation, formal analysis, investigation, validation, writing-original draft, writing-review, editing. (Co-Corresponding Author–SJ): Writing-Original draft, writing-review draft, editing; Investigation; editing (Co-Corresponding Author–GM): Conceptualization; Methodology. (LT): editing. (HT): editing. (LN): editing, resource. (GX): resource.

Funding

This work was jointly supported by the Youth Fund of the National Natural Science Foundation (42104053) and the Research Project Fund of the Institute of Geophysics, China Earthquake Administration (DQJB22B21, DQJB22R30).

Acknowledgments

We would like to express our thanks to the Institute of Engineering Mechanics of China Earthquake Administration for providing the CENC seismic data. We also thank two reviewers and the editor-in-chief and associate editors for their careful reading and valuable suggestions.

Conflict of interest

The authors declare that the research was conducted in the absence of any commercial or financial relationships that could be construed as a potential conflict of interest.

Publisher's note

References

Ansal, A., Akinci, A., Cultrera, G., Erdik, M., Pessina, V., Tönük, G., et al. (2009). Loss estimation in istanbul based on deterministic earthquake scenarios of the marmara sea region (Turkey). *Soil Dyn. Earthq. Eng.* 29, 699–709. doi:10.1016/j.soildyn.2008.07.006

Aochi, H., and Douglas, J. (2006). Testing the validity of simulated strong ground motion from the dynamic rupture of a finite fault, by using empirical equations. *Bull. Earthq. Eng.* 4, 211–229. doi:10.1007/s10518-006-0001-3

Aoi, S., and Fujiwara, H. (1999). 3D finite-difference method using discontinuous grids. *Bull. Seismol. Soc. Am.* 89, 918–930. doi:10.1785/BSSA0890040918

Atkinson, G. M., and Beresnev, I. A. (2002). Ground motions at memphis and st. Louis from m7.5-8.0 earthquakes in the new madrid seismic zone. *Bull. Seismol. Soc. Am.* 92, 1015–1024. doi:10.1785/0120010203

Boore, D. M., Stewart, J. P., Seyhan, E., and Atkinson, G. M. (2014). NGA-West2 equations for predicting pga, pgv, and 5% damped psa for shallow crustal earthquakes. *Earthq. Spectra* 30, 1057–1085. doi:10.1193/070113EQS184M

Causse, M., Cotton, F., Cornou, C., and Bard, P.-Y. (2008). Calibrating median and uncertainty estimates for a practical use of empirical green's functions technique. *Bull. Seismol. Soc. Am.* 98, 344–353. doi:10.1785/0120070075

Cultrera, G., Cirella, A., Spagnuolo, E., Herrero, A., Tinti, E., and Pacor, F. (2010). Variability of kinematic source parameters and its implication on the choice of the design scenario. *Bull. Seismol. Soc. Am.* 100, 941–953. doi:10.1785/0120090044

Deng, Q., Du, S., and Zhao, X. (1994). Tectonics, scismisity and dynamics of longmenshan mountains and its adjacent regions. *Seismol. Geol.* 04, 389–403. (in Chinese).

Gao, M., Chen, G., Xie, F., Xu, X., Li, X., Yu, Y., et al. (2015). *Seismic ground motion parameters zonation map of China: GB18306-2015*. Beijing: Beijing Standards Press of China, 173. (in Chinese).

Geller, R. J. (1976). Scaling relations for earthquake source parameters and magnitudes. *Bull. Seismol. Soc. Am.* 66, 1501–1523. doi:10.1785/BSSA0660051501

Graves, R. W., Aagaard, B. T., Hudnut, K. W., Star, L. M., Stewart, J. P., and Jordan, T. H. (2008). Broadband simulations for Mw7.8 southern san andreas earthquakes: Ground motion sensitivity to rupture speed. *Geophys. Res. Lett.* 35, L22302. doi:10.1029/2008GL035750

Graves, R. W., and Pitarka, A. (2010). Broadband ground-motion simulation using a hybrid approach. *Bull. Seismol. Soc. Am.* 100, 2095–2123. doi:10.1785/0120100057

Hanks, T. C., and Kanamori, H. (1979). A moment magnitude scale. *J. Geophys. Res.* 84, 2348–2350. doi:10.1029/JB084iB05p02348

Hartzell, S., Harmsen, S., Frankel, A., and Larsen, S. (1999). Calculation of broadband time histories of ground motion: Comparison of methods and validation using strong-ground motion from the 1994 Northridge earthquake. *Bull. Seismol. Soc. Am.* 89, 1484–1504. doi:10.1785/BSSA0890061484

Hartzell, S. H. (1978). Earthquake aftershocks as green's functions. *Geophys. Res. Lett.* 5, 1–4. doi:10.1029/GL005i001p00001

Huang, S., Wang, Y., Dai, G., Fu, G., Luo, K., Li, X., et al. (2015). *Code for seismic design of buildings: GB50011-2010*. Beijing: China Architecture Building Press, 33. (in Chinese).

Idriss, I. M. (2014). An NGA-West2 empirical model for estimating the horizontal spectral values generated by shallow crustal earthquakes. *Earthq. Spectra* 30, 1155–1177. doi:10.1193/070613EQS195M

Imperatori, W., and Mai, P. M. (2012). Sensitivity of broad-band ground-motion simulations to earthquake source and Earth structure variations: An application to the messina straits (Italy). *Geophys. J. Int.* 188, 1103–1116. doi:10.1111/j.1365-246X.2011.05296.x

Irikura, K., and Kamae, K. (1994). Estimation of strong ground motion in broad-frequency band based on seismic source scaling model and an empirical green's function technique. *Ann. Geophys.* 37.

Irikura, K., and Miyake, H. (2011). Recipe for predicting strong ground motion from crustal earthquake scenarios. *Pure Appl. Geophys.* 168, 85–104. doi:10.1007/s00024-010-0150-9

Iwaki, A., Fujiwara, H., and Aoi, S. (2016b). Broadband ground-motion simulation based on the relationship between high- and low-frequency acceleration envelopes: Application to the 2003 Mw 8.3 tokachi-oki earthquake. *Bull. Seismol. Soc. Am.* 106, 632. doi:10.1785/0120150273

Iwaki, A., and Iwata, T. (2010). Simulation of long-period ground motion in the osaka sedimentary basin: Performance estimation and the basin structure effects. *Geophys. J. Int.* 181, 1062–1076. doi:10.1111/j.1365-246X.2010.04556.x

Iwaki, A., Maeda, T., Morikawa, N., Miyake, H., and Fujiwara, H. (2016a). Validation of the recipe for broadband ground-motion simulations of Japanese crustal earthquakes. *Bull. Seismol. Soc. Am.* 106, 2214. doi:10.1785/0120150304

Ji, Z., Li, Z., Chen, X., Li, T., Wu, Q., Zhang, B., et al. (2022). Uncertainties in prediction of near-fault long-period ground motion: An application to the 1970 tonghai earthquake (Ms7.8). *Pure Appl. Geophys.* 179, 2637–2660. doi:10.1007/s00024-022-03094-w

Jones, L. M., Han, W., Hauksson, E., Jin, A., Zhang, Y., and Luo, Z. (1984). Focal mechanisms and aftershock locations of the songpan earthquakes of august 1976 in sichuan, China. *J. Geophys. Res.* 89, 7697–7707. doi:10.1029/JB089iB09p07697

Kirby, E., Harkins, N., Wang, E., Shi, X., Fan, C., and Burbank, D. (2007). Slip rate gradients along the eastern kunlun fault. *Tectonics* 26. doi:10.1029/2006TC002033

Li, F., Liu, G., Jia, Q., Xu, X., Zhang, X., and Gong, F. (2018). Holocene active characteristics of the northern segment of the Minjiang fault in the eastern margin of the Tibetan plateau. *Seismol. Geol.* 01, 97–106. (in Chinese). doi:10.3969/j.issn.0253-4967.2018.01.008

Li, J. (1988). Laminar and turbulent flow in the mammalian aorta: Reynolds number. *J. Theor. Biol.* 04, 409–414. (in Chinese). doi:10.1016/s0022-5193(88)80255-8

Li, Z., Sun, J., Fang, L., Chen, X., Gao, M., Luo, Q., et al. (2021). Reproducing the spatial characteristics of high-frequency ground motions for the 1850 M7.5 xichang earthquake. *Seismol. Res. Lett.* 93, 100–117. doi:10.1785/0220210076

Li, Z., Sun, J., Gao, M., Fu, G., An, Z., Zhao, Y., et al. (2022). Evaluation of horizontal ground motion waveforms at sedongpu glacier during the 2017 M6.9 mainling earthquake based on the equivalent green's function. *Eng. Geol.* 306, 106743. doi:10.1016/j.enggeo.2022.106743

Long, F. (2008). *The velocity structure of the longmenshan fault zone and its neighborhoods and the focal mechanism solutions of the 2008 wenchuan earthquake sequence*. Hefei: University of Science and Technology of China. [dissertation/master's thesis]. [Hefei](in Chinese).

Luo, Q., Dai, F., Liu, Y., and Chen, X. (2020). Simulating the near-field pulse-like ground motions of the imperial valley, California, earthquake. *Soil Dyn. Earthq. Eng.* 138, 106347. doi:10.1016/j.soildyn.2020.106347

Mai, P. M., Imperatori, W., and Olsen, K. B. (2010). Erratum to hybrid broadband ground-motion simulations: Combining long-period deterministic synthetics with high-frequency multiple S-to-S backscattering. *Bull. Seismol. Soc. Am.* 100, 3338–3339. doi:10.1785/0120100283

Miyake, H., Iwata, T., and Irikura, K. (2003). Source characterization for broadband ground-motion simulation: Kinematic heterogeneous source model and strong motion generation area. *Bull. Seismol. Soc. Am.* 93, 2531–2545. doi:10.1785/0120020183

Morikawa, N., Senna, S., Hayakawa, Y., and Fujiwara, H. (2011). Shaking maps for scenario earthquakes by applying the upgraded version of the strong ground motion prediction method "recipe". *Pure Appl. Geophys.* 168, 645–657. doi:10.1007/s00024-010-0147-4

Motazedian, D., and Atkinson, G. M. (2005). Stochastic Finite-Fault modeling based on a dynamic corner frequency. *Bull. Seismol. Soc. Am.* 95, 995–1010. doi:10.1785/0120030207

Pitarka, A., Graves, R., Irikura, K., Miyake, H., and Rodgers, A. (2017). Performance of irikura recipe rupture model generator in earthquake ground motion simulations with graves and pitarka hybrid approach. *Pure Appl. Geophys.* 174, 3537–3555. doi:10.1007/s00024-017-1504-3

Razafindrakoto, H. N. T., Bradley, B. A., and Graves, R. W. (2018). Broadband ground-motion simulation of the 2011 Mw 6.2 christchurch, New Zealand, earthquake. *Bull. Seismol. Soc. Am.* 108, 2130–2147. doi:10.1785/0120170388

Roten, D., Olsen, K. B., and Pechmann, J. C. (2021). 3D simulations of M7 earthquakes on the Wasatch Fault, Utah, Part Ⅱ: Broadband (0-10 Hz) ground motions and nonlinear soil behavior. *Bull. Seismol. Soc. Am.* 102, 2008–2030. doi:10.1785/0120110286

Ripperger, J., Mai, P. M., and Ampuero, J.-P. (2008). Variability of near-field ground motion from dynamic earthquake rupture simulations. *Bull. Seismol. Soc. Am.* 98, 1207–1228. doi:10.1785/0120070076

Schmedes, J., Archuleta, R. J., and Lavalle, D. (2010). Correlation of earthquake source parameters inferred from dynamic rupture simulations. *J. Geophys. Res.* 115, B03304. doi:10.1029/2009JB006689

Somerville, P., Irikura, K., Graves, R., Sawada, S., Wald, D., Abrahamson, N., et al. (1999). Characterizing crustal earthquake slip models for the prediction of strong ground motion. *Seismol. Res. Lett.* 70, 59–80. doi:10.1785/gssrl.70.1.59

Song, S. G. (2015). Developing a generalized pseudo-dynamic source model of Mw 6.5–7.0 to simulate strong ground motions. *Geophys. J. Int.* 204, 1254–1265. doi:10.1093/gji/ggv521

Sørensen, M. B., Pulido, N., and Atakan, K. (2007). Sensitivity of ground-motion simulations to earthquake source parameters: A case study for istanbul, Turkey. *Bull. Seismol. Soc. Am.* 97, 881–900. doi:10.1785/0120060044

Sun, J., Jin, X., Lin, J., Ma, Q., Zhang, L., Sun, B., et al. (2020). *The Chinese seismic intensity scale:GB/T17742-2020*. Beijing: China Earthquake Administration, 4–7. (in Chinese).

Tang, R., and Liu, L. (1981). On the seismogeological characteristics of 1976 songpan-pingwu earthquakes. *Seismol. Geol.* 02, 41–86. (in Chinese).

Wang, H. (2004). Finite fault source model for predicting near-field strong ground motion. *Institute of engineering mechanics*.

Wang, H., Igel, H., Gallovič, F., Cochard, A., and Ewald, M. (2008). Source-related variations of ground motions in 3-D media: Application to the newport-inglewood fault, los angeles basin. *Geophys. J. Int.* 175 (1), 202–214. doi:10.1111/j.1365-246X.2008.03878.x

Xu, X., Wen, X., Chen, G., and Yu, G. (2008). Discovery of the longriba fault zone in eastern bayan har block, China and its tectonic implication. *Sci. China Ser. D-Earth. Sci.* 05, 1209–1223. (in Chinese). doi:10.1007/s11430-008-0097-1

Yao, H., Yang, Y., Wu, H., Zhang, P., and Wang, M. Crustal shear velocity model in Southwest China from joint seismological inver-sion CSES scientific products. (2019), doi:10.12093/02md.02.2018.01.v1

Zeng, Y., Anderson, J. G., and Yu, G. (1994). A composite source model for computing realistic synthetic strong ground motions. *Geophys. Res. Lett.* 21, 725–728. doi:10.1029/94GL00367

Zhao, X., Deng, Q., and Chen, S. (1994). Tectonic geomorphology of the Minshan uplift in Western Sichuan, southwestern China. *Seismol. Geol.* 04, 429–439. (in Chinese).

Zhou, R., Li, Y., Alexander, L. D., Michael, A. E., He, Y., Wang, F., et al. (2006). Active tectonics of the eastern margin of the tibet plateau. *Mineralogy Petrology* 02, 40–51. (in Chinese). doi:10.19719/j.cnki.1001-6872.2006.02.007

frontiers | Frontiers in Earth Science

TYPE Original Research
PUBLISHED 17 January 2023
DOI 10.3389/feart.2022.950582

OPEN ACCESS

EDITED BY
Yefei Ren,
Institute of Engineering Mechanics,
China Earthquake Administration, China

REVIEWED BY
Luc Chouinard,
McGill University, Canada
Boumediene Derras,
University of Tlemcen, Algeria

*CORRESPONDENCE
Wenxin Liu,
wenxinl@zstu.edu.cn

SPECIALTY SECTION
This article was submitted to Structural Geology and Tectonics,
a section of the journal
Frontiers in Earth Science

RECEIVED 23 May 2022
ACCEPTED 31 October 2022
PUBLISHED 17 January 2023

CITATION
Liu W, Peng Y and Wang J (2023), Spatially correlated V_{s30} estimation in the Beijing area.
Front. Earth Sci. 10:950582.
doi: 10.3389/feart.2022.950582

Spatially correlated V_{s30} estimation in the Beijing area

Wenxin Liu[1]*, Yanjv Peng[2] and Jingjing Wang[3]

[1]College of Civil Engineering and Architecture, Zhejiang Science and Technology University, Hangzhou, China, [2]National Institute of Natural Hazards, Ministry of Emergency Management, Beijing, China, [3]Testing Center, Hangzhou Survey, Design and Research Institute, Hangzhou, China

Beijing is an international metropolis, that is also an earthquake-prone city. The aims of this study are detailed quantifying and qualifying soil layer properties for an accurate seismic safety evaluation in the Beijing area. The time average shear-wave velocity in the first 30 m of subsoil, V_{s30}, is an important site parameter used in site response analysis, site classification, and seismic loss estimation. Mapping of V_{s30} over a city-scaled region is commonly done through proxy-based methods by correlating V_{s30} with geological or topographic information. In this paper, a geostatistical-based random field model is presented and applied to mapping V_{s30} over extended areas. This random field model is then coupled with Monte Carlo simulations to obtain an averaged V_{s30} map and its associated uncertainties. Unlike the traditional deterministic prediction model, this framework accounts for spatial variations of V_{s30} values and uncertainties, which makes the prediction more reliable. A total of 388 shear wave velocity measurements in the Beijing area are used to calculate V_{s30} values, from which the statistical and spatial properties for the random field realizations are inferred. New spatially correlated probabilistic V_{s30} maps for the Beijing area are then represented, and the effect of the maximum number of previously generated elements to correlate to in estimating V_{s30} maps is tested.

KEYWORDS

shear wave velocity, V_{s30}, random field model, spatial variability, Monte Carlo simulation

1 Introduction

The time-averaged shear-wave velocity in the upper 30 m (V_{S30}) is an important site parameter used in estimating site response, classifying sites, and loss estimation (Boore, 2004; Xie et al., 2016). In the earthquake codes, V_{s30} is used with CPT, SPT value and/or the depth of soil profiles to represent the soil properties. Furthermore, some recent studies, show that coupling between V_{s30} and other site-condition proxies such as resonance frequency and topographical slope may give efficient results in prediction specified with a reduction of ground-motion variability (Derras et al., 2017; Derras et al., 2020). A reasonable and accurate database of V_{s30} is the basis for successfully carrying out seismic effect analysis and research of complex sites and implementing reasonable site classification. However, for large-scale urban areas, the boreholes with shear wave velocity data and meeting the requirements are extremely limited (Seed and Idriss, 1981; Raptakis et al., 1995; Wride et al., 2000; Hasancebi and Ulusay, 2007), which mainly manifested as follows: 1) Boreholes have geotechnical description data but no shear wave velocity data; 2) Because of the different uses of boreholes, the depth of boreholes are different. For example, the depth of boreholes in engineering geotechnical investigation is shallow, even less than 30 m; 3) The boreholes for seismic safety evaluation of major engineering and site control engineering have deep depth and complete wave velocity data, but the number of boreholes is limited and the spatial distribution is uneven. Therefore, in order to meet the needs of urban regional-scale earthquake effect analysis, as well as the requirement of implementing reasonable site classification, it is necessary to accurately describe the complex site conditions with a spatially correlated V_{s30} map in urban areas which combines shear wave velocity measurements and a scientific, reasonable and efficient prediction model.

At present, deterministic methods are mostly used in site shear wave velocity predictions. Commonly used deterministic methods can be roughly divided into two categories: 1) Interpolation prediction of parameter distribution between boreholes based on linear interpolation method (Badal et al., 2004), focusing on prediction between two points, but lacking extension ability; 2) According to the regression analysis method in traditional statistical methods, the regression equation between shear wave velocity and topography, geomorphology, depth, CPT-N, and other parameters is established (Wald and Allen, 2007; Chiou and Youngs, 2008; Ancheta et al., 2013; Stewart et al., 2014; Wills et al., 2015; Xie et al., 2016; Ahdi et al., 2017; Parker et al., 2017; Chen et al., 2018; Rahman et al., 2018; Heath et al., 2020). The above deterministic method determines the spatial distribution pattern and correlation by analyzing the frequency distribution or mean value and variance relationship of sample attribute values and their corresponding rules, but does not consider the difference in spatial orientation.

Moreover, the most fatal disadvantage of the deterministic method is that it can't take into account the uncertainty of parameters. It has been well-recognized that the soil profile and the associated parameters are usually not known with certainty (Liu et al., 2017a,b; Liu et al., 2021; Zhang et al., 2021; Stewart and Afshari, 2021; Ching et al., 2018; Phoon et al., 2022). These uncertainties will eventually be expressed and propagated in further applications such as the uncertainty of site response and the degree of earthquake disasters (Liu et al., 2021). Therefore, other than the accuracy prediction of V_{s30} values for a certain region, the uncertainty distribution of V_{s30} needs to be evaluated. One thing needs to be noticed, there are many sources of uncertainty, such as insufficient *in-situ* geotechnical survey data, the influence of sample disturbance and scaling in laboratory tests, and the natural heterogeneity of soil profiles (Ching and Schweckendiek, 2021; Phoon et al., 2022). It is hard to tell them apart. In this paper, the uncertainties from different sources are integrated, and defined as the "uncertainty of V_{s30}", regardless of their sources.

To remedy the above defects, the application of geostatistical methods in soil properties (V_{s30}, CPT, SPT, et al.) and site condition mapping has been greatly promoted, which takes into account the spatial variability of soil properties and the obvious interdependence among points. Several works have been done along this line:

Thompson et al. (2007) use the geostatistical method for modeling the horizontal variability of near-surface shear wave velocity of soil in the San Francisco Bay Area. Wald et al. (2011) and Yong et al. (2013) applied the kriging-with-a-trend method to mapping V_{s30} considering the topographic slope. Liu et al. (2017a, b) presented a multiscale random field model and applied it to mapping V_{s30} over the Suzhou area, in which areas of high interest can be able to adaptively refined while maintaining a consistent description of spatial dependence. Chen et al. (2018) built a 3D shear wave velocity model for the Suzhou area by using the Kriging method in the horizontal direction. By using the Kriging method, Foster et al. (2019) developed a geology-based and terrain-based models V_{S30} map for New Zealand and compared it with a flexible multivariate normal approach. Li et al. (2021) developed a Texas-specific V_{S30} map by using the geostatistical kriging method which integrated with a region-specific geologic proxy and field measurements of V_{S30}. All these works show that by using geostatistical methods, the spatial variation of shear wave velocity can be well considered during estimation.

In this paper, a random field-based approach is presented and adopted to simulate and predict the V_{s30} in the study area, more importantly, the uncertainty distribution of V_{s30} is evaluated. In the meantime, the effect of the maximum number of previously generated elements to correlate to is also been tested. The presented approach accounts for the spatial variability of V_{s30} and incorporates the database of geotechnical measurements. The order of presentation of this paper goes as follows: Section 2 presents the key components of the developed geostatistical tools for mapping V_{s30}; Engineering geology and field data for the Beijing area are summarized in Section 3; In Section 4, the statistical and spatial characterizations of the known V_{s30} data are discussed in detail; New V_{s30} maps are represented in Section 5 and the effect of N value in estimating V_{s30} maps will be discussed in Section 6.

2 Geo-statistical approach to characterize the spatial variability of V_{s30}: Random field model

The key component of this section is to present the shear wave velocity estimation model by using the random field method in geostatistical theory. Geostatistical theory shows that the geotechnical or geological characteristics of the regional areas usually show spatial variability and spatial correlation, which means the soil parameters measured at each observation point are correlated with those at adjacent locations, and with the increase of distance, the correlation between the parameters decreases gradually. According to that, this method can be used to simulate various parameters with time-space variation attributes in nature, such as soil characteristics in a certain space range, or ground motion changes at different times and locations. Therefore, it is proposed to use this theory to establish a prediction model of V_{s30}. With the spatial distribution characteristics of V_{s30}, the accuracy of V_{s30} estimation at unsampled points can be improved. Moreover, other than improving the accuracy of the estimation, one of the strengths of this random field method is the ability to estimate the associated uncertainties with the maps when coupled with Monte Carlo simulation.

Semi-variogram is known as a form of covariance and can be related to other commonly used measures to quantify the spatial correlation (Baise et al., 2006; DeGroot and Baecher, 1993; Goovaerts, 1997). Usually, the filed measured data will be used to fit the best curve of the semi-variogram and expressed as s linear combination of basic models such as the exponential model, spherical model, and Gaussian model. The geo-statistics community is preferred using the semi-variograms to describe the spatial structure since it only requires the increment of the random variable at two locations with distance h to be second-order stationery, which is a weaker requirement. The Hence, in this study, the spatial structure is characterized by the semi-variogram model as follows:

$$\gamma(h) = \frac{1}{2}\mathrm{Var}\left[Z(u) - Z(u+h)\right] \tag{1}$$

In which, $Z(u)$ is the random variable at location u, and h is the distance between any two locations.

Under the condition of second-order stationarity, the spatial correlation $\rho_{(h)}$ can be defined as related to the semi-variogram by:

$$\rho_{(h)} = 1 - \frac{\gamma(h)}{\mathrm{cov}(0)} \tag{2}$$

where COV(0) is the covariance at h = 0.

With the correlation between the two elements, the covariance matrix Σ consists of the covariance (COV) between any two points/elements (Z_i and Z_j) within the random field t can be calculated as:

$$COV\left[Z_i, Z_j\right] = \rho_{Z_i,Z_j}\sigma_{Z_i}\sigma_{Z_j} \tag{3}$$

where ρ_{Z_i,Z_j} is the correlation between the two elements, σ_{Z_i} and σ_{Z_j} are the corresponding standard deviations respectively.

Once the covariance between any two elements in the random field is determined, a conditional sequential simulation procedure is taken for the simulation. In this work, it is assumed that the V_{s30} obeys lognormal distributions, which can be converted into normal distributions using statistical transformations. Based on the conditional random field theory, the random variable Z_n can be characterized by a joint normal distribution as

$$\begin{bmatrix} Z_n \\ \boldsymbol{Z_p} \end{bmatrix} \sim N(\boldsymbol{\mu}, \boldsymbol{\Sigma}) = N\left(\begin{bmatrix} \mu_n \\ \boldsymbol{\mu_p} \end{bmatrix}, \begin{bmatrix} \Sigma_{nn} & \boldsymbol{\Sigma_{np}} \\ \boldsymbol{\Sigma_{pn}} & \boldsymbol{\Sigma_{pp}} \end{bmatrix}\right) \tag{4}$$

The process simulates each value individually, conditional upon all known data and previously generated values. Using such a process, the conditional distribution of the next value to be simulated in the random field, denoted as Z_n, is given by a univariate normal distribution with the updated mean and the variance as:

$$\left(Z_n|Z_p\right) \sim N\left(\Sigma_{np}\cdot\Sigma_{np}^{-1}\cdot Z_p, \sigma_n^2 - \Sigma_{np}\cdot\Sigma_{np}^{-1}\cdot\Sigma_{pn}\right) \tag{5}$$

where Z_p is a vector of all known or previously simulated points; the subscription "p" means "previous" simulated points and "n" refers to the "next" point to be simulated. Once Z_n is generated, it is inserted into the "previous" vector, upon which the "next" unknown value at another unsampled location will be generated. Such a process is repeated until all the values in the field are simulated, and then, a map of V_{s30} is generated for the region of interest. The flowchart of the random field implementation is shown in Figure 1.

3 The Beijing site: Engineering geology and field data

Beijing is an international metropolis and is also one of the capitals of three countries in the world that have suffered earthquakes of magnitude eight or above in history (Peng et al., 2011; Yuan et al., 2019; Peng et al., 2020). Beijing is located at the intersection of the Yanshan seismic zone and the central seismic zone of North China Plain and is close to Fenwei seismic zone and Tanlu deep fault seismic zone (Peng et al., 2020). Many earthquake fault zones are passing through the urban area, which makes Beijing an earthquake-prone city. It has been damaged and affected by many strong earthquakes in history, among which the Mafang earthquake in 1,679 and the Xijiao earthquake in 1,730 have the greatest impact (Min et al., 1995; Wang et al., 1999). More than 600 earthquakes have been felt in the Beijing area and more than 5,000 earthquakes have been recorded by instrumentation since records of earthquakes began (Peng et al., 2011).

3.1 Engineering geology

For engineering geology, the southeast terrain of the Beijing area is low and flat, and the terrain gradually rises to the west and north. Hebei Plain and the Bohai Sea are in the southeast of the region, and Taihang Mountain and Yanshan Mountain are located in the northwest part of the region. Due to the influence of regional neotectonic movement and active faults, different geomorphic tectonic units have been formed in the region, mainly including uplifted mountains,

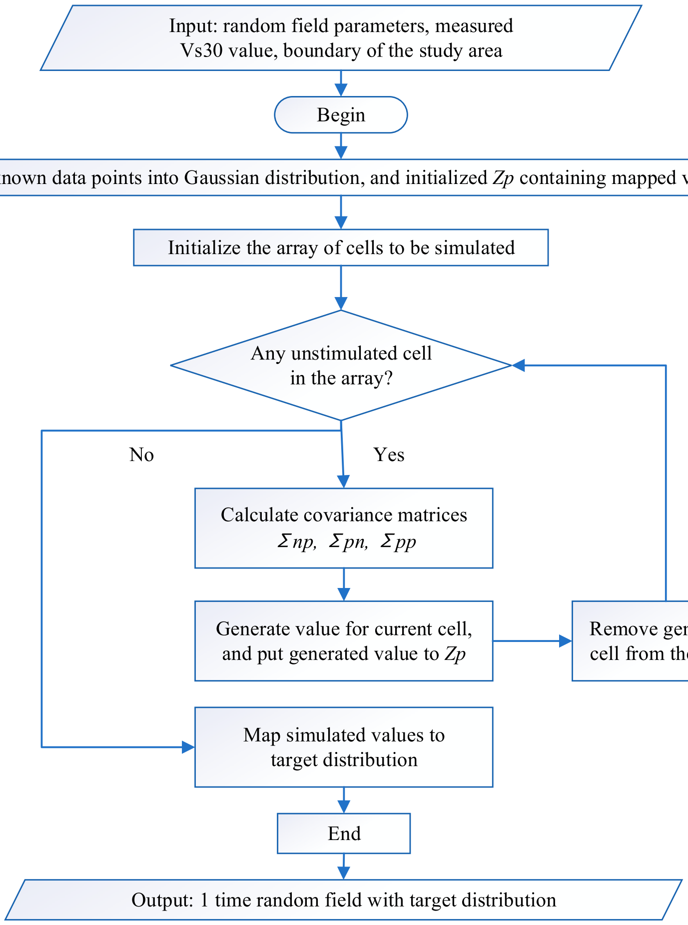

FIGURE 1
Flowchart of the random field model implementation.

intermountain subsidence basins, and sedimentary plains (Peng et al., 2020). The soil mass in the Beijing area is mainly silty clay mixed with fine sand and medium sand, and the lower bedrock is mainly round gravel. Quaternary sediments are widely distributed in the plain area, followed by the foothills. Sedimentary types are different in different structural areas and geomorphic areas (Beijing Institute of Hydrogeology and Engineering Geology, 1979). Alluvial and alluvial-proluvial facies are mainly developed in western mountainous areas, and flood-alluvial facies and cave accumulation are developed in western mountainous areas. Sand, gravel, and loess accumulation of residual slope facies and flood-slope facies are the main deposits in the piedmont, forming alluvial fans or platforms. The south part of the plain is dominated by lacustrine facies and fluvial facies, while the north part is mostly alluvial sand and gravel deposits (Cai et al., 2016). The thickness of Quaternary sediments varies greatly, from several meters to several hundred meters from the western piedmont to the eastern plain (Wang and Han, 2012). An example of a borehole joint profile in the Beijing area is shown in Figure 2, from the profile, it can be seen that there are approximately 10 layers of soil, which are: ①Miscellaneous fill; ②Yellow-brown silty fine sand; ③Yellow-brown silty clay; ④Grey fine sand; ⑤Gray-brown silty clay with sand; ⑥Silty fine sand with horizontal clay strip; ⑦Gray-brown silty sand mixed with silty clay; ⑧Gray silty fine sand is mixed with silty clay, and horizontal bedding is developed; ⑨Gray-brown, yellow-brown silty clay; ⑨-1 Gray silty clay; ⑨-2 Yellow-brown silty clay; ⑩Dark gray silty clay. Also, a potential fault crossing several soil layers can be found here and the maximum stratum drop reached 10 m.

3.2 Field data

For this study, a total number of 418 borehole data were collected. Information including project name, location,

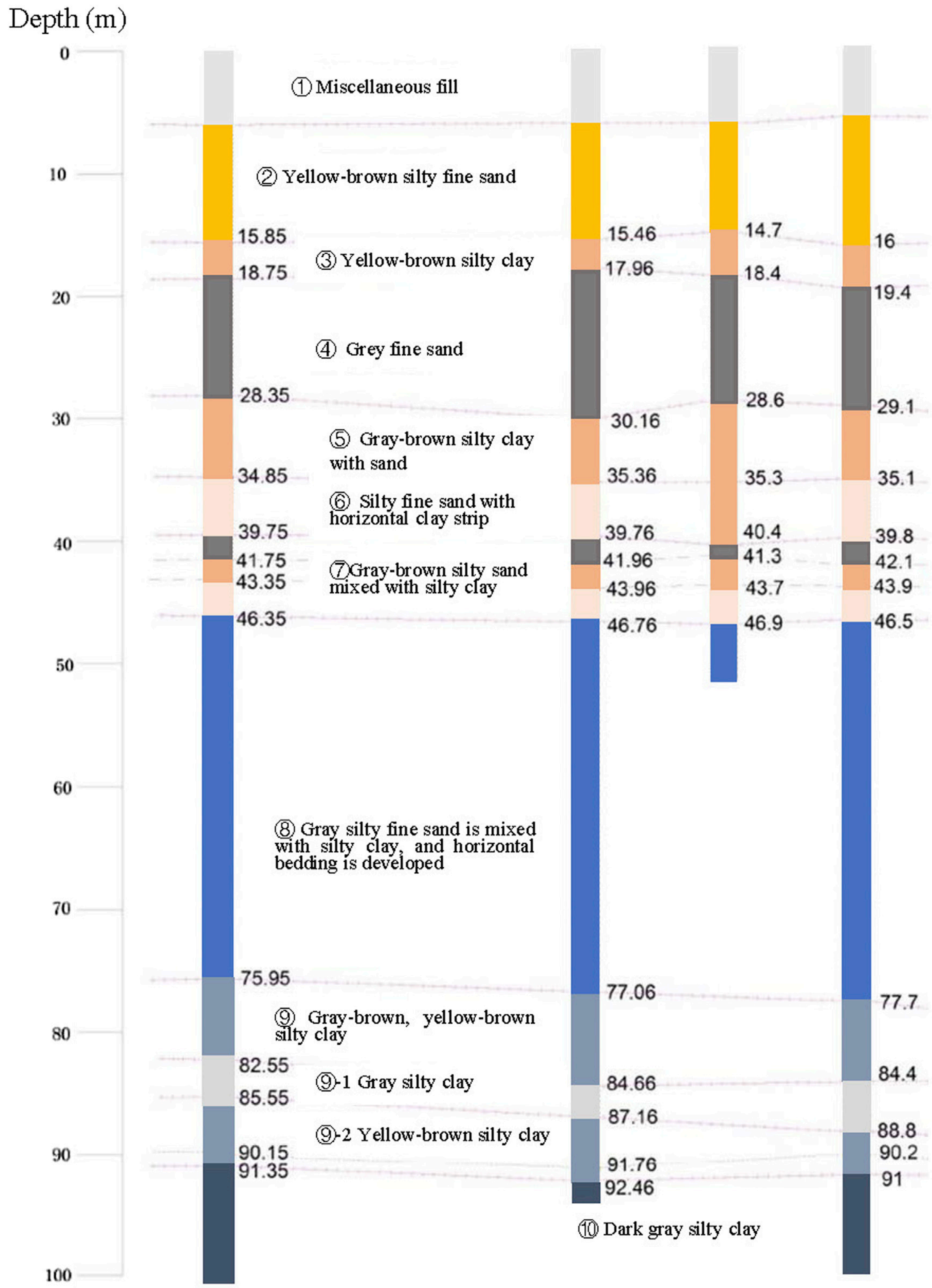

FIGURE 2
An example borehole joint profile in the Beijing area.

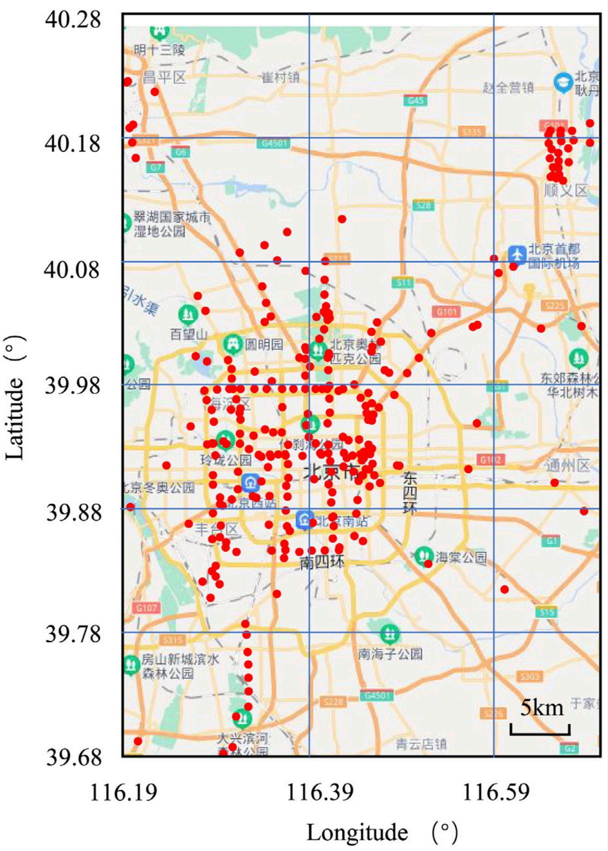

FIGURE 3
Distribution of selected measured data, red dots represent the borehole locations.

date, shear wave velocity along with the depth, depth of soil layers, descriptions of soil, V_{s15}, V_{s20}, and V_{s30}. The shear-wave velocity data are obtained from the suspension P-S velocity logging method. The original study area is relatively wide with latitude boundaries ranging from 39.3° to 40.5° and longitude boundaries ranging from 115.7° to 117.3°. Ignoring the projection error of the curved surface, it is transformed into spherical coordinates as a rectangular zone, with a width of 136.5 km and a height of 133.4 km. The original data uses latitude (Beijing, 1979) and longitude as coordinates to represent the positioning of points. Because latitude and longitude are inconvenient to be directly computed as horizontal and vertical coordinates, it is necessary to convert them to plane coordinates in kilometers. For easy calculation in this study, the point (115.7°, 39.3°) is set as the origin. Through simple mathematical calculation, It can be known that longitude corresponds to 85.3125 km per degree (e.g., 136.5/(117.5–115.7) =85.3125) and latitude corresponds to 111.1667 km per degree (e.g., 133.4/(40.5–39.3)=111.1667). Hence, the coordinate points can be transformed into XY coordinates as follows:

$$X = (x - 115.7) \times 85.3125 \tag{6}$$

$$Y = (y - 39.3) \times 111.1667 \tag{7}$$

where x is the longitude of the data point and y is the latitude of the data point. X and Y are the transverse and ordinate values of the converted data points (X and Y are in the unit of km). Since the measured data points are unevenly distributed in the original study area, with dense data points in some areas and scattered data points distributed around them. Therefore, in order to facilitate the smooth implementation of the project, as well as the accuracy of the prediction, the scope of the study area is narrowed. After adjustment, the study area has a latitude boundary of 39.6778°–40.2895° and a longitude boundary of 116.1923°–116.7081°. The range of study area and distribution of measured data points is shown in Figure 3.

Therefore, according to Eqs 6, 7, the boundary of the study area can be transformed into XY coordinate system, where the range in the X direction is 42.5–85.7 km and the range in the Y direction is 42.2–109.6 km, which constitutes a rectangular range with a width of 44 km and a height of 68 km.

Given the shear wave velocity - depth measurement data, a time-averaged shear wave velocity to a profile depth z, denoted as V_{sz}, can be calculated at each measurement location as

$$V_{sz} = \frac{z}{\Delta t_z} \tag{8}$$

$$\Delta t_z = \int_0^z \frac{dz}{V_s(z)} \tag{9}$$

where Δt_z is the travel time for shear waves from depth z to the ground surface; $V_s(z)$ is the shear wave velocity at depth z. In this work, z is taken as 30m.

4 Data inference - Statistical and spatial characterizations of the V_{s30} data

The data set was randomly divided into two groups: training data (388 measurements) and testing data (30 measurements). Among them, the testing data will not participate in random field simulation but only be used to evaluate the accuracy of prediction. Figure 4 plots the histogram of the selected 388 V_{s30} measurements, and it fit the lognormal distribution. These values are only available at locations with measured shear wave velocity profiles. And these measured data will be used as input information in random field estimation of V_{s30} in this study area. A more detailed value can be seen in Table 1. It summarizes the statistical characteristics (e.g., mean, variance, maximum, median, minimum) of the 388 V_{s30} values.

The empirical semi-variogram of V_{s30} measurements is also computed to infer their spatial structure in the studied region. According to Goovaerts (1997), the empirical semi-variogram can be calculated as follow:

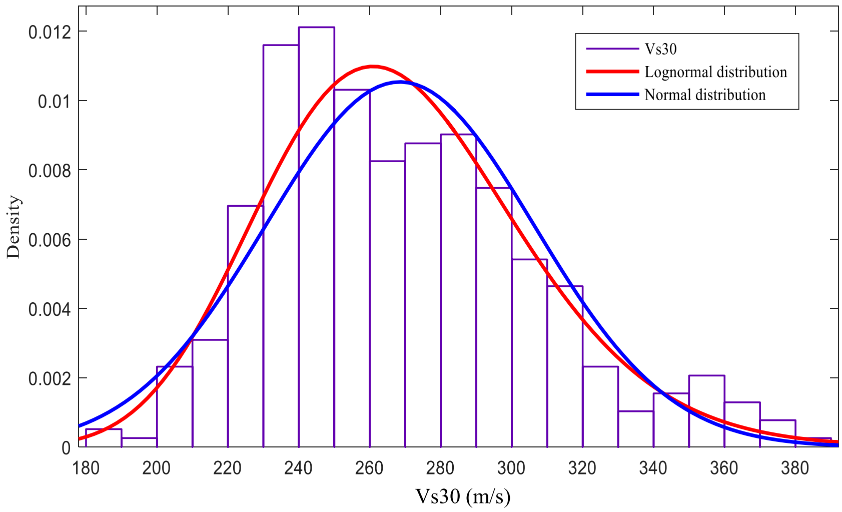

FIGURE 4
Histogram of selected 388 V_{s30} values calculated from shear wave velocity measurements.

TABLE 1 Statistical characteristics of the known V_{s30}.

Statistical parameter	Study area
Data count	388
Mean	268 m/s
Standard deviation	37.85
Maximum	388 m/s
Minimum	185 m/s
Median	263 m/s

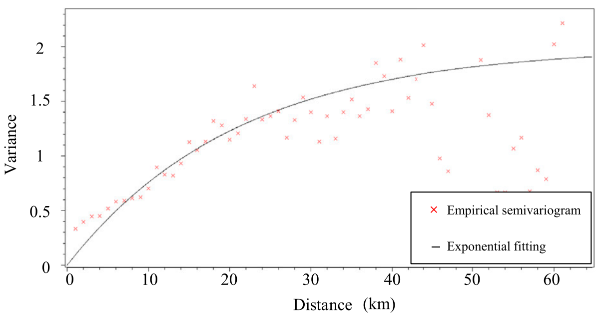

FIGURE 5
Empirical and fitted semi-variogram based on known V_{s30} at measurement locations.

$$\gamma(h) = \frac{1}{2N(h)} \sum_{\alpha=1}^{N(h)} \left[Z(u_\alpha) - Z(u_\alpha + h)\right]^2 \tag{10}$$

In which, N(h)is the number of pairs of data with a distance of h.

To facilitate the incorporation of the semi-variogram into random field models, the empirical semi-variogram has to be fitted by a basic semi-variogram model or a linear combination of several basic semi-variogram models that are permissible. The three most commonly used models for fitting semi-variogram are the Exponential model, the Spherical model, and the Gaussian model (Liu et al., 2017a). Figure 5 plots the empirical semi-variogram model as well as the fitted exponential model of the form:

$$\gamma(h) = \omega\left[1 - \exp\left(-\frac{3h}{a}\right)\right] + \tau \tag{11}$$

In which, h is the separation distance between any two points; a is the range, representing the distance at which the semi-variogram levels off. The fitted range of this study site is 19.67 km, and the nugget effect is neglected here for a better fit of the exponential model.

5 Random field realization of the Beijing area

With the statistical distribution of V_{s30} values and the spatial structure of V_{s30} at different locations, random field models are used to generate V_{s30} maps of the Beijing area. A grid with the element size of 1 km*1 km is used, since the size of the study area is rectangular with a width of 44 km and a height of 68 km, so 2,992 elements are generated. The grid can be refined if it is necessary for future studies. Random field realization will be carried out based on this grid form, and finally, the

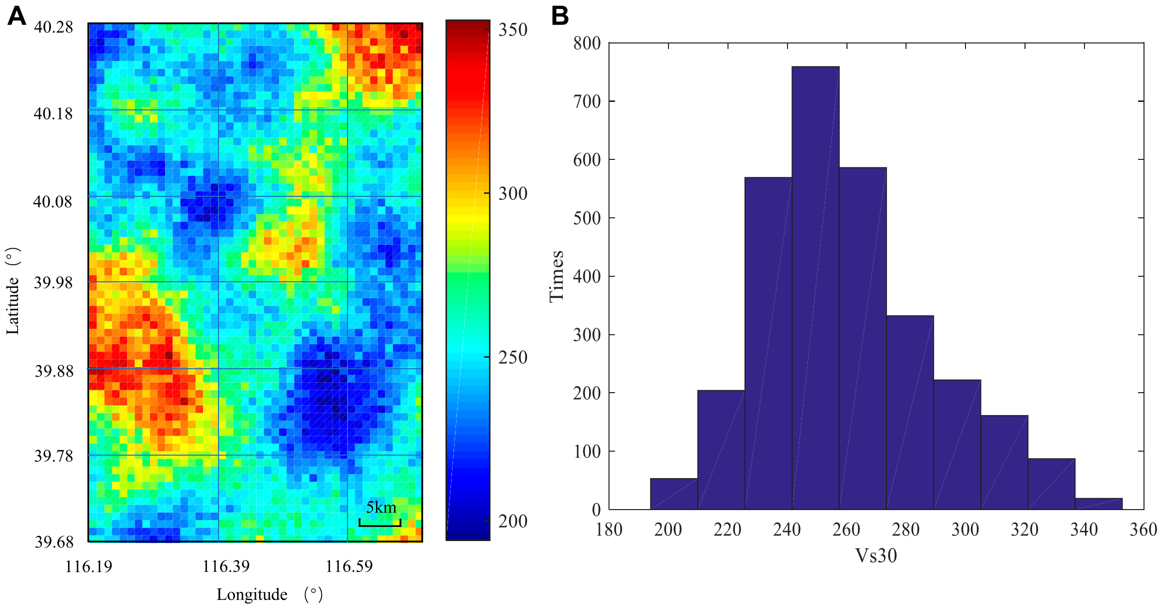

FIGURE 6
One-time random field realization of V_{s30} in the Beijing area.**(A)** Map of V_{s30} realization; **(B)** Histogram of V_{s30}.

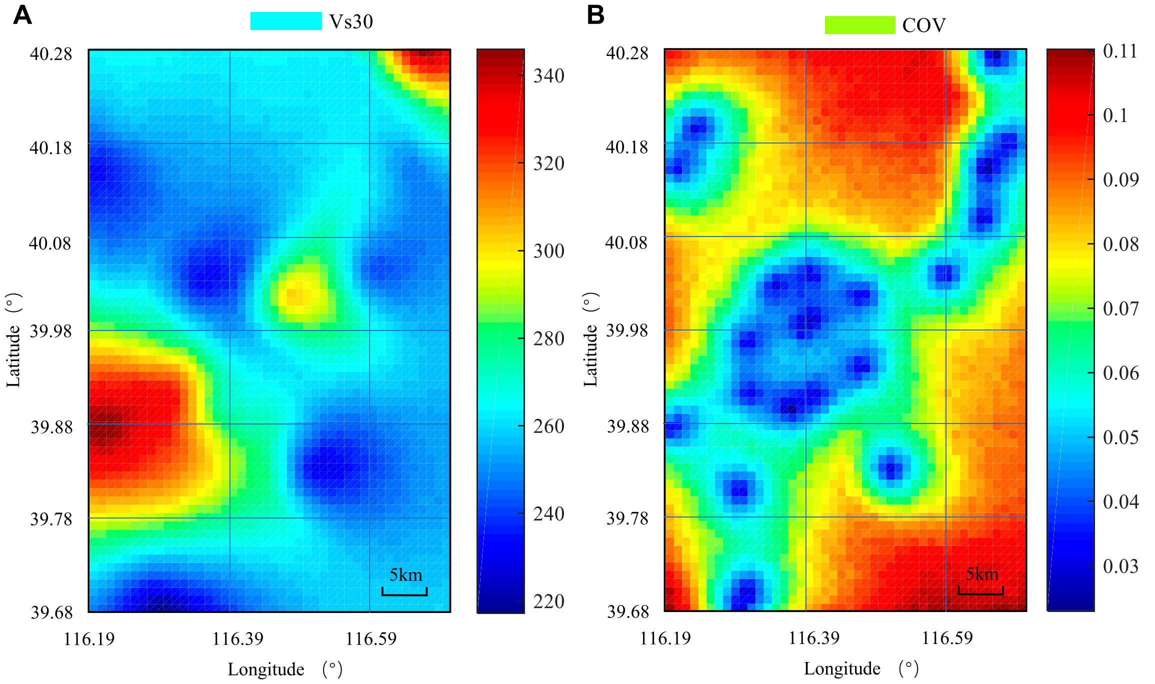

FIGURE 7
Expected V_{s30} values and associated uncertainties (coefficient of variations) in the Beijing area. **(A)** Map of average V_{s30}; **(B)** Map of COV of V_{s30}.

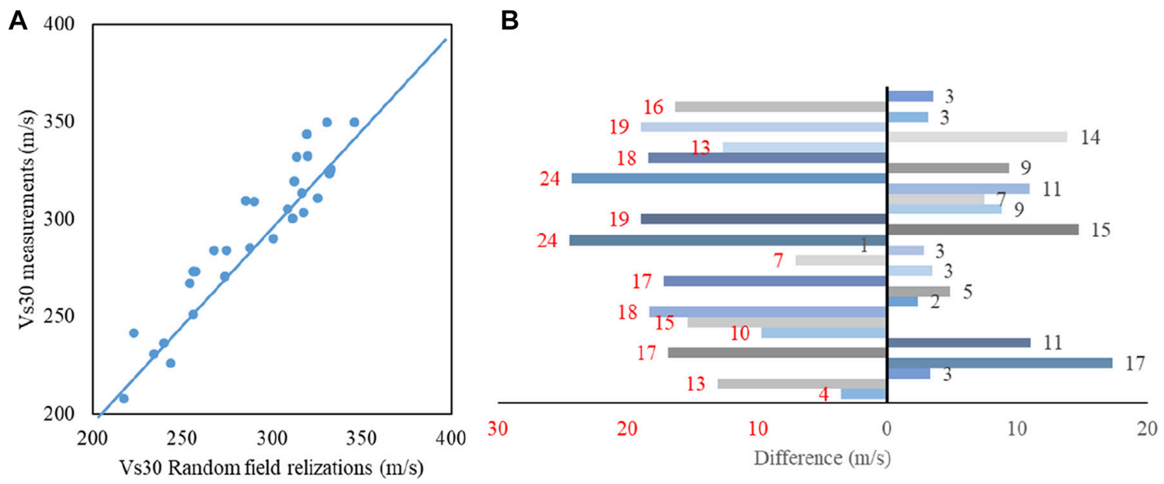

FIGURE 8
Cross-validation result of V_{s30} realizations. **(A)** Comparison between random field realizations and measurements; **(B)** Differences of random field realizations and measurements.

corresponding V_{s30} estimation value will be obtained in each element, which will be finally displayed in the form of a digital V_{s30} map. The new map accounts for and preserves the site-specific shear wave velocity measurements and the soil spatial structure.

One time of V_{s30} realization and its corresponding histogram is shown in Figure 6. The histogram shows that the simulation preserves the statistical characterizations of V_{s30} inferred from the known V_{s30} data.

A single random field simulation is only a random sampling based on a given distribution, and the result can not represent the true V_{s30} value. Therefore, random field realization and the Monte Carlo sampling method are combined to carry out a large number of independent simulations. Coupling the random field model with Monte Carlo simulations, the expected V_{s30} value across the Beijing area can be obtained, as well as its uncertainty distribution. Here, 1,000 times Monte Carlo simulations are operated and 1,000 independent maps can be generated. In other words, for the V_{S30} of each 1 km*1 km element, 1,000 simulation calculations have been carried out. According to the simulation results of 1,000 times realizations, the mean value and coefficient of variation of the V_{s30} prediction value can be obtained statistically for each element. Among them, the mean value of 1,000 simulations of each element represents the expected value of V_{s30} of the element, and the variance and coefficient of variation represent the uncertainty of the shear wave (Crespo MariaJ. et al., 2022) velocity value at this point. By combining 2,992 elements, the V_{s30} distribution and uncertainty distribution in the study area can be obtained. The expected V_{s30} map is shown in Figure 7A. And it is averaged from these 1,000 times independent Monte Carlo simulations. An obvious trend in this map is that the overall soil quality in the study area is normal, ranging from 217.1623 m/s to 346.9406 m/s, the west-south part of this area has a relatively higher V_{s30} value, which represents the Fang Shan hilly area. And the northeast corner also has high V_{s30} values, which can be seen from the geology map as a hilly area too.

Unlike the deterministic method, one of the strengths of the random field method is its ability to estimate the uncertainty distribution associated with the generated V_{s30} map. Here, the coefficient of variation (COV) calculate from 1,000 independent Monte Carlo simulations at each location is calculated to quantify the uncertainties. The COV map is plotted in Figure 7B. As shown in the figure, the COVs are generally very small (ranging from 0.023 to 0.1102) and approach zero around locations with measurement data. And for the location without measured data, the COV value will be higher but still acceptable. It is worth noting that, in the (Crespo MJ. et al., 2022) simulation of this random field model, the study area is divided into 2,992 square elements, and the center point of each element is focused, the simulated V_{s30} value of the center point is assigned to the whole square element. Hence, if the center point happens to be the measured data point, the COV of the cell is 0. If there are measured data points in the cell, but the measured data points are not exactly at the center point of the element, the simulated value of the cell will not be completely equal to the measured data value. But it will be very close, and the COV value of this cell will be very small (shown in dark blue in Figure 7B).

Since the V_{s30} map has been generated, the accuracy of the prediction can be verified by using the testing data (30 measurements). According to the location of 30 testing data points, the corresponding element in the map can be found. Obtaining the corresponding V_{s30} value of each element, cross-validation can be operated. The comparison

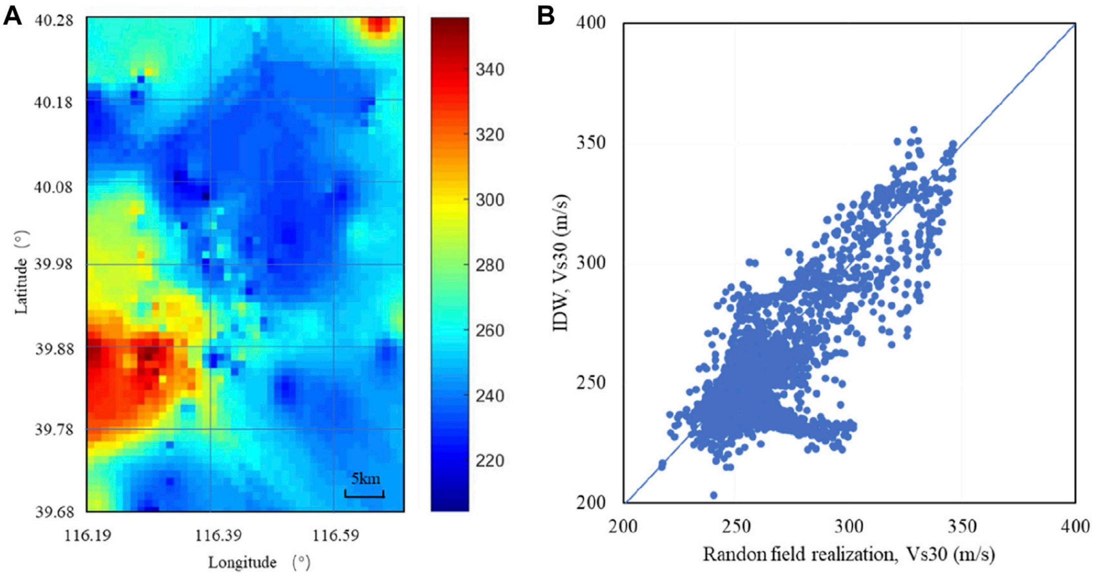

FIGURE 9
Comparison between IDW and Random field model: **(A)** V_{s30} realizations calculated by IDW; **(B)** Comparison of results between two methods.

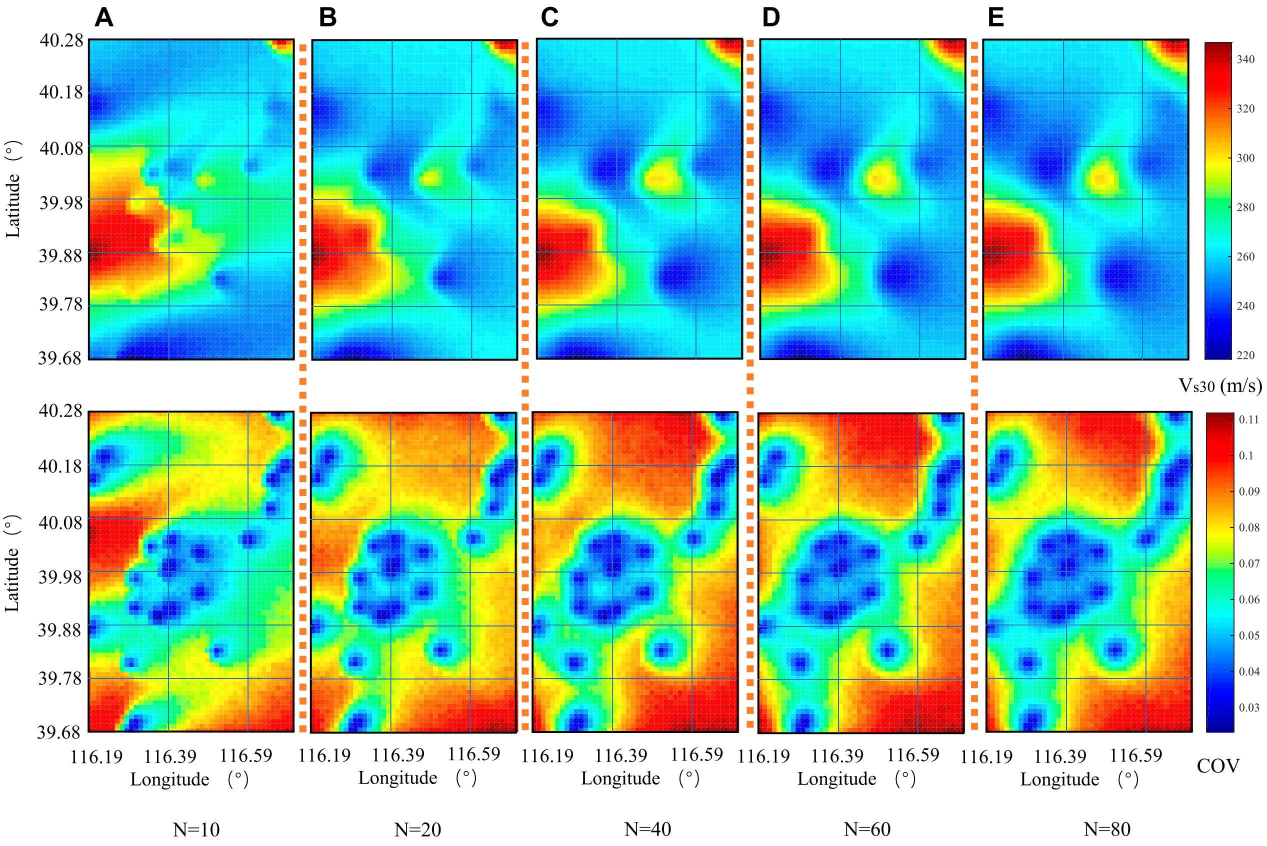

FIGURE 10
Expected V_{s30} values and associated uncertainties in the Beijing area with different values of N. **(A)** N=10; **(B)** N=20; **(C)** N=40; **(D)** N=60; **(E)** N=80.

TABLE 2 Variability of V_{s30} realizations under different N values.

	V_{s30}			COV		
	Average	Maximum	Minimum	Average	Maximum	Minimum
N=10	271.2419	344.2349	219.5146	0.0744	0.1129	0.0251
N=20	267.0315	345.2037	217.2584	0.0739	0.1136	0.0238
N=40	265.7826	345.8909	217.6856	0.0732	0.1102	0.0237
N=60	265.0711	345.9406	217.1623	0.0714	0.1102	0.0230
N=80	264.6746	346.6608	216.9359	0.0702	0.1117	0.0227

results are shown in Figure 8. As can be seen from the figure, the prediction results are reasonable.

Also, the inverse distance weighted method (IDW) is operated here to verify the result. Because both methods consider the variation of parameter values with spatial distance, hence, the two methods get similar results with an average difference of 13.95 m/s (Figure 9). The random field method describes spatial correlation by semi-variogram, which is more accurate than the inverse distance difference method. Moreover, the random field V_{s30} map could provide both the expectation and uncertainty of a site parameter, which could be further integrated into the reliability analysis of the site response or earthquake disaster degree evaluation.

6 Effects of N

As described in Section 2, the unknown value Z_n at an unmeasured location can be drawn from the conditional normal distribution. Once Z_n is generated, it is inserted into the "previous" vector, upon which the "next" unknown value at another unsampled location will be generated. Hence, the "previous" vector is getting bigger during the simulation, it is unnecessary to use all of them to do the estimation. Therefore, it is necessary to define the "N" value (maximum number of previously generated elements to correlate to) when predicting value at unsampled locations, which will have a noticeable influence on the calculation results. After we set the value of N at the beginning of the estimation (e.g., 40), this value will keep constant for the whole simulation. This means when generating each unknown value at the unsampled location, only 40 "previous" data closest to this point will participate in the prediction, the nearest 40 data points are included in the covariance matrix calculation. And the values of other points will not have a direct impact on the prediction of this point. The principle behind this is that in geostatistical theory, the geotechnical or geological characteristics of the regional areas usually show spatial variability and spatial correlation, which means the soil parameters measured at each observation point are correlated with those at adjacent locations, and with the increase of distance, the correlation between the parameters decreases gradually. Therefore, five different values of N are selected, namely, 10, 20, 40, 60, and 80, and the simulation results are used to evaluate the influence of N.

Similar to Section 3, for each N value, the random field model is coupled with 1,000 times independent Monte Carlo simulations. So five sets of expected V_{s30} values and their uncertainty distribution across the Beijing area are obtained (Figure 10).

It can be seen from Figure 10 that with the increase of the N value (from 10 to 80), the prediction results gradually tend to be stable, and the change in the V_{s30} map becomes invisible. Among them, for N changes from 10 to 40, the V_{s30} distribution map has obvious changes, and in COV maps, the blue area expanded and the red area turns orange, which means the COV values turn smaller. And for N changes from 60 to 80, the predicted V_{s30} distribution map is almost no different, similar to the COV maps. Detailed statistical results are listed in Table 2. It can be seen that the coefficient of variation (COV) is gradually decreasing with the increase of N, indicating that its prediction reliability is also gradually increasing. It is worth noting that for N changes from 10 to 60, the decreasing rate is large, and when N is larger than 60, the average COV value continues to decline, but the rate of decline is likely to remain steady.

The above observation shows that in the simulation process, the more "known values" are considered, the more accurate the results are (the lower the COV value is), and the improvement rate of its accuracy is gradually stable after reaching the peak with the increase of N. However, with the increase of the N value, the calculation matrix also increases, which increases the calculation workload and storage space required for calculation. Therefore, it is necessary to comprehensively consider the calculation efficiency and accuracy, and cannot blindly increase the N value. The appropriate N value can give us an appropriate result with a high calculation efficiency. So in this case, 60 is appropriate for this case study.

7 Conclusion

In this work, a random field prediction model of V_{s30} is presented. And this prediction model is applied to map V_{s30}

and its uncertainty over the Beijing area. By operating statistical and geostatistical analysis of 388 measured bore data, the distribution and spatial variation of V_{s30} are studied. Combining conditional sequence simulation technology and the Monte Carlo sampling method, the random field simulation of V_{s30} at the city scale is carried out, and the two-dimensional V_{s30} map and uncertainty distribution for the Beijing area are established. This new map can be applied to site classification and amplification factor characterization in the studied region in the future. Also, the effect of random filed model parameter N is tested. All the calculations and simulations in this paper are realized by self-made MATLAB code. In summary, it is found that:

1) V_{s30} estimates over the entire studied region can be obtained using the random field model. The resulting map can give a detailed and reliable estimation of V_{s30} at the unsampled location, meanwhile, the local measurement data are incorporated and preserved to make the new map consistent with the actual situation.
2) Coupled with the Monte Carlo simulation, the coefficient of variation (COV) can be easily obtained and is used to quantify the uncertainty distribution of V_{s30} in the Beijing area. In general, COV is close to zero around locations with measured data, while COV gradually increases in areas without any measured V_{s30} values.
3) The model parameter *N* (maximum number of previously generated elements to correlate to) will have a noticeable influence on the estimating V_{s30} value at un-measured locations. The results show that with the increase of the N value, the prediction results gradually tend to be stable and the prediction reliability is gradually enhanced. However, the increase in the N value may cause an increase in the calculation workload and storage space required for calculation. Therefore, it is necessary to consider the calculation efficiency and accuracy comprehensively, and cannot blindly increase the N value.
4) Random field model and IDW method get similar results since both methods consider the variation of parameter values with spatial distance. However, the random field method describes spatial correlation by semi-variogram, which is more accurate than the inverse distance difference method. The presented methods are directly applicable to the site involving more complex property conditions. Moreover, the random field approach could provide both the expectation and uncertainty of a site parameter, which could be further integrated into the reliability analysis of the site response or earthquake disaster degree evaluation.
5) It is realized that estimation errors will be obtained when the geological conditions change abruptly (for example, from mountain to plain). So, it is necessary to use geological conditions to constrain the V_{s30} estimation. And this will be the next step to improve this random field model by combining geological data and geotechnical data in V_{s30} estimation.

Data availability statement

The datasets generated and analyzed during the current study are not publicly available but are available from the corresponding author on reasonable request. Requests to access the datasets should be directed to Wenxin Liu, wenxinl@zstu.edu.cn.

Author contributions

WL and YP conceived the presented idea. WL developed the theory and performed the computations. WL wrote the manuscript with support from YP and JW. All authors provided critical feedback and helped shape the research, analysis, and manuscript. YP supervised the project.

Funding

This work was supported by the National Natural Science Foundation of China (5210082052), the Zhejiang Provincial Natural Science Foundation (LQ22E080028), and the Science Foundation of Zhejiang Sci-Tech University (19052459-Y).

Acknowledgments

These financial supports are gratefully acknowledged.

Conflict of interest

The authors declare that the research was conducted in the absence of any commercial or financial relationships that could be construed as a potential conflict of interest.

Publisher’s note

References

Ahdi, S. K., Stewart, J. P., Ancheta, T. D., Kwak, D. Y., and Mitra, D. (2017). Development of VS profile database and proxy-based models for VS 30 prediction in the Pacific Northwest region of North America. *Bull. Seismol. Soc. Am.* 107 (4), 1781–1801.

Ancheta, T. D., Darragh, R., Stewart, J. P., Seyhan, E., Silva, W. J., Chiou, B. S. J., et al. (2013). *PEER NGA-West2 database, PEER Report 2013/03*. Berkeley, California: Pacific Earthquake Engineering Research Center.

Badal, J., Dutta, Serón F., and Biswas, N. (2004). Three-dimensional imaging of shear wave velocity in the uppermost 30 m of the soil column in Anchorage, Alaska. *Geophys. J. Int.* 158 (3), 983–997. doi:10.1111/j.1365-246x.2004.02327.x

Baise, L. G., Higgins, R. B., and Brankman, C. M. (2006). Liquefaction hazard mapping statistical and spatial characterization of susceptible units. *J. Geotech. Geoenviron. Eng.* 132 (6), 705–715. doi:10.1061/(asce)1090-0241(2006)132:6(705)

Beijing Institute of Hydrogeology and Engineering Geology (1979). *The bedrock geological map of Beijing plain*. Biejing: Geological Publishing House. (in Chinese).

Boore, D. M. (2004). Estimating s(30) (or NEHRP site Classes) from shallow velocity models (depths < 30 m). *Bull. Seismol. Soc. Am.* 94 (2), 591–597. doi:10.1785/0120030105

Cai, X. M., Luan, Y. B., Guo, G. X., and Liang, Y. N. (2016). 3D Quaternary geological structure of Beijing plain. *Geol. China* 36 (5), 1021–1029. (in Chinese).

Chen, G. X., Zhu, J., Qiang, M. Y., and Gong, W. P. (2018). Three-dimensional site characterization with borehole data-a case study of Suzhou area. *Eng. Geol.* 234, 65–82. doi:10.1016/j.enggeo.2017.12.019

Ching, J., and Schweckendiek, T. (2021). State-of-the-art review of inherent variability and uncertainty in geotechnical properties and models. *ISSMGE Tech. Comm.*, 304.

Chiou, B. S. J., and Youngs, R. R. (2008). *NGA model for average horizontal component of peak ground motion and response spectra, PEER Report 2008/09*. Berkeley, California: Pacific Earthquake Engineering Research Center.

Crespo, Maria J., Benjumea, Beatriz, Moratalla, José M., Lacoma, Luis, Albert, Macau, González, Álvaro, et al. (2022b). A proxy-based model for estimating V30 in the Iberian Peninsula. *Soil Dyn. Earthq. Eng.* 155, 107165. doi:10.1016/j.soildyn.2022.107165

Crespo, M. J., Benjumea, B., Moratalla, J. M., Lacoma, L., Macau, A., Gonzalez, A., et al. (2022a). A proxy-based model for estimating VS30 in the Iberian Peninsula. *Soil Dyn. Earthq. Eng.* 155, 107165.

DeGroot, D. J., and Baecher, G. B. (1993). Estimating autocovariance of *in-situ* soil properties. *J. Geotech. Engrg.* 119, 147–166. doi:10.1061/(asce)0733-9410(1993)119:1(147)

Derras, B., Bard, P. Y., and Cotton, F. (2017). V_{S30}, slope, H800 and f0: Performance of various site-condition proxies in reducing ground-motion aleatory variability and predicting nonlinear site response. *Earth Planets Space* 69, 133. doi:10.1186/s40623-017-0718-z

Derras, B., Bard, P. Y., Régnier, J., and Cadet, H. (2020). Non-linear modulation of site response: Sensitivity to various surface ground-motion intensity measures and site-condition proxies using a neural network approach. *Eng. Geol.* 269, 105500. doi:10.1016/j.enggeo.2020.105500

Foster, K. M., Bradley, B. A., McGann, C. R., and Wotherspoon, L. M. (2019). A V_{S30} map for New Zealand based on geologic and terrain proxy variables and field measurements. *Earthq. Spectra* 35 (4), 1865–1897. doi:10.1193/121118eqs281m

Goovaerts, P. (1997). *Geostatistics for natural resources evaluation*. Duke: Oxford University Press on Demand.

Hasancebi, N., and Ulusay, R. (2007). Empirical correlations between shear wave velocity and penetration resistance for ground shaking assessments. *Bull. Eng. Geol. Environ.* 66 (2), 203–213. doi:10.1007/s10064-006-0063-0

Heath, D. C., Wald, D. J., Worden, C. B., Thompson, E. M., and Smoczyk, G. M. (2020). A global hybrid V_{S30} map with a topographic slope–based default and regional map insets. *Earthq. Spectra* 36 (3), 1570–1584. doi:10.1177/8755293020911137

Li, M., Rathje, E. M., Cox, B. R., and Yust, M. (2021). A Texas-specific VS 30 map incorporating geology and VS 30 observations. *Earthq. Spectra* 24, 87552930211033622.

Liu, W. X., Chen, Q. S., Wang, C. F., Chen, G. X., and Juang, C. H. (2017b2017). Multiscale random field-based shear wave velocity mapping and site classification. *Geo-Risk*, 410–419.

Liu, W. X., Chen, Q. S., Wang, C. F., Chen, G. X., and Juang, C. H. (2017a). Spatially correlated multiscale Vs30 mapping and a case study of the suzhou site. *Eng. Geol.* 220, 110–122. doi:10.1016/j.enggeo.2017.01.026

Liu, W. X., Juang, C. H., Chen, Q. S., and Chen, G. X. (2021). Dynamic site response analysis in the face of uncertainty–an approach based on response surface method. *Int. J. Numer. Anal. Methods Geomech.* 45, 1854–1867. doi:10.1002/nag.3245

Min, Z. Q., Wu, G., Jiang, Z. X., Liu, C. S., and Yang, Y. L. (1995). *A Catalog of strong Historical earthquakes in China (from 2300 BC to 1911 AD)*. Beijing, China: Seismology Publishing House. (in Chinese).

Parker, G. A., Harmon, J. A., Stewart, J. P., Hashash, Y. M. A., Kottke, A. R., Rathje, E. M., et al. (2017). Proxy-based V_{S30} estimation in central and eastern North America. *Bull. Seismol. Soc. Am.* 107 (1), 117–131. doi:10.1785/0120160101

Peng, H., Wu, Z., Wu, Y. M., Yu, S., Zhang, D., and Huang, W. (2011). Developing a prototype earthquake early warning system in the Beijing capital region. *Seismol. Res. Lett.* 82 (3), 394–403. doi:10.1785/gssrl.82.3.394

Peng, Y., Wang, Z., Woolery, E. W., Lyu, Y., Carpenter, N. S., Fang, Y., et al. (2020). Ground-motion site effect in the Beijing metropolitan area. *Eng. Geol.* 266, 105395. doi:10.1016/j.enggeo.2019.105395

Phoon, K. K., Cao, Z. J., Ji, J., Leung, Y. F., Najjar, S., Shuku, T., et al. (2022). Geotechnical uncertainty, modeling, and decision making. *Soils Found.* 62 (5), 101189. doi:10.1016/j.sandf.2022.101189

Rahman, M., Kamal, A. S. M., and Siddiqua, S. (2018). Near-surface shear wave velocity estimation and V_{s30} mapping for Dhaka City, Bangladesh. *Nat. Hazards (Dordr).* 92 (3), 1687–1715. doi:10.1007/s11069-018-3266-3

Raptakis, D. G., Anastasiadis, S. A. J., Pitilakis, K. D., and Lontzetidis, K. S. (1995). "Shear wave velocities and damping of Greek natural soils," in *Proceedings of 10th European Conference of earthquake engineering* (Vienna, 477–482.

Seed, H. B., and Idriss, I. M. (1981). Evaluation of liquefaction potential sand deposits based on observation of performance in previous earthquakes. *InASCE Natl. Conv. (MO)*, 481–544.

Stewart, J. P., and Afshari, K. (2021). Epistemic uncertainty in site response as derived from one-dimensional ground response analyses. *J. Geotech. Geoenviron. Eng.* 147 (1), 04020146. doi:10.1061/(asce)gt.1943-5606.0002402

Stewart, J. P., Klimis, N., Savvaidis, A., Theodoulidis, N., Zargli, E., Athanasopoulos, G., et al. (2014). Compilation of a local VS profile database and its application for inference of VS30 from geologic- and terrain-based proxies. *Bull. Seismol. Soc. Am.* 104 (6), 2827–2841. doi:10.1785/0120130331

Thompson, E. M., Baise, L. G., and Kayen, R. E. (2007). Spatial correlation of shear-wave velocity in the san Francisco Bay area sediments. *Soil Dyn. Earthq. Eng.* 27 (2), 144–152. doi:10.1016/j.soildyn.2006.05.004

Wald, D. J., and Allen, T. I. (2007). Topographic slope as a proxy for seismic site conditions and amplification. *Bull. Seismol. Soc. Am.* 97 (5), 1379–1395. doi:10.1785/0120060267

Wald, D. J., McWhirter, L., Thompson, E., and Hering, A. S. (2011). "A new strategy for developing VS30 maps," in *Proc. 4th Int. Effects of surface geology on seismic motion Symp*.

Wang, J. H., and Han, X. (2012). Preliminary study on Tertiary engineering geological conditions in Beijing Plain area. *J. Eng. Geol.* 20 (5), 682–686. (in Chinese).

Wang, S. Y., Wu, G., and Shi, Z. L. (1999). *A Catalog of modern earthquakes in China (1912–1990)*. Beijing, China: China Science and Technology Press. (in Chinese).

Wills, C. J., Gutierrez, C. I., Perez, F. G., and Branum, D. M. (2015). A next generation V_{S30} map for California based on geology and topography. *Bull. Seismol. Soc. Am.* 105 (6), 3083–3091. doi:10.1785/0120150105

Wride, C. E., Robertson, P. K., Biggar, R. G., Campanella, R. G., Hofmann, B. A., Hughes, J. M. O., et al. (2000). Interpretation of *in situ* test results from the CANLEX sites. *Can. Geotech. J.* 37 (3), 505–529. doi:10.1139/t00-044

Xie, J. J., Zimmaro, P., Li, X. J., Wen, Z., and Song, Y. S. (2016). V_{S30} empirical prediction relationships based on a new soil-profile database for the Beijing Plain Area, China. *Bull. Seismol. Soc. Am.* 106 (6), 2843–2854. doi:10.1785/0120160053

Yong, A., Martin, A., Stokoe, K., and Diehl, J. (2013). ARRA-funded VS30 measurements using multi-technique approach at strong-motion stations in California and central-eastern United States (No. 2013-1102). *U. S. Geol. Surv.* 47, 5765.

Yuan, H., Gao, X., and Qi, W. (2019). Modeling the fine-scale spatiotemporal pattern of earthquake casualties in cities: Application to Haidian District, Beijing. *Int. J. disaster risk Reduct.* 34, 412–422. doi:10.1016/j.ijdrr.2018.12.010

Zhang, J. Z., Huang, H. W., Zhang, D. M., Phoon, K. K., Liu, Z. Q., and Tang, C. (2021). Quantitative evaluation of geological uncertainty and its influence on tunnel structural performance using improved coupled Markov chain. *Acta Geotech.* 16 (11), 3709–3724. doi:10.1007/s11440-021-01287-6

frontiers | Frontiers in Earth Science

TYPE Original Research
PUBLISHED 19 January 2023
DOI 10.3389/feart.2022.1054448

Spatial variation of strong ground motions in a heterogeneous soil site based on observation records from a dense array

Qianli Yang[1], Ruifang Yu[1]*, Peng Jiang[2] and Kexu Chen[1]

[1]Institute of Geophysics, China Earthquake Administration, Beijing, China, [2]Sichuan Earthquake Administration, Chengdu, China

EDITED BY
Yefei Ren,
China Earthquake Administration,
Harbin, China

REVIEWED BY
Chaoying Zhao,
Chang'an University, China
Ping Wang,
China Earthquake Administration,
Lanzhou, China

*CORRESPONDENCE
Ruifang Yu,
yrfang126@126.com

SPECIALTY SECTION
This article was submitted to Structural Geology and Tectonics,
a section of the journal
Frontiers in Earth Science

RECEIVED 26 September 2022
ACCEPTED 15 November 2022
PUBLISHED 19 January 2023

CITATION
Yang Q, Yu R, Jiang P and Chen K (2023), Spatial variation of strong ground motions in a heterogeneous soil site based on observation records from a dense array.
Front. Earth Sci. 10:1054448.
doi: 10.3389/feart.2022.1054448

The difference in local sediment thickness and soil properties has a significant impact on the spatial variation mechanism of seismic ground motion in the engineering scale. Due to the scarcity of observation data of dense arrays, the existing theoretical studies are mostly developed by numerical simulation methods, including human factors and a large number of assumptions. In view of this, based on the multistation observation records of the Luxian MS 6.0 earthquake and Yibin MS 5.1 earthquake obtained using a Zigong dense array, the study quantitatively analyzes the spatial characteristics of ground motion in heterogeneous soil sites by integrating a theoretical model with numerical analysis. In this study, many popular approaches including root-mean-square acceleration, horizontal-to-vertical spectral ratio (HVSR) of microtremor and strong motion records, and lagged coherency are comprehensively utilized to make the conclusion accurate and reliable. The results show that local soil conditions could affect the attenuation of coherence function with distance. The station-pairs with similar HVSR characteristics generally present a higher coherence level when the difference of the interstation distance is less than 100 m. In addition, the coherency function between stations will be greatly reduced when the H/V spectral ratio characteristics differ greatly, which is also obvious in the low-frequency part below 5 Hz. Finally, a lagged coherency model that considers the influence of heterogeneous soil is constructed in this study. The model has a definite physical meaning and can better represent the spatial variation of ground motion at nonbedrock sites.

KEYWORDS

heterogeneous soil site, dense array, spatial variation of ground motion, H/V spectral ratio method, lagged coherency

1 Introduction

The amplitude and phase of ground motion change with the spatial position affected by the seismic source model, propagation mechanism, and site conditions (Kiureghian, 1996; Zerva, 2009). This characteristic directly affects the seismic response of lifeline projects such as bridges, pipelines, and communication transmission systems. When an earthquake occurs, these facilities will be subject to additional pseudostatic action. If the seismic response analysis is conducted under simple support excitation, then this phenomenon will be ignored, resulting in a large deviation between the calculation results and the actual vibration. For the aforementioned reasons, in the seismic fortification of long-span structures, it is an urgent problem to accurately describe the spatial variation law of ground motion at the engineering scale and then establish a mathematical model to obtain the spatially relevant multipoint ground motion input suitable for engineering applications.

Research on the spatial variation of ground motion can be traced back to the early 1980s. The establishment of dense seismic arrays in various countries provides reliable data support for the research on spatial variation of ground motion. The SMART-1 soil array, located in northeastern Taiwan, was built in 1980 (Chern, 1982; Abrahamson et al., 1987). Throughout its operation, it has recorded 60 different seismic events and generated nearly 1,000 sets of three-component waveform records. The UPSAR bedrock array (Schneider et al., 1992), located on the San Andreas fault in the US, recorded the San Simeon earthquake in 2003 and the Parkfield earthquake in 2004, the data from which have been widely used in engineering seismic research (Konakli et al., 2014; Yu et al., 2020). In addition, the Chiba array in Japan (Katayama, 1991) and Argostoli array in Greece (Svay et al., 2017) provide valuable observation data for the study on the spatial variation law of ground motion at the engineering scale (Zerva and Zhang, 1997; Boissières and Vanmarcke,1995; Goda and Hong, 2008; Chen et al., 2021).

The spatial variation of ground motion mainly includes four components. 1) Phase diversity caused by the propagation of seismic waves to different positions on the surface (i.e., wave passage effect). 2) Spatial coherency loss of ground motion caused by moderate scattering and refraction (i.e., incoherent effect). 3) Amplitude attenuation caused by energy dissipation in the process of seismic wave propagation (i.e., attenuation effect), which can be basically ignored at the engineering scale. 4) Changes in the frequency and amplitude of bedrock incident waves in varying degrees caused by the changes in site geology and terrain (i.e., site effect). From the perspective of seismic design, the spatial variation characteristics of ground motion are mainly described by the standardized cross power spectrum of different measuring points, that is, the coherency function. Based on the observation data of dense seismic array, researchers in both China and around the world have proposed a variety of mathematical models for the attenuation of coherency functions with frequency and distance (Loh et al., 1982; Harichandran and Vanmarcke, 1986; Loh and Yeh, 1988; Hao et al., 1989; Abrahamson et al., 1991; Wang, 2012; Yu et al., 2021). Due to the lack of physical significance and low universality of empirical models, some scholars have proposed models combining theory and experience by analyzing the factors influencing the spatial variation of ground motion, for example, the Luco–Wong model, Somerville model (Somerville et al., 1988), and Kaiureghian model (Kiureghian, 1996). These models first establish the basic relations of coherency function based on theoretical analysis, then determine the model parameters according to the actual ground motion records, and are more flexible in application. However, the aforementioned research assumes that the ground surface is homogeneous, and fails to consider the influence of local site conditions on lagged coherency. As a result, the conclusions and models obtained are difficult to apply to structural response analysis under different site conditions.

Local site conditions are among the important factors affecting the spatial characteristics of ground motion (Nour et al., 2003; Kwok et al., 2008; Sadouki et al., 2012), and the thickness of overburden and the difference in the geotechnical properties of flat soil sites also impact the coherency function. For example, Kiureghian's research showed that the different soil layer responses between two points only changed the phase angle of the coherency function (Kiureghian, 1996), while having no effect on the amplitude (i.e., lagged coherency). Zerva and Harada deduced an analytical model for the coherency function of the seismic displacement field reflecting the spatial variability of the soil according to the kinematic differential equation. The results showed that the local soil layer effect did not change the overall attenuation trend of the lagged coherency, yet a small range of "drop-in-coherence" would appear in the curve near the average natural frequency of the site. In consideration of the complexity of soil conditions, Liao and Li (2002) evaluated the influence of soil property uncertainty on the coherency function with the orthogonal multinomial expansion coefficient method. The results showed that randomness in the soil layer often led to a decrease in the coherency function near the resonance frequency of the site, which was consistent with the research results of Zerva and Harada (1997). In addition, Bi and Hao (2012) generated spatial two-point ground motions under the joint action of the undulating surface and random soil properties with the combined spectral representation method. They found that the coherency function was directly related to the spectral ratio of two local sites, and the role of random change in the shear modulus of the soil layer on the coherency loss could not be ignored. Laib et al. (2015) established an analytical formula for the coherency function of the ground acceleration on the flat heterogeneous soil site according to the theoretical basis given by Zerva and Harada. They found that the lateral change in the natural frequency of the site not only led to the "coherence-hole" but also reduced the overall value of the coherency curve. Moreover, the results of the seismic response analysis on the double fulcrum structure of the single degree of freedom system show that the soil heterogeneity significantly increases the dynamic displacement and shear stress at the fulcrum, resulting in serious damage to the structure. The aforementioned research has played a positive role in the theoretical development of the spatial variation of strong ground motion. However, the theoretical analysis and numerical simulation methods involve many human factors and scientific assumptions in the calculation process (e.g., the soil properties change randomly with space). As a result, the conclusions and models obtained may be contrary to the actual situation. To make matters worse, the current observation of local site characteristics mainly focuses on mountain terrain (Nechtschein et al., 1996; Cornou et al., 2003; Wang and Xie, 2010; Zerva and Stephenson,2011; Imtiaz et al., 2018), while the dense array that can record the spatial variation of ground motion on the flat soil layer is extremely scarce. Therefore, actual flat site data are urgently needed to explain the spatial variation of heterogeneous soil layers.

In 2021, we set up a dense array of eight observation points in Zigong City, Sichuan Province. The sediments in this area exhibit the geological characteristics of uneven thickness (Yang, 2008), making them quite suitable for observing the spatial variation of strong ground motion in heterogeneous soil sites. All seismic stations are distributed on a nearly flat soil site, and the distance between the stations varies within the range of 50–1,000 m. The test run of the array began in early September 2021, during which the MS 6.0 earthquake in Luxian County and the MS 5.1 earthquake in Wenxing County of Yibin City in April 2022 were successfully recorded. In this work, the spatial variation characteristics of strong ground motion are studied by combining the theoretical model and numerical analysis based on the acceleration records of the two earthquakes. First, the spatial variation of the root mean square (RMS) acceleration and Fourier spectrum are analyzed, and the site response was quantified and classified by the horizontal-to-vertical spectral ratio. Second, Thomson’s multitaper method is used to calculate the lagged coherency curves between different stations, and the influence of either the same or different soil layers on the spatial variation law of ground motion is analyzed. Third, the main factors affecting the spatial variation of ground motion are discussed, and the influence degree of local soil conditions on the spatial variation of ground motion at the engineering scale is qualitatively analyzed. Fourth and finally, a lagged coherency model that can characterize the spatial variation characteristics of strong ground motion in heterogeneous soil sites is established, and the empirical parameters in different frequency bands are obtained by the nonlinear fitting method. The conclusions and models in this paper are based on two earthquake events, which can be used for reference in similar studies in the future.

2 Spatial variation characteristics of seismic acceleration

2.1 Data source

Zigong City is located in the hilly area of the southern Sichuan Basin, characterized by vertical and horizontal valleys and a small relative elevation difference. The Quaternary overburden is scattered near the riverbed and flood plain of the Fuxi River. The geotechnical properties are artificial backfill, clay, and silty sand mixed with each other. The thickness of the soil cover layer is relatively small yet significantly different, at just over 10 m in local areas. This geological background provides the necessary conditions for observing the spatial characteristics of strong ground motion in heterogeneous soil sites. To study the spatial variation of ground motion within the scope of the engineering scale, a dense array of eight stations with separation distances of no more than 1,000 m was established. The array is composed of eight observation substations (Figure 1). These observation points are distributed in relatively flat bushes in the urban area, and the relative elevation difference is negligible. Specifically, stations S02–S05 are closely distributed, and the distance between adjacent stations is about 100 m, while the distances between S01, S06, S07, and S08 are slightly larger. The distances between the eight stations are shown in Table 1. A GL-PA4-integrated strong motion seismograph with high sensitivity is adopted for all observation points, and the sampling rate is 200 Hz. Continuous microtremor waveforms can be recorded while observing earthquake events. During its operation, the array recorded the MS 6.0 earthquake that occurred in Luxian County on 16 September 2021, and the MS 5.1 earthquake that occurred in Wenxing, Yibin, in April 2022. The basic information of these is shown in Table 2. These events provide necessary observation records for this study.

2.2 Spatial variation of root-mean-square acceleration

To accurately quantify the amplitude level of acceleration time history, the root mean square acceleration a_{rms} of each observation point is calculated according to the following formula:

$$x_{rms}^{2} = \frac{1}{T_d}\int_{T_1}^{T_2} x^2(t)dt, \quad (1)$$

where Td=T_1-T_2 represents the relative duration of ground motion. In this paper, the S-bands of the earthquake events in Luxian and Yibin are the main research objects; thus, T1 and T2 are the start and end times, respectively, of the S-waves in the observation records. Before starting the calculation, the following processes must be carried out for the two sets of observation records. 1) Subtract the average value of noise 10 s before the event from the original data to return the observed waveform to zero (Boore, 2001). 2) Perform bandpass filtering in the range of 0.05–50 Hz on the data using the fourth-order Butterworth filter to eliminate the influence of environmental factors and instrument self-noise on the acceleration time history. 3) Eliminate the first arrival time fluctuations caused by the wave passage effect using the waveform cross-correlation method, and

FIGURE 1
Location map of the dense array.

TABLE 1 Separation distance of station-to-station (unit: m).

Station	S01	S02	S03	S04	S05	S06	S07	S08
S01	0	285.95	343.85	430.95	382.27	575.52	817.46	916.04
S02	285.95	0	121.89	197.17	226.87	302.82	544.74	730.54
S03	343.85	121.89	0	88.4	110.91	338.61	565.42	813.63
S04	430.95	197.17	88.4	0	111.86	328.68	533.66	826.01
S05	382.27	226.87	110.91	111.86	0	432.58	677.48	919.84
S06	575.52	302.82	338.61	328.68	432.58	0	242.73	505.44
S07	817.46	544.74	565.42	533.66	677.48	242.73	0	432.58
S08	916.04	730.54	813.63	826.01	919.84	505.44	432.58	0

TABLE 2 Parameters of strong motion recordings.

ID	Occurrence time (UTC+8)	Latitude/°N	Longitude/°E	M_s	Station available	Mean R_{epi}/km
1	2021-09-16, 04:33:31	29.20	105.34	6.0	S01–S05, S08	57.4
2	2022-04-06, 07:50:05	28.22	105.03	5.1	All	125.9

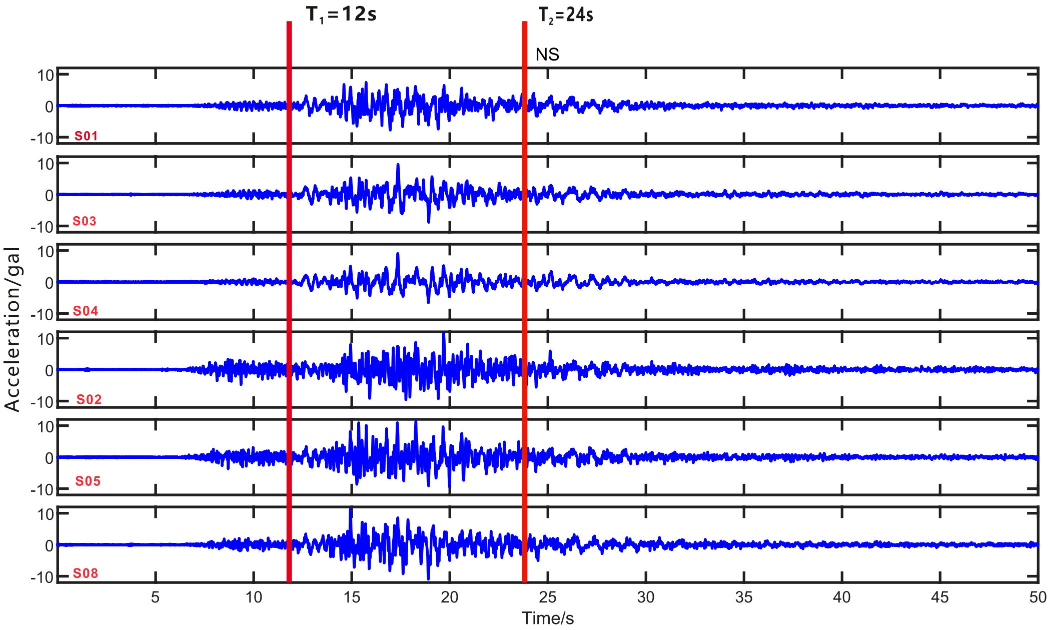

FIGURE 2
Schematic diagram of time window interception (NS component of the Luxian earthquake).

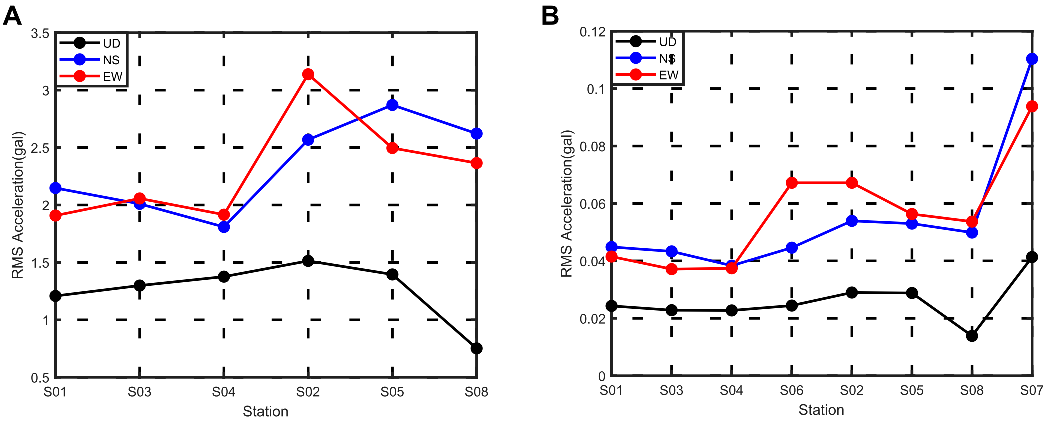

FIGURE 3
Spatial distribution of root-mean-square acceleration: **(A)** RMS acceleration of the Luxian earthquake; **(B)** RMS acceleration of the Yibin earthquake.

align the waveform (Boissières and Vanmarcke, 1995). The S-wave time window is intercepted as shown in Figure 2:

For the Luxian earthquake, the time windows of each component are set to the range of 12–24 s, which covers the whole period from the first arrival of shear waves to the maximum energy, thereby effectively avoiding the interference of a signal singular value on peak ground acceleration (PGA). The window selection principle of the Yibin earthquake records is the same as that of the Luxian earthquake, with a time truncation of 20–32 s, and the relative duration is 12 s. The slight difference in the S-wave delay caused by different source parameters does not affect the final calculation result. The calculation results of the RMS acceleration are shown in Figure 3.

Comparing the earthquake events, a_{rms} of all of the stations differs significantly, but the amplitude changes with space in the same law. For NS and EW components (red and blue broken

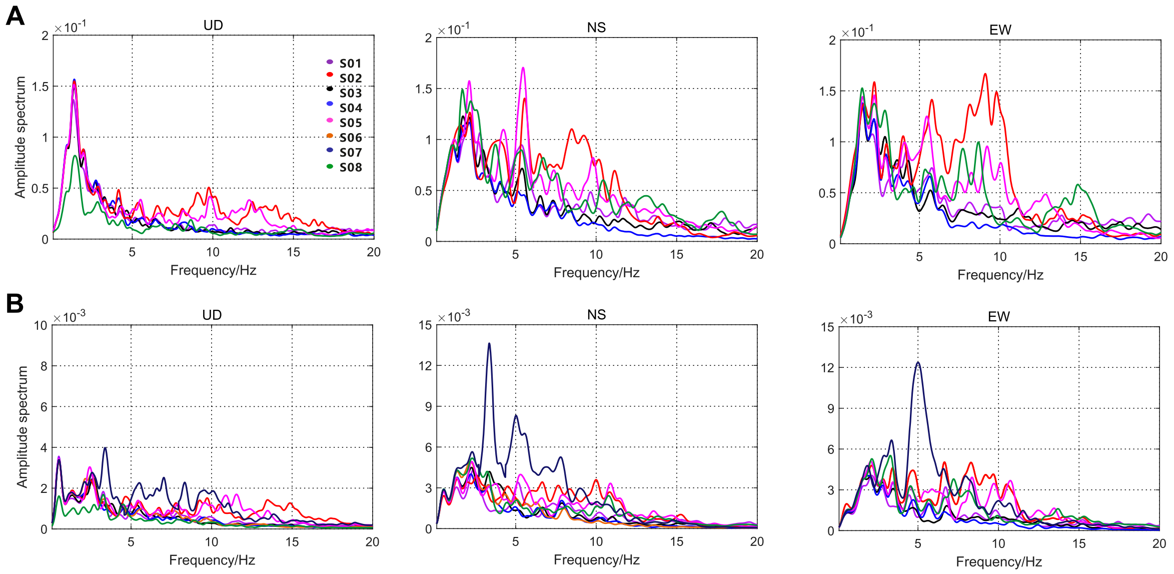

FIGURE 4
Acceleration amplitude spectra of different observation points: **(A)** amplitude spectra of the Luxian earthquake and **(B)** amplitude spectra of the Yibin earthquake.

lines), a_{rms} of S01, S06, S03, and S04 is at the same amplitude level, and that of S02, S05, and S08 is higher than that of the aforementioned four stations, but there is little difference among them. As shown in Figure 3B, a_{rms} of S07 is about 0.1 gal, much higher than that of other stations. For the vertical component (black broken line), the amplitude level of each substation is significantly lower than those of the two horizontal components. With the exception of S08, the a_{rms} variation trend of all observation points is similar to that of the horizontal components. However, the variation in amplitude is much smaller, indicating that the local soil conditions may be the main factor causing the change in the acceleration amplitude, and the horizontal component is far more greatly affected than the vertical component. The vertical a_{rms} of the two earthquake events at S08 is much smaller than that of the other stations, which is also a result of the changes in local site conditions.

2.3 Variation of the Fourier amplitude spectrum

The acceleration Fourier spectra are shown in Figure 4, which are divided into two groups, one for each earthquake event. The amplitude spectrum curve is smoothed using the Konno–Ohmachi algorithm (the smoothing coefficient is 50) so as to suppress random disturbances (Konno and Ohmachi, 1998). For the same observation station, affected by the magnitude and epicenter distance, the Fourier spectrum of the Luxian earthquake (Figure 4A) is several tens of times higher than that of the Yibin earthquake (Figure 4B), and its effective frequency signal band is 0.05–20 Hz, slightly wider than that of the Yibin earthquake. The following trends can also be seen in the figure.

1) In Figure 4A (the Luxian earthquake), the amplitude spectra of the three-component record at each station are in high consistency below 5 Hz (except S08), but spectra of S02 and S05 are amplified compared with those of S01, S03, and S04 when the frequency exceeds 5 Hz. This amplification is particularly obvious in the horizontal component. The amplitude spectrum of S08 in the vertical component is lower than that of the other stations below 5 Hz, but the low-frequency part is consistent with that of the other stations in the horizontal component, indicating that site conditions at this point are distinctive. The amplitude spectrum of this point is also amplified to different degrees in the two horizontal components, and the affected frequency band is wider than that of S02 and S05.
2) In Figure 4B (the Yibin earthquake), the spatial variation characteristics of the spectra in common stations resemble the observation results of the Luxian earthquake. The frequency-domain amplification of S07 is most obvious, starting at 2.5 Hz, and the corresponding root mean square acceleration shown in Figure 3B is also the greatest.

The observation results show that the energy of the two groups of the acceleration time histories is limited, but its characteristics of spatial variation are obvious. In addition, the amplitude–frequency difference of the horizontal component is much larger than that of the vertical component, which is mainly reflected in the frequency domain above 2.5 Hz. The heterogeneity of the site soil layer is the fundamental cause of the aforementioned changes, and this will be studied and discussed in the following section.

3 Estimation of station site conditions

The array is located in the southern limb of the Ziliujing Anticline, where the site is relatively flat and free of large faults; therefore, the geological structure is simple. The exposed soil of the site mainly includes the Quaternary Holocene backfill (backfill time is 7–20 years) and residual slope clay, and the estimated shear wave velocity is close to 200 m/s. The influence of this soil layer on ground motion is mainly manifested as an amplification effect therefore, the horizontal-to-vertical spectrum ratio (H/V) can be calculated to distinguish site types in the absence of borehole data. In this section, this method is adopted to simultaneously analyze the microtremor and acceleration records and then evaluate the heterogeneity of the soil layer from the perspectives of predominant frequency and amplification.

3.1 Estimation based on microtremor records

The three-component microtremor data are selected from the continuous waveform recorded using the instrument at night (after 22:00). Next, the anti-STA/LTA algorithm is used to eliminate short-time interference, and a period of 30 min is intercepted to calculate the spectrum ratio according to Eq. 2:

$$(H/V) = \sqrt{F_N(f)F_E(f)}/F_U(f), \tag{2}$$

where $F_N(f)$, $F_E(f)$, and $F_U(f)$ represent the noise Fourier spectrum of the NS, EW, and vertical components, respectively. The smoothing method used in the spectrum calculation is consistent with that in Section 2.3 of this paper. The H/V spectrum ratio assumes that the vertical component of the microtremor is not affected by the terrain and local soil conditions. Although the calculated result is slightly smaller than the actual response amplitude, it is simple and efficient. In addition, the error is within a controllable range. Therefore, this result is an important index for site classification (Nakamura and Saito, 1983; Zhao et al., 2006; Rosalba et al., 2018). Figure 5 shows the H/V calculation results of the microtremor; the predominant frequency (f0) of S01, S03, S04, and S06 is higher than 20 Hz, and that of station S06 even reaches 47.5 Hz. According to the latest site classification criteria in China given by Shi et al. (2022) (I: T≤0.08 s; II: 0.08 s<T≤0.55 s; III: 0.55 s<T≤0.95 s; IV: T>0.95 s;; IV: T > 0.95 s), these stations belong to class I. The f_0 of S02 and S05 is around 9 Hz, slightly lower than that of S08, while S07 has the lowest predominant frequency, which is about 4.7 Hz; the site conditions of all of these stations can be classified into class II. Compared with Figure 3, there is a corresponding relationship between predominant frequency (f_0) and root-mean-square acceleration (a_{rms}). In general, the lower the f_0, the larger the a_{rms}. However, when f_0>20 Hz, the acceleration amplitude no longer changes significantly because the properties of these sites are similar to bedrock and the amplification effect is weak.

Many studies have shown that the predominant frequency of the H/V spectral ratio is nearly close to the resonant frequency of the sedimentary layer, which has a negative exponential relation with the depth of the soil–rock interface. Therefore, the higher the predominant frequency, the smaller the thickness (Ibs-von Seht and Wohlenberg, 1999; Parolai et al., 2002; Dinesh et al., 2010; Rong et al., 2016; Joshi et al., 2018; Peng et al., 2020; Shi and Chen, 2020). In view of this, we can infer that the difference in the overburden thickness is an important factor causing the spatial variation of acceleration amplitude. However, the aforementioned inference cannot explain the low-frequency attenuation of vertical records of S08, which needs to be further analyzed in combination with strong motion acceleration records.

3.2 Estimation based on the acceleration response spectrum ratio

In this section, the horizontal–vertical acceleration response spectrum ratios are used to quantify the amplification effect of the soil layers. The damping ratio of this study is $\xi = 0.05$, and the geometric average of the response spectrum ratios of the two horizontal components is calculated according to Eq. 1, the results of which are shown in Figure 6. All spectrum ratio curves increase abruptly from above 1 Hz, and the amplification exceeds twice the original value before 2 Hz, indicating that the soil layer has a wide range of frequency bands affecting strong ground motion. Compared with Figure 5, the H/V curves calculated by the acceleration response spectrum and microtremor differ significantly. Since the energy of the microtremor is weak, the calculated H/V curves are vulnerable to the external environment therefore, the amplification coefficient has no reference value. In addition, some H/V curves of the acceleration response spectrum cannot distinguish predominant frequencies clearly due to the lack of sample data. However, the soil conditions can be distinguished by the shape and coincidence of the response spectrum H/V curves (Wen, 2011).

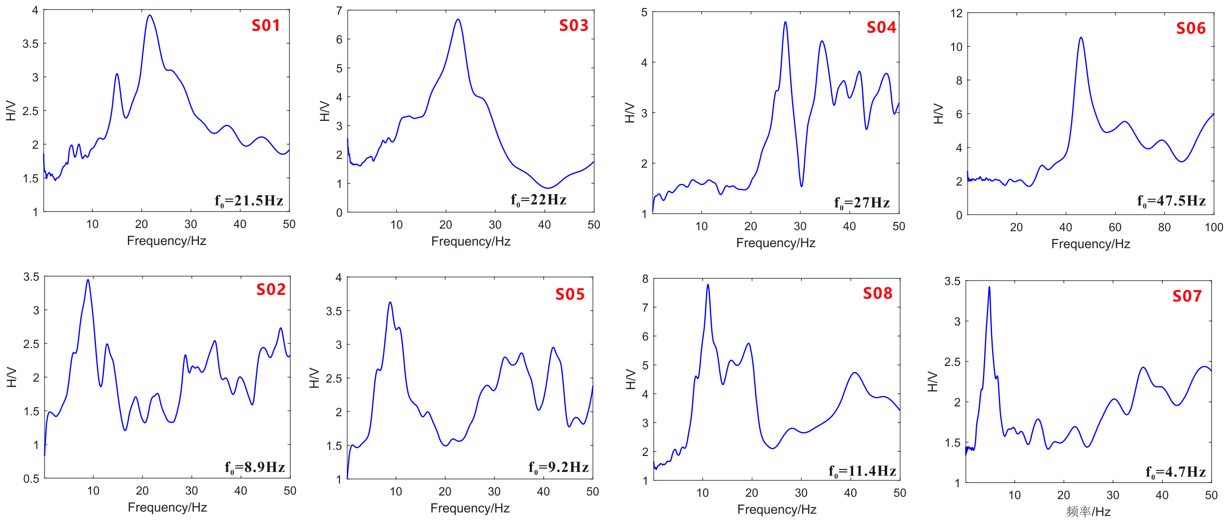

FIGURE 5
Microtremor H/V ratios of each soil station.

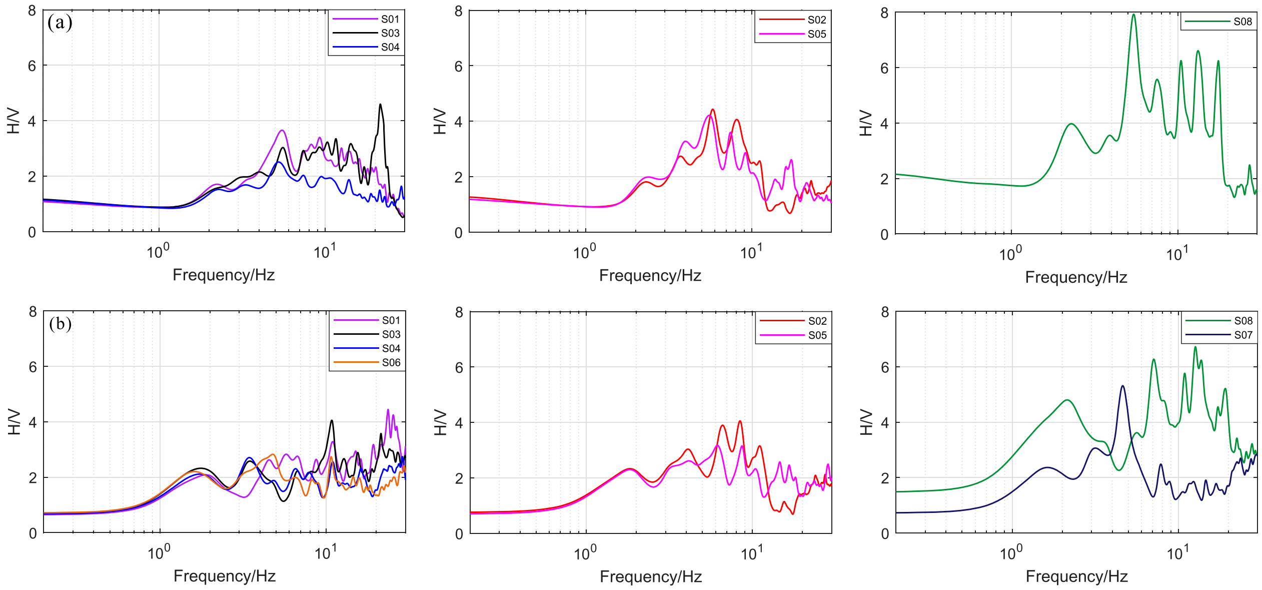

FIGURE 6
Response spectral H/V ratio of each soil station: **(A)** H/V ratios of the Luxian earthquake and **(B)** H/V ratios of the Yibin earthquake.

By comparing S01–S07, the spectrum ratio curves of stations with similar site conditions are also shown to be consistent, such as S01 and S03, and S02 and S05. Additionally, the amplification of the S04 and S06 curves is lower than that of the other soil layer stations, while there is little difference in S01 and S03. The flatness of the response spectrum H/V curves of the seven stations corresponds to the predominant frequency. The higher the predominant frequency, the smaller will be the thickness of the overburden, and the flatter the spectrum ratio curve. The spectral ratio curve of S08 is the most distinctive. For S08, although the estimated soil layer thickness is between S01 and S05, the H/V curve is the steepest, with the highest amplification of 8. It indicates that thickness is not the only factor affecting the amplitude–frequency characteristics of acceleration. Combined with the multipeak characteristics of the curve at this station, it is indicated that S08 has a soft interlayer and tends to be a class III site (Ji, 2014). Considering that there is more noise interference in the case of too little ground motion energy, the amplification effect of the Yibin earthquake is not as obvious as that of the Luxian earthquake. However, after comparing the curve characteristics of the stations, the classification results of the site conditions are consistent (Figure 6B). In addition, the amplification (combined with Figures 4, 5), predominant frequency, and H/V curve characteristics of S07 differ significantly from those of S02 and S05. Although the three stations belong to class II soil layers, in the follow-up study, it is still considered as independent soil conditions.

By analyzing the characteristics of the H/V spectrum ratio, it is inferred that the discrepancy in the overburden thickness leads to the spatial variation in the acceleration amplitude and spectrum. The presence of the soft interlayer increases the complexity and uncertainty of the site effect at S08. It also amplifies the horizontal acceleration and attenuates the vertical acceleration. In conclusion, the properties of the soil contained in the array can be divided into four types, but the specific situation must be determined by subsequent drilling exploration or by referring to strict site classification methods (Wen et al., 2011). This paper mainly aims to study the impact of these differences in soil properties on the spatial variation of ground motion.

4 Spatial variation analysis based on the coherency function

The amplification effect of the classification and thickness of the soil layer on the bedrock incident wave will alter the amplitude and spectrum of the ground motion. With the gradual improvement of the theory, our researchers found that the heterogeneity of the site would also change the shape of the lagged coherency curve, and this mechanism was more complex than we had imagined. In view of this, the lagged coherency of different pairs of the stations is calculated based on the existing observation data, and the variation law of strong motion spatial coherency in heterogeneous soil sites is analyzed from a practical perspective.

4.1 Coherency function

Assuming that the ground motion is an ergodic stationary random process and the acceleration time histories of points k and l at a distance of d are $x_k(n)$ and $x_l(n)$, respectively, the cross-power spectral density function between them is as follows:

$$S_{kl}(f,d) = \sum_{n=0}^{N-1} R_{kl}(n,d)\exp(-i2\pi nf), \tag{3}$$

where N is the time length of the intercepted shear wave, and $R_{kl}(n,d)$ is the cross-correlation function of k and l, which is expressed as follows:

$$R_{kl}(n,d) = \sum_{m=0}^{N-1} x_k(m)x_l(m+n). \tag{4}$$

After further derivation,

$$\begin{aligned} S_{kl}(f,d) &= \sum_{n=0}^{N-1}\sum_{m=0}^{N-1} x_k(m)x_l(m+n)\exp(-i2\pi nf) \\ &= F_k(f)F_l^*(f), \end{aligned} \tag{5}$$

where $F_k(f)$ and $F_l(f)$ are the Fourier spectra of $x_k(n)$ and $x_l(n)$, respectively, and the asterisk "*" represents conjugation. Similarly, the following can be obtained:

$$\begin{cases} S_{kk}(f,d) = F_k(f)F_k^*(f) \\ S_{ll}(f,d) = F_l(f)F_l^*(f) \end{cases}. \tag{6}$$

Next, combining Formulas (5), (6) and (7), the cross-power spectral density is normalized to obtain the coherency function expression:

$$\gamma_{kl}(f,d) = \frac{S_{kl}(f,d)}{\sqrt{S_{kk}(f)S_{ll}(f)}} = |\gamma_{kl}(f,d)|\exp[i\theta(f,d)]. \tag{7}$$

The absolute value of the coherency function is between 0 and 1, representing the correlation of different frequency components of multipoint ground motions. In engineering practice, this is called lagged coherency and is regarded as an important index to measure the spatial variation of strong ground motions. The imaginary part $\exp[i\theta(f,d)]$ is used to express the wave passage effect, that is, the arrival time difference of each point.

The spectrum obtained by the traditional Fourier transform will contain much spike interference, causing the lagged coherency to remain constant at 1 throughout the frequency band. In this regard, the power spectral density is smoothed by referring to the multiorder Slepian window proposed by Thomeson (1982), and the result is obtained by weighted summation. The specific implementation steps are shown in Supplementary Appendix S1. Compared with the single-window smoothing power spectrum estimation method, the multiwindow spectrum analysis has a small deviation and variance, and the result is closer to the real spectrum.

4.2 Variation of lagged coherency with frequency

The lagged coherency curved surface between different pairs of stations is estimated based on the multiwindow spectrum

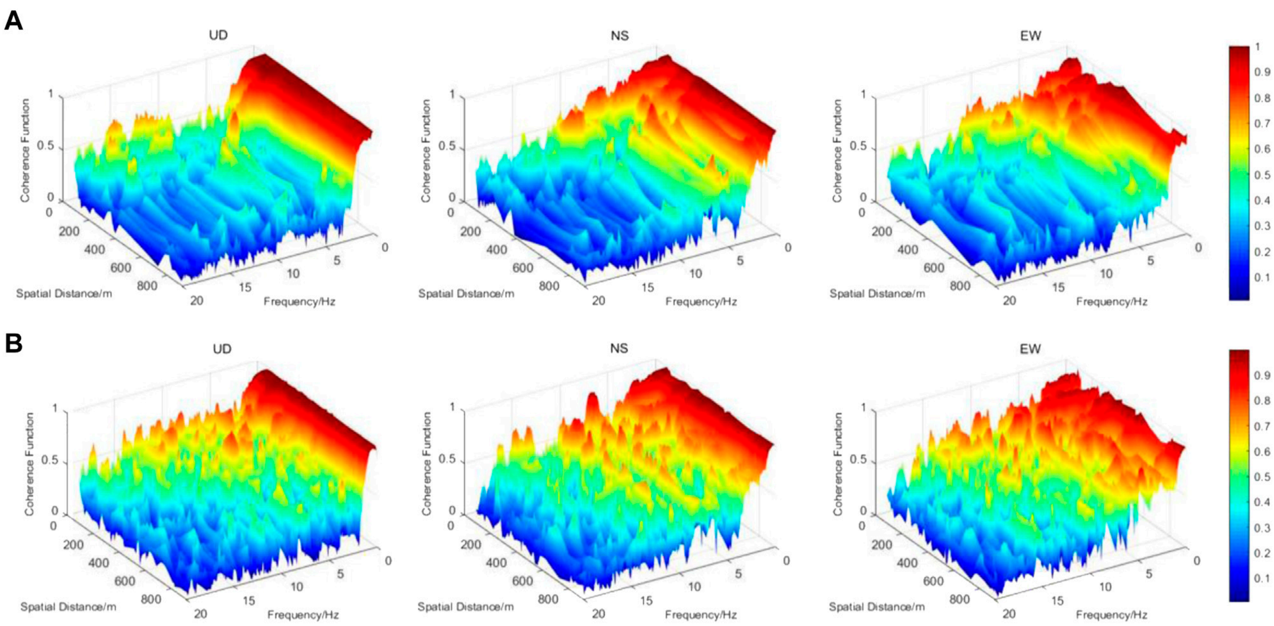

FIGURE 7
Lagged coherency 3D stereogram: **(A)** stereogram of the Luxian earthquake and **(B)** stereogram of the Yibin earthquake.

theory, as shown in Figure 7. The variation amplitude of the coherency function with frequency is greater than that with spatial distance, and there are several rules. First, with the increase of frequency, the values of the lagged coherency first rapidly decay and then fluctuate slightly, exhibiting multipeak characteristics in the middle- and high-frequency band (5–20 Hz). The variation laws of different vibration directions also differ. The vertical component decays faster with frequency, and the peak jitter of the high-frequency part is not as obvious as that of the horizontal component. Meanwhile, the coherency of the EW and NS components has a trend similar to that of the frequency. As shown by the comparison result of the two groups of calculations, overall, the lagged coherency of the Yibin earthquake is higher than that of the Luxian earthquake. Since there are many station pairs, the stereogram is clearer.

The comparison of the lagged coherency curves of station pairs is shown in Figure 8, arranged from small to large spatial distance. It is observed that the coherency function curve of the vertical component first decays with the frequency, shows the first “valley” at 3–7 Hz, and then increases slightly and decays in an oscillatory manner. This “valley” is called a “coherency hole” in the work of Zerva, and the corresponding frequency is the average of the predominant frequency (f0) of the whole heterogeneous soil site (Zerva and Harada, 1997). However, this concept does not apply here because f0 of most sites exceeds 8 Hz and falls within this range only in S07. Therefore, the theoretical model has certain limitations, and this paper instead refers to it as the “frequency inflection point.” Compared with the vertical component, the “inflection points” in the two horizontal directions are slightly blurred, and the oscillation amplitude of the curve at a high frequency is greater.

The local soil conditions are obviously correlated with the lagged coherency between stations. First, the records of the Luxian earthquake are analyzed (Figure 8A). The separation distance between S03 and S04 is about 88.4 m, and the three components show the highest correlation as a whole, while the lagged coherency of their horizontal components remains around 0.8 even in the middle frequency band (5–12 Hz). The predominant frequency and flatness of the corresponding H/V curves of the two stations are also similar (Figures 5, 6). The site effects of the station pair S02–S05 are basically the same, and the coherency of the whole frequency band is significantly higher than that of S02–S01. Similarly, the coherency of S03–S01 is also greater than that of S02–S01 with slightly smaller station spacing, indicating that the difference in soil conditions will cause coherency loss. However, this is not the only factor affecting the coherency function, since the station-to-station distance also plays a role.

Compared with S03–S05, the horizontal component of S02–S05 does not exhibit obvious site advantages. The reason for this is that the latter has a larger distance than the former, with a difference of more than 100 m. Although the response spectrum H/V curves of S03 and S01 are in the highest agreement (Figure 6), the separation distance d exceeds 300 m, and the coherency function is generally (f>5) lower than those of

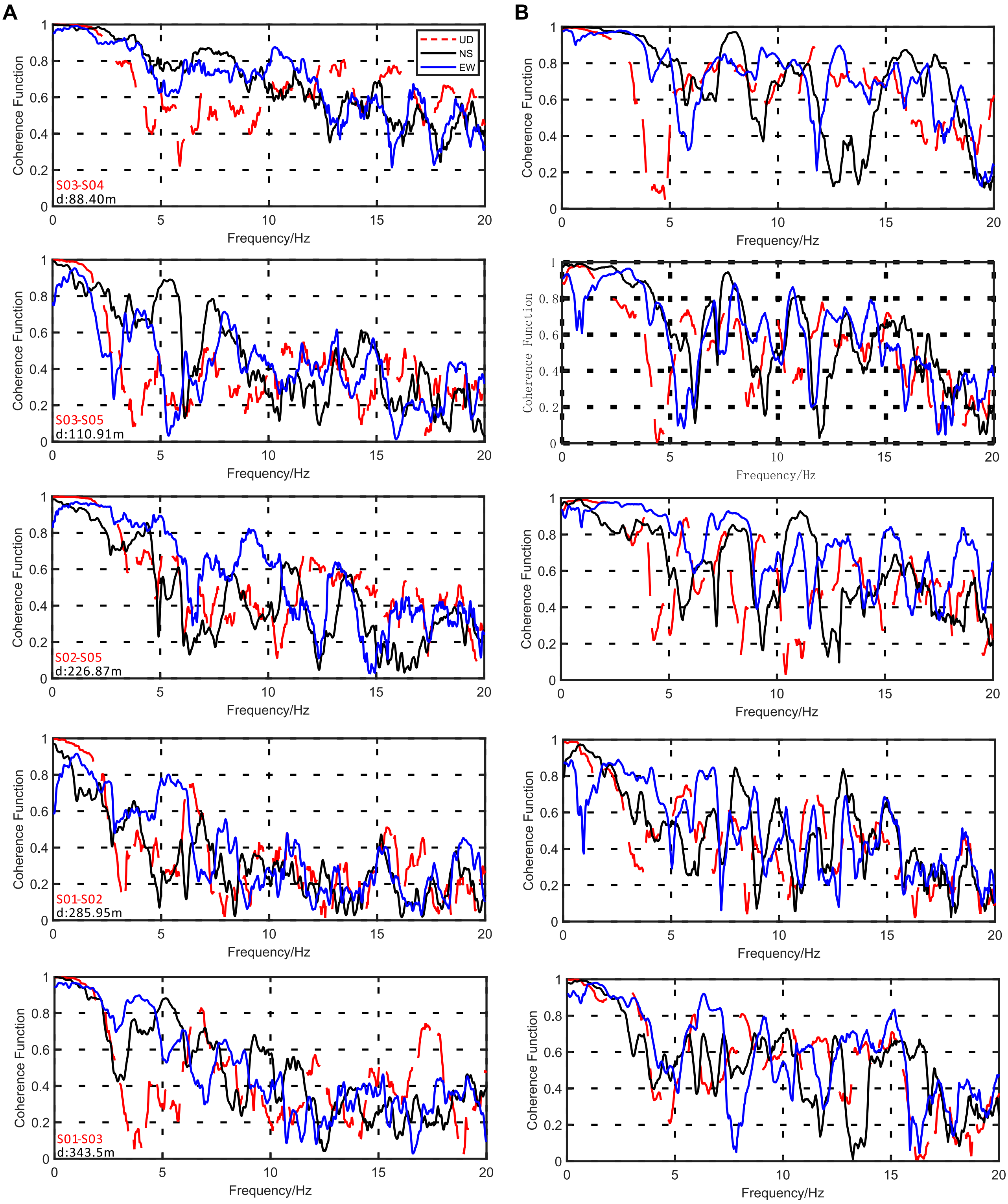

FIGURE 8
Variation in lagged coherency as functions of frequency: **(A)** coherency curves of the Luxian earthquake and **(B)** coherency curves of the Yibin earthquake.

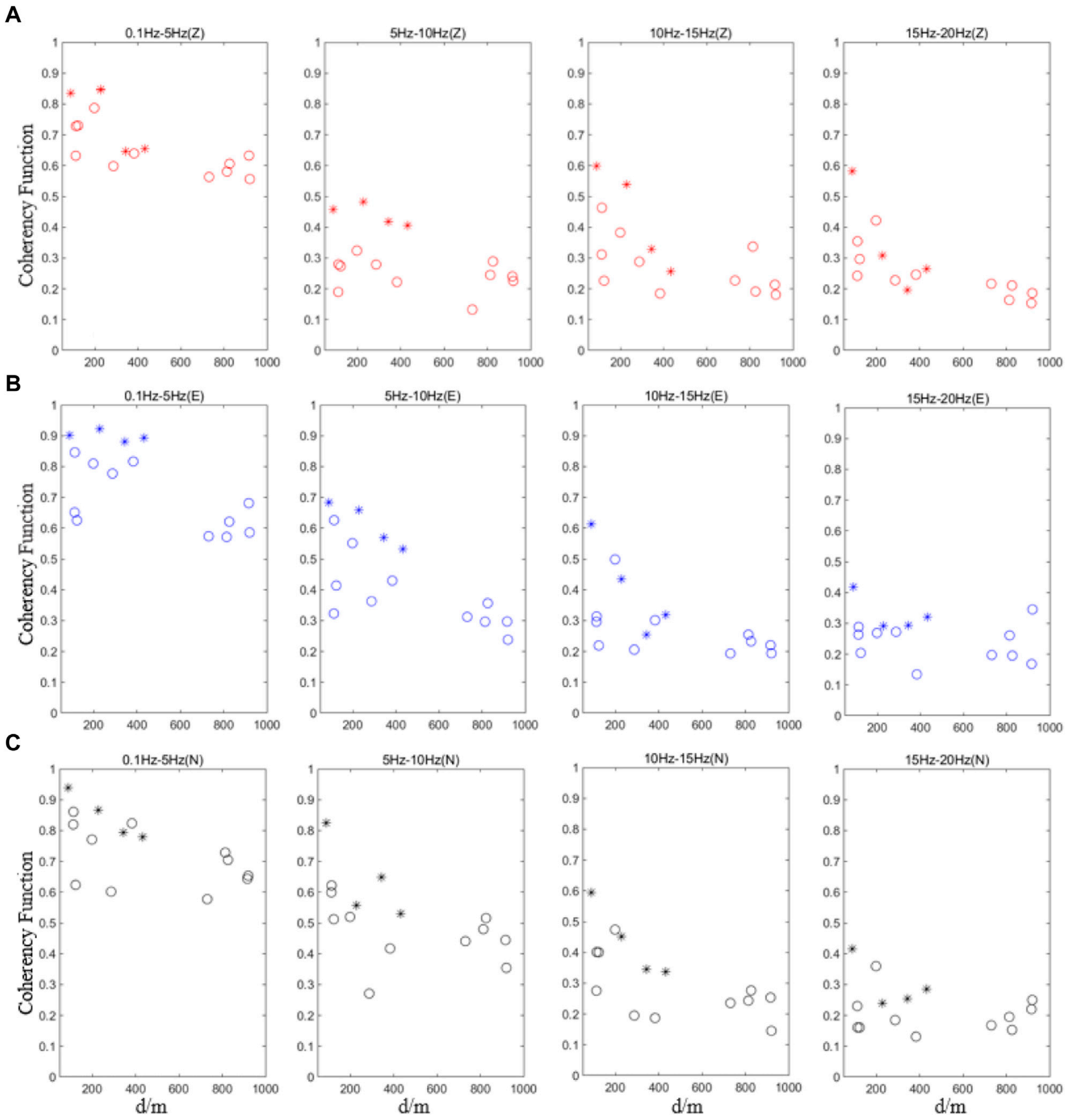

FIGURE 9
Variation in lagged coherency as functions of distance (the Luxian earthquake). The asterisk (*) represents the station pairs of the same site type, and the circle (O) represents the station pairs between other different site types. **(A)** UD component, **(B)** EW component, and **(C)** NS component.

S03–S04 and S03–S05. The analysis results show that the station spacing d and site conditions jointly affect the coherency of soil ground motions. However, when d does not differ much, the site conditions have a greater impact on the coherency function, and this influence mechanism is also quite obvious in the calculation results of the vertical direction.

After observing the corresponding calculation results of the Yibin earthquake (Figure 8B), almost the same conclusion can be drawn, even though the coherency loss in the horizontal direction caused by heterogeneous site conditions is not as obvious as that of the Luxian earthquake.

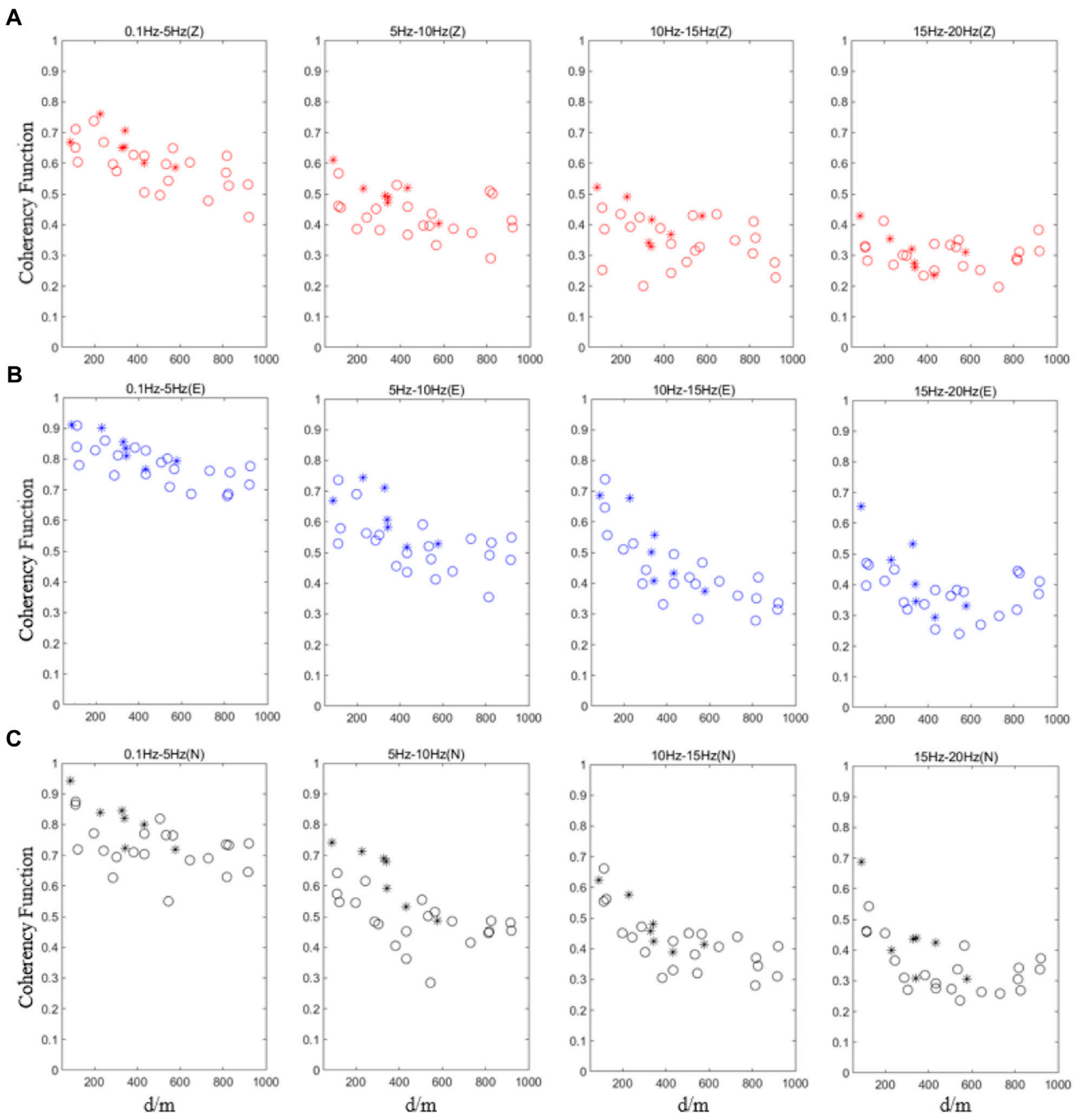

FIGURE 10
Variation in lagged coherency as functions of distance (the Yibin earthquake). The asterisk (*) represents the station pairs of the same site type, and the circle () represents the station pairs between other different site types. **(A)** UD component, **(B)** EW component, and **(C)** NS component.

4.3 Variation in lagged coherency with spatial distance

To avoid the subjectivity of artificially selecting coherency samples, all lagged coherency curves are summed and averaged according to the four frequency bands of 0.1–5, 5–10, 10–15, and 15–20 Hz (representing low, medium, medium-high, and high frequency, respectively). Then, the scatter plots of the coherency function change with station spacing d at different scales are drawn. According to the discussion results in Section 3, the asterisk "*" represents the station pairs of the same site type (including the station pairs between S01, S03, S04 and S06, and

S02-S05), and the circle "○" represents the station pairs between other different site types. Figures 9, 10 show the two sets of scatter points. All of the scatter points of the lagged coherency attenuate with the increase in the separation distance d and decrease with the increase of the frequency. Specifically, the values of the vertical component decrease faster with the frequency, and the attenuation trend of the mid-high-frequency band (5–20 Hz) with the distance is blurred compared with the horizontal component. Comparing different types of scatter distribution, the two earthquake events show similar characteristics. In other words, the scatter-lagged coherency distribution of the station pair with the same soil conditions is more concentrated, and the value is higher. Due to the uncertainty of the spatial variation of ground motion, it is also observed that the coherency coefficient of some "○" scatter points is larger than that of "*" scatter points with equal (or even smaller) station spacing, but the high coherency brought by site consistency is a common phenomenon.

In summary, the heterogeneity of the soil layer will also bear an impact on the lagged coherency. In the case of little difference in the separation distance, the station pairs with similar soil conditions tend to have higher coherency. Different soil conditions will not only reduce the coherency between two points but also make the distribution of coherency more discrete in the spatial domain. Thus, the influence mechanism will not change the general attenuation of coherency with frequency and distance because the influence of the propagation path (incoherency effect) must not be ignored (Abrahamson et al., 1991; Zerva, 2009).

5 Coherency function model characterizing the influence of the heterogeneous soil layer

5.1 Frequency-dependent coherence function model

Mathematical modeling is a key step in applying theoretical research to engineering practice. Researchers have established a variety of lagged coherency models according to seismological methods and observation results and then regressed corresponding parameters through observation data to further guide multipoint ground motion input. The coherency loss caused by site heterogeneity has been confirmed in the previous section of this paper, but this change mechanism cannot be directly explained by the transfer function of a soil seismic response, since lagged coherency is the standardization of cross-power spectrum amplitude, and the transfer function will be canceled out in the calculation process. Some scholars have derived the expression of the coherency function in the heterogeneous soil site through the response spectrum theory. However, it is also a macro-model given under the assumption that the soil characteristics are randomly distributed and thus cannot explain the observation results in this study. The results of this study agree with Kiureghian's view that the coherency loss caused by the heterogeneity of the soil layer is also attributed to the incoherency effect, ignoring the influence of the medium attenuation and finite source (Somerville et al., 1988). The lagged coherency function can be expressed in the following form:

$$\left|\gamma(f,d)\right| = C_{\text{site}}(f,d)\cdot C_{\text{icoh}}(f,d), \tag{8}$$

where $C_{\text{icoh}}(f,d)$ represents the incoherency effect of seismic waves when they propagate from the source to the underground bedrock. In this paper, referring to the frequency band coherency function model given by Yu et al. (2020), $C_{\text{icoh}}(f,d)$ is written as a rational fraction:

$$C_{\text{icoh}}(f,d) = \frac{1}{1+\alpha(f_{cc})\mathrm{d}^{q(f_{cc})}f^4}\exp(-\beta(f_{cc})d), \tag{9}$$

where $\alpha(f_{cc})$、$\beta(f_{cc})$、$q(f_{cc})$ are empirical parameters related to the coherency cut-off frequency f_{cc}, which can be obtained by nonlinear fitting. This model is of clear physical meaning, with which the resolution of the coherency function in the response spectrum analysis under multipoint excitation can be obtained, and good results in fitting multiple events are achieved.

In Yu's study, the cut-off frequency f_{cc} is represented as the starting point where the rate of coherency attenuation based on the interstation distances is obviously different. This point can divide lagged coherency into two frequency ranges, and satisfactory fitting results can be obtained if different model parameters are used for different frequency ranges. Although the cut-off frequency has a theoretical basis, it is difficult to observe accurately in practical applications. To further improve the accuracy of multivariate fitting, a more flexible way is adopted to determine the frequency range of piecewise fitting, and the model parameters are expressed in a more general form: $\alpha(f)$、$\beta(f)$、$q(f)$.

$C_{\text{site}}(f,d)$ represents the coherency loss caused by additional scattering and refraction when the bedrock incident wave vertically passes through (O' Rourke et al., 1980) the heterogeneous cover. This influence mechanism is quite complex and difficult to deduce using the random process theory, but it can be expressed by empirical exponential function. From the perspective of engineering application and considering the accuracy and practicability of the model, the site impact is expressed in the following form:

$$C_{\text{site}}(f,d) = \exp\left[-\xi\left(c(f)+e(f)f^2\right)d^{r(f)}\right], \tag{10}$$

where parameters $c(f)$, $e(f)$, and $r(f)$ control the overall value of the lagged coherency and the rate of decline with frequency and distance, and ξ is the site impact factor, which reflects the difference in soil conditions between two points in space. When $\xi = 0$, the two points in space are in almost the same site

TABLE 3 Empirical lagged coherency model for comparison (according to the research content in this section, the model expression had been slightly modified).

Proposer	Model for comparison	Parameters to be fitted
Loh and Lin	$\lvert\gamma(f,d)\rvert = \exp[-(a(f)+b(f)f^2)d]$	$a(f)b(f)$
Harichandran and Vanmarcke	$\lvert\gamma(f,d)\rvert = A(f)\times exp\left[-\frac{2Bd}{a(f)\times\theta}\right]+(1-A(f))\times\exp\left[-\frac{2Bd}{a(f)\times\theta(f)}\right]$ $\theta = k(f)\left[1+\left(\frac{f}{\delta_0(f)}\right)^b\right]^{-1/2};B=(1+A(f)-a(f)A(f))$	$A(f),a(f),k(f),\delta_0(f),b(f)$

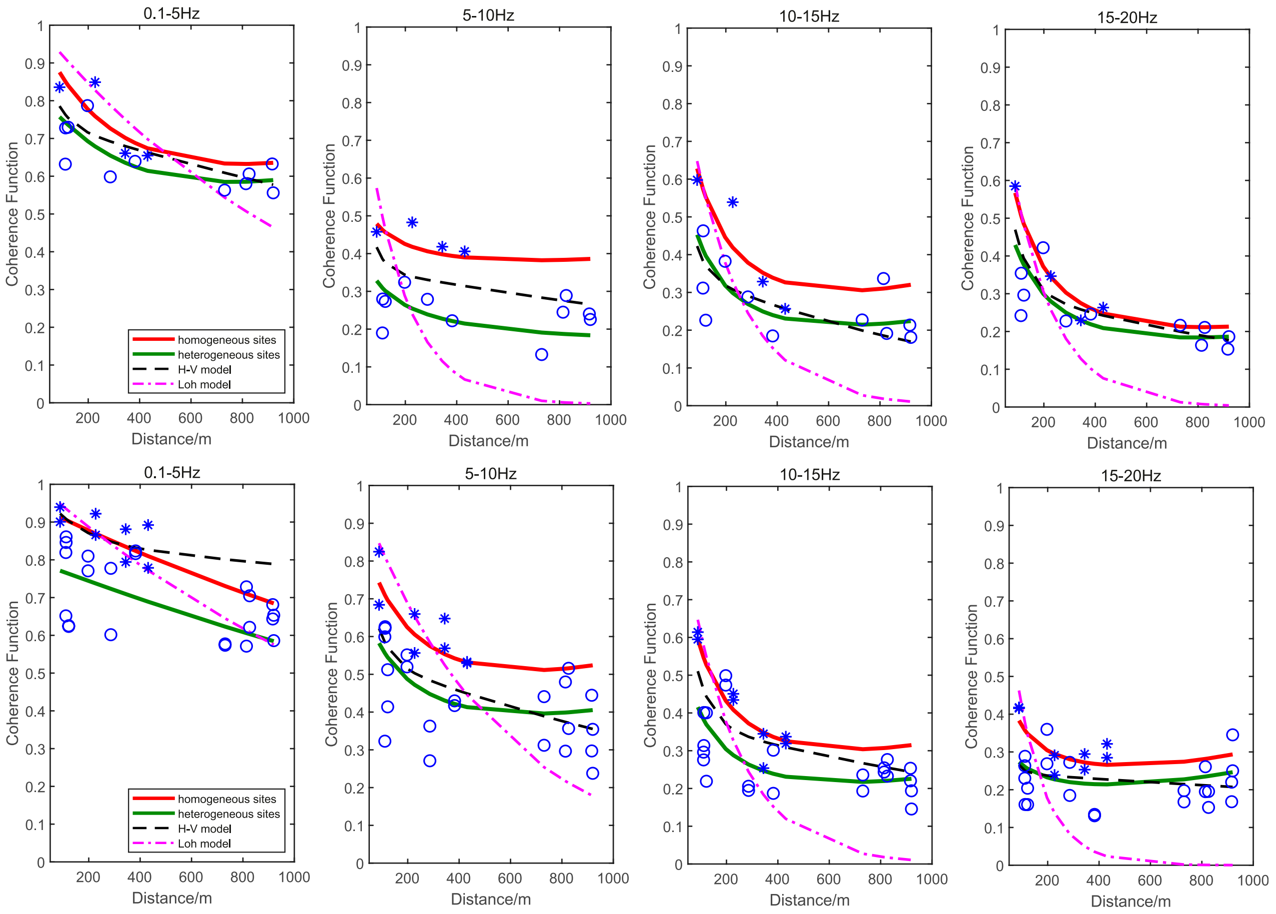

FIGURE 11
Fitting results for the Luxian earthquake: **(A)** vertical direction and **(B)** horizontal direction.

conditions, and the soil has no effect on the coherency function. However, when two points in space are located in different soil layers, then $\xi = 1$, and heterogeneous soil will cause a loss of the coherency function. Due to the limited number of samples, the station pairs in different site conditions are not subdivided in this paper. Substituting Eqs 9, 10 into Equation 8, a new lagged coherency expression is then obtained as follows:

$$\lvert\gamma(f,d,\xi)\rvert = \frac{1}{1+\alpha(f)\mathrm{d}^{q(f)}f^4}\exp(-\beta(f)d) \cdot \exp\left[-\xi\left(c(f)+e(f)f^2\right)d^{r(f)}\right]. \quad (11)$$

The model is controlled by three variables, that is, frequency (f), separation distance (d), and site impact factor (ξ), and can be applied to many flat soil sites in theory.

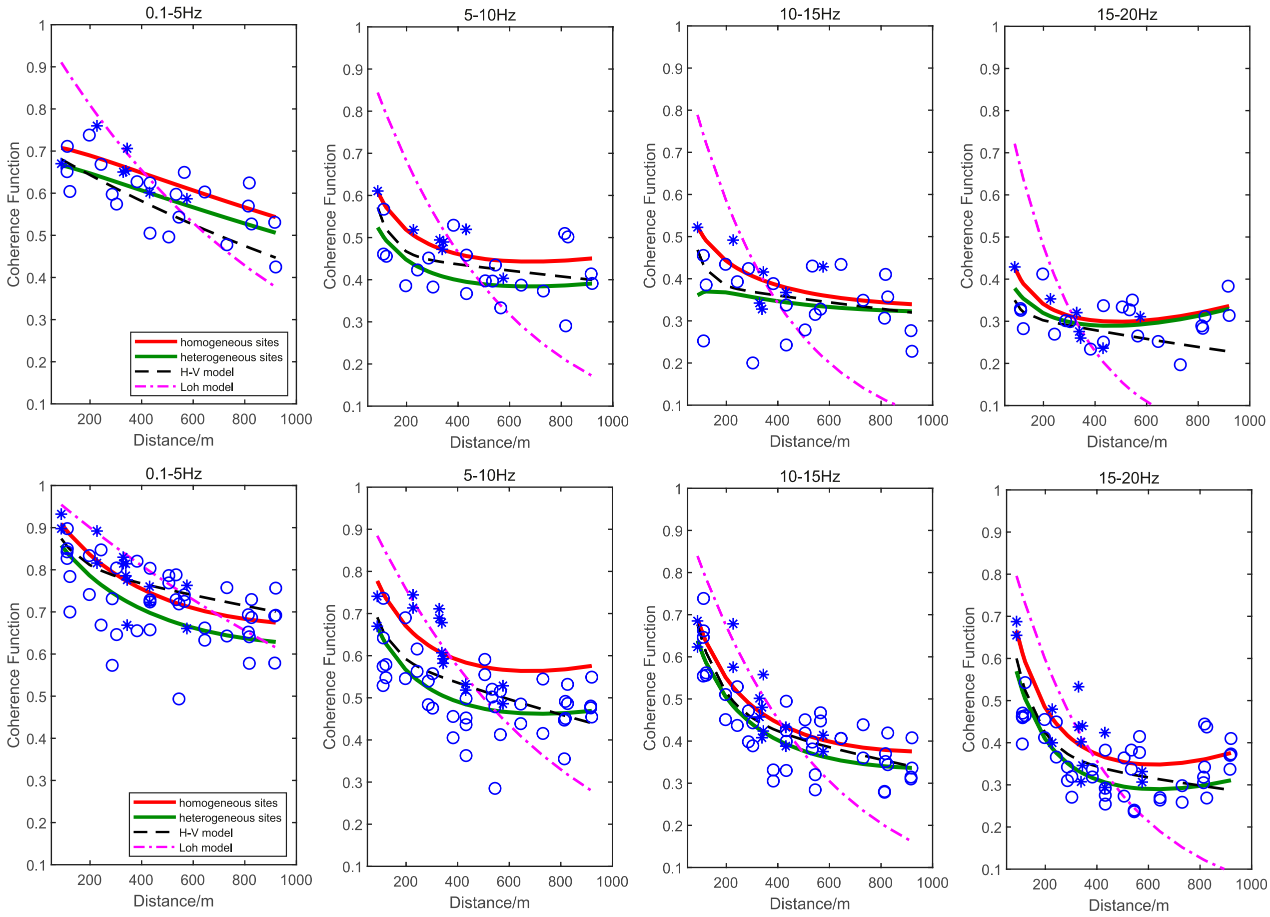

FIGURE 12
Fitting results for the Yibin earthquake: **(A)** vertical direction and **(B)** horizontal direction.

TABLE 4 RMSE of different models' fitting results for the Luxian Earthquake.

Comp	Frequency (Hz)	Loh	H-V	Proposed model
Hor	0.1–5 Hz	0.123	0.143	0.078
	5–10 Hz	0.200	0.11	0.079
	10–15 Hz	0.187	0.097	0.071
	15–20 Hz	0.186	0.07	0.058
	Mean	0.174	0.105	0.072
Ver	0.1–5 Hz	0.132	0.065	0.052
	5–10 Hz	0.223	0.096	0.058
	10–15 Hz	0.186	0.102	0.076
	15–20 Hz	0.160	0.071	0.059
	Mean	0.175	0.084	0.061

TABLE 5 RMSE of different models' fitting results for the Yibin Earthquake.

Comp	Freq. (Hz)	Loh	H-V	Proposed model
Hor	0.1–5 Hz	0.102	0.077	0.072
	5–10 Hz	0.147	0.082	0.068
	10–15 Hz	0.133	0.074	0.059
	15–20 Hz	0.169	0.081	0.061
	Mean	0.138	0.079	0.065
Ver	0.1–5 Hz	0.163	0.069	0.053
	5–10 Hz	0.175	0.057	0.055
	10–15 Hz	0.162	0.073	0.069
	15–20 Hz	0.193	0.058	0.045
	Mean	0.173	0.064	0.056

5.2 Model parameter fitting and test

In order to verify the reliability of the proposed model, Eq. 11 is used to perform nonlinear fitting on the two sets of observation records. The Loh model (Loh and Lin, 1990) and Harichandran–Vanmarcke model (1986, " H-V "for short), which are widely used in earthquake engineering today, are selected as references for fitting results in different frequency bands; corresponding empirical formulas are shown in Table 3. Considering that the coherency functions of the NS and EW components are close, the samples of the two are pooled. In the calculation, the frequency increment is df=0.1 Hz, and the lagged coherency curve shown in Figure 9 is fitted according to four frequency bands of 0.1–5, 5–10, 10–15, and 15–20 Hz to ensure the accuracy of results.

Figures 11, 12 show the comparison of the arithmetic mean value between fitting curves and the mean coherency observed from two events. The solid lines in red and green represent the coherency coefficients of this proposed model when $\xi = 0$ (same soil conditions, compared with blue "*" points in Figures 11, 12) and $\xi = 1$ (different soil conditions, compared with blue 'o' points in Figures 11, 12), respectively. The pink dot-and-dash lines and black dotted lines represent the fitting results of the Loh model and H-V model, respectively, both of which correspond to all scattered points due to the inability to distinguish between site types. We can obtain the following insights from the figure: 1) due to the simple form and few parameters, the Loh model presents a poor fitting in the middle- and high-frequency band (>5 Hz) and 2) the H-V model can well simulate the overall trend of coherency scatter attenuation with frequency and distance. However, like the Loh model, it is established under the assumption of homogeneous site conditions and cannot distinguish the different types of coherency points, and 3) the proposed model established in this paper takes into account the contribution of site heterogeneity on the spatial variation of ground motion, and the fitting results can effectively distinguish the attenuation patterns of different scatter points. Even for the Yibin earthquake (Figure 12), where the influence of heterogeneous soil is less obvious, the accuracy is higher than that of the H-V model with only one fitting curve. The fitted parameters of all models for different frequency bands are shown in Supplementary Appendix S2.

Residual analysis was carried out on the fitting results, and the root mean square error (RMSE) was selected as the accuracy evaluation criteria:

$$RMSE = \sqrt{1/N\sum_{i=1}^{N}\left(\gamma_i - \hat{\gamma}_i\right)^2}, \tag{12}$$

where γ_i is the coherency function estimated from observation records, $\hat{\gamma}_i$ is the corresponding fitting result, and N is the total number of lagged coherency samples in each frequency range. The smaller the RMSE is, the smaller the error between the simulation results and the original records, and the higher the fitting precision. The RMSE of the three models is shown in Tables 4, 5:

The Loh model has the worst fitting performance, and the fitting RMSE in some frequency bands exceeds 0.2 (Table 4, 5-10 Hz); the RMSE of the H-V model is generally lower than that of the Loh model but higher than our proposed model in each bands. Comparing the mean RMSE, we can find that the residuals of three fitting models for the Luxian earthquake are higher than those of the Yibin earthquake due to smaller sample size and more discrete distribution of lagged coherency. However, our model takes into account the effect of site heterogeneity, and the fitting RMSE could be controlled below 0.08 in each frequency band.

Practical application shows that the ideal simulation results throughout the frequency range can be obtained with the soil-heterogeneity lagged coherency model developed in this study.

6 Conclusion

Based on observation records of the Luxian MS 6.0 earthquake and Yibin MS 5.1 earthquake obtained using the Zigong dense array, we first studied the spatial variability of strong motion in heterogeneous soil from a practical perspective. Multiple technical methods are then comprehensively utilized to quantify the amplification effects and classify the site conditions in the study. On this basis, the lagged coherency of different station pairs was analyzed, and the impact of local soil conditions on the lagged coherency was emphatically discussed, which led to a fascinating new insight. Finally, a coherency function model considering the influence of a heterogeneous soil site is constructed using a mathematical method, and the nonlinear fitting results are compared with two traditional empirical models. The following conclusions can be drawn from this study:

1) The amplitude characteristics of ground motion change with the spatial position attributed to local soil conditions, and the affected frequency bands also differ. The root-mean-square acceleration of most stations increases with the decrease of the dominant frequency, and the horizontal component is much more affected than the vertical component. The H/V spectrum ratio method can be used to clearly show the site effect of each station, making site classification, and assist in studying the spatial variation of strong ground motion.
2) As shown by the calculation results of lagged coherency, the correlation between stations decreases with frequency and separation distance. However, the heterogeneity of the soil layer interferes with this change trend. The station pairs with

similar H/V spectrum ratio characteristics have higher coherency and may be larger than those with smaller distance. When the site conditions differ greatly, the coherency is greatly reduced, thus making the scatter distribution more discrete. This effect is also quite obvious in the low-frequency part below 5 Hz. Comparing the calculation results of the two groups of observation data of the Luxian MS 6.0 earthquake and Yibin MS 5.1 earthquake, the conclusion is consistent.

3) Considering that the bedrock incident wave may be affected by additional incoherency effects when passing through the heterogeneous soil layer, a novel coherency function model is established. The proposed model was controlled by three variables, namely, frequency, interstation distance, and site impact factor, and the lagged coherency attenuation trend of different station pairs can be simulated through a set of parameters. In addition, its fitting precision was obviously better than that of the Loh model and H-V model which are popular in engineering at present.

In this study, the influence of soil heterogeneity on the spatial variation of ground motion could not be ignored. The previous lagged coherency models obtained based on the dense array are all in accordance with the soil homogeneous assumption, which could not reflect the change in the coherency coefficient by local site factors. The new model proposed in this paper could make up for such shortcomings to some extent and is an advance in research methods. For middle- and far-field earthquakes (R>50 km), the spatial coherence of observation records is mainly affected by the propagation path and site conditions (incoherent effect). The source finiteness contributes little to the coherency loss (Huda and Langston, 2021; Abbas and Tezcan 2020). Consequently, the conclusions and model summarized in this paper are also of high reference value and at least provide good lower-bound estimates of the spatial incoherence of larger magnitude earthquakes for earthquake fortification. However, this proposed model cannot distinguish soil heterogeneity in detail due to the limited observation data. Therefore, it is needed to collect more strong motion records of dense arrays and borehole data in heterogeneous soil sites, optimize the classification of the heterogeneous soil layer, and achieve better application results (Supplementary Appendix S1).

Data availability statement

The raw data supporting the conclusions of this article will be made available by the authors, without undue reservation.

Author contributions

QY: data analysis, numerical calculation and model building, and writing of manuscript with RY; RY: daily advisor, conception and design of the study, and writing of manuscript with QY; PJ: operation and maintenance of the array, data reception, and data preprocessing; and KC: providing codes for response spectrum calculation and drawing H/V spectral ratio curves with QY.

Funding

This study is supported by the Natural Science Foundation of China (No. 51878627) and the Special Foundation of Geophysics, China Earthquake Administration (No. DQJB 21B36).

Conflict of interest

The authors declare that the research was conducted in the absence of any commercial or financial relationships that could be construed as a potential conflict of interest.

Publisher's note

Supplementary material

The Supplementary Material for this article can be found online at: https://www.frontiersin.org/articles/10.3389/feart.2022.1054448/full#supplementary-material

References

Abbas, H., and Tezcan, J. (2006). Analysis and modeling of ground motion coherency at uniform site conditions. *Soil Dynamics and Earthquake Engineering* 133, 106124. doi:10.1016/j.soildyn.2020

Abrahamson, N. A., Schneider, J. F., and Stepp, J. C . (1991). Empirical spatial coherency functions for application to soil-structure interaction analyses. *Earthq. Spectra* 7 (1), 1–27. doi:10.1193/1.1585610

Abrahamson, N. A., Bolt, B. A., Darragh, R. B., Penzien, J., and Tsai, Y. B. (1987). The smart I accelerograph array (1980-1987): A review. *Earthq. Spectra* 3, 263–287. doi:10.1193/1.1585428

Bi, K. M., and Hao, H. (2012). Influence of ground motion spatial variations and local soil conditions on the seismic responses of buried segmented pipelines. *Struct. Eng. Mech.* 44 (5), 663–680. doi:10.12989/sem.2012.44.5.663

Boissières, H., and Vanmarcke, E. H. (1995). Spatial correlation of earthquake ground motion: Non-parametric estimation. *Soil Dyn. Earthq. Eng.* 14 (1), 23–31. doi:10.1016/0267-7261(94)00027-e

Boore, D. M. (2001). Effect of baseline corrections on displacements and response spectra for several recordings of the 1999 chi-chi, taiwan, earthquake. *Bull. Seismol. Soc. Am.* 91 (5), 1199–1211. doi:10.1785/0120000703

Chen, Y., Bradley, B. A., and Baker, J. W. (2021). Nonstationary spatial correlation in New Zealand strong ground-motion data. *Earthq. Eng. Struct. Dyn.* 50 (13), 3421–3440. doi:10.1002/eqe.3516

Chern, C. C. (1982). "Preliminary report on the smart 1 strong motion array in taiwan," in *Earthquake engineering research center report No. UCB/EERC-82/13* (Berkeley CA: Univ of California).

Cornou, C., Bard, P-Y., and Dietrich, M. (2003). Contribution of dense array analysis to the identification and quantification of basin-edge-induced waves, Part II: Application to grenoble basin (French alps). *Bull. Seismol. Soc. Am.* 93, 2624–2648. doi:10.1785/0120020140

Dinesh, B. V., Nair, G. J., Prasad, A. G. V., Nakkeeran, P., and Radhakrishna, M. (2010). Estimation of sedimentary layer shear wave velocity using micro-tremor H/V ratio measurements for Bangalore city. *Soil Dyn. Earthq. Eng.* 30 (11), 1377–1382. doi:10.1016/j.soildyn.2010.06.012

Goda, K., and Hong, H. P. (2008). Spatial correlation of peak ground motions and response spectra. *Bull. Seismol. Soc. Am.* 98 (1), 354–365. doi:10.1785/0120070078

Hao, H., Oliveira, C. S., and Penzien, J. (1989). Multiple-station ground motion processing and simulation based on smart-1 array data. *Nucl. Eng. Des.* 111 (3), 293–310. doi:10.1016/0029-5493(89)90241-0

Harichandran, R. S., and Vanmarcke, E. H. (1986). Stochastic variation of earthquake ground motion in space and time. *J. Eng. Mech.* 112 (2), 154–174. doi:10.1061/(asce)0733-9399(1986)112:2(154)

Huda, M. M., and Langston, C. A. (2021). Coherence and variability of ground motion in New Madrid Seismic Zone using an array of 600 m. *J. Seismol.* 25 (2), 433–448. doi:10.1007/s10950-020-09970-z

Ibs-von Seht, M., and Wohlenberg, J. (1999). Microtremor measurements used to map thickness of soft sediments. *Bull. Seismol. Soc. Am.* 89 (1), 250–259. doi:10.1785/bssa0890010250

Imtiaz, A., Cornou, C., Bard, P. Y., and Zerva, A. (2018). Effects of site geometry on short-distance spatial coherency in Argostoli, Greece. *Bull. Earthq. Eng.* 16 (5), 1801–1827. doi:10.1007/s10518-017-0270-z

Ji, K. (2014). *Estimation on site characteristic based on H/V spectral ratio method [D]*. Harbin: Institute of Engineering Mechanics, CEA.

Joshi, A. U., Sant, D. A., Parvez, I. A., Rangarajan, G., Limaye, M. A., Mukherjee, S., et al. (2018). Subsurface profiling of granite pluton using microtremor method: Southern Aravalli, Gujarat, India. *Int. J. Earth Sci.* 107 (1), 191–201. doi:10.1007/s00531-017-1482-9

Katayama, T. (1991). Use of dense array data in the determination of engineering properties of strong motions. *Struct. Saf.* 10, 27–51. doi:10.1016/0167-4730(91)90005-t

Kiureghian, A. D. (1996). A coherency model for spatially varying ground motions. *Earthq. Eng. Struct. Dyn.* 25 (1), 99–111. doi:10.1002/(sici)1096-9845(199601)25:1<99::aid-eqe540>3.0.co;2-c

Konakli, K., Der Kiureghian, A., and Dreger, D. (2014). Coherency analysis of accelerograms recorded by the UPSAR array during the 2004 Parkfield earthquake. *Earthq. Eng. Struct. Dyn.* 43 (5), 641–659. doi:10.1002/eqe.2362

Konno, K., and Ohmachi, T. (1998). Ground-motion characteristics estimated from spectral ratio between horizontal and vertical components of microtremor. *Bull. Seismol. Soc. Am.* 88 (1), 228–241. doi:10.1785/bssa0880010228

Kwok, A. O. L., Stewart, J. P., and Hashash, Y. M. A. (2008). Nonlinear ground-response analysis of Turkey flat shallow stiff-soil site to strong ground motion. *Bull. Seismol. Soc. Am.* 98 (1), 331–343. doi:10.1785/0120070009

Laib, A., Laouami, N., and Slimani, A. (2015). Modeling of soil heterogeneity and its effects on seismic response of multi-support structures. *Earthq. Eng. Eng. Vib.* 14 (3), 423–437. doi:10.1007/s11803-015-0034-1

Liao, S., and Li, J. (2002). A stochastic approach to site-response component in seismic ground motion coherency model. *Soil Dyn. Earthq. Eng.* 22, 813–820. doi:10.1016/s0267-7261(02)00103-3

Loh, C. H., and Lin, S. G. (1990). Directionality and simulation in spatial variation of seismic waves. *Eng. Struct.* 12 (2), 134–143. doi:10.1016/0141-0296(90)90019-o

Loh, C. H., Penajien, J., and Tsai, Y. B. (1982). Engineering analysis of smart-1 seismic data. *Int. J. Earthq. engineering\&\structural Dyn.* 10, 575–591.

Loh, C. H., and Yeh, Y. T. (1988). Spatial variation and stochastic modelling of seismic differential ground movement. *Earthq. Eng. Struct. Dyn.* 16 (4), 583–596. doi:10.1002/eqe.4290160409

Nakamura, Y., and Saito, A. (1983). "Estimations of amplification characteristics of surface ground and PGA using strong motion records (in Japanese) [C]," in Proceeding of the 17th JSCE Earthquake Eng. Symp, 25–28.

Nechtschein, S., Ba, Rd P. Y., Gariel, J. C., Meneroud, J. P., Dervin, P., Gaubert, C., et al. (1996). "A topographic effect study in the Nice region[C]," in Proceeding of the International conference on seismic zonation, Jaunary 1996.

Nour, A., Slimani, A., Laouami, N., and Afra, H. (2003). Finite element model for the probabilistic seismic response of heterogeneous soil profile. *Soil Dyn. Earthq. Eng.* 23 (5), 331–348. doi:10.1016/s0267-7261(03)00036-8

O' Rourke, M. J., Castro, G., and Centola, N. (1980). Effects of seismic wave propagation upon buried pipelines. *Earthq. Eng. Struct. Dyn.* 8 (5), 455–467. doi:10.1002/eqe.4290080507

Parolai, S., Bormann, P., and Milkereit, C. (2002). New relationships between VS, thickness of sediments, and resonance frequency calculated by the H/V ratio of seismic noise for the Cologne Area (Germany). *Bull. Seismol. Soc. Am.* 92 (6), 2521–2527. doi:10.1785/0120010248

Peng, F., Wang, W. J., and Kou, H. D. (2020). Microtremer H/V spectral ratio investigation in the sanhe-pinggu area: Site responses, shallow sedimentary structure, and fault activity revealed. *Chin. J. Geophys* 63 (10), 3775–3790. (in Chinese). doi:10.6038/cjg2020O0025

Rong, M. S., Li, X. J., Wang, Z. M., Lv, Y. Z., et al. (2016). Applicability of HVSR in analysis of site-effects caused by earthquakes. *Chin. J. Geophys* 59 (8), 2878–2891. (in Chinese). doi:10.6038/cjg2018L0171

Rosalba, M., Lucia, N., Terenzio, G. F., and Potenza, M. R. (2018). Ambient noise HVSR measurements in the Avellino historical centre and surrounding area (southern Italy). Correlation with surface geology and damage caused by the 1980 Irpinia-Basilicata earthquake. *Measurement* 130, 211–222. doi:10.1016/j.measurement.2018.08.015

Sadouki, A., Harichane, Z., and Chehat, A. (2012). Response of a randomly inhomogeneous layered media to harmonic excitations. *Soil Dyn. Earthq. Eng.* 36, 84–95. doi:10.1016/j.soildyn.2012.01.007

Schneider, J. F., Stepp, J. C., and Abrahamson, N. A. (1992). "The spatial variation of earthquake ground motion and effects of local site" in Proc. Earthquake Engng. 10th World Conf. Madrid, Spain, 967–972

Shi, L. J., and Chen, S. Y. (2020). The applicability of site characteristic parameters measurement based on micro-tremor's H/V spectra. *J. Vib. Shock* 39 (11), 138–145. doi:10.13465/j.cnki.jvs.2020.11.018

Shi, L. J., Liu, J. X., and Chen, S. Y. (2022). Site classification based on predominant period of microtremor 's H/V spectral ratio. *J. Vib. Shock* 41 (13), 34–42. doi:10.13465/j.cnki.jvs.2022.13.00

Somerville, P. G., McLaren, J. P., Saikia, C. K., and Helmberger, D. V. (1988). Site-specific estimation of spatial incoherence of strong ground motion. *Geotech. Spec. Publ.*, 188–202.

Svay, A., Perron, V., Imtiaz, A., Zentner, I., Cottereau, R., Bard, P., et al. (2017). Spatial coherency analysis of seismic ground motions from a rock site dense array implemented during the Kefalonia 2014 aftershock sequence. *Earthq. Eng. Struct. Dyn.* 46 (12), 1895–1917. doi:10.1002/eqe.2881

Thomeson, D. J. (1982). Spectrum estimation and harmonic analysis. *Proc. IEEE* 70 (9), 1055–1096. doi:10.1109/proc.1982.12433

Wang, H. Y., and Xie, L. L . (2010). Effects of topography on ground motion in the xishan park, zigong city. *Chin. J. Geophys.* 53 (7), 1631–1638. doi:10.3969/j.issn.0001-5733.2010.07.014

Wang, Z. Z. (2012). *Coherence variation of ground motion with depths[D]*. Dalian: Dalian University of Technology.

Wen, R., Ren, Y., and Shi, D. (2011). Improved HVSR site classification method for free-field strong motion stations validated with Wenchuan aftershock recordings. *Earthq. Eng. Eng. Vib.* 10 (3), 325–337. doi:10.1007/s11803-011-0069-x

Yang, Q. M. (2008). *The divisional evaluation of urban environmental geology in Zigong City[M]*. Chendu: Chengdu University of Technology.

Yu, R. F., Abduwaris, A., and Yu, Y. X. (2020). Practical coherency model suitable for near- and far-field earthquakes based on the effect of source-to-site distance on spatial variations in ground motions. *Struct. Eng. Mech.* 73 (6), 651–666. doi:10.12989/sem.2020.73.6.651

Yu, R. F., Wang, S. Q., and Yu, Y. X. (2021). Reviewing of stochastic description of the spatial variation of ground motion and coherence function model. *Rev. Geophys. Planet. Phys.* 52 (2), 194–204. doi:10.19975/j.dqyxx.2020-012

Zerva, A. (2009). *Spatial variation of seismic ground motion[M]*. Boca Raton: CRS Press, Talor and Francis Group.

Zerva, A., and Stephenson, W. R. (2011). Stochastic characteristics of seismic excitations at a non-uniform (rock and soil) site. *Soil Dyn. Earthq. Eng.* 31, 1261–1284. doi:10.1016/j.soildyn.2011.05.006

Zerva, A., and Zhang, O. (1997). Correlation patterns in characteristics of spatially variable seismic ground motions. *Earthq. Eng. Struct. Dyn.* 26 (1), 19–39. doi:10.1002/(sici)1096-9845(199701)26:1<19::aid-eqe620>3.0.co;2-f

Zerva, A., and Harada, T. (1997). Effect of surface layer stochasticity on seismic ground motion coherence and strain estimates. *Soil Dyn. Earthq. Eng.* 16 (7-8), 445–457. doi:10.1016/s0267-7261(97)00019-5

Zhao, J. X., Irikura, K., and Zhang, J. (2006). An empirical site-classification method for strong-motion stations in Japan using H/V response spectral ratio. *Bull. Seismol. Soc. Am.* 96 (3), 914–925. doi:10.1785/0120050124

frontiers | Frontiers in Earth Science

TYPE Original Research
PUBLISHED 25 January 2023
DOI 10.3389/feart.2022.1058701

OPEN ACCESS

EDITED BY
Giovanni Lanzano,
Istituto Nazionale di Geofisica e Vulcanologia (INGV), Italy

REVIEWED BY
Danqing Song,
Tsinghua University, China
Yankun Wang,
Yangtze University, China

*CORRESPONDENCE
Wu Zhijian,
✉ zhijian@njtech.edu.cn

SPECIALTY SECTION
This article was submitted to Structural Geology and Tectonics, a section of the journal Frontiers in Earth Science

RECEIVED 30 September 2022
ACCEPTED 06 December 2022
PUBLISHED 25 January 2023

CITATION
Wujian Y, Xinxin T, Zhijian W, Ping W and Lin K (2023), Seismic effects of loess slopes using physical modeling and numerical simulation.
Front. Earth Sci. 10:1058701.
doi: 10.3389/feart.2022.1058701

Seismic effects of loess slopes using physical modeling and numerical simulation

Yan Wujian[1,2,3], Tian Xinxin[3], Wu Zhijian[4]*, Wang Ping[3] and Kang Lin[3]

[1]Key Laboratory of Earthquake Engineering and Engineering Vibration, Institute of Engineering Mechanics, Harbin, China, [2]Key Laboratory of Earthquake Disaster Mitigation, Ministry of Emergency Management, Harbin, China, [3]Key Laboratory of Loess Earthquake Engineering, Lanzhou Institute of Seismology, China Earthquake Administration, Lanzhou, China, [4]College of Transportation Engineering, Nanjing Tech University, Nanjing, China

A large shaking-table test of a loess slope with a geometric similarity ratio of 1:25 was established as a prototype model of the loess landslide in Yongguang Village, which occurred during the 2013 Minxian–Zhangxian *M*6.6 earthquake. Combined with finite-element–numerical-simulation software, the dynamic response characteristics of the loess slope were compared and analyzed under the action of the same Minxian horizontal seismic wave characteristics. The results show that the seismic waves observed in the model test and numerical simulation clearly exhibit non-linear amplification effects along the slope surface and in the loess vertical direction, reaching a maximum value at the top of the slope. The ground-motion acceleration waveforms observed in the model test and numerical simulation at each observation point of the slope were similar, and the horizontal peak ground acceleration (PGA) obtained from the numerical simulation at these locations was larger than that of the slope top. The horizontal $a_{\text{Simulated-max}}/a_{\text{Model-max}}$ values ranged from 1.5 to 2.2 and the vertical $a_{\text{Simulated-max}}/a_{\text{Model-max}}$ values were more discrete in the range of 0.5–2.7, while the horizontal and vertical-PGA-amplification factors at the slope surface were similar. The Fourier amplitude and main horizontal frequencies were mainly distributed between 0.1 and 12 Hz. The Fourier spectrum observed in the model test was approximately 0.5 Hz, while the main frequency of the vertical Fourier spectrum was approximately 4 Hz. Additionally, the main frequency of the horizontal and vertical Fourier spectra observed in the numerical simulation was approximately 2 and 1.2 Hz, respectively.

KEYWORDS

low-angle loess slope, shaking-table model test, numerical simulation, dynamic response, spectral analysis, Fourier spectrum

1 Introduction

The Loess Plateau is located in China's northeast edge of the Qinghai–Tibet Plateau seismic belt and the north–south seismic belt. Its geological structure is complex, and it experiences strong neotectonic movement, which contributes to the frequent mega-geological disasters experienced in China, mainly in the form of strong earthquakes. The Loess Plateau area has a large number of slopes, loess, beams, mountings, and other special topographic features. Compared with other soil types, loess is a special Quaternary deposition of porous and weakly cemented material, with strong water sensitivity and very high dynamic vulnerability (Liu et al., 1985). Geological hazards, such as loess landslides and liquefaction, can be induced under the action of moderate-to-strong earthquakes (Wang, 2003). A previous study showed that the amplification effects of ground motion caused by thick loess deposits were the main cause of intensity anomalies (Wang and Xie, 2010; Wang et al., 2013). On September 6, 2018, a 6.7-magnitude earthquake that occurred in Hokkaido, Japan, triggered more than 4,000 landslides, and 44 casualties were reported as predominantly caused by these landslides (Wang L. et al., 2019). Most of the landslides formed at an angle of 15–30°, with very few forming between 30 and 39°. The same situation occurred in China, where an M6.6-magnitude earthquake occurred on July 22, 2013, at the border of Min and Zhang counties, which triggered more than 2,330 landslides that resulted in 95 deaths. Most of these landslides have slopes ranging between 10 and 20° (Wang et al., 2017a, Wang et al., 2017b, Wang et al., 2017c). A massive mudslide with a slope angle of 18° in Yongguang Village, Minxian County, formed a part of these landslides.

With the "Belt and Road" initiative and the rapid development of China's social and economic development, the center of gravity of national infrastructure construction is gradually shifting to the west, along with an increasing scale of cities and human engineering activities, leaving more people increasingly vulnerable to sudden earthquakes owing to the loess slopes. To prevent and better mitigate disasters, it is necessary to study deformation, damage mechanisms, and response laws of loess slopes under the action of earthquakes. Current analysis methods for slope dynamic responses are divided into three types: analytical methods, numerical calculations, and physical models. Owing to the discontinuity and inhomogeneity of the soil medium, as well as the complexity of slope dynamics, it is very difficult to solve slope dynamic problems using theoretical derivations. The theory of geotechnical slope dynamic response is far from mature, and its accuracy is to be tested yet (Bouckovalas and Papadimitriou, 2005). Wu et al. (2015) used shaking table model tests to study the destabilization damage process and acceleration response characteristics of pure loess slopes with low moisture contents and slope angles under earthquake excitation. Wang et al. (2018) conducted shaking-table model tests on loess slopes and studied the dynamic response law under the coupled action of earthquakes and rainfall. Song et al. (2021a) studied the seismic cumulative failure effects on a reservoir-bank slope with a complex geological structure, considering its plastic-deformation characteristics using shaking-table tests. Zhang et al. (2018) analyzed the damage characteristics and dynamic response law of loess-mudstone slopes under different amplitudes using centrifuge shaking-table tests and numerical simulations. To investigate the seismic response of pile systems in multi-tilted and layered soils under earthquake and rainfall conditions, two models were built and tested using a large 1-g shaking table (Jian Zhang et al., 2022). The shaking-table test by Wang and Wang (1987) indicated that the peak acceleration response at the crest of a slope was amplified more than that at the foot. Studies have also demonstrated that surficial soil and rock-mass structures have a pronounced effect on the seismic response of slopes (He et al., 2020; He et al., 2021; Song et al., 2021b; Song et al., 2021c; Song et al., 2021d). Murphy (2006) conducted a study based on the landslide data from the 1970 Peru and 1999 Taiwan Jiji earthquakes to investigate the amplification effect of mountains and found that the amplification effect of ground shaking was the most obvious at ridge locations. By studying the distribution maps of earthquake landslides near the Northridge region in California, United States, the Chiji region in Taiwan, and the Finisterre Mountains in Papua New Guinea, Meunier et al. (2008) found that earthquake-induced landslides were clustered near ridges, the peak ground acceleration (PGA) occurred at the top of the ridges, and the sudden change in the slope on both sides of the ridges was significantly amplified. Wang et al. (2010) conducted a study on the amplification effect of site conditions and soil structure on ground shaking based on the time course of mainshock acceleration recorded by the Zigong topographic table array during the Wenchuan earthquake. Chen and Wu (2012) conducted a dynamic response analysis of the Loess Plateau with different cover thicknesses and slopes under earthquake loads by deploying a strong ground-motion observation array and using a two-dimensional equivalent linear time-response–dynamic-analysis method. The results showed that the amplification effects of peak seismic acceleration, loess cover thickness, and angle of the loess slope were related. Mitani et al. (2013) investigated the amplification effect of ground motion on homogeneous slopes with different heights and slopes using a finite-element–numerical-analysis method. Wang et al. (2018) numerically analyzed the amplification effect of earthquake ground motion in terms of the loess-layer thickness and slope. The results show that the amplification effect is more evident as the thickness of the loess layer and slope increase. However, under the action of dynamic loads, the loess microstructure is gradually damaged and deformed, such that the macroscopic properties of the soil are continuously degraded. Finite-element–numerical-simulation software cannot simulate this degradation–evolution process, and the laws summarized by its numerical analysis need to be mutually verified by actual earthquake or model tests (Jiang, 2019). Qi et al. (2003) and Qi (2006) investigated the topographic effect of a single surface slope on an entire slope section using numerical simulations and reported two types of slope dynamic responses. Bouckovalas and Papadimitriou (2005) stated that this

FIGURE 1
Shaking table and model box.

type of topography may lead to intense amplification or deamplification variability at neighboring points (within a few tens of meters) behind the crest of the slope, particularly during high-frequency motion. He et al. (2020) demonstrated that the combined effect of superficial soil and topography resulted in a complex seismic response on the Lengzhuguan slope.

To study the ground-motion response characteristics of a low-angle loess slope, we combined shaking-table model tests with simulation calculations. We adopted this approach because shaking-table model tests are more complex, costly, and reliable than numerical simulations. However, although numerical simulations are simple and less costly, they lack validation. A comparative study between shaking-table model tests and numerical simulations of the same loess-slope model can be conducted to verify the reliability of both methods and establish a relationship between the two seismic parameters, thus establishing reliable samples for future numerical calculations. By selecting a low-angle (approximately 20°) loess slope as the prototype, the dimensions and materials of the low-angle slope model were determined according to the law of similarity. Additionally, the dynamic response characteristics of the low-angle loess slope under the strong motion load of the Minxian Station during the M6.6 earthquake in Minxian, Zhangxian County, were observed using seismic acceleration sensors. Additionally, a two-dimensional soil model was constructed using the geo-mechanical and physical–mechanical parameters obtained from an indoor test of the *in situ* loess of the prototype slope. Simultaneously, this model was simulated using the finite-element method, and the same seismic wave used in the model test was incorporated in the numerical simulation of the ground-motion amplification effect of the prototype loess slope. Based on the model test and simulation calculation results, the acceleration, amplification factor, displacement, and other dynamic response laws of a low-angle loess slope under earthquake conditions were compared and analyzed to reveal the characteristics of the ground-motion amplification effect.

2 Ground-motion response of the shaking-table test on loess slopes

2.1 Test setup

The test was conducted on a large electric-servo shaking table at the Key Laboratory of Loess Earthquake Engineering, China Earthquake Administration (Figure 1). The shaking table size is 4 × 6 m, driven by 28 servo motors, which can realize horizontal (x), vertical (z), and horizontal–vertical coupling vibrations. Maximum load capacity: $F_x = 250$ kN and $F_z = 150$ kN; frequency range in x and z directions: $f_x = 0.1$–70.0 Hz and $f_z = 0.1$–50.0 Hz; maximum displacement in x and z directions: $u_x = \pm 250$ mm and $u_z = \pm 100$ mm; maximum acceleration: $a_x = 1.7$ g and $a_z = 1.2$ g for x and z directions independently; $a_x = 1.2$ g for x and z directions combined; and maximum acceleration: $a_x = 1.7$ g and $a_z = 1.2$ g for x- and z-directional vibration independently; $a_x = 1.2$ g and $a_z = 1.0$ g for combined x- and z-directional vibration.

2.2 Slope prototype

The landslide of the loess slope from Min County to Zhang County was triggered by an $M6.6$ earthquake in the west of Yongguang Village and was selected as a prototype for this study

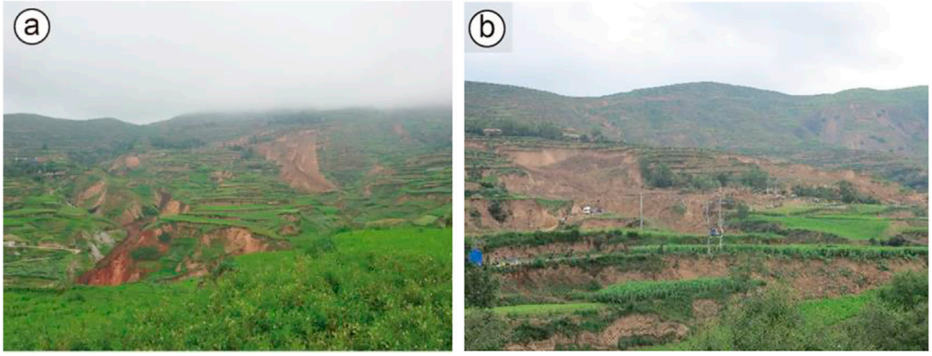

FIGURE 2
Prototype slope. **(A)** Distant view of the landslide in Yongguang Village; **(B)** close-range view of the landslide in Yongguang Village.

(Figure 2). The parameters measured on site include the prototype slope height of 20.00 m, slope bottom length of 70.50 m, slope top length of 9.25 m, slope width of 35.00 m, slope body leading edge of 6.25 m, leading edge thickness of 2.5 m, and average slope of 20°. The prototype slope-soil body was used for Q_3 loess.

2.3 Boundary conditions and shaking-table similar design

Broadly speaking, a slope is a semi-infinite geological body with a slope that has at least one side exposed to air and possesses no theoretical boundary. However, the model soil is placed in a model box of finite size during the test, which results in wave reflection at the boundary, producing the "model-box effect" and changing the motion pattern of the entire system, as well as causing secondary damage to the model slope (Lu et al., 2000). Therefore, measures must be taken to mitigate these effects at the boundaries. The general approach is to add a liner inside the model box or to change the box structure and material. In this experiment, a 5-cm-thick polystyrene foam sponge was attached to each side of the box to absorb the energy at the boundary.

The biggest challenge in the model design is to accurately reflect the properties of the prototype slope; therefore, it is necessary to use a similarity theory design to guide the test. Model tests include geometric, kinematic, and kinetic similarities. If two physical quantities are similar in terms of geometry and kinematics, their dynamics are also similar. However, owing to the complexity of the model and limitations of the objective conditions, it is difficult to satisfy the similarity of all parameters. Thus, it was necessary to select the primary control parameters and ignore the secondary control parameters according to the purpose of the test. In this test, geometry, material density, and gravitational acceleration were used as the basic magnitudes, and their similarity constants were taken as $C_L = 25$, $C_\rho = 1$, and $C_a = 1$, respectively. The remaining physical quantities were derived according to Buckingham's theory (π theorem) and magnitude analysis (Yuan, 1998; Gao et al., 2000). The final similarity constants are listed in Table 1.

2.4 Model design and sensor arrangement

The geometric similarity ratio between the model and prototype slope was 1:25. The slope model has a slope height of 0.8 m, slope bottom length of 2.82 m, slope top length of 0.37 m, slope width of 1.4 m, and slope gradient of 20°. The loess-slope model is illustrated in Figure 3. This test used a rigid closed model box with an inner size of $L \times W \times H = 2.8 \times 1.4 \times 1$ m, with Plexiglas plates installed in the length direction to facilitate the observation of macroscopic phenomena during the experiment and organic carbon steel plates in the width direction to increase the strength of the model box.

Remodeled loess was used as the primary material in the model tests because the prototype slope was a pure loess slope. The internal friction angle and cohesion parameters of the material were controlled by restricting the water content and density of the remodeled soil to achieve physical properties that were similar to those of the prototype material. Loess, fly ash, light foam soil, heavy gold stone powder, and water were used as the test materials. Through several material proportioning tests, it was determined that the ratio of loess: fly ash: light foam soil: heavy gold stone powder: water was 10:3:3:3:1. The physical and mechanical parameters of the prototype and model materials measured by multiple sets of static triaxial and direct shear tests are listed in Table 2, which shows that the internal friction angle and density satisfy a similar theory and the modulus of elasticity and cohesion decrease significantly and converge to the target value of the model soil.

TABLE 1 Similarity constants for the shaking model test.

Physical quantity	Similarity relationship	Similarity constant
Length (control quantity)	C_L	25
Density (control quantity)	C_ρ	1
Cohesion (control quantity)	$C_C = C_\rho \cdot C_L$	25
Velocity	$C_v = C_L \cdot C_t^{-1} = C_L^{1/2}$	5
Acceleration	$C_a = C_L \cdot C_t^{-2}$	1
Time	$C_t = \sqrt{C_L}$	5
Frequency	$C_f = C_L^{-1/2}$	0.2
Modulus of elasticity	$C_E = C_\rho \cdot C_L$	25
Stress	$C_\sigma = C_\rho \cdot C_L$	25
Strain	C_ε	1
Angle of internal friction	C_φ	1
Poisson's coefficient	C_μ	1

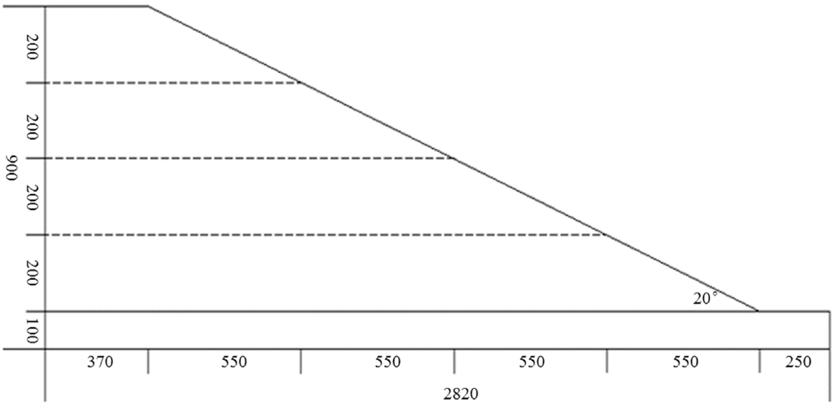

FIGURE 3
Loess-slope model (unit: mm).

TABLE 2 Soil parameters.

	Modulus of elasticity E (MPa)	Cohesive force C (kPa)	Density ρ(g/cm^3)	Angle of internal friction φ (°)
Actual value of the prototype soil	70	23.3	1.38	14
Target value of the model soil	2.8	0.932	1.38	14
Measured value of the model soil	20	7.79	1.38	19.5

The test used a three-phase capacitive DH301-type acceleration sensor, and the detailed parameters are listed in Table 3. Only two horizontal and vertical channels of the sensor were selected for the test because only horizontal and vertical two-directional seismic loadings were tested. The arrangement of the acceleration sensors used in the test is shown in Figure 4.

TABLE 3 Main technical specifications of a DH301 series three-way capacitive acceleration sensor.

Index type	Detailed parameter	Index type	Detailed parameter
Sensitivity (Mv/m·s^{-2})	*X*-axis: 68.0	Frequency range (Hz) (±3 dB)	*X*-axis: 0–1,500 Hz
	Y-axis: 68.0		*Y*-axis: 0–1,500 Hz
	Z-axis: 66.6		*Z*-axis: 0–800 Hz
Range	±20 m/s^2	Install the resonance	12 kHz
Impact limit	50 × 10^4 m/s^2	Transverse sensitivity	<5%

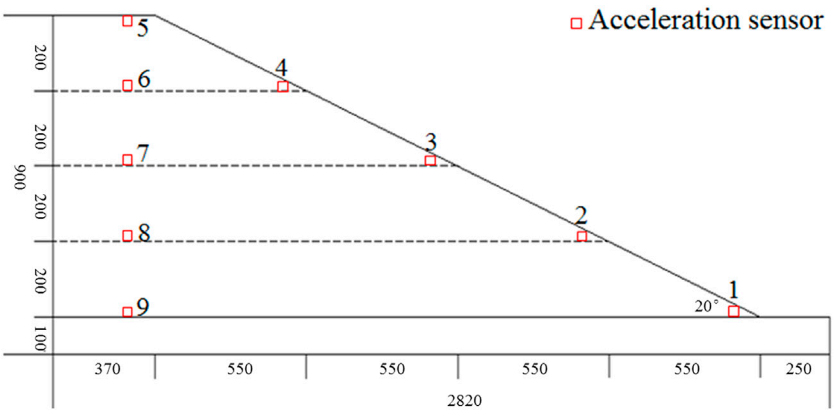

FIGURE 4
Layout scheme of the acceleration sensor (unit: mm).

TABLE 4 Waveform input parameters of ground-motion loading.

Loading condition	Tabletop input ground-motion waveform	Mesa input PGA	Duration of the seismic wave (s)	Loading way
VIII degree basic earthquake (0.20 g)	Minxian seismic wave	183.2 gal	84.32	*x*

2.5 Loaded waveform and spectral characteristics

According to a similar design and the dimensional analysis method used to simulate the original site conditions, only the dimensional and material similarities are considered in this study because dynamic similarity is difficult to achieve. To study the dynamic response characteristics of low-angle pure loess slopes under the effect of strong earthquakes, shaking-table physical model tests and numerical simulations were used for comparison and analysis. The loading waveforms and Minxian seismic wave (NS direction, horizontal component) were used, and the specific parameters are listed in Table 4. The Minxian seismic wave was the mainshock acceleration time course recorded by the Minxian strong seismic station of the 2013 Minxian–Zhangxian *M*6.6 earthquake. The waveform of the horizontal component of the Minxian seismic wave is shown in Figure 5 with a time interval of 0.005 s and waveform holding time of 84.23 s, and the maximum acceleration amplitude is 183.2 gal, which occurs near 24.56 s. Figure 6 shows the spectrum of the horizontal component of the Minxian seismic wave, from which it can be observed that its frequency is concentrated at approximately 5 Hz. The waveform of the vertical component of the Minxian seismic wave is shown in Figure 7, with a time interval of 0.005 s, a waveform holding time of 84.32 s, and a maximum acceleration amplitude of 86.8 gal, which occurs near 24.92 s.

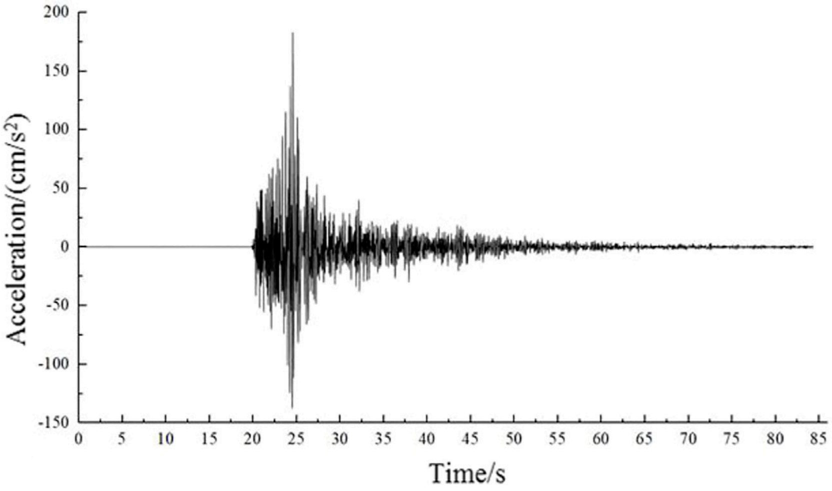

FIGURE 5
Seismic waveform of the horizontal component of the Minxian seismic wave.

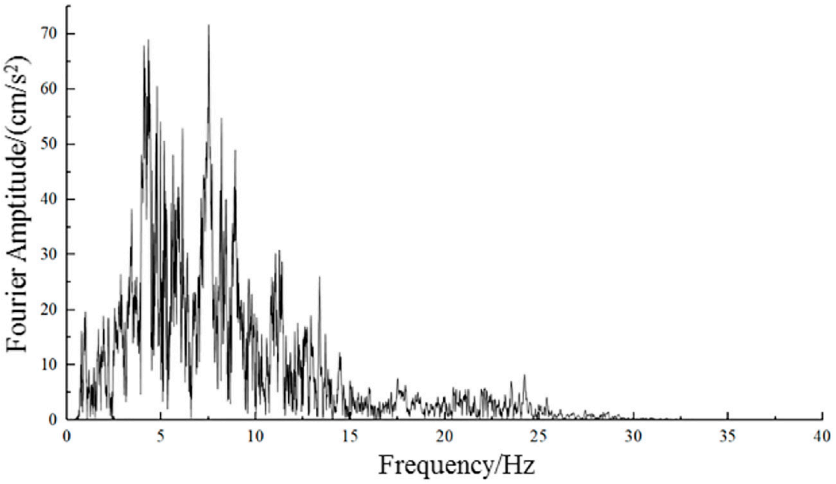

FIGURE 6
Seismic spectrum of the horizontal component of the Minxian seismic wave.

3 Ground-motion response of the loess slope by numerical simulation

3.1 Numerical simulation principle of dynamic response

3.1.1 Basic equation for the analysis of soil-layer earthquake response

When analyzing loess soil using the finite-element method, a limited range of soil layers must be intercepted for the calculation because the real soil has a semi-infinite space. After intercepting a reasonable soil-layer range, the analysis of the soil-layer seismic reaction is equivalent to solving the dynamic reaction of a discrete system with “n” supports under the earthquake action. We performed a transformation from the soil-layer fluctuation analysis problem under external excitation in the semi-infinite domain to the soil-layer motion analysis problem of the finite domain under basic excitation. Figure 7 shows a schematic of the finite-element model of this finite soil layer, where seismic wave excitation occurred in the bedrock surface at

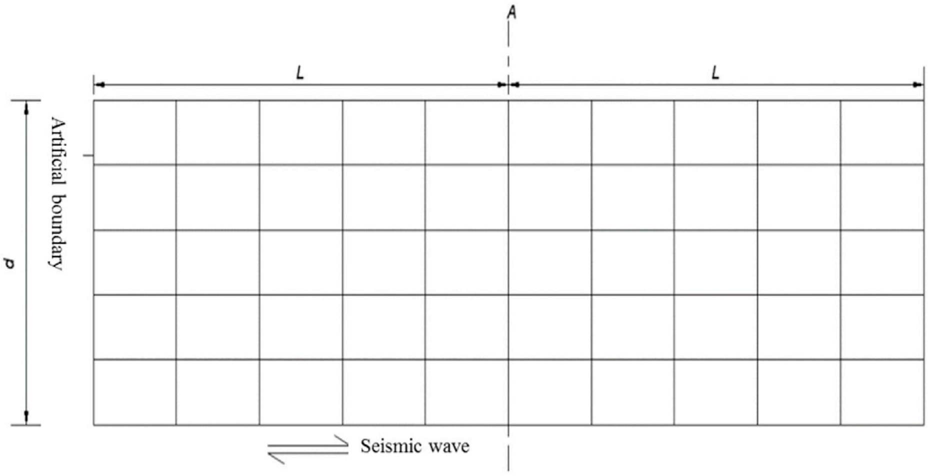

FIGURE 7
Schematic diagram of the finite-element calculation model of the soil layer.

the bottom of the soil layer. The basic equations of the seismic response analysis in the soil layer are divided into two categories: equations of motion under consistent and multi-point seismic excitation. The following is a brief introduction to the equations of motion under consistent seismic excitation (Bai, 2010).

The structural dynamics method can be used to establish the equations of motion when the soil layer is discretized into a motion system with finite elements. The discrete soil-layer system is a structural system with finite degrees of freedom, and the bedrock surface is a structural foundation surface. The equation of motion of the structural time domain under a consistent seismic input is:

$$[M]\{\ddot{u}_d(t)\} + [C]\{\dot{u}_d(t)\} + [K]\{u_d(t)\} + [M]\{I\}\ddot{u}_g(t) = 0. \quad (1)$$

In this equation, $[C]$, $[K]$, and $[M]$ are the damping, stiffness, and mass matrices after the discrete structure finite-element structure, respectively; $\{I\}$ is a unit array, whose elements are 0 and 1, indicating whether the dynamic action–reaction of seismic motion in all degrees of freedom is present; $\ddot{u}_g(t)$ is the seismic-wave acceleration time course input; and $\{u_d\}$ is the displacement component of each node relative to the structural substrate and caused by seismic motion. The absolute acceleration $\{\ddot{u}\}$ of the nodes in the structure can be expressed as

$$\{\ddot{u}\} = \{\ddot{u}_d\} + \{I\}\ddot{u}_g(t). \quad (2)$$

Because the order of the finite-element model is higher in practical problems, two types of solutions are generally adopted to solve the equation of motion for the aforementioned system: motion-type superposition and direct integration methods. The motion-type superposition method regards the dynamic reaction of the soil as a reaction (motion-type) produced by the soil under a series of motions at different frequencies. The motion-type superposition method is theoretically concise; however, it is complicated and unsuitable for non-linear dynamic analyses. The direct integration method can solve the internal force and displacement of each moment without the self-motion frequency of the system. The common direct integration methods include Newmark, Wilson-θ, linear acceleration, and central difference methods.

3.1.2 Newmark method

Assuming a finite-element discrete system with n degrees of freedom, n differential equations of motion can be established and expressed in the form of a matrix:

$$[M]\{\ddot{u}\} + [I] - [P] = 0, \quad (3)$$

where $[M]$ is the mass matrix, $[I]$ is the viscous damping matrix, $[P]$ is the external load, and $\{u\,\dot{}\}$ is the acceleration of the unit node.

The differential equations of motion at moments t and $t + \Delta t$ are expressed as follows:

$$[M]\{\ddot{u}\}_t + [I]_t - [P]_t = 0, \quad (4)$$

$$[M]\{\ddot{u}\}_{t+\Delta t} + [I]_{t+\Delta t} - [P]_{t+\Delta t} = 0. \quad (5)$$

To facilitate this solution, Eqs 4, 5 can be rewritten as follows:

$$[M]\{\ddot{u}\}_{t+\Delta t} + [C]\{\dot{u}\}_{t+\Delta t} + K\{u\}_{t+\Delta t} = [P]_{t+\Delta t}. \quad (6)$$

The displacement and velocity at moment $t + \Delta t$ can be obtained using the Newmark-β method, which can be expressed as

$$\{u\}_{t+\Delta t} = \{u\}_t + \{\dot{u}\}_t\Delta t + \left[\left(\frac{1}{2} - \beta\right)\{\ddot{u}\}_t + \beta\{\ddot{u}\}_{t+\Delta t}\right]\Delta t^2, \quad (7)$$

$$\{\dot{u}\}_{t+\Delta t} = \{\dot{u}\}_t + \left[(1-\gamma)\{\ddot{u}\}_t + \gamma\{\ddot{u}\}_{t+\Delta t}\right]\Delta t, \tag{8}$$

where $\beta \in (0, \frac{1}{2})$ and $\gamma \in (0, 1]$ are the weighting factors.

The accuracy of the Newmark-β method and its convergence and stability are influenced by the values of β and γ. Many researchers have developed kinetic equations that consider different values.

When $\beta = 1/6$ and $\gamma = 1/2$, this is termed the linear acceleration method. When $\beta = 1/4$ and $\gamma = 1/2$, Eqs 7, 8 can be rewritten as

$$\{u\}_{t+\Delta t} = \{u\}_t + \{\dot{u}\}_t\Delta t + \frac{\Delta t^2}{4}\left[\{\ddot{u}\}_t + \{\ddot{u}\}_{t+\Delta t}\right], \tag{9}$$

$$\{\dot{u}\}_{t+\Delta t} = \{\dot{u}\}_t + \frac{\Delta t}{2}\left[\{\ddot{u}\}_t + \{\ddot{u}\}_{t+\Delta t}\right]. \tag{10}$$

Eqs 9, 10, that is, when $\beta = 1/4$ and $\gamma = 1/2$, can be termed the inertia table shape rule.

A transformation of the Newmark-β method using the displacement at moment $t + \Delta t$ and the acceleration, velocity, and displacement at moment t can be used to calculate the acceleration and velocity at moment $t + \Delta t$ in the following form:

$$\{\ddot{u}\}_{t+\Delta t} = \frac{1}{\beta\Delta t^2}\left(\{u\}_{t+\Delta t} - \{u\}_t\right) - \frac{1}{\beta\Delta t}\{\dot{u}\}_t - \left(\frac{1}{2\beta} - 1\right)\{\ddot{u}\}_t, \tag{11}$$

$$\begin{aligned}\{\dot{u}\}_{t+\Delta t} &= \{\dot{u}\}_t + \{(1-\gamma)\ddot{u}\}_t + \gamma\left[\frac{1}{\beta\Delta t^2}\left(\{u\}_{t+\Delta t} - \{u\}_t\right) - \frac{1}{\beta\Delta t}\{\dot{u}\}_t\right.\\ &\quad \left.-\left(\frac{1}{2\beta} - 1\right)\{\ddot{u}\}_t\right]\}\Delta t\\ &= \{\dot{u}\}_t + \Delta t\,(1-\gamma)\{\ddot{u}\}_t + \frac{\gamma}{\beta\Delta t}\left(\{u\}_{t+\Delta t} - \{u\}_t\right) - \frac{\gamma}{\beta}\{\dot{u}\}_t\\ &\quad -\gamma\left(\frac{\Delta t}{2\beta} - \Delta t\right)\{\ddot{u}\}_t\\ &= \frac{\gamma}{\beta\Delta t}\left(\{u\}_{t+\Delta t} - \{u\}_t\right) + \left(1 - \frac{\gamma}{\beta}\right)\{\dot{u}\}_t\\ &\quad +\Delta t\left(1 - \frac{\gamma}{2\beta}\right)\{\ddot{u}\}_{t.}\end{aligned} \tag{12}$$

To solve the linear problem using the stiffness matrix $[K]$, the internal force $Q_{t+\Delta t}$ can be expressed as

$$\{Q\}_{t+\Delta t} = [K]\{u\}_{t+\Delta t}. \tag{13}$$

Thus, the Newmark-β method was implemented using the following equation:

$$\begin{aligned}&\left(\frac{1}{\beta\Delta t^2}[M] + \frac{\gamma}{\beta\Delta t}[C] + [K]\right)\{u\}_{t+\Delta t}\\ &= \{Q\}_{t+\Delta t} + [M]\left(\frac{1}{\beta\Delta t^2}\{u\}_t + \frac{1}{\beta\Delta t}\{\dot{u}\}_t + \left(\frac{1}{2\beta} - 1\right)\{\ddot{u}\}_t\right)\\ &\quad +[C]\left(\frac{\gamma}{\beta\Delta t}\{u\}_t + \left(\frac{\gamma}{\beta} - 1\right)\{\dot{u}\}_t + \left(\frac{1}{2\beta} - 1\right)\Delta t\{\ddot{u}\}_t\right).\end{aligned} \tag{14}$$

A linear program can be used when the stiffness matrix $[K]$ is substituted with $(\frac{1}{\beta\Delta t^2}[M] + \frac{\gamma}{\beta\Delta t}[C] + [K])$. When solving linear problems, the solutions of the dynamic equations are not affected by the value of Δt, when $\beta = 1/4$ and $\gamma = 1/2$, and they are all satisfied. In addition, when $\beta = 1/6$ and $\gamma = 1/2$, the solution is stable when Δt is less than a certain value, resulting in a conditional stable solution. However, when $\gamma > 1/2$, the solution exhibits a numerical decay.

3.2 Dynamic analysis model of the loess slope

3.2.1 Overview of the model

This numerical analysis of the dynamic response of a loess slope under seismic loading used a typical loess-slope model as the research object and established a two-dimensional simplified numerical calculation model, as shown in Figure 8. The model stratification was based on Kun (2020) for the stratification of the borehole data of the landslide. The distribution of the model soil layers from the top to bottom was Malan loess, Lishi loess, and bedrock. The thickness of the Malan loess layer is 15 m, Lishi loess layer is 7.5 m, and bedrock layer is 13.5 m. A finite-element two-dimensional slope model with a slope of 20° was established, and in order to compare it with the ground motion of the shaking-table model test, a total of nine observation points for the ground-motion parameter were arranged at the corresponding locations, including five slope locations (points 1–5) and four vertical slope top locations (points 6–9), as shown in Figure 9. An infinite-element boundary was used for the left and right boundaries of the model, and a fixed boundary was used at the bottom of the model. The finite-element cell size of the model was 2.5 × 2.5 m, and the infinite-element cell size was 2.5 × 10 m. Before the dynamic calculation, the model must be equilibrated for ground stresses because the soil material is used in an elastoplastic instantaneous model. Numerical calculations were first performed for the gravity analysis of the model (Bai, 2010), and predefined fields were created in the ground stress analysis step. The stresses obtained in the gravity analysis step were used as the initial stress conditions for ground stress analysis to achieve ground stress equilibrium. Finally, the model was dynamically analyzed.

3.2.2 Numerical calculation parameters and loadings of the loess slope

The kinetic parameters for the numerical calculation were adopted from the results of dynamic triaxial tests conducted by Zhijian et al. (2020) on *in situ* soil samples, and the soil material was selected as an elastoplastic material, satisfying the Moore–Coulomb yield criterion. The mechanical parameters of the model are listed in Table 5. The loading waveform had the same ground-motion acceleration time course as that of the shaking-table model test, as shown in Figure 5.

3.2.3 Numerical simulation acceleration and displacement clouds of the loess slope

The horizontal seismic acceleration distribution characteristics of the Minxian–Zhangxian *M*6.6 earthquake prototype loess slope were obtained using finite-element calculations (Figure 10). It can be observed from the figure that the acceleration response had an amplification effect with an increase in the slope height, and the

FIGURE 8
Structure of the finite-element 2D model of the prototype loess slope.

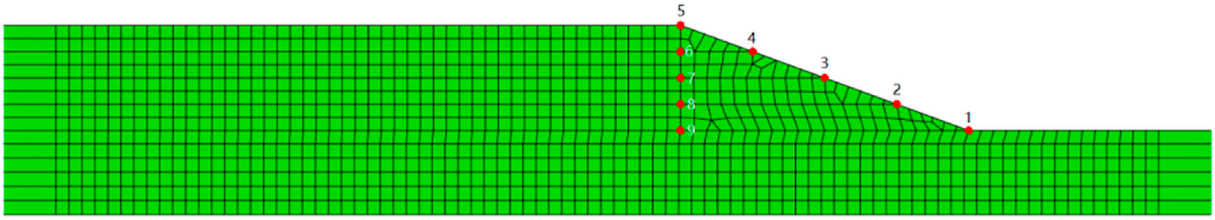

FIGURE 9
Grid division and observation point arrangement of the ground motion parameters of the prototype loess slope.

TABLE 5 Slope model mechanical parameters of soil layers.

Soil-layer name	Density (kg/m^3)	Modulus of elasticity (MPa)	Poisson's ratio	Cohesion (kPa)
Malan loess	1,520	61	0.33	25
Lishi loess	1,630	75	0.34	48
Bedrock	2,200	200	0.20	—

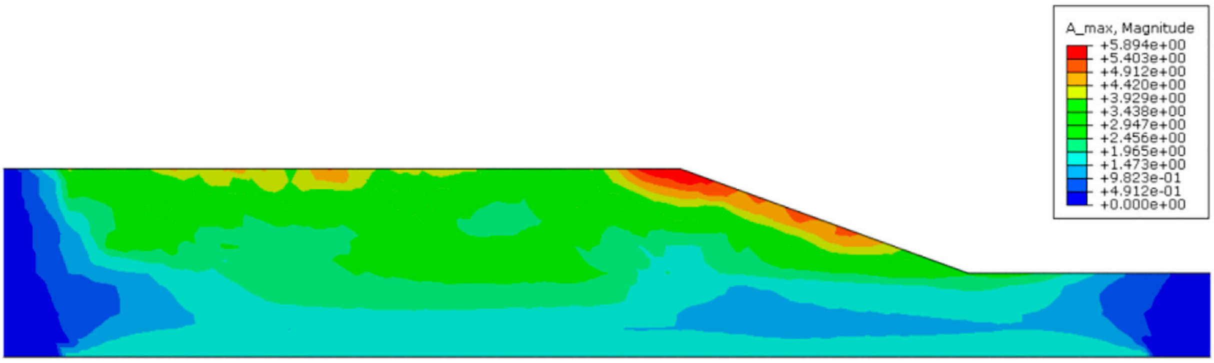

FIGURE 10
Seismic acceleration cloud of the loess slope by numerical simulation.

maximum value appeared at the top loess and the leading edge of the slope. The seismic displacement value showed a decreasing trend as the distance from the top loess edge of the slope increased.

The horizontal seismic displacement distribution characteristics of the Minxian–Zhangxian *M*6.6 earthquake prototype loess slope were obtained using finite-element

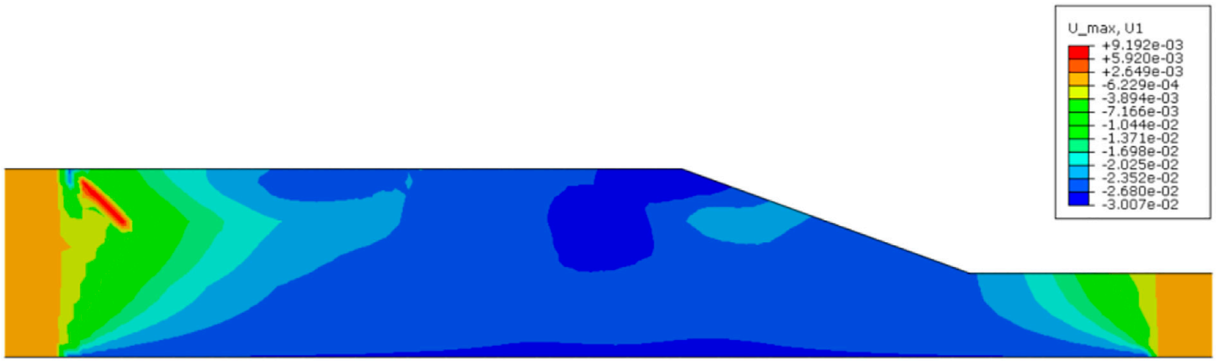

FIGURE 11
Seismic displacement cloud of the loess slope by numerical simulation.

calculations (Figure 11). It can be observed from the figure that the seismic displacement and acceleration response changes show a similar trend, and the seismic displacement response has an amplification effect with an increase in the slope height. The maximum value appeared at the top loess and leading edge of the slope, and the seismic acceleration value showed a decreasing trend as the distance from the top loess edge of the slope increased.

4 Comparative analysis of the shaker-model test and numerical simulation calculation results

4.1 Acceleration time range

Owing to the acquisition process, seismic acceleration waveforms are subjected to sensor drift and high-frequency noise interference from the surrounding environment, such as those originating from the model-box resonance. To eliminate these effects, all PGA data were baseline-corrected using SeismoSignal software during the post-processing stage of the experiment, and the corrected seismic acceleration waveforms were band-pass-filtered from 0.1 to 40 Hz. Figure 12 shows the time course of horizontal ground-shaking acceleration at each observation point when the shaking table and numerical simulation were subjected to a horizontal seismic wave with a PGA of 183.2 gal, in accordance with the Minxian–Zhangxian *M*6.6 earthquake. The ground-motion acceleration waveforms at these slope observation points were similar to the clear amplification effect, and the peak horizontal ground-motion acceleration observed in the numerical simulation was larger than that observed in the shaking-table test.

This study explored the dynamic response law of loess slopes by considering the variation characteristics of the slope surface seismic acceleration and internal vertical direction. For comparison, the dimensionless acceleration amplification factor (M_{PGA}) was introduced, and the ratio of the PGA at each measuring point of the slope surface and vertical section to that at measuring point 1 of the table surface, and measuring point 9 of the vertical section, was defined as the PGA amplification factor. The distribution law of the amplification factor represents that of seismic acceleration.

4.2 Comparative analysis of seismic acceleration response between the slope-model test and numerical simulation

Figures 13, 14 show the horizontal and vertical PGA and amplification factor curves for the model test and numerical simulation at each slope-measuring point under seismic-wave excitation, with a PGA of 183.2 gal, respectively. Figure 15 shows the PGA ratio of each measuring point in the model test and numerical simulation of the loess slope.

As shown in Figure 13, the horizontal PGA and amplification factors of the loess-slope surface and vertical section measured during the model test and numerical simulation under the same seismic wave excitation showed a clear linearity in elevation with great similarity, and the PGA measured by the model test was lower than that of the corresponding numerical simulation. The distribution of acceleration in the slope surface and vertical section showed regularity; that is, the PGA and amplification factors showed a linearly increasing trend with increasing elevation, and the amplification factors were similar at the same slope-measuring point.

From Figures 13A, C, it can be seen that under seismic wave excitation with a PGA of 183.2 gal, the horizontal PGAs of slope-measuring points 1, 2, 3, 4, and 5 of the model test were 1.55 m/s^2, 2.27 m/s^2, 2.22 m/s^2, 3.09 m/s^2, and 3.31 m/s^2, respectively, and the amplification factors of measuring points 2, 3, 4, and 5 were 1.46, 1.43, 1.99, and 2.14, respectively. The horizontal PGAs of

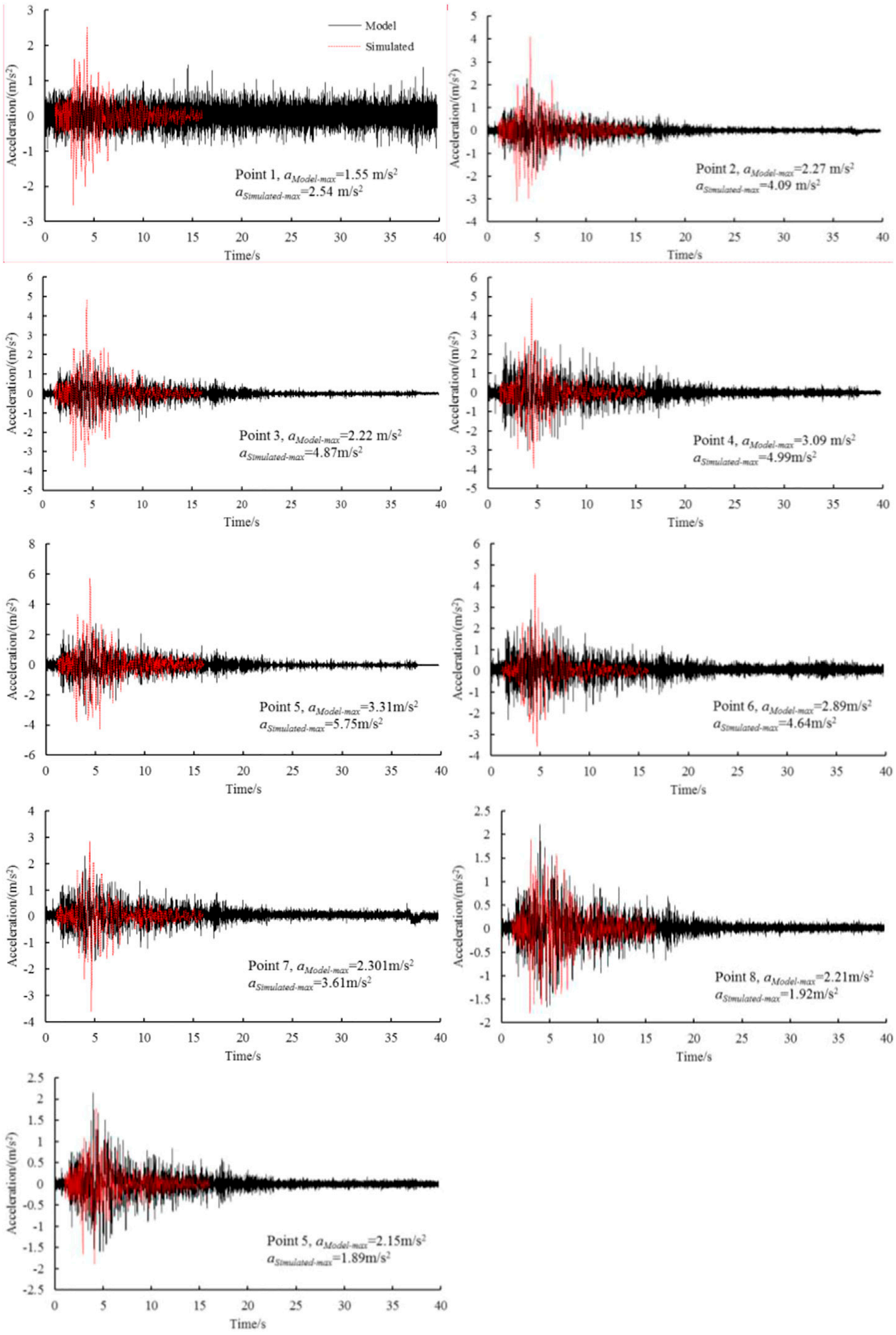

FIGURE 12
Time course of horizontal ground-motion acceleration at each measuring point of the slope under seismic wave excitation with a peak ground acceleration (PGA) of 183.2 gal used in the model test and numerical simulation.

slope-measuring points 1, 2, 3, 4, and 5 of the numerical simulation were 2.54 m/s^2, 4.09 m/s^2, 4.86 m/s^2, 4.99 m/s^2, and 5.75 m/s^2, respectively, and the amplification factors of measuring points 2, 3, 4, and 5 were 1.61, 1.92, 1.96, and 2.27, respectively, whereas the PGA amplification factors of both were extremely close to each other (Figure 13C). From Figures 13B, D, it can be observed that the horizontal PGAs of measuring points 9, 8, 7, 6, and 5 of the vertical section of the

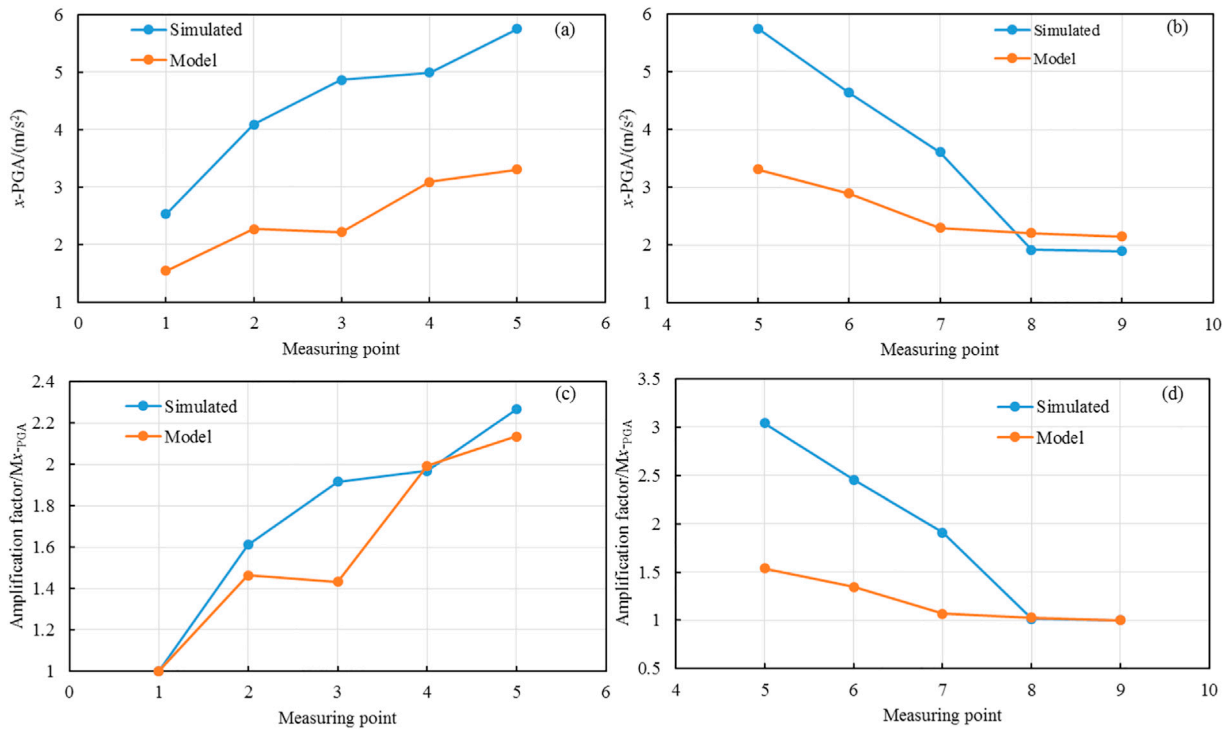

FIGURE 13
Horizontal PGA and amplification factors of each measurement point of the slope. **(a)** x-PGA of the loess-slope surface; **(b)** x-PGA of vertical section; **(c)** Amplification factor of x-PGA of the loess-slope surface; **(d)** Amplification factor of x-PGA of vertical section.

slope tested under seismic wave excitation with a PGA of 183.2 gal were 2.15 m/s^2, 2.21 m/s^2, 2.30 m/s^2, 2.89 m/s^2, and 3.31 m/s^2, respectively, and the amplification factors of measuring points 8, 7, 6, and 5 were 1.03, 1.07, 1.34, and 1.54, respectively. The horizontal PGA of the vertical section of the slope corresponding to its height was much lower than the value of the measuring point at the same height of the slope, and the amplification factor of the PGA was also lower than that at the same height of the slope (Figure 13B). The horizontal PGAs of measuring points 9, 8, 7, 6, and 5 of the numerical simulation of the slope were 1.89 m/s^2, 1.92 m/s^2, 3.61 m/s^2, 4.64 m/s^2, and 5.75 m/s^2, respectively, and the amplification factors of measuring points 8, 7, 6, and 5 were 1.02, 1.91, 2.45, and 3.04, respectively, whereas the amplification factors of both were similar to those of the horizontal direction with the change in elevation. However, the values differ greatly; that is, the amplification factors increased overall with increasing section elevation, but the amplification factors of the same measuring point in the numerical simulation were much larger than those of the shaking-table model test (Figure 13D).

From Figures 14A, C, it is observed that under seismic wave excitation with a PGA of 183.2 gal, the vertical PGAs of slope-measuring points 1, 2, 3, 4, and 5 of the model test were 0.60 m/s^2, 1.09 m/s^2, 1.07 m/s^2, 1.69 m/s^2, and 1.90 m/s^2, respectively, and the amplification factors of measuring points 2, 3, 4, and 5 were 1.81, 1.77, 2.80, and 2.99, respectively. The vertical PGAs of measuring points 1, 2, 3, 4, and 5 on the slope surface of numerical simulation were 0.33 m/s^2, 0.75 m/s^2, 1.27 m/s^2, 2.42, and 1.74 m/s^2, respectively, and the amplification factors of measuring points 2, 3, 4, and 5 were 2.29, 3.87, 7.35, and 5.31, respectively. However, the vertical PGA of the two were closer (Figure 14A), while the difference in amplification factors was larger (Figure 14C). Compared with the horizontal PGA values and amplification factors on the loess slope, the vertical PGA values were significantly smaller, but the amplification factors of the vertical PGA were larger. From Figures 14B, D, it can be observed that the vertical PGAs of the vertical section of the slope at measuring points 9, 8, 7, 6, and 5 of the model test under seismic wave excitation with a PGA of 183.2 gal were 0.56 m/s^2, 0.66 m/s^2, 1.37 m/s^2, 1.80 m/s^2, and 1.90 m/s^2, respectively, and the amplification factors of measuring points 8, 7, 6, and 5 were 1.18, 2.43, 3.21, and 3.39, respectively. The amplification factors of both were similar to the amplification factors of the vertical PGA with elevation, but the values were different; that is, the overall amplification factors increase with an increasing section elevation, but the amplification factors of the same measuring point in the numerical simulation were much

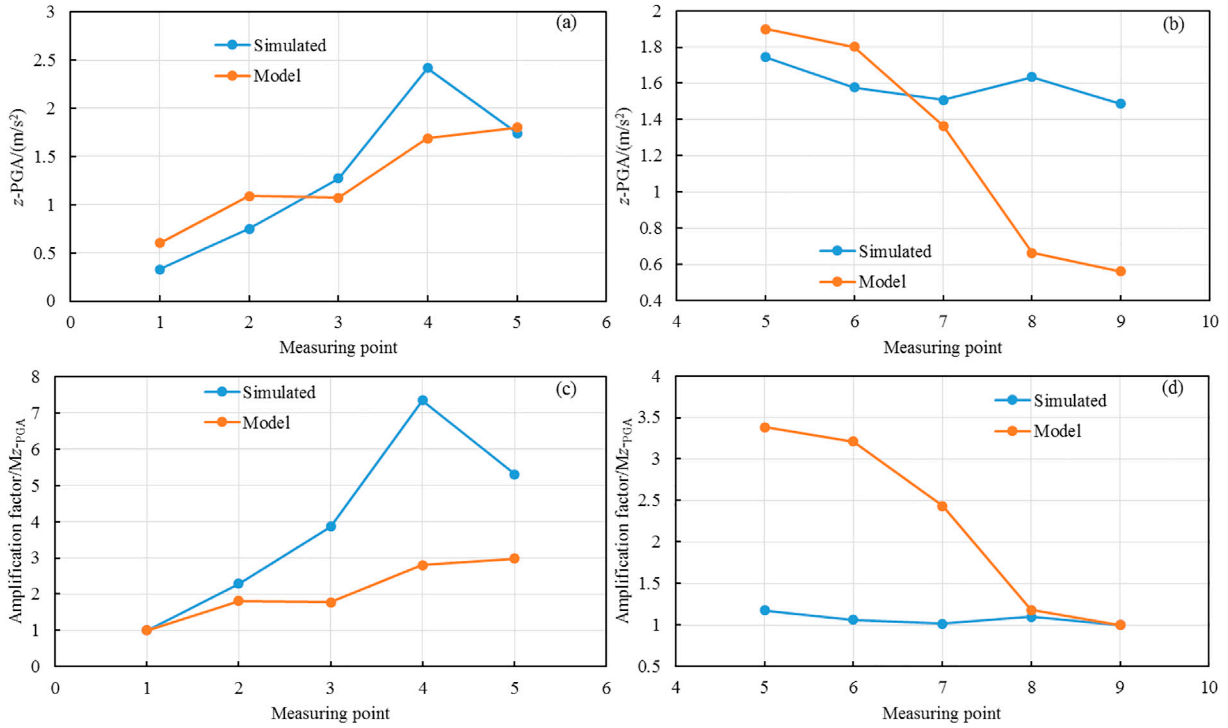

FIGURE 14
Vertical PGA and amplification factors of each measurement point of the slope. **(a)** z-PGA of the loess-slope surface; **(b)** z-PGA of vertical section; **(c)** Amplification factor of z-PGA of the loess-slope surface; **(d)** Amplification factor of z-PGA of vertical section.

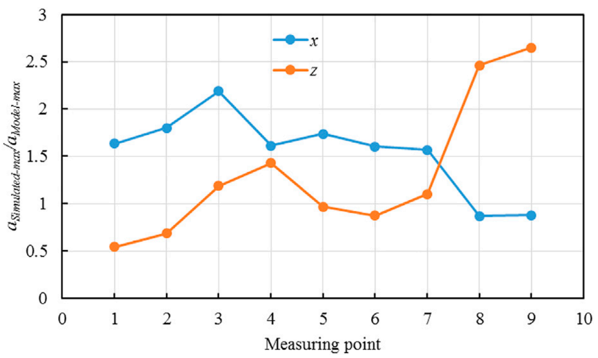

FIGURE 15
Ratio of the PGA at each measuring point using the model test and numerical simulation of the loess slope.

smaller than those of the shaking-table model test (Figure 14D) and the horizontal PGA.

As shown in Figures 13, 14, both the model tests and numerical simulations under the same seismic wave excitation conditions indicate that the loess slope exhibits a significant amplification effect along the elevation, and that there is a linear amplification of ground motion with a consistent trend on the slope surface. The results from both the model tests and numerical simulations verify that horizontal seismic forces under the natural earthquake action may be the main cause of loess slope damage.

It can be observed from Figure 15 that there is a similarity between the PGA ratios of measuring points 1–7 at the same elevation for the slope surface and vertical sections. The values of the horizontal PGA $a_{\text{Simulated-max}}/a_{\text{Model-max}}$ range from 1.5 to 2.2 and the values of the vertical PGA $a_{\text{Simulated-max}}/a_{\text{Model-max}}$ range from 0.5 to 1.5, indicating that the horizontal PGA measured by the numerical simulation is much larger than that measured by the model test for the slope surface and vertical section at the same elevation. However, the ratio of the vertical PGA was closer to 1.0, and the horizontal PGA measured by the numerical simulation was smaller than that measured by the model test. At measuring points 8–9 of the vertical section of the slope, the values of the horizontal PGA $a_{\text{Simulated-max}}/a_{\text{Model-max}}$ range from 0.86 to 0.88 and the values of the vertical PGA $a_{\text{Simulated-max}}/a_{\text{Model-max}}$ range from 2.45 to 2.65, which are different from the corresponding PGA ratios at measuring points 1–7. This large difference indicates that for the same elevation of the loess slope with a lower vertical section elevation, the position of the PGA inside the slope body is influenced by the physical model conditions and numerical simulation parameter settings, resulting in a large dispersion. This means that the numerical simulation is closer to the real measured ground-motion characteristics, whereas the model test displayed differences in the ground motion and curves owing to factors such as reshaping the soil and parameter settings. There are some differences between the main ground motions and the curves.

4.3 Spectrum analysis

4.3.1 Spectrum analysis method of strong ground motion

The spectral analysis of data from strong ground-motion observations is a process of Fourier transform and Fourier inverse transform. The value of N (even) of the time function at equal time interval points $x_m\,(m = 0, 1, 2, \ldots, N-1)$ is

$$\begin{aligned} A_k &= \frac{2}{N}\sum_{m=0}^{N-1} x_m \cos\frac{2\pi km}{N} \qquad k = 0, 1, 2, \ldots, N/2-1, N/2, \\ B_k &= \frac{2}{N}\sum_{m=0}^{N-1} x_m \sin\frac{2\pi km}{N} \qquad k = 1, 2, \ldots, N/2-1, \end{aligned} \tag{15}$$

where x_m is denoted as a finite trigonometric function with A_k and B_k as coefficients.

$$\begin{aligned} x_m = \frac{A_0}{2} + \sum_{k=1}^{N/2-1}\left[A_k \cos\frac{2\pi km}{N} + B_k \sin\frac{2\pi km}{N}\right] \\ + \frac{A_{N/2}}{2}\cos\frac{2\pi (N/2)m}{N}. \end{aligned} \tag{16}$$

Considering that this function is nothing but an approximation of the metric function x_t, we get

$$\begin{aligned} \tilde{x}(t) = \frac{A_0}{2} + \sum_{k=1}^{N/2-1}\left[A_k \cos\frac{2\pi kt}{N\Delta t} + B_k \sin\frac{2\pi kt}{N\Delta t}\right] \\ + \frac{A_{N/2}}{2}\cos\frac{2\pi (N/2)t}{N\Delta t}. \end{aligned} \tag{17}$$

Eq. 17 is a finite Fourier approximation of function *xt*. The coefficients *Ak* and *Bk* in Eq. 15 are を finite Fourier coefficients. The calculation of Eq. 15 is called the Fourier transform of the discrete value *xm*, and Eq. 16 is called the inverse Fourier transform.

Here, the introduction of the complex Fourier coefficient C_k implies

$$x_m = \sum_{k=0}^{N-1} C_k e^{i(2\pi km)} \qquad m = 0, 1, 2, \ldots, N-1. \tag{18}$$

More concisely, it can be expressed by the following equation, called the finite complex Fourier series:

$$C_k = \frac{1}{N}\sum_{m=0}^{N-1} x_m e^{-i(2\pi km/N)} \qquad k = 0, 1, 2, \ldots, N-1. \tag{19}$$

Eq. 19 is the Fourier transform, and Eq. 18 is the inverse Fourier transform. Using this calculation method, the observed data can be subjected to spectral analysis.

4.3.2 Comparative analysis between the model test and numerical simulation of the Fourier spectrum of each loess slope-measuring point

The Fourier spectrum characteristics of each measuring point of the slope surface and vertical section from model tests and numerical simulations were compared and analyzed by the Fourier transform. This was performed from the perspective of variations in seismic wave frequencies to explore the possible causes of differences in the seismic acceleration response of the slope due to model conditions and numerical simulation parameters.

The Fourier spectra of the horizontal and vertical seismic accelerations at each measuring point on the slope surface and vertical section of the loess slope for the model test and numerical simulation under the same ground motion are shown in Figure 16. The magnitude of the amplitude in the Fourier spectrum represents the amount of energy contained at the measuring point, and the difference in amplitude between the spectral lines represents the change in energy between the measuring points as the seismic wave passes through various parts of the soil. It can be observed from this figure that with an increase in the elevation, the spectral-line shapes of the different measuring points of the slope from both the model tests and numerical simulations were similar. From Figures 16A–I, it can be observed that under seismic wave excitation with a PGA of 183.2 gal, the horizontal first-principal frequency of the slope surface and vertical section of the model test was mainly concentrated at approximately 0.5 Hz at low frequency, the Fourier amplitude frequencies were mainly distributed between 0.1 and 12 Hz, and the amplitude value was between 2.83 and 3.81 m/s^2. The amplitude value was positively correlated with the overall slope height, and the spectral-line shapes of different measuring points showed similarities at different measuring points. The first main frequency in the horizontal direction of each measuring point in the numerical simulation of the slope surface and vertical section was concentrated around 2.0 Hz at low frequencies. The Fourier amplitude frequencies were distributed between 0.1 and 12 Hz, with an amplitude value ranging from 2.08 to 6.57 m/s^2. The amplitude was positively correlated with the overall slope height, and the spectral-line shapes of the different measuring points showed similarities. Figures 16A–I show seismic wave excitation with a PGA of 183.2 gal.

The first main frequency in the vertical direction at each measuring point of the slope surface and vertical section of the model test was similar to that in the horizontal direction, mainly concentrated at approximately 0.5 Â Hz, with low frequencies. The amplitudes were between 0.50 and 1.96 m/s^2, which are positively correlated with the overall slope height, and the spectral-line shapes of the different measuring points showed similarities. The first main frequency of the vertical direction of each measuring point in the numerical simulation of the slope surface and vertical section was mainly concentrated around

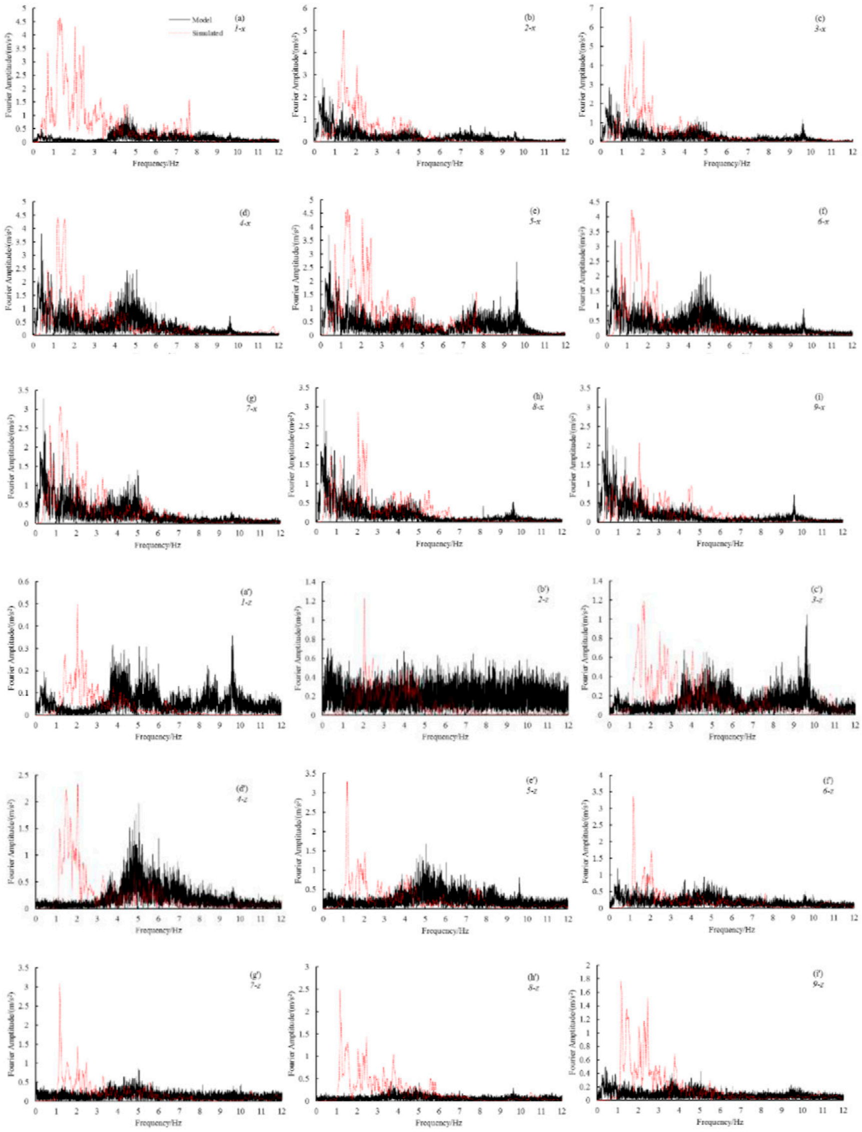

FIGURE 16
Fourier spectrum of each measuring point of the slope in the model test and numerical simulation.

2.0 Hz, with a low frequency, and the amplitude was between 1.19 and 3.36 m/s^2. The amplitude was positively correlated with the overall slope height, and the spectral-line shapes of the different observation points showed similarities. From the aforementioned details, although the same seismic wave input was used, the main frequencies of the Fourier spectrum of the model test and numerical simulation were different, and the latter was approximately four times that of the former. However, the main frequency of the Fourier spectrum of each measuring point of the model test and numerical simulation is different from that of the seismic wave input; however, the numerical simulation is closer and the curve is more similar, which means that the numerical simulation is closer to the real observed ground-motion spectrum characteristics, while the model test showed differences between the main frequency of the Fourier spectrum and the curve owing to the non-primary loess, the similarity ratio, and other possible factors.

It can be observed from Figure 17 that the Fourier spectrum amplitudes of measuring points 2–9 of the slope surface and vertical section, taking into account both the model test and numerical simulation of the slope at the same elevation measuring points, increased with the increasing elevation, and the trend was similar; however, the Fourier spectrum amplitudes of the numerical simulation were higher than those of the model test, and there were significant similarities between them and the corresponding PGA. The inconsistencies between the Fourier

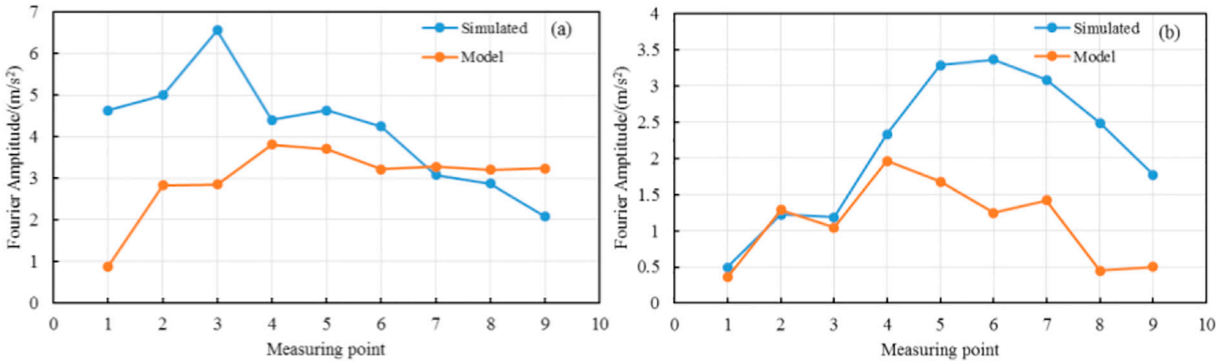

FIGURE 17
Comparison of Fourier spectrum amplitude at each measuring point of the slope between the model test and numerical simulation: **(A)** horizontal direction; **(B)** vertical direction.

spectrum amplitude at individual points and the overall trend in the figure are due to the presence of data errors caused by the discrete-model test-measuring data.

5 Conclusion

The dynamic response characteristics of a low-angle loess slope under the input of the same horizontal seismic wave load were studied through a combination of shaking-table model test and simulation calculations. The response law of seismic waves on the slope surface and body of the loess slope was explored, and the seismic acceleration Fourier spectra of the slope surface and section were analyzed. The following conclusions were drawn:

1) The PGA and peak ground displacement on the slope surface and internal vertical section of the loess slope both exhibited elevation amplification effects; that is, the closer to the top of the slope, the more evident the amplification effects. Under the same seismic load, the seismic acceleration waveforms of each loess slope-measuring point in the model test and numerical simulation were similar.
2) Under the same seismic load, the PGA and amplification factors of the slope and loess-slope vertical sections measured by the model test and numerical simulation showed clear linearity in elevation with great similarity, and the PGAs measured by the model test were lower than those of the corresponding numerical simulation. The Fourier spectrum amplitude for the same elevation measuring point of the slope in both the model test and numerical simulation increased with an increasing elevation, and there was a similar trend. However, the overall Fourier spectrum amplitude of the numerical simulation was higher than that of the model test, and there was a significant similarity between amplitude and the corresponding PGA.
3) There was a similarity between the ratios of the measuring points at the same elevation, with the values of the horizontal PGA $a_{\text{Simulated-max}}/a_{\text{Model-max}}$ ranging from 1.5 to 2.2 and the vertical PGA $a_{\text{Simulated-max}}/a_{\text{Model-max}}$ ranging from 0.5 to 1.5, indicating that for the loess slope at the same elevation and vertical section. However, for the vertical PGA, the ratio of the two was predominantly close to 1.0, and the horizontal peak acceleration measured by the numerical simulation was smaller than that measured by the model test.
4) Under the same seismic load, the first predominant frequency of the slope surface Fourier spectrum and the vertical section of the model test was concentrated at approximately 0.5 Hz (low frequency) and the amplitude was positively correlated with the overall slope height, whereas the spectral-line shapes at different measuring points exhibited similarities. The first predominant frequency of the Fourier spectra at the slope and vertical section of the numerical simulation was approximately 2.0 Hz, and the amplitude was positively correlated with the slope height.

Data availability statement

The original contributions presented in the study are included in the article/Supplementary Material, Further inquiries can be directed to the corresponding author.

Author contributions

YW: writing—original draft, visualization, formal analysis, and writing—review and editing. TX: numerical simulation. WZ: conceptualization, methodology, formal analysis, and writing—review and editing. WP: writing—review and editing. KL: physical modeling test.

Funding

Financial support for this project was provided by the Scientific Research Fund of Institute of Engineering Mechanics, China Earthquake Administration (Grant No. 2020EEEVL0304), the Second Tibetan Plateau Scientific Expedition and Research Program (STEP) (Grant no. 2019QZKK0905), the Scientific Research Fund of Institute of Earthquake Forecasting, China Earthquake Administration (Grant no. 2014IESLZ01), the National Natural Science Foundation of China (Grant nos. 51678545, 41472297, and U1939209), and the Topics of Gansu Province Key R&D Program (Grant no. 18YF1FA101).

Conflict of interest

The authors declare that the research was conducted in the absence of any commercial or financial relationships that could be construed as a potential conflict of interest.

Publisher's note

References

Bai, Jianfang (2010). *Introduction to site seismic response analysis*. Beijing, China: China Railway Press.

Bouckovalas, G. D., and Papadimitriou, A. G. (2005). Numerical evaluation of slope topography effects on seismic ground motion. *Soil Dyn. Earthq. Eng.* 25 (7-10), 547–558. doi:10.1016/j.soildyn.2004.11.008

Chen, T., Wu, Z. J., Ma, W, Wang, L. M, and Zeng, L. F. (2012). Study on the influence of site conditions on ground vibration amplification effect in loess areas. *J. Undergr. Space Eng.* 8 (05), 969–974.

Gao, Lin, Zhu, Tong, and Lin, Bei (2000). Similarity technique for dynamic structural model test. *J. Dalian Univ. Technol.* 40 (1), 1–8.

Jiang, Ming-jing (2019). New paradigm for modern soil mechanics: Geomechanics from micro to macro. *Chin. J. Geotechnical Eng.* 41 (2), 195–254. doi:10.11779/CJGE201902001

Liu, Kung (2020). "Earthquake-induced failure mechanism and stability evaluation of loess slope under rainfall effects," (Lanzhou, China: Lanzhou University). PhD Thesis.

Liu, T. S. (1985). *Loess and the environment*. Beijing, china: Ocean Press.

Lu, Xi-lin, Yue-qing, C. H. E. N., Chen, Bo, Huang, W., and Zhao, L. (2000). Shaking table test of dynamic soil-structure interaction system. *Seismic Eng. Eng. Vib.* 20 (4), 20–29.

Meunier, P., Hovius, N., and Haines, J. A. (2008). Topographic site effects and the location of earthquake induced landslides. *Earth Planet. Sci. Lett.* 275 (3-4), 221–232. doi:10.1016/j.epsl.2008.07.020

Murphy, W. (2006). "The role of topographic amplification on the initiation of rock slopes failures during earthquake," in *Landslides from massive rock slope failure*. Editors S. G. Evans, G. S. Mugnozza, A. Strom, and R. L. Hermanns (Springer), 49, 139–154.*Celano, Italy*2

Wang, H. Y., and Xie, L. L. (2010). Influence of topography on ground shaking in xishan park, Zigong. *J. Geophys.* 53 (7), 1631–1638.

Wang, Lanmin (2003). *Loess dynamics*. San Diego, CA: Seismic Press.

Wang, Lanmin, Pu, Xiaowu, Wu, Zhi-jian, Xu, X., and Liu, K. (2018). Shaking table tests of dynamic response of loess slopes under the coupling effects of earthquake and rainfalls. *Chin. J. Geotechnical Eng.* 40 (7), 1287–1293.

Wang, L. M., Che, A. L., and Wang, L. (2019). Characteristics and enlightenment of Hokkaido Ms6.7 earthquake disaster in Japan. *City Disaster Reduct.* 1, 1–8.

Wang, L. M., Pu, X. W., Chai, S., Wang, P., and Wang, Q. (2017c). "A performance-based design method of loess slopes under the coupling effects of earthquakes and rainfalls," in PBD III VANCOUVER Earthquake Geotechnical Engineering, Vancouver, Canada, July 16-19, 2017.

Wang, L. M., Wang, Q., Wu, Z. J., and Che., A. L. (2017a). "Loessial landslides induced by the minxian–zhangxian Ms6.6 earthquake of China in 2013," in *Geotechnical hazards from large earthquakes and heavy rainfalls* (Tokyo, Japan: Springer).

Wang, L., Sun, J., Wang, Q., Pu, X., and Wang, N. (2017b). "Physical mechanism and prevention method of loess slope failure induced by the coupling effect of earthquake and rainfall," in 16th World Conference on Earthquake, Santiago, Chile, January 09-13 2017.

Wang, L., Wua, Zhijian, Xia, Kun, Liu, K., Wang, P., Pu, X., et al. (2019). Amplification of thickness and topography of loess deposit on seismic ground motion and its seismic design methods. *Soil Dyn. Earthq. Eng.* 126, 105090–105112, 1–12. doi:10.1016/j.soildyn.2018.02.021

Wu, Zhi-jian, Wang, Lan-min, Wang, Ping, Chen, T., Shi, H., and Yang, X. p. (2013). Influence of site conditions on ground motion at far field loess sites during strong earthquake. *J. Cent. South Univ.* 20, 2333–2341. doi:10.1007/s11771-013-1741-2

Wu, Zhijian, Tian, Lei, Chen, Yujin, Wang, Ping., and Chai, Shao-feng. (2015). Deformation and instability characteristics of loess slope base on shaking table model. *J. Shanghai Jiaot. Univ.* 49 (7), 940–945.

Yasuhiro, Mitani, Wang, Fawu, Okeke, Austin Chukwueloka, and Qi, W. (2013). "Dynamic analysis of earthquake amplification effect of slopes in different topographic and geological conditions by using ABAQUS," in *Environmental science and engineering* (Berlin, Heidelberg: Springer).

Yuan, Wen-zhong (1998). *Similar theoretical and static model test*. Chengdu, China: Southwest Jiaotong University Press.

Zhang, Zelin, Wu, Shuren, and Wang, Tao (2018). Influence of seismic wave amplitude on dynamic response of loess-mudstone slope. *Rock Soil Mech.* 39 (7), 2403–2412.

frontiers | Frontiers in Earth Science

TYPE Original Research
PUBLISHED 30 January 2023
DOI 10.3389/feart.2022.1058386

EDITED BY
Yefei Ren,
China Earthquake Administration, China

REVIEWED BY
Ba Zhenning,
Tianjin University, China
Yushi Wang,
Beijing University of Technology, China

*CORRESPONDENCE
Yushan Zhang,
✉ hyszhang@163.com

SPECIALTY SECTION
This article was submitted to Structural Geology and Tectonics, a section of the journal Frontiers in Earth Science

RECEIVED 30 September 2022
ACCEPTED 05 December 2022
PUBLISHED 30 January 2023

CITATION
Yan J and Zhang Y (2023), One dimensional time-domain non-linear site seismic response analysis program integrating two hysteresis models of soil.
Front. Earth Sci. 10:1058386.
doi: 10.3389/feart.2022.1058386

One dimensional time-domain non-linear site seismic response analysis program integrating two hysteresis models of soil

Jingru Yan and Yushan Zhang*

China Earthquake Disaster Prevention Center, Beijing, China

In the numerical simulation of site seismic responses, traditional equivalent linearization methods typically realized in the frequency domain cannot satisfactorily analyze the high-degree non-linearity of soil under strong input motions. Therefore, the "true" non-linear numerical methods performed in the time domain are often utilized in such cases. However, a crucial element of the time-domain non-linear method, which is the hysteresis model of soil that describes the rule controlling the loading–unloading behavior of soil, has no established guidelines for earthquake engineering. Different researchers presented different models, revealing the epistemic uncertainty related to the dynamic properties of soil. Thus, the time-domain non-linear method should consider this uncertainty in practice. Therefore, in this study, a one-dimensional (1D) time-domain non-linear site seismic response analysis program was developed. The developed program was coded using Fortran95 and integrates two kinds of soil hysteresis models (i.e., extended Masing model and dynamic skeleton curve model). In both models, the damping correction was introduced to calibrate the hysteresis loop area toward the damping ratio measured in the dynamic triaxial test or resonant column test. Moreover, the temporospatial finite difference algorithm was used to resolve the 1D non-linear wave equation, and its precision was demonstrated in comparison with the results of the frequency-domain program for the linear case. Finally, the non-linear seismic response of a specific site was calculated by the proposed program. The findings of the fitting were compared to those of the two popular time-domain non-linear programs DEEPSOIL (Hashash, V6.1) and CHARSOIL (Streeter et al., CHARSOIL, Characteristics Method Applied to Soils, 1974 March 25). Simultaneously, the Japanese KIK-net strong motion observation station data were applied to validate the reliability of this program.

KEYWORDS

soil dynamics, soil modulus, non-linear hysteretic response, backbone curve, soil seismic response

1 Introduction

Many data on earthquake investigation and observation show that (Seal, 1988; Gao et al., 1996; Beresnev, 2002; Kokusho et al., 2008; Kim et al., 2013) local site conditions will directly affect the ground motion amplitude, spectral characteristics, and the distribution of earthquake disaster degree. The amplification effect of ground-to-ground motion must be considered in seismic zoning, seismic safety evaluation, and seismic design analysis of engineering sites. When the ground motion parameters of engineering site design are determined, it has to consider the influence of site conditions on ground motion amplification by using corresponding adjustment methods (Li, 2013). The adjustment relationship of site ground vibration parameter should be established based on many obtained strong vibration observation data and numerical calculation results of site model. In addition, the statistical relationship of site characteristic data and ground motion property spectrum has to be analysis to determine the adjustment model of site ground vibration parameters. This requires collecting sufficient basic data for research in addition to ensuring reasonable and reliable results. Site model with numerical calculation by means of the study of field adjustment should involve the soil seismic response calculation, the construction of the theoretical model, and the reasonable descriptions on the non-linear change of stress and strain of soil constitutive relationship. In this case, it can support the large-scale site numerical model for computing platform and improve the field response calculation efficiency.

At present, the frequency-domain equivalent linearization method and time-domain non-linear (TNL) method are the most widely applied in soil seismic response analysis. The influence of site soil conditions is analyzed by using a frequency-independent equivalent linearization method in China (Bo, 1998; Li et al., 2005; Li, 2010), which is widely used in engineering due to simple concept and small calculation. However, the equivalent linearization method is often no longer applicable in weak sites with large strain and strong non-linearity (Qi et al., 2010). To ensure the calculated results being consistent with the observed results, the TNL stepwise integration rule is proposed, which is a seismic response analysis method with clear physical significance and can more truly reflect the non-linear physical process of soil under stress state (Li, 1992). The true non-linear analysis method can describe the dynamic stress-strain non-linear hysteresis model of soil (Luan et al., 1994).

There are three aspects for the one-dimensional (1D) time-domain calculation method of the site non-linear seismic response, including the model of the soil skeleton curve, the soil loading-unloading-reloading criterion, and the time-domain integration method. The soil loading-unloading-reloading criterion was firstly established by Masing in 1926 (Masing, 1926). Later, it is revised continually and the empirical function form of the skeleton curve is proposed, which is a constitutive model that can better fit the test results (Pyke, 1979; Matasovic et al., 1993; Wang et al., 1981; Li, 1992; Luan, 1992; Chen, 2006; Qi et al., 2010; Martin et al., 1982; Yee et al., 2013). At present, the TNL constitutive models are widely applied in China, including Wang Zhiliang's extended Masing criterion (Wang et al., 1981), Li Xiaojun's dynamic skeleton curve (Li, 1992), Luan Maotian's true non-linear model (Luan et al., 1992), and Qi Wenhao's UE model (Qi et al., 2010). With the development of computer technology and engineering fluctuation, various site seismic reaction analysis programs have been developed based on soil constitutive model and time-domain numerical integration methods, which are widely applied in the international geotechnical seismic engineering. At present, the internationally well-known CHARSOIL program proposed by Streeter in 1974 (Streeter et al., 1974) is based on the finite difference method and uses the Ramberg-Osgood constitutive model to reflect the dynamic non-linear characteristics of soil. It is the first TNL soil seismic response analysis program in the world. However, it uses rigid boundary conditions, so sometimes the calculation results are not consistent with the actual situation. DEEPSOIL (Hashash, 2009) is a non-linear seismic response analysis program of 1D soil layer widely used abroad. It adopts a variety of numerical analysis methods (frequency-domain equivalent linearization methods and TNL methods), and introduces several constitutive models to describe the non-linear changes of soil in the TNL method. It can be applied for different soil layer earthquake responses. In addition to that, similar programs include DesRA-2C (Idriss et al., 1968), MASH (Martin et al., 1978), D-MOD (Kavazanjian and Matasovic, 1995), and ONDA (Diego et al., 2006).

The current dilemma of the TNL methods is analyzed as follows. On the one hand, the key elements of the current TNL method, namely the soil constitutive model describing the behavior of soil addition and unloading hysteresis, is not a universally accepted rule in seismic engineering. Therefore, most research focuses on developing a more scientific and reasonable method which can actually describe the non-linear dynamic changes of soil constitutive relationship. Based on previous studies and combination of the experiment data, a simplified constitutive model for complex mathematical correction with a variety of test soil parameters can be more reasonable to describe the dynamic skeleton curve model of the relationship. However, it ignores the analysis of cognitive uncertainty related to soil dynamic properties revealed by different constitutive models. In practical engineering applications, the TNL method considers this uncertainty and the good combination of developing constitutive models and engineering applications. On the other hand, more mature international geotechnical TNL method generally exist interface interaction with poor intuition and efficiency and more complex modelling process. In addition, it gives an upper limit on the calculation scale of site model and seismic

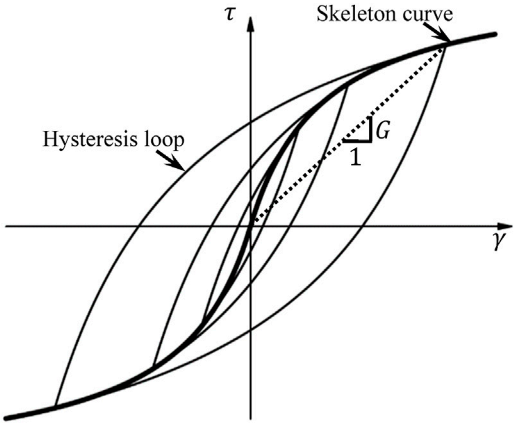

FIGURE 1
Soil skeleton curve.

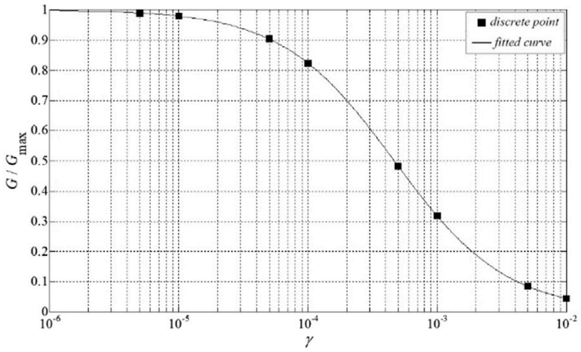

FIGURE 2
The shear modulus ratio curve.

input. The research trend of the field adjustment model based on many statistical results is to adopt a variety of computational methods and constitutive models for large-scale site seismic response, so as to eliminate the uncertain impact caused by the single frequency-domain equivalent linearization method and the small calculation site type. Therefore, it is imperative to develop efficient and diversified geotechnical non-linear calculation methods with independent property rights.

This work develops a new non-linear seismic response analysis program based on Fortran95, which integrates two hysteresis models of soil, namely extended Masing criterion and dynamic skeleton curve. Meanwhile, it introduces the damping correction coefficient to calibrate the lag ring area to match the damping ratio measured in dynamic triaxial test or resonance column test. It can store data by using dynamic array technology. In principle, there is no limit on the number of site models and the calculation scale of time and space points of input and output data. The results of this work can be used for calculation of large-scale site seismic response and uncertainty analysis of site calculation method, based on which the influence characteristics of site conditions on ground motion can be studied.

2 Soil skeleton curve model

The hyperbolic skeleton model is adopted to describe the soil skeleton curve, namely, a function of strain-stress. The soil skeleton curve model is described below by taking the shear deformation as an example. The vertices of stress-strain hysteresis cycles corresponding to different strain amplitudes are connected to each other to form the soil skeleton curve, as shown in Figure 1. If any point on the skeleton curve is connected to the origin, the slope of the resulting line is the cut modulus G corresponding to the point. In addition, due to the non-linear nature of the soil, the modulus is a function of the strain, namely $G = G(\gamma)$. The stress-strain relationship can be expressed as follows:

$$\boldsymbol{\tau}(\boldsymbol{\gamma}) = \boldsymbol{G}(\boldsymbol{\gamma})\boldsymbol{\gamma} \tag{1}$$

If a hyperbolic function is employed to describe a 1D soil constitutive model, Eq. 1 above can be expressed as follows:

$$\boldsymbol{\tau}(\boldsymbol{\gamma}) = \boldsymbol{G}_{\mathbf{max}} \frac{\boldsymbol{\gamma}_{\mathbf{r}}\boldsymbol{\gamma}}{|\boldsymbol{\gamma}| + \boldsymbol{\gamma}_{\mathbf{r}}} \tag{2}$$

In the equation above, $G_{\max}$ is the maximum shear modulus, and the tangent shear modulus corresponding to the zero strain was shown in Figure 1. Then, if the shear wave velocity is c and the mass density is ρ, then below relation can be obtained:

$$\boldsymbol{G}_{\mathbf{max}} = \boldsymbol{\rho}\boldsymbol{c}^2 \tag{3}$$

In Eq. 2, γ_r is the reference strain that can be obtained from the test data regression. The Eq. 4 can be acquired based on Eqs 1, 2:

$$\boldsymbol{G}(\boldsymbol{\gamma}) = \frac{\boldsymbol{\gamma}_{\mathbf{r}}}{|\boldsymbol{\gamma}| + \boldsymbol{\gamma}_{\mathbf{r}}} \boldsymbol{G}_{\mathbf{max}} \tag{4}$$

Thus:

$$\frac{\boldsymbol{G}_{\mathbf{max}}}{\boldsymbol{G}(\boldsymbol{\gamma})} = \mathbf{1} + \frac{|\boldsymbol{\gamma}|}{\boldsymbol{\gamma}_{\mathbf{r}}} \tag{5}$$

Typically, dynamic triaxial or resonant column tests can provide discrete data between the shear modulus ratio $G(\gamma)/G_{\max}$ and the shear strain γ. Based on the model given in Eq. 5, the reference strain γ_r can be regressed by the least square method. For example, the discrete data points in Figure 2 can be regressed and substituted into Eq. 5, based on which the shear modulus ratio curve can be obtained (the solid line in the figure). The discrete points in Figure 2 are not

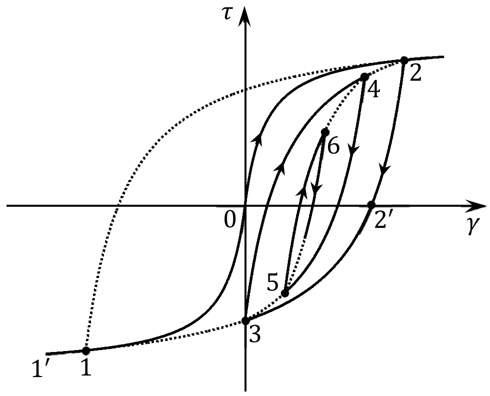

FIGURE 3
The extended Masing criterion (without considering damping correction).

the original test data, but the modulus ratios under different strains are obtained by fitting the test data using Eq. 5. Therefore, the curve by fitting the hyperbolic model shown in Eq. 5 naturally coincides with the discrete data points. Those processed by the actual calculation are the discrete data points shown in Figure 2.

In this work, the hyperbolic model can describe the soil skeleton curve.

3 Soil loading and unloading criterion

After the soil skeleton curve is defined, the corresponding loading and unloading criteria should be set to fully describe the loading-unloading-reloading dynamic process of the soil under the complex cyclic load. This work provides two addition and unloading criteria by previous study: extended Masing criteria proposed by Wang Zhiliang (Wang et al., 1981) and dynamic skeleton curve proposed by Li Xiaojun (Li, 1992).

3.1 Extended Masing criterion

The extended Masing criterion is widely used in seismic engineering. It is developed on the basis of Masing Criterion (Masing, 1926) and proposed by Wang Zhiliang. Its basic rules are as follows:

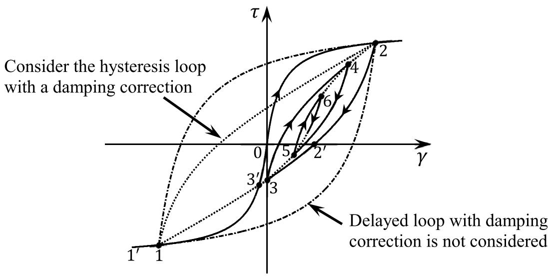

Consider the hysteresis loop with a damping correction

Delayed loop with damping correction is not considered

FIGURE 4
Extended Masing criterion (damping correction not considered).

1) During the initial loading, the stress-strain relationship follows the skeleton curve $\tau(\gamma) = f(\gamma)$.
2) During the unloading and reverse loading, the tangent modulus at the initial unloading is equal to the maximum shear modulus $G_{\max}$ of soil, and the stress-strain relation curve shows the "double" relationship with the original skeleton curve:

   $$\frac{\tau - \tau_c}{2} = f\left(\frac{\gamma - \gamma_c}{2}\right) \tag{6}$$

   If the hyperbolic model shown in Eq. 2 is used, Eq. 6 can be expressed as follows:

   $$\tau = \tau_c + 2G_{\max}\frac{\gamma_r(\gamma - \gamma_c)}{|\gamma - \gamma_c| + 2\gamma_r} \tag{7}$$

   In the above equations, τ_c and γ_c are the stress and strain values corresponding to the nearest inflection point of the stress-strain curve, respectively.

3) If the stress-strain curve of unloading and reverse loading intersects the skeleton curve, the subsequent stress-strain relation curve follows the skeleton curve, satisfying the "upper skeleton curve" rule;
4) If the unloaded and reverse loaded stress-strain curve intersects the previous load-unloading curve, the subsequent stress-strain curve follows the previous stress-strain curve, which is the upper circle rule.

According to the above extended Masing criterion, the 1D non-linear dynamic stress-strain relation of soil can be given for any dynamic loading process.

Figure 3 shows the hysteretic process of soil loading, unloading, and reloading under the extended Masing criterion. During the initial loading, the stress-strain relationship follows the skeleton curve, namely the 0→2 curve. If unloading is performed at point 2 and loading is realized in the direction after unloading to zero stress point 2′, the unloading-reverse loading curve follows curve 2→2′→1 in Figure 3. The unloading-reverse loading curve intersects the skeleton curve at point 1, which is symmetric about the origin. When the stress-strain relationship reaches point 1 along the curve 2→2′→1, the subsequent reverse loading curve follows the skeleton curve 1→1′. If the stress-strain

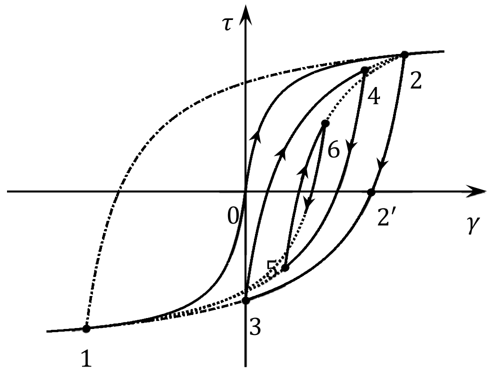

FIGURE 5
Dynamic skeleton curve criterion (damping correction not considered).

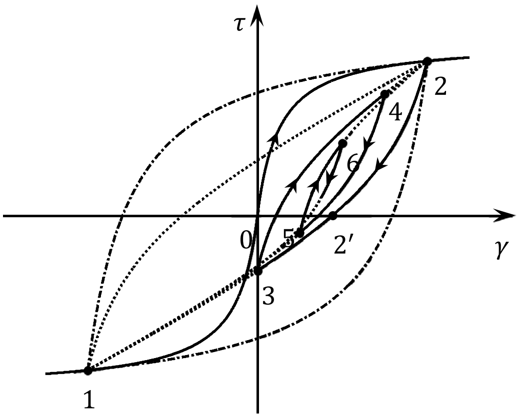

FIGURE 6
Dynamic skeleton curve criterion (damping correction considered).

relationship is reverse unloaded and reloaded along the curve 2→2′→1, the stress-strain curve follows the line 1→2. The expression of the curve 2→2′→1 can be determined by Eq. 7 according to the above rule (2). In the equation, τ_c and γ_c are corresponding stress and strain at point 2, respectively. The slope of tangent line of curve 2→2′→1 at point 2 is equal to that of the skeleton curve at point 0, which is the maximum shear modulus $G_{\max}$.

In the above unloading-reverse loading process 2→2′→1, if reverse loading is carried out at point 3, the reverse unloading-reverse loading curve still can be determined according to Eq. 7. It illustrates that the curve determined in such way necessarily intersects the skeleton curve at point 2 and the unload-reverse loading curve 2→2′→1. Therefore, this reverse unloading-reloading curve will follow the 3→4→2 curve. If this reverse unloading-reloading process reaches point 2, then the skeleton curve is followed if loading continues, and the above unloading-reloading curve 2→2′→1 is followed if unloading.

If the reverse unloading and reloading process 3→4→2 is unloaded and reverse loaded after reaching point 4, the unloading and reverse loading curve 4→5 can be obtained by substituting the stress and strain corresponding to point 4 into Eq. 7. In this case, the extension line of the curve should meet the corresponding "big circle," that is, the unloading and reverse loading curve 2→2′→1 of the upper layer reaches point 3. If the unloading and reverse loading process 4→5→3 reaches point 3, the subsequent reverse loading curve follows the curve 3→1 with the principle of "upper big circle" if the revserse loading continues. If this unload-reverse loading process 4→5→3 reaches point 3, the reverse unloading and reverse loading process 3→4→2 above is repeated.

The figures above illustrate the rules that should be followed in the stress-strain relationship of soil under the extended Masing criterion.

The soil-like non-linear dynamic parameter test demonstrates the relationship between shear modulus ratio and damping ratio-shear strain. An analytical representation of the soil skeleton curve can be obtained based on the relationship between the shear modulus ratio and shear strain shown in Figure 3. In combination with the above expansion Masing criteria, the soil retardation curve under equal amplitude cyclic load is obtained, including the hysteresis loops 2→2′→3→1→2 and 4→5→3→4. The area of the resulting lag loop is different from that of the damping ratio corresponding to the maximum strain (i.e., half of the difference between the maximum strain and the arrested loop). To correct this deviation, the damping correction coefficient $K(\gamma_0)$ should be included in the stress-strain skeleton curve.

After that, the stress-strain relationship of soil is obtained based on the extended Masing criterion, which can be expressed as Eq. 8:

$$\tau(\gamma) = \begin{cases} \tau_{c,i} + K\left(\left|\frac{\gamma_0}{2}\right|\right)\left[\frac{G_0(\gamma - \gamma_{c,i})}{1 + \left|\frac{(\gamma - \gamma_{c,i})}{2\gamma_r'}\right|} - \frac{\tau_0}{\gamma_0}(\gamma - \gamma_C)\right] + \frac{\tau_0}{\gamma_0}(\gamma - \gamma_{c,i}), & \text{Non skeleton curve} \\ \frac{G_0\gamma}{1 + \frac{|\gamma|}{\gamma_r}}, & \textit{Skeleton curve} \end{cases} \tag{8}$$

If the stress-strain state point is under the skeleton curve, the above equation is applicable for calculation; otherwise, the following equations are applicable:

$$\gamma_0 = \left|\gamma_{c,i-1} - \gamma_{c,i}\right| \tag{9}$$

$$\tau_0 = \left|\tau_{c,i-1} - \tau_{c,i}\right| \tag{10}$$

$$\gamma_r' = \left(\frac{2G_0}{\left|\tau_{c,i-1} - \tau_{c,i}\right|} - \frac{2}{\left|\gamma_{c,i-1} - \gamma_{c,i}\right|}\right)^{-1} \tag{11}$$

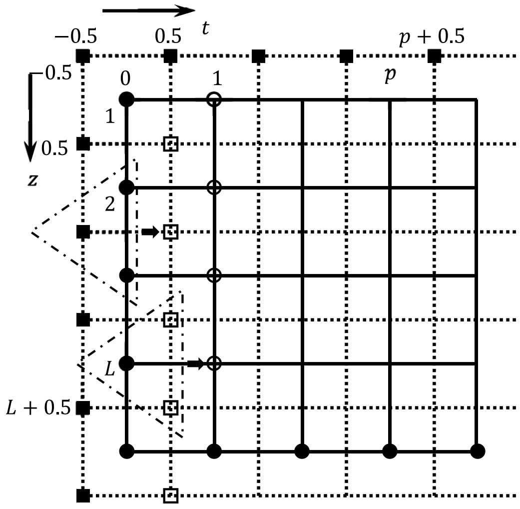

FIGURE 7
Space-time explicit finite difference grid.

$$K(\gamma_0)=\frac{\pi\gamma_0^2\lambda(\gamma_0)}{2\gamma_0(2\gamma_r'+\gamma_0)-4\gamma_r'(\gamma_r'+\gamma_0)\ln\left(1+\gamma_0/\gamma_r'\right)}\qquad(12)$$

In the above equations, $\tau_{c,i}$ and $\gamma_{c,i}$ are the shear stress and shear strain for the current moment before the last inflection point, respectively; $\tau_{c,i-1}$ and $\gamma_{c,i-1}$ are the turning points before $(\gamma_{c,i},\tau_{c,i})$, G_0 is the elastic shear modulus, namely the skeleton curve at the origin of tangent slope ($G_{\max}$), and $\lambda(\gamma_0)$ is the damping ratio corresponding to the strain amplitude γ_0, which can be calculated by fitting the function relation to the discrete data or directly interpolated to the discrete data.

Equation 12 defines the correction coefficient, which is introduced for better consideration of the damping fit. The soil stress-strain change corresponding to Figure 3 is given in Figure 4, which considers the damping correction according to the hysteresis curve. It suggests that after the damping correction, the "double" relationship between the unloading-reverse loading curve and the skeleton curve is no longer satisfied, and the area of the damping correction is the same as the damping circle corresponding to the test damping ratio. Moreover, for the correction case shown in the figure, the two branches of the hysteresis curve intersect in the skeleton curve. In this case, the unloading-reverse loading curve determined in Eq. 8 intersects the skeleton curve in advance without adopting the "upper skeleton curve" criterion. In Figure 4, the unloading-reverse loading curve 2→2′→3→1 intersects the skeleton curve even at the point 3′, but the upper skeleton curve criterion is followed at point 1. Therefore, both the "upper skeleton curve" criterion and the "upper large circle" criterion are based on whether the current stress-strain curve reaches and exceeds the previous inflection point. For the first loading, the first inflection point appears (point 2 in Figure 4), then the previous inflection point is symmetrical with the origin (point 1). Therefore, the unloading-reverse loading process from point 2 follows the curve 2→2′→3→1.

3.2 Dynamic skeleton curve criteria

When the soil stress-strain arrest behavior is described by using the extended Masing criteria, it should repeatedly remember and identify the current inflection point and its previous inflection point. It will be more complex and detrimental to programs when the cyclic load is complex (such as ground motion input). Due to the complexity and uncertainty of the dynamic characteristics of the soil, the hysteresis criterion based on the dynamic skeleton curve proposed by Li (1992) remembers and identifies the current inflection point and the maximum inflection point of stress-strain history while showing the basic characteristics of the Masing criterion, so it is easier to implement.

The dynamic skeleton curve describes the loading-unloading hysteresis criterion for 1D soil based on the following three basic hypotheses:

1) During the initial loading, the stress-strain relationship curve coincides with the soil skeleton curve;
2) During the unloading and reverse loading, the stress-strain relationship curve directly points to the absolute maximum stress-strain point of the stress-strain history or its reverse symmetry point, enabling that the stress and strain relationship curve and the skeleton curve meet the "double" relationship for the equal amplitude cyclic load process;
3) The stress and strain relationship curve of the subsequent loading process after meeting with the skeleton curve will follow the skeleton curve.

The above hypotheses are not the exactly same as those of the extended Masing criterion, where it assumes that hypothesis (3) is the "upper skeleton curve" criterion. The biggest difference between the two is the above hypothesis (2). In the extended Masing criterion, the unloading-reverse loading stress-strain relationship curve points to the previous inflection point of the current inflection point. While in the dynamic skeleton curve criterion, it points directly to the absolute maximum stress-strain point of the stress-strain history or its reverse symmetry point.

According to the above hypotheses, the relationship between soil shear stress and strain corresponding to the hyperbolic dynamic skeleton curve criterion can be obtained as follows:

$$\tau(\gamma)=\begin{cases}\tau_C+K\left(\left|\frac{\gamma_0}{2}\right|\right)\left[\frac{G_0(\gamma-\gamma_C)}{1+\left|\frac{(\gamma-\gamma_C)}{2\gamma_r'}\right|}-\frac{\tau_0}{\gamma_0}(\gamma-\gamma_C)\right]+\frac{\tau_0}{\gamma_0}(\gamma-\gamma_C), & |\gamma|\leq\gamma_M\\ \frac{G_0\gamma}{1+\frac{|\gamma|}{\gamma_r}}, & |\gamma|>\gamma_M\end{cases}\qquad(13)$$

TABLE 1 Computational model of site 1.

Layer number	Soil class	Shear-wave speed (m/s)	Density (g/cm^3)	Depth (m)
1	Sandy soil	300	1.90	50.0
2	Clay	400	2.00	30.0
3	Enter a semi-space	600	2.05	-

TABLE 2 Computational model of site 2.

Layer number	Soil class	Shear-wave speed (m/s)	Density (g/cm^3)	Depth (m)
1	Plain fill	129	1.9	1
2	Medium sand	149	1.95	1.8
3	Medium sand	144	1.95	1.8
4	Silty clay	116	2	1.5
5	Medium weathered basalt	778	2.15	2.7
6	Medium weathered basalt	1088	2.15	2.7
7	Medium weathered basalt	953	2.15	2.7
8	Medium weathered basalt	884	2.15	2.7
9	Medium weathered basalt	1023	2.15	2.7
10	Medium weathered basalt	839	2.15	2.4
11	Strong weathering tuff	391	2.05	1
12	Silty clay	383	2.1	2.4
13	Silty clay	423	2.15	2.9
14	Silty clay	442	2.15	2.9
15	Dilty clay	450	2.15	2.9
16	Silty clay	428	2.15	2.9
17	Silty clay	394	2.15	2.9
18	Silty clay	419	2.15	2.9
19	Silty clay	458	2.15	2.9
20	Silty clay	519	2.15	2.9
21	Silty clay	534	2.15	2.9
22	Silty clay	551	2.15	2.9
23	Silty clay	583	2.15	2.9
24	Silty clay	625	2.15	2.7
25	Enter a semi-space	625	2.15	-

In the above relationship,

$$\gamma_0 = \pm\gamma_M - \gamma_C \tag{14}$$

$$\tau_0 = \pm\tau_M - \tau_C \tag{15}$$

$$\gamma_r' = \left(\frac{\pm 2G_0}{\pm\tau_M - \tau_C} - \frac{\pm 2}{\pm\gamma_M - \gamma_C}\right)^{-1} \tag{16}$$

$$K(\gamma_0) = \frac{\pi\gamma_0^2\lambda(\gamma_0)}{2\gamma_0(2\gamma_r' + \gamma_0) - 4\gamma_r'(\gamma_r' + \gamma_0)\ln\,(1 + \gamma_0/\gamma_r')} \tag{17}$$

γ_M *and* τ_M are the absolute values of the maximum strain and the strain and stress history before the current moment, or the absolute values the maximum inflection point of the strain and stress

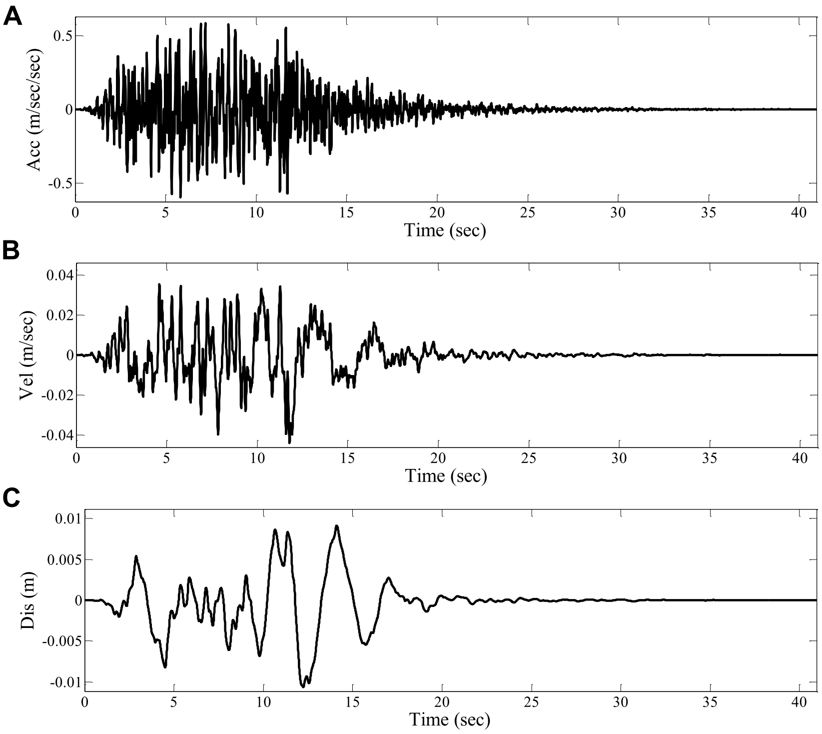

FIGURE 8
Time history curve of upgoing wave at the top of input half space **(A)** Accelerated speed. **(B)** Velocity. **(C)** Displacement.

before the current moment, respectively; γ_C and τ_C are the strain and stress corresponding to the last inflection point before the current moment, respectively; G_0 refers to the elastic shear modulus, namely the slope of the tangent line of the skeleton curve at the origin; $\lambda(\gamma_0)$ is the damping ratio related to the strain amplitude; and $K(\gamma_0)$ is the correction coefficient introduced by considering the damping fitting. In the above format, the selection criterion of ± sign is as follows: if the strain increment is positive, the + sign is selected; otherwise, the - sign is selected.

Equation 17 is the same form as Eq. 12, but the definition γ_r' is different.

Without the damping correction, $K = 1.0$. Figure 5 shows the soil stress-strain relationship curve based on the dynamic skeleton curve criterion. For the initial loading, point 2 and point 1 are the first inflection point and the corresponding previous one, respectively. At this point, point 1 coincides with the historical maximum stress-strain point, so the unloading-reverse loading curve 2→2′→3→1 from point 2 is exactly the same curve under the extended Masing criterion shown in Figure 3. For subsequent unloading inflection points 4 and 6 in the figure, the previous inflection points are inflection points 3 and 5 (defined here as the reverse unloading points). When the historical maximum stress-strain point is point 2, and the reverse point is point 1. Therefore, following the dynamic skeleton curve criterion, the unloading-reverse loading process starting from unloading points 4 and 6 will follow the curves 4→1 and 6→1 in Figures 2.2 and 2.3, respectively, in which the reverse point directly points to the historical maximum stress-strain point. According to the extended Masing criteria, the curves of the two unloading-reverse loading processes will point to the previous inflection point, namely inflection points 3 and 5 (Figure 3), which is the difference between the two criteria. Figure 6 illustrates the stress-strain relation curve obtained by considering the dynamic skeleton curve criterion after damping correction.

3.3 Time-space finite difference method

In this work, the finite difference method is employed to discretize the time-domain and the space-domain. The dynamic equilibrium equation of the 1D wave can be written as follows:

$$\frac{\partial \tau}{\partial z} = \rho \frac{\partial v}{\partial t} \tag{18}$$

The deformation coordination condition is expressed as follows:

$$\frac{\partial \gamma}{\partial t} = \frac{\partial v}{\partial z} \tag{19}$$

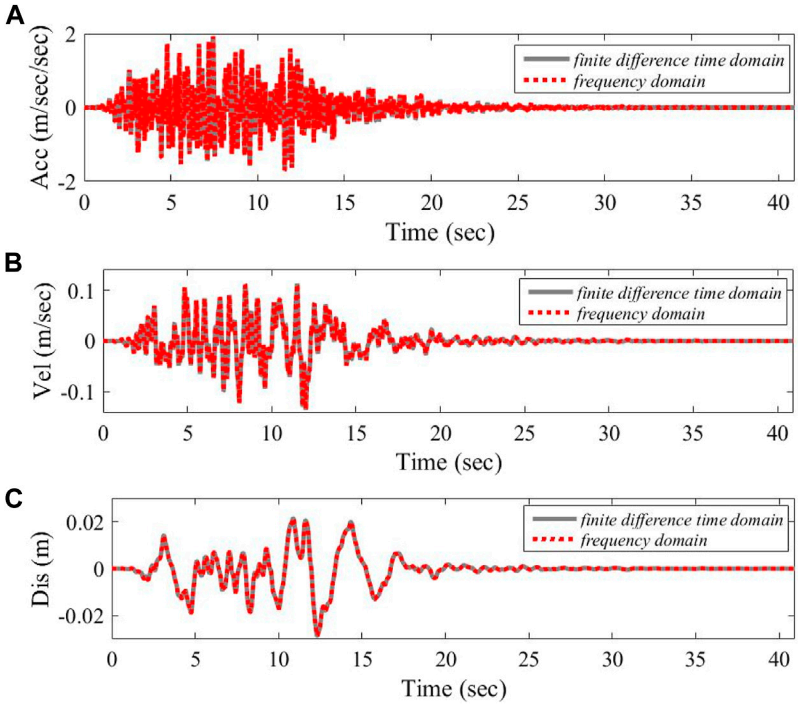

FIGURE 9
Comparison between ground motion time history curves of site 1. **(A)** Accelerated speed. **(B)** Velocity. **(C)** Displacement.

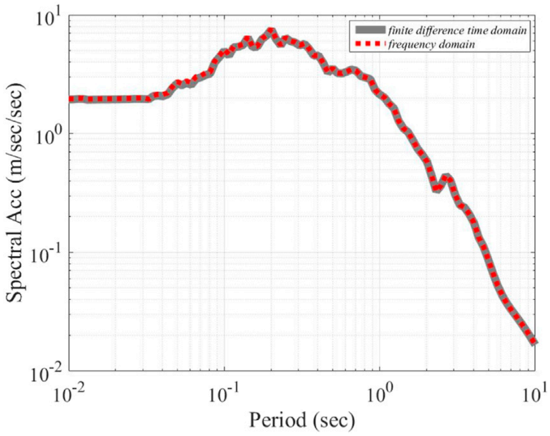

FIGURE 10
Comparison of ground motion response spectrum curves of site 1.

The non-linear constitutive equation between stress and strain is expressed as follows:

$$\tau = \tau(\gamma) \tag{20}$$

In the several equations above, $\tau = \tau(z,t)$ is the shear stress, $v = v(z,t)$ refers to the particle motion velocity, and $\gamma = \gamma(z,t)$ is the medium shear strain. Eqs 18–20 constitute a complete non-linear 1D wave equation.

Before the dynamic equation difference is solved differentially, each soil layer should be subdivided according to corresponding stability conditions of the differential format. Because the space-time center difference scheme is adopted to solve the dynamic equation in this work, the thickness of each soil layer after the subdivision layer should satisfy Eq. 21 below:

$$\Delta z_l \geq c_{s,l} \Delta t \tag{21}$$

Δz_l is the thickness of the first soil layer (sequence numbered from free surface to substrate), $c_{s,l}$ is the shear wave speed of the first soil layer, and Δt refers to the interval of calculation time.

To ensure smaller calculation error caused by spatial discretization, the thickness of each calculated soil should satisfy the below relationship as much as possible:

$$\frac{\Delta z_l}{\Delta z_m} = \frac{C_{s,l}}{C_{s,m}} \tag{22}$$

After spatial-temporal discretization of Eqs 18–20 by using the central difference method, the following explicit difference stepwise integral scheme can be acquired:

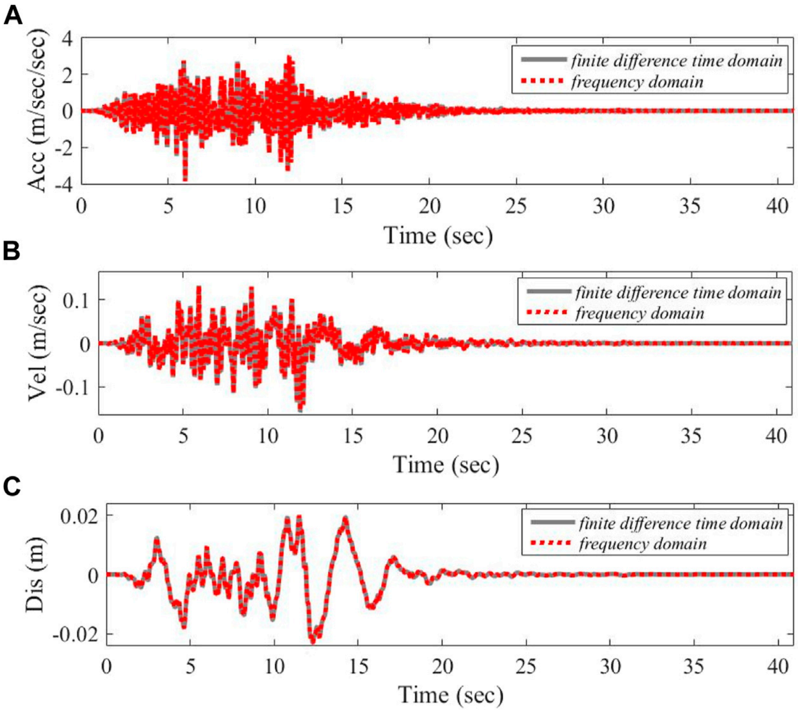

FIGURE 11
Comparison between ground motion time history curves of site 2. **(A)** Accelerated speed. **(B)** Velocity. **(C)** Displacement.

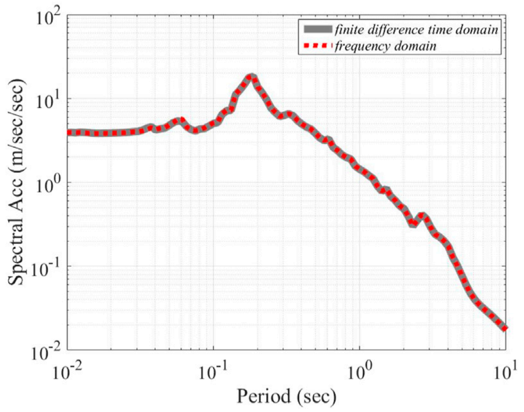

FIGURE 12
Comparison of ground motion response spectrum curves of site 2.

$$\left.\begin{aligned}
&\rho_l^{'}\frac{v_l^p - v_l^{p-1}}{\Delta t} = \frac{\tau_{l+0.5}^{p-0.5} - \tau_{l-0.5}^{p-0.5}}{\Delta z_l^{'}}\\
&\frac{\gamma_{l+0.5}^{p+0.5} - \gamma_{l+0.5}^{p-0.5}}{\Delta t} = \frac{v_{l+1}^p - v_l^p}{\Delta z_l}\\
&\tau_{l'}^{p'} = \tau\left(\gamma_{l'}^{p'}\right)
\end{aligned}\right\} \tag{23}$$

They can be rewritten as follows:

$$\left.\begin{aligned}
&v_l^p = v_l^{p-1} + \frac{\Delta t}{\rho_l^{'}\Delta z_l^{'}}\left(\tau_{l+0.5}^{p-0.5} - \tau_{l-0.5}^{p-0.5}\right)\\
&\gamma_{l+0.5}^{p+0.5} = \gamma_{l+0.5}^{p-0.5} + \frac{\Delta t}{\Delta z_l}\left(v_{l+1}^p - v_l^p\right)\\
&\tau_{l'}^{p'} = \tau\left(\gamma_{l'}^{p'}\right)
\end{aligned}\right\} \tau_{l'}^{p'} = \tau\left(\gamma_{l'}^{p'}\right) \tag{24}$$

In the equations above.

$$\Delta z_l^{'} = \frac{\Delta z_l + \Delta z_{l-1}}{2}, \quad l = 1, 2, \ldots, L$$

$$\rho_l^{'} = \frac{\rho_l \Delta z_l + \rho_{l-1}\Delta z_{l-1}}{2\Delta z_l^{'}}, \quad l = 1, 2, \ldots, L$$

$$\rho_0 = 0, \Delta z_0 = 0$$

v_l^p represents the velocity of the medium at the top of the soil layer calculated at the lth time $p\Delta t$, $\tau_{l+0.5}^{p-0.5}$ and $\gamma_{l+0.5}^{p+0.5}$ represent the shear stress and strain of the medium at the midpoint of the soil layer calculated at the lth time $p\Delta t + 0.5\Delta t$, respectively; ρ_l is the mass density of the medium calculated at the lth time, and L represents the total number of soil layers calculated, excluding the input substrate.

The Eq. 24 is adopted to combine the boundary conditions with initial conditions, it can gradually integrate the velocity of the medium at the top of each layer and the shear stress and shear strain response of the medium at the midpoint of the layer. The corresponding acceleration and displacement can be derived from the velocity response quantity. The initial conditions for calculation are as follows:

$$\boldsymbol{v}_l^0 = \mathbf{0}, \quad \boldsymbol{l} = \mathbf{1}, \mathbf{2}, \ldots, \boldsymbol{L} \tag{25}$$

$$\boldsymbol{\tau}_{l-0.5}^{-0.5} = \mathbf{0}, \quad \boldsymbol{l} = \mathbf{1}, \mathbf{2}, \ldots, \boldsymbol{L} \tag{26}$$

The boundary conditions are defined as follows:

$$\boldsymbol{\tau}_{-0.5}^{p-0.5} = \mathbf{0} \tag{27}$$

$$\boldsymbol{v}_{L+1}^{p} = \boldsymbol{v}_{\mathrm{b}}^{p} \tag{28}$$

In Eq. 28, v_{b}^{p} refers to the motion speed of the medium at the base top surface is calculated at time $p\Delta t$. In practical engineering, only the incident wave field (ascending wave field) in the base half space is given. If the substrate is regarded as an elastic body, the radiation effect of energy from the soil layer to the substrate has to be considered in reaction calculation. In this way, it can estimate the real motion v_{b}^{p}.

$$\boldsymbol{v}_{\mathrm{b}}^{p} = \frac{2\Delta \boldsymbol{t}}{\boldsymbol{\rho}_L \Delta \boldsymbol{z}_L + \boldsymbol{\rho}_{\mathrm{b}} \boldsymbol{c}_{\mathrm{sb}} \Delta \boldsymbol{t}} \left[\frac{\boldsymbol{\rho}_L \Delta \boldsymbol{z}_L - \boldsymbol{\rho}_{\mathrm{b}} \boldsymbol{c}_{\mathrm{sb}} \Delta \boldsymbol{t}}{2\Delta \boldsymbol{t}} \boldsymbol{v}_{\mathrm{b}}^{p-1} + \boldsymbol{\rho}_{\mathrm{b}} \boldsymbol{c}_{\mathrm{sb}} \left(\boldsymbol{v}_{\mathrm{Ib}}^{p} + \boldsymbol{v}_{\mathrm{Ib}}^{p-1} \right) - \boldsymbol{\tau}_{L+0.5}^{p-0.5} \right] \tag{29}$$

In the above equation, ρ_{b} and c_{sb} are the density and shear wave velocity of the substrate medium, respectively; v_{Ib}^{p} is the velocity of the incident wave field at the top of the substrate at time $p\Delta t$, and $\tau_{L+0.5}^{p-0.5}$ represents the shear stress of the medium at the middle point of the Lth soil layer calculated at time $p\Delta t + 0.5\Delta t$, and it satisfies the below relationship:

$$\boldsymbol{\tau}_{L+0.5}^{p-0.5} = \frac{\boldsymbol{\tau}_{L+0.5}^{p} - \boldsymbol{\tau}_{L+0.5}^{p-1}}{\mathbf{2}} \tag{30}$$

Figure 7 presents the explicit space-time finite difference grids. Among them, solid points indicate the known initial conditions or boundary conditions, hollow points represent the spacetime points to be solved, square points mark the stress (or strain) spacetime points, and circular points represent the velocity spacetime points. According to the grid, the speed and stress at each space-time point can be gradually found.

In the above time-domain numerical integration method, the discretized time interval Δt should be small enough to ensure computational stability due to the application of central difference algorithm. Thickness of soil calculation stratification should meet the requirements of Eq. 21.

4 Numerical examples

This section employs several basic numerical examples to validate the reliability of the time-domain non-linear calculation program developed for this paper.

4.1 Example 1

This example verifies the accuracy of the time-space finite difference method, which is introduced in the field seismic response by comparing with an ideal two-layer field and a complex multi-layer field of an actual major project.

As for the mechanical parameters of the two models (Tables 1, 2), site 1 is an ideal two-storey site, and site 2 is a complex multi-storey site for a practical major project, which contains a hard interlayer with thickness of 15.9 m. In this example, all media are assumed to be linear elastic media, and the damping ratio is set to 0.05. Meanwhile, site-2 was chosen to verify the accuracy of the time-space finite difference method when the difference between the upper and lower soil layers is significant. Whereupon, a comparison is performed between the numerical solution and the analytical solution.

The time history curves of upgoing waves at the top of input half space in terms of accelerated speed, velocity and displacement (incident wave) are indicated in Figure 8. Under the ground motion input as indicated in Figure 8, the time-history curve of ground motion on site 1 surface obtained with the time-space finite difference method as described in Section 3.3 is compared with the calculation result obtained with the frequency domain method, as shown in Figure 9, with the comparison result of response spectrum curve presented in Figure 10. Figures 11, 12 indicate the corresponding results of site 2.

It can be observed that the calculation results of the two methods are basically consistent. It needs to be noted that the time-space finite difference method adopts the central difference method to replace the time and spatial derivatives of the wave equation, and then it determines the numerical solution of the fluctuation problem by explicit numerical integration, while the frequency domain method determines the analytical expression of the steady-state solution followed by the transient reaction by Fourier transformation. Moreover, when referring to the time-space finite difference method, the artificial boundary processing method is adopted to handle the infinite domain problem of the input half space, while the frequency domain method may eliminate the infinite domain truncation problem, without considering the exact accuracy of the numerical error of the discrete Fourier transformation itself. The consistency of the calculation results as presented in Figures 9–12 indicates that it is reliable to solve one-dimensional site seismic response with time-space finite difference method by the numerical program developed in this work.

TABLE 3 Computational model of site 3.

Layer number	Soil class	Shear-wave speed (m/s)	Density (g/cm^3)	Depth (m)
1	Sand fill	149	1.83	9.6
2	Sand mix silt	217	1.84	2.4
3	Silty clay	245.5	1.86	3.2
4	Sand mix silt	257	1.89	1.3
5	Silty clay	243	1.91	1.2
6	Residual sandy clay	283	1.94	5.5
7	Completely weathered granite	372	1.98	7.3
8	Gritty weathered granite	438	2.04	5.4
9	Breezetized granite	533	2.15	1.1
10	Enter a semi-space	533	2.15	-

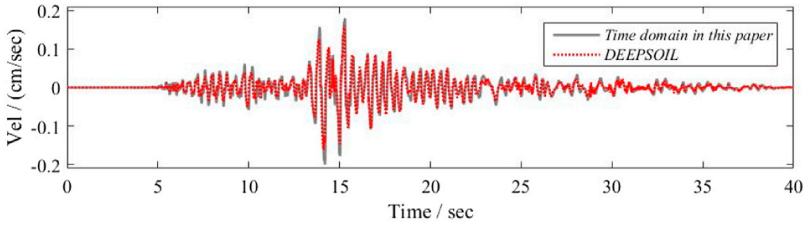

FIGURE 13
Comparison between ground motion time history curves of site 3 (Accelerated speed).

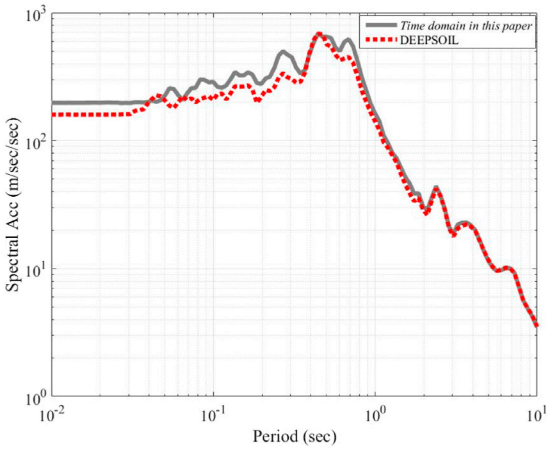

FIGURE 14
Comparison of ground motion response spectrum curves of site 3.

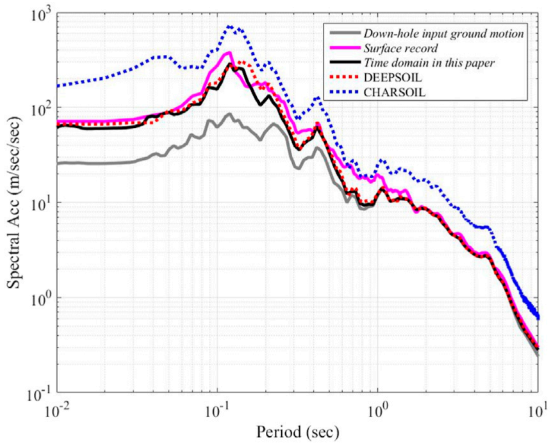

FIGURE 15
Comparison of ground motion response spectrum curves of different programs with actual observation records.

4.2 Example 2

In this section, the data from a certain practical engineering site and the KiK-net station was introduced. With contrastive analysis of DEEPSOIL (Hashash, V6.1) and CHARSOIL (Streeter et al., 1974), the non-linear time-domain programs used worldwide, the reliability of the program developed herein was further demonstrated.

Presently, DEEPSOIL is the most extensively adopted time-domain non-linear soil layer seismic response analysis and calculation program in the world, representing the highest level of time-domain non-linear analysis. Therefore, in this section, the actual project site with silt soil layer is used as the calculation model (the mechanical parameters of the model are shown in Table 3). The Northridge strong seismic observation data is used as input for a comparative analysis of the proposed method (the constitutive model adopts the extended Masing criterion, same as below) and the DEEPSOIL time domain algorithm. Figures 13, 14 depict the calculated surface acceleration time history and response spectrum. In comparison, the proposed method is consistent with the time-history curve of surface acceleration calculated by DEEPSOIL, with a marginally lower amplitude than the DEEPSOIL results. According to the comparison curves of the reaction spectrum, the proposed method for fitting the long-period reaction spectrum is relatively consistent. While the high-frequency component is less than the DEEPSOIL calculation results. The reason for the difference is inferred to be the difference between the backbone curves of the non-linear constitutive model of rock and soil and the finite difference method utilized by the two programs.

Observation station data from the Japanese KiK-net network at a class II site are used concomitantly. The observation point is used as the input; and by comparing and analyzing the calculation results of various time-domain non-linear programs (the proposed method, DEEPSOIL, CHARSOIL) with the actual surface observation records corresponding to the observation points, the reliability of the non-linear program in this paper is verified.

Figure 15 depicts the comparison results of the seismic response spectrum curve at the surface. In accordance with the figure, the research methodology and DEEPSOIL calculation findings are comparable to the actual surface observation record. The overall reaction spectrum curve is essentially consistent with the actual surface observation record, especially the curves of the long period ($T > 2$ s), which completely overlap, with the exception of the large fitting error of individual reaction spectrum periods (such as $T = 0.5$ s ~ 1 s). Whereas the GHARSOIL calculation result represents a significant error.

In terms of this section, the non-linear method is comparable to the internationally recognized DEEPSOIL program's calculation results and is superior to the CHARSOIL when compared to actual observation records. In contrast to DEEPSOIL, the developed procedure is simple, quick, and has a high modeling efficiency, particularly when the site soil layer is thick and the soil is abundant.

5 Conclusion

In order to solve the problems such as the uncertainty of site non-linear seismic response results caused by a single calculation method and the restriction of traditional site non-linear calculation program on the calculation scale, a site non-linear seismic response analysis program is developed based on fortran95 software platform for the time-space finite difference method in this work. To facilitate the consideration of the uncertainty effect of various soil constitutive models under the TNL method, the program is embedded in two relatively mature soil constitutive models at the present stage, namely the extended Masing criterion model and the dynamic skeleton curve model. Simultaneously, port is reserved for the further introduction of various soil constitutive models, and it can be a tool platform for the uncertainty research work of soil non-linear dynamic change. Moreover, the program uses dynamic array technology to store relevant data, and it has no limitation on the computational scale of the site model, the time points and space points of the input and output data principally. In addition, the program can be used for large-scale site seismic response calculation work, and facilitate the research work of site adjustment coefficient in the new generation of zoning map in China. Finally, the reliability of the developed calculation program are verified based on the practical examples, and through a comparative analysis of a relatively mature time-domain non-linear program and testing with actual records from the KiK-net strong motion observation station in Japan, the time-nonlinear program developed in this paper demonstrates a high degree of calculation reliability and modeling efficiency. Consequently, it is applicable to the calculation of more complex site conditions and large-scale site seismic response. Due to the singularity and uniqueness of the example model, additional real site models should be included in the follow-up work to validate the procedure's applicability. Moreover, an uncertainty analysis of various site calculation methods should be carried out.

Data availability statement

The raw data supporting the conclusion of this article will be made available by the authors, without undue reservation.

Author contributions

All authors listed have made a contribution to conception and design of the study, and approved it for publication. Main program development: YZ. Collection and processing of data: YZ and JY. Writing-original draft: JY. Writing-reviewing and editing: YZ and JY. All authors contributed to manuscript revision, read, and approved the submitted version.

Funding

This study is supported by the Science for Earthquake Resilience of China Earthquake Administration (XH22013YA).

Conflict of interest

The authors declare that the research was conducted in the absence of any commercial or financial relationships that could be construed as a potential conflict of interest.

Publisher's note

References

Beresnev, I. A. (2002). Nonlinearity at California generic soil sites from modeling recent strong-motion data. *Bull. Seismol. Soc. Am.* 92 (2), 863–870. doi:10.1785/0120000263

Bo, J. S. (1998). Site Classification and design response spectrum adjustment method (postdoctoral research Report*)*. China Earthquake Administration: Institute of Engineering Mechanics, 55–58.

Chen, X. L. (2006). *Study on soil dynamic properties, and nonlinear seismic response of complex site and its methods*. China Earthquake Administration, Institute of Engineering Mechanics.

Diego, C. F. L. P., Carlo, G. L., and Ignazio, P. (2006). ONDA: Computer code for nonlinear seismic response analyses of soil deposits. *J. Geotech. Geoenviron. Eng.* 132 (2), 223–236.

Gao, S., Liu, H., and Davis, P. M., (1996). Localized amplification of seismic waves and correlation with damage due to the northridge earthquake: Evidence for focusing in santa monica. *Bull. Seismol. Soc. Am.* 869 (1B), 209–230.

Hashash, Y. M. A. (2009). DEEPSOIL V6.1, 12, *user manual and tutorial*.

Idriss, I. M., and Seed, H. B. (1968). Seismic response of horizontal soil layers. *Soil Mechanics and Foundations Division. J. Soil Mech. Found. Div.* 94 (4), 1003–1031. doi:10.1061/jsfeaq.0001163

Kavazanjian, E., and Matasovic, N. (1995)., 46. New Orleans, Louisiana, USA, 1066–1080.Seismic analysis of solid waste landfills*Geoenvironmental 2000, Geotech. Spec. Publ.*2

Kim, B., and Hashash, Y. M. A. (2013). Site response analysis using downhole array recordings during the march 2011 tohoku-oki earthquake and the effect of long-duration ground motions. *Earthq. Spectra* 29 (S1), 37–54. doi:10.1193/1.4000114

Kokusho, T., and Sato, K. (2008). Surface-to-base amplification evaluated from KiK-net vertical array strong motion records. *Soil Dyn. Earthq. Eng.* 28 (9), 707–716. doi:10.1016/j.soildyn.2007.10.016

Li, P. (2010). *The effect of site types on platform value of the design response spectrum*. China Earthquake Administration: Harbin: Institute of Engineering Mechanics.

Li, X. J. (1992). A method for analysing seismic response of nonlinear soil layers. *South China J. Seismol.* 12 (4), 1–8.

Li, X. J. (1992). A simple function expression of the soil dynamic constitutive relationship. *Chin. J. Geotechnical Eng.* (05), 90–94.

Li, X. J. (2013). Adjustment of seismic ground motion parameters considering site effects in seismic zonation map. *Chin. J. Geotechnical Eng.* 35 (S2), 21–29.

Li, Y. Y., Xu, Y., and Li, D. M. (2005). Analysis of earthquake responses for different site categories. *Earthq. Res. Shanxi* 4, 27–33.

Luan, M. T., and Lin, G. (1994). An effective time-domain computational method for nonlinear seismic response analysis of soil deposit. *J. Dalian Univ. Technol.* 34 (2), 228–234.

Luan, M. T., and Lin, G. (1992). Computational model for nonlinear analysis of soil site seismic response. *Eng. Mech.* 9 (1), 94–103.

Luan, M. T. (1992). Ramberg-osgood constitutive model with variable parameters for dynamic nonlinear analysis of soils. *Earthq. Eng. Eng. Vib.* (02), 69–78.

Martin, P. P., and Seed, H. B. (1982). One-dimensional dynamic ground response analyses. *J. Geotech. Engrg. Div.* 108 (7), 935–952. doi:10.1061/ajgeb6.0001316

Martin, P. P., and Seed, H. B. (1978). *MASH-A computer program for the non-linear analysis of vertically propagating shear waves in horizontally layered deposits*. Calif: Report EERC, University of California at Berkeley, 78–23.

Masing, G. (1926). *Eigenspannungeu and verfertigung beim Messing*. Zurich: Proceedings of the 2nd International Congress on Applied Mechanics.

Matasovic, N., and Vucetic, M. (1993). Cyclic characterization of liquefiable sands. *J. Geotech. Engrg.* 119 (11), 1805–1822. doi:10.1061/(asce)0733-9410(1993)119:11(1805)

Pyke, R. M. (1979). Nonlinear soil models for irregular cyclic loadings. *J. Geotech. Engrg. Div.* 105 (6), 715–726. doi:10.1061/ajgeb6.0000820

Qi, W. H., Wang, Z. Q., and Bo, J. S. (2010). Development and verification of a method for analyzing the nonlinear seismic response of soil layers. *J. Harbin Eng. Univ.* 31 (4), 444–450.

Qi, W. H., and WangBo, Z. Q, J. S. (2010). Development and verification of a method for analyzing the nonlinear seismic response of soil layers. *J. Harbin Eng. Univ.* 31 (04), 444–450.

Seed, H. B., Romo, M. P., Sun, J. I., Jaime, A., and Lysmer, J. (1988). The Mexico earthquake of september 19, 1985: Relationships between soil conditions and earthquake ground motions. *Earthq. Spectra* 4 (4), 687–729. doi:10.1193/1.1585498

Streeter, V. L., Wylie, E. B., and Richart, F. E. (1974). CHARSOIL, 100(3), 247-263, *characteristics method applied to soils*.

Wang, Z. L., and Han, Q. Y. (1981). Analysis of wave propagation for the site seismic response, using the visco-elastoplastic model. *Earthq. Eng. Eng. Vibraion* (01), 117–137.

Yee, E., Stewart, J., and Tokimatsu, K. (2013). Elastic and large-strain nonlinear seismic site response from analysis of vertical array recordings. *J. Geotech. Geoenviron. Eng.* 139 (10), 1789–1801. doi:10.1061/(asce)gt.1943-5606.0000900

frontiers | Frontiers in Earth Science

TYPE Original Research
PUBLISHED 22 March 2023
DOI 10.3389/feart.2023.1053085

OPEN ACCESS

EDITED BY
Behzad Hassani,
BC Hydro, Canada

REVIEWED BY
Muhammad Tariq Chaudhary,
Kuwait University, Kuwait
Sujit Kumar Dash,
Indian Institute of Technology Kharagpur,
India

*CORRESPONDENCE
Zifa Wang,
✉ zifa@iem.ac.cn

SPECIALTY SECTION
This article was submitted
to Structural Geology and Tectonics,
a section of the journal
Frontiers in Earth Science

RECEIVED 25 September 2022
ACCEPTED 06 March 2023
PUBLISHED 22 March 2023

CITATION
Wang X, Wang Z, Wang J, Miao P, Dang H and Li Z (2023), Machine learning based ground motion site amplification prediction.
Front. Earth Sci. 11:1053085.
doi: 10.3389/feart.2023.1053085

Machine learning based ground motion site amplification prediction

Xiangqi Wang[1], Zifa Wang[2,3]*, Jianming Wang[3], Pengyu Miao[1], Haotian Dang[1] and Zhaoyan Li[2]

[1]Henan University, Kaifeng, Henan, China, [2]Institute of Engineering Mechanics, China Earthquake Administration, Harbin, Heilongjiang, China, [3]CEAKJ ADPRHexa Inc., Shaoguan, Guangdong, China

Site condition impact on seismic ground motion has been a complex but important subject in earthquake hazard analysis. Traditional studies on site amplification effect are either based on site response *via* wave propagation simulation or regression analysis using parameters such as Vs30, bedrock ground motion and site response period. Ground Motion Prediction Equations (GMPEs) are used for regions where there is limited data of seismic records. The main issues with these approaches are that they cannot demonstrate the complex relationship between site amplification and its various affecting parameters, thus there exists large uncertainty in the results. Recent studies based on machine learning have shown significant improvement in predicting the site amplification, but the result is not well explained. This study assembled the information on 6 parameters including Vs30, magnitude, epicentral distance, earthquake source depth, bedrock ground motion, and altitude of 353,327 records observed during 1997 and 2019 from 698 KiK-net stations. Three machine learning algorithms of Random Forest (RF), XGBoost, and Deep Neural Networks (DNN) were implemented to predict the site amplification factor using these 6 selected parameters. Shapley Additive explanation (SHAP) was used to explain the importance of the 6 parameters. The results show that all three machine learning algorithms performed much better than the traditional GMPE approach with XGBoost's performance the best. The explanation provided by the SHAP analysis further enhanced the reasonability of this study. It is anticipated that the combination of machine learning and SHAP analysis can provide better assessment for site amplification of ground motion with better potential of future application in seismic hazard analysis.

KEYWORDS

site effect, amplification prediction model, machine learning, shap, ground motion

1 Introduction

The effect of site condition on seismic ground motion has been a research focus in geotechnical earthquake engineering and seismic hazard analysis. Numerous records have demonstrated that site conditions amplify the ground motion and further intensify the earthquake damage (Borcherdt, 1970; Borcherdt and Gibbs, 1976; Seed et al., 1988; Dobry et al., 2000; Bala et al., 2009). A large number of studies have been performed to better represent the effect of site amplification, and traditional approaches can be categorized into two groups: site response analysis based on wave propagation simulation and the empirical Ground Motion Prediction Equations (GMPEs). Site response analysis based on site wave propagation simulation is mostly using one-dimensional (1-D) or multi-dimensional models. The non-linear property of the soil is approximated through equivalent linearization (Idriss and Seed, 1968; Seed and Idriss, 1969). Park and Hashash conducted the analysis through improved equivalent linearization of site soil non-linear property (Park and Hashash, 2004; Park and Hashash, 2008), and Gerlymos and Gazetas proposed a new constitutive model in a 1-D analysis (Gerolymos and Gazetas, 2005). Harmon et al. developed the ground motion site amplification model for the West and East part of the US based on extensive site response simulation (Harmon et al., 2019). Site response analysis can provide detailed results of the site amplification, but the analysis requires extensive information on soil property which is often not available. The other approach for site response analysis is through empirical Ground Motion Prediction Equations (GMPEs), which is a statistical model based on earthquake property and simplified parameters of site soil conditions. The early stage GMPEs were usually developed separately for rock and soil site conditions, and ground motion amplification factor was used to consider statistical effect of site conditions (Boore et al., 1997; Sadigh et al., 1997). Abrahamson and Silva considered non-linear effect of the site amplification factor (Abrahamson and Silva, 1997), and Boore et al. (Boore et al., 1997) used the average shear-wave velocity of the top 30 m soils (Vs30) to represent the site effect. Seyhan and Stewart (Seyhan and Stewart, 2014) developed a site amplification model for the West part of the US and used the GMPEs by Boore et al. (Boore et al., 2014) for rock sites to compliment the data scarcity of records on rock sites. Most GMPEs used only Vs30 to express the site condition, which cannot completely represent the complex nature of the various site conditions, thus resulting in a large degree of uncertainty. With the accumulation of a great number of observed records and rapid development of computational resources machine learning algorithms have been actively introduced to predict the site response. Daniel Roten et al. (Roten and Olsen, 2021a) applied machine learning to predict the site amplification factor using records from the KiK-net, and the result was compared against the result by the 1-D site response analysis showing the mean squared logarithm error reduction of at least 50%. Hamidreza et al. (Hamidreza and Soleimani Kutanaei, 2015) compared the site amplification result by Artificial Neural Network (ANN) against the result by 2-D site response analysis and found that the shear wave velocity and soil layer depth are more important than other factors in site amplification. Kveh (Kaveh et al., 2016)and (Derras et al., 2017) predicted the site amplification through M5 decision tree method and ANN, respectively. Chuanbin Zhu (Zhu et al., 2021)compared the performance of RF, GRA, SRI and HVSR methods on the benchmark dataset, and the results showed that RF performance is relatively better. Daniel Roten (Roten and Olsen, 2021b) compared the neural network methods (CNN, MLP) with the theoretical SH1D amplification method, and the results showed that CNN has a smaller MSLE and MAE in the prediction results. Machine learning approach has shown its superiority in predicting site amplification of ground motion, but the approach itself looked like a “black box” approach with results somethings difficult to be explained.

This study utilized the observed ground motion in KiK-net between 1997 and 2019, and applied RF, XGBoost, and DNN approaches to predict site amplification factor for different periods. The results were compared against those by (Yoojoong and Jonathan, 2005), who used Vs30 as the main parameter to predict ground motion site amplification. The comparison demonstrates that machine learning approaches are superior in predicting site amplification with XGBoost performance the best. Shapley additive explanation (SHAP) was then introduced to explain the proposed prediction models, and the contribution of each parameter on site amplification was analyzed to provide better guidance for future similar studies.

2 Data

KiK-net is the ground motion observation network operated by the Japanese National Research Institute for Earth Science and Disaster Resilience (NIED), which is composed of approximately 700 stations (https://www.doi.org/10.17598/NIED.0004). Each station has a pair of high-end sensors placed at the top and bottom of the borehole to record three components (NS, EW, UD) of the earthquake ground motion. In addition, detailed soil profile data has been provided for most stations by NIED. This study conducted the research based the data accumulated by KiK-net during 1997–2019.

2.1 Data preparation

The ground motion records by KiK-net are stored separately for each earthquake event, and this study assembled the records with the following additional parameters. Information on earthquake magnitude (Mag), altitude of the station (S_Altitude), earthquake source depth (Depth), and the latitude and longitude of both the earthquake source and the observation stations are included in the ground motion records. The epicentral distance(R) can be calculated *via* the latitude and longitude of the earthquake source and observation stations. The Vs30 at the stations can be calculated from the borehole data according to Eq. 1 (Yoojoong and Jonathan, 2005). For stations where borehole data does not reach down to 30 m, the last layer will be extended to 30 m deep (Boore, 2004).

$$V_{30} = 30 \Big/ \sum_{1}^{n} \frac{d_i}{Vs_i} \tag{1}$$

where d_i is the depth for the i-th layer, and Vs_i is its corresponding shear wave velocity. The calculation only accounts for soil layers up to 30 m deep. Spectral acceleration Sa is calculated as in Eq. 2 (Chen Longwei Chen Zhuoshi Yuan Xiaoming, 2013).

$$Sa(T) = \sqrt{Sa(T)_{EW} * Sa(T)_{NS}} \tag{2}$$

where $Sa(T)_{EW}$, $Sa(T)_{NS}$ are the spectral acceleration of the EW and NS component for period T.

The site amplification factor (Amp) for Sa can be calculated as in Eq. 3.

$$Amp(T) = \frac{Sa(T)_S}{Sa(T)_R} \tag{3}$$

where $Sa(T)_S$, $Sa(T)_R$ are the SA at surface and bottom respectively for period T. The above computation is repeated for all the records

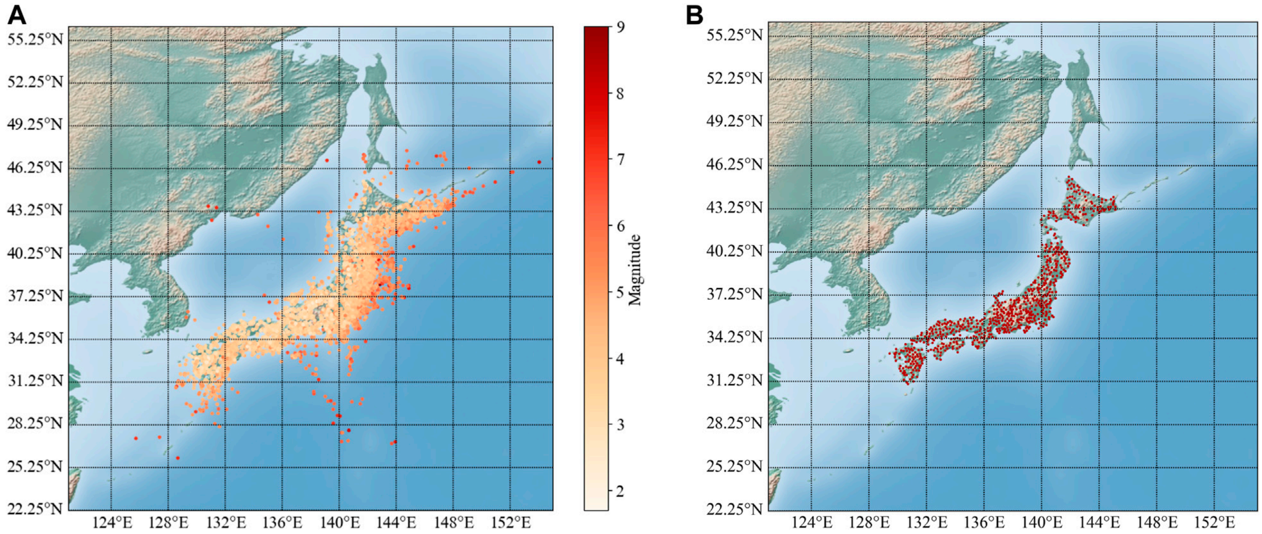

FIGURE 1
Location distribution of earthquake source and observation station. **(A)** Earthquake source location, **(B)** Observation station location.

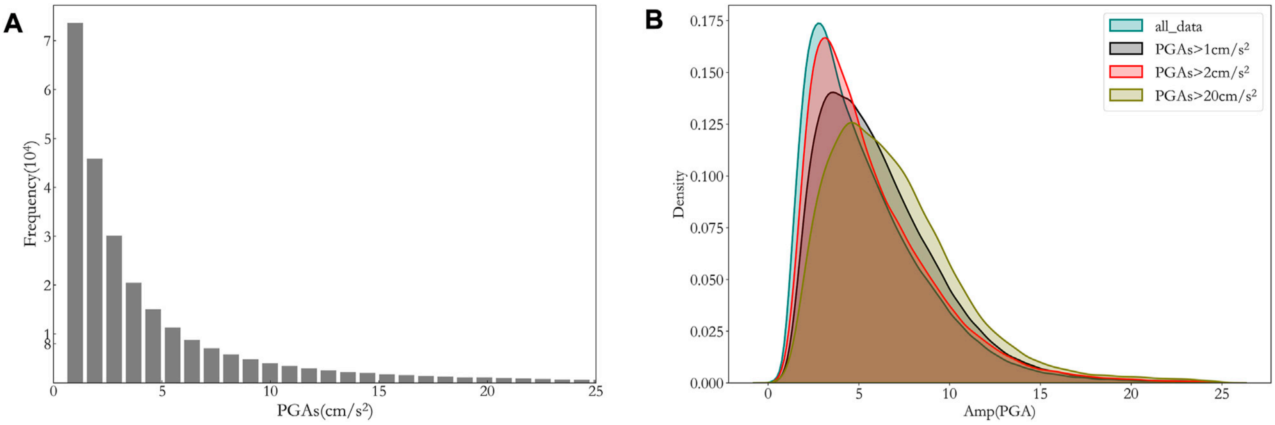

FIGURE 2
Record frequency distribution with PGAs or its amplification. **(A)** PGAs distribution for all records, **(B)** Amp (PGA) distribution of datasets with different filtrating PGA_S.

observed in the KiK-net during 1997–2019, resulting in a data set of Amp for more than 350,000 earthquake records.

2.2 Data filtering and distribution

The location distribution of earthquake source and observation station for the dataset selected in this study is shown in Figure 1. Previous researches (Bommer and Martinez-Pereira, 2000) have shown that only ground motions with PGA more than 20 cm/s² will have impact on our society, engineering structures and living environment. The PGA_S (subscript s stands for surface) distribution of the data collected for this study is shown in Figure 2A, and from Figure 2A it can be seen that PGA_S for most records is below 20 cm/s². For application in future engineering practice, we need to filter the data from the assembled dataset. Figure 2B shows the distribution of Amp with datasets of different minimum PGA_S of 0, 1, 2, and 20 cm/s². As can be seen from Figure 2B, the distribution of Amp for datasets of minimum 1 cm/s² and 20 cm/s² looks similar, therefore, we chose the dataset with minimum PGA_S of 1 cm/s² for this study to ensure that there be enough samples in the dataset. This filtered dataset has more than 260,000 samples. The distribution of Vs30, Mag, R and Depth for the selected dataset is also shown in Figures 3A–D, respectively. As can be seen from Figure 3 Vs30 mostly falls into the range of 250–700 m/s, and M is mostly between 4 and 7, while R is mostly less than 200 km and the source depth is mostly shallower than 60 km.

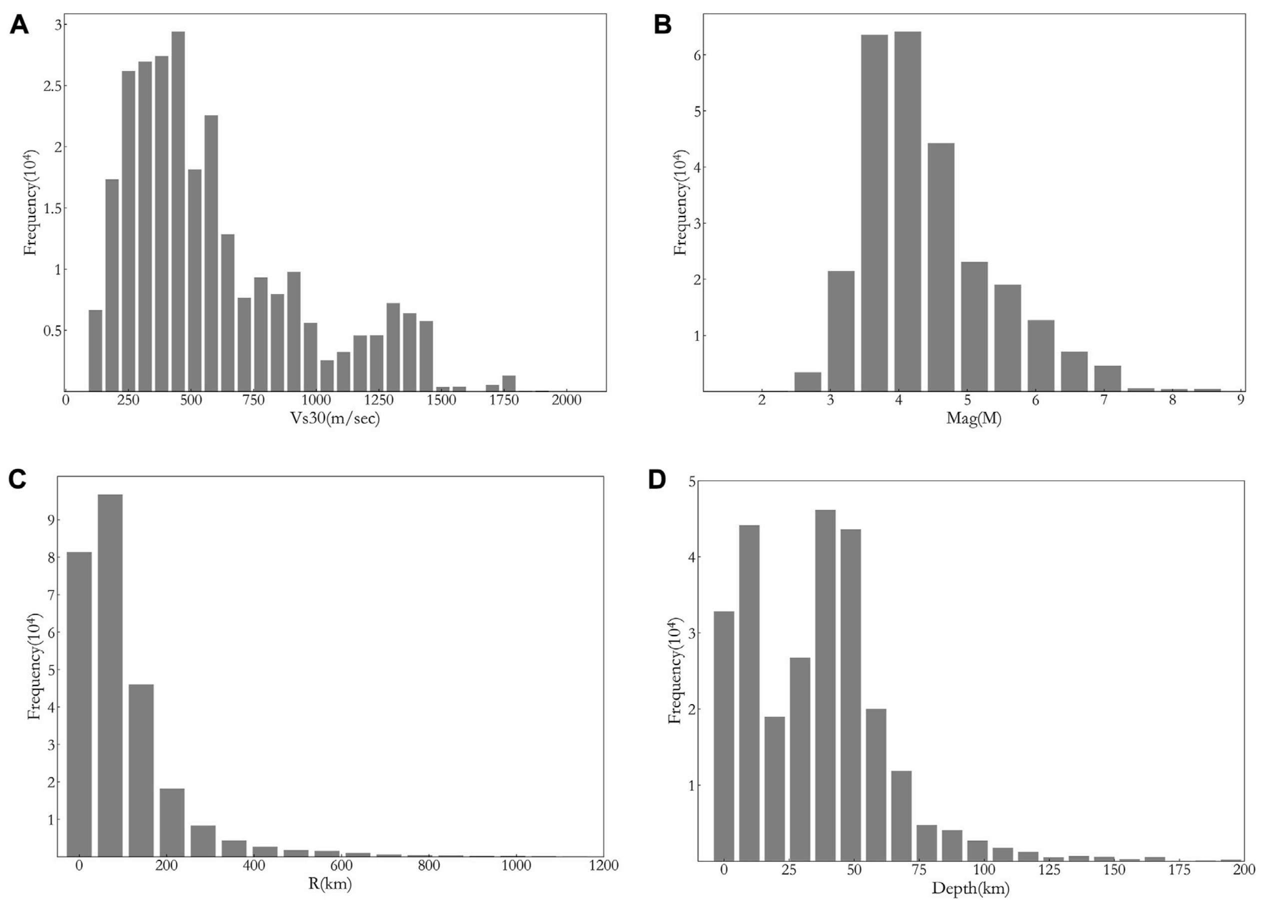

FIGURE 3
Distribution of the dataset for different parameters. **(A)** Vs30, **(B)** Magnitude, **(C)** Epicentral distance and **(D)** Source depth.

TABLE 1 Parameter adjustment results and training time of three models.

Models	Average MSE predicted	Average training time (minutes)
RF	0.07744	31
XGBoost	0.07168	54
DNN	0.07867	62

3 Models for predicting

3.1 Traditional approach

Most traditional approaches use parameters such as Vs30 and PGA_R to predict the site amplification factor. (Yoojoong and Jonathan, 2005) established a site amplification prediction equation using Vs30 and PGA_R and verified its effectiveness *via* comparison with actual amplification based on a large number of ground motion records. Their results also demonstrated explicit deviation from the NEHRP provision of amplification factors. Their prediction formula can be shown in Eq. 4.

$$Ln\left(Amp\right) = c\ln\left(\frac{Vs30}{V_{ref}}\right) + b\ln\left(\frac{PGA_R}{0.1}\right) + \eta + \varepsilon \tag{4}$$

where **c**, V_{ref}, b are regression coefficients, and η is a random factor expressing the ground motion response, and ε is the error of regression.

It is noted that Eq. 4 is only applicable when Vs30 is between 130 and 1,300 m/s and PGA_R is between 0.02 and 0.8 g. This study made sure that the selected dataset also met these conditions for the comparison study.

3.2 Machine learning approaches

Because of the vast advancement of computer technology and computing resources in recent years, machine learning approaches have been extensively applied in many areas of studies, often resulting in much satisfactory results (Jordan and Mitchell, 2015). In this study three

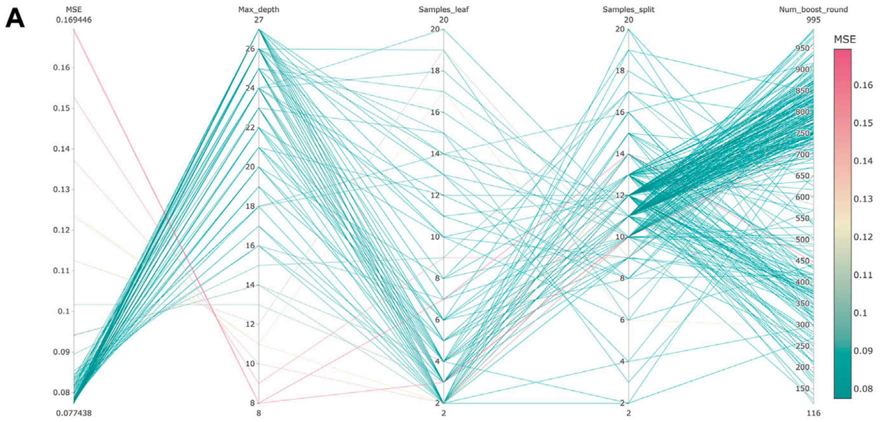

Hyper-parameter optimization process for RF

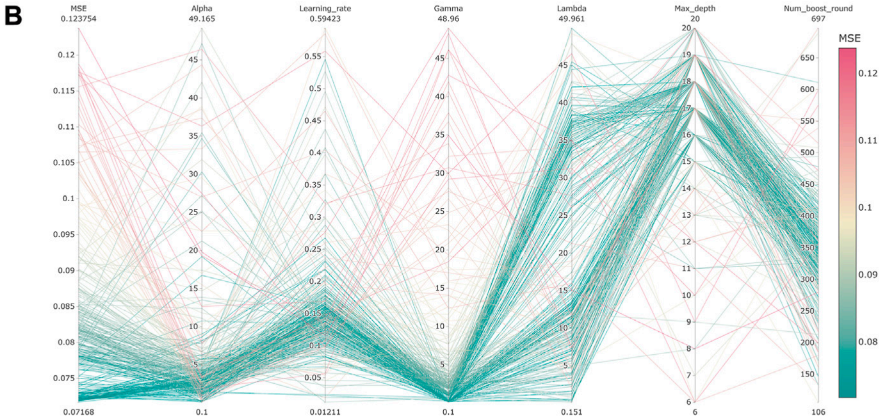

Hyper-parameter optimization process for XGBoost

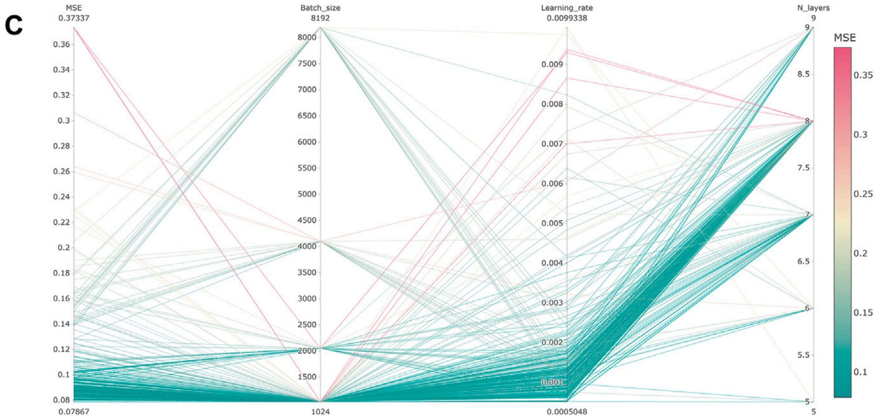

Hyper-parameter optimization process for DNN

FIGURE 4
The Bayesian optimization process for hyper-parameters of the 3 ML models. **(A)**Hyper-parameter optimization process for RF, **(B)**Hyper-parameter optimization process for XGBoost, **(C)**Hyper-parameter optimization process for DNN.

representative machine learning algorithms (RF, XGBoost, DNN) were selected in constructing models to predict the site amplification factor. For the feature parameters in the constructed machine learning models, only parameters which were easily accessible and without regional restrictions were selected, which included Vs30, Mag, R, S_altitude, Depth, Acc_rock. For validating the proposed models, 10% records

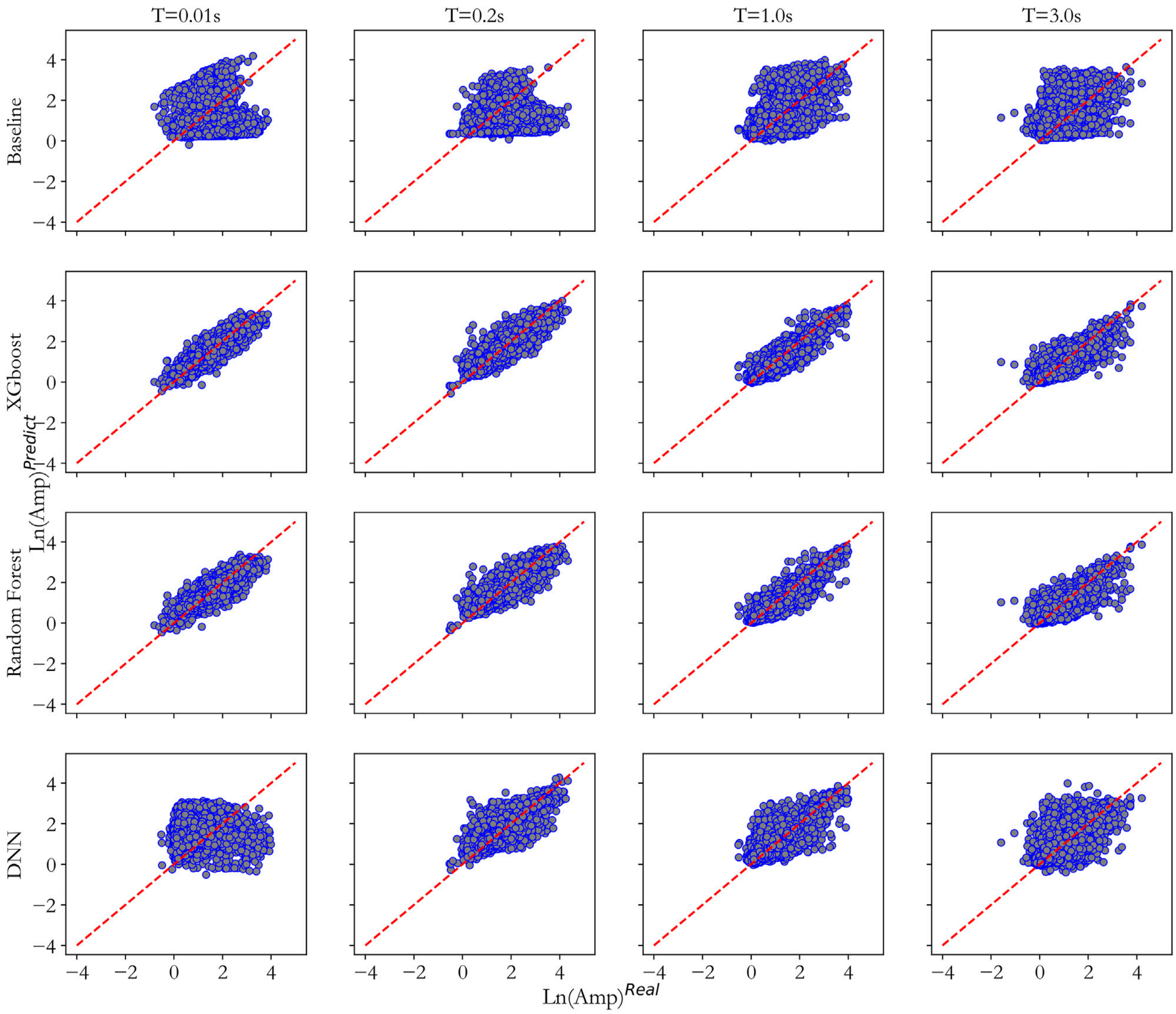

FIGURE 5
The prediction performance of four methods on validation dataset (The closer the scatter distribution is to the 1:1 line, the better the prediction results).

were randomly selected from the dataset. Of the remaining 90% data, 70% were used for training, and the other 30% were used for testing the accuracy and degree of fitting in the prediction.

3.2.1 Random forest

Random Forest (RF) algorithm is a classification prediction approach based on multiple decision trees by Leo Breiman (Breiman, 2001), and it is an extension of decision tree algorithm. The RF algorithm traverses all nodes (trees) to be split, identifies the optimum split variable and its corresponding slipt threshold for maximum impurity reduction for all sub-nodes. The above process is repeated until the threshold value requirement is satisfied, thus resulting in generation of a forest of trees. Impurity is often represented by Gini index, which can be calculated using the following formula:

$$\boldsymbol{Gini(t) = 1 - \sum\nolimits_k^K \left[P\left(\frac{k}{t}\right)\right]^2} \tag{5}$$

where $\boldsymbol{Gini(t)}$ is the Gini index at node $\boldsymbol{t}$, $\boldsymbol{P(\frac{k}{t})}$ is the ratio of k category sample size by the total sample size at node $\boldsymbol{t}$, and $\boldsymbol{K}$ is the number of sample categories at note $\boldsymbol{t}$.

Bagging approach is used as the key algorithm in RF, and each tree in the forest is trained by a randomly selected sample set. The output of the results is an average of results for all the trees, as shown below:

$$\boldsymbol{F(x) = \mathrm{mean}\left(\sum\nolimits_i^n f^i(x)\right)} \tag{6}$$

where $\boldsymbol{F(x)}$ is the output result, $\boldsymbol{f^i(x)}$ is the result for tree $\boldsymbol{i}$, and $\boldsymbol{n}$ is the number of trees in the forest.

3.2.2 XGBoost

XGBoost algorithm is a classification prediction approach based on the iteration of multiple decision trees by Tianqi Chen (Chen and Guestrin, 2016), and boosting is the key algorithm in XGBoost. The

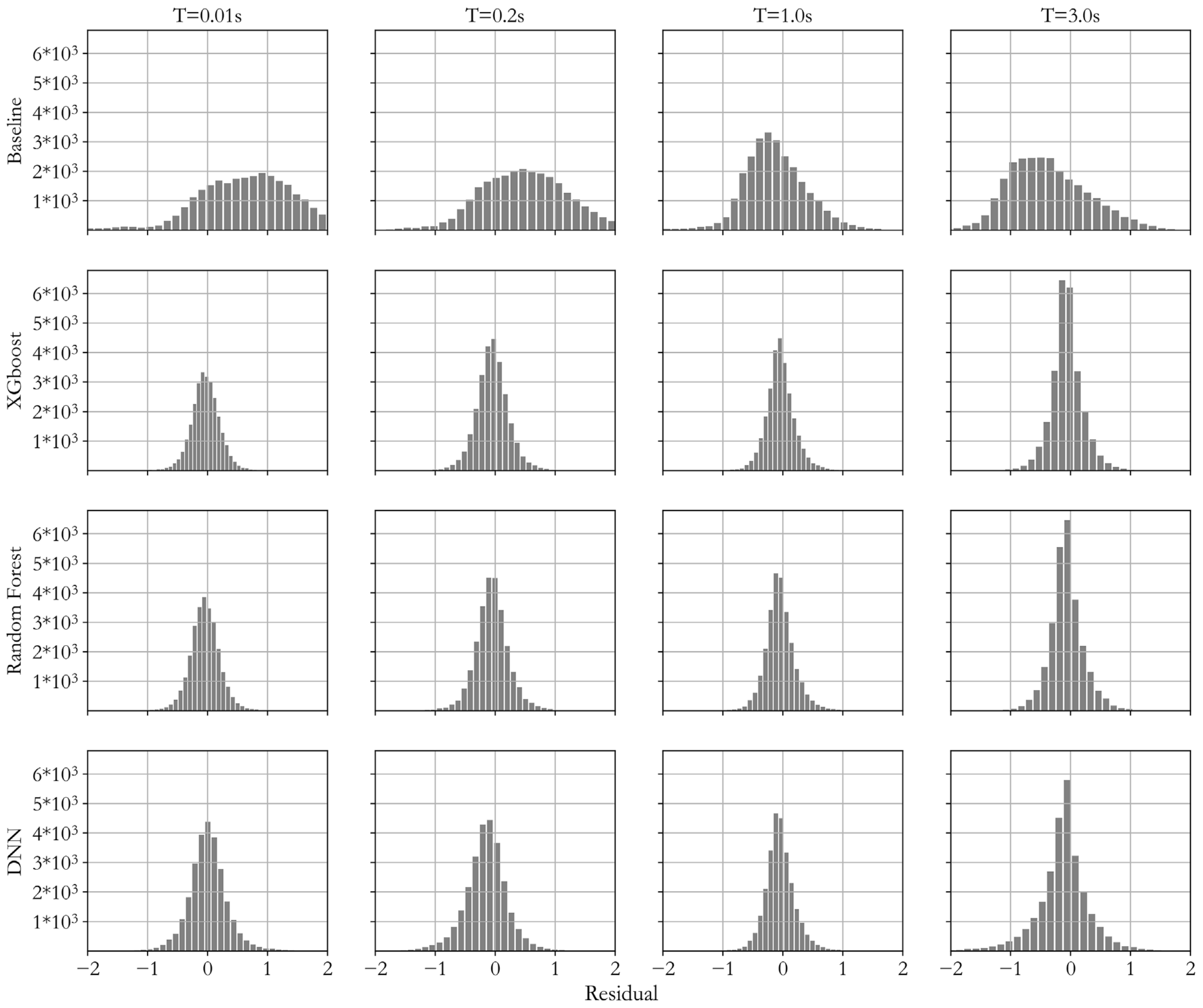

FIGURE 6
The prediction residual of four methods on validation dataset.

XGBoost approach starts from an initial model trained on an initial dataset, and the result is used to reconstruct the next model, and this process repeats until a satisfactory result is obtained. During this iteration process, the newly generated tree is used to approximate the error of the previous tree, and the result can be expressed as the additive tree models. Aggregation can be used to represent the result, as shown below:

$$y_i^{(t)} = \sum_{k=1}^{t} f^k(x_i) = y_i^{(t-1)} + f^n(x_i) \tag{7}$$

where $y_i^{(t)}$ is the model prediction result for the t iteration, $f^k(x)$ is the prediction result for tree k, and t is the number of tree models.

During the iteration process, XGBoost use an approach similar to the one for decision tree, that is, traversing of classification of all feature parameters and using an objective function OBJ to evaluate the performance. Splitting is performed when OBJ increment surpasses pre-determined threshold, and the OBJ can be expressed as in the following:

$$OBj = \sum_i^n l(y_i, \check{y}_i) + \sum_i^t \Omega(f^i) \tag{8}$$

where the first item on the right is the differentiable loss function used to measure the distance between predicted value $\check{y}_i$ and the object value y_i which is differentiable, and the second item Ω is penalty for model's complexity, which is used to reduce the risk of over-fitting.

3.2.3 Deep neural networks

The multi-layer network proposed by Hinton in 2006 opened the door for deep learning (Hinton et al., 2006). Multi-layer perceptron (MLP) is composed of input, hidden (multiple), output layers with full connection between neighboring layers. Each layer can be treated as a logistic regression model, and neuron parameter can be calculated *via* a traversing approach as shown in Eq. 9:

$$a_i^n = \sigma\left(\sum_{k=1}^{K} w_{ik}^{nm} * a_k^m\right) \tag{9}$$

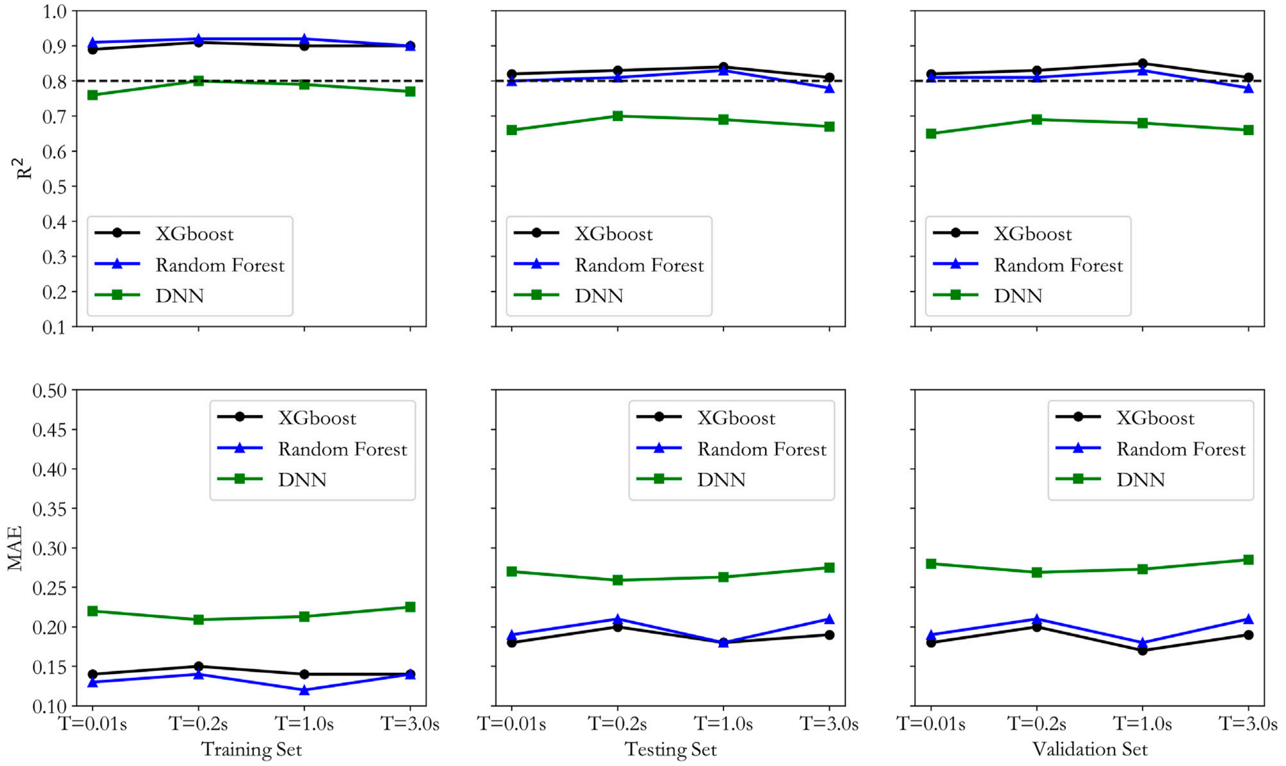

FIGURE 7
R^2 and MAE distribution of the three machine learning models for training, testing and validation datasets.

where $\mathbf{a}_i^n$ is the $\boldsymbol{i}$-th neuron in the nth layer, $\boldsymbol{K}$ is number of neurons in the neighboring layer $\boldsymbol{m}$, $\mathbf{w}_{ik}^{nm}$ is the calculation coefficient for two neurons $(\mathbf{a}_i^n, \mathbf{a}_k^m)$, and $\boldsymbol{\sigma}$ is the activation function to provide non-linear modeling capability for the networks.

3.3 Optimization of hyper-parameters

The hyper-parameters in an ML model are very important in affecting the performance of the models, so identifying the proper setup of hyper-parameters is an important task in building ML models. In this study, based on the Optuna framework of Bayesian optimization, we optimize the important hyper-parameters in the three selected ML models. For RF, the hyper-parameters are maximum depth of decision tree (Max_depth), the number of trees (Num_boost_round), the minimum sample size for splitting (Samples_split) and the minimum sample size in a leaf (Samples_leaf). For XGBoost the hyper-parameters are maximum depth of the decision trees (Max_depth), learning rate (Learning_rate), number of decision trees (Num_boost_round), fitting parameter (Gamma) and normalization parameters (Alpha, Lambda). Similarly, for DNN, the hyper-parameters include learning rate (Learning_rate), number of network layers (N_layers) and sample size in one training (Batch_size). Mean Squared Error (MSE) of the model results was used as the control parameter to determine the hyper-parameters and MSE can be expressed as in the following Equation:

$$\boldsymbol{MSE} = \frac{\mathbf{1}}{\boldsymbol{N}}\sum_i^N (y_i - \check{y}_i)^2 \tag{10}$$

where $\boldsymbol{N}$ represents the number of samples, $\boldsymbol{y_i}$ is the object value of $\boldsymbol{i}$-th sample, $\check{\boldsymbol{y}}_i$ is the predicted value of the $\boldsymbol{i}$-th sample.

The MSE and the average training time for the hyper-parameter optimization of the 3 ML models are shown in Table 1, and the training process is visualized in Figure 4.

3.4 Results for the four models

The traditional model by Yoojoong Choi et al. is used as the baseline model, and the results by the three proposed machine learning models are compared against it from the baseline model at periods of 0.01, 0.2, 1, and 3 s. The results are shown in Figure 5 where the horizontal axis is the actual Amp while the vertical axis is the predicted Amp. For further observing the prediction error of the model, we calculate the residual and the result is shown in Figure 6, where the residual can be calculated based on Eq. 13 which represents the model prediction error. As can be seen clearly from Figures 5, 6, the results from the three machine learning models show much less scattering and smaller residual, indicating better accuracy than it by the traditional approach. To further analyze the prediction accuracy of the three proposed models, R^2 and mean absolute error (MAE) are used to assess the three models for the training, testing and validation datasets. The results are shown in Figure 7, where R^2 represents the ratio of explainable portion in the overall squared summation divided by the predicted squared summation. The closer R^2 is to 1, the better the prediction results. R^2 and MAE can be expressed in the following equations.

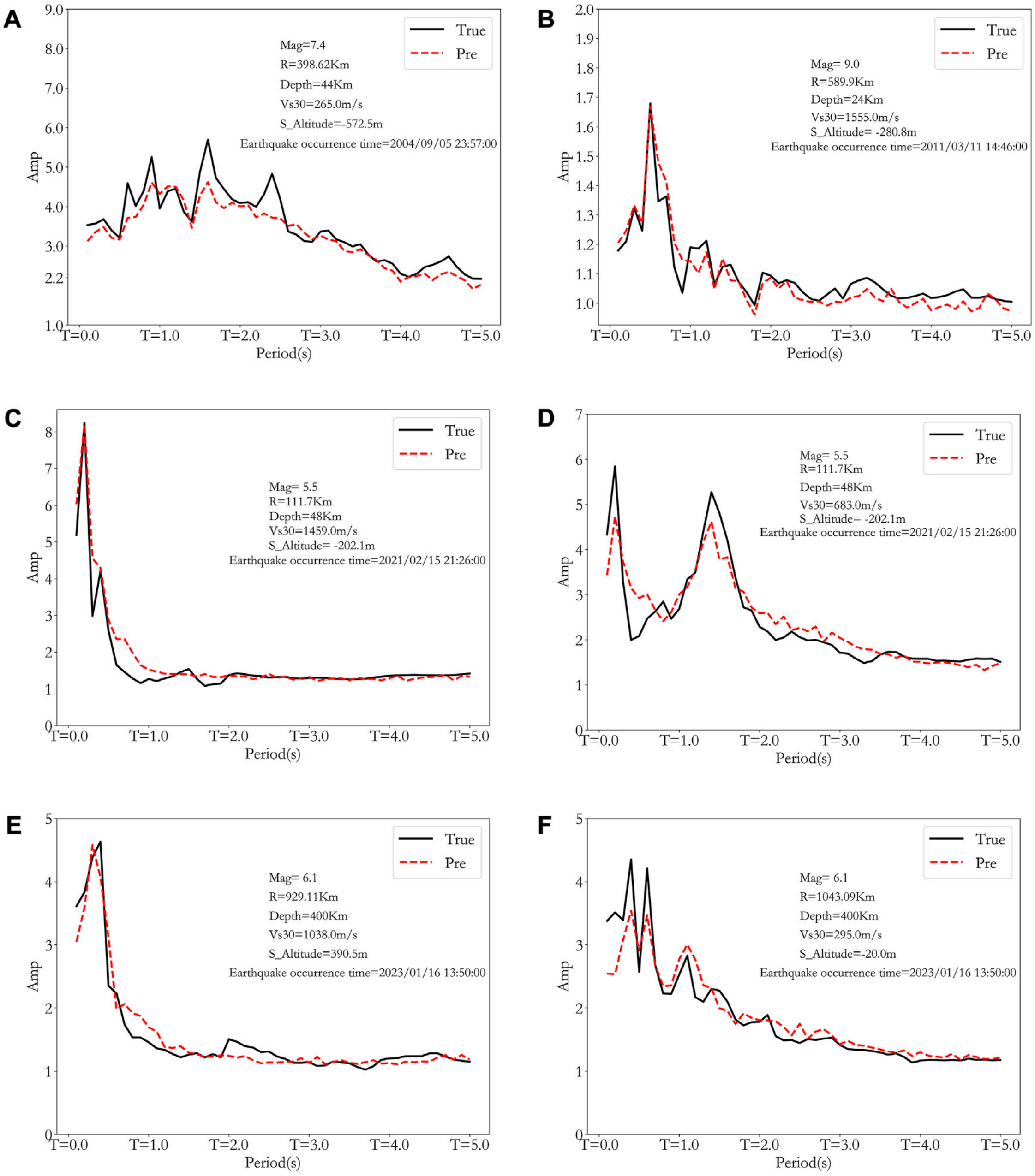

FIGURE 8
Generalization testing of actual events with different Vs30 (black line is the actual amplification while the red dashed line is the predicted amplification). The **A–F** figures represent seismic motion prediction validations for different earthquake events and site conditions, with earthquake events and site conditions presented as legends in each figure.

$$R^2 = 1 - \frac{\sum_{i=0}^{N} (y_i - \check{y}_i)^2}{\sum_{i=0}^{N} (y_i - \overline{y_i})^2} \tag{11}$$

$$MAE = \frac{1}{N}\sum_{i}^{N} (y_i - \check{y}_i) \tag{12}$$

$$\mathbf{Residual} = y_i - \check{y}_i \tag{13}$$

where N represents the number of samples, y_i is the object value of the i-th sample, $\check{y}_i$ is the predicted value of the i-th sample, and $\overline{y_i}$ is the mean value of the object value.

From the R^2 distribution in Figure 7 it can be concluded that DNN has smaller values than the values by both XGBoost and RF for training, testing and validation datasets. RF has higher R^2 value than it by XGBoost for the training dataset, but lower values for both the testing and validation datasets, indicating an overfitting trend by the RF model, which may lead to less generalization capability in future predictions. From the MAE distribution in Figure 7, it can be seen that DNN has the highest values in all three datasets, and RF has lower MAE than XGBoost for the training dataset, but it has higher MAE than XGBoost for both the testing and validation datasets. Based on the above observation, it can be concluded that the DNN model performed the worst, and RF model showed some over-fitting tendency, while the XGBoost model performed the best in predicting the site amplification factor.

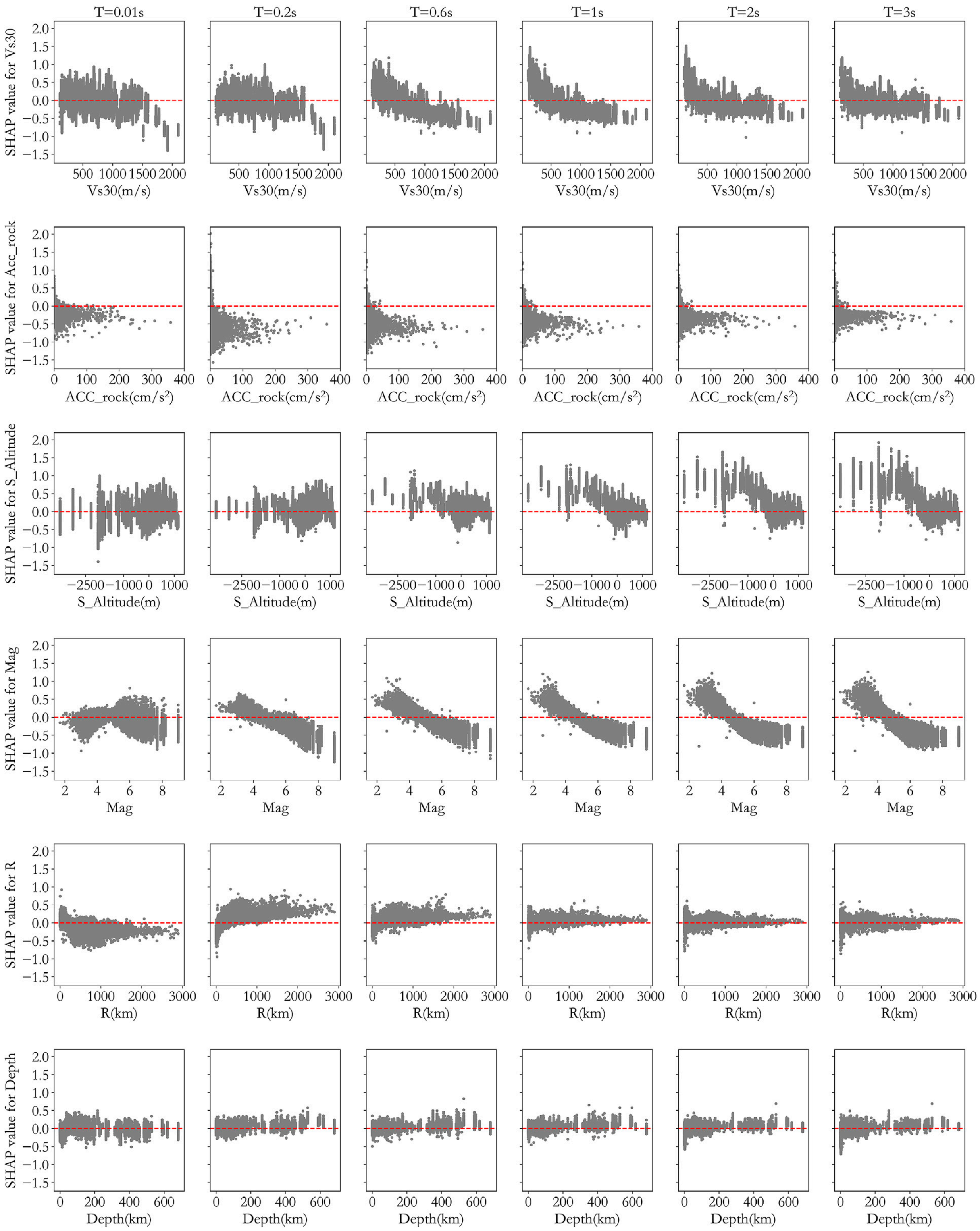

FIGURE 9
Scattering plots for feature parameters and their corresponding SHAP values.

To further study the generalization capability of the proposed XGBoost model, 6 events with different Vs30 values outside the training dataset were chosen to verify the amplification prediction results, as shown in Figure 8. As can be seen from Figure 8, for different Vs30, the predicted amplification factor is pretty close to the actual ratio,

TABLE 2 Average SHAP value of each feature parameter at different periods.

	Vs30	Mag	S_Altitude	Acc_rock	R	Depth
T=0.01s	0.2	0.17	0.24	0.13	0.23	0.16
T=0.2s	0.08	0.13	0.16	0.27	0.18	0.24
T=0.6s	0.19	0.16	0.13	0.18	0.15	0.18
T=1s	0.09	0.09	0.04	0.041	0.03	0.04
T=2s	0.05	0.03	0.03	0.06	0.03	0.043
T=3s	0.04	0.26	0.16	0.08	0.12	0.09

indicating good stability and generalization capability of the proposed model.

4 Explanation of the predicted results

Although machine learning has been increasingly applied in many areas with great success, it is still considered a "black box" approach with little reasonable explanation of the results. In this study the SHAP approach is introduced to explain the prediction models proposed. SHAP was originally constructed by Lundberg (Akiba et al., 2019) in 2017 as an explanation model, and its core is to calculate the contribution (SHAP values) of each feature parameter based on collaborative game theory to reflect the contribution of each parameter in the prediction. The calculation of SHAP value can be expressed in the following.

$$SHAP_{feature}(\mathbf{x}) = \sum\nolimits_{set:\, feature \in set} \left[|\mathbf{set}| * \begin{pmatrix} \mathbf{F} \\ |\mathbf{set}| \end{pmatrix} \right]^{-1} \left[\mathbf{y}_{set}(\mathbf{x}) - \mathbf{y}_{set \setminus feature}(\mathbf{x}) \right] \tag{14}$$

where $\mathbf{y}_{set}(x)$ represents the model prediction when feature parameters are ***set*** and **F** is the feature number.

For assembled tree models, SHAP method considers each feature parameter as a contributor, and the summation of contribution value from every parameter will lead to the final prediction assessment, as in the following (Lundberg and Lee, 2017):

$$y = \mathbf{SHAP_0} + \sum\nolimits_{i=1}^{F} SHAP_i \tag{15}$$

where y is the predicted result by the model, and $\mathbf{SHAP_0}$ is the average prediction for all samples in the training dataset. $SHAP_i$ represents the SHAP value of the i-th feature parameter.

It should be noted that the effect of each feature parameter on the prediction has been studied in the past (Liu and Lei, 2005), but those studies did not consider the coupling effect of other feature parameters in the analysis. Based on collaborative game theory, SHAP approach can well represent the contribution by each feature parameter *via* SHAP value in the prediction results accounting for the coupleinge effect of feature parameters, and the contribution can be both positive and negative, thus well suited for explaining the prediction results (Zhang, 2020).

4.1 Contribution of each feature parameter

As explained in previous sections, XGBoost performed the best in the prediction, therefore it was selected to predict site amplification factor at 6 periods (0.01, 0.2, 0.6, 1, 2, and 3 s) and the corresponding SHAP values were calculated. For observation of the relationship between feature parameter and SHAP value, scattering plots were provided in Figure 9 for all 6 parameters at the 6 periods. From Figure 9 we can make the following observations.

1. SHAP value increases with Vs30 when Vs30 is small, but decreases when Vs30 is large, representing a negative correlation between SHAP value and Vs30. This negative trend increases with increasing period value. The positive

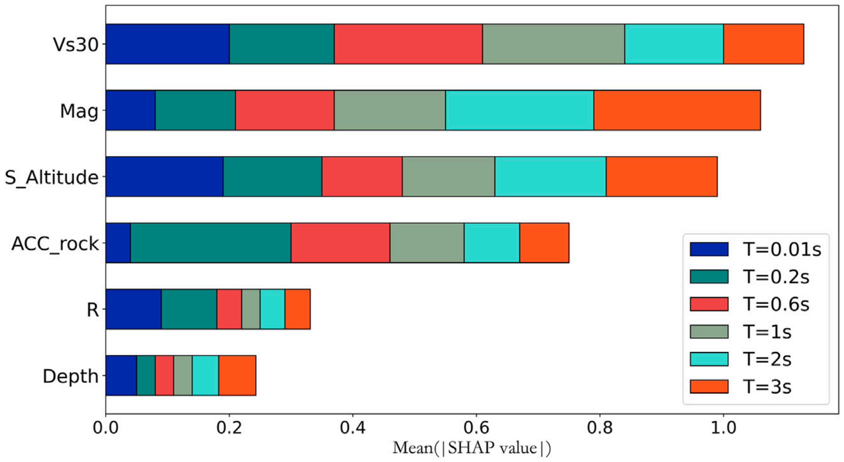

FIGURE 10
Feature importance ranking.

correlation when Vs30 is small indicates that the predicted value for soft soil sites is bigger than actual value, and this over prediction is worse for longer periods. This observation is comparable to the conclusions in previous studies (Emel et al., 2014; Wojtuch et al., 2021), validating the results by this study and providing an evidence to show that SHAP analysis can well explain the model results.

2. There is generally a negative correlation between Mag and its SHAP value, representing over prediction by the model for smaller earthquakes.
3. There is no clear correlation trend between station altitude and its SHAP value when the period is short (0.01 and 0.2 s). When the period increases, the SHAP value is big when the altitude is small, and the SHAP value increases with decreasing station altitude, representing over prediction at low altitude for long periods.
4. There is obvious negative correlation between bedrock acceleration (Acc_rock) and SHAP value, which means that the model overpredicts the site amplification when Acc_rock is small but underestimates the amplification when Acc_rock is big. This observation is also supported by results by Beresnev (Walling et al., 2008), which may be because of non-linear effect of the site.
5. From the perspective of SHAP calculation, the SHAP values for Depth and R do not show a particularly obvious trend.

4.2 Feature parameter importance

The SHAP value analysis has provided a good picture of the impact by each feature parameter, and to further quantify the impact of each parameter on the prediction results, importance analysis was performed for all the feature parameters in this study. In a typical XGBoost model, importance can be ranked using different measures (Gain, Cover, Weight) but the conclusion can be different if using different measures, so it is hard to decide which measure is the best for application. Since SHAP value represents the contribution of each feature parameter on the prediction result, we can use the average of the SHAP value to objectively represent the importance of each feature parameter and rank the absolute mean SHAP value to decide on the importance of each parameter. The results are shown in Table 2. The same results are graphically represented in Figure 9 for better comprehension. As can be seen from both Table 2 and Figure 10 Vs30, Mag, S_Altitude and Acc_rock have relatively large influence on the prediction results while R and Depth show less influence with Vs30 having the largest impact and Depth having the least impact. These results may serve as good reference for future site amplification studies.

5 Conclusion

Based on the observed ground motion between 1997 and 2019 and station information from the KiK-net, a large database was assembled that included both the site amplification factor and 6 feature parameters. Three prediction models for site amplification factor based on machine learning were proposed and prediction results were compared against the result by a traditional approach at 6 different periods. Extensive analysis was conducted to find the best prediction model. SHAP analysis was used on the XGBoost model to provide better explanation of the prediction results and assess the impact and importance of the 6 feature parameters at 6 different periods. The following observations can be made based on this study.

1. In terms of predicting site amplification effect, machine learning algorithms are significantly better than traditional regression methods. Among the three machine learning approaches studied, XGBoost performs the best, followed by RF and DNN.
2. Comparison with the actual ground motion records for site amplification verifies the performance of the XGBoost prediction model, demonstrating huge potential of machine learning in site amplification factor prediction.
3. In the SHAP analysis, Vs30, Acc_rock and Mag are significantly negatively correlated with the predicted value, and S_Altitude is negatively correlated for large periods.

4. Of the 6 feature parameters, Vs30 has the largest impact on the prediction results, followed by Mag, S_Altitude, Acc_rock, R and Depth of the hypocenter.

These conclusions can be used to better quantify the effect of site condition and provide reference for future studies on site conditions.

Data availability statement

Publicly available datasets were analyzed in this study. This data can be found here: https://www.doi.org/10.17598/NIED.0004 https://pan.baidu.com/

Author contributions

XW, ZW, and JW participated in the conception and design of the study and wrote the first draft. PM, HD, and ZL wrote sections of the manuscript. All authors contributed to manuscript revision, read, and approved the submitted version.

Funding

This study is funded by National Natural Science Foundation of China (51978634) and Scientific Research Fund of Institute of Engineering Mechanics, China Earthquake Administration (Grant No. 2021B09).

Acknowledgments

The authors are grateful to NIED for its ground motion database, and to Google for its TensorFlow package used in this study.

Conflict of interest

Authors ZW and JW were employed by CEAKJ ADPRHexa Inc.

The remaining authors declare that the research was conducted in the absence of any commercial or financial relationships that could be construed as a potential conflict of interest.

Publisher's note

References

Abrahamson, N. A., and Silva, W. J. (1997). Empirical response spectral attenuation relations for shallow crustal earthquakes. *Seismol. Res. Lett.* 68 (1), 94–127. doi:10.1785/gssrl.68.1.94

Akiba, T., Sano, S., and Yanase, T. (2019). "Optuna: A next-generation hyperparameter optimization framework," in Proceedings of the 25th ACM SIGKDD international conference on knowledge discovery & data mining, 2623–2631.

Bala, A., Grecu, B., Ciugudean, V., and Raileanu, V. (2009). Dynamic properties of the quaternary sedimentary rocks and their influence on seismic site effect: Case study in bucharest city, Romania. *Soil Dyn. Earthq. Eng.* 29 (1), 144–154.

Bommer, J. J., and Martinez-Pereira, A. (2000). "Strong-motion parameters: Definition, usefulness andpredictability," in Proc. of the 12th World Conference on Earthquake Engineering Auckland, New Zealand.

Boore, D. M., Fumal, T. E., and Joyner, W. B. (1997). Equations for estimating horizontal response spectra and peak acceleration from western north American earthquakes: A summary of recent work. *Seismol. Res. Lett.* 68 (1), 128–153. doi:10.1785/gssrl.68.1.128

Boore, D. M. (2004). Estimating s(30) (or NEHRP site classes) from shallow velocity models (depths < 30 m)[J]. *Bull. Seismol. Soc. Am.* 94 (2).

Boore, D. M., Stewart, J. P., Seyhan, E., and Atkinson, G. M. (2014). NGA-West2 equations for predicting PGA, PGV, and 5% damped PSA for shallow crustal earthquakes. *Earthq. Spectra* 30 (3), 1057–1085. doi:10.1193/070113eqs184m

Borcherdt, R. D., and Gibbs, J. F. (1976). Effects of local geological conditions in the San Francisco Bay region on ground motions and the intensities of the 1906 earthquake. *Bull. Seismol. Soc. Am.* 66 (2), 1170.

Borcherdt, R. D. (1970). Effects of local geology on ground motion near San Francisco Bay. *Bull. Seismol. Soc. Am.* 60 (1), 29–61.

Breiman, L. (2001). Random forests. *Mach. Learn.* 45 (1), 5–32. doi:10.1023/a:1010933404324

Chen Longwei Chen Zhuoshi Yuan Xiaoming (2013). Site-specific amplification function assessment and variability analysis using KiK-Net single-station strong motion data. *China Cicil Eng. J.* 46, 141–145.

Chen, T., and Guestrin, C. (2016). "Xgboost: A scalable tree boosting system," in Proceedings of the 22nd acm Sigkdd International Conference on Knowledge Discovery and Data Mining, 785–794.

Derras, B., Bard, P-Y., and Cotton, F. (2017). VS30, slope, H800 and f0: Performance of various site-condition proxies in reducing ground-motion aleatory variability and predicting nonlinear site response. *Earth Planets Space* 69 (1), 133. doi:10.1186/s40623-017-0718-z

Dobry, R., Borcherdt, R., Crouse, C., Idriss, I. M., Joyner, W. B., Martin, G. R., et al. (2000). New site coefficients and site classification system used in recent building seismic code provisions. *Earthq. Spectra* 16 (1), 41–67. doi:10.1193/1.1586082

Emel, S., Jonathan, P. S., and Eeri, S. (2014). Semi-empirical nonlinear site amplification from NGA-west2 data and simulations. *Earthq. Spectra Prof. J. Earthq. Eng. Res. Inst.* 30 (3), 1241–1256. doi:10.1193/063013eqs181m

Gerolymos, N., and Gazetas, G. (2005). Constitutive model for 1-D cyclic soil behaviour applied to seismic analysis of layered deposits. *Soils Found.* 45 (3), 147–159. doi:10.3208/sandf.45.3_147

Hamidreza, T., and Soleimani Kutanaei, S. (2015). Evaluation of effect of soil characteristics on the seismic amplification factor using the neural network and reliability concept. *Arabian J. Geosciences* 8 (6), 3881–3891. doi:10.1007/s12517-014-1458-z

Harmon, J., Hashash, Y. M. A., Stewart, J. P., Rathje, E. M., Campbell, K. W., Silva, W. J., et al. (2019). Site amplification functions for central and eastern North America – Part II: Modular simulation-based models. *Earthq. Spectra* 35 (2), 815–847. doi:10.1193/091117eqs179m

Hinton, G. E., Osindero, S., and Teh, Y. W. (2006). A fast learning algorithm for deep belief nets. *Neural Comput.* 18 (7), 1527–1554. doi:10.1162/neco.2006.18.7.1527

Idriss, I. M., and Seed, H. B. (1968). Seismic response of horizontal soil layers. *Proc. ASCE* 94 (4), 1003–1031. doi:10.1061/jsfeaq.0001163

Jordan, M. I., and Mitchell, T. M. (2015). Machine learning: Trends, perspectives, and prospects. *Science* 349 (6245), 255–260. doi:10.1126/science.aaa8415

Kaveh, A., Bakhshpoori, T., and Hamze-Ziabari, S. M. (2016). Derivation of new equations for prediction of principal ground-motion parameters using M5′ algorithm. *J. Earthq. Eng.* 20 (6), 910–930. doi:10.1080/13632469.2015.1104758

Liu, Huan, and Lei, Yu (2005). Toward integrating feature selection algorithms for classification and clustering [J]. *IEEET rans Knowled geand Data Eng.* 17 (4), 491–502.

Lundberg, S. M., and Lee, S. I. (2017). "A unified approach to InterpretingModel predictions," in Proceedings of Annual Conference onNeural Information Processing Systems, 4765–4774.

Park, D., and Hashash, Y. M. A. (2008). Rate-dependent soil behavior in seismic site response analysis. *Can. Geotechnical J.* 45 (4), 454–469. doi:10.1139/t07-090

Park, D., and Hashash, Y. M. A. (2004). Soil damping formulation in nonlinear time domain site response analysis. *J. Earthq. Eng.* 8 (2), 249–274. doi:10.1080/13632460409350489

Roten, D., and Olsen, K. B. (2021). Estimation of site amplification from geotechnical array data using neural networks[J]. *Bull. Seismol. Soc. Am.* 111 (4).

Roten, D., and Olsen, K. B. (2021). Estimation of site amplification from geotechnical array data using neural networks[J]. *Bull. Seismol. Soc. Am.* 111 (4), 1784–1794.

Sadigh, K., Chang, C. Y., Egan, J. A., Makdisi, F., and Youngs, R. R. (1997). Attenuation relationships for shallow crustal earthquakes based on California strong motion data. *Seismol. Res. Lett.* 68 (1), 180–189. doi:10.1785/gssrl.68.1.180

Seed, H. B., and Idriss, I. M. (1969). The influence of soil conditions on ground motions during earthquake[J]. *J. Soil Mech. Found. Eng. Div. ASCE* 94, 93–137.

Seed, H. B., Romo, M. P., Sun, J. I., Jaime, A., and Lysmer, J. (1988). The Mexico earthquake of September 19, 1985: Relationships between soil conditions and earthquake ground motions [J]. *Earthq. Spectra* 4, 687–729. doi:10.1193/1.1585498

Seyhan, E., and Stewart, J. P. (2014). Semi-empirical nonlinear site amplification from NGA-West2 data and simulations. *Earthq. Spectra* 30 (3), 1241–1256. doi:10.1193/063013eqs181m

Walling, M., Silva, W., and Abrahamson, N. (2008). Nonlinear site amplification factors for constraining the NGA models. *Earthq. Spectra* 24 (1), 243–255. doi:10.1193/1.2934350

Wojtuch, A., Jankowski, R., and Podlewska, S. (2021). How can SHAP values help to shape metabolic stability of chemical compounds? *J. Cheminformatics* 13 (1), 74–20. doi:10.1186/s13321-021-00542-y

Yoojoong, C., and Jonathan, P. S. (2005). Nonlinear site amplification as function of 30 m shear wave velocity. *Earthq. Spectra* 21. doi:10.1193/1.1856535

Zhang, L. (2020). Prediction of V_{s30} in datong basin and amplification effect of site ground motion based on typical geological characteristics analysis. *IOP Conf. Ser. Earth Environ. Sci.* 455 (1), 012069. (11pp). doi:10.1088/1755-1315/455/1/012069

Zhu, C., Cotton, F., Kawase, H., Haendel, A., Pilz, M., and Nakano, K. (2021). How well can we predict earthquake site response so far? Machine learning vs. Physics-based modeling. *Earthq. Spectra* 38 (2), 1047–1075. doi:10.1177/87552930211060859

frontiers | Frontiers in Earth Science

TYPE Original Research
PUBLISHED 27 March 2023
DOI 10.3389/feart.2023.1028712

OPEN ACCESS

EDITED BY
Yadab P. Dhakal,
National Research Institute for Earth Science and Disaster Resilience (NIED), Japan

REVIEWED BY
Liu Yu,
Southwest Jiaotong University, China
Leonardo Colavitti,
Istituto Nazionale di Geofisica e Vulcanologia, Italy

*CORRESPONDENCE
Zhongxian Liu,
✉ zhongxian1212@163.com

SPECIALTY SECTION
This article was submitted to Structural Geology and Tectonics,
a section of the journal
Frontiers in Earth Science

RECEIVED 12 September 2022
ACCEPTED 09 March 2023
PUBLISHED 27 March 2023

CITATION
Li C, Liu P, Liu Z, Yuan X, Tian Y, Zhang H and Cao Z (2023), 3D seismic simulation analysis of the Longtoushan Town Basin during the 2014 Ludian earthquake, Yunnan province.
Front. Earth Sci. 11:1028712.
doi: 10.3389/feart.2023.1028712

3D seismic simulation analysis of the Longtoushan Town Basin during the 2014 Ludian earthquake, Yunnan province

Chengcheng Li[1,2], Peng Liu[2], Zhongxian Liu[2]*, Xiaoming Yuan[1], Yuan Tian[3], Hai Zhang[2] and Zhenzhong Cao[4]

[1]Institute of Engineering Mechanics, Key Laboratory of Earthquake Engineering and Engineering Vibration, China Earthquake Administration, Harbin, China, [2]Tianjin Key Laboratory of Soft Soil Characteristics and Engineering Environment, Tianjin Chengjian University, Tianjin, China, [3]School of Civil and Resource Engineering, Research Institute of Urbanization and Urban Safety, University of Science and Technology Beijing, Beijing, China, [4]Guangxi Key Laboratory of Geomechanics and Geotechnical Engineering, Guilin University of Technology, Guilin, China

On 3 August 2014, a magnitude Ms 6.5 earthquake struck Ludian County, Zhaotong City, Yunnan Province, causing grave losses of life and property in the Longtoushan Town Basin near the fault. In this study, a three-dimensional model of the Longtoushan Town Basin and the velocity structure of the surrounding area, and the Spectral Elements in Elastic Dynamics code, which combines the discontinuous Galerkin technique and the spectral element method (SEM) are used to simulate and study the entire seismic wave propagation process. The results show that due to the variations in the basin geometry and the impedance ratio of the media inside and outside the basin, the seismic waves incident on the basin edge are refracted and diffracted, further prolonging the ground motion holding time within the basin. In the bedrock outside the basin, the velocity peaks are higher at higher elevations; viceversa within the basin, the locally depressed basement produces an obvious amplification effect. The amplitude of the ground motion is not the greatest in the thickest sedimentary layers in the basin, and it is closely related to the degree of undulation at the base of the sedimentary layers, the overburden thickness, and the basin geometry. The peak ground accelerations (PGAs) of approximately 8 m/s^2 in the east–west (E–W) direction and 3 m/s2 in the north–south (N–S) direction are influenced by the rupture directivity effect (the ruptured surface is the Baogunao–Xiaohe fault that is oriented in the N–W direction). The peak ground velocity with a sedimentary model is 2.6 and 1.6 times that of the non-sedimentary model in the E–W and N–S directions, respectively. The maximum amplification factor for PGA in the E–W direction is 2.8 and that in the N–S direction is approximately 2.3. The results are in agreement with the actual observed seismic station data in terms of the waveforms and peaks, and the intensity distribution map matches the actual damage distribution. This proves the accuracy and rationality of the method used in this study. The results are useful for the seismic zoning of cities, and they can help engineers predict ground motions for future large earthquakes.

KEYWORDS

Longtoushan Town Basin, amplification effect, 3D model, seismic wave propagation, spectral element method

1 Introduction

Numerous cities around the world are located in basins, such as Los Angeles Olsen (2000); Komatitsch et al. (2004), Osaka Pitarka et al. (1998), Taipei Lee et al. (2008), Chengdu Yu (2017), and Xi'an Ren et al. (2013). Therefore, the study of basin effects is an active topic of interest for seismologists and engineers. For example, during the 2008 Wenchuan earthquake, a VII degree intensity anomaly zone (with a VI degree surrounding intensity) was observed in the Baoji–Meixian region, which is located at the edge of the Weihe Basin, and a VI degree anomaly zone within a V degree zone was observed in Xi'an in the interior of the basin (Parsons et al., 2008; Li et al., 2016). On 3 August 2014, a magnitude Ms 6.5 earthquake occurred in Ludian County, Zhaotong City, Yunnan Province, with an epicenter at 27.1° N, 103.3° E and a depth of 12 km (according to the China Earthquake Administration). Although the earthquake was not a mega-quake, the Longtoushan Township Basin, Ludian County, which is located near the epicenter, suffered severe damage, with an intensity reaching IX degrees (Zhang Y. et al., 2014; Lin et al., 2020). The earthquake counts 617 deaths, 112 missing people, 3,143 injured, and its direct economic loss was about 3.46 billion dollars (Li et al., 2016). Most of the buildings in Longtoushan Town were seriously damaged or collapsed due to the strong earthquake. The experts analyzing the damage of Longtoushan Town observed obvious differences in the degree of earthquake damage between two adjacent areas (Lin et al., 2020). Thus, the propagation process and distribution pattern of the ground vibrations within the basin under the effect of earthquake need to be systematically researched and analyzed, which helps in the seismic zoning of cities and the seismic design of structures.

For the Ms 6.5 magnitude earthquake in Ludian County, Zhaotong City, Yunnan Province, that occurred on 3 August 2014, Liu (2021) developed a two-dimensional (2D) basin model of the Longtou Mountain present in this region based on borehole and topographic data. They analyzed the site amplification effect under the action of SV waves (a shear wave that is polarized so that its direction of propagation and particle motion occur in a vertical plane) using the explicit finite element method. However, several previous studies have shown that 2D models do not represent the magnitude and duration of ground shaking in three-dimensional (3D) models. Horike et al. (1990) compared the differences in the amplification effect of ground shaking between 3D and 2D basins and found that the 2D model does not represent the magnitude and duration of the ground shaking in the 3D model. Toshinawa and Ohmachi (1992) used a 3D finite element method to simulate the propagation of Love waves in the Kanto Basin, Japan. They determined that the 3D model yields a larger amplitude and longer duration of ground shaking than the 2D model, and the simulation results obtained by the 3D model were closer to the observed record than those obtained by the 2D model. Ohori et al. (1990) compared the differences between a 3D resonance model and one-dimensional (1D) and 2D resonance models and found that the resonance amplification factors and resonance frequencies were greater in the 3D model than those in the 1D and 2D models. In addition, they found that the 3D basin structures have a significant effect on the ground shaking. Compared to the 2D model, the irregular 3D basin comprises the same edge, focusing, and resonance effects as in the 2D basin, and the 3D basin makes the internal propagation of body and surface waves more complex. Therefore, this study performs a 3D ground motion simulation analysis of the Longtoushan Town Basin after the 2014 Ludian earthquake in the Yunnan region.

The main techniques for studying the seismic effects in the basins are analytical methods, ground vibration observation methods, and numerical simulation methods. Analytical methods are only applicable to regularly shaped basins, wherein the media inside and outside the basin are single or layered linear elastic media. The analytical solutions of 2D sedimentary basins under seismic wave incidence have been relatively well studied (Trifunac, 1971; Wong and Trifunac, 1974; Bard and Bouchon, 1980a; 1980b; Todorovska and Lee, 1990; Yuan and Liao, 1995; Paudyal et al., 2012). Since the real site conditions are complex and the topography is often irregular, obtaining an analytical solution to the corresponding problem is difficult, and thus, the problem is usually solved using numerical analysis. The seismic observation method employs a dense seismic record within the basin, which already considers the influence of the media and site conditions within the basin, making the results highly accurate (Frankel, 1993; Wen and Peng, 1998; Cornou et al., 2003a; 2003b). However, this method has several disadvantages. First, it is computation expensive and requires an intensive seismic record of the basin; thus, the current seismic network is only used for some basins in earthquake-prone areas. Second, it requests high-quality seismic data, e.g., the record cannot contain significant ambient background noise. Third, the number of seismic records obtained is limited; therefore, the method is still under development.

The main numerical simulation methods are the finite element method (Bao et al., 1998), the finite difference method (Olsen and Schuster, 1995; Graves et al., 1998; Lee et al., 2008), the boundary element method (Lee, 2013; Semblat et al., 2022; Huang et al., 2022), and the Spectral Element Method (SEM) (Smerzini and Villani, 2012; Liu et al., 2013; Abraham et al., 2016; Vijaya et al., 2020). Finite difference methods are prone to numerical dispersion near large gradients in the wavefield or when the used grid is too coarse. Thus, they do not achieve the same accuracy when imposing free boundary conditions on the surface cells as that in the inner region. Furthermore, they are only applicable to simple geometrical changes and may affect the calculation stability when a deformed grid is used. The finite element method is based on the variational form of the wave equation. It naturally introduces the free boundary conditions and is suitable for describing complex media with arbitrary shapes but usually has significant numerical dispersion properties, with pseudo-waves appearing in higher-order conventional finite elements. The boundary element method is based on the integral expressions for quantities associated with the physical boundaries and can accurately model the propagation of outgoing waves on the boundary. However, it is often restricted to linear and homogeneous problems and may yield solutions that are not unique. SEM, which was introduced by Patera (1984) for computational fluid dynamics, combines the spectral method with the finite unit method, taking advantage of the fast convergence of the spectral method and the flexibility of the finite unit method. SEM can well adapt to complex terrains and can accurately model surface waves. Hence, it has been increasingly used in recent years for simulating the seismic responses in basins.

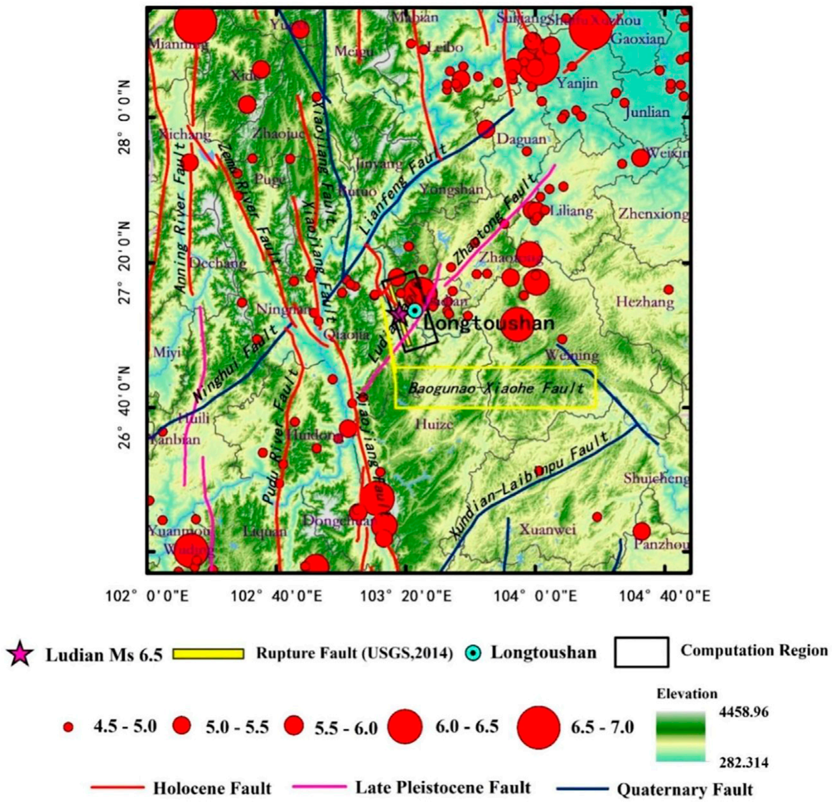

FIGURE 1
Seismogenic structure and historical seismicity around the M6.5 Ludian earthquake. The pink star and the yellow rectangular with black border outline the epicenter and projection of the rupture fault of this earthquake provided by the USGS, respectively. The area within the black rectangular is the study area. Red circles of different sizes represent historical earthquakes of different magnitudes. The red, pink, and blue lines represent Holocene, Late Pleistocene, and Quaternary faults, respectively.

TABLE 1 Medium parameters used in the simulation.

Soil layer number	ρ (kg/m^3)	V_S (m/s)	V_P (m/s)	Q_S	Q_P
Soil layer 1 (inside-basin)	2,000	450	814.5	45	82
Soil layer 2	2,110	1,070	2,500	107	250
Soil layer 3	2,460	2,590	4,600	259	460
Soil layer 4	2,740	3,550	6,100	355	610
Soil layer 5	2,780	3,650	6,300	365	630

Lee et al. (2009) used SEM to simulate the strong ground motion in the Taipei Basin and investigated the interaction between mountains and sedimentary basins as well as the effects of the earthquake source location, depth, and rupture processes on the distribution of the ground motion in the basin. Stupazzini et al. (2009) used a high-performance SEM program to simulate the seismic response of a near-fault earthquake in the Glenoble Valley, France. Hu et al. (2011) employed SEM to simulate the topographic effects of the Wenchuan earthquake that occurred on 12 May 2008. Liu et al. (2013) investigated the amplification effect of seismic wave propagation in the Shidian Basin using SEM. Liu et al. (2017) studied the effects of the wave velocity and dip angle of soil layers under the action of strike–slip faults on the seismic amplification effect of sedimentary basins as well as the seismic response of 3D sedimentary basins under the action of point sources. Yu (2017) used high-precision parallel SEM to better understand the seismic effects in the Shidian Basin and Sichuan Basin.

However, this method has some limitations that need to be addressed, such as the complexity of the geometric constraints and dealing with complex 3D non-homogeneous media while keeping the computational cost low. The Politecnico di Milano, Italy, developed the numerical Spectral Elements in Elastic Dynamics

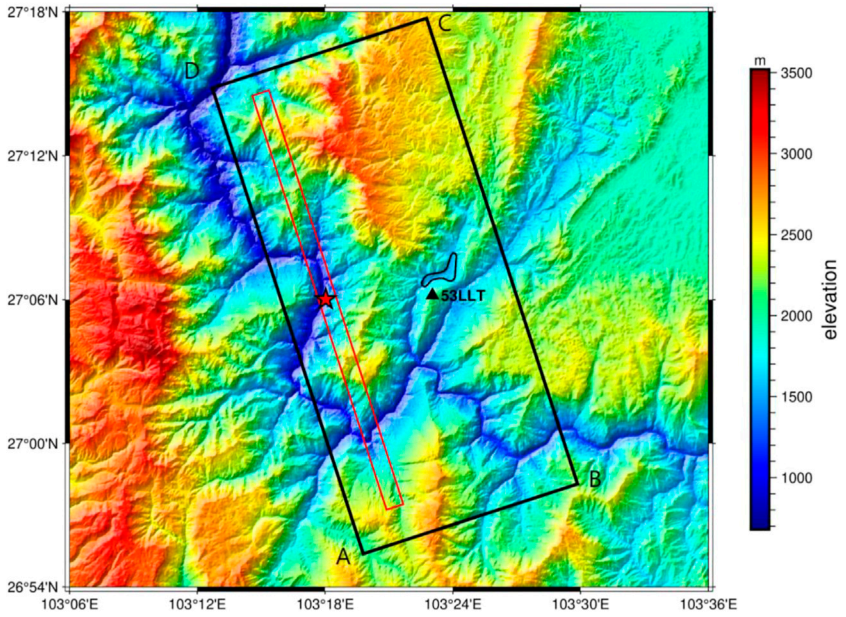

FIGURE 2
Map displaying the source location of the M6.5 Ludian earthquake. The area within the black rectangular outline is the study area. The red rectangular outline is the projection of the rupture fault location of the Ludian earthquake in Yunnan provided by the USGS. The red star denotes the epicenter location provided by the USGS. The black outline denotes the location of the Longtoushan town.

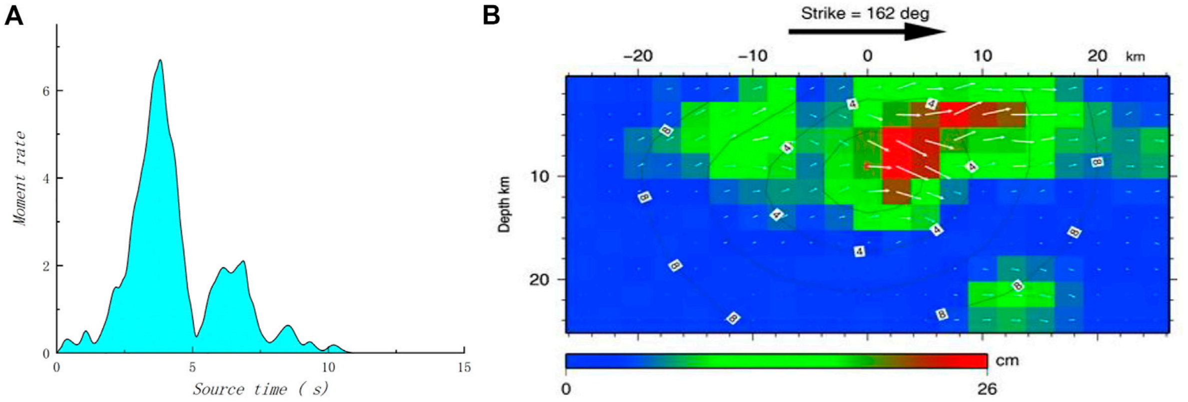

Ludian source time function obtained through inversion by Zhang et al. (2014)

Slip distribution of Ludian earthquake obtained by Hao et al. (2014)

FIGURE 3
Source model of the Ms 6.5 2014 Ludian earthquake. **(A)** Ludian source time function obtained through inversion by Zhang Z. G et al. (2014). **(B)** Slip distribution of Ludian earthquake obtained by Hao et al. (2014).

(SPEED) code (http://mox.polimi.it/it/progetti/speed). This code combines non-coherent discretization methods, discontinuous Galerkin (DG) techniques, and SEM and can handle non-uniform polynomial distributions (N-Adaptive) and locally varying grid sizes (h-Adaptive). SPEED is a numerical code for simulating both linear and non-linear elastodynamic problems in heterogeneous media based on the Spectral Elements (SE) decomposition technique, allowing for non-conforming meshes through a DG approach (Mazzieri et al., 2013).

In this study, the SPEED code is used to simulate the entire seismic wave propagation process that occurred in the Longtoushan Town Basin during the 2014 Ludian earthquake. This basin is narrow and has a width of approximately 3.1 km from the north to south and a length of 2.8 km from the east to west. We investigate

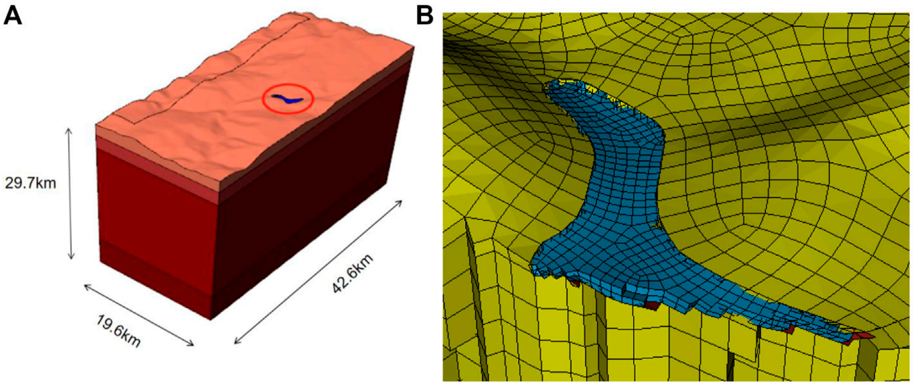

Global 3D model

Locality 3D basin model

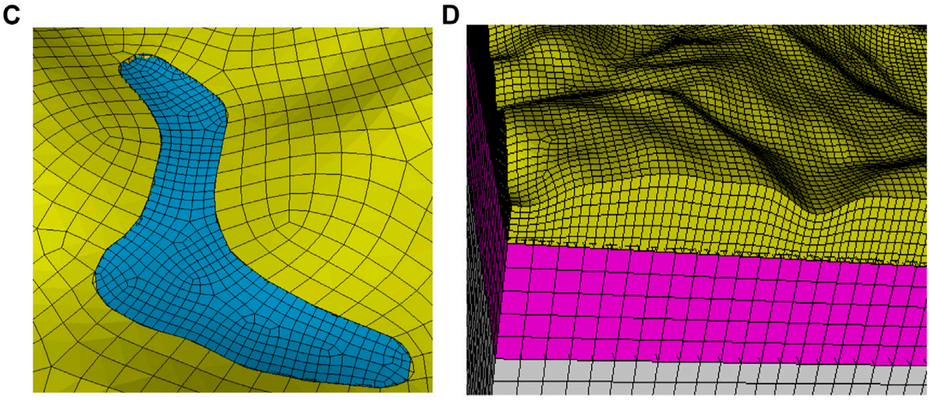

Discontinuous grid in the basin

Discontinuous grid of the model

FIGURE 4
3D computational model of the 2014 M6.5 Ludian–Longtoushan Basin earthquake. **(A)** Global 3D model. **(B)** Locality 3D basin model. **(C,D)** Discontinuous grid in the basin.

the generation and propagation of the seismic waves and we analysed the differences in the ground motion at different locations in the basin and the effect of the topographic reliefs. The correctness and rationality of the study results are verified by comparing them with the observed data from seismic stations and the observed distribution of the damage to buildings caused by the earthquake.

2 Geological framework

As shown in Figure 1, the epicenter of the 2014 Ludian earthquake was located southwest of the Ludian County, and it was along the Lianfengshan fault in the NE direction and the Zhaotong, Zemuhe, Xiaojiang, Anning, and Yuanmou–Lujuijiang faults in the NS direction. The Zhaotong–Ludian fault begins from the west of Yiliang Niujie in the NE and ends SW of the Niulan River after passing through Zhaotong and Ludian. The total length of the Zhaotong–Ludian fault is about 160 km, the overall strike is 30°, the rake direction is southeast, and the dip is 60°–80°(USGS; Zhang et al., 2014). According to the solution of the main seismic source mechanism, aftershock spatial distribution, regional geological structure, seismic intensity, strong ground motion record, and other data, the seismic fault of this earthquake is determined to be NNW to Baogunao–Xiaohe fault, which is the NW secondary slipping fault that is NE to the Zhaotong–Ludian fault system; all the faults belong to the Xiaojiang fault system (USGS; Zhang Z. G. et al., 2014; Li et al., 2015; Zhao and Sun, 2014; Xu et al., 2014; Li and Li, 2016). The Baogunao–Xiaohe fault is a Holocene fault; no earthquake with M ≥ 5.0 has been recorded in its history, and the largest earthquake recorded of this fault and its major fault system was the Ludian earthquake with Ms 4.4 that occurred on 6 August 1989.

3 Source model of the Ms 6.5 2014 Ludian-Longtoushan Basin earthquake

The coverage area of the present research is shown in detail in Figure 2. The elevation data for the sedimentary layer in the basin were obtained from observed data, including the geological cloud

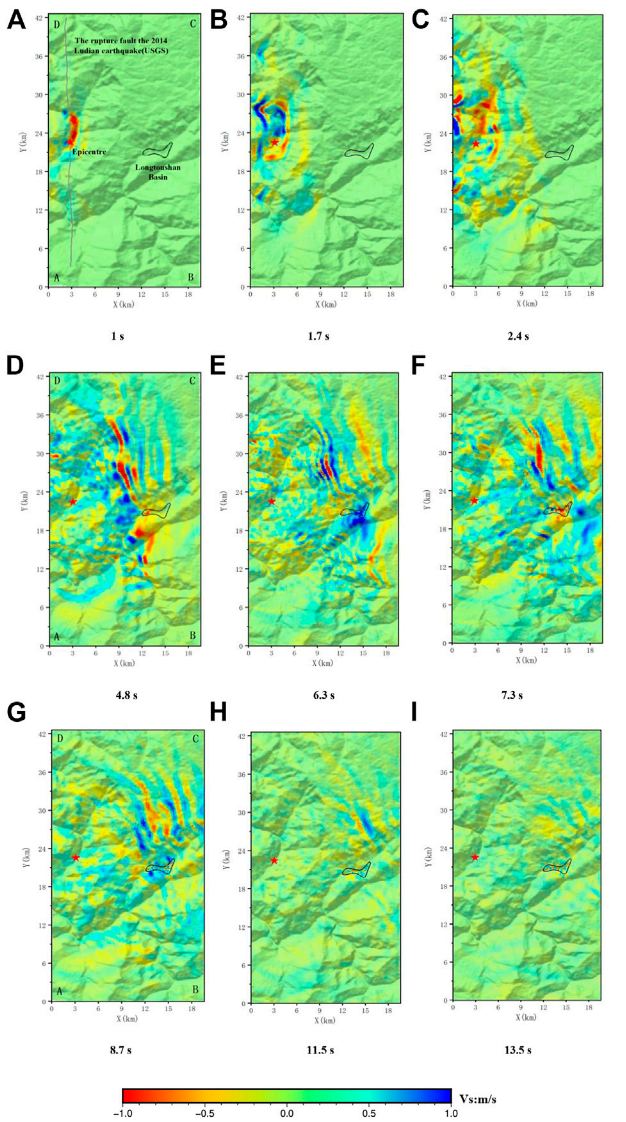

FIGURE 5
Wave field snapshots of east–west components of the surface ground motion. The black outline denotes the basin. The red star and gray line denote the epicenter and rupture fault of this earthquake provided by the USGS, respectively. **(A)** 1 s; **(B)** 1.7 s; **(C)** 2.4 s; **(D)** 4.8 s; **(E)** 6.3 s; **(F)** 7.3 s; **(G)** 8.7 s; **(H)** 11.5 s; **(I)** 13.5 s.

(https://geocloud.cgs.gov.cn/), boreholes in the basin, resistivity profile inversion along the measuring lines (Pang et al., 2016), and a safety evaluation report. The basin model was set to comprise of single depositional layer. The S- and P-wave velocities in the basin were 450 and 814.5 m/s, respectively, and the quality factors Q_S and Q_P were 45 and 82, respectively (Liu et al., 2013). The CRUST1.0 (https://blog.seisman.info/crust1/) model based on the global velocity structure model is used as the calculation parameter in the velocity medium model outside the basin. The model parameters are presented in Table 1.

We simulate the Ms 6.5 earthquake occurred on 3 August 2014 in Ludian County where the source is located on the west side of the basin and at 12 km-depth. The source time function is obtained from the inversion results (Zhang Y. et al., 2014), and the rise time was 0.2 s with a total source duration of about 10.7 s (Figure 3A).

Following this earthquake, many researchers utilized different data and methods to invert a series of source rupture models. In this study, Hao's dislocation model (Hao et al., 2014) is used. It was built based on the near-field ground motion stations, and the rupture process of the earthquake is obtained using the data from this model. Source mechanism solutions are based on the United States Geological Survey (USGS) data (strike, dip, and rake of the nodal plane are 162°, 86°, and 6°, respectively; the second strike, dip, and rake of the nodal plane are 72°, 84°, and 176°, respectively). Herein, the fault style is set as a normal fault. It is 50 km long along the strike direction and 25 km wide along the dip direction. The grid points in the fault profile of the model are taken as the sub-source points and are transformed into second-order spectral element points, and the corresponding seismic moments are applied to each sub-source point. Additionally, the rake is taken to 6°. The epicenter of the earthquake was located at 27.1° N, 103.3° E, and the slip distribution on the fault plane is shown in Figure 3B (Hao et al., 2014).

Figure 3B shows that the fault has a major slip area, which is represented by the red area on the fault plane, with a maximum slip of 26 cm. For the Ludian earthquake, a constant rupture speed of 2.1 km/s is assumed. Then, according to the relative positions of the source and the initial rupture point, the rupture time of each sub-source is defined.

The corresponding slip is assigned to each point according to Figure 3B, and the magnitude of the seismic moment corresponding to each point is obtained according to the shear modulus of the medium for simulating the dislocation of the whole fault. The seismic moment and shear modulus are calculated as follows:

$$M = S \cdot G \cdot A$$
$$G = v_s^2 \cdot \rho$$

where M (N·m) is the seismic moment, S (m) is the slip, G is the shear modulus of the soil, A (m^2) is the control area at each point, vs. (m/s) is the shear wave velocity of the layer, and ρ (kg/m^3) is the density of the medium.

4 Calculation method

The open-source spectral element program SPEED (http://mox.polimi.it/it/progetti/speed) is used to simulate the seismic effect of the Ludian earthquake in the Longtoushan Basin. SEM aims to divide the computational range into finite elements and to configure non-uniformly distributed nodes (Legendre–Gauss–Lobatto points, LGL points) on each element. The approximate solution of the element is expressed as the corresponding truncated orthogonal polynomial, and the Galerkin method is used to solve for the approximate global solution. The main difference method or the Newmark predictor calibration is usually adopted as the time integration scheme (Mazzieri et al., 2013).

The model used herein considers the influence of the 3D terrain (Figure 4A). The regional grid size in the basin is set as 80 m, and the regional grid outside the basin is set as 200–500 m (Figure 4B). To ensure the continuity of the deformation, discontinuous contact surfaces are set between soil layers 1 and 2 and between soil layers

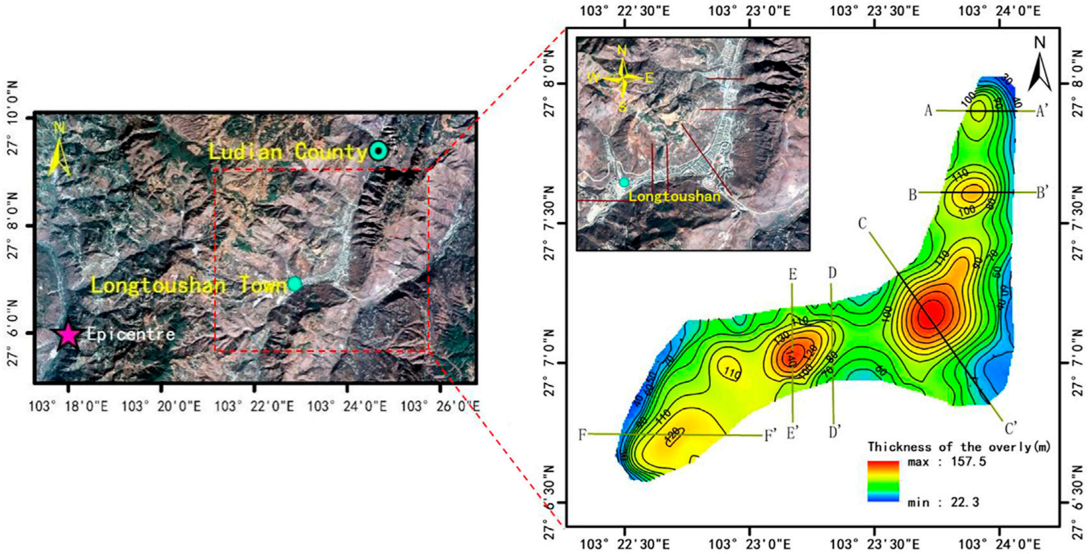

FIGURE 6
Location of the basin and locations of the selected profiles in the basin.

2 and 3. As is shown in Figures 4C, D, the number of grids is greatly reduced using this method, which consequently improves the calculation efficiency. This model comprises 312995 units and 347286 nodes. Absorbing boundary conditions are applied on five boundary surfaces, except the ground surface. In each SE, a polynomial degree N = 2 is used, and thus each element contains $(N + 1)^3 = 27$ LGL integration points. According to the accuracy requirement of spectral element method which contains at least five grid points in the shortest wavelength, and the LGL integration points for the elements at the surface of the basin were about 80 m, so the shortest wavelength is hence equal to about 320 m, which is sufficiently small to accurately model the softest sediments within the plain up to a maximum frequency of about 1.125 Hz (Komatitsch and Tromp, 1999).

The calculation area is divided into five blocks, and the multi-node parallel computing technology based on the Linux system is adopted. The time step is 0.001 s, and the simulation time is 60 s; the total calculation time is about 38 h.

5 Results and discussion

In this section, the calculation results of the wavefield snapshots, time profiles, peak distributions, and amplification coefficients are analyzed to investigate the seismic effects of the Longtoushan Town Basin and its surrounding bedrock sections.

5.1 Wavefield snapshot

A snapshot of the velocity wavefield in the east–west (E–W) direction in the computed area is shown in Figure 5, which displays the propagation of the seismic waves at the surface. At around t = 1–1.7 s, the seismic waves excited by the fault dislocation spread outwards, and the P-waves propagating outwards from the epicenter are roughly elliptical. During this time, the vibrations in the basin are relatively weak, and no significant surface wave generation is observed. At t = 2.4 s, the S-wave reaches the basin. At t = 4.8–6.3 s, the amplitude of the ground shaking within the basin becomes significantly larger than that in the outer bedrock areas due to the presence of low-wave-velocity sedimentary layers. In addition, due to the low wave velocity of the media in the basin, simultaneous arrivals of waves from multiple source points occur in the sedimentary depression region of the Longtoushan Town Basin. They superimpose and interfere in this area, resulting in elevated ground shaking amplitudes and significant delay and bending of the S-wave front. At around t = 7.3–8.7 s, the body wave largely passes through the basin, but most of the fluctuating energy is captured in the basin. At this time, surface waves with large amplitudes are generated and they propagate after the body waves; when they encounter the opposite edge of the basin, some of the surface waves are reflected again into the basin. At around t = 13.5 s, the ground shaking response outside the basin largely dissipates and some residual surface waves remain scattered within the basin, which further prolongs the ground shaking holding time within the basin. This phenomenon indicates that the response time of the seismic waves in the low-velocity basin is greater than that in the surrounding bedrock section, reflecting the strong wake phenomenon of the seismic waves in the low-velocity region.

The snapshot of the wave field (Figure 5) shows that because the basin contains sedimentary layer with low wave velocity, the complex seismic waves radiated by the fault during rupture are captured in the basin and are superimposed in certain areas within the basin. This leads to an interference phase length phenomenon, which increases the duration of the seismic waves in the basin. Due to the above phenomenon and the fact that the basin is along the propagation direction of the wave front generated by the fault movement, the ground shaking is stronger in some areas of the basin.

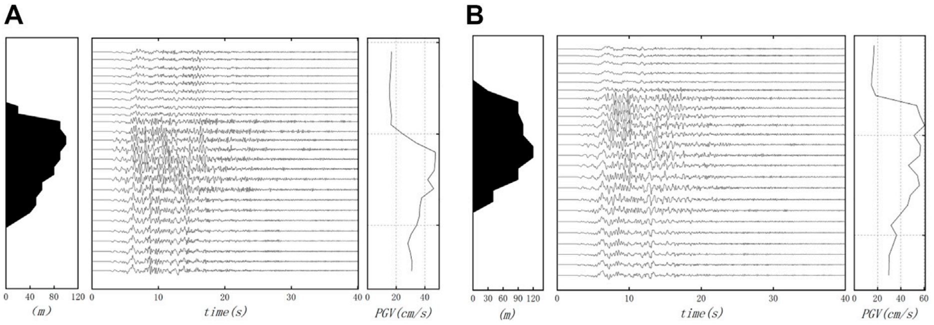

Section A–A’

Section B–B’

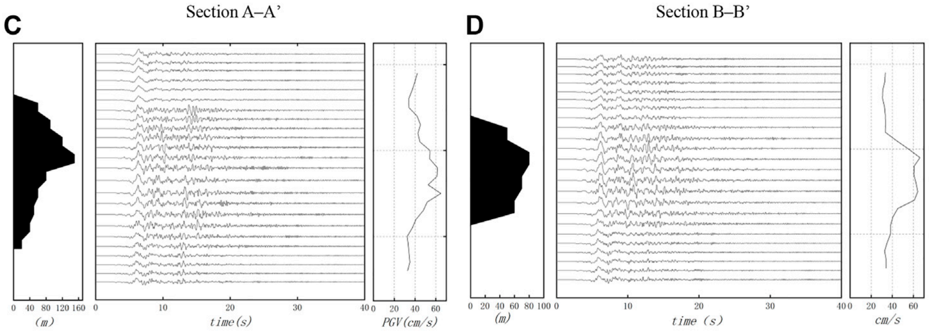

Section C–C’

Section D–D’

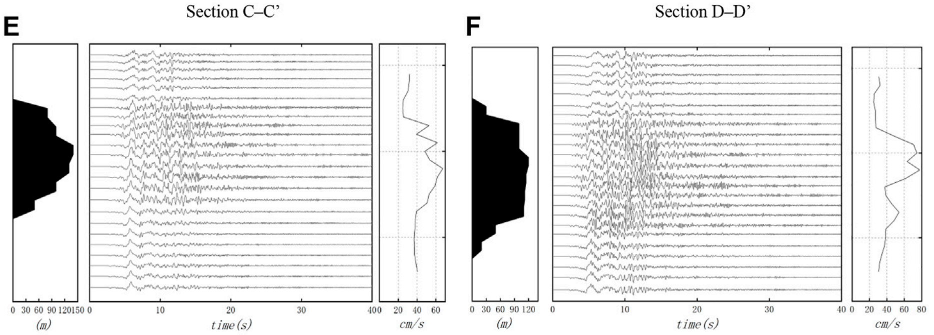

Section E–E’

Section F–F’

FIGURE 7
Ground motion time history. Thickness of the deposit (left, black area) corresponding to the observation points on sections A–A′ to F–F′, velocity time histories at the observation points (middle), and the PGV at the surface of each section (right). **(A)** Section A–A’; **(B)** Section B–B’ **(C)** Section C–C’; **(D)** Section D–D’; **(E)** Section E–E’; **(F)** Section F–F’.

5.2 Time history analysis

Figure 6 displays the outline of Longtoushan Town and six typical profiles. Profiles A–A′, B–B′, C–C′, and F–F′ trend E–W, while profiles D–D′ and E–E’ trend north–south (N–S). Each profile runs through the basin, and for each profile, both the bedrock surface outside the basin and the interior of the basin can be seen. The relief within the Longtoushan Basin is relatively gentle, with surface elevations ranging from 1,550 to 1800 m. In this study, the response pattern of the basin is analyzed under the effect of ground shaking by studying the elevation changes on the profiles and the vibration time range and peak ground velocity (PGV) changes at the selected points on each profile.

The topography of the basin floor, the E–W component velocity timescales, and their peak velocities corresponding to the selected points on all six profiles are shown in Figure 7. The amplification of the ground shaking by the basin and the longer duration of the shaking within the basin than that outside the basin are observed for all the profiles; that is, the amplitude of the velocity timescale within the basin is much greater than that outside the basin. In the bedrock section outside the basin, the profiles exhibit some differences. In profiles A–A′ and B–B′, the western part of the basin has lower elevation than the eastern part; thus, the peak bedrock velocity in the west is significantly lower than that in the east. The peak velocities in the bedrock outside the basin range from approximately 15–40 cm/s, and the durations are approximately 10 s. The peak velocities in the soil within the basin range from 40 to 80 cm/s, and durations are approximately 20 s. The six profiles are analyzed in more detail below.

Profiles A–A′ and B–B′ are located in the northern part of Longtoushan Town, and the surface elevation map shows that the ground surface comprises depressions. In profile A–A′, the maximum thickness of the sediment layer is approximately 150 m; in profile B-B′, it is approximately 200 m. The velocity

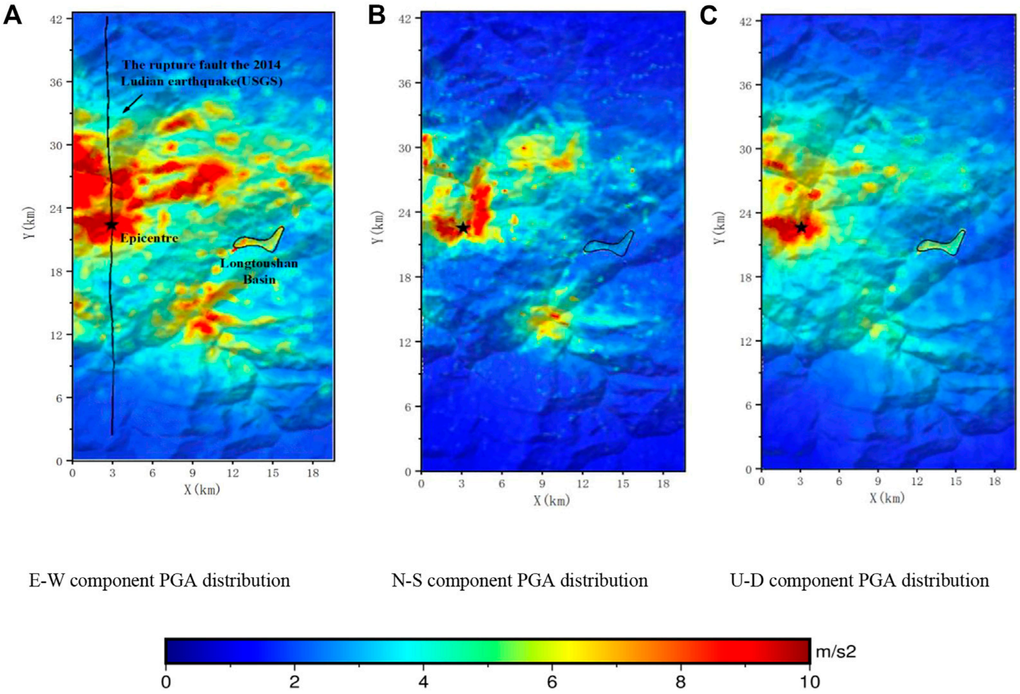

E-W component PGA distribution

N-S component PGA distribution

U-D component PGA distribution

FIGURE 8
PGA distribution of the model. The black star and black line denote the epicenter and rupture fault of this earthquake provided by the USGS, respectively. **(A)** E-W component PGA distribution. **(B)** N-S component PGA distribution. **(C)** U-D component PGA distribution.

curves of both profiles have large amplitudes at the location of the lowest point in the depression. In this area, the waveform dramatically changes, and the peak velocity is roughly 2.5 times that of the surrounding bedrock. The peak velocities in profile A–A′ show that in the bedrock section, the peak velocity is small (approximately 20 cm/s) and the amplitude and waveform little vary. After the seismic waves enter the depression, the seismic intensity gradually increases, with a maximum value of 56 cm/s at approximately the center of the depression. Then, the amplitude decreases, and the amplitude of profile A–A′ is slightly smaller than that of profile B–B′. This may be because the thickness of the deposit in profile B–B′ is larger than that in profile A–A′, with more surface wave development, and the waves reflected from the basin are more likely to be superimposed at this location. It is speculated that the depressed substrate converges the seismic waves at a central location, resulting in a more intense seismic response.

Profile C–C′ is located in the deepest part of the Longtoushan Town Basin and cuts diagonally through several important buildings, such as the Longtoushan Township police station, and through the center of the basin, where the sediments are the thickest. Figure 7 shows that the bottom of the depression in profile C–C′ is relatively smooth, and the velocity–time plot shows that the change of the peak velocity is relatively gentle in the profile, with a peak velocity of 60 cm/s. Due to the low wave velocity of the media in the basin, the arrival of the body waves in the basin lags behind that outside the basin. The ground shaking on the profile is similar in the central part but is smaller at the edges, and the amplitude and duration are not very different. Figure 7 also shows that the peak velocity of profile C–C′ is smaller than that of profile F–F′, which is most likely due to the large width-to-thickness ratio in this region. This causes the surface waves to take longer time to propagate to the middle of the basin and makes them difficult to superimpose. Furthermore, the effect of the basin edge is relatively weak in this area. This phenomenon suggests that the response to ground shaking is not necessarily the greatest in the basin areas with thick sedimentary layer and that the magnitude of the response to ground shaking is closely related to the surrounding topography, the overburden thickness, and the basin shape.

Profiles D–D′ and E–E′ are located in the central part of the Longtoushan Town Basin in a narrow zone between mountains (Figure 6). The two profiles are similar in shape, and the sedimentary layer in profile E–E′ is somewhat thicker than that in profile D–D′; thus, the peak velocity of profile D–D′ is slightly larger. The waveforms show that the velocity peaks in both profiles (D–D′, E–E′) are greater than those in profiles A–A′ and B–B′. This is because the two profiles are located between the two boundaries of the basin, with a narrow N–S extent, and the surface waves propagate back and forth within the basin, with significant basin edge effects.

Profile F–F′ is located in the southernmost part of Longtoushan Town, and the variations in the base of the sediment layer in this profile are greater than those in the other profiles. Moreover, the peak velocity of this profile is greater than that of the other five profiles, with a maximum PGV of approximately 80 cm/s. This is probably due to the narrow of the overlying strata in this profile and the complex undulation of the base of the overburden, which leads to a basin-focusing effect. In addition, the profile is located at the edge of the basin and close to the seismogenic fault. The direct body waves and the surface waves propagating within the basin as well as

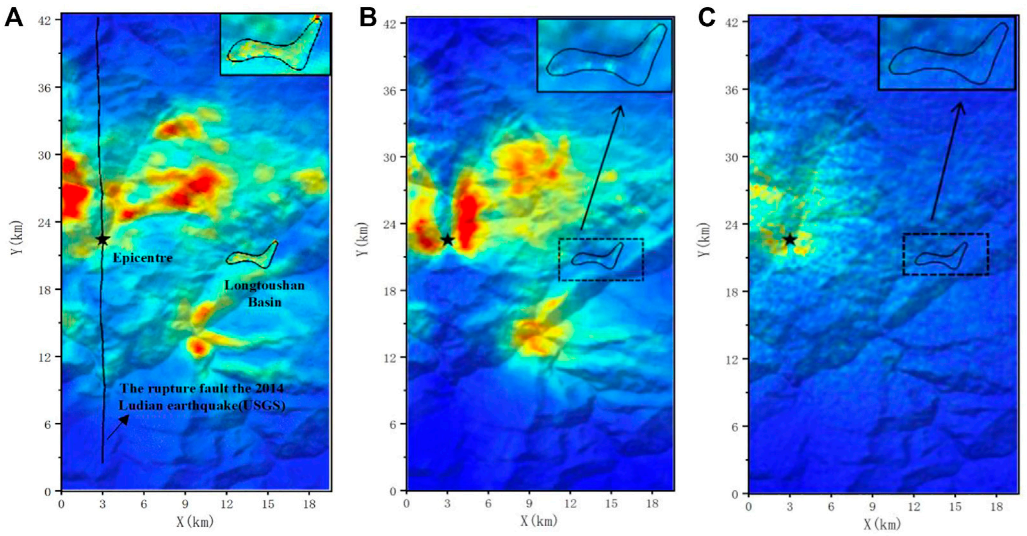

E-W component PGVs (bedrock only model)

N-S component PGVs (bedrock only model)

U-D component PGVs (bedrock only model)

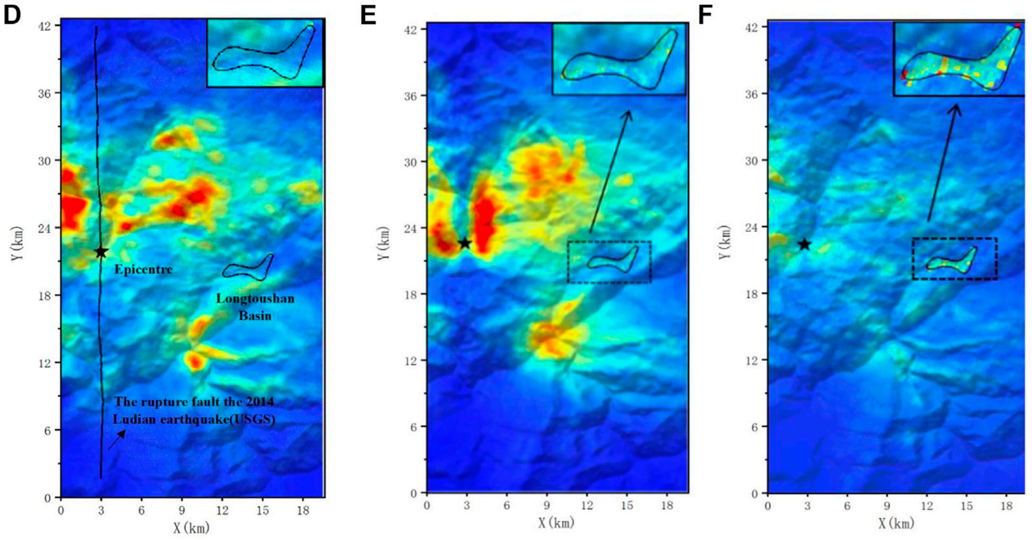

E-W component PGVs (basin model)

N-S component PGVs (basin model)

U-D component PGVs (basin model)

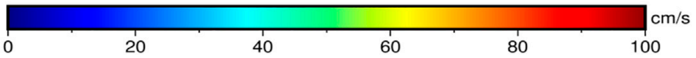

FIGURE 9
PGV (m/s) distribution of E−W, N−S, and U-D components obtained using different models. The black star and black line denote the epicenter and rupture fault of this earthquake provided by the USGS, respectively. **(A)** E-W component PGVs (bedrock only model). **(B)** N-S component PGVs (bedrock only model). **(C)** U-D component PGVs (bedrock only model). **(D)** E-W component PGVs (basin model). **(E)** N-S component PGVs (basin model). **(F)** U-D component PGVs (basin model).

the waves from outside the basin that enter *via* the edge of the basin overlap, resulting in a strong interference phenomenon, thus significantly amplifying some vibration frequencies and exhibiting the edge effect of the basin.

5.3 PGA distribution

Figure 8 shows the peak ground acceleration (PGA) distribution in three directions, E–W, N–S, and vertical (U–D), for the terrain in

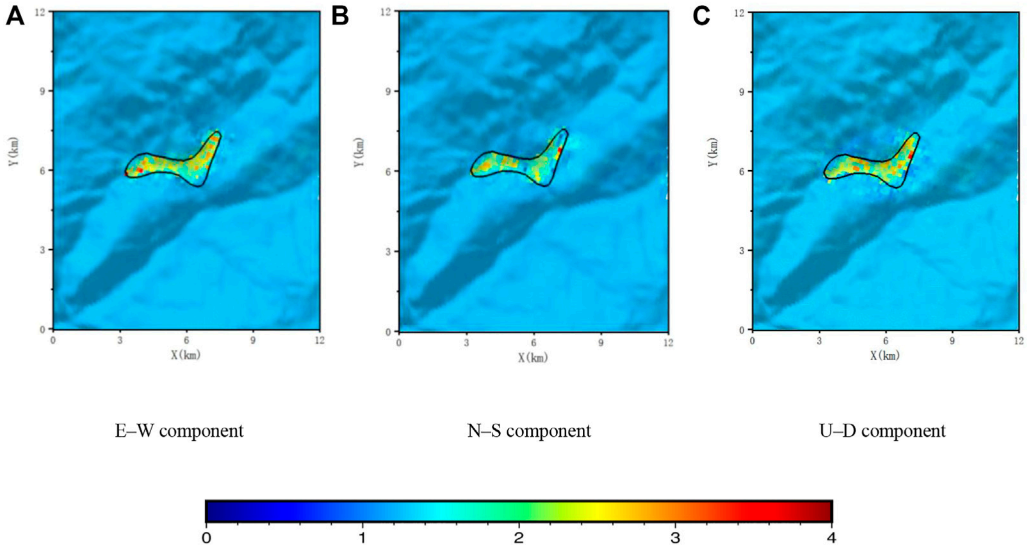

E–W component

N–S component

U–D component

FIGURE 10
Distribution of the amplification factors of PGA (E−W, N−S, and U−D components) in the Longtoushan Town basin model compared with the bedrock site model without the basin. **(A)** E−W component. **(B)** N−S component. **(C)** U−D component.

and around Longtoushan Town, Ludian County, Yunnan Province, during of the earthquake.

Figure 8 shows that the PGA distribution is influenced by the direction of the seismic wave propagation. The PGA distribution is related to the propagation of the wave front in Figure 5, which shows that the wave front passes with larger PGA values are located near the fault surface, within the basin area, and in the hilltop location. The waves within the basin are amplified compared to those in the surrounding bedrock, which is consistent with the observed record.

In the E–W direction, the areas with large PGA values within the basin are concentrated in the southern part of the basin, around profile F–F′, with values of approximately 8 m/s^2. This is caused by the trapping effect of the depressions on the seismic wave energy and the interference among the seismic waves reflected from the basin boundary in different directions, both of which can cause sustained ground shaking with large magnitudes.

The ground shaking in the basin is less intense in the N–S direction than that in the other two directions, and the overall PGA distribution in the basin exhibits a similar pattern. As shown in Figure 8, the PGA in the part of the basin with the deepest cover (157 m) is approximately 2.1 m/s2, which is smaller than that in the other areas (for example, 110 m in F-F′) of the basin. This is mainly because comparing this area with the other areas, the bottom of the depression is flatter, and the secondary surface waves generated are weaker and do not have a significant focusing effect.

In the U–D direction, the average PGA in the basin is approximately 6 m/s^2, which is approximately three times that of the surrounding bedrock.

5.4 PGV distribution

The ground motion velocity is related to the kinetic energy of particle vibration and is often used as a physical quantity to measure the ground motion energy Bao et al. (1998). The shear wave impedance between the basin and bedrock determines the amount of incident wave energy that can pass through the basin–bedrock interface, which affects the generation of secondary surface waves in the basin. Figure 9 presents a model containing a sedimentary basin and a model with bedrock only. The distributions of the PGVs E–W, N–S, and U–D components in the calculated area that are obtained *via* simulation using these two models are used to study the influence of the sedimentary basin in the area affected by seismic activity. The simulations using different models exhibit the same trends of the ground shaking distributions, but the differences in the distribution of the ground shaking in the basin are greater than outside the basin.

In the E–W direction, the peak velocity is approximately 25 cm/s for the bedrock model and 65 cm/s for the basin model. In the N–S direction, the amplitude of the ground shaking in the basin area is approximately 35 cm/s for the bedrock model and 57 cm/s for the basin model. In the U–D direction, the peak velocity is about 18 cm/s for the bedrock model and about 73 cm/s for the basin model.

The results show that the Longtoushan Town Basin significantly influences the distribution of the ground shaking in the E–W and U–D directions. The N–S component is less influenced by the sedimentary layers than the E–W component. The peaks of the seismograms are also high in some areas at the edge of the basin, reflecting the basin edge effect.

5.5 Magnification factor

In order to reflect the amplification of the sedimentary basin, the amplification factor of the basin is defined as the ratio of the PGA simulated using the model containing the basin to the PGA simulated using the model without the basin. Figure 10 illustrates the distribution of the amplification factors for the three PGA

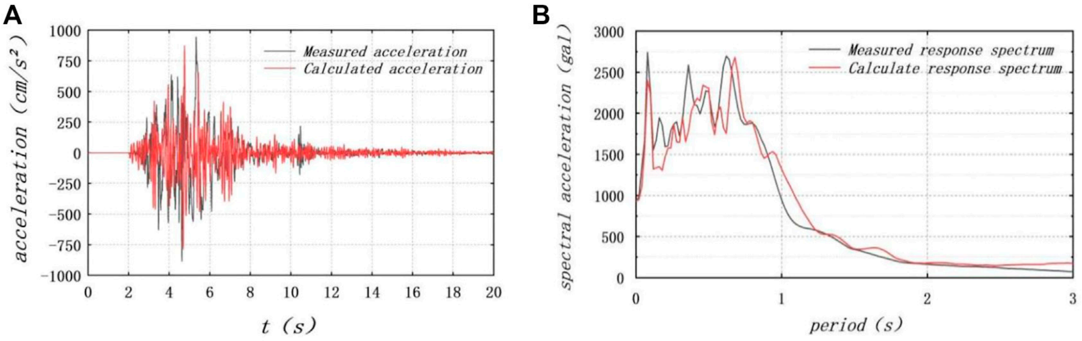

Comparison of acceleration in 53LLT, E–W direction

Comparison of acceleration response spectrum E–W direction

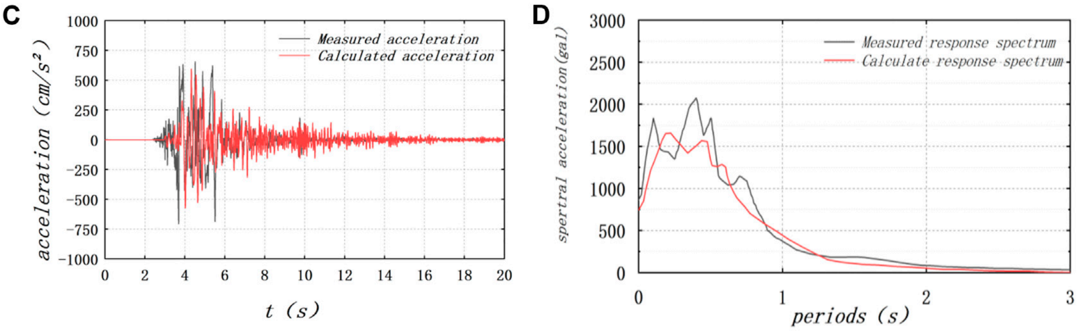

Comparison of acceleration in 53LLT, N–S direction

Comparison of acceleration response spectrum N–S direction

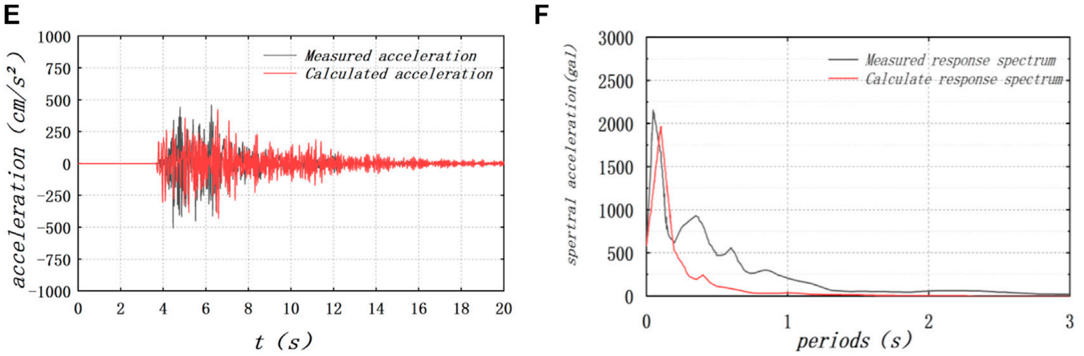

Comparison of acceleration in 53LLT, U-D direction

Comparison of acceleration response spectrum U–D direction

FIGURE 11
Comparison between the simulation and observed records. **(A)** Comparison of acceleration in 53LLT, E−W direction. **(B)** Comparison of acceleration response spectrum E−W direction. **(C)** Comparison of acceleration in 53LLT, N−S direction. **(D)** Comparison of acceleration response spectrum N−S direction. **(E)** Comparison of acceleration in 53LLT, U-D direction. **(F)** Comparison of acceleration response spectrum U−D direction.

components in the Longtoushan Basin. For the E–W component, the areas with larger amplification factors are mainly located in the deeper areas of the basin and the smaller amplification factors are mainly located at the edge of the basin, and the largest amplification coefficient is 2.8, which is located near profile F–F. For the N–S component, the maximum amplification factor is approximately 2.3, which is located at the edge of the basin. For the U–D component, the maximum amplification factor is 2.18, which is smaller than those of the other two components. The amplification effect of the basin mainly stems from two aspects: the influence of the basin geometry and the influence of the difference in the wave impedances of the media inside and outside the basin.

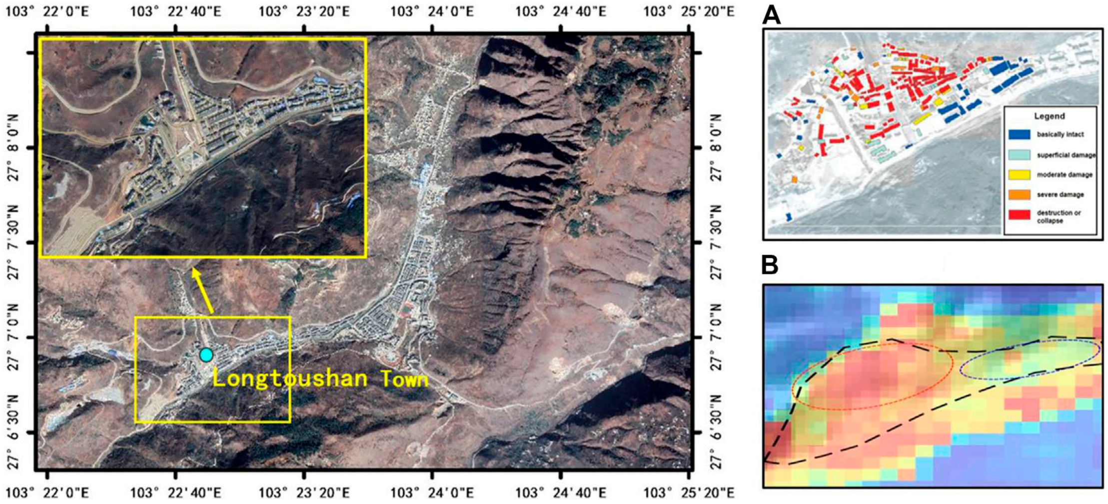

FIGURE 12
Comparison of the actual damage. **(A)** Spatial distribution of the seismic damage to buildings in Longtoushan Town Lin et al. (2020). **(B)** Local PGA map of Longtoushan Town, this study. The colour scale is the same as Figure 8.

6 Validation

6.1 Comparison between simulated time history and observed records

During the strong ground Ludian motions in 2014, strong earthquakes were recorded at stations in the China Strong-Motion Networks Center, which provide a reference for validating the correctness of the simulation results. The site records are used for comparison: 53LLT (27.1°N, 103.4°E) is located about 1 km from the basin and is the only station in the calculation range of this study (Figure 2). The calculation accuracy is verified by the acceleration curve and acceleration response spectrum (Figure 11).

Overall, the calculated results are close to the peak values of the observed records. Particularly, the peak value of the simulation results of the three-component is close to that recorded at 53LLT, but the simulation results after 6 s are greater than the observed values.

The acceleration response spectra obtained from accelerations at 53LLT are compared with the simulation results at the corresponding location, as shown in Figures 11B, D, F. In general, the characteristics of the acceleration response spectra of the three-component match the observations for this site reasonably well, especially in the E–W and N–S directions, which validate the applicability of the proposed method in this paper. Figure 11B, D, F shows that the larger values in the response spectrum of 53LLT are concentrated at periods shorter than 1 s. This may be due to the fact that 53LLT is located close to the fault where the ground motion response is more intense, resulting in the pulse phenomenon.

For the rupture process of the earthquake, we considered the complexity of the structures and the geological conditions. For example, the present model uses a constant rupture velocity and sliding angle, but in the rupture zone in the Ludian region, the geological structure and the rupture process of the earthquake source are very complex. Therefore, the difference between the observed results and the simulation results obtained in this study is considered acceptable, and the calculations reflect the validity of the basin model and the rupture of the earthquake source to a certain extent.

In this research, the maximum frequency was about 1.125 Hz; however, the actual strong ground motion caused by earthquakes is often presented as a wide band signal. The reduction of the grid scale to increase the computing frequency will greatly increase the number of computing nodes and make computation difficult. Owing to the computational and knowledge constraints associated with the rupture process and velocity structure at fine spatial scales, the method of this study is difficult to resolve at high frequencies. In the future, wide-band ground motion simulation will be investigated and more scenarios covering a range of magnitudes and source parameters of basins will be computed, which will provide a better understanding of the seismic effect of the basin for detailed hazard assessment. And we will consider the source directivity effects (Wen et al., 2015; Convertito et al., 2016; Vincenzo et al., 2016; Ross et al., 2020; Colavitti et al., 2022) in our future research in more detail below.

6.2 Comparison of post-earthquake damage investigation

Following the work of Lin et al. (2020), we analyzed the seismic damages for 192 buildings in Longtoushan Town (Figure 12A). Based on the remote sensing data and historical news reported before and after the earthquake (Li et al., 2016; Lin et al., 2020), the spatial distribution of the seismic damage to the buildings caused by the Ludian earthquake in 2014 is obtained. Figure 12A shows that the building damage is mainly divided into five grades, among which the buildings with serious damage are mainly distributed on the left side of the figure and buildings with minor damage are mainly distributed on the right side.

Figure 12B shows the simulated PGA map, and its scope corresponds to Figure 12A. The black line in Figure 12 represents the general outline of Longtoushan Town. The red and blue ellipses denote the areas with more and less serious damage, respectively. The calculation results are consistent with the actual damage.

7 Conclusion

In this study, a three-dimensional model of the Longtoushan Town Basin and the velocity structure of the surrounding area are used to simulate and study the entire seismic wave propagation process in the basin during the 2014 Ludian earthquake using the Spectral Elements in Elastic Dynamics code, which combines the discontinuous Galerkin technique and the spectral element method (SEM). The simulation results were comprehensively analyzed based on the snapshots of the wave field propagation, surface wave characteristics with different geometric features on the profiles, and the distribution of the peak ground shaking (PGA and PGV) in areas with and without sedimentary layers. Analysis was performed by comparing the data with actual station records and the observed distribution of building damage caused by the earthquake.

Due to the special geometry of the basin and the difference in the impedance ratio between the media inside and outside the basin, the seismic waves incident on the basin’s edge were refracted and diffracted, causing the response time of seismic waves in the low-wave-velocity basin media to be significantly greater than that in the surrounding bedrock, which reflects the generation of large amplitude seismic waves in the low-wave-velocity basin media.

Examination of the elevation changes on each profile, the vibration time histories at the simulated points on the profiles, and the PGV change patterns showed that for the bedrock areas outside the basin, the peak velocities were higher at sites with higher topography and the ground vibration holding times were significantly lower than those inside the basin. Inside the basin, the locally depressed substrates had a focusing effect, which resulted in a more intense seismic response. The ground shaking response was not necessarily the greatest in the thickest sedimentary layers within the basin. The ground shaking amplitude was closely related to the degree of undulation of the base of the sedimentary layers, the overburden thickness, and the basin geometry.

The maximum PGA distribution in the E–W direction was higher than that in the N–S direction. The PGA was approximately 8 m/s^2 in the E–W direction and approximately 3 m/s^2 in the N–S direction.

Comparison of the simulation results for the models with and without sedimentary layers showed that for the model with sedimentary layers, PGV was 2.6 times higher in the E–W direction and 1.6 times higher in the N–S direction than that for the model without sedimentary layers. The maximum amplification factor of PGA was 2.8 in the E–W direction, approximately 2.3 in the N–S direction, and approximately 2.18 in the U–D direction, which is smaller than that in the other two directions. The amplification effect of the basin was mainly due to the influence of the basin geometry and the difference in the wave impedances of the media inside and outside the basin.

The acceleration time history and acceleration response spectrum simulated in this study were compared with the actual records for station 53LLT, and the simulated local intensity distribution map of the basin was compared with the spatial distribution of the seismic damage to the building complexes after the 2014 Ludian earthquake. The comparison revealed that the simulated time course was consistent with the records in terms of the waveforms and peaks, and the local intensity distribution cloud map for Longtoushan Town matched the actual damage situation. This proves the accuracy and rationality of the method used in this research.

Data availability statement

The datasets presented in this study can be found in online repositories. The names of the repository/repositories and accession number(s) can be found in the article/supplementary material.

Author contributions

CL: Methodology, software, writing and review, investigation; PL: Software, writing (original draft); ZL: Conceptualization, project administration, resources; XY: Conceptualization, validation, resources; YT: Software, validation, writing (review); HZ: Writing (review and editing); ZC: Validation, writing (review).

Funding

This study was supported by the Scientific Research Fund of Institute of Engineering Mechanics, China Earthquake Administration (2019C07), the National Natural Science Foundation of China (grant nos. 52008287, 51878434, and 51968015), Key project of Tianjin Science and Technology 513 Support Plan (19YFZCSN01180) and Key Laboratory of Earthquake Engineering and Engineering Vibration, China Earthquake Administration (2020EEEVL0302).

Acknowledgments

We thank the editors and reviewers for their very helpful comments and detailed suggestions for improving the manuscript. Data for this study are provided by the Institute of Engineering Mechanics, China Earthquake Administration. We thank Professor Lin Xuchuan for giving us the precise positioning of the station.

Conflict of interest

The authors declare that the research was conducted in the absence of any commercial or financial relationships that could be construed as a potential conflict of interest.

Publisher's note

References

Abraham, J. R., Smerzini, C., Paolucci, R., and Lai, C. G. (2016). Numerical study on basin-edge effects in the seismic response of the Gubbio valley, Central Italy. *Bull. Earthq. Eng.* 14 (6), 1437–1459. doi:10.1007/s10518-016-9890-y

Bao, H., Bielak, J., Ghattas, O., Kallivokas, L. F., O'Hallaron, D. R., Shewchuk, J. R., et al. (1998). Large-scale simulation of elastic wave propagation in heterogeneous media on parallel computers. *Comput. Methods Appl. Mech. Engrg.* 152, 85–102. doi:10.1016/s0045-7825(97)00183-7

Bard, P. Y., and Bouchon, M. (1980a). The seismic response of sediment-filled valleys. Part 1. The case of incidentSHwaves. *Bull. Seism. Soc. Am.* 70 (4), 1263–1286. doi:10.1785/bssa0700041263

Bard, P. Y., and Bouchon, M. (1980b). The seismic response of sediment-filled valleys. Part 2. The case of incidentPandSVwaves. *Bull. Seism. Soc. Am.* 70 (5), 1921–1941. doi:10.1785/bssa0700051921

Colavitti, L., Lanzano, G., Sgobba, S., Pacor, F., and Gallovič, F. (2022). Empirical evidence of frequency-dependent directivity effects from small-to-moderate normal fault earthquakes in Central Italy. *J. Geophys. Res. Solid Earth* 127, e2021JB023498. doi:10.1029/2021jb023498

Convertito, V., Nicola, A. P., and Francesca, D. L. (2016). Investigating source directivity of moderate earthquakes by multiple approach: the 2013 Matese (southern Italy) Mw = 5 event. *Geophys. J. Int.* 207 (3), 1513–1528. doi:10.1093/gji/ggw360

Cornou, C., Bard, P. Y., and Dietrich, M. (2003a). Contribution of dense array analysis to the identification and quantification of basin-Edge-Induced waves, Part I: Methodology. *Bull. Seism. Soc. Am.* 93 (6), 2604–2623. doi:10.1785/0120020139

Cornou, C., Bard, P. Y., and Dietrich, M. (2003b). Contribution of dense array analysis to the identification and quantification of basin-edge-induced waves, Part II: Application to Grenoble basin (French Alps). *Bull. Seism. Soc. Am.* 93 (6), 2624–2648. doi:10.1785/0120020140

Frankel, A. (1993). Three-dimensional simulations of ground motions in the San Bernardino Valley, California, for hypothetical earthquakes on the San Andreas fault. *Bull. Seismol. Soc. Am.* 83 (4), 1020–1041. doi:10.1785/bssa0830041020

Graves, R. W., Pitarka, A., and Somerville, P. G. (1998). Ground-motion amplification in the Santa Monica area: Effects of shallow basin-edge structure. *Bull. Seism. Soc. Am.* 88 (5), 1224–1242. doi:10.1785/bssa0880051224

Hao, J. L., Wang, W. M., and Yao, Z. X. (2014). *Preliminary results of inversion of the source rupture process of Yunnan Ludian M6.5 earthquake on August 3, 2014*. Beijing: Institute of Geology and Geophysics, China Academy of Sciences.

Horike, M., Uebayashi, H., and Takeuchi, Y. (1990). Seismic response in three-dimensional sedimentary basin due to plane S wave incidence. *J. Phys. Earth* 38 (4), 261–284. doi:10.4294/jpe1952.38.261

Hu, Y. X., Liu, X. R., Luo, J. H., and L, Z. (2011). Simulation of three-dimensional topographic effects of ground shaking in Wenchuan earthquake zone by spectral element method. *J. Lanzhou Univ. Nat. Sci. Ed.* 47 (4), 24–32.

Huang, L., Liu, Z. X., Wu, C., and Liang, J. W. (2022). A three-dimensional indirect boundary integral equation method for the scattering of seismic waves in a poroelastic layered half-space. *Eng. Anal. Bound. Elem.* 135, 167–181. doi:10.1016/j.enganabound.2021.11.012

Komatitsch, D., and Tromp, J. (1999). Introduction to the spectral element method for three-dimensional seismic wave propagation. *Geophys. J. Int.* 139 (3), 806–822. doi:10.1046/j.1365-246x.1999.00967.x

Komatitsch, D., Liu, Q. Y., Tromp, J., Suss, P., Stidham, C., and Shaw, J. H. (2004). Simulations of ground motion in the Los Angeles basin based upon the spectral-element method. *Bull. Seismol. Soc. Am.* 94 (1), 187–206. doi:10.1785/0120030077

Lee, J. (2013). Earthquake site effect modeling in the Granada basin using a 3-D indirect boundary element method. *Phys. Chem. Earth* 63, 102–115. doi:10.1016/j.pce.2013.03.003

Lee, S. J., Chen, H. W., and Huang, B. S. (2008). Simulations of strong ground motion and 3D amplification effect in the Taipei Basin by using a composite grid finite-difference method. *Bull. Seismol. Soc. Am.* 98 (3), 1229–1242. doi:10.1785/0120060098

Lee, S. J., Komatitsch, D., Huang, B. S., and Tromp, J. (2009). Effects of topography on seismic-wave propagation: An example from northern Taiwan. *Bull. Seismol. Soc. Am.* 99 (1), 314–325. doi:10.1785/0120080020

Li, P., Liu, H. S., Bo, J. S., Li, X. B., and Yu, X. H. (2016). Effects of river valley topography on anomalously high intensity in the Hanyuan town during the Wenchuan Ms8.0 earthquake. *Chin. J. Geophys.* 59 (01), 174–184.

Li, Y., Chen, X. Z., Chen, L. J., and Guo, X. Y. (2015). Investigation on the rupture process of the Ludian MS6. 5 earthquake sequence on 3 August, 2014 in Yunnan province. *Chin. J. Geophys.* 58 (9), 3232–3238.

Li, Y. Q., and Li, Z. L. (2016). Analysis on casualty caused by the Ludian Yunnan MS 6.5 earthquake in 2014. *Earthq. Res. China* 4, 787–800.

Lin, X. C., Liu, X. Y., Hu, R. K., and Zhang, L. X. (2020). Regional damage analysis and resilience evaluation of buildings in the epicenter region of 2014 Ludian Earthquake. *J. Seismol. Res.* 43 (03), 449–455+601.

Liu, Q. F. (2021). Study on the basin resonance effect in Longtoushan Town during the 2014 Ludian earthquake. *Earthq. Eng. Eng. Dyn.* 41 (02), 43–52.

Liu, Q. F., Yu, Y. Y., and Zhang, X. B. (2013). Study of three-dimensional ground vibrations in the Shidian Basin. *Earthq. Eng. Eng. Vib.* 33 (4), 54–60.

Liu, Z. X., Liu, M. Z., and Han, J. B. (2017). Simulation of strong ground shaking spectral elements in near-fault sedimentary basins. *World Earthq. Eng.* 33 (4), 76–86.

Mazzieri, I., Stupazzini, M., Guidotti, R., and Smerzini, C. (2013). Speed: SPectral elements in elastodynamics with discontinuous Galerkin: A non-conforming approach for 3D multi-scale problems. *Int. J. Numer. Methods Eng.* 95 (12), 991–1010. doi:10.1002/nme.4532

Ohori, M., Koketsu, K., and Minami, T. (1990). Seismic response analyses of sediment-filled valley due to incident plane waves by three-dimensional Aki-Larner method. *Bull. Earthq. Res. Inst., Univ. Tokyo* 65, 433–463.

Olsen, K. B., and Schuster, G. T. (1995). Causes of low frequency ground motion amplification in the salt lake basin: The case of the vertically incident P wave. *Geophys. J. Int.* 122 (3), 1045–1061. doi:10.1111/j.1365-246x.1995.tb06854.x

Olsen, K. B. (2000). Site amplification in the Los Angeles basin from three-dimensional modeling of ground motion. *Bull. Seismol. Soc. Am.* 90 (6B), S77–S94. doi:10.1785/0120000506

Pang, W. D., Yang, R. M., Chen, J. L., Li, Z. G., and Lu, J. G. (2016). High density resistivity exploration method for Ludian MS6.5 earthquake in area of Longtoushan Town in 2014. *J. Seismol. Res.* 39 (04), 622–629+718.

Parsons, T., Ji, C., and Kirby, E. (2008). Stress changes from the 2008 Wenchuan earthquake and increased hazard in the Sichuan basin. *Nature* 454 (7203), 509–510. doi:10.1038/nature07177

Patera, A. T. (1984). A spectral element method for fluid dynamics: Laminar flow in a channel expansion. *J. Comput. Phys.* 54, 468–488. doi:10.1016/0021-9991(84)90128-1

Paudyal, Y. R., Yatabe, R., Bhandary, N. P., and Dahal, R. K. (2012). A study of local amplification effect of soil layers on ground motion in the Kathmandu Valley using microtremor analysis. *Earthq. Eng. Eng. Vib.* 11 (2), 257–268. doi:10.1007/s11803-012-0115-3

Pitarka, A., Irikura, K., Iwata, T., and Sekiguchi, H. (1998). Three-dimensional simulation of the near-fault ground motion for the 1995 Hyogo-Ken Nanbu (Kobe), Japan, earthquake. *Bull. Seismol. Soc. Am.* 88 (2), 428–440. doi:10.1785/bssa0880020428

Ren, J., Feng, F. Y., Fu-Yun, W., Jian-Bing, P., Chen, L., Wang-Qiang, D., et al. (2013). Revealed the fine crust structures of Xi'an sag in Weihe basin by deep seismic reflection profile. *Chin. J. Geophys.* 56 (2), 513–521. doi:10.6038/cjg20130215

Ross, Z. E., Trugman, D. T., Azizzadenesheli, K., and Anandkumar, A. (2020). Directivity modes of earthquake populations with unsupervised learning. *J. Geophys. Res. Solid Earth* 125, e2019JB018299. doi:10.1029/2019jb018299

Semblat, J. F., Dangla, P., Kham, M., and Duval, A. (2022). Seismic site effects for shallow and deep alluvial basins: In-depth motion and focusing effect. *Soil Dyn. Earthq. Eng.* 22, 849–854. doi:10.1016/s0267-7261(02)00107-0

Smerzini, C., and Villani, M. (2012). Broadband numerical simulations in complex near-field geological configurations: The case of the 2009 M w 6.3 L'Aquila earthquake. *Bull. Seismol. Soc. Am.* 102 (6), 2436–2451. doi:10.1785/0120120002

Stupazzini, M., Paolucci, R., and Igel, H. (2009). Near-Fault earthquake ground-motion simulation in the grenoble valley by a high-performance spectral element code. *Bull. Seismol. Soc. Am.* 99 (1), 286–301. doi:10.1785/0120080274

Todorovska, M. I., and Lee, V. W. (1990). A note on response of shallow circular valleys to Rayleigh waves: Analytical approach. *Earthq. Eng. Eng. Vib.* 10 (1), 21–34.

Toshinawa, T., and Ohmachi, T. (1992). Love-wave propagation in a three-dimensional sedimentary basin. *Bull. Seismol. Soc. Am.* 82 (4), 1661–1677. doi:10.1785/bssa0820041661

Trifunac, M. D. (1971). Surface motion of a semi-cylindrical alluvial valley for incident plane SH waves. *Bull. Seismol. Soc. Am.* 61 (6), 1755–1770. doi:10.1785/bssa0610061755

Vijaya, R., Boominathan, A., and Mazzieri, I. (2020). 3D ground response analysis of simplified Kutch Basin by spectral element method. *J. Earthq. Tsunami* 14 (01), 2050003. doi:10.1142/s1793431120500037

Vincenzo, C., Nicola, A. P., and Francesca, D. L. (2016). Investigating source directivity of moderate earthquakes by multiple approach: The 2013 matese (southern Italy) mw = 5 event. *Geophys. J. Int.* 207 (3), 1513–1528. doi:10.1093/gji/ggw360

Wen, K. L., and Peng, H. Y. (1998). Site effects analysis in the Taipei Basin: Results from TSMIP network data. *TAO* 9 (4), 691–704.

Wen, R. Z., Wang, H. W., and Ren, Y. F. (2015). Rupture directivity from strong-motion recordings of the 2013 lushan aftershocks. *Bull. Seismol. Soc. Am.* 105 (6), 3068–3082. doi:10.1785/0120150100

Wong, H. L., and Trifunac, M. D. (1974). Surface motion of a semi-elliptical alluvial valley for incident plane SH waves. *Bull. Seism. Soc. Am.* 64 (5), 1389–1408. doi:10.1785/bssa0640051389

Xu, X. W., Jiang, G. Y., Yu, G. H., Wu, X. Y., Zhang, J. G., and Li, X. (2014). Discussion on seismogenic fault of the Ludian MS6. 5 earthquake and its tectonic attribution. *Chin. J. Geophys.* 57 (9), 3060–3068.

Yu, Y. Y. (2017). Study of seismic effects in three-dimensional sedimentary basins. *Int. Seismol. Update* (6), 33–35.

Yuan, X., and Liao, Z. P. (1995). Scattering of plane SH waves by a cylindrical alluvial valley of circulararc cross-section. *Earthq. Eng. Struct. Dyn.* 24 (10), 1303–1313. doi:10.1002/eqe.4290241002

Zhang Y., Y., Xv, L. S., Chen, Y. T., and Li, R. F. (2014). Rupture process of Mw6.1 (Ms6.5) earthquake in ludian, yunnan province on August 3, 2014. *Chin. J. Geophys.* 57 (9), 3052–3059.

Zhang, Z. G., Sun, Y. C., Xv, J. K., Zhang, W., and Chen, X. F. (2014). Preliminary simulation of strong ground motion for Ludian, Yunnan earthquake of 3 August 2014, and hazard implication. *Chin. J. Geophys.* 57 (09), 3038–3041.

Zhao, X. Y., and Sun, N. (2014). Simultaneous inversion for focal location of Yunnan Ludian M S 6.5 earthquake sequence in 2014 and velocity structure in the source region. *J. Seismol. Res.* 37 (4), 523–531.

Frontiers in Earth Science

TYPE Original Research
PUBLISHED 27 June 2023
DOI 10.3389/feart.2023.1180289

OPEN ACCESS

EDITED BY
Yosuke Aoki,
The University of Tokyo, Japan

REVIEWED BY
Boumediene Derras,
University of Tlemcen, Algeria
Ryota Takagi,
Tohoku University, Japan

*CORRESPONDENCE
Yadab P. Dhakal,
✉ ydhakal@bosai.go.jp

RECEIVED 05 March 2023
ACCEPTED 12 June 2023
PUBLISHED 27 June 2023

CITATION
Dhakal YP and Kunugi T (2023), Preliminary analysis of nonlinear site response at the S-net seafloor sites during three Mw 7 class earthquakes. *Front. Earth Sci.* 11:1180289. doi: 10.3389/feart.2023.1180289

Preliminary analysis of nonlinear site response at the S-net seafloor sites during three Mw 7 class earthquakes

Yadab P. Dhakal* and Takashi Kunugi

National Research Institute for Earth Science and Disaster Resilience, Tsukuba, Japan

In this paper, we investigated the characteristics of nonlinear site response (NLSR) at 23 S-net seafloor sites using strong-motion records obtained during three Mw 7 class earthquakes that occurred directly beneath the network. During the earthquakes, horizontal peak accelerations as large values as 1,400 and 1700 cm/s^2 were recorded at the land (KiK-net) and S-net stations, respectively. The S-net is a large-scale inline-type seafloor observation network for earthquake and tsunami in the Japan Trench area. Characterization of NLSR is important because, in most common cases, it can cause a reduction of higher frequency components and a shift of predominant site frequency to lower one. Obtaining high-quality strong-motion records at seafloor sites is extremely difficult and expensive. Some of the records from the three earthquakes used in this study were contaminated by the rotations of the sensor houses, resulting in the ramps and offsets after the arrival of strong S-wave phases. We used a time window of 10 s starting from the S-wave onset, that avoided the ramps and offsets mostly. Using the horizontal-to-vertical spectral ratio (HVSR) technique, we found that the selected S-net sites might have experienced substantial degrees of NLSR during the three earthquakes with peak accelerations greater than about 60 cm/s^2. To investigate that the obtained features of NLSR were realistic or not at the S-net sites, we examined the NLSR at nine KiK-net sites on land where high-quality strong-motion records were obtained. We found that the KiK-net sites experienced various degrees of NLSR during the three earthquakes, and the obtained characteristics of NLSR at the KiK-net and S-net sites were comparable. We found that the NLSR affected the ground motions at frequencies mainly higher than 1 Hz at both Kik-net and S-net sites. Despite these similarities, by analyzing the spectral ratios between two horizontal component records, we suspected that the induced rotations contributed to some extent in exaggerating the degree of NLSR at the S-net sites, primarily when the components perpendicular to the cable axes were used. We concluded that consideration of induced rotational effects is necessary to understand the NLSR at the S-net sites better.

KEYWORDS

nonlinear site response, horizontal-to-vertical spectral ratio, degree of nonlinearity, peak ground acceleration, S-net, ocean bottom seismograph network, Japan Trench

1 Introduction

S-net is a large-scale cable-linked seafloor observation network for earthquake and tsunami around the Japan Trench area, consisting of 150 observatories laid out in grid pattern covering about 1,000 and 300 km parallel and normal to the Japan Trench, respectively (Kanazawa et al., 2016; Aoi et al., 2020). The network was established after experiencing the devastating effects of the 2011 Mw 9.1 Tohoku-oki earthquake in northeast Japan. The network has been operated by National Research Institute for Earth Science and Disaster Resilience (NIED), and the waveform data recorded by the network has been freely accessible. One of the main objectives of the establishment of the network was to enhance the Japan Meteorological Agency (JMA) earthquake early warning (EEW) and tsunami early warning (Aoi et al., 2020).

In order to improve the EEW, it is crucial to evaluate the characteristics of the recorded motions at the S-net stations. The S-net stations and cables in the shallow water regions (depth <1,500 m) have been buried about 1 m beneath the seafloor, while they have been sited freely on the seafloors in deeper water regions. The waveform records at the S-net stations have been known to be contaminated by induced rotations of the seismometers during strong shakings (e.g., Nakamura and Hayashimoto, 2019; Takagi et al., 2019). The rotations have been attributed to the poor coupling between the cylindrical-shaped pressure vessels in which the seismometers have been housed and the seabed sediments. The S-net records are also known to include the effects of natural vibrations of the pressure vessels, making further difficulty in recovering the true ground motions (Sawazaki and Nakamura, 2020). These effects are discussed in some detail in the next section.

Previous studies showed that the offshore ground motion records contained the strong amplification effect of the unconsolidated sediments in the offshore regions (e.g., Nakamura et al., 2015; Noguchi et al., 2016a; Kubo et al., 2018; Takemura et al., 2019; Hu et al., 2020; Dhakal et al., 2021; Dhakal and Kunugi, 2021; Dhakal et al., 2023). To avoid the overestimation of the magnitudes due to the site amplification effect and also to minimize the effect of

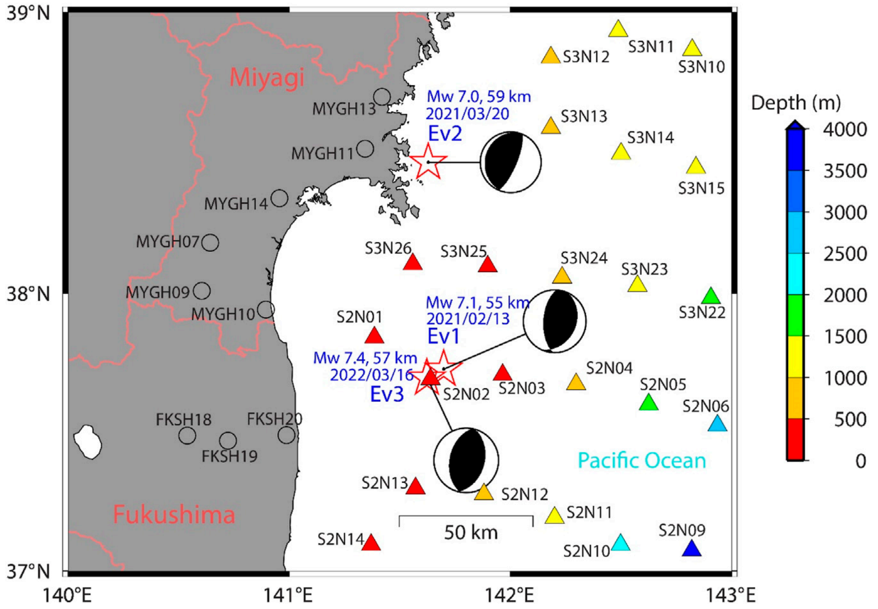

FIGURE 1
Index map. Circles and triangles denote the KiK-net and S-net stations, respectively, used in this study. The S-net stations are color-coded by the depth of water. The stars denote the epicenters of the earthquakes (JMA) used as target events for NLSR analysis. The earthquakes are identified as Ev1, Ev2, and Ev3 according to the order of their occurrences in time. The F-net NIED (Okada et al., 2004) magnitudes (Mw) of the earthquakes were 7.1, 7.0, and 7.4, respectively, while the focal depths were around 55 km. The focal-mechanism plots connected to the epicenters are taken from (Okada et al., 2004) F-net NIED. See Tables 1, 2, and 3 for detail about the earthquakes and sites.

TABLE 1 Source parameters of earthquakes used in the study.

Event code	Date and time (JST)	Japan meteorological agency (JMA)				F-net moment tensor	
		Longitude	Latitude	Focal depth (km)	Mj	Mw	Depth (km)
Ev1	2021/02/13, 23:08	141.6983	37.7283	55	7.3	7.1	53
Ev2	2021/03/20, 18:09	141.6267	38.4667	59	6.9	7.0	62
Ev3	2022/03/16, 23:36	141.6217	37.6967	57	7.4	7.4	56

TABLE 2 List of KiK-net site stations used in this study.

Site number	Site code	Longitude	Latitude	Vs30 (m)	Depth to borehole sensor (m)	Vs at borehole sensor (m/s)
1	FKSH18	140.538	37.4894	307	100	2,250
2	FKSH19	140.7227	37.4703	338	100	3,060
3	FKSH20	140.9871	37.4911	-	109	610
4	MYGH07	140.6405	38.1802	366	142	740
5	MYGH09	140.6027	38.0091	358	100	840
6	MYGH10	140.8924	37.9411	348	205	770
7	MYGH11	141.3421	38.5158	859	207	2,780
8	MYGH13	141.4176	38.6993	571	100	2,740
9	MYGH14	140.9551	38.34	-	1,034	-

TABLE 3 List of S-net site stations used in this study.

Site number	Site code	Longitude	Latitude	Depth (m)	Buried/Unburied
1	S2N01	141.38445	37.84280	102	Buried
2	S2N02	141.63870	37.69217	239	Buried
3	S2N03	141.96498	37.70725	462	Buried
4	S2N04	142.29745	37.67392	786	Buried
5	S2N05	142.62363	37.60158	1781	Unburied
6	S2N06	142.93503	37.52588	2,945	Unburied
7	S2N09	142.81883	37.07413	4,226	Unburied
8	S2N10	142.49793	37.09485	2,417	Unburied
9	S2N11	142.19985	37.19305	1,447	Buried
10	S2N12	141.87903	37.27722	591	Buried
11	S2N13	141.57095	37.30038	212	Buried
12	S2N14	141.37032	37.09523	162	Buried
13	S3N10	142.82122	38.86678	1,310	Buried
14	S3N11	142.48733	38.93490	1,168	Buried
15	S3N12	142.18160	38.84118	558	Buried
16	S3N13	142.18155	38.59010	573	Buried
17	S3N14	142.50023	38.49932	1,092	Buried
18	S3N15	142.83755	38.44867	1,472	Buried
19	S3N22	142.90720	37.98383	1,645	Unburied
20	S3N23	142.57352	38.02700	1,220	Buried
21	S3N24	142.23402	38.05690	849	Buried
22	S3N25	141.89573	38.09720	230	Buried
23	S3N26	141.55717	38.10602	128	Buried

the change in orientation of the sensors during strong motions, Hayashimoto et al. (2019) devised an equation to estimate the magnitude required for the JMA EEW using the vertical-component displacement amplitude, which produced smaller variance compared with those using the horizontal-component records. Moreover, previous studies indicated that the nonlinear

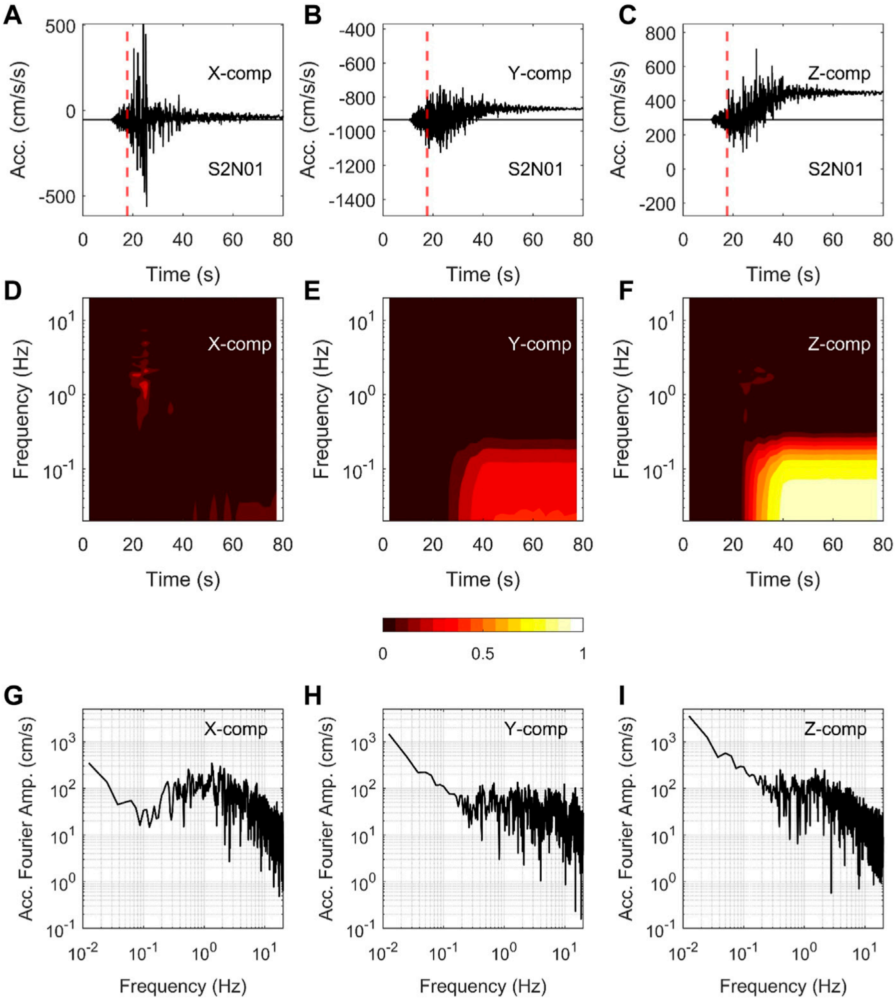

FIGURE 2

Upper panels **(A–C)** show the as recorded original acceleration time histories at the S2N01 site (buried) for the X, Y, and Z components for the 2021 Mw 7.1 earthquake (Ev1 in Table 1). See Figure 1 for the locations of the site and epicenter of the earthquake. Middle panels **(D, E, F)** show the time-frequency plots, and bottom panels **(G–I)** show the Fourier spectra of the waveforms shown in the panels **(A, B, C)**, respectively, after removing the pre-event means of corresponding records. See also the upper three panels of Figure 5, which shows the transformed waveforms into the horizontal and vertical components, respectively.

site response (NLSR) could be commonly observed during strong shakings at the seafloor sites with sediments, thus requiring analysis of the recorded motions from multiple perspectives (e.g., Hayashimoto et al., 2014; Dhakal et al., 2017; Kubo et al., 2019).

A peak ground acceleration (PGA) of 100 cm/s^2 to 200 cm/s^2 has generally been cited as a threshold motion that causes NLSR at soft-soil sites (e.g., Beresnev and Wen, 1996). During a typical NLSR, the predominant frequencies of ground motions shift to the lower ones and the amplitudes of the higher-frequency components decrease compared with those during linear range of motions. It has been demonstrated that these effects are the manifestation of the increase of damping and degradation of soil rigidity during strong motions (e.g., Idriss and Seed, 1968; Hardin and Drnevich, 1978).

In the absence of suitably located reference site with linear site response, horizontal-to-vertical spectral ratios (HVSRs) of S waves recorded at the same site during strong and weak motions have been used to infer NLSR at the soil sites during strong motions (e.g., Wen et al., 2006; Noguchi and Sasatani, 2008). As the S-net stations can experience stronger shakings in wide areas during major and great earthquakes in the offshore regions, in the present study we tried to identify the NLSR at selected S-net sites during three magnitude 7 class earthquakes, described in the next section, using the HVSR method. Due to the various undesirable factors such as the rotations of the sensors and natural vibrations of the sensor houses at the seafloor sites, we first present an analysis of the NLSR at selected stations on land, where high-quality records have been observed, to show that the NLSRs were observed during the three earthquakes. Then, we present and discuss the features of the inferred NLSR at the S-net sites, including intermittent high-frequency spikes on the accelerograms. Ocean-bottom seismograph networks of different scales have been in operation in different parts of the world (e.g., Romanowicz et al., 2009; Hsiao et al., 2014; Barnes et al., 2015; Aoi et al., 2020), and some networks are under

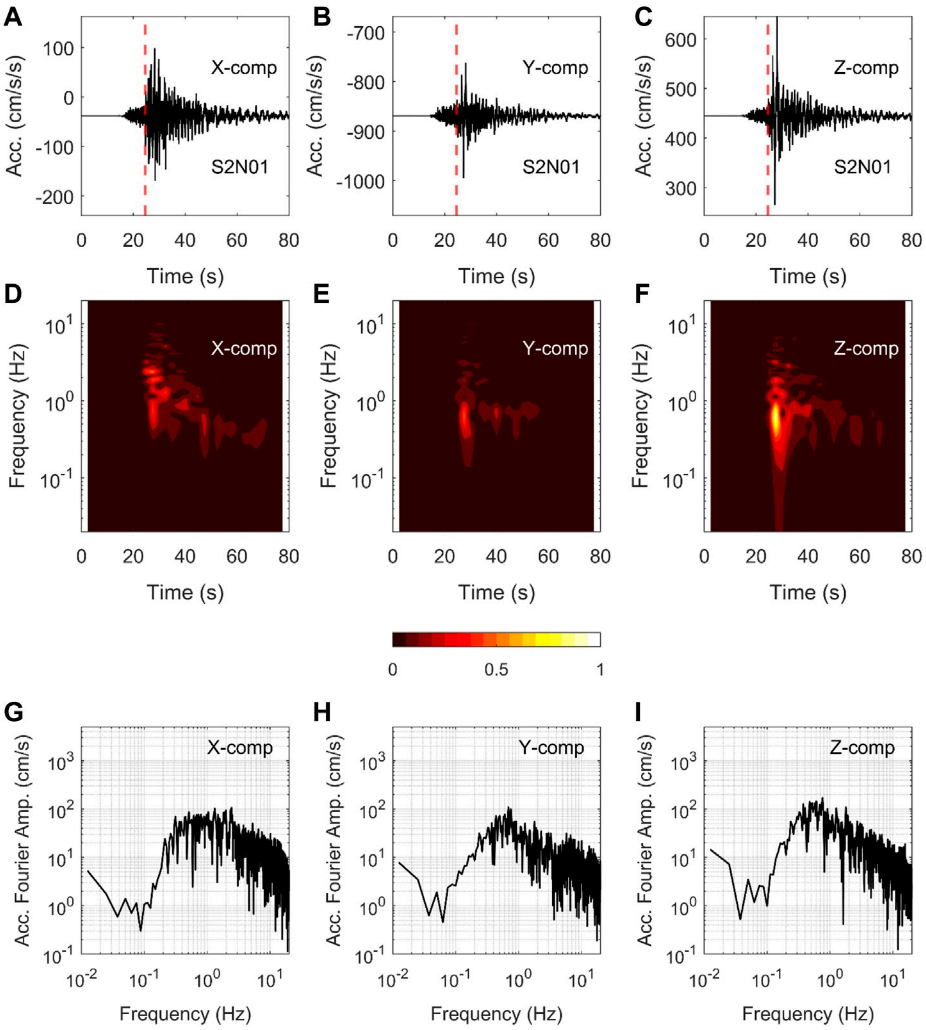

FIGURE 3
Upper panels **(A–C)** show the as recorded original acceleration time histories at the S2N01 site (buried) for the X, Y, and Z components for the 2021 Mw 7.0 earthquake (Ev2 in Table 1). See Figure 1 for the locations of the site and epicenter of the earthquake. Middle panels **(D, E, F)** show the time-frequency plots, and bottom panels **(G–I)** show the Fourier spectra of the waveforms shown in panels **(A, B, C)**, respectively, after removing the pre-event means of corresponding records. See also the lower three panels of Figure 5, which shows the transformed waveforms into the horizontal and vertical components, respectively.

construction (e.g., Aoi et al., 2020) for EEW and other related geophysical studies. Thus, it is expected that the results presented in this study may contribute to the literature in the seismological community for improved prediction of ground motions required for EEW and so on.

2 Data and method

Based on previous studies of NLSR at the offshore sites (e.g., Hayashimoto et al., 2014; Dhakal et al., 2017; Kubo et al., 2019), we obtained weak-motion (reference-motion) records from many earthquakes at 32 sites [23 seafloor sites of S-net (NIED, 2019a) and 9 land sites of KiK-net (NIED, 2019b)] with the property that the vector PGAs of three component records were between 5 and 50 cm/s^2. The weak-motion records were mostly from earthquakes with moment magnitudes (Mw) between 4.5 and 5.5 and epicentral distances between 20 and 200 km. The target records for the identification of NLSR were obtained from three earthquakes of Mw values between 7.0 and 7.4. The locations of the earthquakes and sites are depicted in Figure 1. The earthquakes are listed in Table 1 with their hypocenter information and magnitudes. The KiK-net and S-net sites used in the NLSR analysis are listed in Tables 2 and 3, respectively. The S-wave onsets were picked up manually, and the signal-to-noise (SN) ratios were computed as the ratios of the Fourier spectral amplitudes between the S-wave and pre-event noise windows of 10 s durations. The records used in the analysis had SN ratios greater than two at frequencies of our interest between 0.5 and 20 Hz. The number of used weak-motion records at the S-net stations varied between 31 and 100, while they were between 60 and 240 at the stations on land.

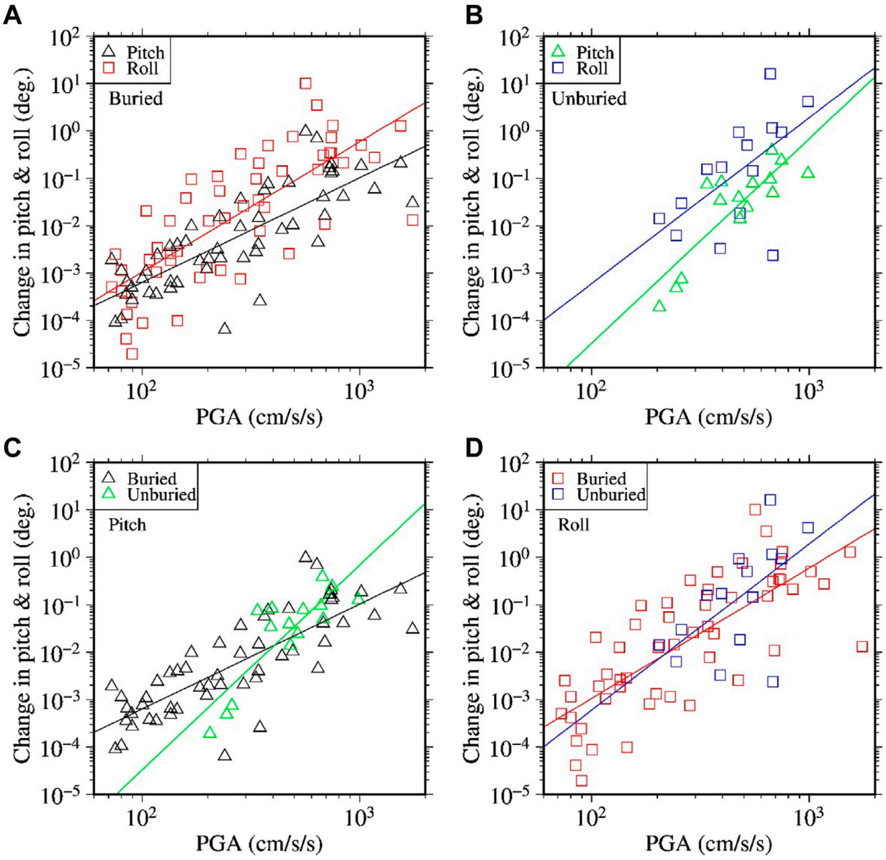

FIGURE 4
Plots of induced rotations of sensors as a function of vector peak accelerations of three component records. The triangles and squares in the plots denote the changes in pitch and roll angles, respectively. Data points in **(A)** show the changes in pitch and roll angles at the buried stations, while those in **(B)** show the changes in pitch and roll angles at the unburied stations. Similarly, data points in **(C)** show the changes in pitch angles, while those in **(D)** show the changes in the roll angles, at the buried and unburied stations as indicated in the plots. For details on the computation of the pitch and roll angles, see the Data and Method section. The solid lines are the regression lines drawn to aid for the visualization of the mean trend of the corresponding data.

The surface-to-borehole spectral ratio (SBSR) method has been proven to be an effective method to identify the NLSR during strong-motions (e.g., Wen et al., 1994; Satoh et al., 1995; Sato et al., 1996; Sawazaki et al., 2006; Assimaki et al., 2008; Noguchi and Sasatani, 2008; Régnier et al., 2013; Kaklamanos et al., 2015; Noguchi et al., 2016b; Dhakal et al., 2019). This is primarily due to that the borehole sensors have been installed in the stiffer layers, and the variations in source and path factors between the surface and borehole stations are negligible in most cases. This study used the SBSR method to detect NLSR at the nine stations of KiK-net shown in Figure 1. However, as the seafloor observation sites lack the vertical array or reference rock-outcrop sites at near distances, the HVSR method is a suitable one, which has been widely applied in the detection of NLSR during strong-motions (e.g., Noguchi and Sasatani, 2008; Wen et al., 2011; Ren et al., 2017; Ji et al., 2020). The HVSR method utilizes the horizontal and vertical component records observed at the same site. This method was first applied in Wen et al. (2006). We also evaluated the NLSR at the land sites using the HVSR method to compare the results with the SBSR method. For an overview of quantification of nonlinear site response by numerical simulations, we refer to the paper by Régnier et al. (2016) and the references therein.

The SBSRs and HVSRs at the KiK-net stations were calculated using Equations 1 and 2, respectively.

$$\mathrm{SBSR} = \sqrt{\frac{NS_s^2 + EW_s^2}{NS_b^2 + EW_b^2}} \tag{1}$$

$$\mathrm{HVSR} = \sqrt{\frac{NS_s^2 + EW_s^2}{UD_s^2}} \tag{2}$$

where NS, EW, and UD denote the acceleration Fourier spectra for the north-south, east-west, and vertical components, respectively. The subscripts, s and b, denote the surface and borehole recordings, respectively.

The S-net seismometers, as mentioned briefly in the previous section, are prone to large induced rotations during strong shakings due to the poor coupling between the sensor houses and seabed sediments. Here, we discuss the example waveforms, their spectrograms based on short-time Fourier transforms (e.g., Rabiner and Schafer, 1978) and Fourier spectra, as depicted in Figure 2. The waveforms plotted in Figure 2 were recorded at the station S2N01 during the 2021 Mw 7.1 earthquake (Ev1 in Table 1). The site was located at the epicentral distance of about 30 km, and the vector PGA of three components was about 560 cm/s^{2}. See

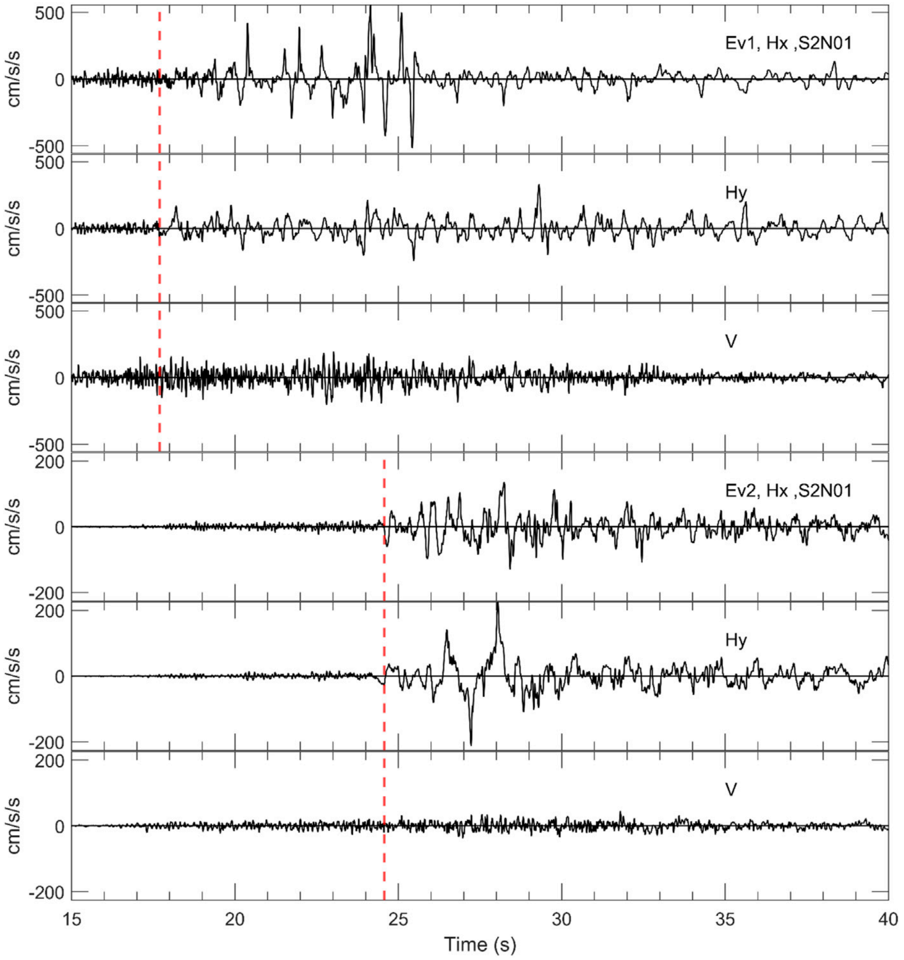

FIGURE 5
The first three traces show the waveforms plotted in Figures 2A–C for the 2021 Mw 7.1 earthquake (Ev1 in Table 1) after transforming them into the horizontal and vertical directions (S2N01 site); the waveforms are shown for the time window between 15 and 40 s after the earthquake origin time for clarity. The two-letter abbreviations Hx and Hy indicate the horizontal components in the direction of and perpendicular to X-axis, respectively. V denotes the vertical component. The lower three traces show the similar plots as described above, but for the waveforms plotted in Figures 3A–C, respectively, for the 2021 Mw 7.0 earthquake (Ev2 in Table 1). The dashed red lines mark the S-wave onsets picked manually. All the waveforms were low-cut filtered at 0.1 Hz.

Figure 1 for the location of the site and epicenter of the earthquake. The upper panels in Figure 2 show the as recorded X-, Y-, and Z-component records from left to right, respectively. *X* axis coincides with the long axis of the cylindrical pressure vessel, and the *Y* and *Z* axes are perpendicular to each other and the *X* axis. It can be seen in Figure 2 that all the three component records include offsets from about 40 s, the larger offsets being observed on the Y and Z components despite the lower peak accelerations (the absolute values after removing the pre-event mean) compared with the peak value on the X-component record. Before the offsets, distinct ramps can be seen on the Y- and Z-component records (Figures 2B,C). These types of features were reported in several previous studies (Hayashimoto et al., 2019; Nakamura and Hayashimoto, 2019; Takagi et al., 2019; Dhakal et al., 2021). The effects of these offsets are reflected in the spectrograms, Figures 2D–F, as continuous large spectral amplitudes towards the lower end frequencies. The acceleration spectral amplitudes should generally be falling off towards the low-frequency end in the absence of noises. But as also shown in the Fourier spectra plots in Figures 2G–I, they grew up towards the low-frequency end from about 0.3 Hz for the Y and Z components and from about 0.1 Hz for the X component.

Another example plot of acceleration time histories recorded at the same site discussed above is given in Figure 3; the records were obtained during the 2021 Mw 7.0 earthquake (Ev2 in Table 1). The site was located at the epicentral distance of about 73 km, and the vector PGA of three components was about 225 cm/s^2, which is about one-third of the value observed during the previous event (Ev1). The time-history plots in Figures 3A–C do not show visible offsets. The time-frequency plots (Figures 3D–F) show that the S-wave parts contain wide-frequency components, while the later parts are richer at frequencies between about 0.3 and 1 Hz. The Fourier spectra plots in Figures 3G–I show that the rise of spectral amplitudes towards the low-frequency end occurs after about 0.04 Hz, which is lower than those seen in Figures 2G–I for the records of Ev1 discussed above.

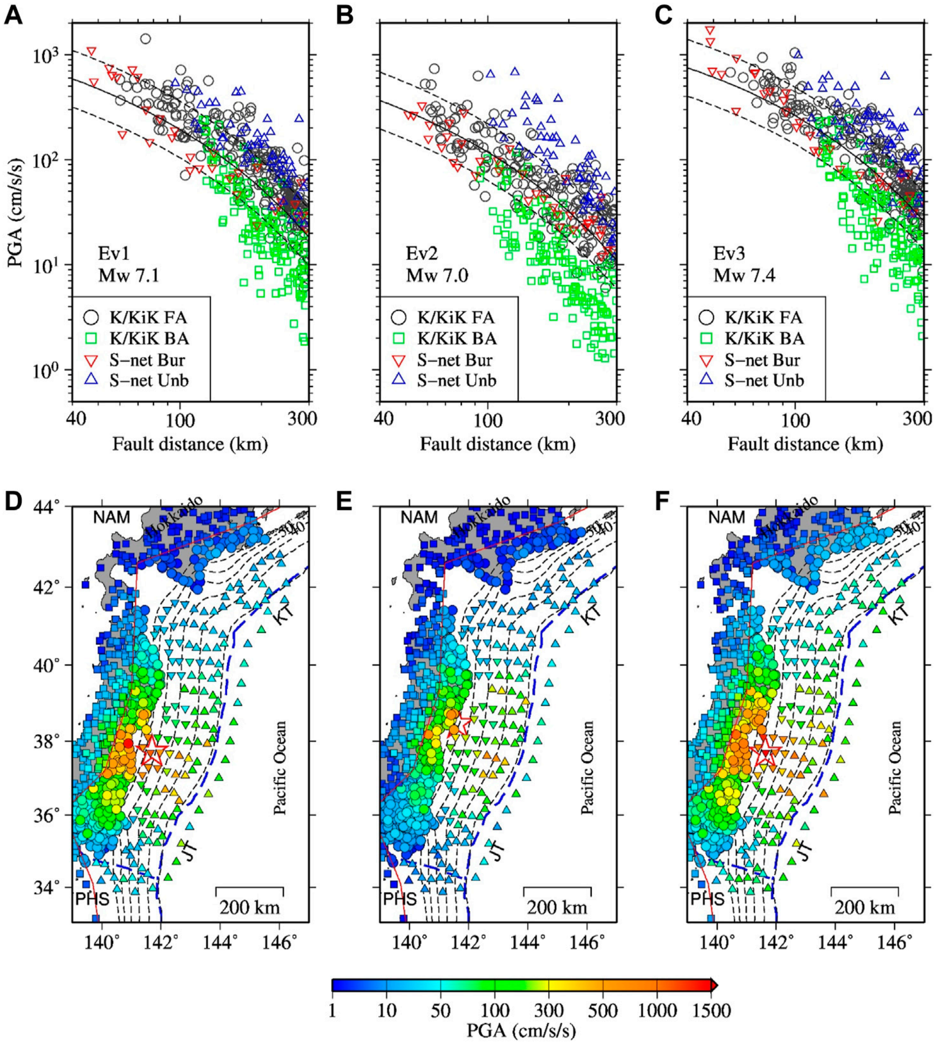

FIGURE 6
Upper panels: PGAs (larger values of two horizontal components) as a function of the shortest fault-rupture distance for three events Ev1, Ev2, and Ev3 (panels **(A, B, C)**), respectively. The symbols, circle and square, denote the fore-arc and back-arc stations of K-net and KiK-net, written as K/KiK FA and K/KiK BA, respectively, in the legends. The inverted and normal triangles denote the buried and unburied stations of S-net, abbreviated as S-net Bur and S-ne Unb, respectively, in the legends. The solid and dashed lines denote the median prediction curve and range of one standard deviation for soil site condition in the GMPE of Si and Midorikawa (1999) for the corresponding event types (Ev1 and Ev3: intraslab; Ev2: interplate). Lower panel: Spatial distribution of the PGAs for the three events, Ev1, Ev2, and Ev3 (panels **(D, E, F)**), respectively. Stars denote the epicenters. The dashed blue lines denote the plate boundaries and the red line denotes volcanic front. The dashed grey lines denote the depth contours of the upper surface of the Pacific Plate at interval of 10 km. The 10 km depth contour coincides roughly with the trench axes (JT: Japan Trench and KT: Kurile Trench). The plate-depth data were taken from Hirose (2022). The NAM and PHS are shorthand for the North-American Plate and Philippine Sea Plate, respectively.

The relationship between the vector PGA of three component records and the induced rotations of the X axis (change in pitch value) and Y (or Z) axis (change in roll value) is given in Figure 4 for the strong-motion records used in the NLSR analysis. Interested readers can find the detailed explanation of pitch and roll angles with illustrations in Takagi et al. (2019). In the present study, the change in pitch and roll were estimated in the following way. The record length was 10 min for each earthquake, beginning from 1 minute before the earthquake origin time. The 1-min time windows at the front and rear ends, respectively, were used to estimate the pitch and roll values at each time step, and the differences in mean pitch and roll values between the two time-windows were calculated. The pitch (β) and roll (γ) values at each time step were calculated using Equations 3 and 4, respectively.

$$\beta = -\arcsin\left(\frac{g_x}{g}\right) \tag{3}$$

$$\gamma = \arctan\left(\frac{g_y}{g_z}\right) \tag{4}$$

where g is the acceleration due to gravity (~980 cm/s^2), and g_x, g_y, and g_z are the components of g as observed on the X, Y, and Z component records. The arctan in Equation 4 is a function that returns the four-quadrant inverse tangent of g_y and g_z.

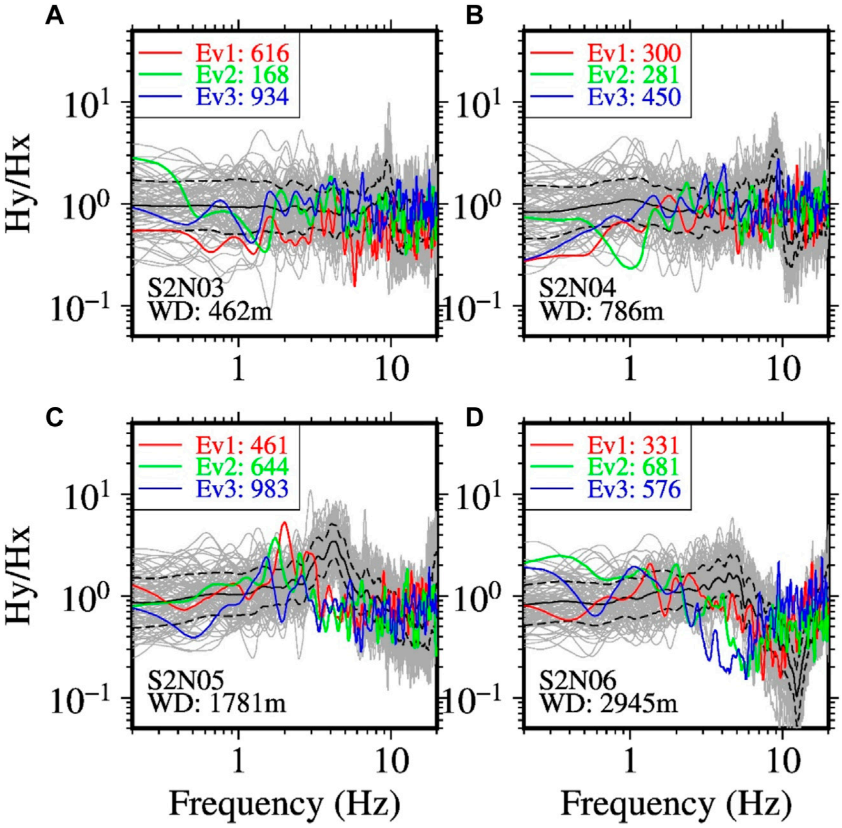

FIGURE 7
Spectral ratios between the horizontal Y- and X-component records at two buried stations [upper panels **(A, B)**] and two unburied stations [lower panels **(C, D)**], computed from the S-wave parts of the records. The site code and water depth (WD) are indicated in each panel. The grey lines denote the spectral ratios for individual earthquake records. The black lines denote the mean spectral ratios, while the dashed lines denote the range of one standard deviation. The red, blue, and green lines denote the spectral ratios for the three target earthquakes, denoted by Ev1, Ev2, and Ev3, respectively (see Table 1 for detail about the earthquakes). The numbers nearby the three event codes indicate the larger peak accelerations in units of cm/s^2 of two horizontal components for the corresponding earthquakes.

As the S-net accelerometers have not been aligned in the horizontal and vertical directions, different from the common deployments on land, the original records need to be transformed into the horizontal- and vertical-component records to examine the NLSR using the HVSR method. The matrix equation for transformation of the records is given in Equation 5.

$$\begin{bmatrix} H_x \\ H_y \\ V \end{bmatrix} = \begin{bmatrix} \cos\beta & \sin\beta\sin\gamma & \sin\beta\cos\gamma \\ 0 & \cos\gamma & -\sin\gamma \\ -\sin\beta & \cos\beta\sin\gamma & \cos\beta\cos\gamma \end{bmatrix} \begin{bmatrix} X \\ Y \\ Z \end{bmatrix} \tag{5}$$

where X, Y, and Z denote the original three component records; β and γ are the pitch and roll angles as defined in Equations 3 and 4, respectively. H_x and H_y denote horizontal component records in the direction of X (cable axis) and perpendicular to it, respectively; V denotes the vertical component record.

For the weak motions, the induced rotations may be considered negligibly small (~10^{-4} degrees or lower). However, the induced rotations during strong shakings can reach to several degrees as shown in Figure 4, and the transformed records may not correctly represent the motions in the horizontal and vertical directions after the ground motions get contaminated by the rotational noises. Example plots of the transformed waveforms after low-cut filtering at 0.1 Hz are shown in Figure 5 for the records drawn in Figures 2 and 3, respectively. In Figure 5, the horizontal X component waveforms for the Ev1 show intermittent acceleration spikes, and the waveforms resemble to some extent to those resulting from the cyclic mobility effects on dilatant soils (e.g., Bonilla et al., 2005). Several records with peak accelerations > about 500 cm/s^2 exhibited spikes on either horizontal X or Y or both components, while none of the records at the land stations of NIED showed spiky waveforms during the earthquakes. The origin of the spiky waveforms obtained at the S-net stations is not investigated well and is a topic for future study. In the present study, we tried to avoid the effects of offsets and induced-rotational noises in the analysis of NLSR by using the records prior to the offsets, and only 10 s length was used beginning from the S-wave onset. All the records (used from both the land and S-net stations) were low-cut filtered at 0.1 Hz with fourth order Butterworth filter to minimize the low-frequency noises. As the SN ratios are smaller at lower frequencies for the weak motions, we primarily focus on the analysis of NLSR at frequencies between 0.5 and 20 Hz for comparison of the results with previous studies (e.g., Noguchi and Sasatani, 2008; Dhakal et al., 2017).

Although it is beyond the scope of this paper to discuss the detailed features of the peak ground motions from the earthquakes

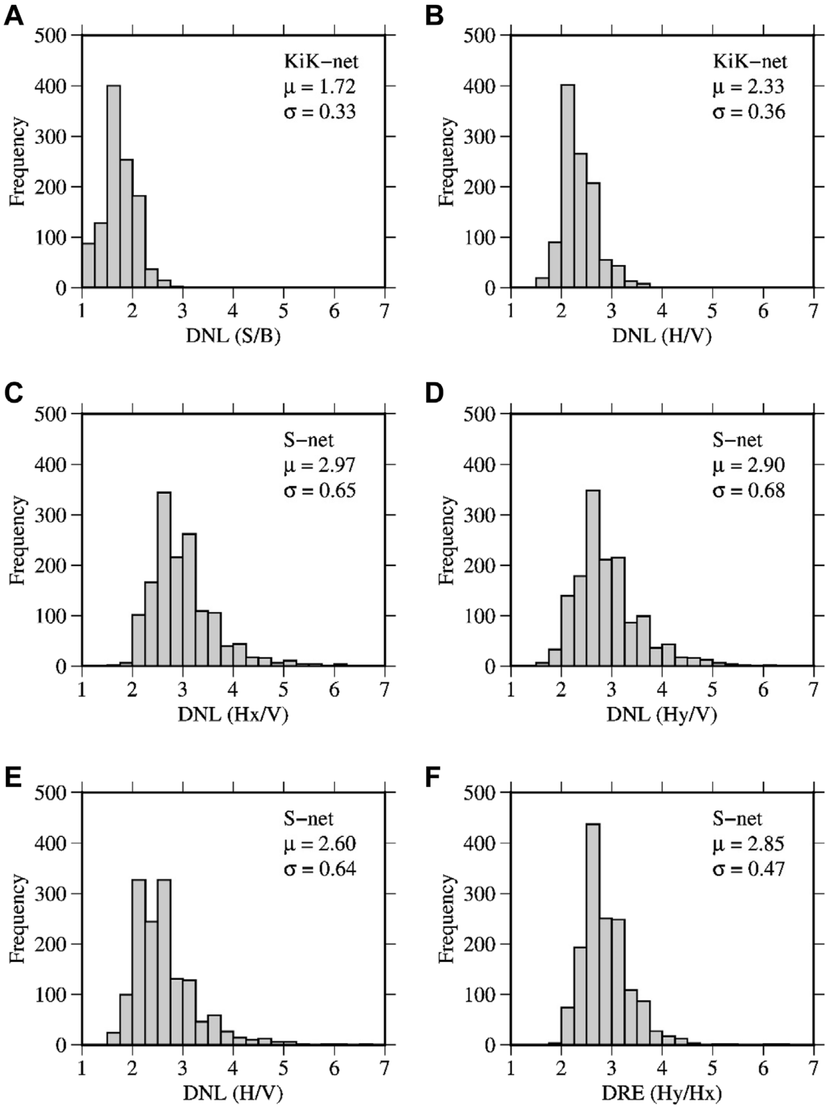

FIGURE 8
Panels **(A–E)**: frequency distributions of the DNL values for the weak-motion records based on the various definitions of the spectral ratios as indicated on the X-axes labels. The panels **(A, B)** show the plots for the DNL values obtained by using the surface-to-borehole (S/B) and horizontal-to-vertical (H/V) spectral ratio methods, respectively, for the KiK-net sites. The panels **(C, D)** show the plots for the DNL values obtained by using the Hx/V and Hy/V spectral ratio methods, respectively, for the S-net sites. Panel **(E)** shows the plot for the DNL values obtained by using the HVSR_h (H/V) spectral ratio method for the S-net sites. Panel **(F)**: frequency distribution of the degree of rotational effect (DRE) described later (see the Discussion section). The mean (*μ*) and standard deviation (*σ*) are indicated in each plot.

considered in this study, we show the horizontal peak accelerations as a function of the shortest fault-rupture distance and their spatial distribution in Figure 6 for the three events listed in Table 1. See Data Availability Statement for the fault models used to calculate the shortest fault-rupture distances. The values plotted in Figure 6 are the larger ones of peak values of the two horizontal components. The largest peak accelerations of about 1,425, 730, and 1,045 cm/s^2 were recorded on land for the Ev1 (Mw 7.1), Ev2 (Mw 7.0), and EV3 (Mw 7.4), respectively, at the fault distances of about 75, 64, and 100 km, respectively. The largest peak accelerations at the S-net sites for the three events were about 1,100, 680, and 1730 cm/s^2, respectively, recorded at the fault distances of about 48, 126, and 48 km, respectively. The peak acceleration data are shown into four groups in each plot in Figure 6. The data from KiK-net sites are grouped into fore-arc (FA) and back-arc (BA) sites while the S-net sites are grouped as buried and unburied sites. It was found that the data generally follow the trends of ground motion prediction curves (Si and Midorikawa, 1999; Si and Midorikawa, 2000) for the three events. However, the BA site records show systematically lower values at longer distances, while the unburied stations, on average, show larger values compared with those at the other site groups. Previous studies (e.g., Kanno et al., 2006; Dhakal et al., 2010; Morikawa and Fujiwara, 2013) showed that the lower Q values in the mantle wedges beneath the volcanic fronts cause stronger attenuation of the high-frequency ground motions passing through them. In contrast, the larger values at the unburied sites

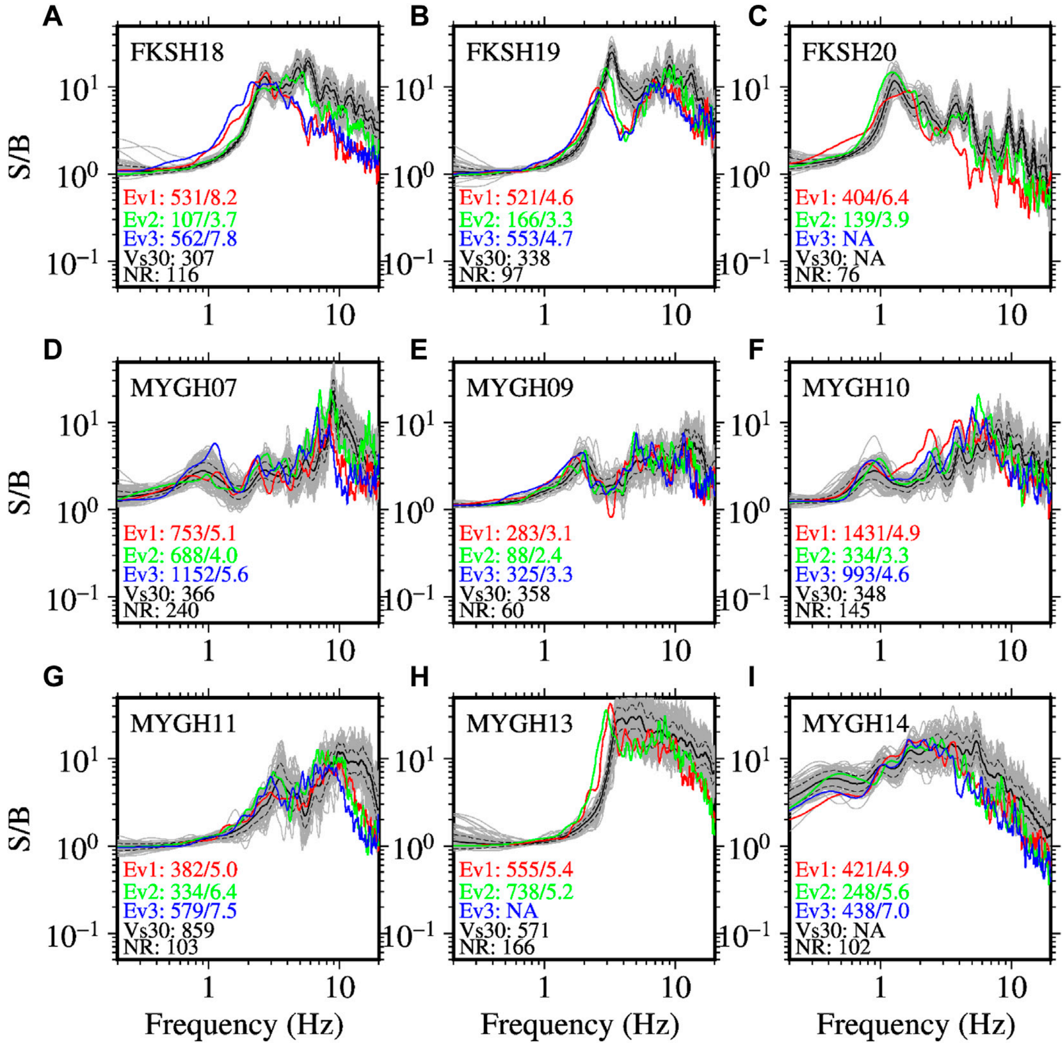

FIGURE 9
Surface-to-borehole (S/B) spectral ratios (SBSR) at the KiK-net sites. The plots **(A–I)** are arranged in order of site codes as listed in Table 2. The red, green, and blue lines denote the SBSRs for Ev1, Ev2, and Ev3, respectively. The black line denotes the mean SBSRs calculated from weak-motion records (grey lines). The dashed grey lines denote the range of one standard deviation from the mean spectral ratios. The first and second numbers separated by forward slash are the PGA (cm/s^2) and DNL values, respectively. Vs30 denotes the average S-wave velocity (m/s) in the upper 30 m soil column, and NR denotes the number of weak-motion records used to compute the mean spectral ratios. The PGAs are the vector peak accelerations of two horizontal components.

may be attributed partly to the lower attenuation of seismic waves in the high-Q Pacific Plate and larger site amplification factors at the unburied sites (Dhakal et al., 2021; Dhakal et al., 2023; Tonegawa et al., 2023).

Sawazaki and Nakamura (2020) showed that the spectral ratios of coda waves between the H_y and H_x components followed the N-shaped pattern with peaks and troughs at about 7 and 13 Hz, respectively. The characteristic N-shaped pattern were conspicuous at the unburied stations, while the spectral ratios were near unity at many buried stations. We show example plots of the spectral ratios between the H_y and H_x component records at two buried (S2N03 and S2N04) and two unburied (S2N05 and S2N06) stations from the S-wave parts of the records in Figure 7 for the weak and strong motions considered in this study. It can be seen in Figures 7A,B that the mean spectral ratios for the weak motions at the two buried stations are about unity except around 10 Hz. Around the 10 Hz, the mean spectral ratios have small peaks and troughs forming minor-type N-shaped patterns, which are more conspicuous in Figure 7B than in Figure 7A. In contrast, the mean spectral ratios plotted in Figure 7C for the unburied station S2N05 show that the peak value is about four at frequency of around 4 Hz, while the mean spectral ratios plotted in Figure 7D for the unburied station S2N06 do not show a conspicuous peak, but show a steep dip at frequency a little over 10 Hz. These observations are generally similar to those reported in Sawazaki and Nakamura (2020). The strong-motion Hy/Hx spectral ratios at the unburied stations indicate a considerable shift of the N-shaped pattern towards lower frequencies, while the spectral ratios at the buried stations appear to be relatively stable for both weak and strong motions. A further comparison of the Hy/Hx spectral ratios between

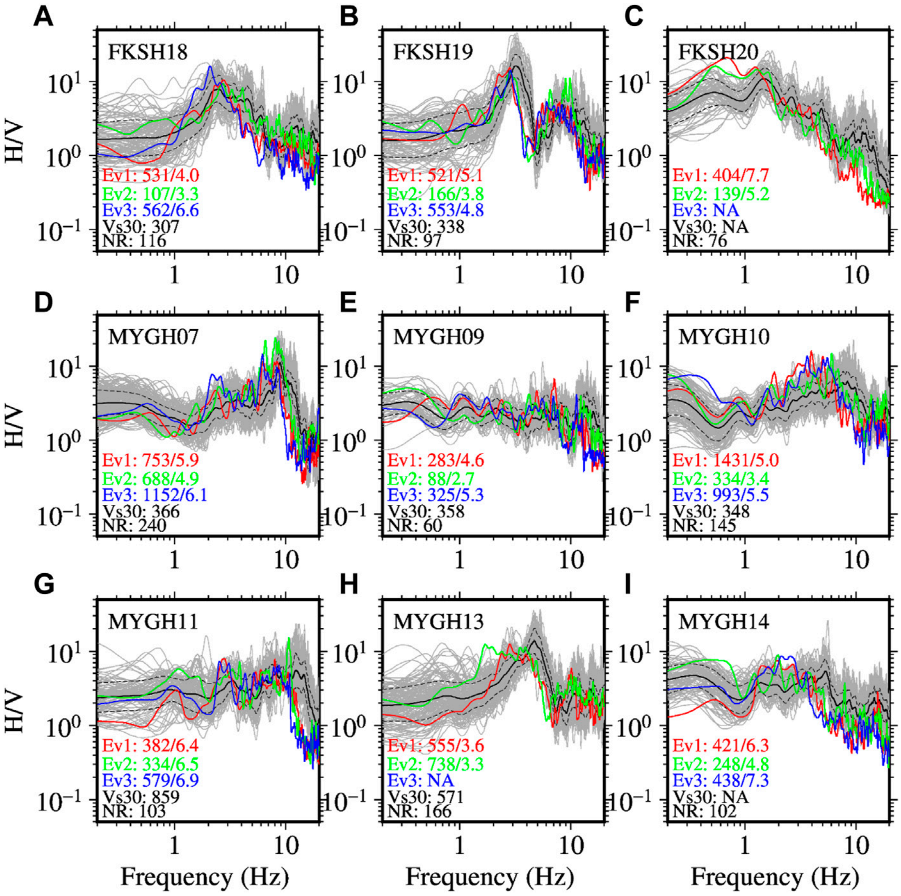

FIGURE 10
Same as Figure 9, but for the horizontal-to-vertical (H/V) spectral ratios (HVSR) at the KiK-net sites. The order of sites in panels **(A–I)** is identical to that in Figure 9. The HVSRs were computed using Eq. 2. See the caption of Figure 9 for detail.

the weak and strong motions is presented in the discussion section. As a result, we obtained the HVSRs at the S-net stations using the following three equations (Equations 6–8).

$$\mathrm{HVSR\_x} = \frac{H_x}{V} \tag{6}$$

$$\mathrm{HVSR\_y} = \frac{H_y}{V} \tag{7}$$

$$\mathrm{HVSR\_h} = \sqrt{\frac{H_x^2 + H_y^2}{V^2}} \tag{8}$$

where H_x, H_y, and V denote the acceleration Fourier spectra for the horizontal X-component, horizontal Y-component, and vertical-component records, respectively, at the S-net sites. The HVSR and HVSR_h defined in Equations 2, 8 are referred simply as H/V in later figures and can be distinguished easily in the context they appear.

Noguchi and Sasatani (2008) proposed the following equation (Equation 9) to express the degree of nonlinearity (DNL) quantitatively.

$$\mathrm{DNL} = \sum \left| \log_{10} \left\{ \frac{R_{strong}}{R_{weak}} \right\} \right| \Delta f \tag{9}$$

where R_{strong} and R_{weak} represent the spectral ratios for strong- and weak-motions, respectively, and Δf is the frequency interval. Noguchi and Sasatani (2008), Noguchi and Sasatani (2011) obtained DNL values from spectral ratios between 0.5 and 20 Hz and suggested threshold DNL values of 2.5 and 4.0 to indicate the NLSR for the SBSR and HVSR methods, respectively. It is to be noted that Equation 9 gives larger weights to higher-frequency components; more than half of the DNL value depends on high-frequency components above 10 Hz (Noguchi and Sasatani, 2008). The suitability of the threshold values to infer NLSR was also confirmed in Dhakal et al. (2017), Dhakal et al. (2019). In the present study also, we computed the DNL values from the spectral ratios between 0.5 and 20 Hz. The frequency distributions of the DNL values for the weak-motion records used in the present study are shown in Figures 8A–E. The mean DNL values were found to be 1.72 and 2.33 for the KiK-net sites with standard deviations of 0.65 and 0.68 for the SBSR and HVSR methods, respectively. Similarly, the mean DNL values for the S-net sites were found to be 2.97 and 2.90 with standard deviations of 0.65 and 0.68 for the HVSR_x and HVSR_y methods, respectively. The mean DNL value for the HVSR_h was found to be 2.60, which may be considered similar to the mean DNL value of 2.33 for the HVSR method at the KiK-net sites considering the range of one standard deviation. The abovementioned DNL values were rounded to two decimal

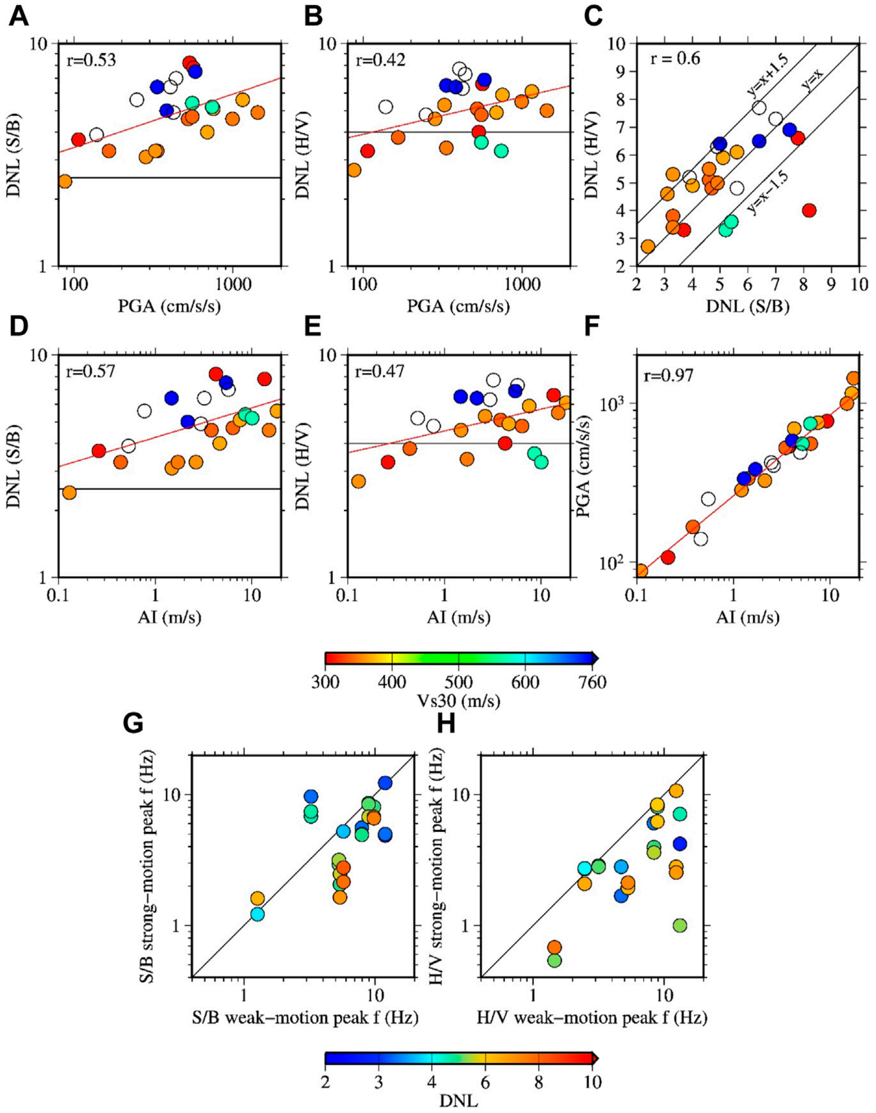

FIGURE 11
Panels **(A, B)** DNL values based on the SBSR **(A)** and HVSR **(B)** methods as a function of the horizontal vector PGAs at the KiK-net sites. The red lines denote the regression lines between the PGAs and DNL values, and the numerals at the upper-left corners indicate the correlation coefficients. Panel **(C)** comparison of the DNL values between the SBSR and HVSR methods. Panels **(D, E)** same as panels **(A, B)** but for the DNL and Arias intensity (AI). Panel **(F)** relationships between the PGAs and AI values. Panels **(G, H)** peak frequencies of the spectral ratios during strong and weak motions based on the SBSR **(G)** and HVSR **(H)** methods.

places. Even though the mean DNL values plus the standard deviations in the present analysis using the HVSR, HVSR_x, HVSR_y and HVSR_h methods are lower than the threshold value of 4 considered in the previous studies, it is somewhat difficult to see the reduction in spectral ratios at higher frequencies and the shift of peak frequencies towards the lower ones for smaller DNL values. Thus, the DNL value of 4 may still be considered a reasonable criterion for the preliminary identification of NLSR using the HVSR methods.

Following Derras et al. (2020), we also computed the Arias intensity (AI) (Arias, 1970) and cumulative absolute velocity (CAV) (Reed et al., 1988) to compare with the DNL values using Equations 10 and 11, respectively. Similar to the use of PGAs, the AI and CAV values were also considered as loading levels in the evaluation of NLSR in Derras et al. (2020).

$$\mathrm{AI} = \frac{\pi}{2g}\int_0^T a^2(t)dt \tag{10}$$

$$\mathrm{CAV} = \int_0^T |a(t)|dt \tag{11}$$

where $a(t)$ is the acceleration time history, T is the total duration of the time history, and g is an acceleration due to gravity. The time lengths of the recordings at the KiK-net stations have been determined by some threshold accelerations, while the S-net stations record waveforms continuously. To compute the AI and

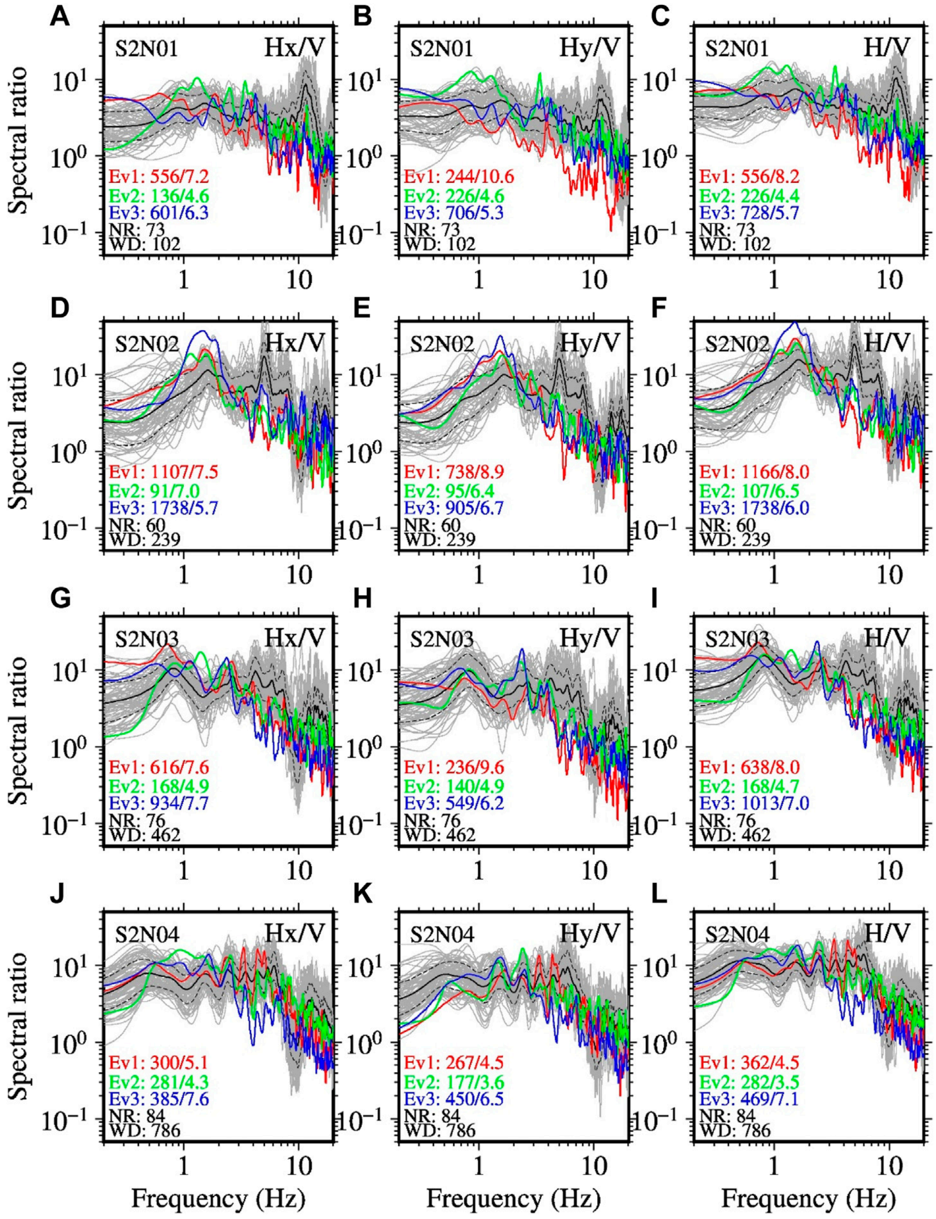

FIGURE 12
Example plots of the HVSRs at the S-net sites. The plots **(A, B, C)** in the top panels show the spectral ratios between the horizontal X and vertical component records (Hx/V; Equation 6), horizontal Y and vertical component records (Hy/V; Equation 7), and vector of two horizontal components and vertical component records (H/V; Equation 8), respectively, at the S2N01 site. The other plots follow similarly for the records at the S2N02 **(D, E, F)**, S2N03 **(G, H, I)**, and S2N04 **(J, K, L)** sites, respectively. WD denotes the depth (m) to the seafloor. The events and related values are identified by the same color schemes as explained in the caption of Figure 9.

CAV values for the same time lengths at the KiK-net and S-net sites, we fixed the value of T equal to 60 s, starting from S-wave onset.

3 NLSR at the KiK-net sites

Here we show the SBSRs and HVSRs at the KiK-net sites for the three events and discuss the nonlinear features with respect to the corresponding weak-motion spectral ratios. Figure 9 shows the plots of SBSRs at the nine KiK-net sites in panels A to I, respectively. The PGAs (peak vector of two horizontal components), DNL values, and Vs30 values are indicated in each plot. The PGAs at the sites were between about 80 and 1,430 cm/s^2. For recordings with larger PGAs, the reduction of SBSRs at higher frequency components can be clearly seen with respect to the weak motion SBSRs (e.g., Figure 9A). The plots of the SBSRs show multiple peaks or small undulations at most sites. During strong motions, the peaks of higher frequencies are reduced mostly while the peaks of the lowest peak frequencies are similar to those of the weak-motion recordings at most sites. The shift in peak frequencies can be seen for several recordings as shown

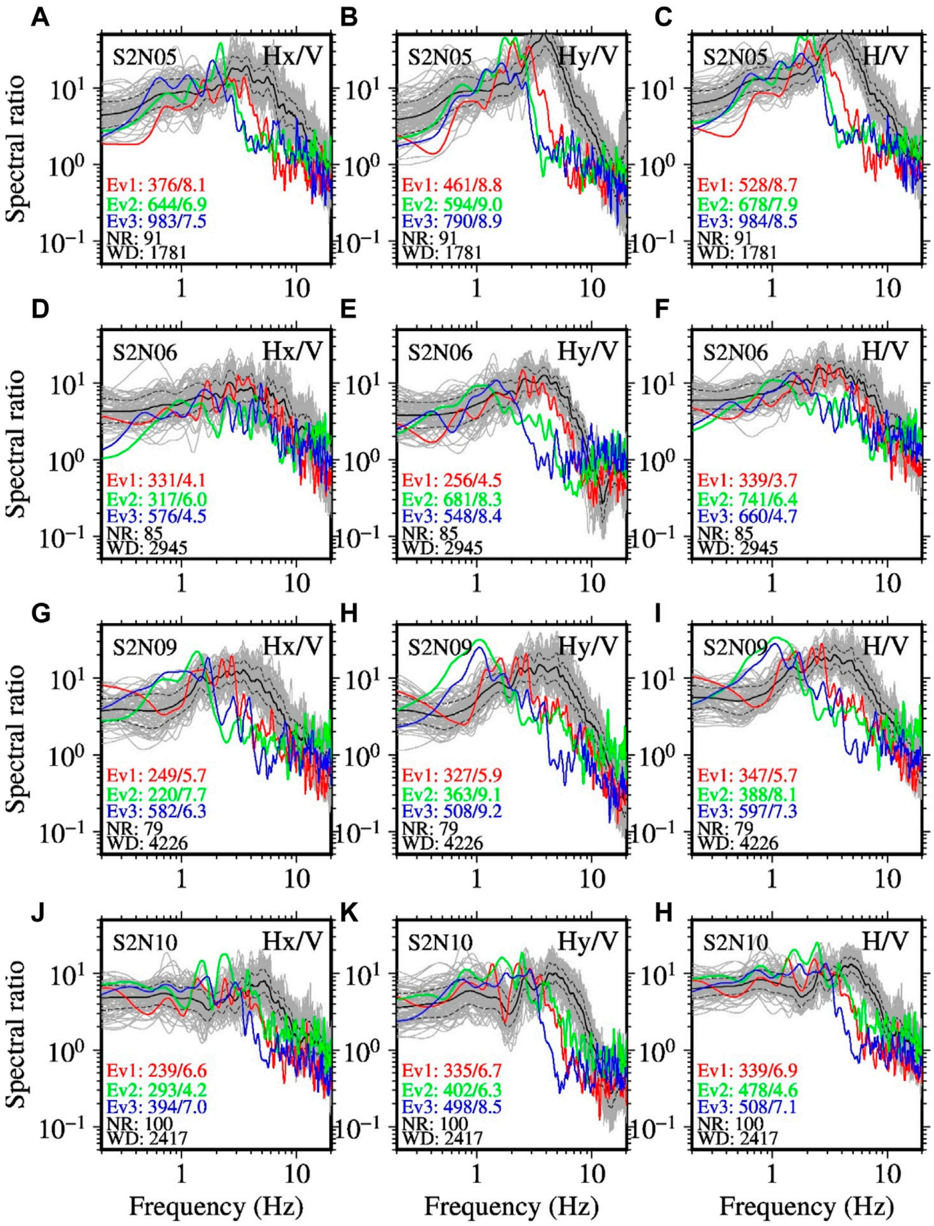

FIGURE 13
Same as Figure 12, but for the sites S2N05 **(A, B, C)**, S2N06 **(D, E, F)**, S2N07 **(G, H, I)**, and S2N10 **(J, K, L)**, respectively. See the caption of Figure 12 for detail. See Supplementary Figures S2–S5 for the plots of the HVSRs at the other sites.

in Figures 9A,B,F,H. The threshold DNL value of 2.5 for identifying the NLSR for the SBSR method as discussed in the previous section was exceeded for all recordings except for the Ev2 at MYGH09 site (Figure 9E). The PGA at the MYGH09 site for the Ev2 was approximately 88 cm/s^2 and was the lowest of all the recordings. The DNL values at the KiK-net sites ranged between 2.4 and 8.2. A larger value of DNL indicates stronger reduction of higher frequency components in the case of typical NLSR. The Vs30 values at the sites ranged between 307 m/s (FKSH18) and 859 m/s (MYGH11). Despite large Vs30 values such as at the MYGH11 (Vs30 = 859 m/s) and MYGH13 (Vs30 = 571 m/s), the features of NLSR were clearly seen at the two sites (see Figures 9G,H). An examination of the PS-logging data indicated soil layers with Vs value of 210 m/s in the top 3 m soil column at the MYGH11 site and 250 m/s in the top 5 m soil column at the MYGH13 site. The presence of these soil layers with lower Vs values might have contributed significantly to the reduction of the higher frequency SBSRs at the two sites.

The HVSRs at the abovementioned KiK-net sites are shown in Figure 10. The reduction of higher frequency components and shift in peak frequencies can be clearly seen for most of the recordings for the three earthquakes. The change in spectral ratio shapes were generally similar to those of the SBSRs at the corresponding sites. The HVSRs for weak motions show a larger scattering compared to the SBSRs. As a result, the threshold DNL value for identifying the

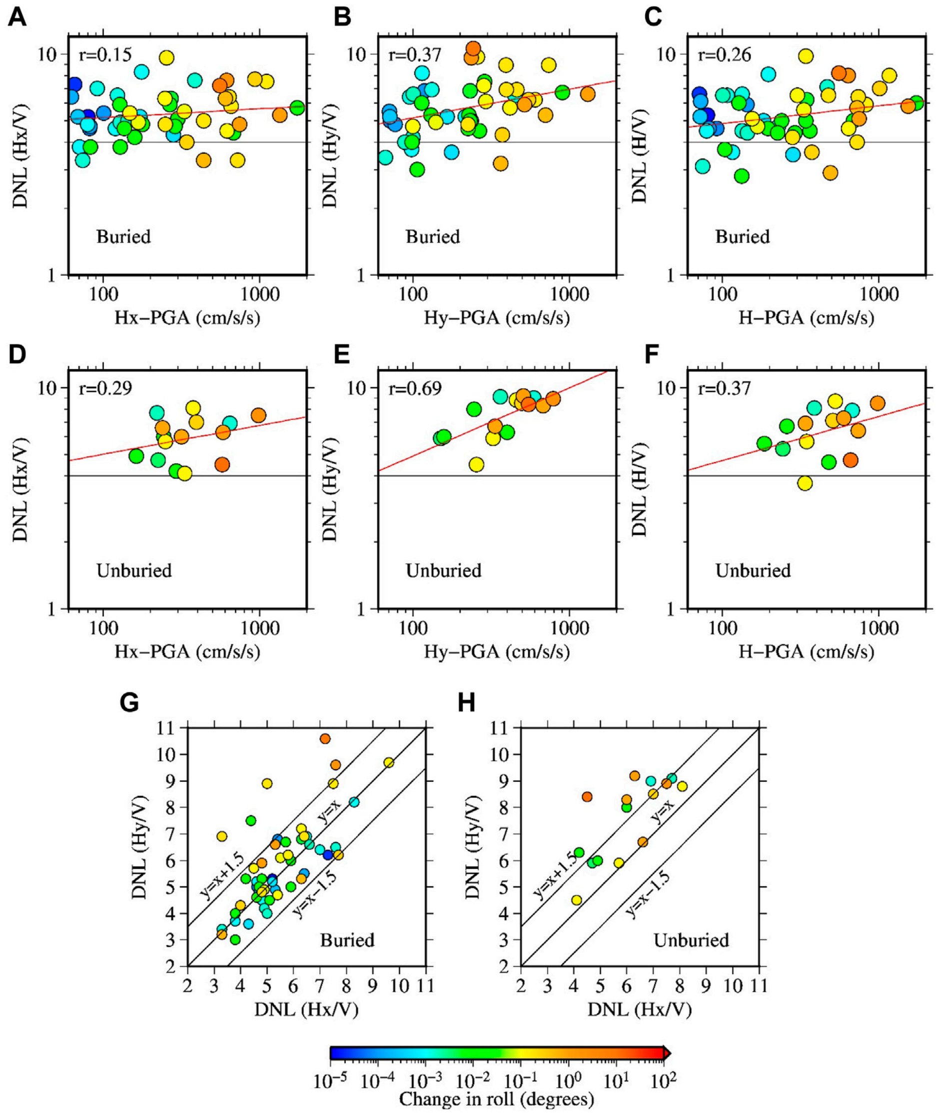

FIGURE 14
DNL values as a function of the PGAs at the S-net sites **(A–F)**. The top **(A, B, C)** and middle **(D, E, F)** panels show the plots for the buried and unburied sites, respectivly, for the three different definitions of spectral ratios given in Equations 6, 7, and , 8, respectively. The x-axes labels, Hx-PGA, Hy-PGA, and H-PGA mean the peak acceleration of the horizontal X, horizontal Y, and vector of the two horizontal component records, respectively. The red lines denote the regression lines between the corresponding PGAs and DNL values, and the numerals at the upper-left corners indicate the correlation coefficients. The bottom panels show the relationships between the DNL values based on the Hx/V and Hy/V spectral ratios at the buried **(G)** and unburied **(H)** sites, respectively.

NLSR using the HVSR method is larger compared to the corresponding threshold value for the SBSR method. The obtained DNL values for the HVSR method were between 2.7 and 7.7 in the present analysis.

The relationships between the DNL values and PGAs for the SBSR and HVSR methods are shown in Figures 11A,B, respectively. A general trend of increasing DNL values can be seen with an increase of PGAs. The plot in Figure 11B (HVSR case) shows four points (recordings) with DNL values ≤4 for PGAs >300 cm/s^2. However, the plot in Figure 11A (SBSR case) shows the DNL values >2.5 for the same recordings, indicating the NLSR. One of the sites with the large difference of the DNL values between the SBSR and HVSR is the MYGH13 site. The DNL values using the HVSR method at the MYGH13 site were 3.6 and 3.3 for the PGAs of 555 and 738 cm/s^2 for the Ev1 and Ev2, respectively. Nonetheless, the HVSRs clearly showed the shift in peak frequencies. A comparison of the DNL values obtained from the SBSR and HVSR methods is shown in Figure 11C, where it can be seen that the DNL values for the HVSR methods tend to be somewhat larger than those for the SBSR methods for a larger number of recordings (18 *versus* 7 data points) and are consistent with the previously reported results (e.g., Noguchi and Sasatani, 2011). But it is noted that the largest DNL value among the KiK-net sites is 8.2 in the present analysis and was obtained using the SBSR method. The DNL value of 8.2 was approximately a factor of two of the DNL value obtained using the HVSR method for the corresponding recording (see Figure 9A, 10A for the Ev1). The plots of DNL values for all recordings

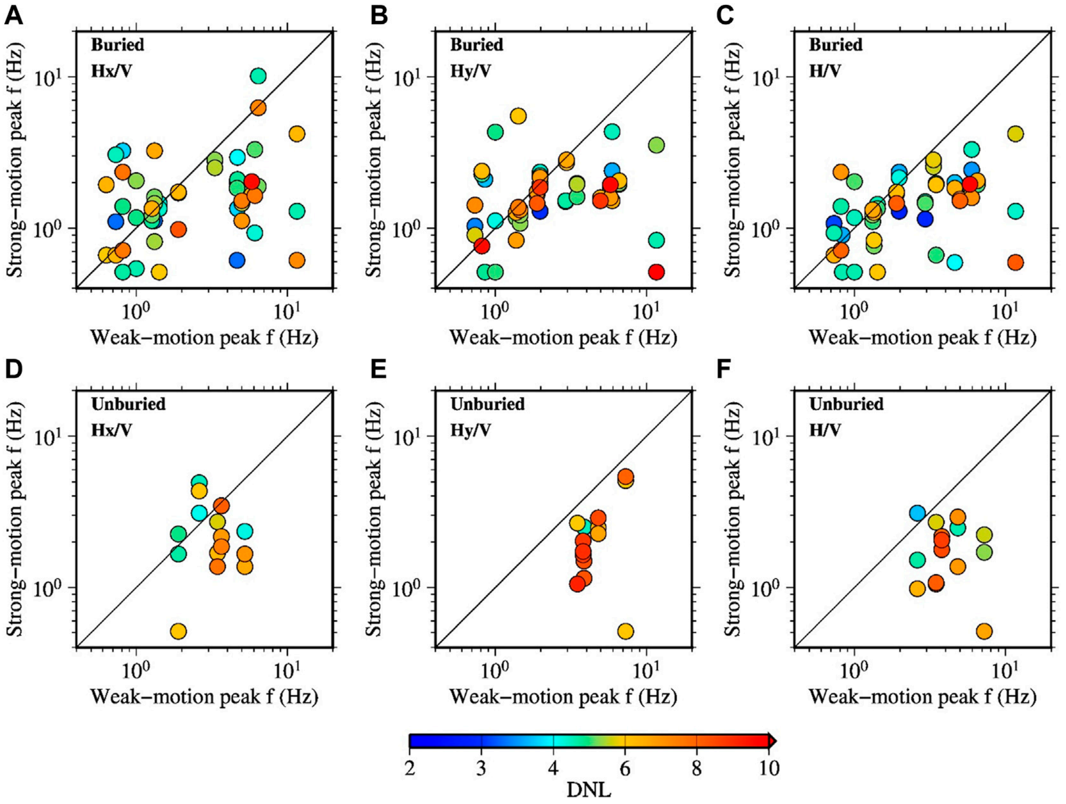

FIGURE 15
Relationships between the peak frequencies of the weak-motion and strong-motion spectral ratios for the recordings obtained at the S-net sites. The upper **(A, B, C)** and lower **(D, E, F)** panels show the plots for the buried and unburied sites, respectivly, for the different definitions of spectral ratios (see the caption of Figure 12 for detail).

identified by site and event codes are shown together with the plots for the S-net sites later (see Figure 16).

The relationships between the DNL and AI values for the SBSR and HVSR methods are shown in Figures 11D,E, respectively. It can be seen that the trends between the DNL and AI values are almost identical to those mentioned above for the DNL and PGAs. This is because the PGAs and AI have a very high correlation, as shown in Figure 11F. The relationships between the DNL and CAV values were also similar to those between the DNL and AI values and are shown in Supplementary Figure S1.

A comparison of the peak frequencies between the weak-motion and strong-motion SBSRs and HVSRs is depicted in Figures 11G, H, respectively. Most of the data points show smaller peak frequencies during the strong motions. A few data points show larger peak frequencies during strong motions compared to the weak-motion peak frequencies. It was found that the difference was simply due to the similar peak ratios at multiple frequencies for the strong motions or the peak frequencies of weak-motion spectral ratios were relatively towards the lower frequencies (e.g., see Figures 9A–C).

4 NLSR at the S-net sites

In this section, the NLSR during the three Mw 7 class earthquakes at the S-net sites are described based on the three types of spectral ratios defined in Equations 6 (HVSR_x), 7 (HVSR_y), and 8 (HVSR_h), respectively. The three types of spectral ratios are referred to simply as Hx/V, Hy/V, and H/V, respectively, for convenience. The number of S-net sites used in the analysis is 23. Therefore, to save space and reduce monotony, example plots of the HVSRs are shown here for only 8 sites, and the plots of the HVSRs at all the remaining sites are provided in the Supplementary Figure S2, S3, S4, S5. The plots of the HVSRs at the S2N01, S2N02, S2N03, and S2N04 are shown in Figure 12. Similarly, the plots of the HVSRs at the S2N05, S2N06, S2N09, and S2N10 are shown in Figure 13. For each site, the HVSRs based on the three equations (Equations 6, 7, and 8) are shown in three different plots. For example, the plots of the Hx/V, Hy/V, and H/V at the S2N01 site are shown in Figures 12A–C, respectively. The plots follow similarly for the other sites. The PGAs of the horizontal X-component records for the three target earthquakes were between about 50 and 1740 cm/s^2, respectively.

In Figures 12A–C (plots for the S2N01 site), it can be seen that the weak-motion spectral ratios have a dominant peak at frequency of a little over 10 Hz. In contrast, the values of the spectral ratios become noticeably smaller for the strong motions at the dominant frequency of weak-motion spectral ratios. Reduction of amplitude of the spectral ratios at higher frequencies compared with the weak-motions was clearly seen for most of the recordings at all the sites. Also, a shift of the peak

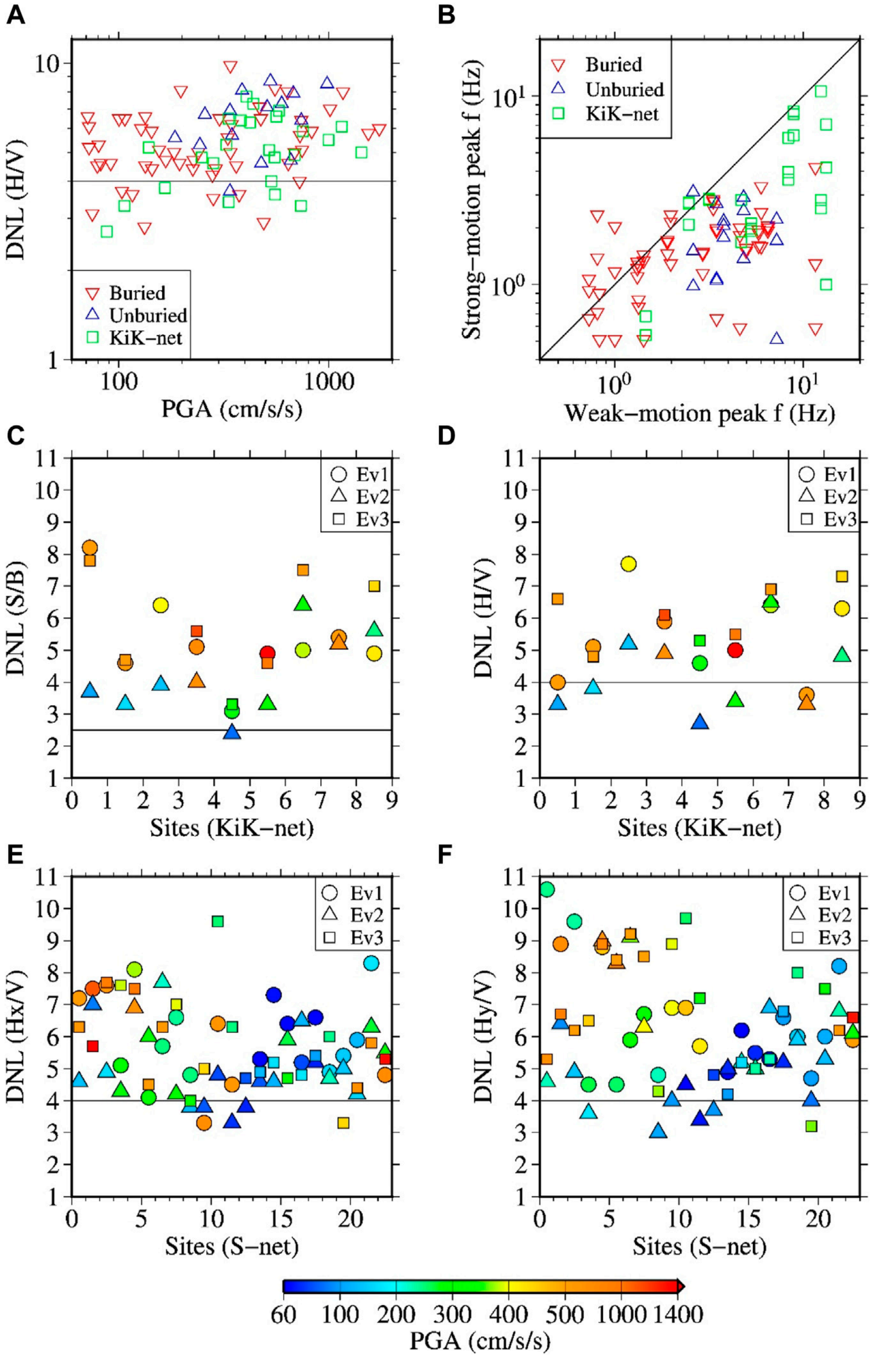

FIGURE 16
Panel **(A)** comparison of the DNL values as a function of the horizontal vector PGAs between the KiK-net and S-net (Buried and Unburied) sites. Panel **(B)** comparison of the peak frequencies of the HVSRs during the weak and strong motions. The HVSRs for the KiK-net and S-net sites were computed identically using Equations 2 and 8, respectively. Panel **(C, D)**: DNL values at the KiK-net sites using the SBSR and HVSR methods, respectively. Panel **(E, F)**: DNL values at the S-net sites using the Hx/V and Hy/V methods, respectively. The tick labels of the X-axes in the panels **(C–F)** indicate the site identification numbers as listed in Tables 2 and 3 for the KiK-net and S-net sites, respectively. The DNL value for a site is plotted 0.5 unit left of its site identification number in the panels **C–F**.

frequency of the spectral ratios was clearly observed for many recordings. This last feature can be seen well in Figure 13. The DNL values for the case of Hx/V ranged between 3.3 and 9.6, while those for the case of Hy/V ranged between 3 and 10.6. The DNL values for the case of H/V were between 2.8 and 9.8.

The plots of DNL values as a function of PGAs for the three definitions of HVSRs are shown in Figures 14A–F for the buried and unburied sites separately. A general trend of increasing DNL values with PGAs can be seen in all the plots for both groups of data. Note that the peak values reported in the HVSR plots and discussed here are from the

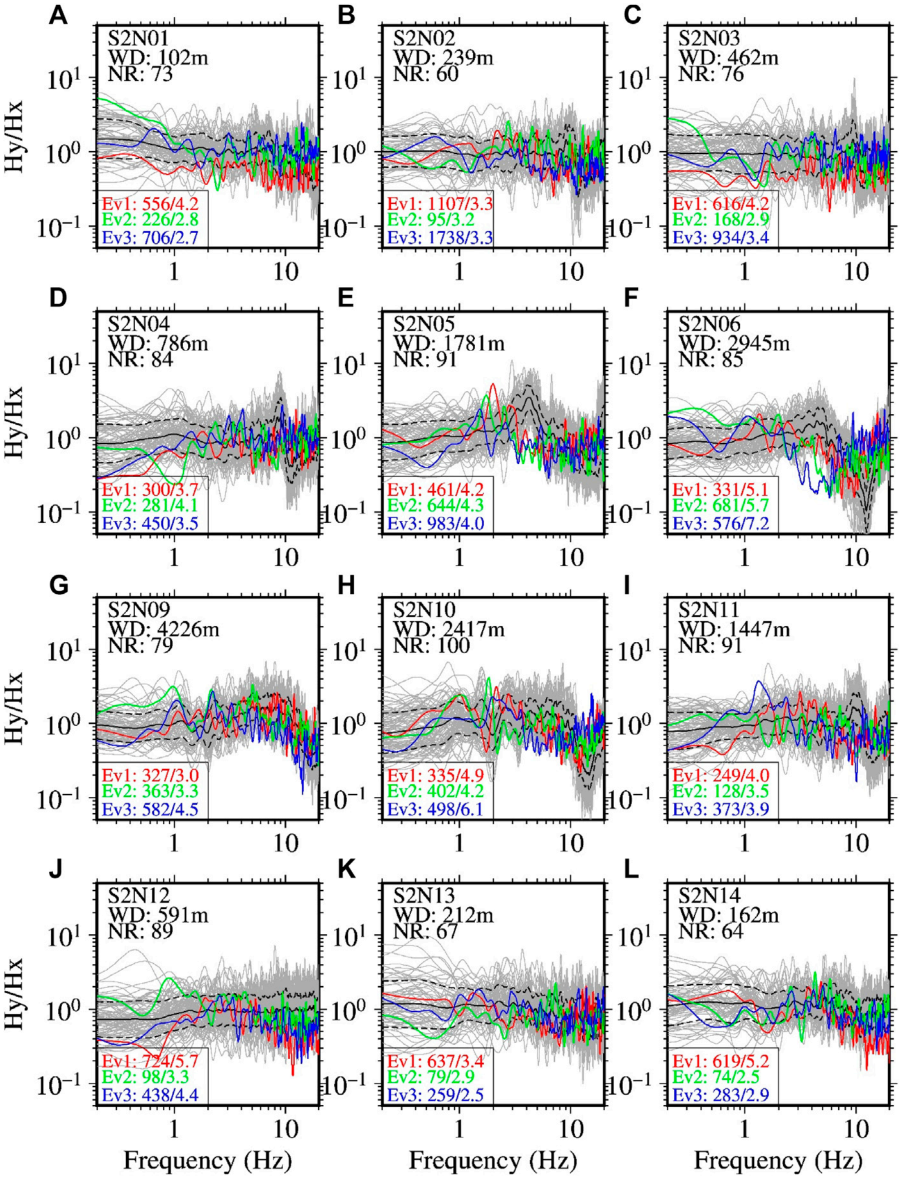

FIGURE 17
Spectral ratios between the horizontal Y- and X-component records at the S-net sites [panels **(A–L)**]. The site codes are indicated in each panel. The two letter codes, WD and NR written beneath the site codes, indicate the water depth and number of weak-motion records at each site. The grey lines denote the spectral ratios for individual earthquake records. The black lines denote the mean spectral ratios, while the dashed lines denote the range of one standard deviation. The red, blue, and green lines denote the spectral ratios for the three target earthquakes, denoted by Ev1, Ev2, and Ev3, respectively (see Table 1 for detail about the earthquakes). The numbers nearby the event codes separated by forward slash (e.g., Ev1: 724/5.7 in panel J) indicate the larger peak acceleration in units of cm/s^2 of two horizontal components and the DRE value for the corresponding earthquake. See Supplementary Figure S8 for similar plots at the other sites.

S-wave window only. A comparison of the DNL values based on the Hx/V and Hy/V spectral ratios is shown in Figures 14G,H, respectively. It was found that the DNL values for the case of Hy/V were somewhat larger than those for the Hx/V case for the recordings that accompanied the larger rotations of the sensors. These features were more obvious for the unburied site conditions. The relationships of the DNL values with AI and CAV are given in Supplementary Figure S6, S7, where results similar to that of the DNL and PGA discussed above can be seen due to the high correlation between the PGAs, AI and CAV values.

A comparison of the peak frequencies between the weak-motion and strong-motion spectral ratios is depicted in Figure 15 for the buried and unburied sites separately. The figure shows that the peak frequencies of the strong-motion spectral ratios are mostly smaller than those of the weak-motion spectral ratios at frequencies over about 3 Hz. The unburied sites have weak-motion peak frequencies of about 2 Hz or higher and the above feature can be seen clearly. At the buried sites, the peak frequencies of the strong-motion spectral ratios are not always smaller than those of the weak-motion spectral

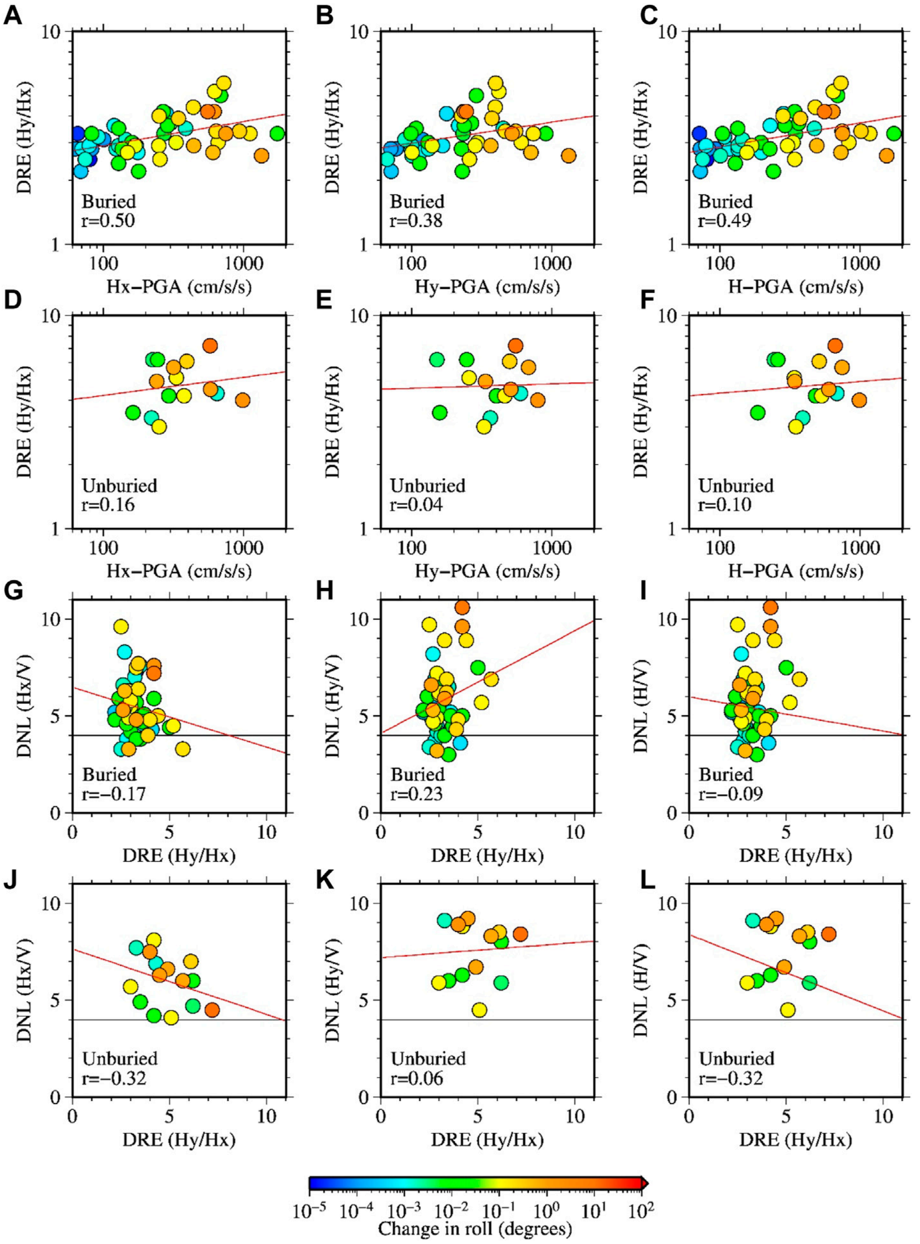

FIGURE 18
Panels **(A–F)** show the relationships between the DRE and PGA values at the buried and unburied sites of S-net as indicated in the plots. The x-axes labels, Hx-PGA, Hy-PGA, and H-PGA mean the peak acceleration of the horizontal X, horizontal Y, and vector of the two horizontal component records, respectively. The red lines denote the regression lines between the corresponding values, and the numerals at the lower-left corners indicate the correlation coefficients. Panels **(G–L)** show the relationships between the DNL and DRE values at the buried and unburied sites as indicated in the plots.

ratios. We found that this is mainly due to the comparable peak values of the spectral ratios at two different frequencies.

5 Discussions

In this section we first discuss the relationships of the DNL values and shift in peak frequencies between the KiK-net and S-net sites. A combined plot of the DNL values for the KiK-net and S-net sites as a function of the PGAs is shown in Figure 16A. Similarly, a combined plot for the KiK-net and S-net sites of the relationship between the peak frequencies of the spectral ratios for the strong- and weak-motions is shown in Figure 16B. It can be seen that the values between the two data sets (KiK-net and S-net) distribute generally similarly except at lower PGAs and lower weak-motion peak frequencies. It is notable that the DNL values are larger than the threshold value of 4 for several recordings at the S-net sites at PGAs lower than about 200 cm/s^2. The DNL values based on the SBSR and HVSR methods at the KiK-net sites for all event-site pairs are shown

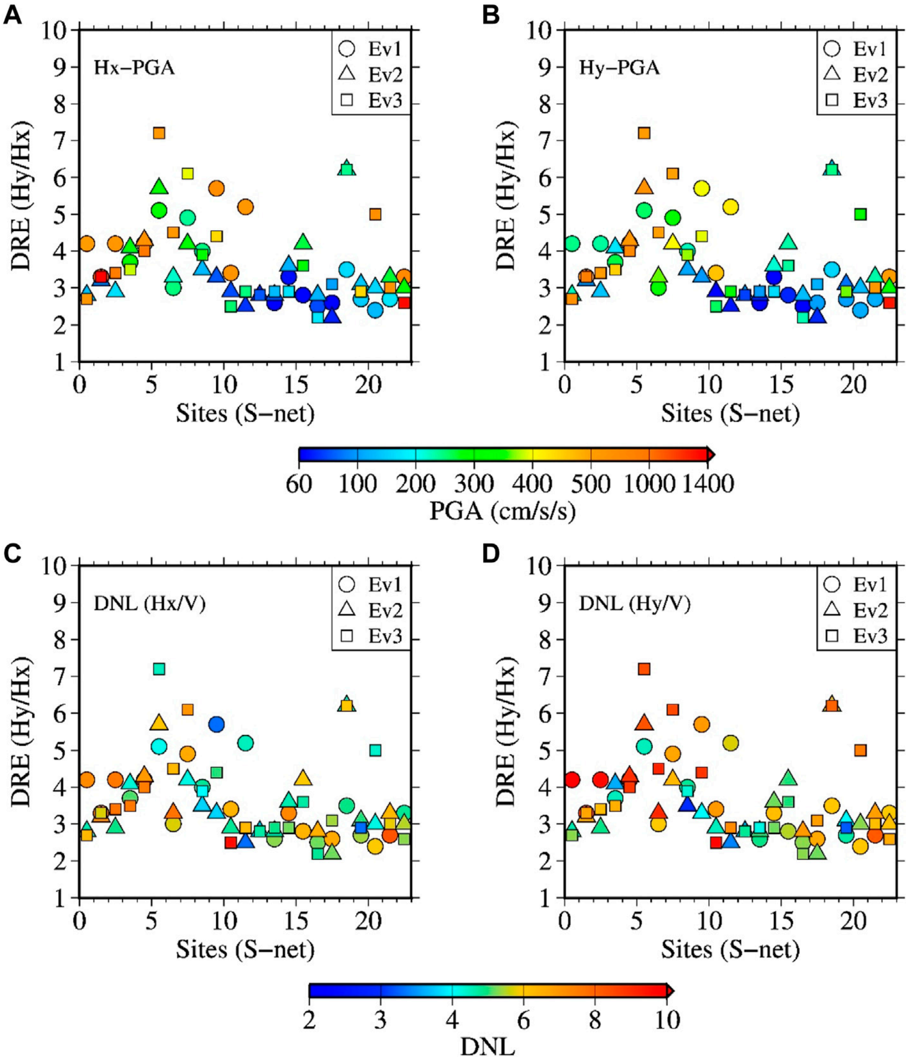

FIGURE 19
Panels **(A)** and **(B)** DRE values with annotations by Hx-PGA and Hy-PGA, respectively, at the S-net sites. The tick labels of the X-axes indicate the site identification numbers as listed in Table 3 for the S-net sites. Panels **(C)** and **(D)** similar to the panels A and B, but with the annotations by DNL values obtained for the Hx/V and Hy/V cases, respectively.

in Figures 16C,D, respectively, while the similar plots for the Hx/V and Hy/V methods at the S-net sites are summarized in Figures 16E,F, respectively. In these plots, it can be clearly noticed the changes in the DNL values with PGAs at the same site.

Even though the measured S-wave velocities are not available for the local soil profiles at the S-net sites, recent studies based on H/V analysis of ambient noise recordings (e.g., Farazi et al., 2023) and seismic interferometric techniques (e.g., Spica et al., 2020; Yamaya et al., 2021; Viens et al., 2023), have revealed the existence of relatively low Vs values in the area around the S-net stations. For example, Farazi et al. (2023) estimated Vs value of about 30 m/s in the top 1.3–1.8 m seabed sediments, and 200–2000 m/s in the next several hundred meters beneath the seafloor, the velocity being increased with depth. Similarly, Viens et al. (2023) suggested a Vs value of about 200 m/s in the shallow layers at some sections of their distributed acoustic sensing profiles. Using the relatively lower amplitude motions than those used in the present study, Viens et al. (2022) reported some signatures of NLSR in the Tohoku offshore region.

A variation of S-wave velocity in the shallow part of the overriding plate beneath the S-net stations was investigated in Tonegawa et al. (2023). The study found a significant reduction of S-wave velocity associated with the large ground motions during Mw six to seven class earthquakes, including the three earthquakes analyzed in the present study. The reduction in S-wave velocity was significant even at longer distances near the Trench axis due to effective trapping of the seismic energy in the upper part of the Pacific Plate. These findings in Tonegawa et al. (2023) support the results shown in the current study, such as the shift in predominant frequencies during strong motions due to reductions of velocity in the shallow sediment layers. The existence of lower Vs values in the shallow layers can produce stronger NLSR during larger input motions. Dhakal et al. (2017) and Kubo et al. (2019), using the same technique as used in the present study, reported that a few offshore sites in the Sagami Trough and Nankai Trough area, respectively, might have experienced NLSR for recordings with PGAs smaller than 100 cm/s^2. All the above discussions and results may suggest that the S-net sites are prone to experience a large degree of NLSR during major earthquakes in the region.

Finally, we discuss that the so-called NLSR presented above for the S-net sites may have been contaminated by the induced rotation of the sensors. We obtained a DNL-like parameter between the weak-motion and strong-motion Hy/Hx spectral ratios for the same set of data used in the computation of the DNL values. The new parameter is called 'degree of rotational effect', abbreviated as DRE for simplicity. The DRE value was also obtained from the same frequency limits, 0.5–20 Hz, as used in the computation of the DNL values. The frequency distribution of the DRE values for the weak motions is shown in Figure 8F. The mean DRE value was found to be 2.85 with standard deviation of 0.47. The DRE values for the target strong-motion records were approximately between 2 and 7. Their relationships with PGAs and DNL values are explained in the next paragraph. The Hy/Hx spectral ratios during the three Mw 7 class earthquakes for the first 12 sites, as listed in Table 3, are compared with the weak-motion Hy/Hx spectral ratios in Figure 17. A similar comparison is shown in Supplementary Figure S8 of the Supplementary File for the remaining 11 sites. The buried stations did not show the typical N-shaped spectral ratios during both weak and strong motions, while three stations out of five unburied stations considered in this study showed the shift in the N-shaped pattern, giving larger DRE values. The three unburied stations are S2N05 (Figure 17E), S2N06 (Figure 17F), and S3N22 (Supplementary Figure S8G). The DRE values at the other two unburied stations were also relatively larger compared with the similar PGA records at buried stations. At a few buried stations such as S2N04 and S2N11 (Figures 17D,I), minor-type N-shaped pattern can be seen around 10 Hz, as mentioned in the Data and Method section. The Hy/Hx spectral ratios for the strong motions were either smooth around the minor-type N-shaped pattern, or they shifted moderately towards lower frequencies. As the computation method for DRE gives larger weights to higher frequencies, relatively larger DRE values were obtained at theses buried sites with the minor-type N-shaped pattern around 10 Hz in comparison to those which did not have the N-shaped spectral ratios.

Plots of the DRE values against the PGAs and DNL values are shown in Figure 18 (A-F) and (G-L), respectively. A moderate positive correlation was found between the DRE and PGA values for the buried sites. The range of PGAs was smaller for the unburied sites compared to that for the buried sites, and hence the trend of DRE values with PGAs was not clearly seen. The DNL values obtained for both Hx/V and Hy/V methods correlated poorly with the DRE values and were inconsistent with the DRE values for the data set considered in this study. The station-wise plots of the DRE values annotated with corresponding PGAs and DNL values are shown in Figures 19A–D, respectively. The DRE values at many sites were larger with higher PGAs at the sites. However, the DRE values at several sites did not show a consistent trend with DNL values based on the Hx/V method, while they were generally larger with larger DNL values based on the Hy/V method. These last results may imply that the NLSR at a site appears to be larger using the Hy/V method without considering the induced rotational effect of the sensors on the recorded Y-component motions.

6 Conclusion

We used the horizontal-to-vertical spectral ratio (HVSR) technique to identify the nonlinear site response (NLSR) at the S-net seafloor observation sites during three Mw 7 class earthquakes. During these earthquakes, large peak ground accelerations were recorded at both onshore and offshore stations. Ramps and significant offsets were seen on some of the acceleration records of S-net with intermittent spikes on accelerations exceeding about 500 cm/s^2.

We used the initial 10 s of the S-wave portions of the records to compute the Fourier spectra for the analysis of HVSRs. This 10 s time window avoided the offsets on the acceleration records. The effect of ramp was minimized by applying low-cut filter at 0.1 Hz. Considering the resonance effect of the S-net sensor houses on the two horizontal components, the HVSRs were computed for each of the horizontal components separately and also for the two horizontal components jointly. Because the qualities of the S-net strong-motion records with high peak accelerations are in doubt due to the issues related with the poor coupling between the sensor houses and the sediments, we first evaluated the NLSR at the KiK-net sites on land, where high quality records were obtained at surface and borehole.

We used the surface-to-borehole spectral ratio (SBSR) and HVSR method to examine the features of NLSR at nine KiK-net sites common to the three events. In these methods, reference spectral ratios are first obtained using weak-motion records for which the site response is mostly linear. Then, the spectral ratios obtained for the records with larger PGAs during the target earthquakes were compared with the weak-motion spectral ratios. We found that the two most common features of the NLSR, the reduction of higher frequency spectral ratios and shift of peak frequencies, were present for most of the recordings at the KiK-net sites analyzed in this study.

By performing the similar analysis of HVSRs at the S-net sites, we found that the S-net sites also experienced various degrees of NLSR during the three earthquakes. The degree of nonlinearity (DNL) values obtained in this study were similar between the KiK-net and S-net sites within the range of comparable peak accelerations with larger data points (between about 300 and 800 cm/s^2). The DNL values increased with the increase of recorded peak accelerations at the both KiK-net and S-net sites on average. The relationship between the weak-motion and strong-motion peak frequencies for the S-net sites were also generally similar to those seen for the KiK-net sites. We found that the reduction of spectral ratios occurred mostly at frequencies higher than about 2 Hz. The shift in peak frequencies were also common for sites with weak-motion peak frequencies higher than 1 Hz. The amplification effect at frequencies lower than about 1 Hz was not so evident associated with the shift in peak frequencies except at few sites.

The DNL values based on the Hy/V spectral ratios were somewhat larger than those based on the Hx/V spectral ratios, and this difference was more evident at the unburied sites. The shift in peak frequencies were also more obvious in the Hy/V spectral ratios. These component-wise differences were most probably related with the different degrees of rotations of the *X* and *Y* axes of the sensors even in the S-wave windows used in this study. An analysis of the Hy/Hx spectral ratios during the strong and weak motions indicated a distinct effect of induced rotations at the unburied stations. To some extent, the radiation pattern and directivity effects may have also caused the discrepancies between the two horizontal components, and hence between the Hx/V and Hy/V spectral ratios. Nonetheless, the general similarities of the results between the KiK-net and S-net sites for the same set of earthquakes suggests that the S-net sites are prone to undergo NLSR widely during major offshore earthquakes due to the presence of relatively softer sediments in the top layers. Analysis of the data from broad magnitude ranges and various source-to-site distances is expected to elucidate further the degrees of NLSR at the S-net sites. Based on the present analysis of Mw 7 class earthquake records at relatively short distances, it is concluded that the analysis of strong ground motions at the S-net sites requires consideration of the NLSR, but considersation of the effects of induced rotations of the sensors is necessary to understand the NLSR at the S-net sites better.

Data availability statement

The K-NET and KiK-net strong-motion records and the Vs30 values at the KiK-net sites used in this study were obtained from the website http://www.kyoshin.bosai.go.jp/. The S-net records were obtained from the website https://hinetwww11.bosai.go.jp/auth/download/cont/?LANG=en. The hypocenter information of the events were taken from https://www.data.jma.go.jp/svd/eqev/data/bulletin/hypo_e.html. The moment magnitude for the events were taken from http://www.fnet.bosai.go.jp/event/joho.php?LANG=en. The fault models used to calculate the shortest fault-rupture distance to the sites were obtained from the following websites (in Japanese). Ev1:https://www.kyoshin.bosai.go.jp/kyoshin/topics/FukushimakenOki_20210213/inversion/inv_index.html Ev2:https://www.kyoshin.bosai.go.jp/kyoshin/topics/MiyagikenOki_20210320/inversion/inv_index.html Ev3:https://www.hinet.bosai.go.jp/topics/off-fukushima220316/?LANG=ja&m=source All the above links were last accessed on 2023/03/01.

Author contributions

YD performed analysis of data and drafted the manuscript. TK guided the first author through the data processing and interpretation. All authors contributed to the article and approved the submitted version.

Funding

This study was supported by "Advanced Earthquake and Tsunami Forecasting Technologies Project" of NIED and JSPS KAKENHI Grant Number JP20K05055.

Acknowledgments

We would like to thank the Japan Meteorological Agency for providing us with hypocenter information for the earthquakes used in this study. We would also like to thank Wessel and Smith (1998) for providing us with Generic Mapping Tools, which were used to make some figures in the manuscript. We express our gratitude to Hisahiko Kubo for providing us with the fault plane data, which were used to calculate the shortest fault distances at the observation sites. We are very thankful to the reviewers for providing us with helpful and constructive comments.

Conflict of interest

Publisher's note

Supplementary material

The Supplementary Material for this article can be found online at: https://www.frontiersin.org/articles/10.3389/feart.2023.1180289/full#supplementary-material

References

Aoi, S., Asano, Y., Kunugi, T., Kimura, T., Uehira, K., Takahashi, N., et al. (2020). Mowlas: NIED observation network for earthquake, tsunami and volcano. *Earth Planets Space* 72, 126. doi:10.1186/s40623-020-01250-x

Arias, A. (1970). "A measure of earthquake intensity," in *Seismic design for nuclear power plants*. Editor R. Hansen (Cambridge, Massachusetts: MIT Press), 438–483.

Assimaki, D., Li, W., Steidl, J. H., and Tsuda, K. (2008). Site amplification and attenuation via downhole array seismogram inversion: A comparative study of the 2003 miyagi-oki aftershock sequence. *Bull. Seismol. Soc. Am.* 98, 301–330. doi:10.1785/0120070030

Barnes, C. R., Best, M. M. R., Johnson, F. R., and Pirenne, B. (2015). "NEPTUNE Canada: Installation and initial operation of the world's first regional cabled ocean observatory," in *Seafloor observatories* (Berlin, Heidelberg: Springer Praxis Books). doi:10.1007/978-3-642-11374-1_16

Beresnev, I. A., and Wen, K. L. (1996). Nonlinear soil response - a reality? *Bull. Seismol. Soc. Am.* 86, 1964–1978. doi:10.1785/BSSA0860061964

Bonilla, L. F., Archuleta, R. J., and Lavallée, D. (2005). Hysteretic and dilatant behavior of cohesionless soils and their effects on nonlinear site response: Field data observations and modeling. *Bull. Seismol. Soc. Am.* 95, 2373–2395. doi:10.1785/0120040128

Derras, B., Bard, P. Y., Régnier, J., and Cadet, H. (2020). Non-linear modulation of site response: Sensitivity to various surface ground-motion intensity measures and site-condition proxies using a neural network approach. *Eng. Geol.* 269, 105500. doi:10.1016/j.enggeo.2020.105500

Dhakal, Y. P., and Kunugi, T. (2021). An evaluation of strong-motion parameters at the S-net ocean-bottom seismograph sites near the Kanto basin for earthquake early warning. *Front. Earth Sci.* 9, 699439. doi:10.3389/feart.2021.699439

Dhakal, Y. P., Takai, N., and Sasatani, T. (2010). Empirical analysis of path effects on prediction equations of pseudo-velocity response spectra in northern Japan. *Earthq. Eng. Struct. Dyn.* 39, 443–461. doi:10.1002/eqe.952

Dhakal, Y. P., Shin, A., Kunugi, T., Suzuki, W., and Kimura, T. (2017). Assessment of nonlinear site response at Ocean bottom seismograph sites based on S-wave horizontal-to-vertical spectral ratios: A study at the Sagami bay area K-net sites in Japan. *Earth, Planets Space* 69, 29. doi:10.1186/s40623-017-0615-5

Dhakal, Y. P., Kunugi, T., Kimura, T., Suzuki, W., and Aoi, S. (2019). Peak ground motions and characteristics of nonlinear site response during the 2018 Mw 6.6 Hokkaido eastern Iburi earthquake. *Earth, Planets Space* 71, 56. doi:10.1186/s40623-019-1038-2

Dhakal, Y. P., Kunugi, T., Suzuki, W., Kimura, T., Morikawa, N., and Aoi, S. (2021). Strong motions on land and Ocean bottom: Comparison of horizontal PGA, PGV, and 5% damped acceleration response spectra in northeastnortheast Japan and the Japan Trench area. *Bull. Seism. Soc. Am.* 111, 3237–3260. doi:10.1785/0120200368

Dhakal, Y. P., Kunugi, T., Yamanaka, H., Wakai, A., Aoi, S., and Nishizawa, A. (2023). Estimation of source, path, and site factors of S waves recorded at the S-net sites in the Japan Trench area using the spectral inversion technique. *Earth, Planets Space* 75, 1. doi:10.1186/s40623-022-01756-6

Farazi, A. H., Ito, Y., Garcia, E. S. M., Lontsi, A. M., Sánchez-Sesma, F. J., Jaramillo, A., et al. (2023). Shear wave velocity structure at the Fukushima forearc region based on H/V analysis of ambient noise recordings by ocean bottom seismometers. *Geophys. J. Int.* 233 (3), 1801–1820. doi:10.1093/gji/ggad028

Hardin, B. O., and Drnevich, V. P. (1978). Shear modulus and damping in soils: Design equations and curves. *J. soil Mech. Found. Div.* 98 (SM7), 667–692. doi:10.1061/jsfeaq.0001760

Hayashimoto, N., Nakamura, T., and Hoshiba, M. (2014). "The characteristics of unusual OBS data exposed to strong shaking and the influence of applying these data to EEW processing: Examples of off-kushiro OBS, JAMSTEC," in *AGU fall meeting*, S33C–S4543.

Hayashimoto, N., Nakamura, T., and Hoshiba, M. (2019). A technique for estimating the UD-component displacement magnitude for earthquake early warnings that can be applied to various seismic networks including ocean bottom seismographs. *Q. J. Seismol.* 83, 1–10. (in Japanese with English abstract).

Hirose, F. (2022). *Plate configuration*. Available from: https://www.mri-jma.go.jp/Dep/sei/fhirose/plate/en.index.html (Accessed May 10, 2022).

Hsiao, N. C., Lin, T. W., Hsu, S. K., Kuo, K. W., Shin, T. C., and Leu, P. L. (2014). Improvement of earthquake locations with the marine cable hosted observatory (MACHO) offshore NE taiwan. *Mar. Geophys Res.* 35, 327–336. doi:10.1007/s11001-013-9207-3

Hu, J., Tan, J., and Zhao, J. X. (2020). New GMPEs for the Sagami Bay Region in Japan for moderate magnitude events with emphasis on differences on site amplifications at the seafloor and land seismic stations of K-NET. *Bull. Seism. Soc. Am.* 110, 2577–2597. doi:10.1785/0120190305

Idriss, I. M., and Seed, H. B. (1968). Seismic response of horizontal soil layers. *J. soil Mech. Found. Div.* 94 (SM4), 1003–1031. doi:10.1061/jsfeaq.0001163

Ji, K., Wen, R., Ren, Y., and Dhakal, Y. P. (2020). Nonlinear seismic site response classification using K-means clustering algorithm: Case study of the September 6, 2018 Mw6.6 Hokkaido Iburi-Tobu earthquake, Japan. *Soil Dyn. Earthq. Eng.* 128, 105907. doi:10.1016/j.soildyn.2019.105907

Kaklamanos, J., Baise, L. G., Thompson, E. M., and Dorfmann, L. (2015). Comparison of 1D linear, equivalent-linear, and nonlinear site response models at six KiK-net validation sites. *Soil Dyn. Earthq. Eng.* 69, 207–219. doi:10.1016/j.soildyn.2014.10.016

Kanazawa, T., Uehira, K., Mochizuki, M., Shinbo, T., Fujimoto, H., Noguchi, S., et al. (2016). S-net project, cabled observation network for earthquakes and tsunamis. *SubOptic* 2016, WE2B–3.

Kanno, T., Narita, A., Morikawa, N., Fujiwara, H., and Fukushima, Y. (2006). A new attenuation relation for strong ground motion in Japan based on recorded data. *Bull. Seism. Soc. Am.* 96, 879–897. doi:10.1785/0120050138

Kubo, H., Nakamura, T., Suzuki, W., Kimura, T., Kunugi, T., Takahashi, N., et al. (2018). Site amplification characteristics at Nankai seafloor observation network, DONET1, Japan, evaluated using spectral inversion. *Bull. Seismol. Soc. Am.* 108, 1210–1218. doi:10.1785/0120170254

Kubo, H., Nakamura, T., Suzuki, W., Dhakal, Y. P., Kimura, T., Kunugi, T., et al. (2019). Ground-motion characteristics and nonlinear soil response observed by DONET1 seafloor observation network during the 2016 southeast off-Mie, Japan, earthquake. *Bull. Seism. Soc. Am.* 109, 976–986. doi:10.1785/0120170296

Morikawa, N., and Fujiwara, H. (2013). A new ground motion prediction equation for Japan applicable up to M9 mega-earthquake. *J. Disast. Res.* 8, 878–888. doi:10.20965/jdr.2013.p0878

Nakamura, T., and Hayashimoto, N. (2019). Rotation motions of cabled ocean-bottom seismic stations during the 2011 Tohoku earthquake and their effects on magnitude estimation for early warnings. *Geophys. J. Int.* 216, 1413–1427. doi:10.1093/gji/ggy502

Nakamura, T., Takenaka, H., Okamoto, T., Ohori, M., and Tsuboi, S. (2015). Long-Period ocean-bottom motions in the source areas of large subduction earthquakes. *Sci. Rep.* 5, 16648. doi:10.1038/srep16648

NIED (2019a). *NIED S-net*. Tsukuba: National Research Institute for Earth Science and Disaster Resilience. doi:10.17598/NIED.0007

NIED (2019b). *NIED K-net, KiK-net*. Tsukuba: National Research Institute for Earth Science and Disaster Resilience. doi:10.17598/NIED.0004

Noguchi, S., and Sasatani, T. (2008). "Quantification of degree of nonlinear site response," in *Proceedings of the 14th world conf. On earthq. Engg.* (Beijing, China. Paper ID: 03-03-0049.

Noguchi, S., and Sasatani, T. (2011). Nonlinear soil response and its effects on strong ground motions during the 2003 Miyagi-Oki intraslab earthquake. *Zisin* 63, 165–187. (in Japanese with English abstract). doi:10.4294/zisin.63.165

Noguchi, S., Maeda, T., and Furumura, T. (2016a). Ocean-influenced Rayleigh waves from outer-rise earthquakes and their effects on durations of long-period ground motion. *Geophys. J. Int.* 205, 1099–1107. doi:10.1093/gji/ggw074

Noguchi, S., Sato, H., and Sasatani, T. (2016b). Evaluation of nonlinear soil response during the 2011 off the pacific coast of Tohoku earthquake by means of a simple Index of soil nonlinearity. *J. Jpn. Assoc. Earthq. Eng.* 16 (4), 93–94. (in Japanese with English abstract). doi:10.5610/jaee.16.4_93

Okada, Y., Kasahara, K., Hori, S., Obara, K., Sekiguchi, S., Fujiwara, H., et al. (2004). Recent progress of seismic observation networks in Japan —hi-net, F-net, K-net and KiK-net. *Earth Planets Space* 56, xv–xxviii. doi:10.1186/bf03353076

Rabiner, L. R., and Schafer, R. W. (1978). *Digital processing of speech signals*. Englewood Cliffs, NJ: Prentice-Hall, 528.

Reed, J. W., Anderson, N., Chokshi, N. C., Kennedy, R. P., Metevia, W. J., Ostrom, D. K., et al. (1988). A criterion for determining exceedance of the operating basis earthquake: Final report. *EPRI-NP* 5930, 301.

Régnier, J., Cadet, H., Bonilla, L. F., Bertrand, E., and Semblat, J. F. (2013). Assessing nonlinear behavior of soils in seismic site response: Statistical analysis on KiK-net strong-motion data. *Bull. Seismol. Soc. Am.* 103, 1750–1770. doi:10.1785/0120120240

Régnier, J., Bonilla, L. F., Bard, P. V., Bertrand, E., Hollender, F., Kawase, H., et al. (2016). International benchmark on numerical simulations for 1D, nonlinear site response (PRENOLIN): Verification phase based on canonical cases. *Bull. Seismol. Soc. Am.* 106, 2112–2135. doi:10.1785/0120150284

Ren, Y., Wen, R., Yao, X., and Ji, K. (2017). Five parameters for the evaluation of the soil nonlinearity during the Ms8.0 Wenchuan Earthquake using the HVSR method. *Earth, Planets Space* 69, 116. doi:10.1186/s40623-017-0702-7

Romanowicz, B., McGill, P., Neuhauser, D., and Dolenc, D. (2009). Acquiring real time data from the broadband ocean bottom seismic observatory at Monterey Bay (MOBB). *Seismol. Res. Lett.* 80 (2), 197–202. doi:10.1785/gssrl.80.2.197

Sato, K., Kokusho, T., Matsumoto, M., and Yamada, E. (1996). Nonlinear seismic response and soil property during strong motion. *Soils Found.* 36, 41–52. doi:10.3208/sandf.36.Special_41

Satoh, T., Sato, T., and Kawase, H. (1995). Nonlinear behavior of soil sediments identified by using borehole records observed at the Ashigra Valley, Japan. *Bull. Seismol. Soc. Am.* 85, 1821–1834. doi:10.1785/bssa0850061821

Sawazaki, K., and Nakamura, T. (2020). N"-shaped Y/X coda spectral ratio observed for in-line-type OBS networks; S-net and ETMC: Interpretation based on natural vibration of pressure vessel. *Earth Planets Space* 72, 130. doi:10.1186/s40623-020-01255-6

Sawazaki, K., Sato, H., Nakahara, H., and Nishimura, T. (2006). Temporal change in site response caused by earthquake strong motion as revealed from coda spectral ratio measurement. *Geophys. Res. Lett.* 33, L21303. doi:10.1029/2006GL027938

Si, H., and Midorikawa, S. (1999). New attenuation relations for peak ground acceleration and velocity considering effects of fault type and site condition. *J. Struct. Constr. Eng. Trans. AIJ* 523, 63–70. (in Japanese with English abstract). doi:10.3130/aijs.64.63_2

Si, H., and Midorikawa, S. (2000). "New attenuation relations for peak ground acceleration and velocity considering effects of fault type and site condition," in Proceedings of the 12th World Conference on Earthquake Engineering, Auckland, New Zealand, January-February 2000. paper no. 0532.

Spica, Z. J., Nishida, K., Akuhara, T., Petrelis, F., Shinohara, M., and Yamada, T. (2020). Marine sediment characterized by ocean-bottom fiber-optic seismology. *Geophys. Res. Lett.* 47, e2020GL088360. doi:10.1029/2020GL088360

Takagi, R., Uchida, N., Nakayama, T., Azuma, R., Ishigami, A., Okada, T., et al. (2019). Estimation of the orientations of the S-net cabled ocean-bottom sensors. *Seismol. Res. Lett.* 90, 2175–2187. doi:10.1785/0220190093

Takemura, S., Kubo, H., Tonegawa, T., Saito, T., and Shiomi, K. (2019). Modeling of long-period ground motions in the Nankai subduction zone: Model simulation using the accretionary prism derived from oceanfloor local S-wave velocity structures. *Pure Appl. Geophys.* 176, 627–647. doi:10.1007/s00024-018-2013-8

Tonegawa, T., Takagi, R., Sawazaki, K., and Shiomi, K. (2023). Short-term and long-term variations in seismic velocity at shallow depths of the overriding plate west of the Japan Trench. *J. Geophys. Res. Solid. Earth)* 128, e2022JB025262. doi:10.1029/2022JB025262

Viens, L., Bonilla, L. F., Spica, Z. J., Nishida, K., Yamada, T., and Shinohara, M. (2022). Nonlinear earthquake response of marine sediments with distributed acoustic sensing. *Geophys. Res. Lett.* 49, e2022GL100122. doi:10.1029/2022GL100122

Viens, L., Perton, M., Spica, Z. C., Nishida, K., Yamada, T., and Shinohara, M. (2023). Understanding surface wave modal content for high-resolution imaging of submarine sediments with distributed acoustic sensing. *Geophys. J. Int.* 232 (3), 1668–1683. doi:10.1093/gji/ggac420

Wen, K. L., Beresnev, I. A., and Yeh, Y. T. (1994). Nonlinear soil amplification inferred from downhole strong seismic motion data. *Geophys. Res. Lett.* 21 (24), 2625–2628. doi:10.1029/94GL02407

Wen, K. L., Chang, T. M., Lin, C. M., and Chiang, H. J. (2006). Identification of nonlinear site response using the H/V spectral ratio method. *Terr. Atmos. Ocean. Sci.* 17 (3), 533–546. doi:10.3319/tao.2006.17.3.533(t)

Wen, K. L., Huang, J. Y., Chen, C. T., and Cheng, Y. W. (2011). "Nonlinear site response of the 2010 Darfield, New Zealand earthquake sequence," in *Fourth intl. Symp. On the effects of surface Geology on seismic motion* (Santa Barbara: University of California), 1–8.

Wessel, P., and Smith, W. H. F. (1998). New, improved version of generic mapping tools released. *Eos, Trans. AGU* 79, 579. doi:10.1029/98EO00426

Yamaya, L., Mochizuki, K., Akuhara, T., and Nishida, K. (2021). Sedimentary structure derived from multi-mode ambient noise tomography with dense OBS network at the Japan Trench. *J. Geophys. Res. Solid Earth* 126, e2021JB021789. doi:10.1029/2021JB021789

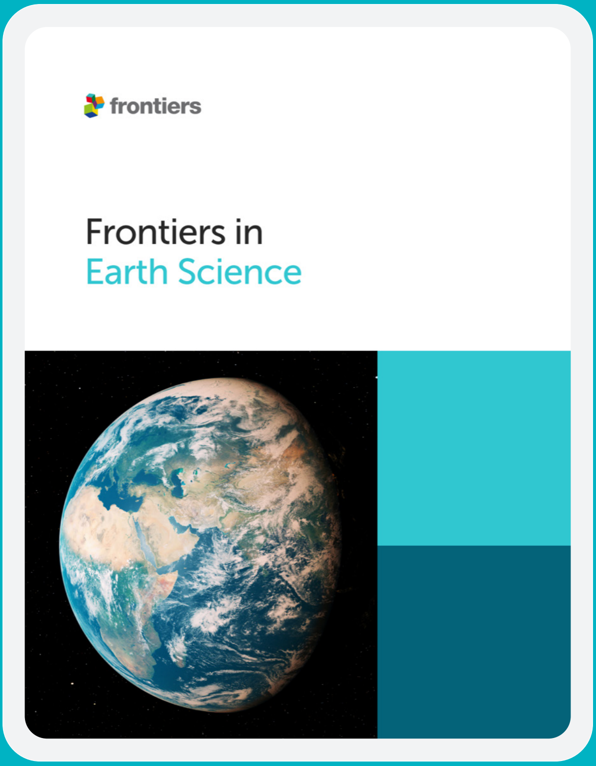

Frontiers

Avenue du Tribunal-Fédéral 34
1005 Lausanne, Switzerland
frontiersin.org

Contact us

+41 (0)21 510 17 00
frontiersin.org/about/contact